



The University of Sydney

**School of Civil Engineering
Sydney NSW 2006
AUSTRALIA**

<http://www.civil.usyd.edu.au/>

Centre for Advanced Structural Engineering

**Numerical Investigation and Design
Methods for Stainless Steel Columns
failing by Interaction of Local and
Overall Buckling**

Research Report No R888

**Jurgen Becque, BASc, MSc
Kim JR Rasmussen, MScEng, PhD**

January 2008

ISSN 1833-2781



The University of Sydney

School of Civil Engineering

Centre for Advanced Structural Engineering

<http://www.civil.usyd.edu.au/>

Numerical Investigation and Design Methods for Stainless Steel Columns failing by Interaction of Local and Overall Buckling

Research Report No R888

Jurgen Becque, BSc, MSc

Kim Rasmussen, MScEng, PhD

January 2008

Abstract:

This report describes research carried out at the University of Sydney to study the interaction of local and overall buckling in stainless steel compression members.

A finite element model was developed taking into account the specific material properties of stainless steel: non-linear stress-strain behaviour, anisotropy and enhanced corner properties as a result of cold-working. The model was verified against experimental data and subsequently used in parametric studies. Simulations were run for lipped channels, plain channels, SHS and I-sections, covering the practical ranges of overall and cross-sectional slenderness values.

The current Australian/North-American and European design guidelines were assessed using the available experimental and numerical data. Finally, a direct strength approach for stainless steel compression members was proposed.

Keywords:

Stainless steel, interaction buckling, local buckling, overall buckling, non-linear material, finite element, cold-formed sections, lipped channels, plain channels, SHS, back-to-back channels, design guidelines, Direct Strength Method.

Copyright Notice

School of Civil Engineering, Research Report R888

**Numerical Investigation of the Interaction of Local and Overall Buckling of
Stainless Steel Columns**

© 2008 Jurgen Becque, Kim JR Rasmussen

J.Becque@civil.usyd.edu.au

K.Rasmussen@civil.usyd.edu.au

ISSN 1833-2781

This publication may be redistributed freely in its entirety and in its original form without the consent of the copyright owner.

Use of material contained in this publication in any other published works must be appropriately referenced, and, if necessary, permission sought from the author.

Published by:

School of Civil Engineering
The University of Sydney
Sydney NSW 2006
AUSTRALIA

January 2008

This report and other Research Reports published by the School of Civil Engineering are available on the Internet:

<http://www.civil.usyd.edu.au>

Table of Contents

Table of Contents.....	4
List of Tables	7
List of Figures.....	8
List of Symbols.....	11
1 Introduction and Scope.....	15
2 Numerical Investigation	15
2.1 General	15
2.2 Model Calibration.....	16
2.2.1 Introduction	16
2.2.2 Material Properties	16
2.2.3 Specimen Boundary Conditions.....	23
2.2.4 Imperfections.....	24
2.2.5 Type of Analysis	25
2.2.6 Element Type and Mesh	26
2.2.7 End Section Eccentricity	30
2.2.8 Analysis Results	31
2.2.9 Discussion	37
2.3 Parametric Studies of Lipped Channels	44
2.3.1 Introduction.....	44
2.3.2 Cross-section Design	45
2.3.3 Imperfections.....	47
2.3.4 Material Properties	50
2.3.5 FE Analysis Results.....	51
2.4 Parametric Studies of Plain Channels	52
2.4.1 Introduction	52
2.4.2 Cross-Section Geometry.....	52

2.4.3	Imperfections.....	54
2.4.4	Material Properties	55
2.4.5	FE Analysis Results.....	55
2.5	Parametric Studies of Tubular Sections.....	58
2.5.1	Introduction	58
2.5.2	Verification	59
2.5.2.1	Test Program.....	59
2.5.2.2	FE Model.....	62
2.5.2.3	FE Results	64
2.5.3	Parametric Studies.....	66
2.6	Parametric Studies of Back-to-Back Channels	70
2.6.1	FE Model.....	70
2.6.1.1	Contact	70
2.6.2.2	Convergence and Stabilization	73
2.6.2	Verification	74
2.6.2.1	Introduction	74
2.6.2.2	Material Properties	75
2.6.2.3	Imperfections.....	75
2.6.2.4	Results	79
2.6.3	Parametric Studies	84
2.7	Summary	88
3	Evaluation of Current Design Practices	89
3.1	Introduction	89
3.2	Effective Width Approach	89
3.2.1	General	89
3.2.1.1	AS/NZS 4673	89
3.2.1.2	prEN 1993-1-4.....	91
3.2.2	Lipped Channels.....	93

3.2.2.1	AS/NZS 4673	93
3.2.2.2	prEN 1993-1-4.....	95
3.2.3	Plain Channels.....	97
3.2.3.1	AS/NZS 4673	97
3.2.3.2	prEN 1993-1-4.....	98
3.2.4	Hollow Sections	98
3.2.4.1	AS/NZS 4673	98
3.2.4.2	prEN 1993-1-4.....	99
3.2.5	I-Sections.....	99
3.2.5.1	AS/NZS 4673	99
3.2.5.2	prEN 1993-1-4.....	99
3.2.6	Reliability Analysis	100
3.2.7	Conclusions	103
3.3	Direct Strength Approach.....	104
3.3.1	Current Formulation for Carbon Steel Columns	104
3.3.2	Proposed DSM for Stainless Steel Columns based on the AS/NZS 4673 Direct Column Strength Equations.....	106
3.3.3	Proposed DSM for Stainless Steel Columns based on the AS/NZS 4673 Tangent Equation for Column Strength.....	111
3.3.4	Proposed DSM for Stainless Steel Columns based on the Eurocode.....	114
4	Conclusions	117
	References	119
	Appendix A.....	123
	Appendix B.....	126
	Appendix C.....	199
	Appendix D	247
	Appendix E.....	287

List of Tables

Table 2.1. Anisotropy Coefficients	21
Table 2.2. Influence of the Mesh Size	27
Table 2.3. 3Cr12 Series: Concentric Tests	34
Table 2.4. 304 Series: Concentric Tests	35
Table 2.5. 430 Series: Concentric Tests	36
Table 2.6. FE Results for L/1500 Eccentricity	44
Table 2.7. Specimen Dimensions (Lipped Channels).....	46
Table 2.8. Specimen Dimensions (Plain Channels).....	53
Table 2.9. Summary: FE modeling of (Rasmussen and Hancock 1993).....	61
Table 2.10. Compressive Material Properties (Rasmussen and Hancock 1993)	62
Table 2.11. Specimen Dimensions (SHS).....	66
Table 2.12. Anisotropy Coefficients	75
Table 2.13. I-Sections: 304 Series	76
Table 2.14. I-Sections: 404 Series	77
Table 2.15. Specimen Dimensions (I-Sections).....	85
Table 3.1. Values of α , β , λ_o and λ_1 (AS/NZS 4673; 2004)	91
Table 3.2. Reliability Analysis: Lipped Channels	101
Table 3.3. Reliability Analysis: Plain Channels	101
Table 3.4. Reliability Analysis: Hollow Sections	102
Table 3.5. Reliability Analysis: I-Sections	102
Table 3.6. Reliability Analysis: All Sections	103
Table 3.7. DSM for Carbon Steel: Reliability Analysis.....	106
Table 3.8. DSM for Particular Cross-Sections	111
Table 3.9. Tangent Approach based DSM for Particular Cross-Sections	114
Table 3.10. DSM for EC3 for Particular Cross-Sections.....	116

List of Figures

Figure 2.1. Longitudinal compressive (engineering) stress-strain curves.	17
Figure 2.2. Corner Properties	18
Figure 2.3. Orientation of the Local Coordinate System.....	22
Figure 2.4. Local Coordinate Systems.....	23
Figure 2.5. Specimen End Conditions.....	24
Figure 2.6. Specimen Imperfections.....	25
Figure 2.7. Effect of the Mesh Size on Peak Load and CPU Time	28
Figure 2.8. Load-Displacement Behaviour	29
Figure 2.9. Effect of Reduced Integration	30
Figure 2.10. 3Cr12: Comparison between Test Results and FE Results	32
Figure 2.11. 304: Comparison between Test Results and FE Results	32
Figure 2.12. 430: Comparison between Test Results and FE Results	33
Figure 2.13a. C3Cr12_920_2: Axial Load vs. Axial Shortening	39
Figure 2.13b. C3Cr12_920_2: Axial Load vs. Lateral Displacement	39
Figure 2.13c. C3Cr12_920_2: Axial Load vs. End Rotations	40
Figure 2.13d. C3Cr12_920_2: Axial Load vs. Local Displacements.....	40
Figure 2.14a. C304_400_1: Post-Peak Buckled Shape	41
Figure 2.14b. C304_636_2: Post-Peak Buckled Shape.....	41
Figure 2.14c. C3Cr12_400_2: Post-Peak Buckled Shape	42
Figure 2.14d. C3Cr12_400_1: Post-Peak Buckled Shape.....	42
Figure 2.15. Deformations under Progressive Loading (Lipped Channel)	43
Figure 2.16. Specimen Dimensions (Lipped Channels).....	46
Figure 2.17. Initial Imperfection.....	48
Figure 2.18 Specimen Dimensions (Plain Channels)	53
Figure 2.19. ThinWall Analysis Output.....	54
Figure 2.20. Initial Imperfection (PC3Cr12_180_1000).....	55

Figure 2.21. Deformations under Progressive Loading (Plain Channel)	56
Figure 2.22. Load vs. Axial Shortening (PC3Cr12_1.80_1000)	57
Figure 2.23. Location of the Compression Coupons	60
Figure 2.24. Compressive Stress-Strain Curves	60
Figure 2.25. Membrane Residual Stresses.....	63
Figure 2.26. Buckled Shape of Specimen S1L3000C	65
Figure 2.27. Initial Imperfections (SHS).....	67
Figure 2.28. Deformations under Progressive Loading (SHS).....	68
Figure 2.29. Load vs. Axial Shortening (SHS304L_0.80_1000)	69
Figure 2.30. Gap Distance along Specimen Length	71
Figure 2.31. Cross-sectional Cut	72
Figure 2.32. Contour Plot of the Gap Distance	72
Figure 2.33. FE Modeling of 304 I-Sections	78
Figure 2.34. FE Modeling of 404 I-Sections	78
Figure 2.35a. I404_500_2: Post-Peak Deformations	80
Figure 2.35b. I304_1500_1:	80
Figure 2.35d. I404_3000_2:	81
Figure 2.37. Specimen Dimensions (I-Sections).....	85
Figure 2.38. Initial Imperfection (I-Section)	86
Figure 2.39. Deformations under Progressive Loading (I-Sections).....	87
Figure 2.40. Available Data	88
Figure 3.1. Comparison of Proposed DSM with Test Results.....	108
Figure 3.2. DSM for Lipped Channels	109
Figure 3.3. DSM for SHS/RHS	109
Figure 3.4. DSM for I-Sections	110
Figure 3.5. Experimental and Numerical Data by Cross-Section Type.....	110
Figure 3.6. Comparison of Tangent Approach Based DSM with Test Results.....	113
Figure 3.7. Tangent Approach Based DSM by Cross-Section Type.....	113

Figure 3.8. Comparison of DSM for EC3 with Test Results	115
Figure 3.9. DSM for EC3 by Cross-Section.....	115
Figure 3.10. DSM (EC3) for Lipped Channels	116

List of Symbols

a	= coefficient in Eq. (48)
A_e	= effective area
A_g	= gross cross-sectional area
b	= overall flange width; coefficient in Eq. (48)
b_{flat}	= flat width of the flange
c	= overall width of the lip; coefficient in Eq. (48)
C_{my}	= moment gradient factor in Eq. (41) (AS/NZS 4673)
COV	= coefficient of variation
d	= overall depth of the section
e_N	= shift in effective centroid
E_0	= initial Young's modulus
E_t	= tangent modulus
f^*	= stress at ultimate member capacity (AS/NZS 4673)
f_{Ed}	= stress at design member capacity (EC3)
f_n	= overall buckling stress (AS/NZS 4673)
F	= coefficient in Hill's anisotropic yield criterion, defined by Eq. (4); ratio of the actual to the nominal cross-sectional dimensions
F_m	= mean value of F
\mathbf{F}_v	= vector containing the viscous damping forces
G	= coefficient in Hill's anisotropic yield criterion, defined by Eq. (5)
H	= coefficient in Hill's anisotropic yield criterion, defined by Eq. (6)
k	= local buckling factor
k_z	= interaction factor defined by Eq. (45) (EC3)
L	= coefficient in Hill's anisotropic yield criterion, defined by Eq. (7); length
L_e	= effective length

- M = coefficient in Hill's anisotropic yield criterion, defined by Eq. (8); ratio of the actual to the nominal material properties
- M_m = mean value of M
- \mathbf{M}^* = mass matrix
- M_{by} = weak axis bending capacity (AS/NZS 4673)
- N = coefficient in Hill's anisotropic yield criterion, defined by Eq. (9)
- N^* = design load (AS/NZS 4673)
- $N_{b,Rd}$ = design buckling resistance (EC3)
- N_c = axial compressive capacity (AS/NZS 4673)
- N_{cr} = elastic local buckling load (EC3)
- N_e = Euler load (AS/NZS 4673)
- N_{Ed} = design member capacity (EC3)
- $P_{0.2\%}$ = yield load
- P_{cr} = elastic local buckling load
- P_{ne} = inelastic overall buckling load
- P_{nl} = local-overall interaction buckling capacity
- P_u = ultimate load
- $P_{u,n}$ = ultimate load obtained from experiment or numerical study
- $P_{u,p}$ = predicted ultimate load
- r = radius of gyration
- t = thickness
- R_{11}, R_{22}, R_{33} = ratio of the yield stress in the 1-, 2- or 3-direction to the reference yield stress (Eq. 11)
- R_{12}, R_{23}, R_{13} = ratio of yield stress in shear within the respective plane to the reference yield stress in shear (Eq. 12)
- \mathbf{v} = vector containing the nodal velocities
- v_o = overall imperfection at mid-height
- $v_{o,x}$ = overall imperfection about the x-axis at mid-height

$v_{o,y}$	= overall imperfection about the y-axis at mid-height
V_D	= coefficient of variation of the dead load
V_F	= coefficient of variation of F
V_L	= coefficient of variation of the live load
V_M	= coefficient of variation of M
$W_{e,z}$	= effective section modulus about the weak axis (EC3)
α	= alloy dependent coefficient in Eq. (31)
α_{ny}	= moment amplification factor (AS/NZS 4673)
β	= alloy dependent coefficient in Eq. (31); reliability index
γ_{M0}	= partial safety factor (EC3)
γ_{M1}	= partial safety factor (EC3)
Δt	= time increment
$\Delta \mathbf{u}$	= vector containing an increment in the nodal displacements
ε	= strain; material parameter defined by Eq. (36) (EC3)
ε_t	= true strain
η	= variable defined by Eq. (31)
λ	= slenderness
λ_{limit}	= limit slenderness
λ_l	= slenderness for interaction buckling, defined by Eq. (46)
λ_o	= overall slenderness
λ_p	= plate slenderness
λ_s	= cross-sectional slenderness
μ	= damping coefficient
ρ	= ratio of the effective width to the width
σ	= stress
σ_0	= reference yield stress
$\sigma_{0.01\%}$	= proportionality limit (0.01% proof stress)
$\sigma_{0.2\%}$	= 0.2% proof stress

- $\sigma_{0.2\%,c}$ = 0.2% proof stress of the corner material
 $\sigma_{0,11}, \sigma_{0,22}, \sigma_{0,33}$ = yield stress in the 1-, 2- and 3-direction
 $\sigma_{11}, \sigma_{22}, \sigma_{33}$ = normal stress components in the 1-, 2- and 3-direction
 $\sigma_{11,0.2\%}$ = 0.2% proof stress in the 1-direction
 $\sigma_{22,0.2\%}$ = 0.2% proof stress in the 2-direction
 $\sigma_{D,0.2\%}$ = 0.2% proof stress in the diagonal direction within the 1, 2-plane
 σ_c = compressive residual stress
 σ_{cr} = elastic local buckling stress
 σ_E = elastic overall buckling stress
 σ_t = true stress
 τ_0 = reference yield stress in shear
 $\tau_{0,12}, \tau_{0,13}, \tau_{0,11}$ = yield stress in shear within the respective plane
 $\tau_{12}, \tau_{23}, \tau_{13}$ = shear stress components within the respective plane
 ϕ = variable defined by Eq. (30)/ Eq. (38)
 ϕ_b = resistance factor in bending (AS/NZS)
 ϕ_c = resistance factor in compression (AS/NZS)
 χ = overall buckling coefficient, defined by Eq. (39) (EC3)
 ω_d = amplitude of the local buckling imperfection

1 Introduction and Scope

This report aims to investigate the interaction of local and overall buckling in stainless steel columns.

A finite element (FE) model has been developed for this purpose. Experimental data from (Becque and Rasmussen 2006), (Becque and Rasmussen 2007) and (Rasmussen and Hancock 1993) was used to evaluate the performance of the FE model. Subsequently, parametric studies were carried out to increase the amount of available data.

The current Australian, North-American and European design guidelines for stainless steel were assessed using the experimentally and numerically obtained data.

The data was further used to develop a Direct Strength Method for stainless steel compression members.

2 Numerical Investigation

2.1 General

A detailed FE model has been developed to study the interaction of local and overall buckling in stainless steel columns. In order to obtain a realistic model which recognizes the specific properties of stainless steel, the model includes non-linear stress-strain behaviour, anisotropy and enhanced corner properties.

After calibration against experiments, parametric studies were carried out to generate additional data. Simulations were run for lipped channels, plain channels, SHS and I-sections comprised of back-to-back channels, thus including singly symmetric as well as doubly symmetric cross-sections, and cross-sections composed of doubly supported

plate elements as well as cross-sections including singly supported plate elements. Parametric studies were carried out covering the practical ranges of overall slenderness values and cross-sectional slenderness values. All columns were modeled with pinned end conditions.

ABAQUS/CAE v.6.4 and v.6.5 were used in the numerical simulations. All FE runs were performed on a Dell PWS650 workstation with a 3.06GHz Intel Xeon processor and 2.0GB of internal memory.

2.2 Model Calibration

2.2.1 Introduction

The FE model was first calibrated against the experimental data reported in Becque and Rasmussen (2006), which includes a total of 36 column tests on lipped channels. These columns were tested with pinned end conditions and incorporated three different stainless steel alloys: austenitic AISI304, ferritic AISI430 and ferritic-like 3Cr12.

2.2.2 Material Properties

2.2.2.1 Material Properties of the Flats

The FE model was based on the measured material properties. The material testing program is described in detail in (Becque and Rasmussen 2006). Figure 2.1 shows the compressive stress-strain curves of the flat material of the 304, 3Cr12 and 430 alloys in the rolling direction, which corresponds to the longitudinal axis of the specimens. Static material properties were used as input in the FE model.

ABAQUS requires the input of the material stress-strain curves in the form of true stress σ_t versus true strain ϵ_t . The true stresses and true strains, σ_t and ϵ_t , were calculated from

the engineering stresses and engineering strains, σ and ϵ , as follows:

$$\epsilon_t = \ln(1 + \epsilon) \quad (1)$$

$$\sigma_t = \sigma (1 + \epsilon) \quad (2)$$

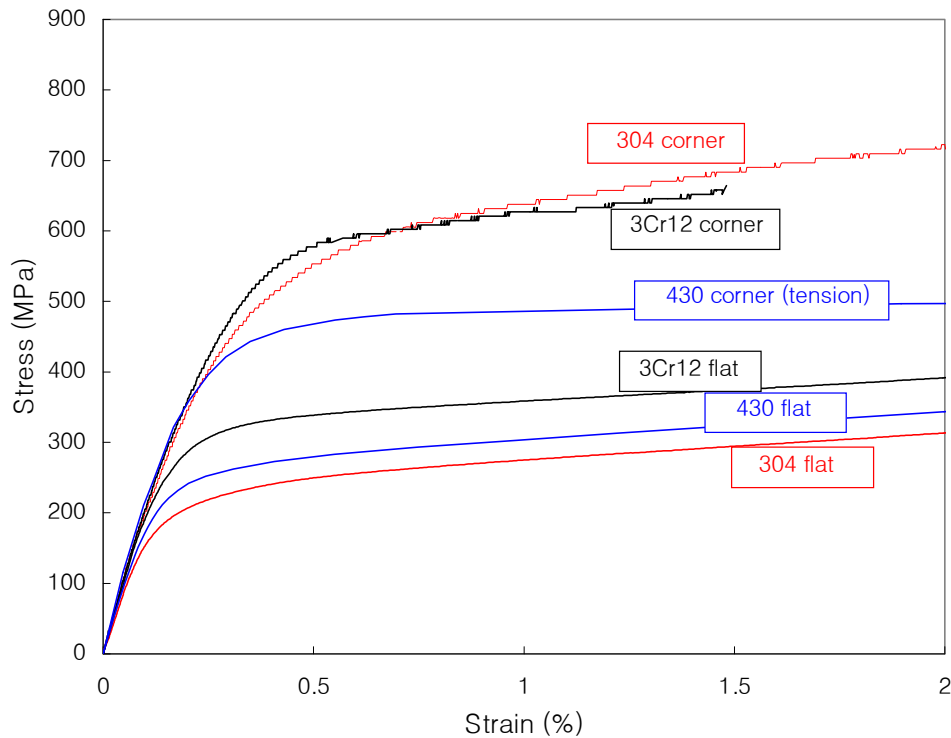


Figure 2.1. Longitudinal compressive (engineering) stress-strain curves.

2.2.2.2 Enhanced Corner Properties

Lecce and Rasmussen (2005) and Becque and Rasmussen (2006) demonstrated that significant strength enhancement can be achieved in the stainless steel alloys under consideration as a result of cold-working. The effect is most pronounced in the austenitic 304 alloy. Figure 2.1 includes the results of compression tests on coupons cut from the corners of the brake-pressed lipped channels. Since compression tests on the

430 corner material proved to be impractical due to its narrow thickness and small corner radius, the results of longitudinal tension tests on corner coupons were substituted for their compressive counterparts and were used instead as FE input.

The stress-strain curves of the enhanced corner materials were input into ABAQUS in the form of true stress versus true strain data points. Static values were used. The increased properties were applied to the rounded corner areas in the way shown in Figure 2.2.

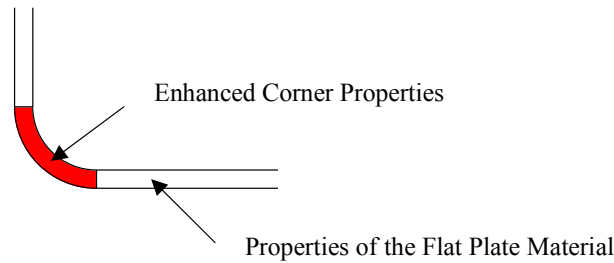


Figure 2.2. Corner Properties

2.2.2.3 Anisotropy

Anisotropic yielding was accounted for by means of Hill's criterion (1950), which is a built-in feature of ABAQUS. According to Hill's theory, the yield surface is described by the following equation:

$$\sigma_0^2 = F(\sigma_{22} - \sigma_{33})^2 + G(\sigma_{33} - \sigma_{11})^2 + H(\sigma_{11} - \sigma_{22})^2 + 2L\tau_{23}^2 + 2M\tau_{13}^2 + 2N\tau_{12}^2 \quad (3)$$

where the coefficients F , G , H , L , M and N are given by:

$$F = \frac{\sigma_0^2}{2} \left(\frac{1}{\sigma_{0,22}^2} + \frac{1}{\sigma_{0,33}^2} - \frac{1}{\sigma_{0,11}^2} \right) = \frac{1}{2} \left(\frac{1}{R_{22}^2} + \frac{1}{R_{33}^2} - \frac{1}{R_{11}^2} \right) \quad (4)$$

$$G = \frac{\sigma_0^2}{2} \left(\frac{1}{\sigma_{0,33}^2} + \frac{1}{\sigma_{0,11}^2} - \frac{1}{\sigma_{0,22}^2} \right) = \frac{1}{2} \left(\frac{1}{R_{33}^2} + \frac{1}{R_{11}^2} - \frac{1}{R_{22}^2} \right) \quad (5)$$

$$H = \frac{\sigma_0^2}{2} \left(\frac{1}{\sigma_{0,11}^2} + \frac{1}{\sigma_{0,22}^2} - \frac{1}{\sigma_{0,33}^2} \right) = \frac{1}{2} \left(\frac{1}{R_{11}^2} + \frac{1}{R_{22}^2} - \frac{1}{R_{33}^2} \right) \quad (6)$$

$$L = \frac{3}{2} \left(\frac{\tau_0^2}{\tau_{0,23}^2} \right) = \frac{3}{2} \left(\frac{1}{R_{23}^2} \right) \quad (7)$$

$$M = \frac{3}{2} \left(\frac{\tau_0^2}{\tau_{0,13}^2} \right) = \frac{3}{2} \left(\frac{1}{R_{13}^2} \right) \quad (8)$$

$$N = \frac{3}{2} \left(\frac{\tau_0^2}{\tau_{0,12}^2} \right) = \frac{3}{2} \left(\frac{1}{R_{12}^2} \right) \quad (9)$$

σ_0 is the reference yield stress and τ_0 is the reference shear yield stress, with:

$$\tau_0 = \sigma_0 / \sqrt{3} \quad (10)$$

The R-coefficients are defined as follows:

$$\begin{aligned} R_{11} &= \frac{\sigma_{0,11}}{\sigma_0} & R_{22} &= \frac{\sigma_{0,22}}{\sigma_0} & R_{33} &= \frac{\sigma_{0,33}}{\sigma_0} \\ R_{12} &= \frac{\tau_{0,12}}{\tau_0} & R_{13} &= \frac{\tau_{0,13}}{\tau_0} & R_{23} &= \frac{\tau_{0,23}}{\tau_0} \end{aligned} \quad (11)$$

In Eqs. (3)-(9), the 1-, 2- and 3-directions align with the principal axes of anisotropy. In what follows the 1-axis is chosen to coincide with the rolling direction of the plate, the 2-axis corresponds with the transverse plate direction and the 3-axis lies along the

normal to the plate.

Hill's yield surface was combined with an isotropic hardening rule, meaning that the surface will expand relative to the origin of the principal stress space, while retaining its shape as strain hardening occurs.

ABAQUS requires the user to input the 6 R-coefficients. R_{11} and R_{22} can directly be determined from the compression test results in the rolling direction and the transverse direction. When choosing the 0.2% proof stress in the rolling direction, $\sigma_{11,0.2\%}$, as the reference stress σ_0 :

$$R_{11} = 1 \quad R_{22} = \frac{\sigma_{22,0.2\%}}{\sigma_{11,0.2\%}}, \quad (12)$$

where $\sigma_{22,0.2\%}$ is the 0.2% proof stress in the transverse plate direction.

When performing a compression coupon test under an angle α with the rolling direction, the non-zero stress components are given by:

$$\sigma_{11} = \sigma \cos^2 \alpha \quad \sigma_{22} = \sigma \sin^2 \alpha \quad \sigma_{12} = \sigma \sin \alpha \cos \alpha, \quad (13)$$

where σ is the applied compressive stress. When choosing α as 45 degrees, the 0.2% proof stress in the diagonal direction $\sigma_{D,0.2\%}$ is reached when:

$$\sigma_{11} = \sigma_{22} = \sigma_{12} = \sigma_{D,0.2\%} / 2 \quad (14)$$

Substituting the stresses (14) into Eq. (3) yields:

$$4 \frac{\sigma_{11,0.2\%}}{\sigma_{D,0.2\%}} = F + G + 2N \quad (15)$$

Subsequently substituting Eqs. (4), (5) and (9) into Eq. (15) results in:

$$4 \frac{\sigma_{11,0.2\%}}{\sigma_{D,0.2\%}} = \frac{1}{R_{33}^2} + \frac{3}{R_{12}^2} \quad (16)$$

Eq. (16) establishes a relationship between R_{33} and R_{12} . Carrying out a coupon test under a different angle α will result in linearly dependent equations and an in-plane

shear test is necessary to determine R_{33} and R_{12} individually. Seen the technical difficulty of performing a shear test, it is instead assumed that:

$$\tau_{12,0.2\%} = \frac{\sigma_{D,0.2\%}}{\sqrt{3}}, \quad (17)$$

where $\tau_{12,0.2\%}$ is the in-plane 0.2% proof stress in shear. Through Eqs. (10) and (11), this eventually results in:

$$R_{33} = R_{12} = \frac{\sigma_{D,0.2\%}}{\sigma_{11,0.2\%}} \quad (18)$$

It was further assumed that in the thickness direction:

$$R_{13} = R_{23} = 1 \quad (19)$$

Hill's anisotropic yield criterion is available in ABAQUS through use of the *POTENTIAL keyword, which is listed under the *PLASTIC option.

Based on the experimental data available in Becque and Rasmussen (2006), the R-coefficients of the stainless steel alloys under consideration were calculated. They are listed in Table 2.1.

Table 2.1. Anisotropy Coefficients

Material	R_{11}	R_{22}	R_{33}	R_{12}	R_{13}	R_{23}
3Cr12	1.00	1.15	1.10	1.10	1.00	1.00
304	1.00	1.05	1.02	1.02	1.00	1.00
430	1.00	1.12	1.10	1.10	1.00	1.00

2.2.2.4 Material Orientation

ABAQUS aligns the principal axes of material anisotropy with the local 1, 2 and 3 axes of the plate element. It is therefore important to ensure that the local coordinate systems have the right orientation. If needed, the orientation of the local coordinate system can be altered using the *ORIENTATION command. By default ABAQUS relates the local coordinate system of a plate element to the global coordinate system by upholding the

following convention (ABAQUS Manual 2005):

“The local 1-direction is the projection of the global 1-axis onto the surface. If the global 1-axis is within 0.1° of being normal to the surface, the local 1-direction is the projection of the global 2-axis onto the surface. The local 2-direction is then at right angles to the local 1-direction, so that the local 1-direction, local 2-direction and the normal to the surface form a right-handed set (See Figure 2.3).”

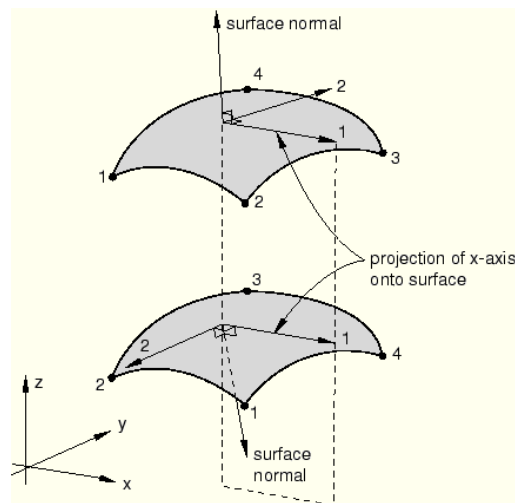


Figure 2.3. Orientation of the Local Coordinate System

When aligning the longitudinal axis of a lipped channel with the global 1-direction, the local coordinate systems on each surface have the default orientations displayed in Figure 2.4, which can be directly accepted. However, when creating a model through extrusion of a cross-section, by default the global 2-axis is the axis of extrusion and the model needs to be rotated over 90 degrees about the 3-axis to obtain the configuration displayed in Fig. 2.4.

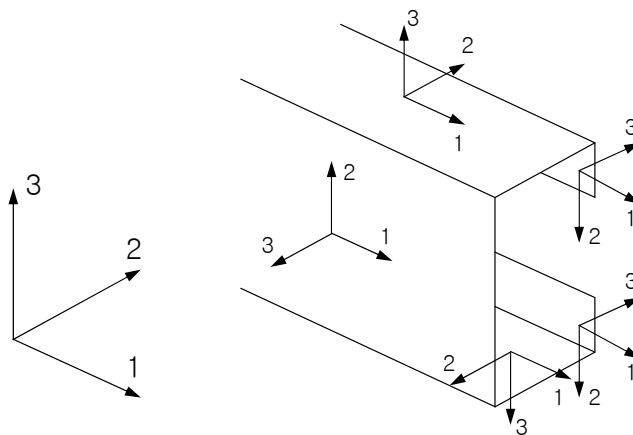


Figure 2.4. Local Coordinate Systems

2.2.3 Specimen Boundary Conditions

The laboratory specimens were tested between pinned ends. The distance between the centerline of the pin and the top plate of the hinge assembly measured 68mm. The hinges were therefore modeled as solid blocks of 68mm depth, which were allowed to rotate about the pin axis, as illustrated in Fig. 2.5. Contact between the specimen and the hinges was modeled by means of a node-to-surface contact pair, where the top surface of the hinges constituted the element-based master surface and the edge of the channel was defined as a node-based slave surface. The normal contact properties were defined as “hard”, meaning that no penetration of the slave nodes into the master surface was allowed. However the slave nodes on the specimen were allowed to separate from the hinge plate and no tensile stresses could develop in the interface. The two surfaces were specified to be precisely in contact with each other at the start of the analysis. The tangential properties were set to “rough”, indicating that infinite friction restrained any tangential slip between the specimen and the hinge plate. These settings can be manipulated through the *Contact->Properties->Edit* entry of the *Interaction* module in

ABAQUS/CAE.

The axial load was applied through incremental displacements in the axial direction of the rotational points of the hinge block on one side of the specimen.

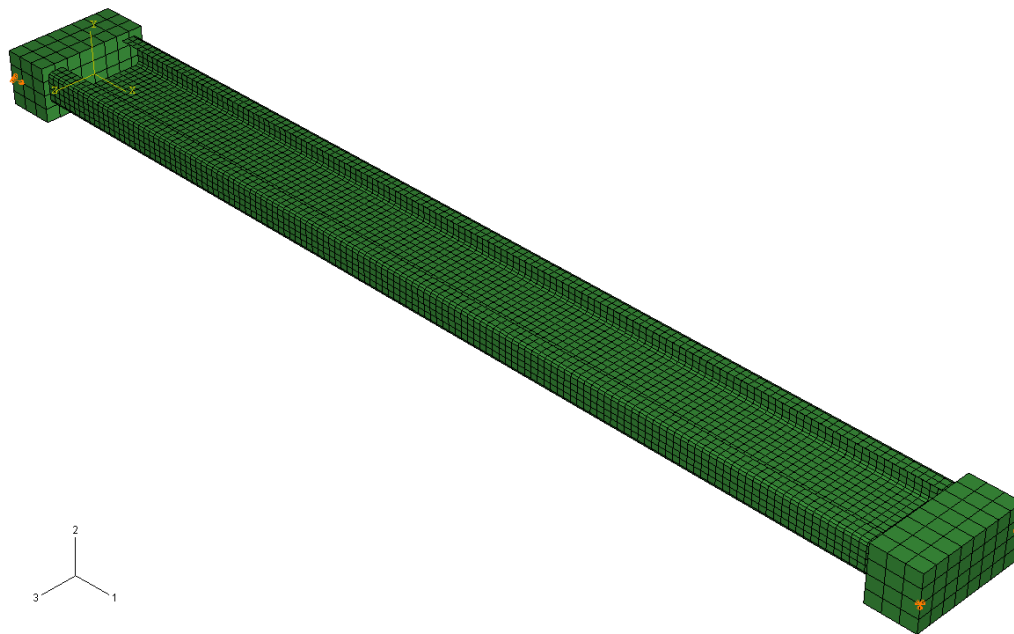


Figure 2.5. Specimen End Conditions

2.2.4 Imperfections

Since the interaction buckling phenomenon is highly imperfection-sensitive, it is important to accurately incorporate the imperfections into the FE model. Imperfections were measured along five longitudinal lines, as indicated in Fig. 2.6, by means of laser-interferometers. Details of the procedure can be found in Becque and Rasmussen (2006). The raw data were decomposed into their respective Fourier series to filter out noise and to obtain a useful mathematical representation, which determines the magnitude of the imperfections along the five given lines for any cross-section with coordinate x along the longitudinal axis of the specimen. The Fourier series were truncated after 10 to 12 terms for the short specimens, and 20 to 35 terms for the longest specimens. Within a given cross-section the magnitude of the imperfection at the location of each node of the

FE mesh was determined by interpolation. Quadratic interpolation was used for the web imperfections, while linear interpolation was used at the flanges, as illustrated in Fig. 2.6. An EXCEL spreadsheet was used to calculate the magnitude of the imperfection at each node of the FE model and to subsequently determine the new nodal coordinates. The results were saved as a comma-separated CSV-file and then cut-and-pasted into the ABAQUS input file (*.INP). The model was then reloaded into ABAQUS/CAE by using the *File->Load->Model* entry. A 3D representation of the (exaggerated) imperfections of each specimen can be found in Appendix C of Becque and Rasmussen (2006).

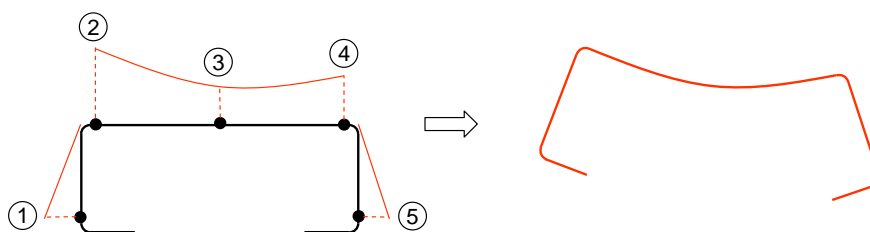


Figure 2.6. Specimen Imperfections

2.2.5 Type of Analysis

A geometric and material non-linear analysis was performed. In order to accurately model the descending branch of the load-deflection curve, a STATIC-RIKS analysis was selected. Automatic incrementation was used with an initial step equal to 0.002 times the estimated arc length. The default settings of the matrix solver were accepted.

2.2.6 Element Type and Mesh

2.2.6.1 Element Type

S4R, a 4-node shell element with reduced integration, was selected from the ABAQUS element library. This element uses three translational and three rotational degrees of freedom at each node. The element accounts for finite membrane strains and arbitrarily large rotations. Therefore, it is suitable for large-strain analyses and geometrically non-linear problems. Elements with five degrees of freedom, such as S4R5, can be computationally more economical. However, they cannot be used in finite-strain applications.

Seen the fact that the plate components constituting the cross-section are fairly slender for all specimens under consideration, transverse shear deformations were not deemed to have a major effect on the solution. Nevertheless, they are accounted for in the S4R element formulation.

Reduced integration was carried out according to the Simpson rule, using five integration points through the shell thickness. Since S4R is a linear element, the hourglass control settings needed to be activated.

2.2.6.2 Convergence Study

In order to study the effect of the mesh parameters on the accuracy of the results, four different mesh configurations were studied. A 400 mm long lipped channel in 3Cr12 stainless steel, identical in dimensions to test specimen C3Cr12_400_1, formed the subject of the study. The non-linear material behaviour of the flats and the corners was included in the model. Seen the elaborate work involved in recalculating the initial imperfections for each mesh configuration, imperfections are not yet included in the model at this stage.

Three different meshes employing square elements were conceived. The element sizes considered were 20 mm, 8 mm and 5 mm. This corresponds to a respective total number of elements of 320, 1700 and 4240. The solid elements constituting the end blocks are not included in these numbers.

A fourth mesh configuration was considered employing rectangular elements with an approximate size of 5 mm by 8 mm. The model, exclusive of the end blocks, then consisted of a total of 2960 elements.

Illustrations of all five meshes can be found in Appendix A. Table 2.2 lists the results of the FE runs.

The CPU time needed to complete the run was chosen as a representative proportional indication of the total amount of time needed for completion. It should be noted however that the total time is an order of magnitude larger than the CPU time due to comparatively time-consuming input/output operations to disk.

Table 2.2. Influence of the Mesh Size

Mesh	Element Size (mm)	Number of Elements	Peak Load (kN)	CPU Time (s)
1	20 x 20	320	124.352	84.7
2	8 x 8	1700	123.529	307.5
3	5 x 8	2960	123.463	534.3
4	5 x 5	4240	123.417	946.6

The peak load as well as the CPU time are pictured against the number of elements in Fig. 2.7.

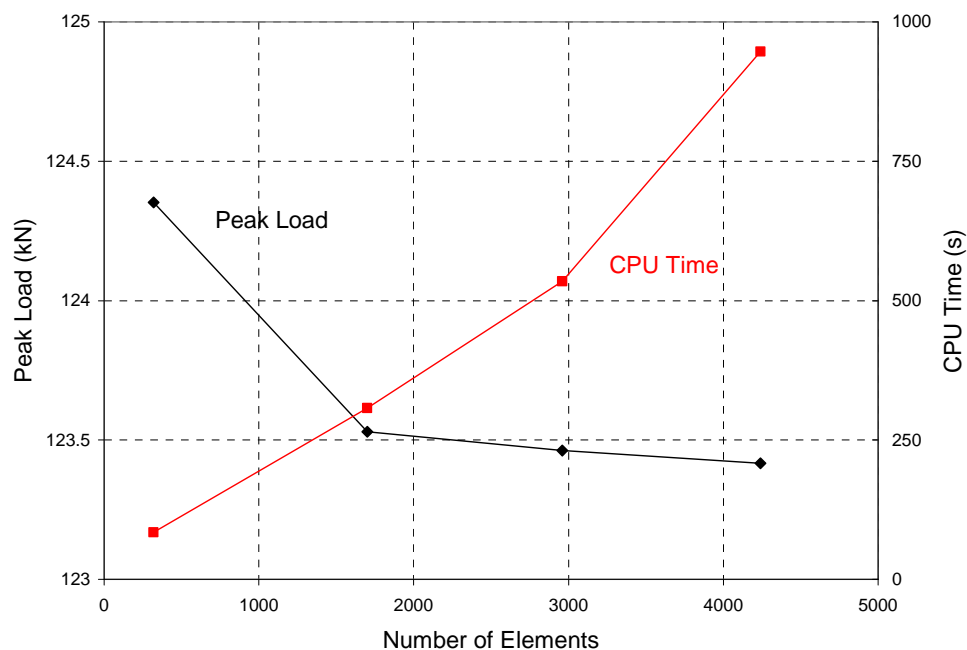


Figure 2.7. Effect of the Mesh Size on Peak Load and CPU Time

A number of conclusions can be drawn from Fig. 2.7 and Table 2.2.

As the mesh size decreases, results converge asymptotically. Mesh refinement beyond the 8 mm mesh (1700 elements) results in little gain in accuracy.

The rectangular 5x8 mm elements (2960 elements) yield good results and the accuracy is not adversely affected by the choice of rectangular elements with an aspect ratio of approximately 1:1.5.

Figure 2.8 displays the load-displacement behaviour obtained for the different meshes. There is no noticeable difference in the results of the 8x8 mm, 8x5 mm and 5x5 mm meshes until well into the post-peak range, at which point the practical significance of the difference becomes irrelevant.

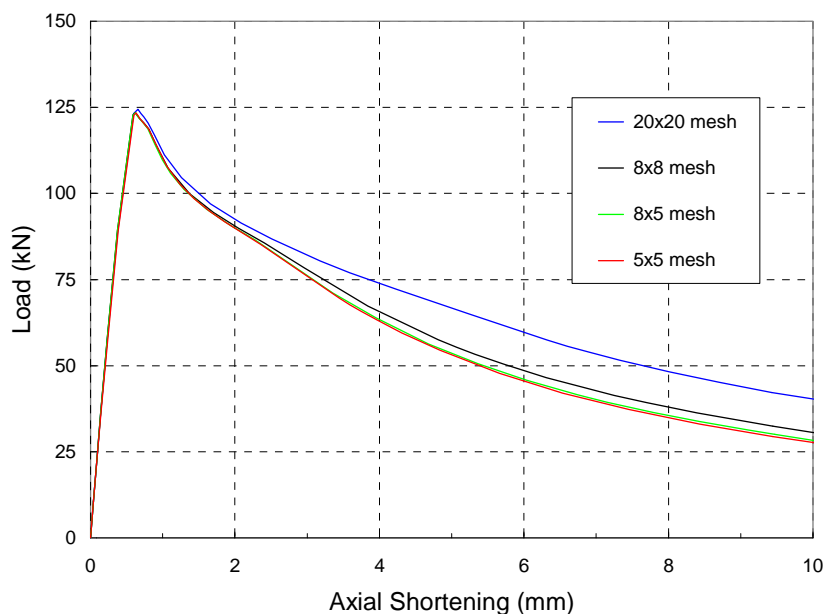


Figure 2.8. Load-Displacement Behaviour

The 8x8 mm mesh was selected for the numerical work. Compared to the 5x5 mm mesh, the difference in peak load is less than 0.1%, while it is substantially more computationally efficient. It also guarantees that the load-displacement curve is accurately modeled. Square elements were used as much as possible. Whenever rectangular elements needed to be used because of geometric constraints, the aspect ratio was kept below 1:1.5.

2.2.6.3 Effect of Reduced Integration

In order to investigate the effect of the reduced integration, an FE analysis was performed with fully integrated S4 elements replacing the S4R elements. Figure 2.9 compares the load-displacement results for both element types. Within the numerical accuracy of the results, there is no difference in peak load or load-displacement behaviour between S4 and S4R.

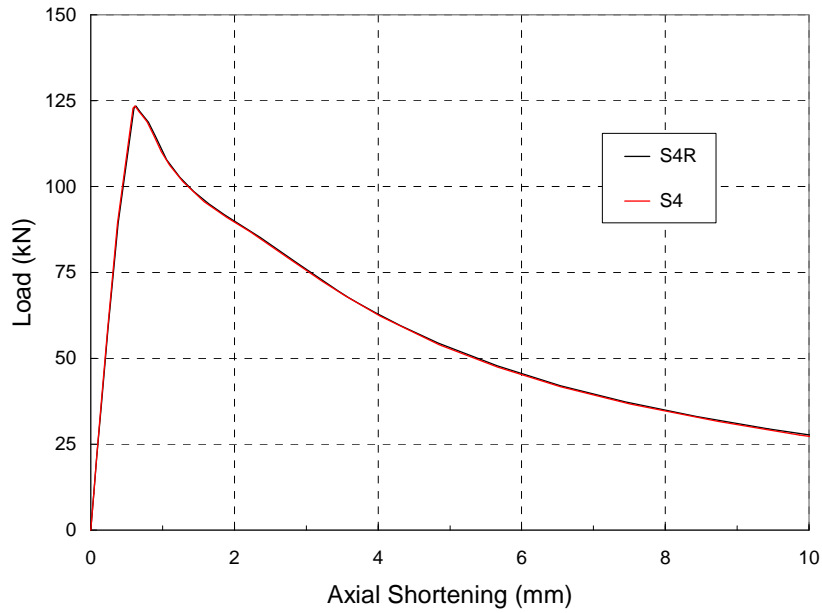


Figure 2.9. Effect of Reduced Integration

2.2.7 End Section Eccentricity

Becque and Rasmussen (2006) reported the eccentricities of the centroids of the end sections relative to the line of loading at the beginning of each test. These eccentricities were measured using the scribed lines on the hinge top plates, or in a number of cases, using strain gauges. They are listed in Tables 2.3, 2.4 and 2.5 for the 3Cr12, 304 and 430 specimens respectively. With the adopted sign conventions, the (initial) load eccentricity at mid-length $e_{o,mid}$, the (initial) load eccentricity at the specimen ends $e_{o,end}$, and the imperfection at mid-length Δ_{mid} (obtained from the Fourier representation of the imperfection readings) relate to each other as:

$$e_{o,end} = e_{o,mid} + \Delta_{mid} \quad (20)$$

The measured eccentricities were incorporated into the FE models by offsetting the specimen relative to the end blocks over the appropriate distance.

2.2.8 Analysis Results

The different aspects of FE modeling discussed in the preceding paragraphs were combined to construct an FE model which incorporates the non-linear stress-strain behaviour of the stainless steel alloys, the increased corner properties, material anisotropy, measured specimen dimensions, measured imperfections, measured load eccentricities and actual boundary conditions.

2.2.8.1 3Cr12 Specimen Results

Table 2.3 and Fig. 2.10 summarize the load capacities obtained from the FE models of the 12 3Cr12 specimens and compares them to the experimentally obtained values.

The deformational behaviour of each 3Cr12 specimen as predicted by the FE model is checked against the experimentally recorded behaviour in Appendix B. Four graphs are provided for each specimen, comparing the axial deformations, lateral deformations at mid-height, end rotations and local displacements of the transducer frame LVDTs.

2.2.8.2 304 Specimen Results

Table 2.4 and Fig. 2.11 compare the ultimate load predicted by the FE model of each 304 specimen with the experimental value. Appendix B graphically compares the predicted 304 specimen deformations with the actual measured deformations.

2.2.8.3 430 Specimen Results

Table 2.5 and Fig. 2.12 compare the ultimate load predicted by the FE model of each 430 specimen with the experimental value. Appendix B compares predicted and actual deformations of each 430 specimen.

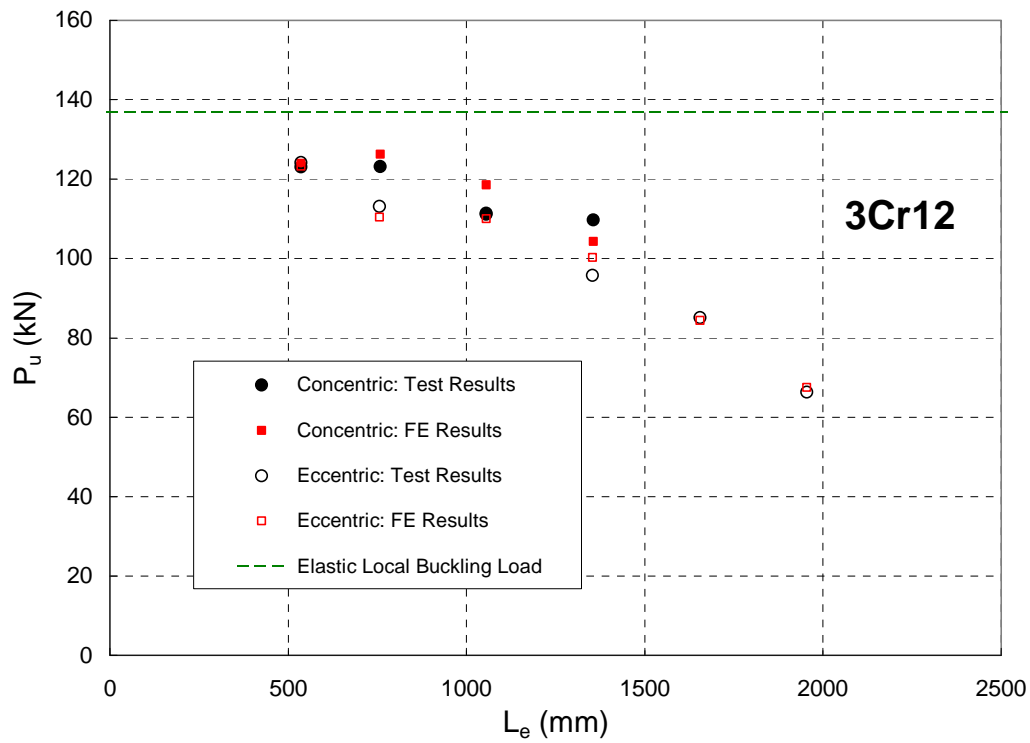


Figure 2.10. 3Cr12: Comparison between Test Results and FE Results

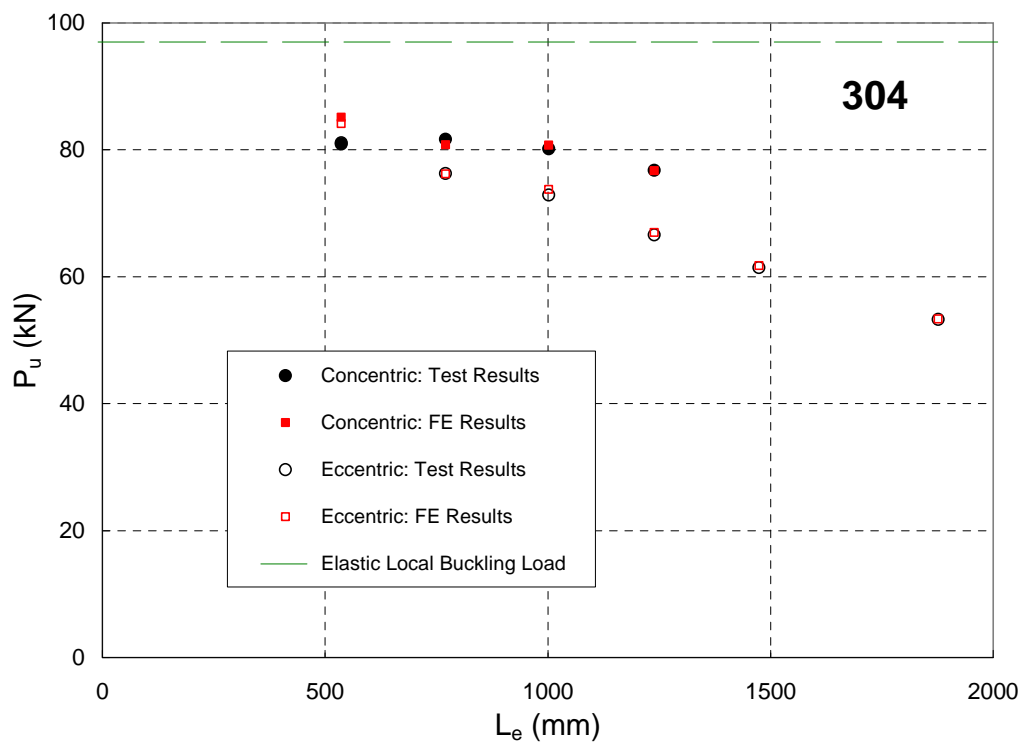


Figure 2.11. 304: Comparison between Test Results and FE Results

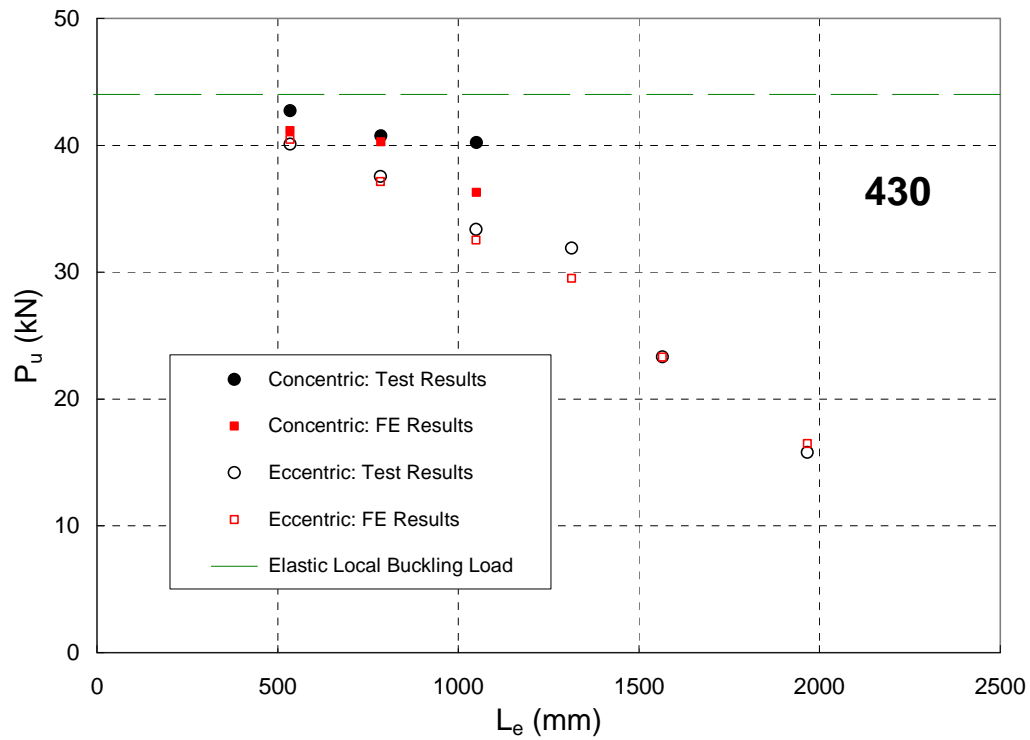


Figure 2.12. 430: Comparison between Test Results and FE Results

3Cr12 Series: Concentric Tests**Table 2.3**

Specimen	Material	Length		Eccentricity			Imperfection	Ultimate Load P_u		Ratio
		L	L_e	$e_{o,end}$	$e_{o,mid}$		Δ_{mid}	Test	FE	FE/Test
		(mm)	(mm)	(mm)	(mm)	-	(mm)	(kN)	(kN)	-
C3Cr12_400_1	3Cr12	400	536	0.000	-0.034	$-L_e/16000$	0.034	123.01	123.95	1.008
C3Cr12_620_1	3Cr12	622	758	-0.053	-0.162	$-L_e/4700$	0.109	123.12	126.29	1.026
C3Cr12_920_1	3Cr12	920	1056	0.184	0.201	$L_e/5300$	-0.017	111.13	118.55	1.067
C3Cr12_1220_1	3Cr12	1220	1356	0.446	0.470	$L_e/2900$	-0.024	109.70	104.26	0.950
C3Cr12_1520_1	3Cr12	1520	1656	0.000	0.147	$L_e/11000$	-0.147	-	90.83	-
C3Cr12_1819_1	3Cr12	1819	1955	0.000	-0.628	$-L_e/3100$	0.628	-	64.87	-
Average										1.013
St. Dev.										0.048

3Cr12 Series: Eccentric Tests

Specimen	Material	Length		Eccentricity			Imperfection	Ultimate Load P_u		Ratio
		L	L_e	$e_{o,end}$	$e_{o,mid}$		Δ_{mid}	Test	FE	FE/Test
		(mm)	(mm)	(mm)	(mm)	-	(mm)	(kN)	(kN)	-
C3Cr12_400_2	3Cr12	400	536	0.357	0.332	$L_e/1600$	0.025	124.15	123.24	0.993
C3Cr12_620_2	3Cr12	620	756	2.17	2.100	$L_e/360$	0.069	113.09	110.43	0.976
C3Cr12_920_2	3Cr12	920	1056	1.072	0.930	$L_e/1100$	0.142	111.40	109.98	0.987
C3Cr12_1220_2	3Cr12	1218	1354	0.818	0.890	$L_e/1500$	-0.072	95.76	100.19	1.046
C3Cr12_1520_2	3Cr12	1520	1656	1.104	0.681	$L_e/2400$	0.423	85.03	84.41	0.993
C3Cr12_1819_2	3Cr12	1819	1955	1.303	0.901	$L_e/2200$	0.402	66.25	67.45	1.018
Average										1.002
St. Dev.										0.026

304 Series: Concentric Tests**Table 2.4**

Specimen	Material	Length		Eccentricity			Imperfection	Ultimate Load P_u		Ratio
		L	L_e	$e_{o,end}$	$e_{o,mid}$		Δ_{mid}	Test	FE	FE/Test
		(mm)	(mm)	(mm)	(mm)	-	(mm)	(kN)	(kN)	-
C304_400_1	304	400	536	0.000	-0.048	$-L_e/11000$	0.048	80.90	85.13	1.052
C304_636_1	304	636	772	-0.038	-0.107	$-L_e/7200$	0.069	81.63	80.75	0.981
C304_866_1	304	866	1002	-0.335	-0.385	$-L_e/2600$	0.050	80.12	80.72	1.007
C304_1103_1	304	1103	1239	0.204	0.081	$L_e/15000$	0.123	76.78	76.67	0.999
C304_1339_1	304	1339	1475	0.169	-0.001	$-L_e/2 \times 10^6$	0.170	-	74.72	-
C304_1741_1	304	1741	1877	0.000	-0.226	$-L_e/8300$	0.226	-	54.33	-
Average										1.012
St. Dev.										0.028

304 Series: Eccentric Tests

Specimen	Material	Length		Eccentricity			Imperfection	Ultimate Load P_u		Ratio
		L	L_e	$e_{o,end}$	$e_{o,mid}$		Δ_{mid}	Test	FE	FE/Test
		(mm)	(mm)	(mm)	(mm)	-	(mm)	(kN)	(kN)	-
C304_400_2	304	400	536	0.357	0.331	$L_e/1600$	0.026	81.12	84.09	1.037
C304_636_2	304	635	771	1.235	1.180	$L_e/650$	0.055	76.27	76.22	0.999
C304_866_2	304	866	1002	0.735	0.733	$L_e/1400$	0.002	72.88	73.75	1.012
C304_1103_2	304	1103	1239	1.766	1.691	$L_e/730$	0.075	66.57	66.99	1.006
C304_1339_2	304	1338	1474	2.010	2.044	$L_e/720$	-0.034	61.42	61.72	1.005
C304_1741_2	304	1741	1877	1.251	1.360	$L_e/1400$	-0.109	53.27	53.30	1.001
Average										1.010
St. Dev.										0.014

430 Series: Concentric Tests**Table 2.5**

Specimen	Material	Length		Eccentricity			Imperfection	Ultimate Load P_u		Ratio
		L	L_e	$e_{o,end}$	$e_{o,mid}$		Δ_{mid}	Test	FE	FE/Test
		(mm)	(mm)	(mm)	(mm)	-	(mm)	(kN)	(kN)	-
C430_399_1	430	399	535	0.000	0.001	$L_e/390000$	-0.001	42.71	41.14	0.963
C430_650_1	430	650	786	0.000	-0.031	$-L_e/26000$	0.031	40.74	40.27	0.988
C430_915_1	430	915	1051	0.236	0.226	$L_e/4700$	0.010	40.22	36.27	0.902
C430_1178_1	430	1178	1314	0.063	-0.010	$-L_e/126000$	0.073	-	32.18	-
C430_1430_1	430	1430	1566	0.000	-0.114	$-L_e/14000$	0.114	-	25.00	-
C430_1831_1	430	1831	1967	0.000	-0.073	$-L_e/27000$	0.073	-	18.06	-
Average										0.951
St. Dev.										0.045

430 Series: Eccentric Tests

Specimen	Material	Length		Eccentricity			Imperfection	Ultimate Load P_u		Ratio
		L	L_e	$e_{o,end}$	$e_{o,mid}$		Δ_{mid}	Test	FE	FE/Test
		(mm)	(mm)	(mm)	(mm)	-	(mm)	(kN)	(kN)	-
C430_399_2	430	399	535	0.357	0.355	$L_e/1500$	0.002	40.07	40.46	1.010
C430_650_2	430	649	785	0.524	0.507	$L_e/1500$	0.017	37.53	37.14	0.990
C430_915_2	430	913	1049	0.935	0.921	$L_e/1100$	0.014	33.37	32.52	0.974
C430_1178_2	430	1178	1314	0.592	0.485	$L_e/2700$	0.107	31.88	29.51	0.926
C430_1430_2	430	1429	1565	1.044	0.926	$L_e/1700$	0.118	23.31	23.30	0.999
C430_1831_2	430	1831	1967	1.311	1.326	$L_e/1500$	-0.015	15.80	16.49	1.043
Average										0.990
St. Dev.										0.039

2.2.9 Discussion

2.2.9.1 Load Capacities

Tables 2.3 to 2.5 demonstrate that the FE model succeeded in accurately predicting the load carrying capacities. Based on all specimens, the average ratio of the predicted ultimate load to the experimental ultimate load is 0.999 with a standard deviation of 0.035. Typically the predictions were slightly more accurate for the eccentrically loaded specimens compared to the concentrically loaded ones. This can be attributed to the fact that variations in initial small eccentricities have a more severe effect on the load carrying capacity than variations of larger eccentricities.

It should be noted that static material properties were used in the FE model and that the predicted ultimate loads are thus compared to the static experimental values.

The FE analysis confirms the earlier suspicion that the experimental results of the longer concentrically loaded specimens C3Cr12_1520_1, C3Cr12_1819_1, C304_1339_1, C304_1741_1, C430_1178_1, C430_1430_1 and C430_1831_1 were affected by initial bearing friction.

2.2.9.2 Specimen Behaviour

By way of an example, Figs. 2.13a to 2.13d compare the predicted deformations of specimen C3Cr12_920_2 with the experimentally recorded deformations. It should again be noted that the FE analysis was based on static material properties and that the predicted load vs. deformation curves should be compared to the static points of the experimental curves, obtained by halting the test repeatedly and allowing the load to settle down to a static value.

Figure 2.13a reveals excellent agreement between the predicted and the experimental load vs. axial shortening curves until well into the post-ultimate range. Typically, the FE

model displays a slightly higher stiffness compared to the actual specimen for very large deformations past the ultimate load. This difference however is irrelevant from a practical perspective.

Figure 2.13b compares the predicted lateral displacements of the FE model with the experimentally recorded values. The displacements derived from the FE model were obtained from the nodes corresponding with the locations of LVDTs D1 and D2 in the test: at mid-height near the corners on either side of the web. Good agreement between predicted and recorded displacements was observed.

Figure 2.13c shows the end rotations of specimen C3Cr12_920_2, as predicted by the FE model, and compares them to the experimentally observed rotations. Good agreement between predicted and experimental behaviour was again obtained.

Figure 2.13d compares the recorded displacements of the LVDTs W1, R1 and L1, mounted on the transducer frame at mid-height, with the displacements of corresponding nodes in the FE model. The W1 reading is to be compared with the nodal 2-displacement of the node at the centre of the web at mid-height, while the L1 and R1 readings correspond with the 3-displacement of nodes on the flanges at mid-height, located approximately 5 mm in from the rounded part of the corner. It should be noted that the post-ultimate W1, R1 and L1 readings are highly sensitive to the location where the local buckling pattern eventually localizes. A small shift in this location results in vastly different readings. Nevertheless in many cases good agreement was observed between predicted and experimental displacements.

Figs. 2.14a, 2.14b, 2.14c and 2.14d show some examples of specimens after failure, accompanied by their corresponding FE models. It can be seen that the buckled shape of the failed specimens is well represented by the FE models.

By way of an example, Figure 2.15 shows the FE deformations of a typical specimen (C304_636_1) under progressive loading. The contours represent Von Mises surface stresses.

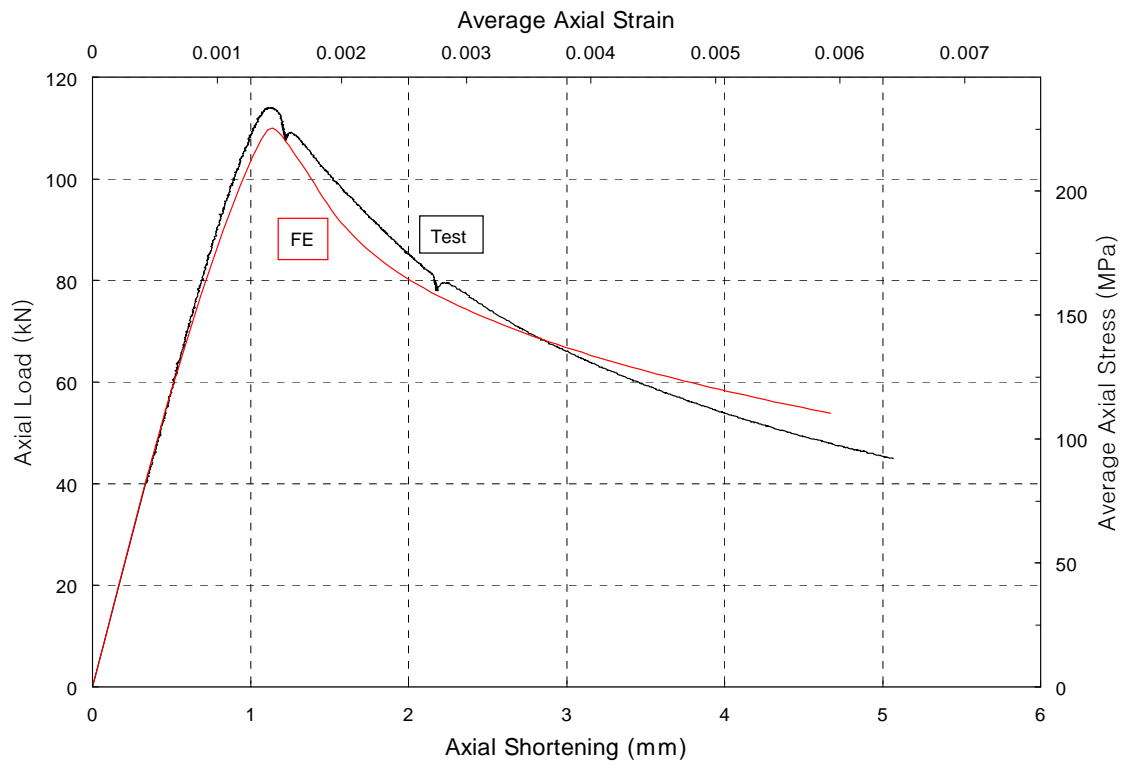


Figure 2.13a. C3Cr12_920_2: Axial Load vs. Axial Shortening

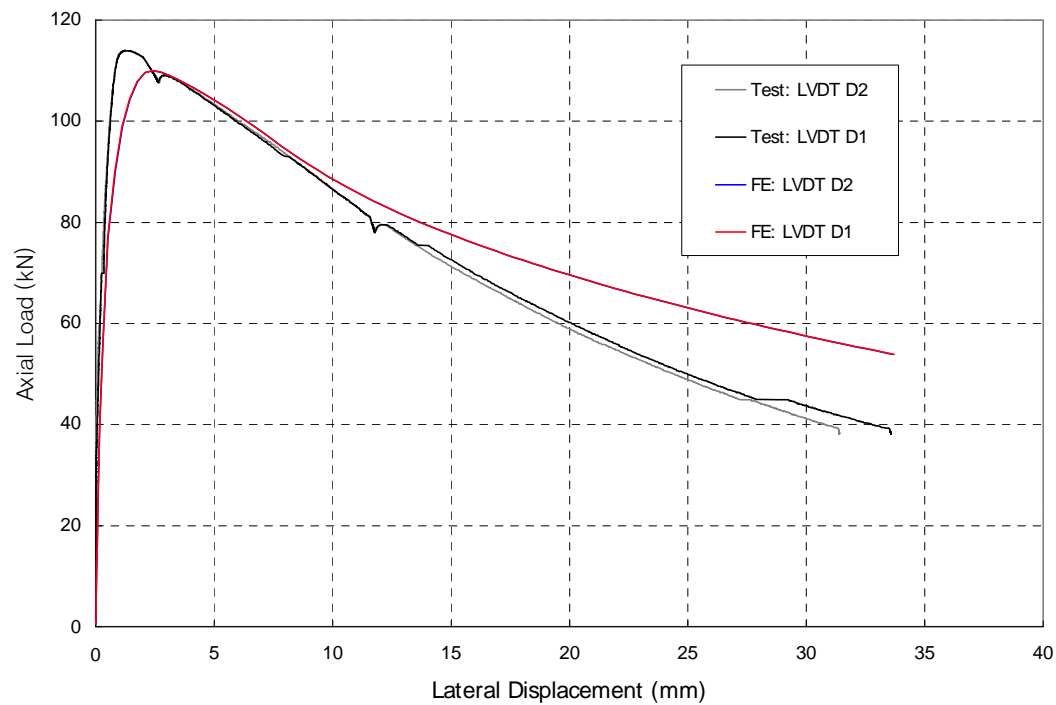


Figure 2.13b. C3Cr12_920_2: Axial Load vs. Lateral Displacement

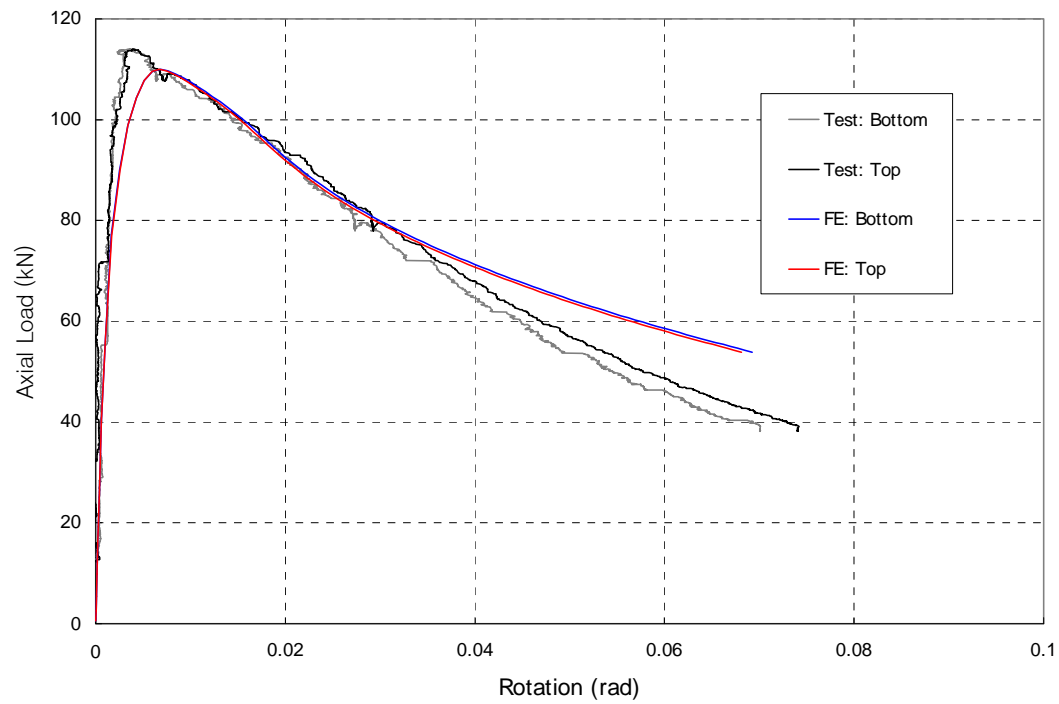


Figure 2.13c. C3Cr12_920_2: Axial Load vs. End Rotations

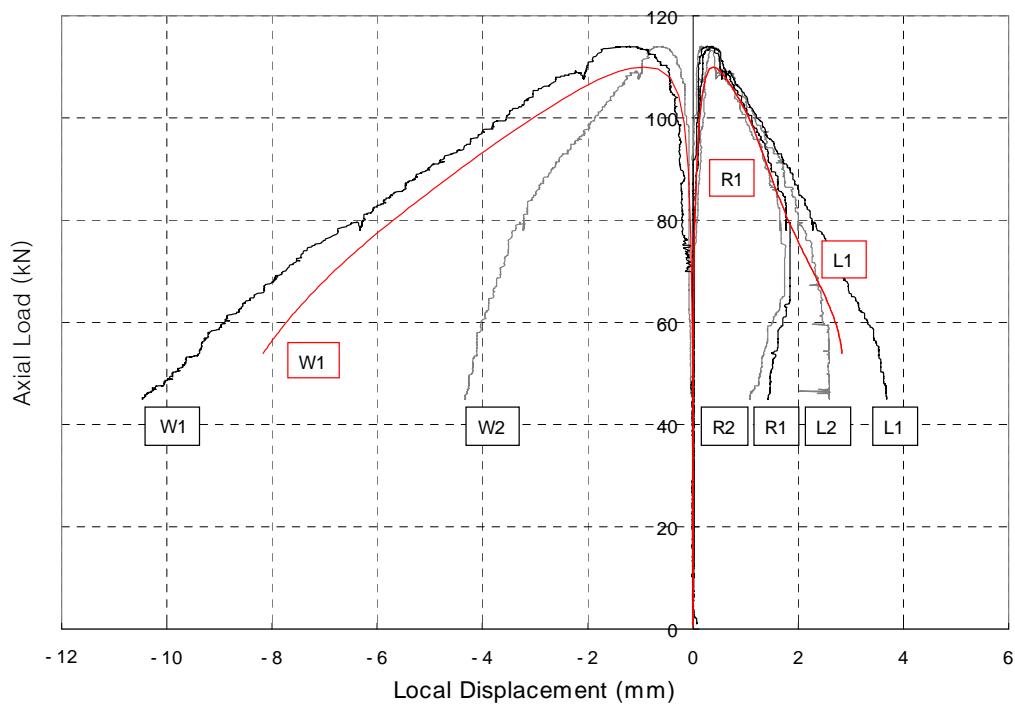


Figure 2.13d. C3Cr12_920_2: Axial Load vs. Local Displacements

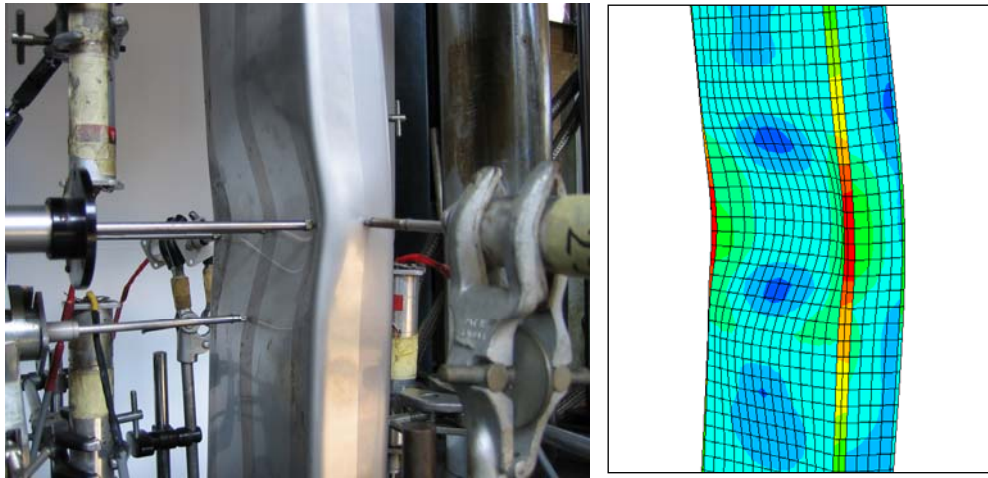


Figure 2.14a. C304_400_1: Post-Peak Buckled Shape

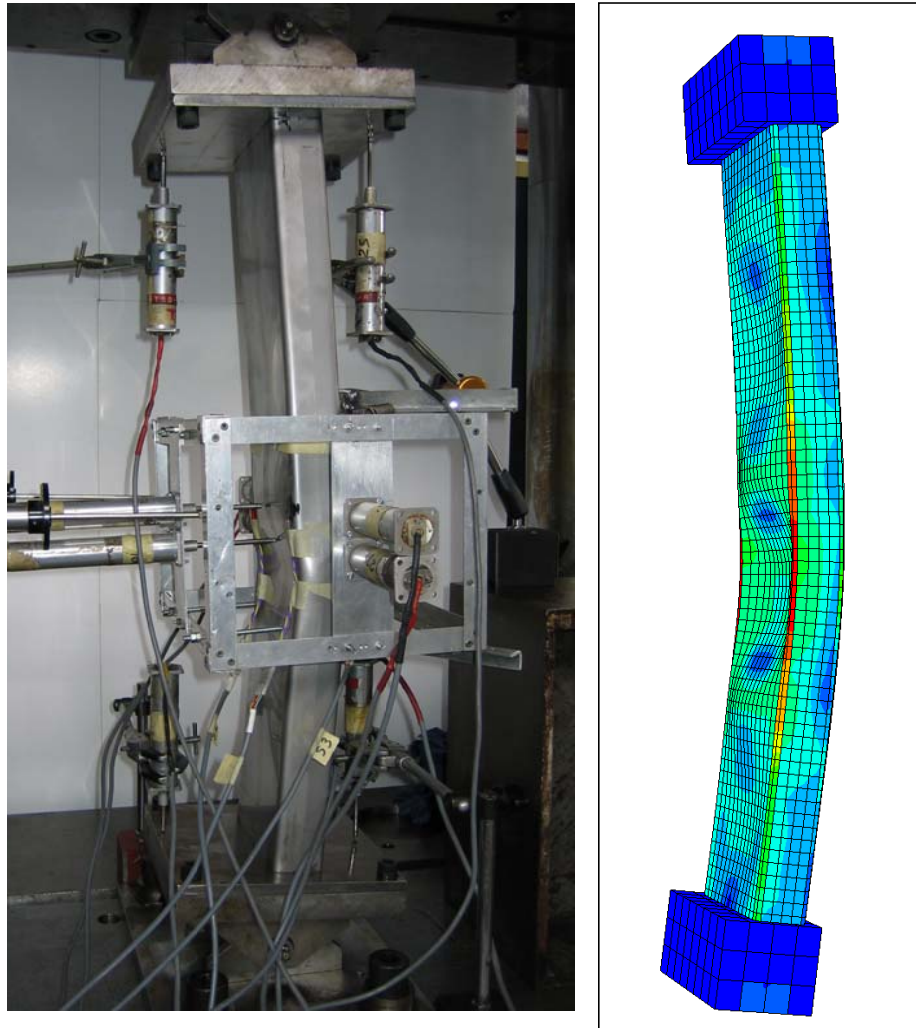


Figure 2.14b. C304_636_2: Post-Peak Buckled Shape

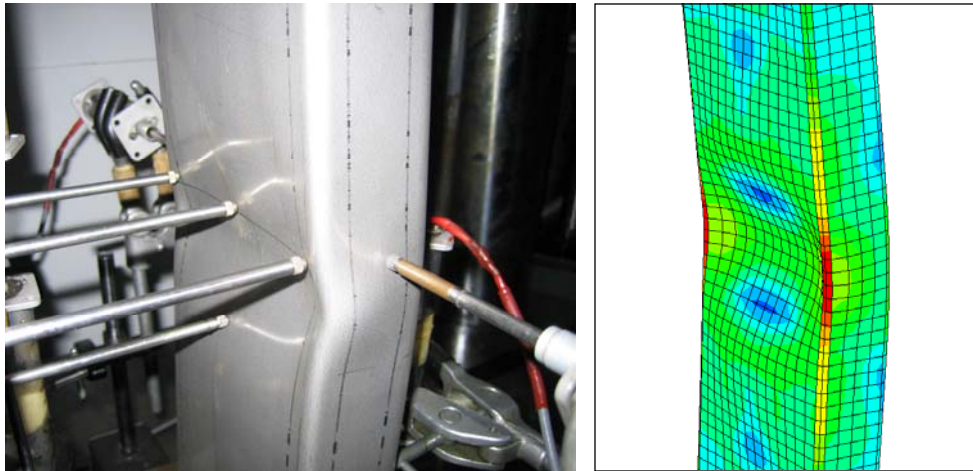


Figure 2.14c. C3Cr12_400_2: Post-Peak Buckled Shape

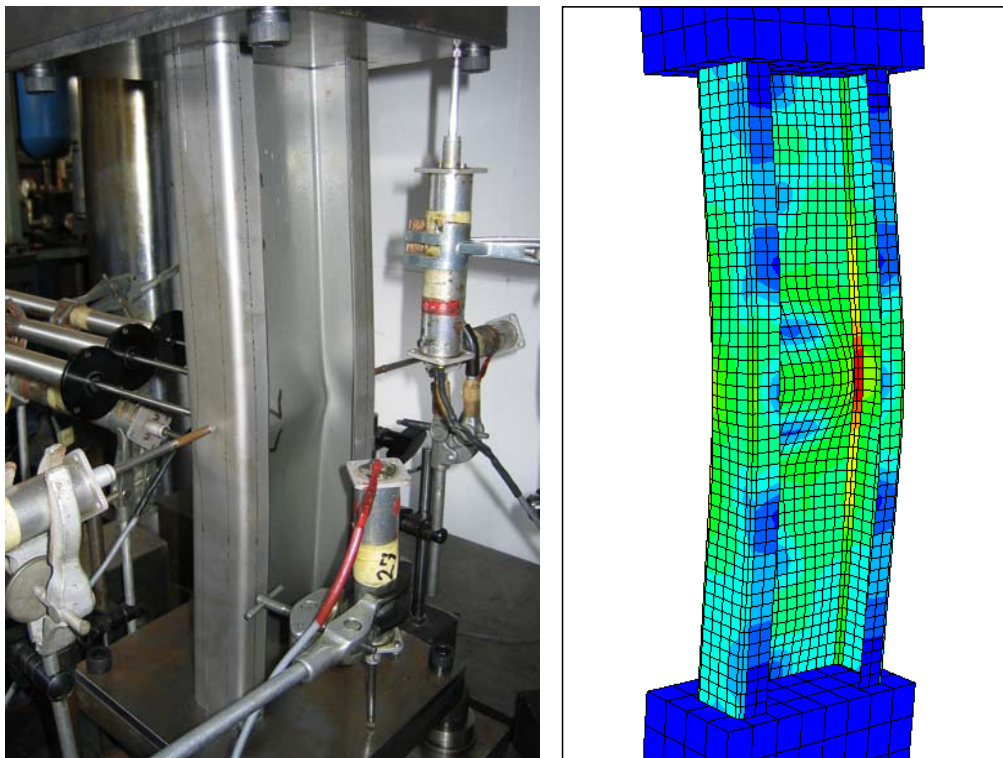


Figure 2.14d. C3Cr12_400_1: Post-Peak Buckled Shape

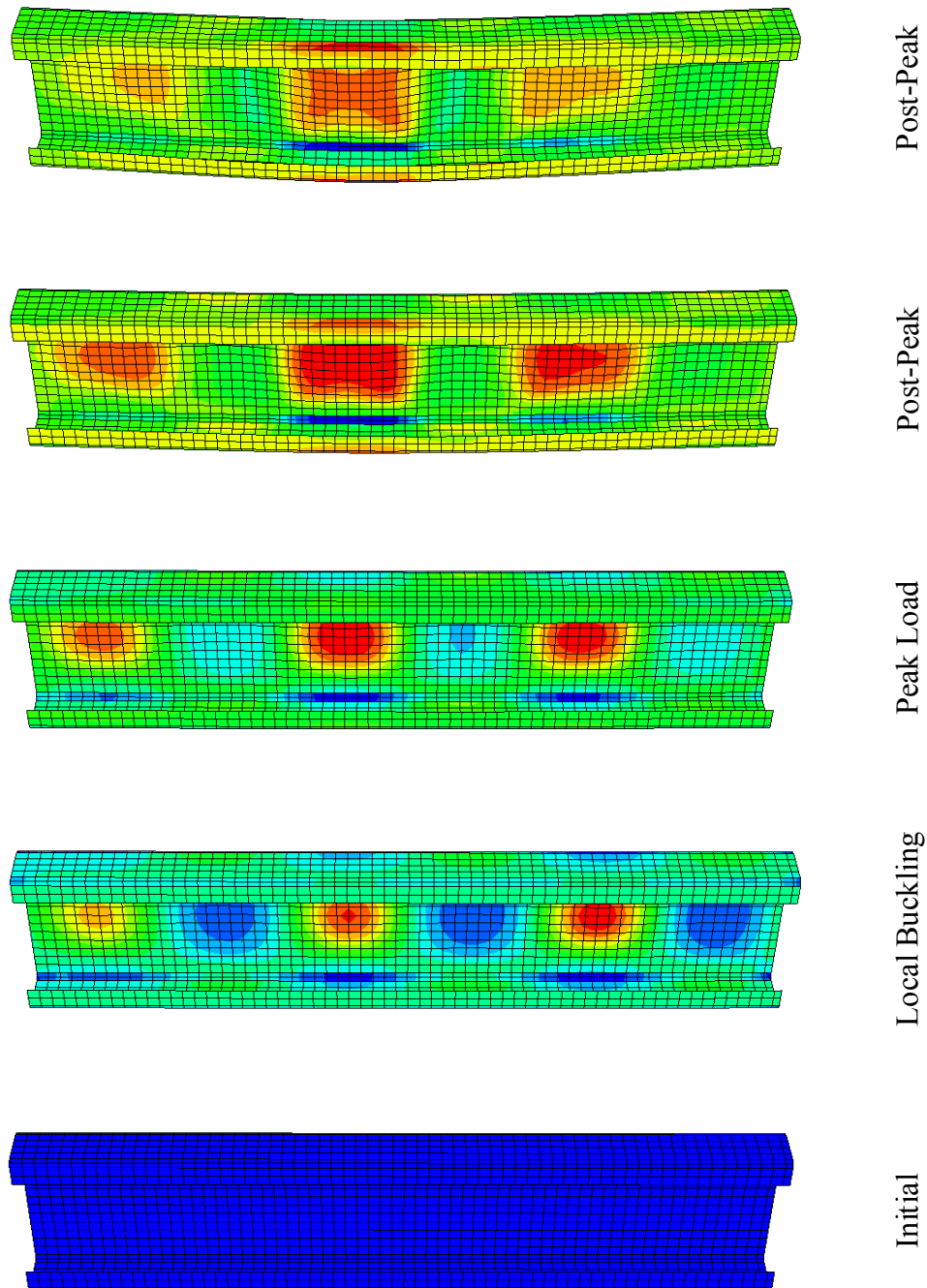


Figure 2.15. Deformations under Progressive Loading (Lipped Channel)

Table 2.6. FE Results for L/1500 Eccentricity

Specimen	Material	L_e (mm)	P_u (kN)
C3Cr12_400_2	3Cr12	536	123.20
C3Cr12_620_2	3Cr12	756	120.36
C3Cr12_920_2	3Cr12	1056	112.24
C3Cr12_1220_2	3Cr12	1354	100.18
C3Cr12_1520_2	3Cr12	1656	81.66
C3Cr12_1819_2	3Cr12	1955	65.92

Specimen	Material	L_e (mm)	P_u (kN)
C304_400_2	304	536	84.01
C304_636_2	304	771	78.77
C304_866_2	304	1002	74.03
C304_1103_2	304	1239	70.67
C304_1339_2	304	1474	66.34
C304_1741_2	304	1877	53.55

Specimen	Material	L_e (mm)	P_u (kN)
C430_399_2	430	535	40.45
C430_650_2	430	785	37.08
C430_915_2	430	1049	33.29
C430_1178_2	430	1314	28.32
C430_1430_2	430	1565	23.08
C430_1831_2	430	1967	16.50

Table 2.6 displays FE generated results for the eccentric tests, where the eccentricity at mid-height was adjusted to be exactly $L_e/1500$. These values form a first set of results which are further used to evaluate the current design standards.

2.3 Parametric Studies of Lipped Channels

2.3.1 Introduction

The overall slenderness λ_o of a stainless steel column is commonly defined as:

$$\lambda_o = \sqrt{\frac{\sigma_{0.2\%}}{\sigma_E}} = \left(\frac{L_e}{r} \right) \sqrt{\frac{\sigma_{0.2\%}}{\pi^2 E_0}} \quad (21)$$

which results from the equivalent definition for carbon steel columns with the 0.2% proof stress substituted for the yield stress f_y . Note that the definition is based on the elastic Euler buckling stress σ_E , calculated with the initial modulus E_0 .

In a similar way the cross-sectional slenderness λ_s is defined as:

$$\lambda_s = \sqrt{\frac{\sigma_{0.2\%}}{\sigma_{cr}}} \quad (22)$$

where σ_{cr} is the elastic local buckling stress.

The test specimens described in (Becque and Rasmussen 2006) were designed to exhibit local buckling in the inelastic stress range to illustrate the non-linear stress-strain behaviour of stainless steel alloys. The sections were constructed with an inelastic local buckling stress above the proportionality limit $\sigma_{0.01\%}$. Consequently, within the range of λ_s values pertaining to sections of interest to this research (i.e. sections susceptible to local buckling), the test specimens exhibit relatively low cross-sectional slenderness values. λ_s varies around 1.1, more accurately: $\lambda_s = 1.08$ for the 3Cr12 section, $\lambda_s = 1.12$ for the 304 section and $\lambda_s = 1.11$ for the 430 section.

The following section describes how the FE model was used to generate additional data for 3Cr12, 304 and 430 stainless steel lipped channel sections with nominal cross-sectional slenderness values λ_s of 1.6 and 2.4. The overall slenderness λ_o was varied between 0.25 and 2.0 in 0.25 increments. Thus the parametric studies comprehensively covered the practical range of both cross-sectional and overall slenderness values.

2.3.2 Cross-section Design

The elastic local buckling stress σ_{cr} is proportional to t^2 . However, since the aim of this research is to investigate the interaction between local and overall buckling, and since the cross-section is susceptible to local buckling, the cross-sectional slenderness cannot

simply be increased by reducing the wall thickness t . To suppress the distortional buckling mode, the cross-section needs to be redesigned. Typically this will result in a reduced flange width b and an increased lip size c with increasing λ_s . The software package ThinWall (Papangelis and Hancock 1995) was used to ensure that the (elastic) distortional buckling stress was sufficiently larger than the (elastic) local buckling stress. The output of the ABAQUS finite element software was checked after each analysis to ensure that the out-of-plane displacements of the flange-to-lip junction were negligible compared to the other displacements, indicating no influence of the distortional buckling mode. The dimensions of the cross-sections used in the parametric studies are listed for each alloy in Table 2.7, using the conventions illustrated in Figure 2.16.

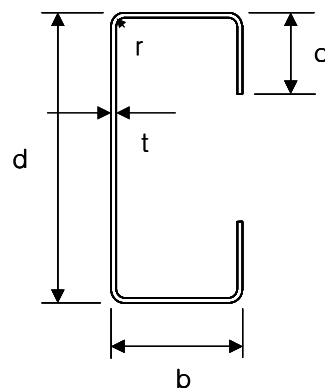


Figure 2.16. Specimen Dimensions (Lipped Channels)

Table 2.7. Specimen Dimensions (Lipped Channels)

Material	λ_s	d mm	b mm	c mm	r mm	t mm	σ_{cr} MPa	ω_d mm
3Cr12	1.60	125.32	35.00	22.66	4.14	1.32	128.0	0.62
3Cr12	2.38	125.32	24.00	22.66	4.14	0.87	57.7	0.63
304	1.61	144.38	40.00	24.00	5.14	1.35	90.2	0.65
304	2.37	144.38	27.00	27.00	5.14	0.90	41.5	0.64
430	1.59	79.73	24.00	18.00	3.00	0.78	104.6	0.37
430	2.38	79.73	16.00	16.00	3.00	0.51	46.8	0.36

2.3.3 Imperfections

In the FE model specimens were given an overall imperfection, as well as a local imperfection.

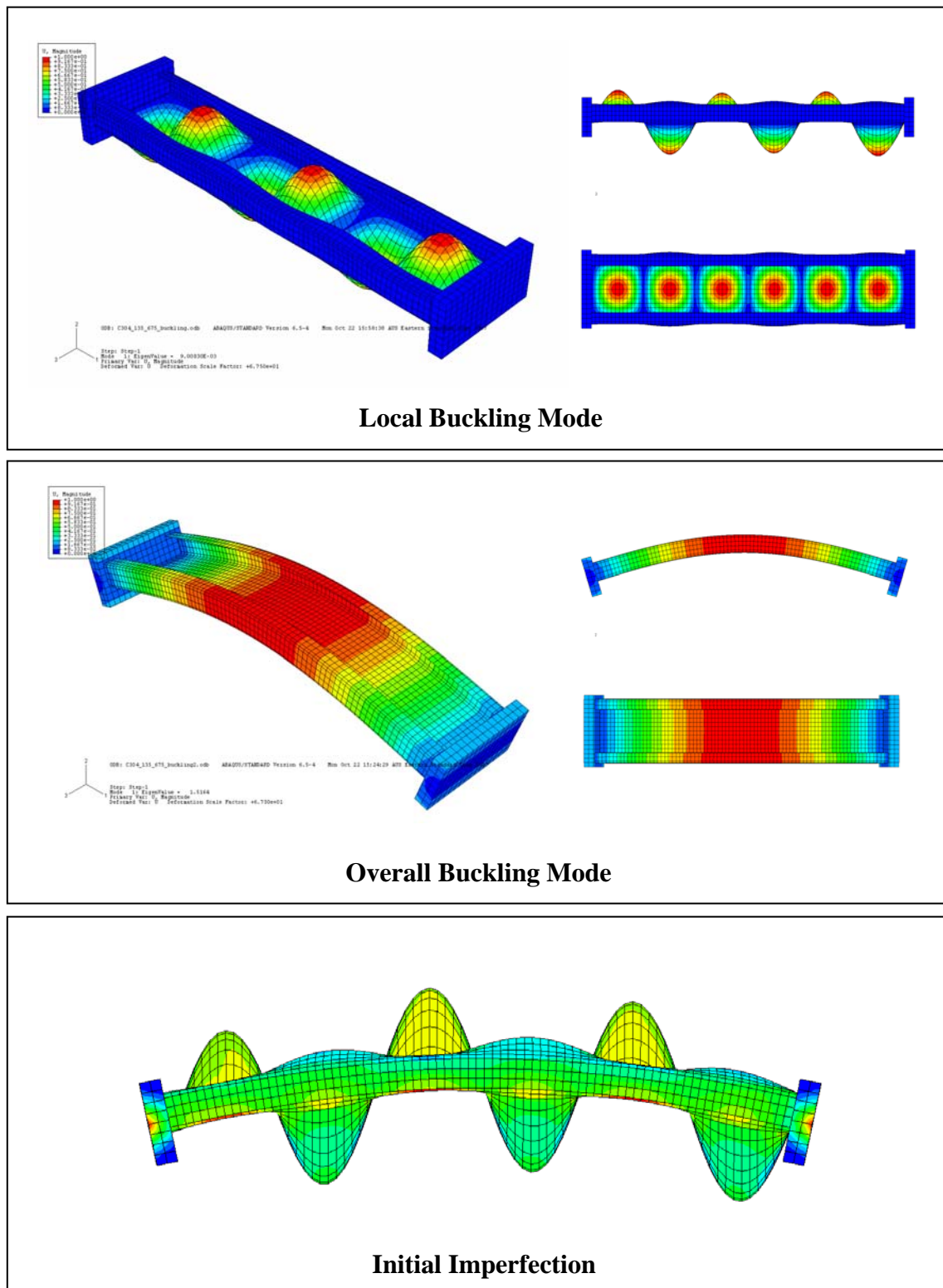
An overall imperfection in the shape of one half-sinewave was used with an amplitude of $L_e/1500$. It was ensured that this imperfection caused the load to be eccentric towards the web, thus adding to the shift in effective centroid caused by local buckling and constituting a worst case scenario.

A local imperfection in the shape of the local buckling eigenmode was also incorporated into the model. The amplitude ω_d was calculated based on the work by Walker (1975):

$$\omega_d = 0.3t \sqrt{\frac{\sigma_{0.2\%}}{\sigma_{cr}}} = 0.3t\lambda_s \quad (23)$$

The Walker equation takes into account the 0.2% proof stress of the material and the elastic local buckling stress and was therefore preferred over the equations proposed by Schafer and Pekoz (1998b), where ω_d is a linear function of the plate thickness only. Such a linear function yields unrealistic results for stockier sections, which are less susceptible to developing large initial imperfections. The Walker equation on the other hand predicts smaller imperfections for sections with a lower cross-sectional slenderness.

The overall and local buckling modes were obtained from a (linear elastic) buckling analysis in ABAQUS. The coordinates of the (normalized) eigenmodes obtained from this analysis are by default stored in file with extension *.fil and can subsequently be used as input for the *IMPERFECTION command in the actual simulation. The *IMPERFECTION command allows for a linear combination of eigenmodes to be used as an initial imperfection, as long as the coordinates of these eigenmodes can be read from a single *.fil file. The *.fil file may be written in binary or ASCII format.



In most cases no clear local or overall buckling mode could be found amongst the eigenmodes produced by the buckling analysis and the desired buckling shapes were coupled with other eigenmodes. In this case the following procedure was followed:

In a first step, the shell thickness was increased sufficiently to enforce overall buckling as the primary eigenmode of the specimen. Indeed, the second moment of area, and by consequence, the Euler buckling load, are proportional to the thickness t , while the elastic local buckling stress is proportional to t^2 .

A second buckling analysis was performed where the shell thickness was reduced sufficiently to ensure a purely local primary eigenmode without any influence of overall buckling modes.

The *.fil result files of both analyses were then combined into one single file. To achieve this, the result files were first converted into ASCII format using the ASCFIL command from the ABAQUS prompt. The ASCFIL command produces a *.fin file, which is the ASCII translation of the original *.fil file. The *.fin files were renamed into *.fil files and combined into one file using the APPEND command. In summary, the following commands were typed at the ABAQUS prompt (using specimen C304_1.35_675 as an example):

```
C:> abaqus ascfil job = C304_135_675_buckling_overall
C:> abaqus ascfil job = C304_135_675_buckling_local
C:> del C304_135_675_buckling_overall.fil
C:> del C304_135_675_buckling_local.fil
C:> ren C304_135_675_buckling_overall.fin C304_135_675_buckling_overall.fil
C:> ren C304_135_675_buckling_local.fin C304_135_675_buckling_local.fil
C:> abaqus append job = C304_135_675_imperfection
First input file name: C304_135_675_buckling_overall
Second input file name: C304_135_675_buckling_local
```

In the above commands, `C304_135_675_buckling_overall.fil` and `C304_135_675_buckling_overall.fil` are the result files of an ABAQUS buckling analysis forcing the specimen to buckle in an overall and a local shape respectively. The resulting file `C304_135_675_imperfection.fil` contains the eigenmodes of both buckling analyses in ASCII format. A text editor such as WordPad or NotePad can then be used to renumber the eigenmodes in consecutive order, so that they can be properly referred to in the `*IMPERFECTION` command, which also specifies the scaling factors to be applied to each mode.

Figure 2.17 illustrates the local buckling mode, the overall buckling mode and the (exaggerated) initial imperfection, which is a linear combination of both, for specimen C304_1.35_675. ABAQUS normalizes the eigenmodes such that the largest displacement is equal to the unit.

2.3.4 Material Properties

Three different alloys were considered: austenitic 304, ferritic 430 and ferritic-like 3Cr12. The material properties which were experimentally determined in (Becque and Rasmussen 2006) and which were previously used to calibrate the FE model, were utilized as input for further parametric studies. Anisotropic yielding was catered for by means of Hill's criterion, using the coefficients listed in Table 2.1. The corner regions were given the increased material properties determined from the experiment (Becque and Rasmussen 2006). It should be noted that, as the cross-sectional slenderness of the specimens listed in Table 2.7 increases and the wall thickness decreases, the r_i/t ratio of the corners increases. For the original test specimens, on which the corner properties were measured, the r_i/t ratios lie in the range of 1.6-2.1, while for the specimens with the highest cross-sectional slenderness ($\lambda_s = 2.4$) the r_i/t ratios range from 4.2 to 5.4. However, a number of equations have been proposed by van den Berg and van der Merwe (1992), Ashraf et al. (2005) and AS/NZS 4673 (2004) to predict the influence of

the r_i/t ratio on the 0.2% proof stress of the corner material $\sigma_{0.2\%,c}$. For the above case, all equations predict a change of approximately 10% in $\sigma_{0.2\%,c}$ of the 430 and 3Cr12 alloys as a result of the change in r_i/t . Therefore the change in $\sigma_{0.2\%,c}$ with varying r_i/t was ignored. The predicted change in $\sigma_{0.2\%,c}$ of the 304 material is roughly 20%, which is still deemed acceptable since the area of the corner regions is fairly small.

2.3.5 FE Analysis Results

48 parametric studies were carried out for lipped channels, encompassing any combination of the two cross-sectional slenderness values ($\lambda_s = 1.6$ and 2.4), the eight overall slenderness values ($\lambda_o = 0.25, 0.50, 0.75, 1.00, 1.25, 1.50, 1.75$ and 2.00) and the three stainless steel alloys mentioned in Section 2.3.4.

The element size of approximately 8 mm obtained from the calibration process was maintained. All columns were modeled with pinned end conditions.

The ultimate capacities obtained from the FE analyses are summarized in Table D1 of Appendix D. They are listed under the heading “Test”. The FE results are identified by a unique label, starting with “C” to indicate a channel, followed by the alloy, the wall thickness (in mm) and the effective length (in mm). For instance, C304_1.35_675 is a 675mm long lipped channel in 304 stainless steel with a plate thickness of 1.35 mm. Table D1 lists the 48 parametric studies of lipped channels, together with 18 results obtained from Table 2.6, renamed to fit the aforementioned convention. The 66 data points thus obtained compose a basis for evaluating the current design guidelines and developing improved design rules for this particular type of section.

The results are also presented graphically in Figures D.1 to D.9 of Appendix D. The strength curves plot the load capacity P_u versus the effective length L_e for a specific value of λ_s , or in non-dimensional form, $P_u/P_{0.2\%}$ versus the overall slenderness λ_o . It is noted that:

$$P_{0.2\%} = A_g \cdot \sigma_{0.2\%} \quad (24)$$

where A_g is the gross cross-sectional area.

The elastic local buckling load P_{cr} is also indicated in the graphs.

2.4 Parametric Studies of Plain Channels

2.4.1 Introduction

No data are available in literature relating to the column behaviour of singly symmetric stainless steel plain channels. The FE model was used to generate 72 data points for this particular case, comprising three alloys (3Cr12, 304 and 430), three cross-sectional slenderness values ($\lambda_s \approx 1.1, 1.6$ and 2.4) and eight overall slenderness values ($\lambda_s = 0.25, 0.50, 0.75, 1.00, 1.25, 1.50, 1.75$ and 2.00).

2.4.2 Cross-Section Geometry

The ThinWall software package (1995) was used to design cross-sections with the desired nominal λ_s values of 1.1, 1.6 and 2.4. Table 2.8 summarizes the cross-sectional dimensions, using the conventions of Figure 2.18. Figure 2.19 shows the output of ThinWall for a 3Cr12 cross-section with thickness 1.20 mm, by way of an example. The minimum in the curve corresponds to the local buckling stress, while the asymptotic part of the curve represents Euler buckling. The initial modulus E_0 was used in the analysis. Since distortional buckling is not an issue, the cross-sectional slenderness could be increased by simply decreasing the section thickness. The comments made in Section 2.3.5 regarding the r_i/t ratios apply.

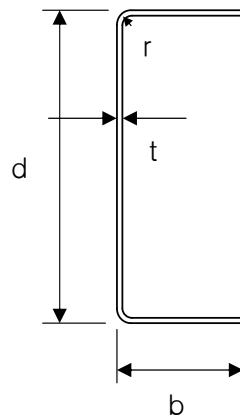


Figure 2.18 Specimen Dimensions (Plain Channels)

Table 2.8. Specimen Dimensions (Plain Channels)

Material	λ_s	d	b	r	t	σ_{cr}	ω_d
	-	mm	mm	mm	mm	MPa	mm
3Cr12	1.18	100.00	40.00	4.00	1.80	236.6	0.65
3Cr12	1.76	99.40	39.70	4.00	1.20	105.9	0.65
3Cr12	2.47	99.05	39.53	4.00	0.85	53.7	0.65
304	1.08	100.00	40.00	4.00	1.80	200.2	0.65
304	1.62	99.40	39.70	4.00	1.20	89.7	0.65
304	2.27	99.05	39.53	4.00	0.85	45.5	0.65
430	1.10	100.00	40.00	4.00	1.80	219.5	0.65
430	1.64	99.40	39.70	4.00	1.20	98.3	0.65
430	2.31	99.05	39.53	4.00	0.85	49.8	0.65

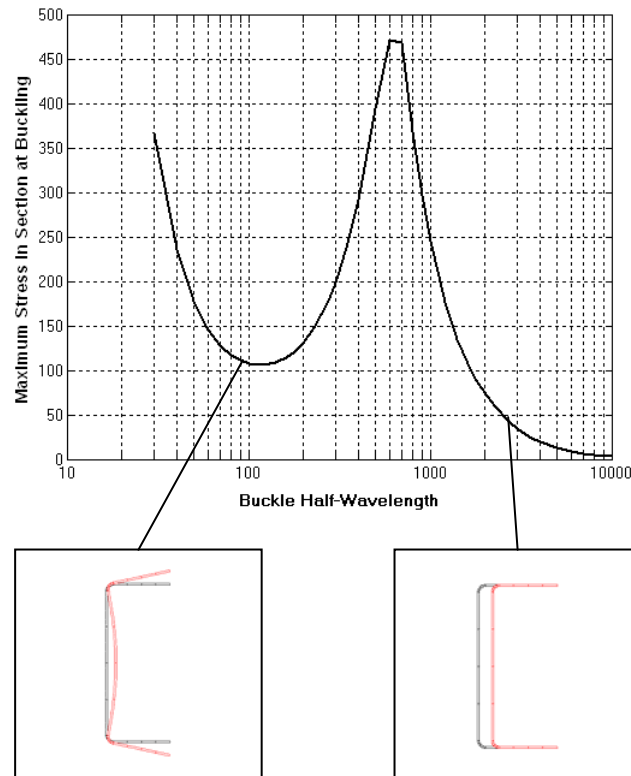


Figure 2.19. ThinWall Analysis Output

2.4.3 Imperfections

An overall imperfection in the shape of a half sine-wave with amplitude $L_e/1500$ was included in the analysis. Since local buckling causes the effective centroid to shift towards the web in this type of section, it was ensured that the overall imperfection resulted in a load eccentricity away from the web, thus simulating a worst case scenario. The overall imperfection was combined with an imperfection in the shape of the local buckling eigenmode. The amplitude was calculated using the Walker equation (Eq. 23). Figure 2.20 shows an exaggerated picture of the initial imperfection of a 1000 mm long 3Cr12 channel with a thickness of 1.8 mm.

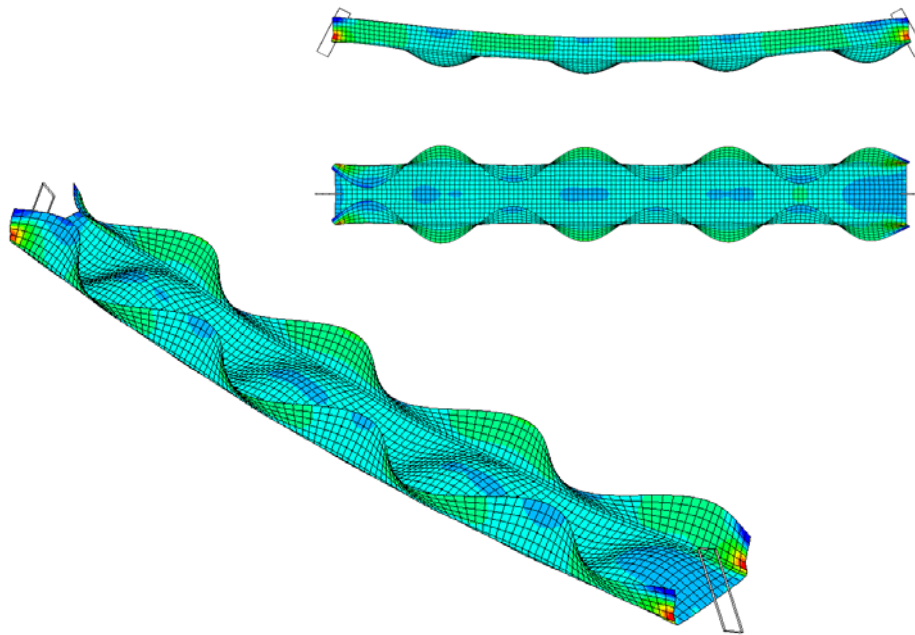


Figure 2.20. Initial Imperfection (PC3Cr12_180_1000)

2.4.4 Material Properties

The material properties of the 3Cr12, 304 and 430 alloys obtained in the experimental program (Becque and Rasmussen 2006) were used as input in the FE model. Anisotropic yielding was taken into account using Hill's criterion. The corner regions were given increased material properties in accordance with the experimental measurements.

2.4.5 FE Analysis Results

72 parametric studies were performed, including any combination of the three alloys, the three λ_s values and the eight λ_o values. All tests were modeled with pinned end conditions.

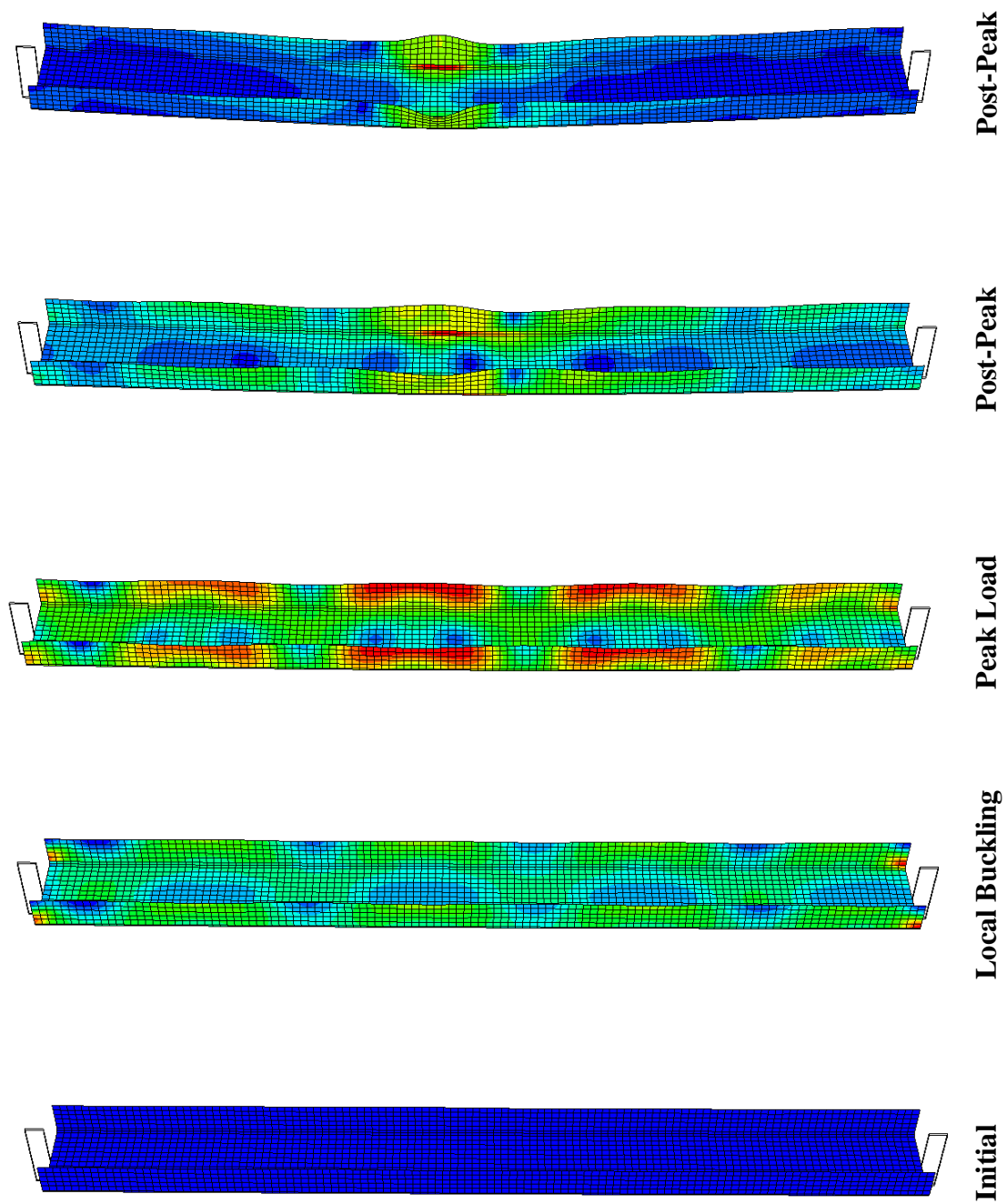


Figure 2.21. Deformations under Progressive Loading (Plain Channel)

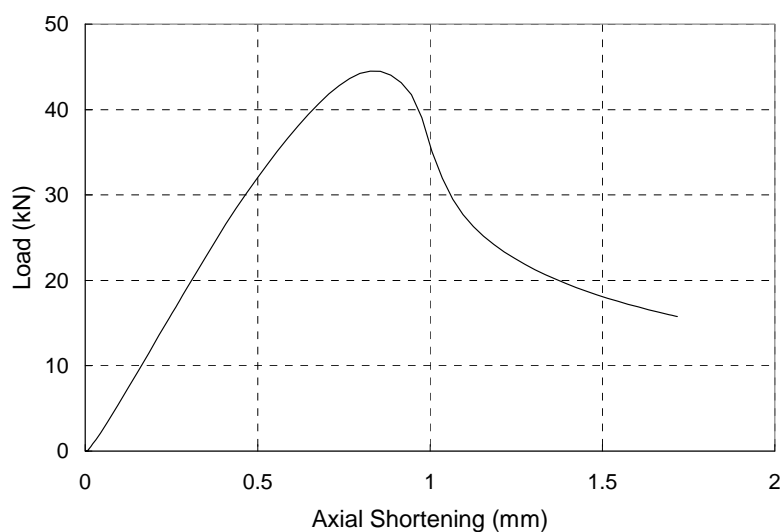


Figure 2.22. Load vs. Axial Shortening (PC3Cr12_1.80_1000)

The ultimate load P_u of each specimen is listed in Table D2 of Appendix D under the heading “Test”. Each specimen is identified by a unique label, starting with “PC” to indicate a plain channel, followed by the alloy, the wall thickness (in mm) and the effective length (in mm). For instance, PC430_1.20_500 is a plain channel with an effective length of 500 mm, manufactured from 430 stainless steel plate with a thickness of 1.20 mm.

The results are also presented graphically in Figures D.10 to D.18 of Appendix D, which plot the load capacity P_u versus the effective length L_e for a specific value of λ_s , or in non-dimensional form: $P_u/P_{0.2\%}$ versus the overall slenderness λ_o .

As an example, Figure 2.21 shows the deformations of specimen PC3Cr12_1.80_1000 obtained from ABAQUS at various steps of loading. The contours represent Von Mises surface stresses. Figure 2.22 shows the load vs. axial shortening output of the same specimen.

2.5 Parametric Studies of Tubular Sections

2.5.1 Introduction

A reasonable amount of test results on stainless steel SHS and RHS columns are available in literature. Experimental work has been carried out by Rasmussen and Hancock (1993), Talja and Salmi (1995), Liu and Young (2002), Gardner and Nethercot (2003), Young and Liu (2003), Young and Lui (2006), and Gardner et al. (2006). A total of 112 data points are available. However, a large amount of the collected data relates to overall buckling without the influence of local buckling. Only those tests were retained where the cross-sectional slenderness λ_s reached above 0.673. According to the Winter equation only sections with $\lambda_s > 0.673$ are susceptible to local buckling. The 60 selected data points are listed in Table D3a of Appendix D and presented graphically in Figures D.19 to D.24 (SHS) and D.28 to D.32 (RHS).

The cross-sectional slenderness values λ_s of the experimental results in Table D3a range from 0.69 to 1.27. No experimental data are available for hollow sections with a λ_s value above 1.27. Additional data was therefore generated for SHS with high cross-sectional slenderness using the FE model, in particular for $\lambda_s = 1.1$, $\lambda_s = 1.7$, and $\lambda_s = 2.3$. Realistic material properties which reflect the high degree of cold-working undergone by SHS and RHS sections during their manufacturing process were needed as input in the FE analysis. They were obtained from an experimental program carried out by Rasmussen and Hancock (1993) on austenitic SHS columns. This particular program was selected because the material properties of both the side surfaces and the corners regions were well reported. Making use of these material properties, the FE model was first verified against the eight tests described in (Rasmussen and Hancock, 1993). Subsequently, parametric studies were performed where the section thickness was gradually reduced to match the desired λ_s values.

2.5.2 Verification

2.5.2.1 Test Program

The experimental program described in (Rasmussen and Hancock 1993) includes two stub column tests and six long column tests on 80x80x3.0 SHS. The long columns were tested between spherical rotational bases, ensuring pinned end conditions, and were all observed to fail by overall buckling without any local buckling. Three nominal specimen lengths were considered: 1000 mm, 2000 mm and 3000 mm. For each length, one specimen was tested under a concentric axial force, applied at the geometric centroid of the section, while its twin specimen was tested with a nominal eccentricity of $L_e/1000$ at mid-length. The effective length L_e , measured between the centre points of the bearings, equaled the specimen length plus an additional 450 mm. The exact eccentricities at mid-length about both principal axes, $v_{o,x}$ and $v_{o,y}$, were calculated from the measured values of overall imperfections and end eccentricities and are listed in Table 2.9, together with the measured dimensions and the ultimate load P_u of each specimen.

All eight specimens were cold-formed from annealed austenitic type 304L stainless steel virgin coil. Compression coupons were cut from the face adjacent to the seam weld, from the face opposite to the weld, and from the corner area, as illustrated in Figure 2.23. The resulting compressive stress-strain curves are plotted in Figure 2.24, while the material properties are summarized in Table 2.10. The corner regions again demonstrated an elevated 0.2% proof stress, as a result of the more pronounced cold-working they underwent during the cold-rolling process.

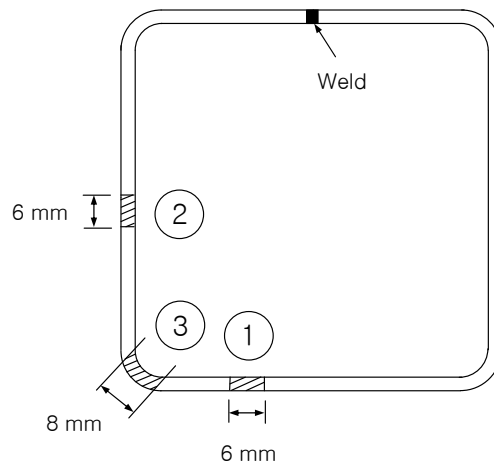


Figure 2.23. Location of the Compression Coupons

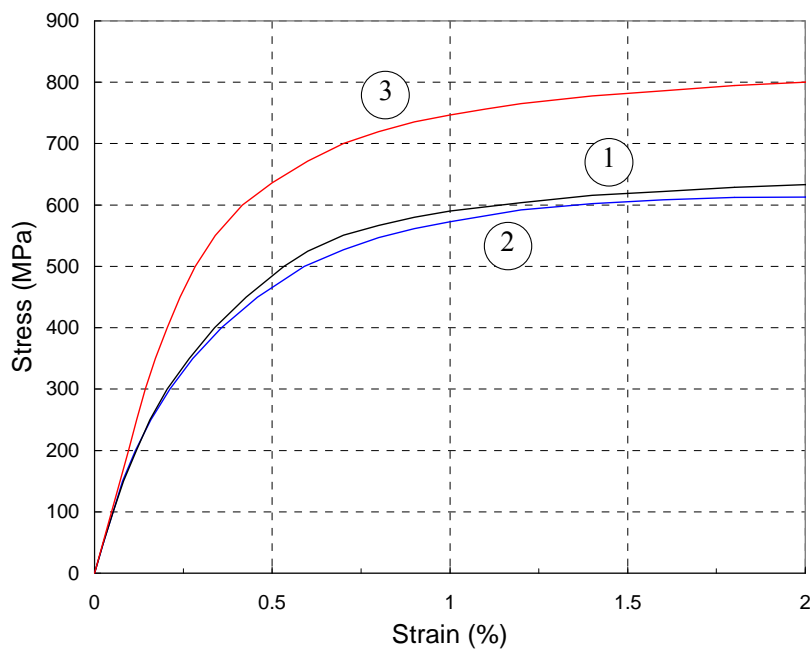


Figure 2.24. Compressive Stress-Strain Curves

Table 2.9. Summary: FE modeling of (Rasmussen and Hancock 1993)

Specimen	Alloy	L	L _e	b	t	r	v _{o,x}	v _{o,y}	P _u (Test)	P _u (FE)	FE/Test
	-	mm	mm	mm	mm	mm	-	-	kN	kN	-
S1SC1	304L	300	150	80.4	3.00	4.0	-	-	485	482.4	0.995
S1SC2	304L	298	149	79.7	3.00	4.0	-	-	471	482.4	1.024
S1L1000C	304L	1001	1451	80.5	2.90	4.5	L/2070	0	390	329.3	0.844
S1L1000E	304L	1001	1451	80.3	2.98	3.5	L/1610	L/2900	344	334.7	0.973
S1L2000C	304L	2000	2450	80.4	2.99	4.5	L/4080	L/4080	193	198.0	1.026
S1L2000E	304L	2000	2450	80.6	2.93	4.5	L/600	L/2720	158	171.3	1.084
S1L3000C	304L	3002	3452	80.7	2.95	4.0	L/1640	L/2300	96	108.6	1.131
S1L3000E	304L	3001	3451	80.2	2.98	4.0	L/650	L/6900	98	102.7	1.048
Average				80.4	2.97	4.1					1.016
St. Dev.				0.3	0.04	0.4					0.085

Table 2.10. Compressive Material Properties (Rasmussen and Hancock 1993)

Coupon	E_0	$\sigma_{0.2\%}$	n
	GPa	MPa	-
Face 1	195	420	3.1
Face 2	197	410	3.5
Corner	210	645	5.7

2.5.2.2 FE Model

The experimentally measured stress-strain curves were input in the FE model in the form of true stress vs. true strain curves, as required by ABAQUS. The corner properties were assigned to an 8 mm strip around the corners, equal to the width of the test coupons, as shown in Fig. 2.23. Anisotropy was neglected since no tests were carried out to determine the variation of the material properties in different directions relative to the rolling direction. Material testing on the 304 alloy by Becque and Rasmussen (2006, 2007) previously indicated a fairly low amount of anisotropy to be present in this alloy, especially when compared to the ferritic alloys. Typically the 0.2% proof stress in the transverse direction was shown to be only 3-5% higher than the 0.2% proof stress in the rolling direction. Thus it was deemed acceptable to neglect anisotropy.

The measured specimen dimensions were used in the FE model. The end sections were allowed to rotate about both principal axes of the cross-section to simulate the actual boundary conditions imposed by the rotating seats.

Residual stresses are generally introduced into cold-formed tubes as a result of the deformations undergone during the cold-forming fabrication process, and due to the thermal gradients which are induced during the welding of the seam. When cutting coupons from the stainless steel tubes, it was observed that they curved longitudinally as a result of the through-thickness bending residual stresses. However, during the tension tests the coupons are straightened out again by the testing machine, which

approximately reintroduces the bending residual stresses. Therefore, if the material properties are established from tension coupons cut from the cross-section, the effects of bending residual stresses are inherently taken into account. The same rationale holds true for the compressive coupons, which are straightened out again when tightening the compressive test jig.

Research has been conducted on the magnitude of the membrane residual stresses induced by welding into stainless steel tubes (Bredenkamp et al. 1992, Lagerqvist and Olsson 2001). For modeling purposes an idealized distribution, based on the work by Masubuchi (1980) and shown in Figure 2.25, can be used. It is recommended that c be taken as $b/5$, where b is the plate width. The maximum tensile residual stress can be assumed equal to the 0.2% proof stress. Consequently the compressive residual stress σ_c can be calculated from equilibrium.

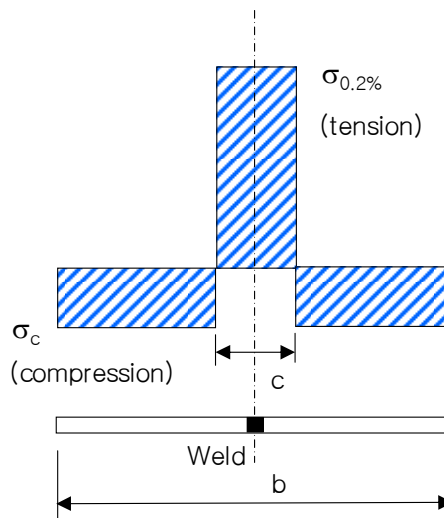


Figure 2.25. Membrane Residual Stresses

The residual stress distribution shown in Figure 2.25 should be applied to the welded face of the cross-section. Measurements of the membrane residual stresses on the face opposite to the welded seam, as part of (Rasmussen and Hancock 1993) confirm that the

membrane residual stresses on this face are indeed negligible.

The proposed stress distribution shown in Fig. 2.25 was incorporated into the ABAQUS model of specimen S1L3000C. The *INITIAL CONDITIONS command was thereby used to model the residual stresses. The difference in ultimate load P_u , when compared to the same model without residual stresses, was 0.4% and deemed negligible. This conclusion concurs with a more extensive study into the sensitivity of square and rectangular hollow sections to residual stresses by Gardner and Nethercot (2004), who ran ABAQUS simulations for stub columns and long columns, with and without the effect of residual stresses. It was concluded that, while residual stresses typically cause a minor reduction in stiffness prior to ultimate load, the ultimate load carrying capacity itself is unaffected.

Since the main focus of this section of the research is to predict the load carrying capacity P_u for specimens with different slenderness values λ_s and λ_o , residual stresses were not incorporated in the parametric studies of hollow sections, or in the modeling of the experimental program by Rasmussen and Hancock (1993).

The magnitude of local imperfections was not investigated as part of the experimental program. Since all six long columns fail by overall buckling, the magnitude of the local imperfections is not deemed a critical parameter. An imperfection in the shape of the local buckling eigenmode with amplitude 0.2 mm was added to the model. This amplitude yielded good predictions of the stub column capacity, and was further used in the modeling of the long columns. The overall imperfections were modeled as a half sine-wave about each principal axis and were given the amplitudes $v_{o,x}$ and $v_{o,y}$ listed in Table 2.9.

2.5.2.3 FE Results

The FE model was successful in predicting the observed failure modes of overall buckling in the long columns and local buckling in the stub columns. Figure 2.26 shows

the failed shape of specimen S1L3000C.

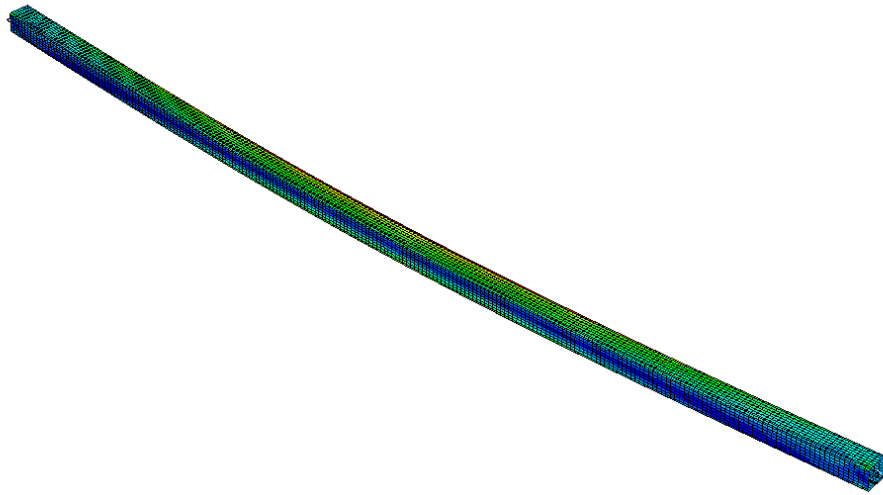


Figure 2.26. Buckled Shape of Specimen S1L3000C

Table 2.9 indicates that the ultimate load capacities P_u were generally well predicted. The average ratio of the predicted load capacity to the experimentally measured load capacity was 1.016 with a standard deviation of 0.085. The standard deviation was slightly higher than the value of 0.035, obtained in Section 2.2 when modeling the experimental program of the lipped channels. It is believed that this higher standard deviation can mainly be attributed to a higher variability in material properties. Square hollow sections undergo significant strain-hardening as a result of cold-working during the manufacturing process, resulting in varying material properties throughout the section as well as a greater variability of properties between specimens. By comparison, an extensive FE modeling program of stainless steel SHS and RHS pin-ended columns by Gardner and Nethercot (2004), using similar modeling techniques, obtained an average ratio of the predicted capacity to the test result of 1.03 and 0.97 for the SHS and RHS sections respectively, with respective standard deviations of 0.16 and 0.10.

2.5.3 Parametric Studies

The experimental program by Rasmussen and Hancock (1993) formed the starting point for parametric studies. Retaining the cross-sectional shape and the material properties of the side surfaces and the corners, the wall thickness was reduced to obtain the desired λ_s values. The ThinWall software (1995) was used to calculate the elastic local buckling stresses. Table 2.11 summarizes the results.

Table 2.11. Specimen Dimensions (SHS)

Material	λ_s	b	r	t	σ_{cr}	ω_d
	-	mm	mm	mm	MPa	mm
304L	1.10	78.7	4.25	1.70	345	0.55
304L	1.67	78.1	4.25	1.10	148	0.55
304L	2.26	77.8	4.25	0.80	81	0.55

The specimens were modeled with pinned ends, allowing overall buckling to occur about one principal axis. Eight overall slenderness values were considered, ranging from 0.25 to 2.0 in 0.25 increments. An overall eccentricity of $L_e/1500$, in the shape of the first overall buckling mode, was incorporated into the model. In addition, a local imperfection in the shape of the local buckling eigenmode with an amplitude ω_d calculated from Eq. (23), was also included. Figure 2.27 illustrates the initial imperfections. Only half of the tube was modeled with symmetry boundary conditions applied along the centerline.

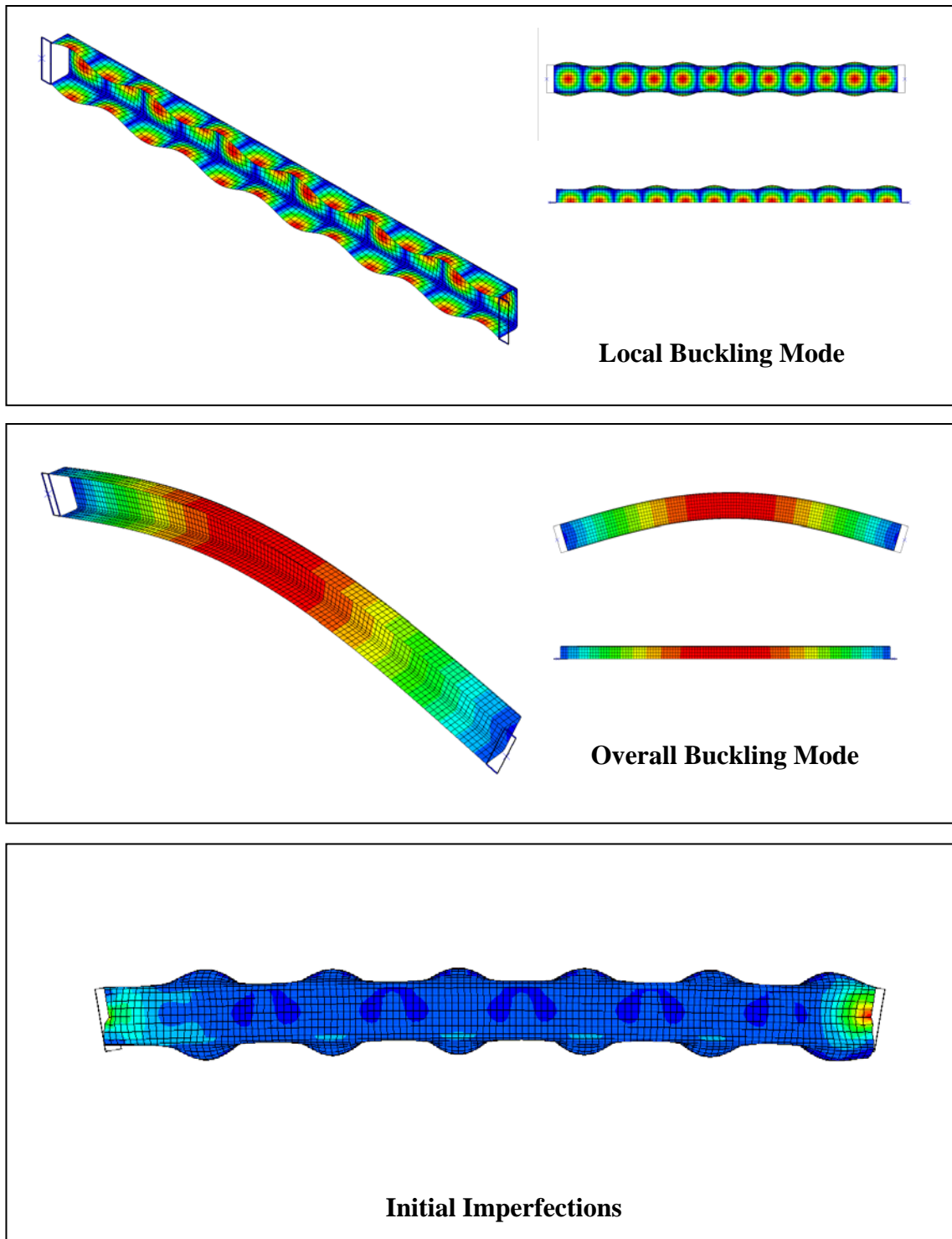


Figure 2.27. Initial Imperfections (SHS)

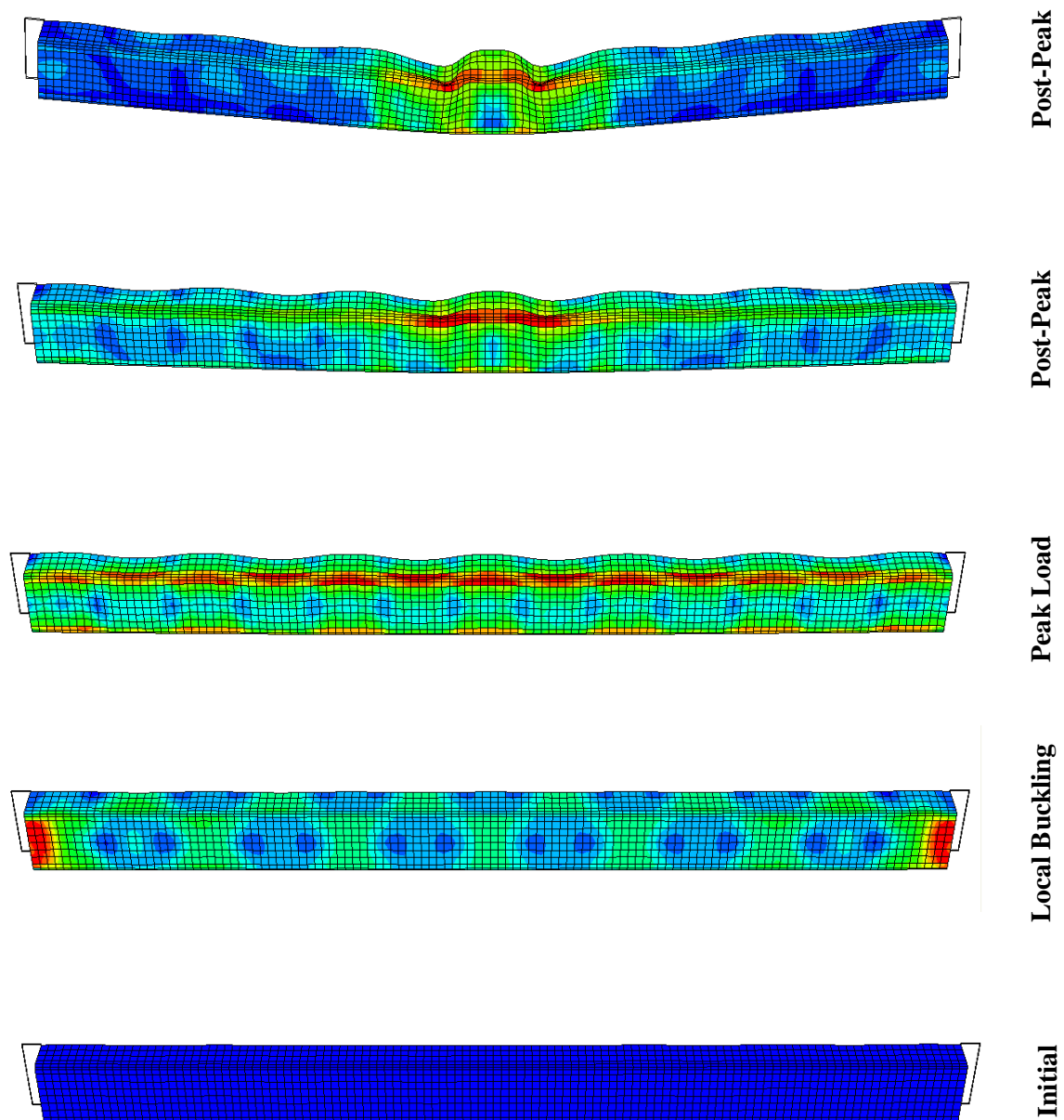


Figure 2.28. Deformations under Progressive Loading (SHS)

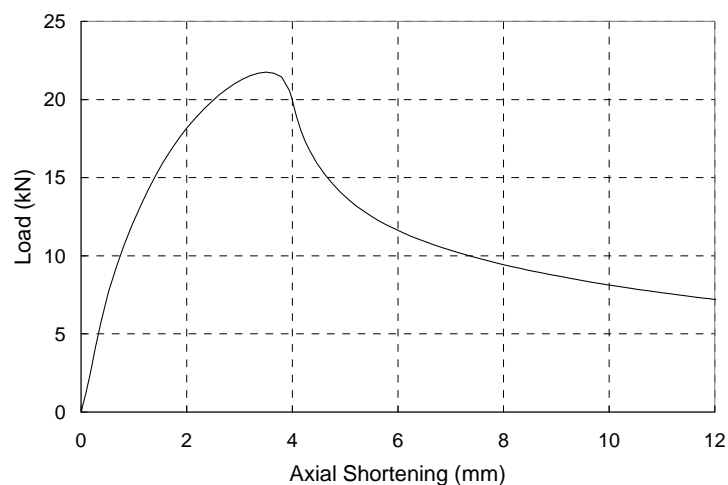


Figure 2.29. Load vs. Axial Shortening (SHS304L_0.80_1000)

The results of the FE studies on SHS columns are summarized in Table D3b of Appendix D, with the ultimate load P_u listed under the heading “Test”. Consistent with previous labeling conventions, the specimens are identified by their cross-section, alloy, thickness and effective length. For instance, SHS304L_0.80_1000 is a 1000 mm long SHS specimen of 304L stainless steel with a wall thickness of 0.80 mm. The results are also presented graphically in Figures D.25 to D.27 of Appendix D, which indicate the load capacity as a function of the effective length or the overall slenderness.

By way of an example, Figure 2.28 shows the deformed state of specimen SHS304L_0.80_1000 at various stages of loading. The contours represent von Mises surface stresses. Figure 2.29 shows the axial shortening vs. load diagram of the same specimen.

2.6 Parametric Studies of Back-to-Back Channels

2.6.1 FE Model

2.6.1.1 Contact

When modeling back-to-back channels, the additional problem of physical contact between the webs needs to be addressed. If not, the channels are able to deform into each other, since ABAQUS does not recognize contact between surfaces unless it is explicitly accounted for in the model. Surface-to-surface type contact was defined between the outside surfaces of the webs. Despite the fact that the mid-surfaces of the plate components are modeled, ABAQUS takes into account the plate thickness, such that contact occurs between the outer surfaces. The interface of the surfaces was modeled as frictionless.

The physical connections between the two channels, such as bolts or screws, were not explicitly modeled. Figure 2.30 provides a plot of the gap distance along the edge of the channels and along the centerline of the webs, for a 500 mm long, a 1000 mm long and a 2000 mm long specimen in the post-ultimate range. From observation of the gap distances over the whole load history, it was concluded that the two channels always remain in contact with each other at discrete points and never separate. The contact points are located along the edges of the channels for the shorter specimens, as illustrated in Figure 2.31, while they can occur along the centerline of the web for the longer specimens. In all cases the gap distance along the edges remains small. Figure 2.32 provides a contour plot of the gap distance for a 1500 mm long specimen. The dark blue areas represent the locations where the gap is virtually closed, while the red areas experience the largest gap. Without explicitly modeling the connectors, the output of the model thus provides an acceptable solution for channels which are connected back-to-back by means of discrete connectors such as screws, spot welds or bolts. These

connections ensure that the channels remain in contact with each other at certain points along the length, while being allowed to separate in between. In case bolts are used, a finite sliding of the web surfaces relative to each other at the bolt location is also possible, while the formation of a sub millimeter gap at the connector is not unimaginable. By not explicitly modeling the connectors, no interaction takes place between the local buckling pattern and the connector spacing, which does not unnecessarily complicate the problem. It could be argued that if connectors put any additional restraints on the local buckling shape, this could marginally increase the load bearing capacity, proving that the proposed solution errs on the safe side. It should be noted moreover that the restrictions imposed by the design standards on the connector spacing in compression members are rather lenient. For the I-sections under consideration in the next paragraph, AS/NZS:4673 (2004) requires connectors at the third points of the member length only, independent of the member length.

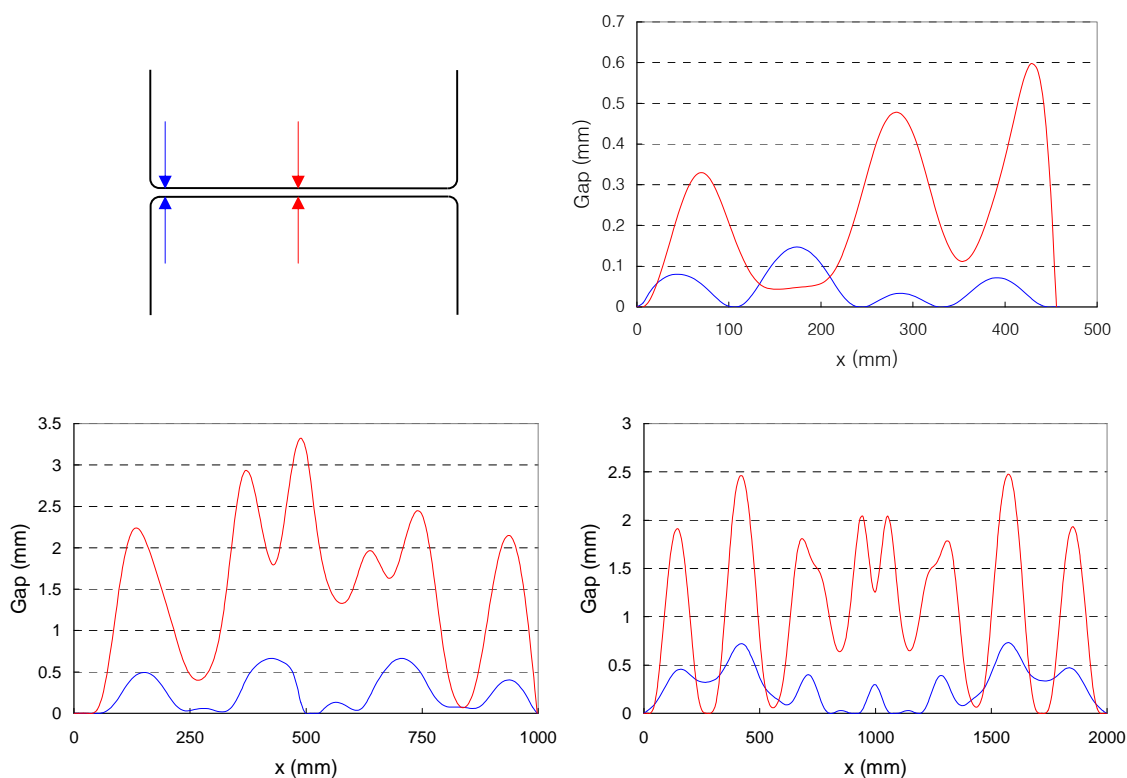


Figure 2.30. Gap Distance along Specimen Length

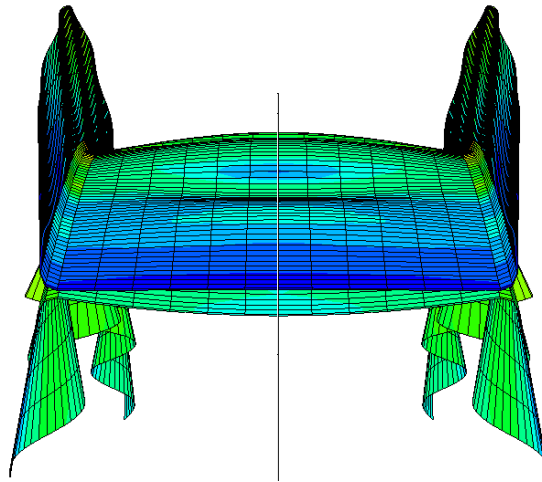


Figure 2.31. Cross-sectional Cut

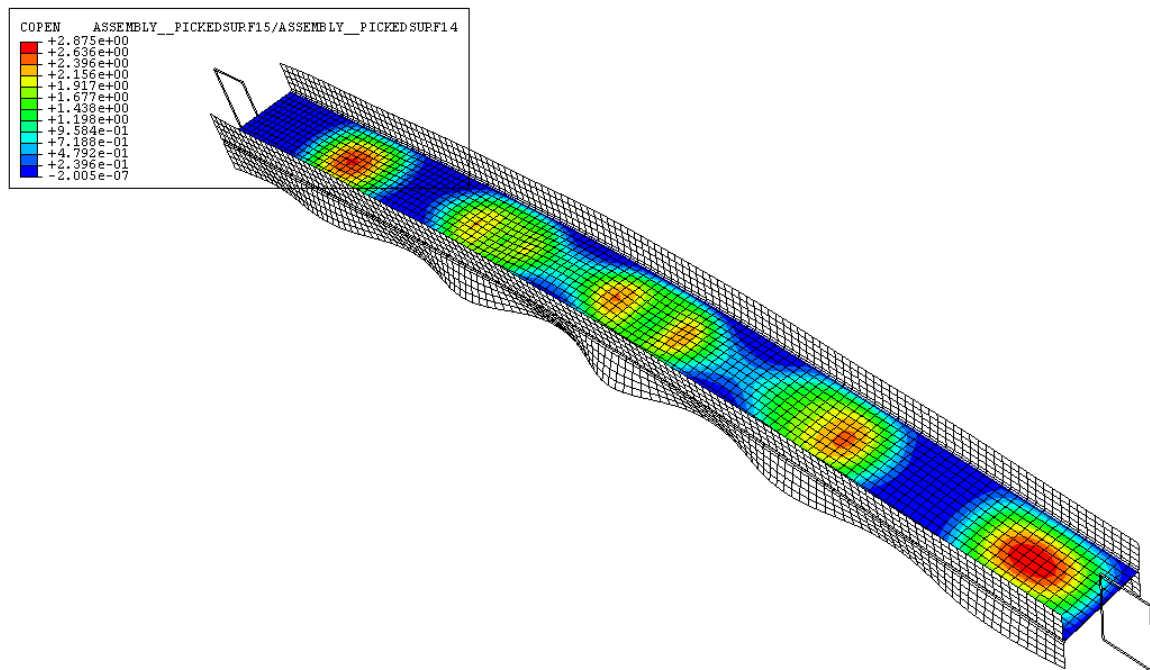


Figure 2.32. Contour Plot of the Gap Distance

2.6.2.2 Convergence and Stabilization

The inclusion of surface-to-surface contact into the model adds a discrete aspect to the problem, in a sense that the gap between the surfaces at a certain location can either be open or closed. This necessitates contact iterations within each load increment, where initial assumptions are made about each gap being open or closed, with these assumptions being adjusted in the next iteration. Not only does this significantly prolong the running time of the program, but many problems involving contact experience convergence problems and terminate prematurely. For the problem under consideration, ABAQUS was unable to reach a convergent solution in the initial step of the analysis, even though the problem was well-defined and the surfaces were in contact with each other at the beginning of the analysis. After more conventional efforts, such as reducing the initial step size, refining the mesh on either master or slave surface, choosing a coarser mesh, changing the matrix solving method or modifying the contact parameters, were exhausted, the problem was overcome by adding artificial damping to the problem. In this method viscous damping forces of the form:

$$\mathbf{F}_v = \mu \mathbf{M}^* \mathbf{v} \quad (25)$$

are added to the global equilibrium equations of the system. \mathbf{M}^* is an artificial mass matrix calculated with unit density, μ is the damping factor, $\mathbf{v} = \Delta \mathbf{u} / \Delta t$ is the vector of the nodal velocities and Δt is the time increment (which does not have a physical meaning in the context of this problem). The ABAQUS user can control the amount of damping added to the problem by specifying the damping factor μ . The default value of μ is 2×10^{-4} . Adding a large amount of damping to the problem may significantly alter the solution. Ideally, sufficient damping should be added to stabilize the calculations, yet not enough to adversely affect the accuracy of the solution. Trial-and-error runs indicated that, in the problem under consideration, stabilization was mainly required in the initial step to get the analysis underway. A damping factor μ_1 was therefore applied

over a first step, where both μ_1 and the step size were kept as small as possible by trial-and-error runs. In many cases, damping was terminated after this first step. Other cases required a more extensive second step with a reduced damping factor μ_2 , followed by a third analysis step without damping. The effect of damping on the solution can be checked by comparing the following ABAQUS output variables at the end of the analysis: ALLSD (= the total amount of energy dissipated through artificial damping), ALLSE (= the total amount of elastic strain energy), ALLPD (= the amount of energy dissipated through plasticity) and ALLIE (= the total internal energy of the system = ALLSE + ALLPD). If the total amount of energy dissipated through artificial damping is negligible compared to the other energy variables, the effect of the stabilization through damping on the solution can be ignored. Table D5 of Appendix D lists ALLSD, ALLSE, ALLPD and ALLIE for each of the analyses discussed in Section 2.6.2 (verification) and Section 2.6.3 (parametric studies). The table also lists the damping factor μ and the step size for each step involving damping. In the final column the ratio of ALLSD over ALLSE is calculated, as recommended by the ABAQUS manual (2005). It is seen that in all cases ALLSD is several orders of magnitude smaller than ALLSE. The average ratio of ALLSD/ALLSE is 0.1%. The ratio is less than 0.5% in all parametric studies. It is therefore concluded that the results are virtually unaffected by adding damping in the initial step(s).

2.6.2 Verification

2.6.2.1 Introduction

The FE model, inclusive of the additions discussed in Section 2.6.1, was verified against the experimental data presented in (Becque and Rasmussen 2007). The test program includes a total of 24 columns, constructed by connecting channels in a back-to-back configuration with sheet metal screws. Twelve 304 austenitic columns were tested, as

well as twelve 404 ferritic columns. All columns were tested with a nominal load eccentricity of $L_e/1500$ and failed by local-overall interaction buckling. The reader is referred to the full report for details.

2.6.2.2 Material Properties

The measured compressive stress-strain curves were incorporated into the model as true stress vs. true strain relationships. Static properties in the rolling direction (which is the longitudinal axis of the specimens) were used. Anisotropy was accounted for by means of Hill's criterion with the coefficients listed in Table 2.12, derived from the experiment.

Table 2.12. Anisotropy Coefficients

Material	R_{11}	R_{22}	R_{33}	R_{12}	R_{13}	R_{23}
304	1.00	1.03	1.01	1.01	1.00	1.00
404	1.00	1.12	1.10	1.10	1.00	1.00

Increased corner properties, obtained from tension tests on corner coupons, were assigned to the rounded parts of the corners.

2.6.2.3 Imperfections

The tests were conducted with a nominal end eccentricity of $L_e/1500$. This value needs to be corrected with the overall specimen imperfection v_o , obtained from the imperfection measurements, to find the eccentricity at mid-height. Tables 2.13 and 2.14 indicate that v_o is generally small and within the margin of error associated with positioning the specimens in the set-up with a certain end eccentricity. Therefore, one FE model was assembled for each set of twin specimens of a certain length, with the load applied at an eccentricity of $L_e/1500$ at both ends.

Table 2.13. I-Sections: 304 Series

Specimen	Material	Length		Eccentricity			Imperfection		Ultimate Load P_u		Ratio
		L	L_e	$e_{o,end}$	$e_{o,mid}$		v_o	ω_d	Test	FE	FE/Test
		(mm)	(mm)	(mm)	(mm)	-	(mm)	(mm)	(kN)	(kN)	-
I304_500_2	304	501	637	0.42	0.33	$L_e/1912$	0.092	0.42	55.24	58.87	1.066
I304_1000_1	304	999	1135	0.76	0.75	$L_e/1516$	0.008	0.42	47.25	45.30	0.959
I304_1000_2	304	999	1135	0.76	0.76	$L_e/1492$	-0.004	0.42	47.43	45.30	0.955
I304_1500_1	304	1499	1635	1.09	1.15	$L_e/1420$	-0.061	0.42	38.67	34.46	0.891
I304_1500_2	304	1498	1634	1.09	1.09	$L_e/1503$	0.002	0.42	37.63	34.46	0.916
I304_2000_1	304	2000	2116	1.41	1.38	$L_e/1532$	0.030	0.42	31.37	32.59	1.039
I304_2000_2	304	2000	2116	1.41	1.12	$L_e/1883$	0.287	0.42	31.07	32.59	1.049
I304_2500_1	304	2497	2613	1.74	1.14	$L_e/2291$	0.602	0.42	22.71	23.87	1.051
I304_2500_2	304	2497	2613	1.74	0.69	$L_e/3798$	1.054	0.42	22.94	23.87	1.040
I304_3000_1	304	2999	3115	2.08	1.91	$L_e/1634$	0.171	0.42	20.62	19.14	0.928
I304_3000_2	304	3000	3116	2.08	2.05	$L_e/1519$	0.026	0.42	18.30	19.14	1.046
Average											0.995
St. Dev.											0.065

Table 2.14. I-Sections: 404 Series

Specimen	Material	Length		Eccentricity			Imperfection		Ultimate Load P_u		Ratio
		L	L_e	$e_{o,end}$	$e_{o,mid}$		v_o	w_d	Test	FE	FE/Test
		(mm)	(mm)	(mm)	(mm)	-	(mm)	(mm)	(kN)	(kN)	-
I404_500_1	404	499	635	0.42	0.38	$L_e/1663$	0.041	0.45	69.83	68.45	0.980
I404_500_2	404	499	635	0.42	0.41	$L_e/1531$	0.009	0.45	71.79	68.45	0.953
I404_1000_1	404	999	1135	0.76	0.73	$L_e/1562$	0.030	0.45	56.53	55.10	0.975
I404_1000_2	404	999	1135	0.76	0.79	$L_e/1433$	-0.035	0.45	56.22	55.10	0.980
I404_1500_1	404	1500	1636	1.09	1.27	$L_e/1285$	-0.182	0.45	40.96	42.23	1.031
I404_1500_2	404	1499	1635	1.09	1.26	$L_e/1298$	-0.170	0.45	42.00	42.23	1.005
I404_2000_1	404	1999	2115	1.41	1.56	$L_e/1355$	-0.151	0.45	37.91	32.59	0.860
I404_2000_2	404	1999	2115	1.41	1.40	$L_e/1514$	0.013	0.45	37.48	32.59	0.869
I404_2500_1	404	2497	2613	1.74	1.59	$L_e/1645$	0.154	0.45	29.90	26.67	0.892
I404_2500_2	404	2499	2615	1.74	1.80	$L_e/1455$	-0.054	0.45	27.24	26.67	0.979
I404_3000_1	404	3001	3117	2.08	1.85	$L_e/1681$	0.224	0.45	21.20	20.85	0.984
I404_3000_2	404	2999	3115	2.08	1.18	$L_e/2637$	0.895	0.45	24.42	20.85	0.854
Average											0.947
St. Dev.											0.059

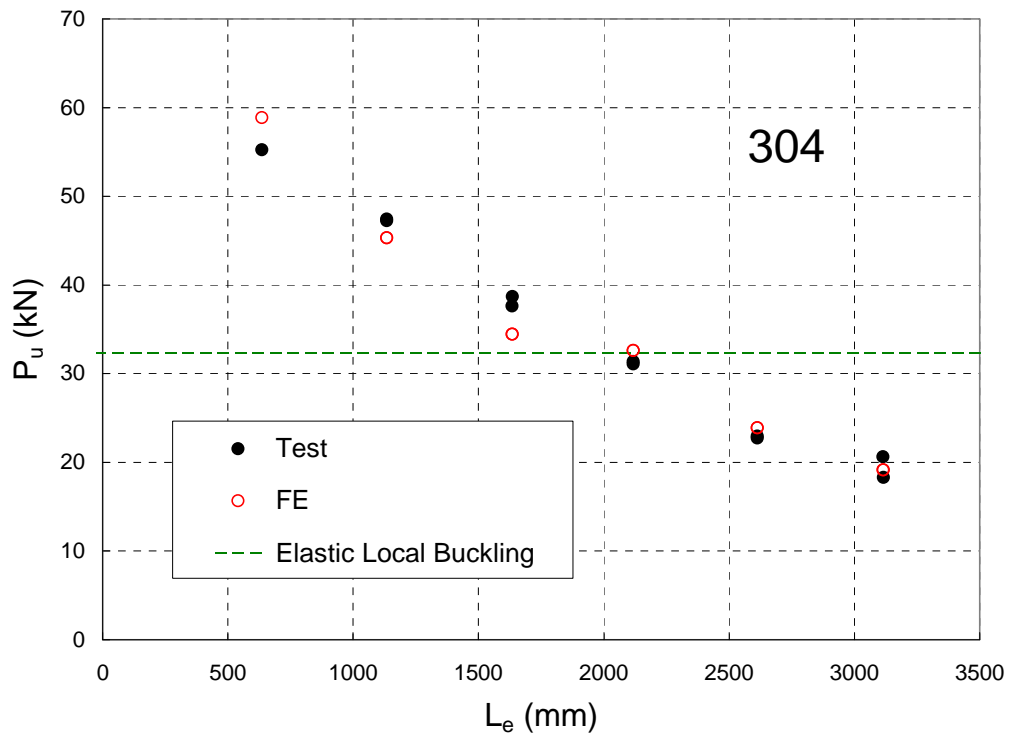


Figure 2.33. FE Modeling of 304 I-Sections

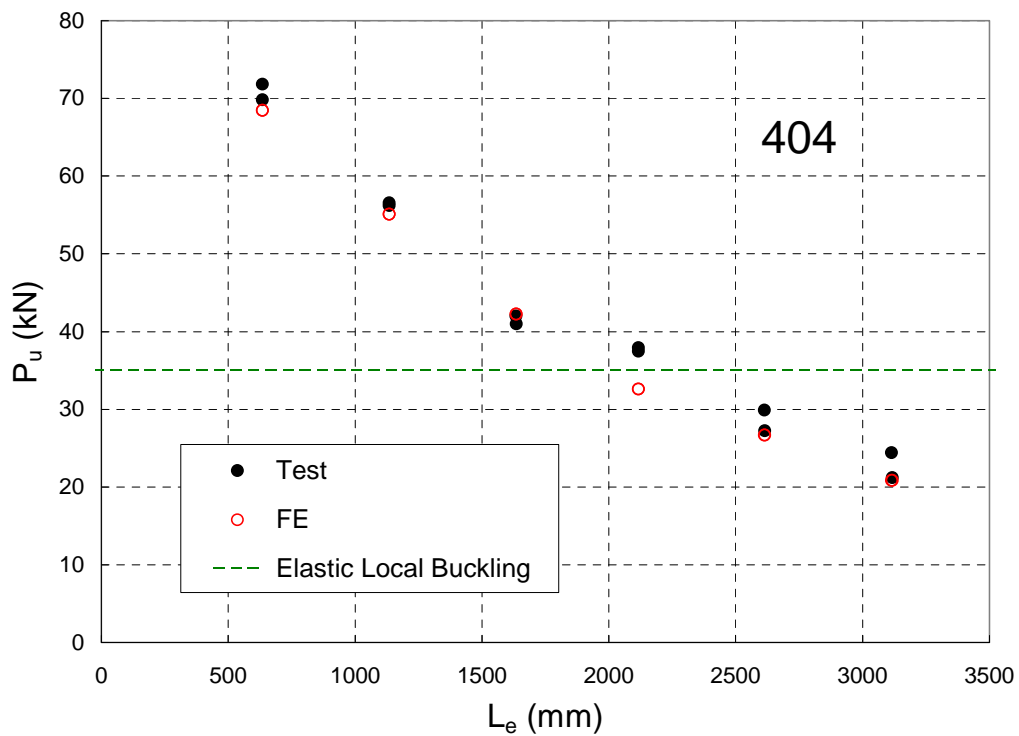


Figure 2.34. FE Modeling of 404 I-Sections

A local imperfection in the shape of the local buckling eigenmode was also included in the model. A realistic value of the local buckling amplitude was previously deducted from the measured imperfection data in (Becque and Rasmussen 2007). The calculations resulted in: $\omega_d = 0.42$ mm for the 304 specimens and $\omega_d = 0.45$ mm for the 404 specimens.

2.6.2.4 Results

Tables 2.13 and 2.14 compare the ultimate loads P_u generated by the FE model to those obtained from the experiment, for the 304 and the 404 alloy specimens respectively. Good agreement was obtained: the average ratio of the FE predicted load capacity to the experimentally measured load capacity was 0.97 with a standard deviation of 0.06. The results are presented graphically in Figures 2.33 and 2.34. It is seen that, both for the 304 and 404 specimens, the largest discrepancy between the FE prediction and the experiment occurs around the local buckling load. This is attributed to the imperfection sensitivity of the test points in this region.

In all analyses, the FE model predicted the right failure mode of interaction between local and overall flexural buckling, and accurately displayed the failed shape. Figures 2.35a to 2.35d show the failed shape of a number of back-to-back channels of various lengths, as observed in the experiment, and as predicted by the FE model.

Figure 2.36 shows the experimentally measured deformations of a typical specimen (I404_1500_2) and compares them to the deformations predicted by the FE model. Figure 2.36a plots the axial shortening of the specimen over the load history, Figure 2.36b provides the lateral displacement at mid-height and Figure 2.36c shows the rotations at both ends. Figure 2.36d displays the local displacements of the flange measured at specific locations by LVDTs L1 and L2, located on the tension flange tips near the end of the specimen (Figs. 2.17 and 2.21 of (Becque and Rasmussen 2007)), and compares them to the displacements of the corresponding nodes in the FE model.

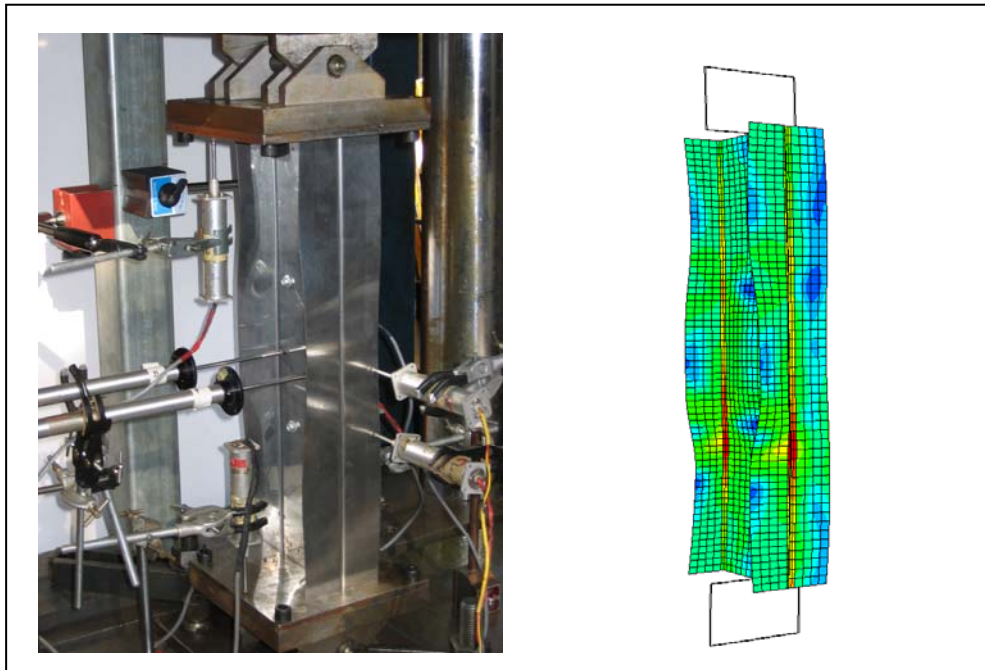
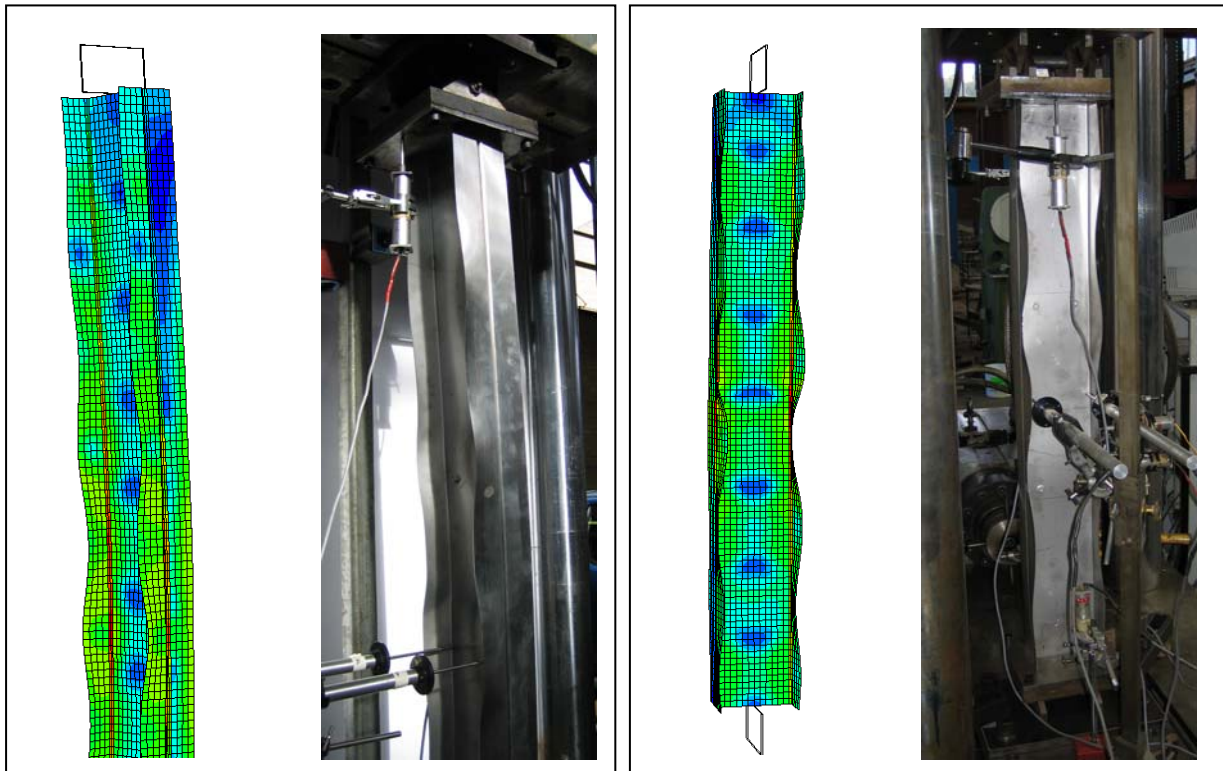
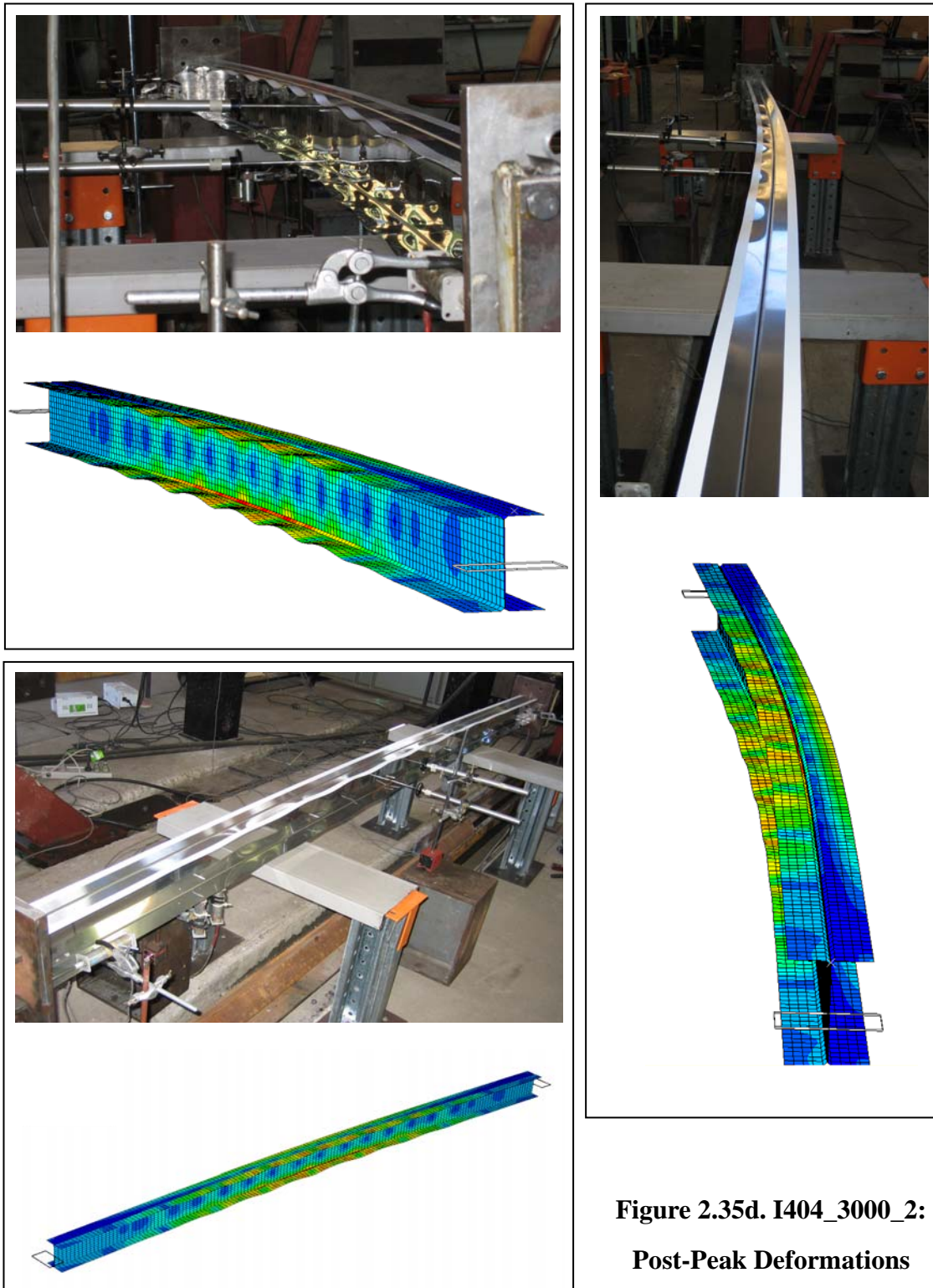


Figure 2.35a. I404_500_2: Post-Peak Deformations



**Figure 2.35b. I304_1500_1:
Post-Peak Deformations**

**Figure 2.35c. I304_1000_1:
Post-Peak Deformations**



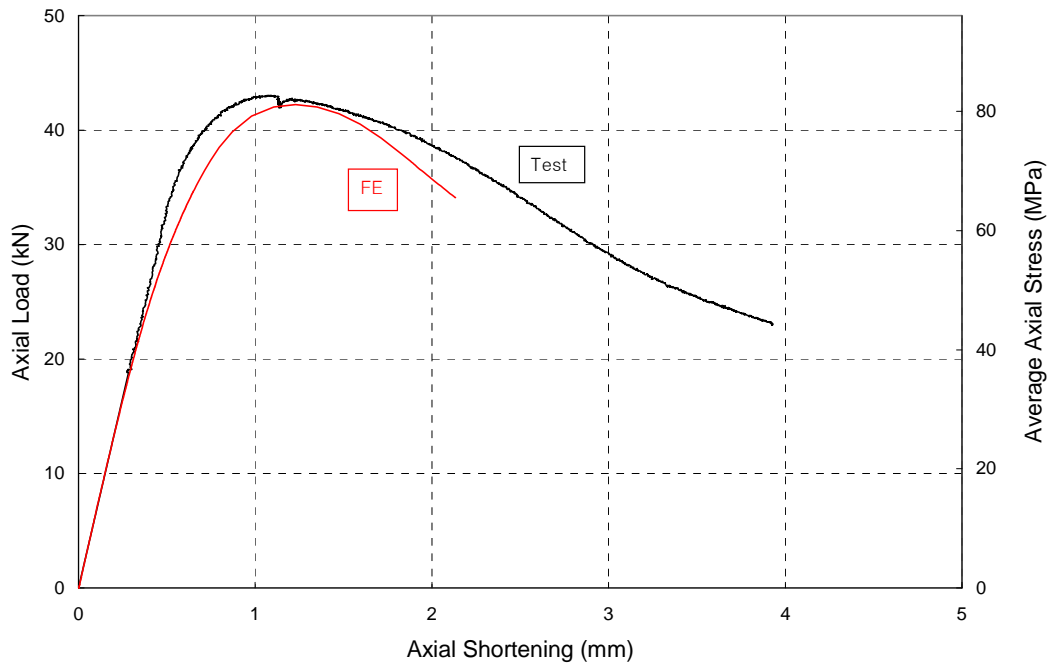


Figure 2.36a. I404_1500_2 : Axial Load vs. Axial Shortening

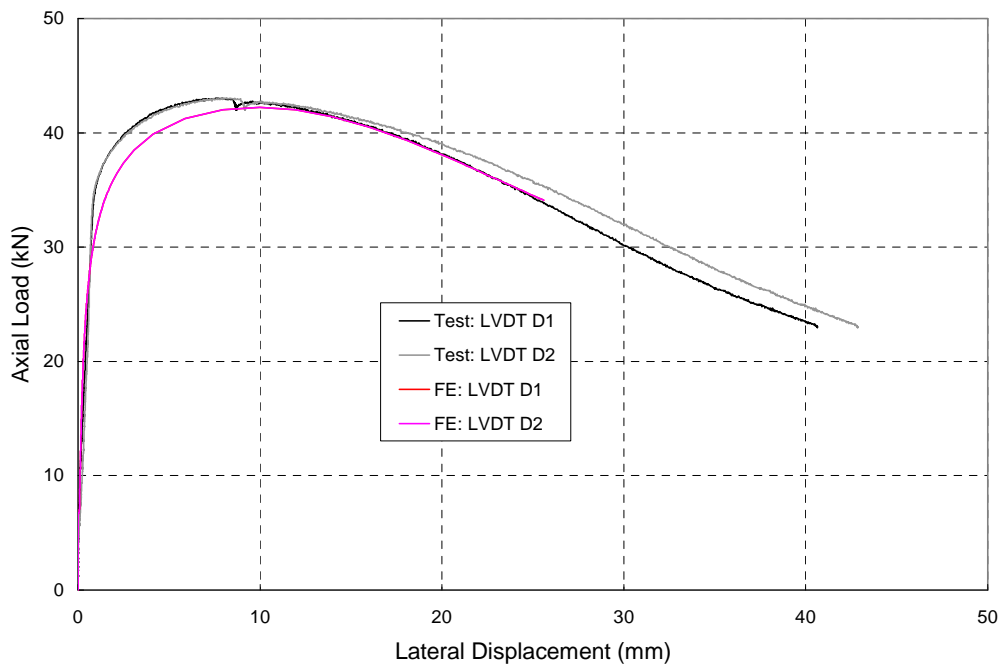


Figure 2.36b. I404_1500_2 : Axial Load vs. Lateral Displacement

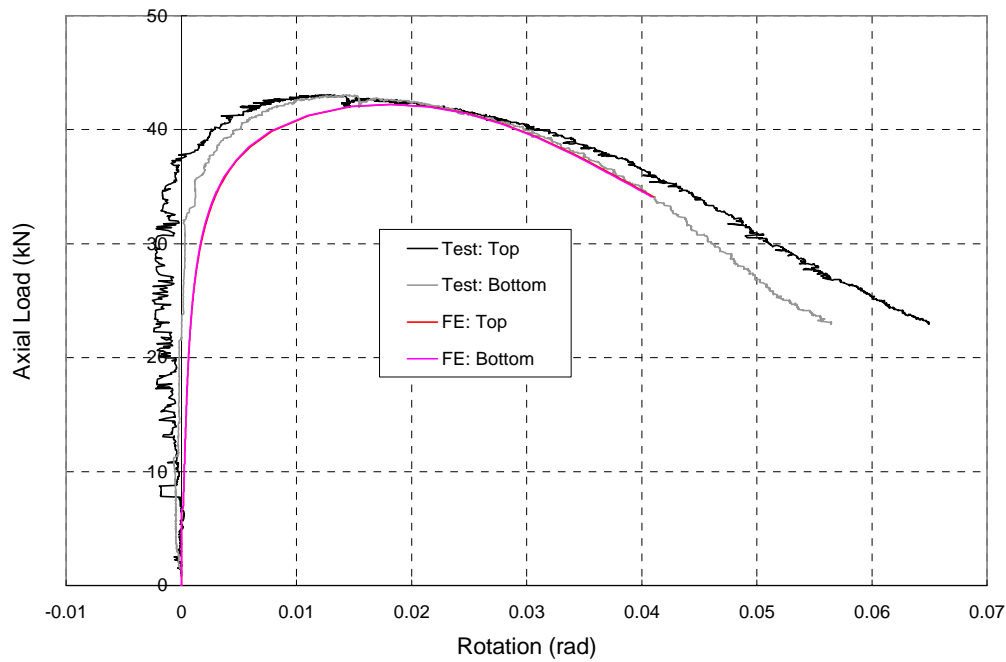


Figure 2.36c. I404_1500_2 : Axial Load vs. End Rotations

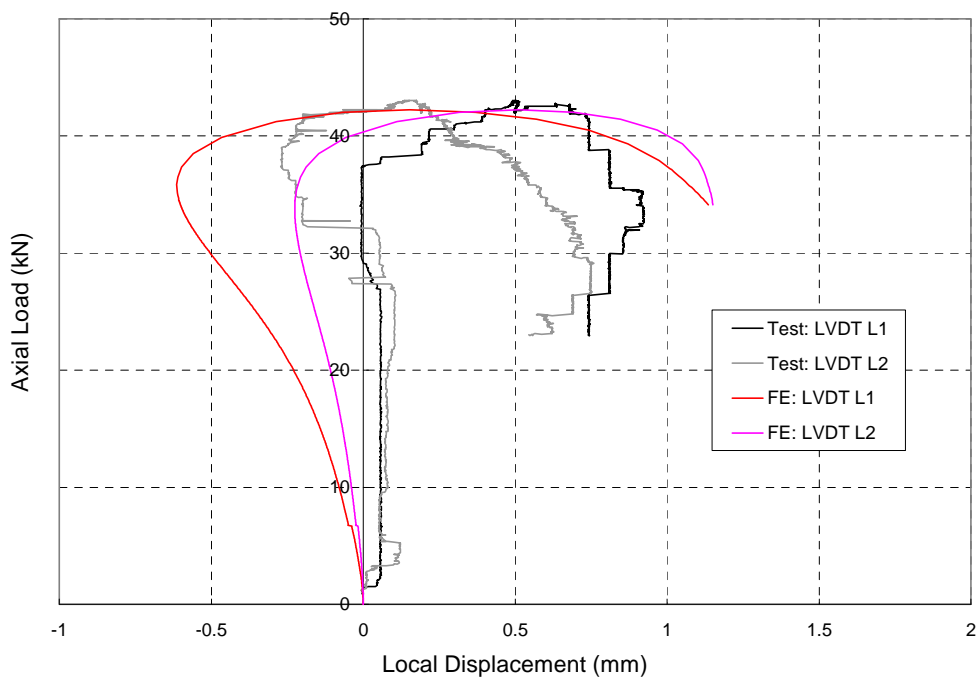


Figure 2.36d. I404_1500_2 : Axial Load vs. Local Displacements

Four similar graphs are provided in Appendix C for each of the 24 specimens included in the experimental program. It should be noted that static material properties were used in the FE model and that consequently, the FE generated curves should be compared to the (static) low points of the experimental curves, obtained by halting the test for 2 minutes. It is concluded that the deformations are generally well predicted by the FE model. The local buckling displacements are rather sensitive to the location of the measurements, but nevertheless the general local buckling behaviour is reasonably well predicted in most cases. Exaggerated local buckling deformations were typically predicted below the local buckling load, since an explicit initial imperfection in the shape of the local buckling mode was included in the model.

In conclusion, the proposed FE model was successful in predicting the failure mode, the ultimate load capacity and the deformations of the stainless steel back-to-back channels.

2.6.3 Parametric Studies

ThinWall (1995) was used to design cross-sections composed of back-to-back channels with the desired nominal cross-sectional slenderness values ($\lambda_s = 1.1, 1.7$ and 2.4). The wall thickness was gradually reduced to increase λ_s . Three alloys were considered: 3Cr12, 304 and 430. The results of the calculations are listed in Table 2.15, using the notations introduced in Figure 2.37. For each combination of the alloy and the cross-sectional slenderness, eight overall slenderness values were considered, ranging from 0.25 to 2.0 in 0.25 increments. The specimens were labeled with “I”, indicating the cross-sectional shape, followed by the alloy, the thickness (in mm) and the effective length (in mm). For instance, I430_1.80_500 is a 430 alloy, 500 mm long specimen with a thickness of 1.80 mm.

The material properties obtained in (Becque and Rasmussen 2006) for the 3Cr12, 304 and 430 alloys were used in the model. Anisotropy was taken into account using Hill’s criterion with the coefficients listed in Table 2.1. Increased material properties of the

corners were also obtained from (Becque and Rasmussen 2006).

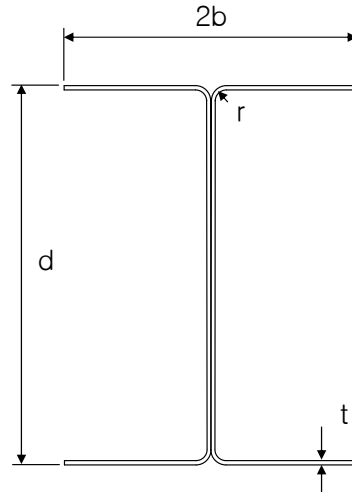


Figure 2.37. Specimen Dimensions (I-Sections)

Table 2.15. Specimen Dimensions (I-Sections)

Material	λ_s	d	2b	r	t	σ_{cr}	ω_d
	-	mm	mm	mm	mm	MPa	-
3Cr12	1.12	100.00	70.00	4.00	1.80	261	0.60
3Cr12	1.83	99.30	69.30	4.00	1.10	98	0.60
3Cr12	2.52	99.00	69.00	4.00	0.80	52	0.60
304	1.03	100.00	70.00	4.00	1.80	221	0.60
304	1.68	99.30	69.30	4.00	1.10	83	0.60
304	2.31	99.00	69.00	4.00	0.80	44	0.60
430	1.05	100.00	70.00	4.00	1.80	242	0.60
430	1.71	99.30	69.30	4.00	1.10	91	0.60
430	2.35	99.00	69.00	4.00	0.80	48	0.60

An overall imperfection of $L_e/1500$ was included in the model. In addition, a local imperfection in the shape of the local buckling mode with an amplitude given by Eq. (23) was incorporated. Figure 2.38 shows the shape of the local imperfection, the overall imperfection and the combined initial imperfection of specimen I304_110_750. All specimens were modeled with pinned end conditions.

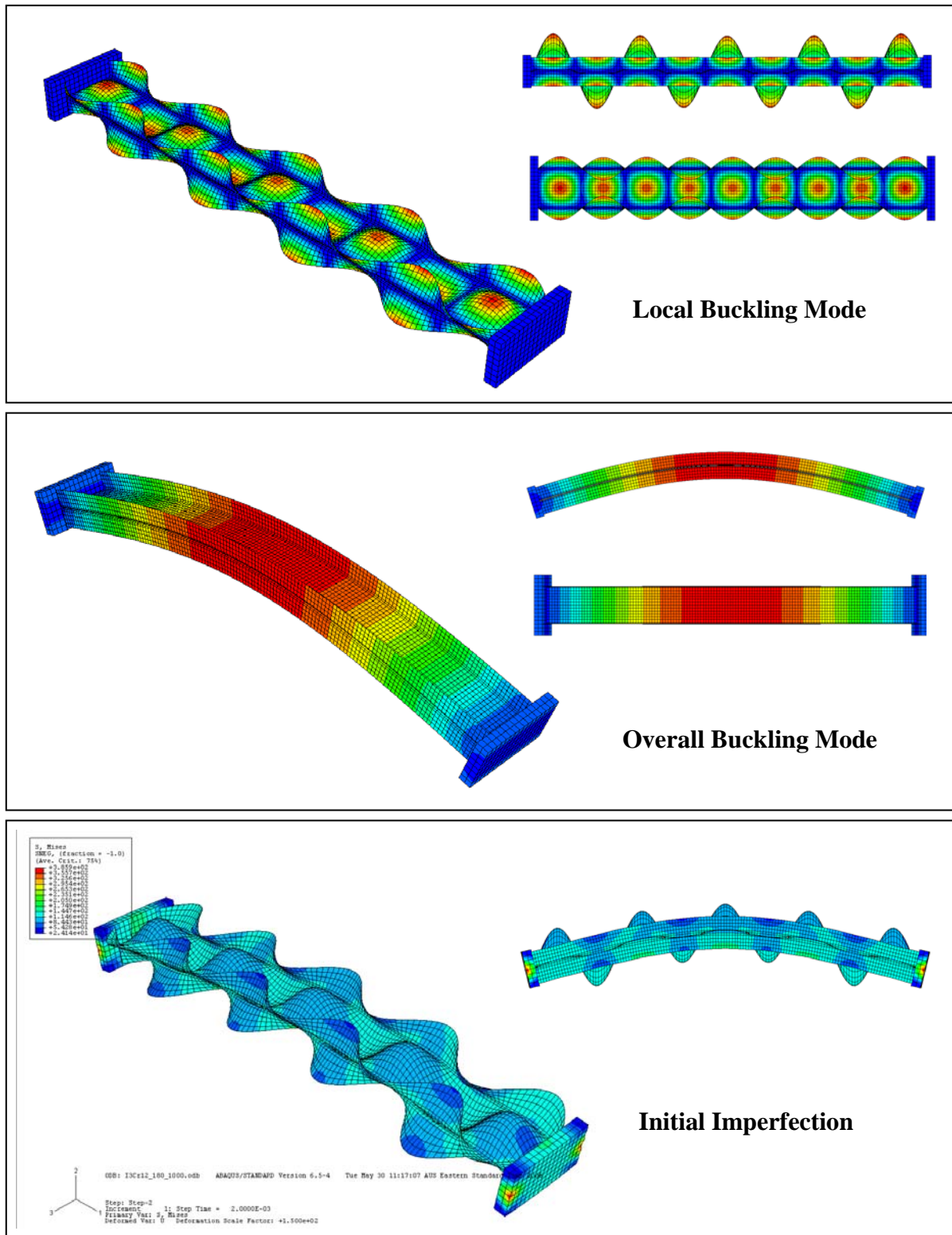


Figure 2.38. Initial Imperfection (I-Section)

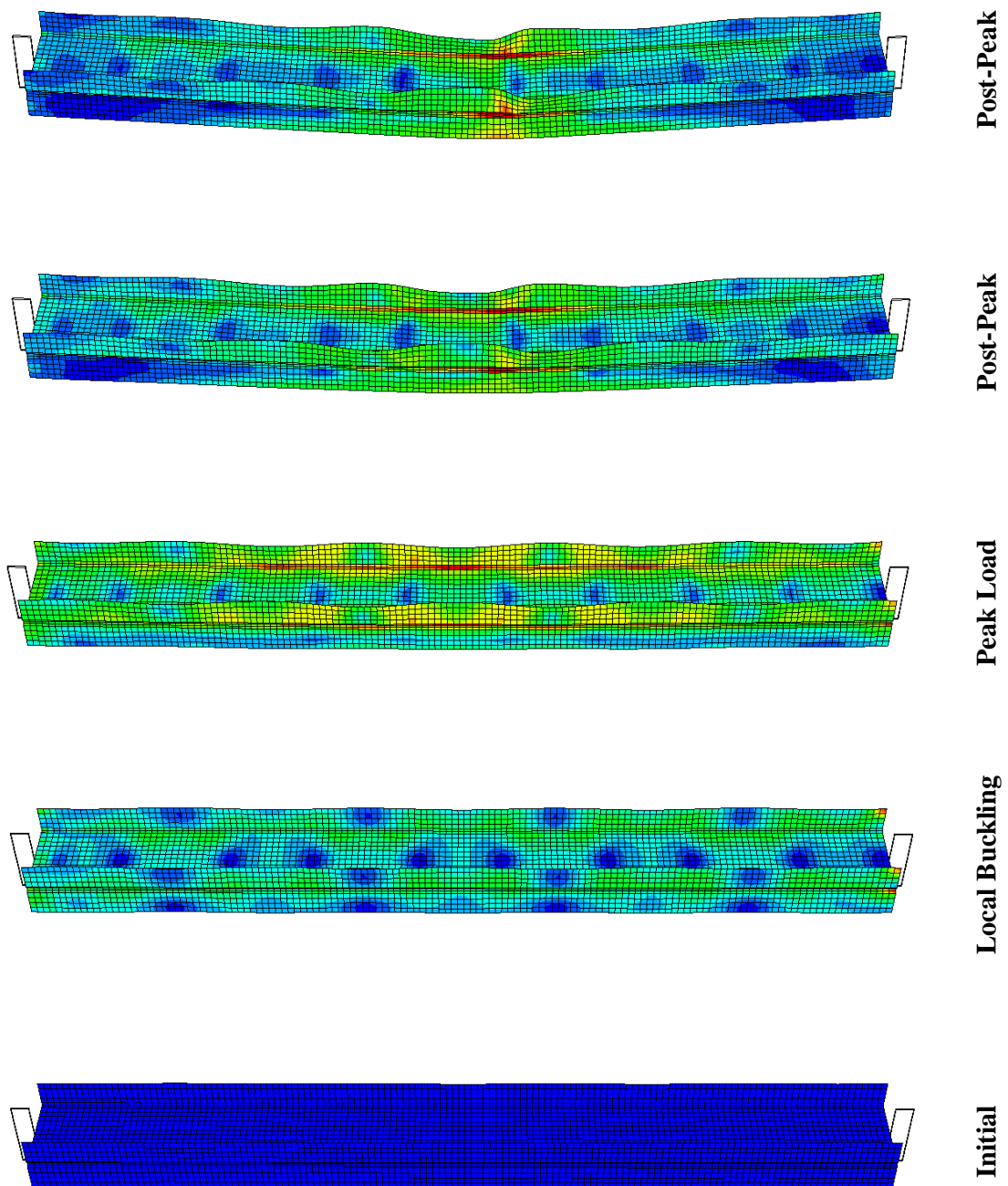


Figure 2.39. Deformations under Progressive Loading (I-Sections)

Table D4 of Appendix D contains the results of the FE studies under the heading “Test”. Figures D35 to D43 plot the specimen load capacities against the effective length L_e or the overall slenderness λ_o .

Figure 2.39 shows the deformations of a typical specimen (I430_080_1000) at various stages of loading. The contour plots represent von Mises surface stresses.

2.7 Summary

Figure 2.40 provides an overview of the data available in Appendix D. A total of 216 ultimate strength results were generated through FE studies. 101 experimental results are also available, amounting to a total of 317 data points. The data is used in the next section of this report to evaluate the current design guidelines and propose a Direct Strength approach for stainless steel columns.


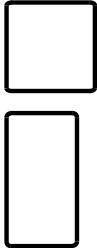

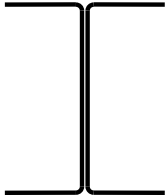
	Singly Symmetric	Doubly Symmetric
Stiffened	 <p>Lipped Channels</p> <p>Exp.: 18 FE: 48</p>	 <p>RHS and SHS</p> <p>Exp.: 60 FE: 24</p>
Unstiffened	 <p>Plain Channels</p> <p>Exp.: – FE: 72</p>	 <p>Back-to-Back Channels</p> <p>Exp.: 23 FE: 72</p>

Figure 2.40. Available Data

3 Evaluation of Current Design Practices

3.1 Introduction

In this section the available data on local-overall interaction buckling is compared to the current Australian/New Zealand, North-American and European design guidelines for stainless steel structures. The most recent Australian design rules are comprised in AS/NZS 4673 (2004), and are largely concurrent with the North American ASCE (2002) rules. The European design guidelines for stainless steel are specified in Eurocode 3 prEN 1993-1-4 (2004). All mentioned design standards have been based on the design rules for cold-formed carbon steel members. Since stainless steel has material properties which are distinctively different from those of carbon steel, it is unclear whether this approach results in conservative or unconservative predictions.

The current Australian, North-American and European design rules for cold-formed stainless steel are based on the effective width concept. A Direct Strength Method (DSM) has recently been included in the Australian standards for cold-formed carbon steel structures AS/NZS 4600 (2005) and in Appendix I of the North American Specifications (NAS) for Cold-Formed Steel Structural Members (2004). A DSM for stainless steel compression members, based on the data presented in this report, is proposed in Section 3.3.

3.2 Effective Width Approach

3.2.1 General

3.2.1.1 AS/NZS 4673

AS/NZS 4673 calculates the effective width ρb of a plate element in a plate assembly using the Winter equation (1940), based on the design stress f_n :

$$\rho = \left(1 - \frac{0.22}{\lambda_p} \right) \frac{1}{\lambda_p} \leq 1.0 \quad (26)$$

where the slenderness λ_p is determined from:

$$\lambda_p = \left(\frac{1.052}{\sqrt{k}} \right) \left(\frac{b}{t} \right) \left(\sqrt{\frac{f_n}{E_0}} \right) \quad (27)$$

b is the flat width of the plate element, t is the plate thickness, E_0 is the initial modulus and k is the plate buckling coefficient. f_n is the least of the flexural, torsional and flexural-torsional buckling stresses of the member, calculated on the basis of the unreduced (gross) cross-section. For compression members subject to flexural buckling AS/NZS 4673 provides two options for calculating f_n . The first option is to use the tangent modulus approach:

$$f_n = \frac{\pi^2 E_t}{(L_e/r)^2} \leq f_y \quad (28)$$

E_t is the tangent modulus corresponding to the buckling stress f_n , so that an iterative approach is necessary. L_e is the effective length and r is the radius of gyration of the unreduced cross-section. In the context of stainless steel, f_y carries the meaning of the 0.2% proof stress. Alternatively, f_n may be calculated using a direct approach:

$$f_n = \frac{f_y}{\phi + \sqrt{\phi^2 - \lambda^2}} \leq f_y \quad (29)$$

$$\phi = \frac{1}{2} (1 + \eta + \lambda^2) \quad (30)$$

$$\eta = \alpha((\lambda - \lambda_1)^\beta - \lambda_o) \quad (31)$$

$$\lambda = \left(\frac{L_e}{r} \right) \sqrt{\frac{f_y}{\pi^2 E_0}} \quad (32)$$

The values of α , β , λ_o and λ_1 for the materials under consideration are shown in Table 3.1. They were either directly obtained from AS/NZS 4673, or in the case of the 404 alloy, calculated from the underlying equations presented in (Rasmussen and Rondal 1997).

In the context of obtaining the overall buckling stress, the two methods will from hereon be referred to as the “tangent approach” and the “direct approach” respectively.

Table 3.1. Values of α , β , λ_o and λ_1 (AS/NZS 4673; 2004)

	Alloy				
	304	430	404	3Cr12	S31803
α	1.59	1.04	0.73	0.94	1.16
β	0.28	0.14	0.15	0.15	0.13
λ_o	0.55	0.59	0.57	0.56	0.65
λ_1	0.20	0.33	0.25	0.27	0.42

3.2.1.2 prEN 1993-1-4

The European approach, outlined in prEN 1993-1-4 (2004) differs from AS/NZ 4673 in that the 0.2% proof stress f_y is used to calculate effective areas. The equations used to calculate the effective width p_b are as follows:

- For cold-formed or welded internal elements:

$$\rho = \left(0.722 - \frac{0.125}{\lambda_p} \right) \frac{1}{\lambda_p} \leq 1 \quad (33)$$

- For cold-formed outstand elements:

$$\rho = \left(1 - \frac{0.231}{\lambda_p} \right) \frac{1}{\lambda_p} \leq 1 \quad (34)$$

where the element slenderness λ_p is defined as:

$$\lambda_p = \frac{b/t}{28.4\epsilon\sqrt{k}} \quad (35)$$

and:

$$\epsilon = \left[\frac{235}{f_y} \frac{E_0}{210000} \right]^{0.5} \quad (36)$$

Eq. (35) is equivalent to Eq. (27) with $f_n = f_y$. The definition of the width b in Eq. (35) is rather inconsistent and depends on the type of cross-section, but usually pertains to the flat width, except for outstand elements, where the overall width is considered.

The overall buckling slenderness λ of a Class 4 (slender) cross-section is then defined as:

$$\lambda = \sqrt{\frac{A_e f_y}{N_{cr}}} \quad (37)$$

where A_e is the effective area and N_{cr} is the elastic overall buckling load. λ is subsequently used to calculate:

$$\phi = 0.5(1 + \alpha(\lambda - \lambda_0) + \lambda^2) \quad (38)$$

$$\chi = \frac{1}{\phi + [\phi^2 - \lambda^2]^{0.5}} \leq 1 \quad (39)$$

$$N_{b,Rd} = \chi A_e f_y / \gamma_{M1} \quad (40)$$

$N_{b,Rd}$ is the design buckling resistance, including a partial safety factor γ_{M1} . The values of α and λ_0 corresponding to the appropriate buckling curve should be used. For flexural buckling of cold-formed open sections and hollow sections: $\alpha = 0.49$ and $\lambda_0 = 0.40$.

3.2.2 Lipped Channels

3.2.2.1 AS/NZS 4673

Section 3.4 of AS/NZS 4673 discusses concentrically loaded compression members and defines these as: “members in which the resultant of all loads acting on the member is an axial load passing through the centroid of the effective section calculated at the stress f_n ”. Therefore, pin-ended members with singly symmetric cross-sections subject to local buckling need to be designed as beam-columns, taking into account the shift of the effective centroid. They need to satisfy:

$$\left(\frac{1}{\phi_c N_c} + e_N \frac{C_{my}}{\phi_b M_{by} \alpha_{ny}} \right) N^* \leq 1.0 \quad (41)$$

where:

$$N_c = A_e (f_n) f_n \quad (42)$$

N^* is the design load ($N^* = A_e(f^*).f^*$) and e_N is the shift of the effective centroid, calculated at the design stress f^* . Iterations are therefore necessary to find the stress f^* which equates Eq. (41) to 1.0. M_{by} is the nominal bending capacity about the weak axis, $C_{my} = 1.0$, $\alpha_{ny} = 1 - N^*/N_e$ and N_e is the Euler buckling load. Actual capacities are meant to be considered in the comparison with the experimental and FE generated results, and therefore the capacity factors ϕ_c and ϕ_b are set equal to 1.0.

When calculating the effective area of a lipped channel in compression, a local buckling factor k of 4.0 should be used for the web. The flange-and-lip assemblies are considered as “elements with an edge stiffener” and their effective areas are determined according to Clause 2.4.3.

The bending capacity about the weak axis M_{by} is calculated according to Clause 3.3.2, considering a moment which puts the web of the channel in compression and causes tension in the flange lips. AS/NZS 4673 allows for the inelastic reserve capacity to be used if the conditions of Clause 3.3.2.3 are met, which is the case for the channels under consideration. Due to the geometry of the channels the compressive strain factor C_y in Clause 3.3.2.3 equals 1.0, meaning that the bending capacity may be determined assuming that the channel web reaches the yield strain, with the cross-section being partially plastified on the tension side.

Appendix E contains the detailed calculations for a typical lipped channel C3Cr12_1.32_1100. Section E1 calculates the member capacity utilizing the tangent approach to find the overall buckling stress, while section E2 repeats the calculations with the overall buckling stress determined from the direct strength equations.

AS/NZS 4673 was used to predict the ultimate capacity of all 66 lipped channels listed in Table D1 of Appendix D. The results are listed in Table D1 under the heading “AS(t)” when the tangent approach was used, and under the heading “AS(d)” when the direct approach was taken.

It should be noted that the lipped channels with the highest cross-sectional slenderness values ($\lambda_s \geq 2.4$) fall outside the scope of AS/NZS 4673. The ratio c/b_{flat} of these

channels, where c is the overall width of the lip and b_{flat} is the flat width of the flange, is greater than the allowed value of 0.8 and results in some cases in negative predictions of the local buckling factor k (Eq. 2.4.3.2(8) of Clause 2.4.3.2). No predictions are listed for the lipped channels with $\lambda_s \geq 2.4$ which are subject to local buckling. Nevertheless, in the finite element simulations, the high ratio of c/b_{flat} is necessary to suppress the distortional buckling mode.

A graphical comparison between the predictions of AS/NZS 4673 and the experimental or FE generated ultimate capacities is made in Figures D1 to D9 of Appendix D. The graphs also show the concentric column strength predicted by AS/NZS 4673 in dashed line i.e. the column capacity $N_c = A_e f_n$, without taking into account the shift of the effective centroid. The stepped curve in Figure D8 is the result of a discontinuous transition under Clause 3.4.3.2 from Case I into Case II as L_e increases.

3.2.2.2 prEN 1993-1-4

Pin-ended members with a singly symmetric cross-section subject to local buckling undergo a shift in effective centroid and need to satisfy (Clause 5.5: “Axial Compression and Uniaxial Minor Axis Moment”):

$$\left(\frac{1}{N_{b,Rd}} + e_N \frac{k_z}{W_{e,z} f_y / \gamma_{M1}} \right) N_{Ed} \leq 1.0 \quad (43)$$

where e_N is the shift of the effective centroid under uniform compression, calculated at a stress f_{Ed} , with:

$$N_{Ed} = A_e f_{Ed} \quad (44)$$

$N_{b,Rd}$ is the overall buckling capacity, calculated according to Eq. (40) and k_z is an interaction factor taken as:

$$k_z = 1 + 2(\lambda - 0.5) \frac{N_{Ed}}{N_{b,Rd}} \quad \text{but} \quad 1.2 \leq k_z \leq 1.2 + 2 \frac{N_{Ed}}{N_{b,Rd}} \quad (45)$$

where λ is defined by Eq. (37).

Iterations are necessary to determine N_{Ed} from Eq. (43).

First yielding in bending is reached on the tension side, at the lips of the channel. Therefore, Clause 6.1.4.2 of EN 1993-1-3 applies and the effective section modulus $W_{e,z}$ can be determined assuming a partially plastified cross-section on the tension side and a linear stress distribution with maximum stress f_y on the compression side.

For the purpose of evaluating the design standards, the partial factor γ_{M1} is set equal to 1.0.

An example of the detailed calculations according to prEN 1993-1-4 is included in Section E3 of Appendix E for a typical channel C3Cr12_1.32_1100. prEN 1993-1-4 states that the local buckling factor k should be obtained from prEN 1993-1-5 (2004) “Plated structural elements”, which results in $k = 4.0$ for the web. The procedure outlined in EN 1993-1-3, Clause 5.5.3.2. “Plane elements with edge stiffener” was used to check for distortional buckling of the flange-lip assembly. It was found that $\chi_d = 1.0$ for all lipped channels under consideration, indicating that no distortional buckling takes place. The procedure also provides the k value of the flange and the lip.

Technically the scope of EN 1993-1-3 and prEN 1993-1-4 is limited to cases where $c/b < 0.6$, where c and b are the overall widths of the lip and the flange respectively. Some of the lipped channels with higher cross-sectional slenderness listed in Table D1 of Appendix D do not satisfy this criterion. A prediction of the ultimate capacity is nevertheless listed for all lipped channels in Table D1 under the heading “EC3”.

The strength curves predicted by prEN 1993-1-4 are also included in Figures D1 to D9 of Appendix D. The concentric column strength, ignoring any shift in effective centroid, is also shown for comparison.

3.2.3 Plain Channels

3.2.3.1 AS/NZS 4673

Pin-ended plain channel columns subject to local buckling need to be designed as elements in combined axial compression and bending because of the shift in effective centroid. The comments made previously in Section 3.2.2.1 apply.

When calculating the effective area under uniform compression, a k value of 4.0 should be used for the web, while 0.5 is the appropriate value for the flanges.

Since the effective centroid shifts towards the web, the nominal bending capacity M_{by} needs to be calculated assuming the channel web undergoes tension and the flange tips are in compression. The k value of the flanges is in this case determined from Appendix I (“Unstiffened Elements with Stress Gradient”) of AS/NZS 4673. The yield strain is first reached in compression at the flange tips. No extra capacity can be obtained from taking into account the inelastic reserve capacity provisions of Clause 3.3.2.3, where the compressive strain factor C_y has to be taken as 1.0 for an unstiffened element.

An example of the detailed calculations is included in Section E4 of Appendix E for a typical specimen PC304_1.80_750. The overall buckling stress is calculated using the tangent approach. Section E5 repeats the calculations with the overall buckling stress determined from the direct approach.

AS/NZS 4673 was used to determine the ultimate capacities of all 72 plain channel columns included in Table D2 of Appendix D. The results are listed under the headings “AS(t)” (tangent approach) and “AS(d)” (direct approach) in Table D2. Figures D10 to D18 provide a graphical comparison between the design code predictions and the FE generated data. The concentric column capacities, assuming no additional bending is caused by the shift in effective centroid, are also shown.

3.2.3.2 prEN 1993-1-4

prEN 1993-1-4 was used to predict the ultimate capacities of the plain channels in Table D2 of Appendix D. The results are listed in Table D2 under the heading “EC3”.

The detailed calculations of a sample specimen PC304_1.80_750 are included in Section E6 of Appendix E. In accordance with prEN 1993-1-5, k equals 4.0 for the web and k equals 0.43 for the flanges. Eq. (33) was used to determine the effective width of the web, while Eq. (34) was used for the flanges. The shift in effective centroid was taken into account using Eq. (43). The effective section modulus W_e was determined according to EN 1993-1-3, Clause 6.1.4.1, assuming a linear stress distribution which reaches f_y at the compressed flange tips.

The strength curves predicted by EC3 are also shown in Figures D10 to D18 of Appendix D.

3.2.4 Hollow Sections

3.2.4.1 AS/NZS 4673

The ultimate capacities, calculated according to AS/NZS 4673, are listed in Tables D3a and D3b of Appendix D for the 60 experimental and the 24 FE generated results respectively. The columns “AS(t)” and “AS(d)” contain the AS/NZS predictions using the tangent approach and the direct approach to calculate the overall buckling stress respectively.

Detailed calculations are included in Section E7 of Appendix E for a sample specimen R1L1200 from the experimental program by Young and Liu (2003). In agreement with Clause 2.2.1.2 of the Standard, a k value of 4.0 was used for all plate components.

A graphical comparison between the strength curves predicted by AS/NZS 4673 and the experimental and FE generated results is presented in Figures D19 to D27 of Appendix

D for the square hollow sections, and in Figures D28 to D32 for the rectangular hollow sections.

3.2.4.2 prEN 1993-1-4

The ultimate capacities predicted by prEN 1993-1-4 are listed in Tables D3a and D3b of Appendix D under the heading “EC3”. The predicted strength curves are also included in Figures D19 to D32.

Sample calculations for specimen R1L1200 are included in Section E8 of Appendix E. prEN 1993-1-5 dictates a k value of 4.0 for all plate components. This value is to be used in combination with Eq. (33) to determine the effective width.

3.2.5 I-Sections

3.2.5.1 AS/NZS 4673

AS/NZS 4673 was used to predict the capacities of all 95 I-columns (comprised of back-to-back channels) listed in Table D4 of Appendix D. The results are found in Table D4 under the headings “AS(t)” (tangent approach) and “AS(d)” (direct approach).

A sample calculation for specimen I404_1.20_1000 is included in Section E9 of Appendix E. As prescribed by AS/NZS 4673, a k value of 0.5 was used for the flanges, while the k value of the webs is 4.0.

Figures D33 to D43 of Appendix D graphically compare the predictions of AS/NZS 4673 with the experimental and FE generated results.

3.2.5.2 prEN 1993-1-4

prEN 1993-1-4 was used to predict the capacity of all 95 I-columns in Table D4 of

Appendix D. The results are listed in Table D4 under the heading “EC3” and graphically presented in Figures D33 to D43.

The detailed calculations are presented in Section E10 of Appendix E for a sample specimen I404_1.20_1000. A k value of 4.0 is prescribed for the webs, in combination with Eq. (33), while the k value of the flanges is 0.43, used in combination with Eq. (34).

3.2.6 Reliability Analysis

A first order second moment (FOSM) reliability analysis was performed to evaluate the current design guidelines. The analysis is based on (Lin et al. 1992) and adopts the following statistical data:

- The variable F , defined as the ratio of the actual to the nominal cross-sectional dimensions, has a mean value $F_m = 1.0$ and a coefficient of variation $V_F = 0.05$.
- The variable M , defined as the ratio of the actual to the nominal material properties, has a mean value $M_m = 1.10$ and a coefficient of variation $V_M = 0.10$.
- A representative ratio of dead load to live load for cold-formed structures is $1/5$.
- The coefficient of variation of the live load V_L is 0.25.
- The coefficient of variation of the dead load V_D is 0.1.

These assumptions are in line with the LRFD approach for cold-formed carbon steel, which underpins the ASCE (2002), AS/NZS 4673 (2004), AS/NZS 4600 (2005) and NAS (2001) guidelines.

Reliability analyses were performed with target reliability indices β of 2.5 and 3.0. The cold-formed carbon steel standards adopt $\beta = 2.5$. A higher value of $\beta = 3.0$ was set for the stainless steel standards due to an initial lack of general experience with the material. As this obstacle gets overcome over time, the opinion arises in the field that conformity with the carbon steel codes on the issue of the reliability index should be aimed for.

Table 3.2 summarizes the results of a reliability analysis performed on the lipped

channel data in Table D1 of Appendix D. The resistance factor ϕ was determined for AS/NZS 4673 (tangent approach and direct approach) and EC3. In this context, it is noted that AS/NZS 4673 prescribes $\phi = 0.85$ when the tangent approach is used, but $\phi = 0.90$ when the direct approach is used. prEN 1993-1-4 recommends to use partial safety factors $\gamma_{M0} = \gamma_{M1} = 1.1$, with $1/\gamma_{M0} = 1/\gamma_{M1} = 0.91$. Table 3.2 also lists the mean value of $P_{u,n}/P_{u,p}$ for the different design codes (where $P_{u,n}$ is the test result or FE generated result and $P_{u,p}$ is the code predicted ultimate capacity), together with the coefficient of variation (COV).

Table 3.2. Reliability Analysis: Lipped Channels

		AS/NZS 4673	AS/NZS 4673	EC3
		Tangent Approach	Direct Approach	
$P_{u,n}/P_{u,p}$	Mean	1.02	1.11	1.13
	COV	0.12	0.10	0.11
ϕ	$\beta = 2.5$	0.79	0.88	0.89
	$\beta = 3.0$	0.68	0.76	0.77

Table 3.3 lists the resistance factors obtained from a reliability analysis on the data in Table D2 of Appendix D (plain channels), for AS/NZS 4673 and EC3. The high COV-values are in this case responsible for the low ϕ -values.

Table 3.3. Reliability Analysis: Plain Channels

		AS/NZS 4673	AS/NZS 4673	EC3
		Tangent Approach	Direct Approach	
$P_{u,n}/P_{u,p}$	Mean	1.10	1.15	1.63
	COV	0.25	0.22	0.32
ϕ	$\beta = 2.5$	0.71	0.79	0.94
	$\beta = 3.0$	0.59	0.66	0.77

Table 3.4 contains the results of a reliability analysis on the available data on square and rectangular hollow sections, contained in Tables D3a and D3b of Appendix D.

Table 3.4. Reliability Analysis: Hollow Sections

		AS/NZS 4673	AS/NZS 4673	EC3
		Tangent Approach	Direct Approach	
$P_{u,n}/P_{u,p}$	Mean	1.03	1.18	1.15
	COV	0.12	0.15	0.13
ϕ	$\beta = 2.5$	0.84	0.92	0.94
	$\beta = 3.0$	0.74	0.80	0.82

Table 3.5 lists the resistance factors obtained from a reliability analysis on the available data on I-sections (Table D4 of Appendix D).

A reliability analysis was also performed including all 317 available data points of various cross-sections, listed in Tables D1 to D4 of Appendix D, in order to allow a general conclusion on the performance of the design standards to be made. The results are shown in Table 3.6.

Table 3.5. Reliability Analysis: I-Sections

		AS/NZS 4673	AS/NZS 4673	EC3
		Tangent Approach	Direct Approach	
$P_{u,n}/P_{u,p}$	Mean	0.83	0.91	0.97
	COV	0.15	0.10	0.16
ϕ	$\beta = 2.5$	0.65	0.76	0.77
	$\beta = 3.0$	0.57	0.67	0.67

Table 3.6. Reliability Analysis: All Sections

		AS/NZS 4673	AS/NZS 4673	EC3
		Tangent Approach	Direct Approach	
$P_{u,n}/P_{u,p}$	Mean	0.99	1.08	1.21
	COV	0.21	0.19	0.31
ϕ	$\beta = 2.5$	0.69	0.78	0.71
	$\beta = 3.0$	0.58	0.66	0.58

3.2.7 Conclusions

It is apparent from Table 3.6 that in general, the current design guidelines are unable to appropriately account for the interaction effect between local and overall buckling of stainless steel columns. The calculated resistance factors are all significantly lower than the ones prescribed by the respective standards.

Table 3.4 demonstrates however that the current Australian/North-American and European guidelines are safe and reasonably accurate for stainless steel square and rectangular hollow sections. The same conclusion can be drawn from observing Figures D19 to D32. As the cross-sectional slenderness λ_s increases to its high-end values (Figs. D25 to D27), the design codes keep performing relatively well, although EC3 becomes increasingly less conservative.

Figures D1 to D9 show that the design guidelines can be quite conservative for lipped channels with low cross-sectional slenderness ($\lambda_s = 1.1$), and more so for ferritic alloys than for austenitic alloys, but become less conservative for higher cross-sectional slenderness values. EC3 consistently underestimates the stub column strength of lipped channel sections. The recommended resistance factors for lipped channels, based on $\beta = 2.5$ (Table 3.2), lie slightly below the code prescribed values.

The capacity of plain channels with low cross-sectional slenderness ($\lambda_s = 1.1$) is well predicted by the direct approach of AS/NZS 4673, while the tangent approach can be

unconservative (Figs. D10 to D18). For plain channels with higher cross-sectional slenderness values however ($\lambda_s = 1.6$, $\lambda_s = 2.3$), AS/NZS becomes overly conservative. EC3 results in overly conservative predictions for plain channels of any slenderness λ_s . Nevertheless, because of the high COV values, the calculated resistance factors are significantly lower than the values specified by EC3.

Figures D33 to D43 demonstrate that AS/NZS 4673 and EC3 result in unconservative predictions of the capacity of stainless steel I-sections with intermediate and high cross-sectional slenderness values ($\lambda_s = 1.6 - 2.5$). This is true for ferritic as well as austenitic sections. This unconservatism mainly demonstrates itself around the local buckling load and in the transition towards pure (inelastic) overall buckling. The inability of the design standards to capture the pronounced interaction effect in I-sections results in recommended resistance factors (Table 3.5) which are significantly lower than the code prescribed values.

The conclusion emerges that the current Australian/North-American and European design guidelines for stainless steel are increasingly unable to accurately and conservatively predict the specimen capacity as the cross-sectional slenderness increases and the interaction effect between local and overall buckling becomes more pronounced.

3.3 Direct Strength Approach

3.3.1 Current Formulation for Carbon Steel Columns

The direct strength method (DSM) has recently been included the North-American Specifications for Cold-Formed Steel Structural Members (NAS 2004) and the Australian Standard for cold-formed (carbon) steel AS/NZS 4600 (2005). The equations are based on a slenderness λ_l , with:

$$\lambda_1 = \sqrt{\frac{P_{ne}}{P_{cr}}} \quad (46)$$

where P_{ne} is the overall buckling strength and P_{cr} is the elastic local buckling load. The compressive member capacity P_{nl} , accounting for local buckling, can then be calculated using the DSM equations:

$$P_{nl} = \begin{cases} P_{ne} & \text{for } \lambda_1 \leq 0.776 \\ \left[\left(1 - \frac{0.15}{\lambda_1^{0.8}} \right) \frac{1}{\lambda_1^{0.8}} \right] P_{ne} & \text{for } \lambda_1 > 0.776 \end{cases} \quad (47)$$

According to Eqs. (46) and (47) the interaction between local and overall buckling is taken into account by relating P_{cr} to the overall buckling strength P_{ne} in the expression for the slenderness λ_1 , rather than to the section yield strength P_y , as is the case when determining the pure local buckling strength.

Eq. (47) was applied to the available stainless steel data, where the overall buckling capacity P_{ne} was calculated using the direct approach of AS/NZS 4673, outlined in Eqs. (29) to (32). A reliability analysis, conforming to the principles discussed in Section 3.2.6, was performed. The resulting resistance factors are listed in Table 3.7. A target reliability index β of 2.5 was used.

It is seen from Table 3.7 that the capacity factor of $\phi = 0.9$, specified in AS/NZS 4600 and the NAS specification is only achieved for SHS and RHS section columns. Hence, Eq. (47) can only be relied on to predict the capacity of stainless steel SHS and RHS sections, but fails to deliver reliable predictions for other types of cross-sections.

Table 3.7. DSM for Carbon Steel: Reliability Analysis

	$P_{u,p}/P_{u,n}$		ϕ
	Mean	COV	
Lipped Channels	1.00	0.08	0.81
Plain Channels	0.73	0.16	0.55
SHS/RHS	1.17	0.15	0.92
I-Sections	0.90	0.09	0.76
Overall	1.03	0.16	0.79

3.3.2 Proposed DSM for Stainless Steel Columns based on the AS/NZS 4673 Direct Column Strength Equations

Eq. (47) was modified to develop a specific DSM for stainless steel columns. A general expression is presented, based on the data of stainless steel SHS, RHS, I-sections and lipped channels. The shift in effective centroid in plain channels is too significant and has too severe an effect on the (pin-ended) member capacity to include the plain channel data into the development of the DSM. However, the proposed DSM may still be applied to plain channel columns with fixed ends, or with sufficient end restraint to minimize the effect of the shift in effective centroid.

An equation is proposed of the form:

$$P_{nl} = \begin{cases} P_{ne} & \text{for } \lambda_1 \leq \lambda_{limit} \\ \left[\left(a - \frac{b}{\lambda_1^c} \right) \frac{1}{\lambda_1^c} \right] P_{ne} & \text{for } \lambda_1 > \lambda_{limit} \end{cases} \quad (48)$$

where a , b and c are coefficients. P_{ne} is the overall buckling strength determined with the direct equations (29) to (32) obtained from AS/NZS 4673. The slenderness λ_1 is still determined by Eq. (46), where P_{cr} is the elastic local buckling load of the cross-section.

The limit slenderness λ_{limit} is given by:

$$\lambda_{\text{limit}} = \left[\frac{a - \sqrt{a^2 - 4b}}{2b} \right]^{-\frac{1}{c}} \quad (49)$$

A reliability analysis was performed on the 245 data points of lipped channels, I-sections and SHS/RHS, contained in Appendix D to determine the coefficients a , b and c . A target reliability index β of 2.5 was used, in conjunction with a resistance factor ϕ of 0.9. By trial-and-error the following values were determined: $a = 0.95$; $b = 0.22$; $c = 0.8$. Eq. (49) then results in $\lambda_{\text{limit}} = 0.474$. The mean value of predicted to experimental (or FE generated) capacity was 1.16 with a COV of 0.15. The Direct Strength equation is:

$$P_{\text{nl}} = \begin{cases} P_{\text{ne}} & \text{for } \lambda_1 \leq 0.474 \\ \left[\left(0.95 - \frac{0.22}{\lambda_1^{0.8}} \right) \frac{1}{\lambda_1^{0.8}} \right] P_{\text{ne}} & \text{for } \lambda_1 > 0.474 \end{cases} \quad (50)$$

Figure 3.1 compares the proposed DSM (Eq. 50) with the experimental and numerical data of Appendix D. Eq. (47), representing the DSM for carbon steel included in AS/NZS 4600 and NAS, is also shown for comparison, as is the Winter equation (26).

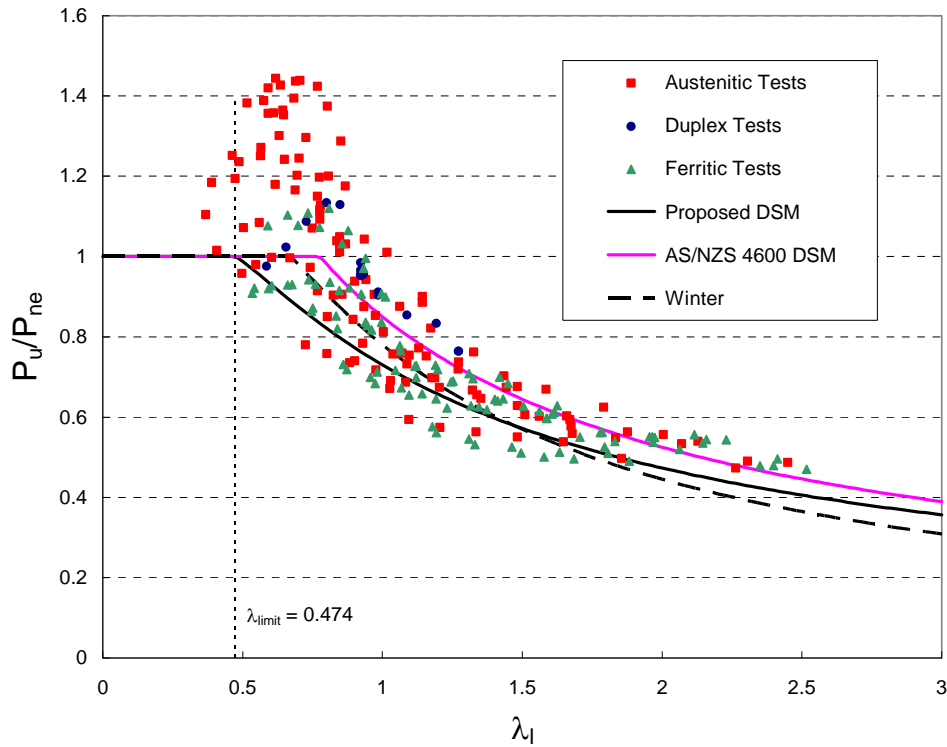


Figure 3.1. Comparison of Proposed DSM with Test Results

Figures 3.2, 3.3 and 3.4 separate the data by cross-section type: lipped channels, SHS/RHS and I-sections. It is seen from these figures that within each cross-section type no significant grouping of the data per material alloy (austenitic, ferritic or duplex) occurs. This justifies the approach of presenting one direct strength curve, without distinguishing between the different alloys. The material properties of a specific alloy are indirectly accounted for by basing the slenderness λ_l on the inelastic overall buckling strength P_{ne} , because the parameters α , β , λ_o and λ_l in Eq. (29) to (32) are alloy specific.

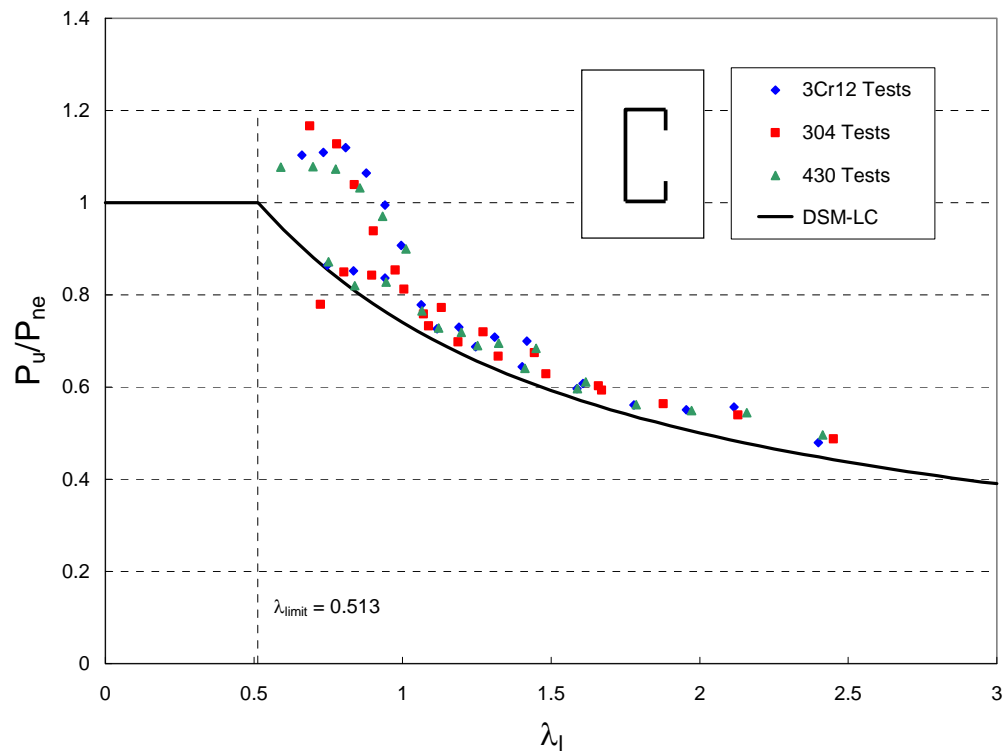


Figure 3.2. DSM for Lipped Channels

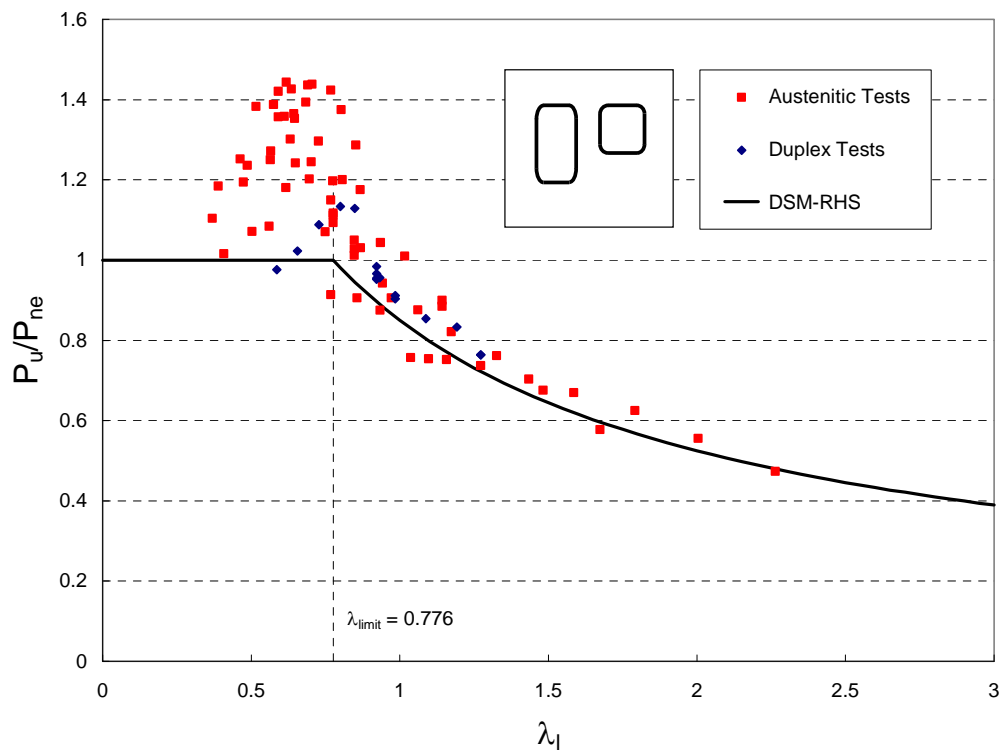


Figure 3.3. DSM for SHS/RHS

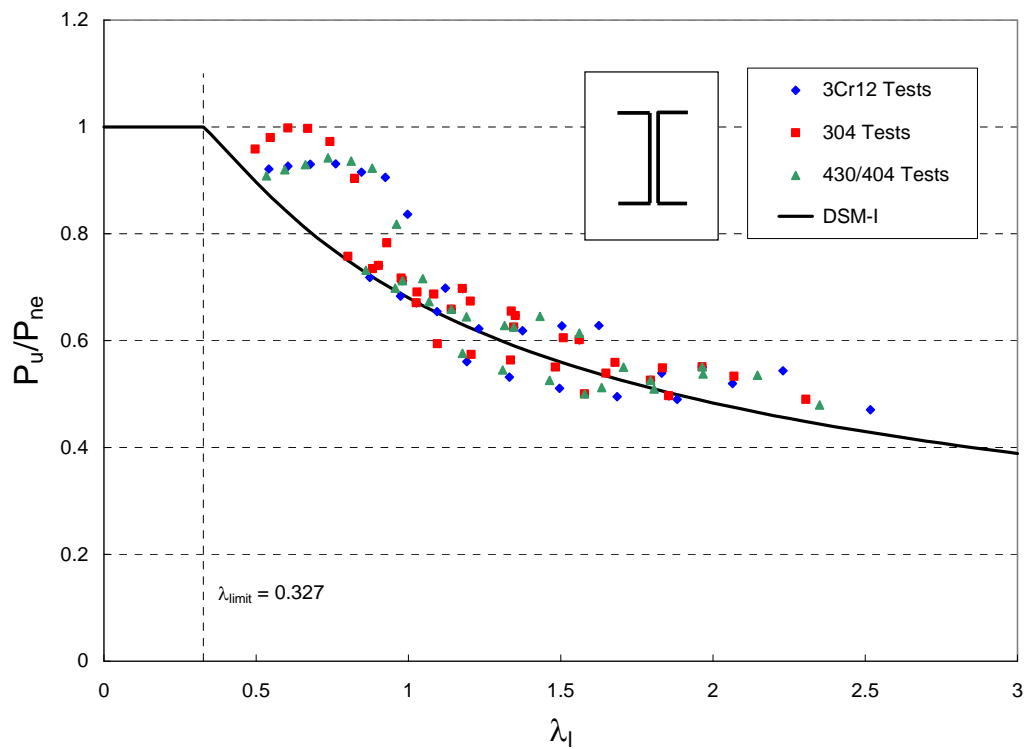


Figure 3.4. DSM for I-Sections

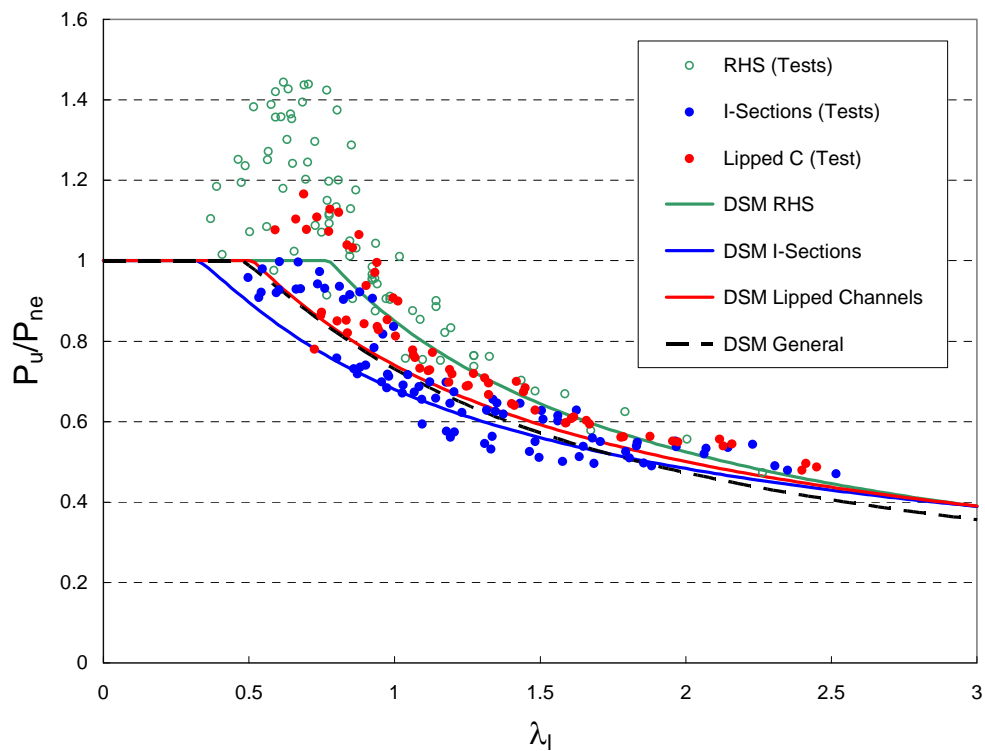


Figure 3.5. Experimental and Numerical Data by Cross-Section Type

Figures 3.2 to 3.4 show that the largest scatter of data occurs between $\lambda = \lambda_{\text{limit}}$ and $\lambda = 1.0$. This corresponds to the imperfection sensitive region where the column strength transitions from P_{cr} into the region of inelastic overall buckling P_{ne} . The scatter is most pronounced for the SHS/RHS data, which are mostly experimental.

Figure 3.5 suggests a slight clustering of the data by cross-section. While the interaction effect is more pronounced in I-sections compared to SHS and RHS, lipped channels are affected by a shift in effective centroid. A DSM is here proposed for each of these cross-section types, in case a more accurate prediction of the compressive capacity is desired for a member with any of these particular types of cross-section. A reliability analysis with reliability index $\beta = 2.5$ and resistance factor $\phi = 0.9$ was performed on the applicable data to determine the coefficients a , b and c in Eq. (48). The results are listed in Table 3.8. The DSM for each cross-section type is compared to the relevant numerical and experimental data in Figures 3.2 to 3.4.

Table 3.8. DSM for Particular Cross-Sections

	Coefficients			λ_{limit}	$P_{u,p}/P_{u,n}$		
	a	b	c		Mean	COV	ϕ
Lipped Channels	0.93	0.19	0.7	0.513	1.12	0.09	0.90
SHS/RHS	1.00	0.15	0.8	0.776	1.17	0.15	0.92
I-Sections	0.86	0.18	0.6	0.327	1.07	0.09	0.90
All Sections	0.95	0.22	0.8	0.474	1.16	0.15	0.90

3.3.3 Proposed DSM for Stainless Steel Columns based on the AS/NZS 4673 Tangent Equation for Column Strength

In Section 3.3.2 the inelastic column strength P_{ne} needed in Eqs. (46) and (50) was calculated using the direct strength approach of AS/NZS 4673 (Eqs. (29) to (32)).

However, AS/NZS 4673 also provides the option of calculating P_{ne} using the tangent approach:

$$P_{ne} = \frac{\pi^2 E_t}{(L_e/r)^2} A \leq P_{0.2\%} \quad (51)$$

This approach has the disadvantage that iterative calculations are necessary to determine P_{ne} .

A reliability analysis was again performed on the 245 data points contained in Appendix D to determine the coefficients a , b and c in Eq. (48), under the assumption that P_{ne} is calculated using the tangent approach. A target reliability index β of 2.5 was used. A resistance factor $\phi = 0.85$ was targeted, consistent with the AS/NZS 4673 prescribed value when using the tangent approach. The resulting Direct Strength equation is:

$$P_{nl} = \begin{cases} P_{ne} & \text{for } \lambda_1 \leq 0.463 \\ \left[\left(0.9 - \frac{0.2}{\lambda_1^{0.9}} \right) \frac{1}{\lambda_1^{0.9}} \right] P_{ne} & \text{for } \lambda_1 > 0.463 \end{cases} \quad (52)$$

Figure 3.6 plots Eq. (52) against the available data and also shows the Winter equation and the current DSM for carbon steel. No clustering of the data by alloy type is observed.

A cross-section specific DSM was also derived for SHS/RHS, lipped channels and I-sections, by applying a reliability analysis with $\beta = 2.5$ and $\phi = 0.85$ to the relevant data. The a , b and c coefficients are listed in Table 3.9. The corresponding curves are shown in Fig. 3.7.

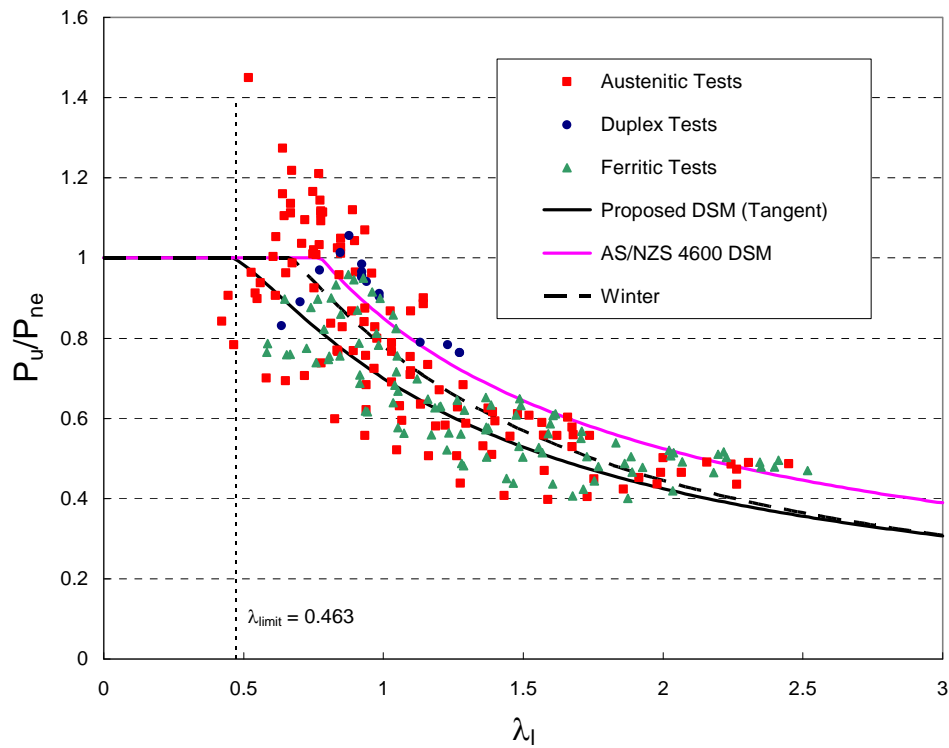


Figure 3.6. Comparison of Tangent Approach Based DSM with Test Results

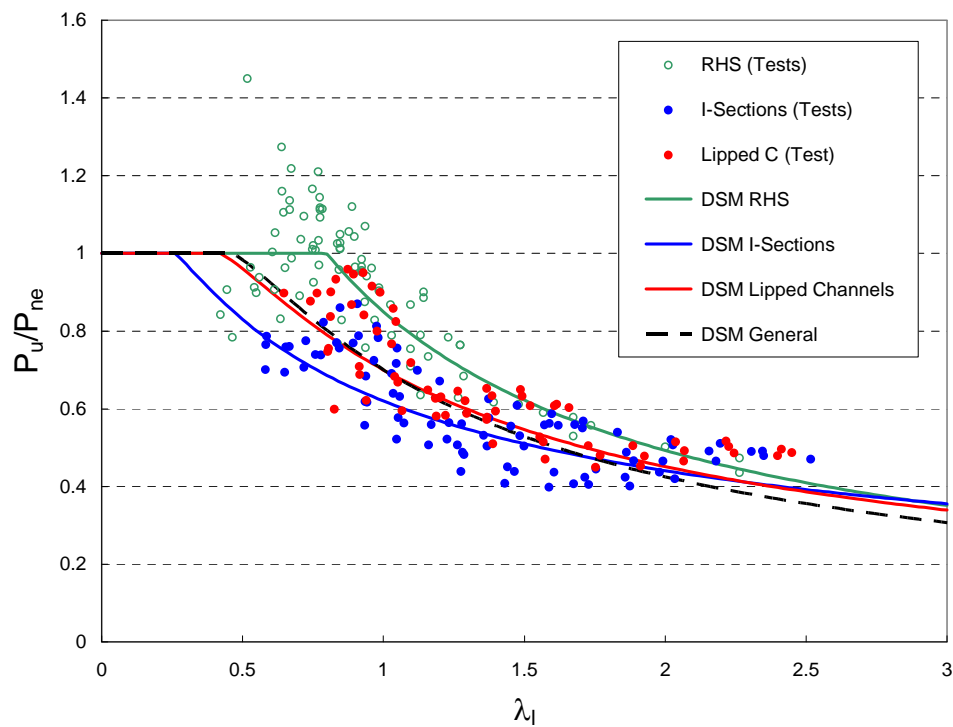


Figure 3.7. Tangent Approach Based DSM by Cross-Section Type

Table 3.9. Tangent Approach based DSM for Particular Cross-Sections

	Coefficients			λ_{limit}	$P_{u,p}/P_{u,n}$		ϕ
	a	b	c		Mean	COV	
Lipped Channels	0.90	0.20	0.8	0.420	1.07	0.11	0.85
SHS/RHS	1.00	0.15	0.9	0.798	1.03	0.11	0.85
I-Sections	0.76	0.14	0.6	0.261	1.05	0.13	0.85
All Sections	0.90	0.20	0.9	0.463	1.10	0.16	0.85

3.3.4 Proposed DSM for Stainless Steel Columns based on the Eurocode

To develop a DSM for stainless steel columns which fits within the framework of EC3, P_{ne} is calculated as:

$$P_{ne} = \chi P_{0.2\%} \quad (53)$$

where χ is calculated using Eqs. (39) and (38) with $\alpha = 0.49$ and $\lambda_0 = 0.40$. The slenderness λ to be used in Eqs. (39) and (38) is the overall slenderness:

$$\lambda = \sqrt{\frac{P_{0.2\%}}{P_E}} \quad (54)$$

where P_E is the Euler buckling load.

A reliability analysis on the 245 available data points with $\beta = 2.5$ and $\phi = 1/\gamma_M = 1/1.1 = 0.91$ yields the following Direct Strength equation:

$$P_{nl} = \begin{cases} P_{ne} & \text{for } \lambda_1 \leq 0.55 \\ \left[\left(0.95 - \frac{0.22}{\lambda_1} \right) \frac{1}{\lambda_1} \right] P_{ne} & \text{for } \lambda_1 > 0.55 \end{cases} \quad (55)$$

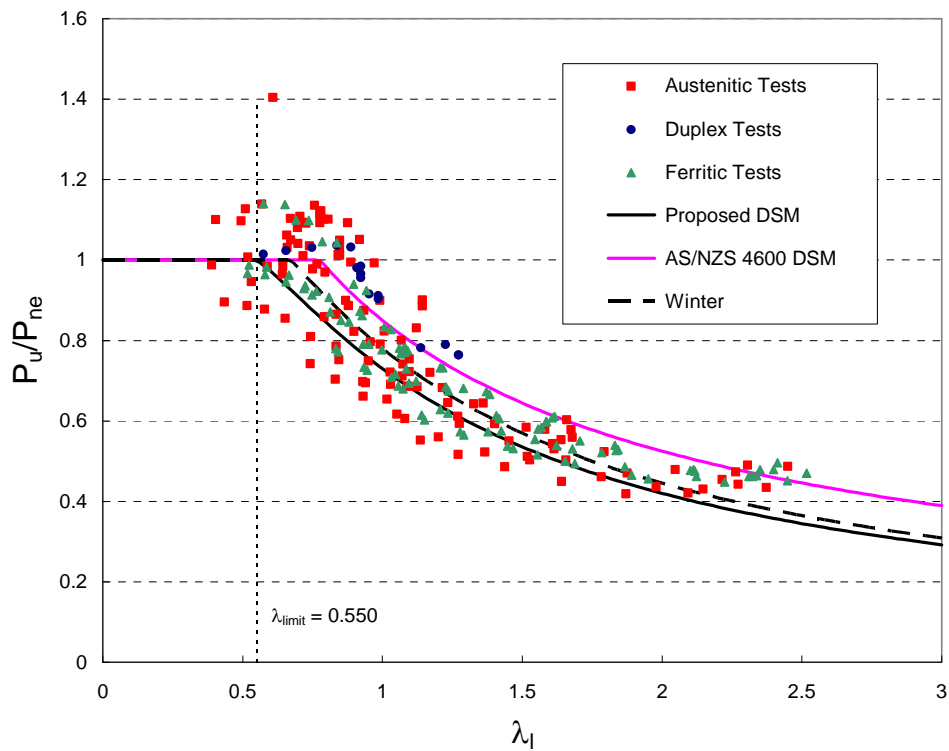


Figure 3.8. Comparison of DSM for EC3 with Test Results

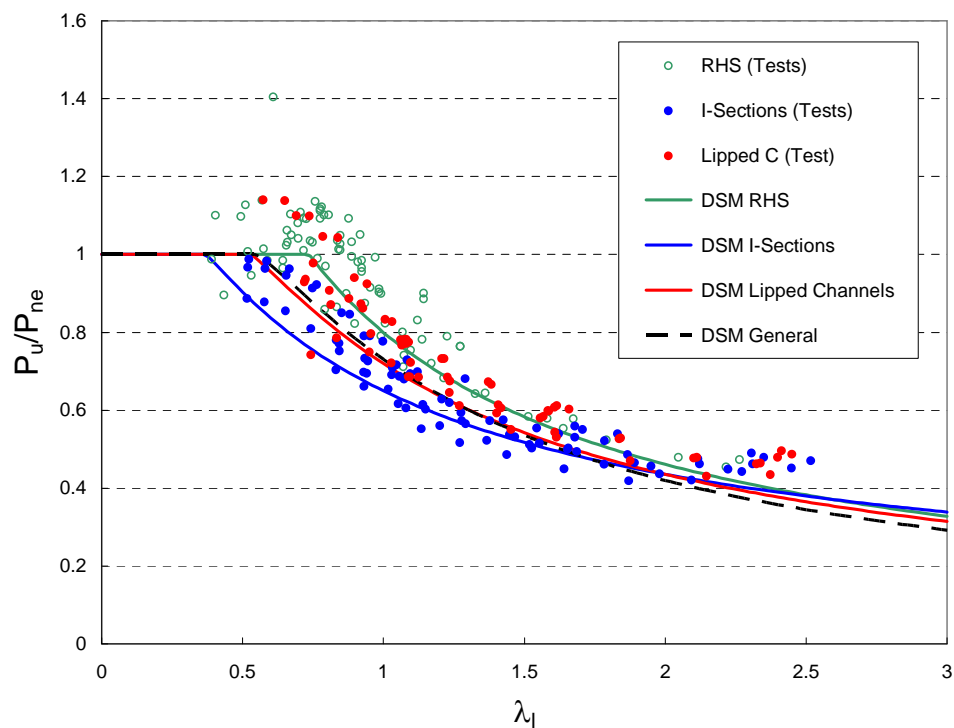


Figure 3.9. DSM for EC3 by Cross-Section

The a , b and c coefficients for cross-section specific DSM equations are listed in Table 3.10. They resulted from a reliability analysis on the relevant data with $\beta = 2.5$ and $\phi = 0.91$.

Table 3.10. DSM for EC3 for Particular Cross-Sections

	Coefficients			λ_{limit}	$P_{u,p}/P_{u,n}$		ϕ
	a	b	c		Mean	COV	
Lipped Channels	0.92	0.2	0.9	0.533	1.12	0.08	0.91
SHS/RHS	0.93	0.14	0.9	0.717	1.10	0.10	0.91
I-Sections	0.80	0.15	0.7	0.371	1.08	0.08	0.91
All Sections	0.95	0.22	1.0	0.550	1.11	0.12	0.91

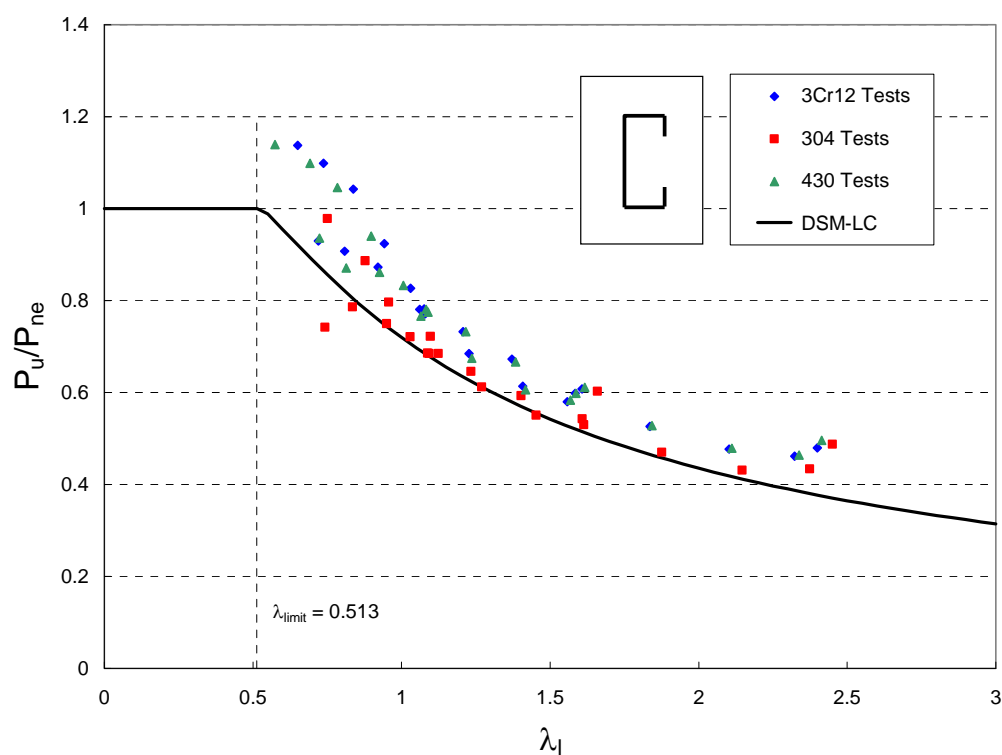


Figure 3.10. DSM (EC3) for Lipped Channels

When considering the data by cross-section, a clustering of the data by alloy type can be observed. This is illustrated in Fig. 3.10 for lipped channels: the austenitic data points on average display lower P_u/P_{ne} values than the ferritic (or ferritic-like 3Cr12) data points. This can be attributed to the fact that EC3 does not distinguish between different alloys when specifying the overall buckling strength, providing only one buckling curve for all alloys. However, study of Figs. 3.8 and 3.9 indicates that the clustering by cross-section is still more pronounced than the clustering by alloy type.

4 Conclusions

A detailed FE model was developed for the purpose of studying the interaction of local and overall buckling in stainless steel columns. The model accounted for the specific material characteristics of stainless steel: non-linear stress-strain behaviour, anisotropy and increased corner properties due to cold-working. The model was verified against an experimental program on stainless steel lipped channels failing in interaction buckling (Becque and Rasmussen 2006), an experimental program on stainless steel back-to-back channels failing in interaction buckling (Becque and Rasmussen 2007), and a test program on stainless steel SHS failing in overall buckling (Rasmussen and Hancock 1993). The study revealed that the FE model was capable of generating accurate predictions of the load carrying capacity, the failure mode and the specimen deformations.

The FE model was used to generate additional ultimate strength data for stainless steel lipped channels, plain channels, SHS and I-sections, the latter comprised of back-to-back channels. The parametric studies covered the practical ranges of cross-sectional and overall slenderness values for each cross-section type. Austenitic as well as ferritic alloys were considered.

The database of 317 experimental and numerical results was used to evaluate the current

Australian, North-American and European design guidelines for stainless steel. It was concluded that the design standards are unable to appropriately account for the interaction effect between local and overall buckling of stainless steel columns. As the cross-sectional slenderness increases and the interaction effect becomes more pronounced, the design standards become less conservative. All current design standards overestimate the load carrying capacity of stainless steel I-sections with intermediate and high cross-sectional slenderness.

Based on the available data, a direct strength method was proposed for stainless steel columns. A general method for stainless steel columns was presented, as well as specific equations for stainless steel SHS/RHS, lipped channels and I-sections.

References

- ABAQUS. (2005). "ABAQUS/standard user's manual, Volumes I-III" and "ABAQUS/CAE manual, v6.5." Hibbit, Karlsson, and Sorensen, ABAQUS Inc., Pawtucket, RI.
- AS/NZS:4600. (2004). "Cold-Formed Steel Structures." Australian Standard/New Zealand Standard, Standards Australia, Sydney, Australia.
- AS/NZS:4673. (2004). "Cold-Formed Stainless Steel Structures." Australian Standard/New Zealand Standard, Standards Australia, Sydney, Australia.
- Ashraf, M., Gardner, L., and Nethercot, D. A. (2005). "Strength Enhancement of the Corner Regions of Stainless Steel Cross-Sections." *Journal of Constructional Steel Research*, 61(1), 37-52
- Becque, J., and Rasmussen, K.J.R. (2006). "Experimental Investigation of the Interaction of Local and Overall Buckling of Cold-Formed Stainless Steel Sections." Research Report No. 873, School of Civil Engineering, University of Sydney, Sydney.
- Becque, J., and Rasmussen, K.J.R. (2007). "Experimental Investigation of the Interaction of Local and Overall Buckling of Stainless Steel I-Sections." Research Report No. 887, School of Civil Engineering, University of Sydney, Sydney.
- Bredenkamp, P. J., van den Berg, G. J., and van der Merwe, P. (1992). "Residual Stresses and the Strength of Stainless Steel I-Section Columns." *Proc., Structural Stability Research Council, Annual Technical Session*, Pittsburg, 69-86.
- Eurocode3-1.1 (1992). "Eurocode3: Design of Steel Structures.", Part 1.1: "General Rules and Rules for Buildings.", EN-1993-1-1, European Committee for Standardization, Brussels.
- Eurocode3-1.3 (2002). "Eurocode3: Design of Steel Structures.", Part 1.3: "Supplementary Rules for Cold-Formed Thin Gauge Members and Sheeting.", EN-1993-1-3, European Committee for Standardization, Brussels.

- Eurocode3-1.4 (2004). “Eurocode3: Design of Steel Structures.”, Part 1.4: “Supplementary Rules for Stainless Steel.”, prEN-1993-1-4, European Committee for Standardization, Brussels.
- Eurocode3-1.5 (2004). “Eurocode3: Design of Steel Structures.”, Part 1.5: “Plated Structural Elements.”, prEN-1993-1-5, European Committee for Standardization, Brussels.
- Gardner, L., and Nethercot D.A. (2003). “Experiments on Stainless Steel Hollow Sections-Part 2: Member Behaviour of Columns and Beams” *Journal of Constructional Steel Research* 60, 1319-1332.
- Gardner, L., and Nethercot, D. A. (2004). “Numerical Modeling of Stainless Steel Structural Components-A Consistent Approach.” *Journal of Structural Engineering* 130(10), 1586-1601.
- Gardner, L., Talja, A., and Baddoo, N. R. (2006). “Structural Design of High-Strength Austenitic Stainless Steel” *Thin-Walled Structures* 44, 517-528.
- Hill, R. (1950). “The Mathematical Theory of Plasticity.” Oxford University Press, London.
- Lagerqvist, O., and Olsson, A. (2001). “Residual Stresses in Welded I-Girders made of Stainless Steel and Structural Steel.” *Proc., 9th Nordic Steel Construction Conference*, Makelainen et al., eds., Helsinki, Finland, 737-744.
- Lecce, M., and Rasmussen, K.J.R. (2005). “Experimental Investigation of the Distortional Buckling of Cold-Formed Stainless Steel Sections.” Research Report No. 844, School of Civil Engineering, University of Sydney, Sydney.
- Lin, S. H., Yu, W. W., and Galambos, T. V. (1988). “Load and Resistance Factor Design of Cold-Formed Stainless Steel – Statistical Analysis of Material Properties and Development of the LRFD Provisions.” *Fourth Progress Report*, University of Missouri-Rolla.
- Lin, S. H., Yu, W. W., and Galambos, T. V. (1992). “ASCE LRFD Method for Stainless Steel Structures.” *Journal of Structural Engineering*, 118(4), 1056-1070.

- Liu, Y., and Young, B. (2003). "Buckling of Stainless Steel Square Hollow Section Compression Members" *Journal of Constructional Steel Research* 59, 165-177.
- Masubuchi, K. (1980). *Analysis of Welded Structures*. Pergamon, New York.
- NAS. (2001). "North American Specification for the Design of Cold-Formed Steel Structural Members." American Iron and Steel Institute, Washington, D.C.
- NAS. (2004). "Appendix I Design of Cold-Formed Steel Structural Members with the Direct Strength Method." American Iron and Steel Institute, Washington, D.C.
- Papangelis, J.P., and Hancock, G.J. (1995). "Computer Analysis of Thin-walled Structural Members." *Computers and Structures* 56(1):157-176.
- Rasmussen, K.J.R., Hancock, G.J. (1993). "Design of Cold-Formed Stainless Steel Tubular Members. I: Columns." *Journal of Structural Engineering* 119(8):2349-2367.
- Rasmussen, K., and Rondal, J. (1997). "Explicit Approach to Design of Stainless Steel Columns." *Journal of Structural Engineering* 123(7), 857-863.
- Schafer, B. W., and Pekoz, T. (1998). "Computational Modeling of Cold-Formed Steel: Characterizing Geometric Imperfections and Residual Stresses." *Journal of Constructional Steel Research*, 47(3), 193-210.
- Talja, A., and Salmi, P. (1995). "Design of Stainless Steel RHS Beams, Columns and Beam-Columns." Research Note 1619, VTT Building Technology, Helsinki, Finland.
- van den Berg, G. J., and van der Merwe, P. (1992). "Prediction of Corner Mechanical Properties for Stainless Steels due to Cold-Forming." *Proc. 11th Specialty Conference on Cold-Formed Steel Structures*, St. Louis, USA, 571-586.
- Walker, A. C. (1975). *Design and Analysis of Cold-Formed Sections*. International Textbook Company Ltd., London.

Winter, G. (1940). "Strength Distribution in and Equivalent Width of Flanges of Wide, Thin-Walled Steel Beams." *NACA Technical Note (784)*.

Winter, G. (1947). "Strength of Thin Steel Compression Flanges." *Transactions*, 112, 527-554.

Young, B., and Liu, Y. (2003). "Experimental Investigation of Cold-Formed Stainless Steel Columns" *Journal of Structural Engineering*, 129(2), 169-176.

Young, B., and Lui W. M. (2006). "Tests of Cold-Formed High Strength Stainless Steel Compression Members" *Thin-Walled Structures* 44, 224-234.

Appendix A

This appendix presents illustrations of the different mesh configurations discussed in paragraph 2.2.6.2 of the main text. A picture of the deformed shape with the Von Mises surface stress contours is also presented for each mesh.

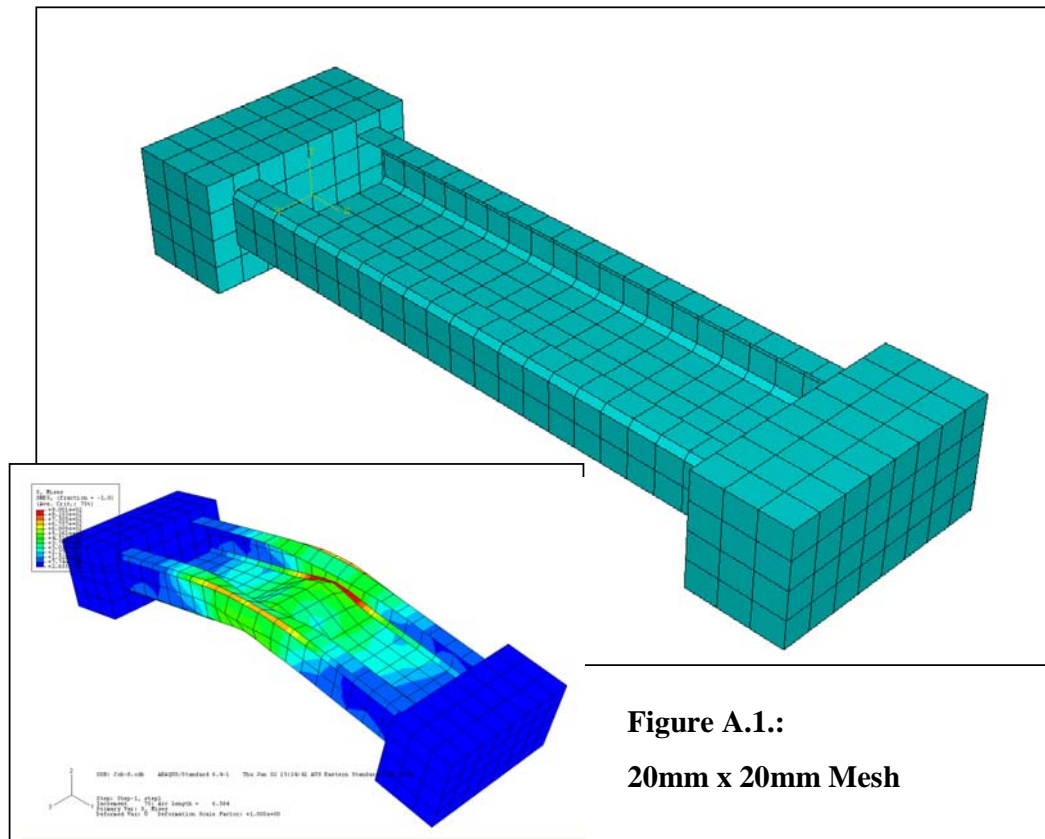


Figure A.1.:
20mm x 20mm Mesh

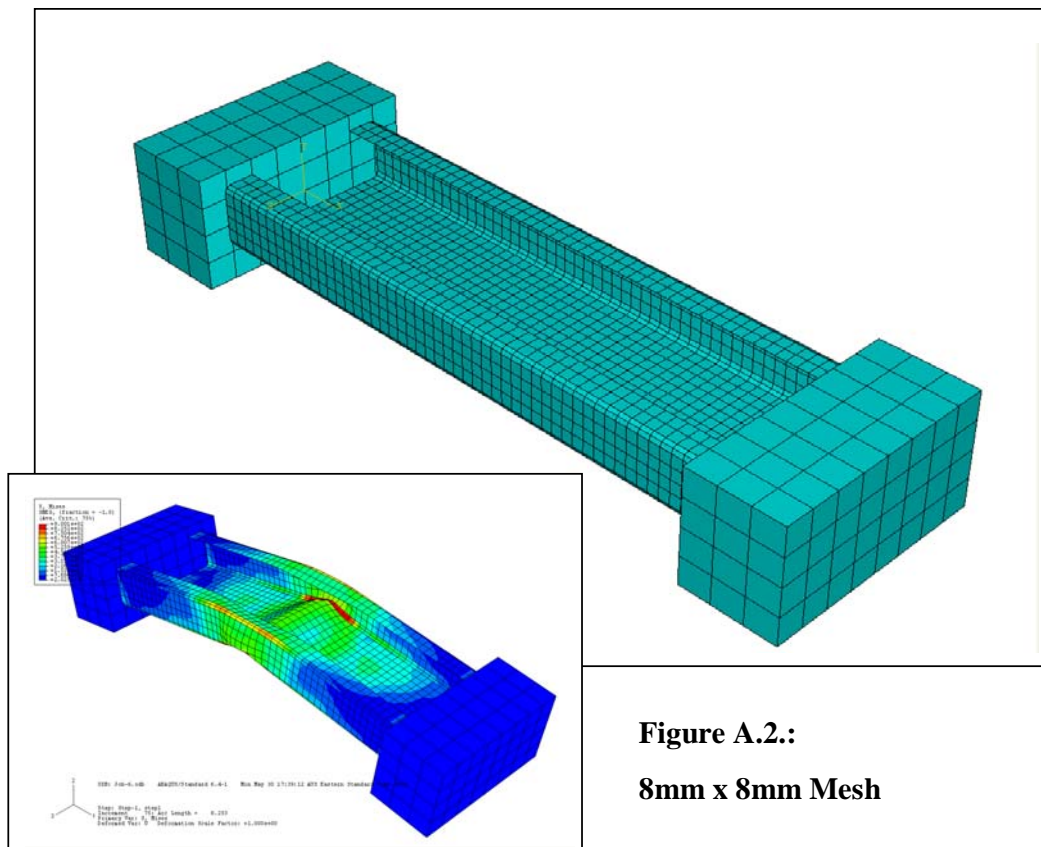


Figure A.2.:
8mm x 8mm Mesh

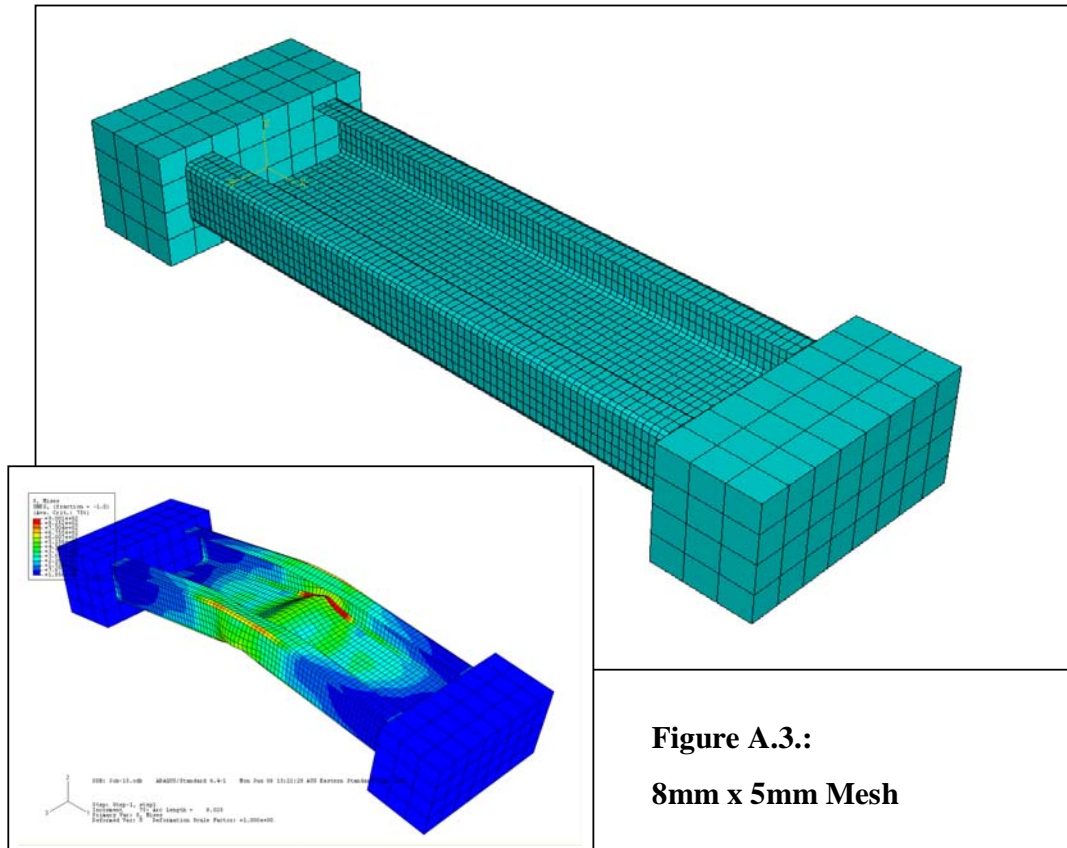


Figure A.3.:
8mm x 5mm Mesh

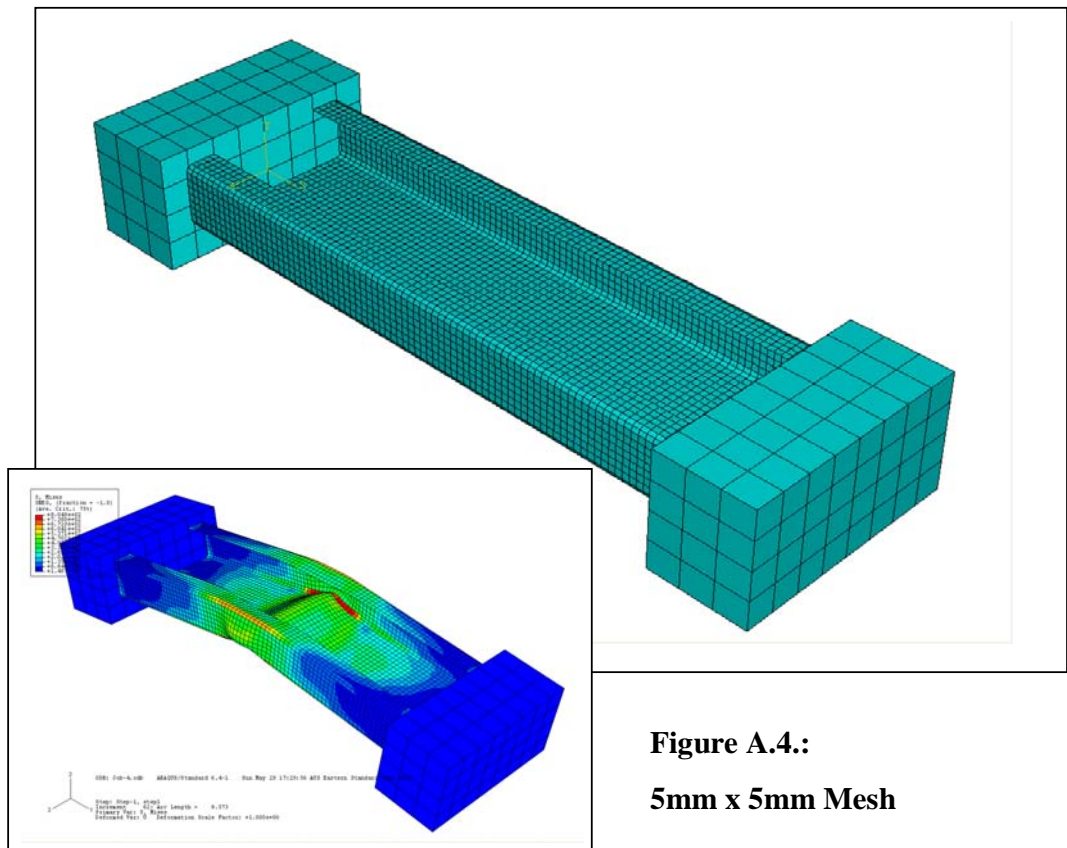


Figure A.4.:
5mm x 5mm Mesh

Appendix B

Appendix B compares the output results of the Finite Element model with the test data on lipped channels (Becque and Rasmussen 2006). The comparison is made for the axial displacements, lateral displacements, end rotations and local buckling displacements of each specimen.

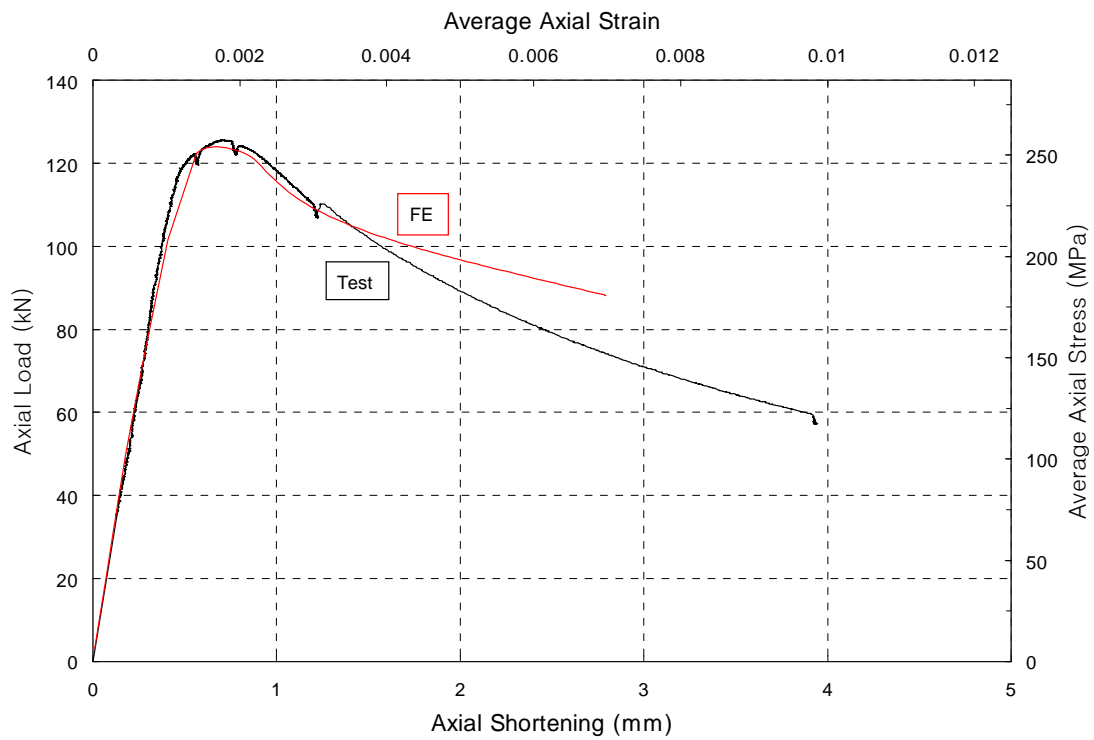


Figure B1.a. C3Cr12_400_1: Axial Load vs. Axial Shortening

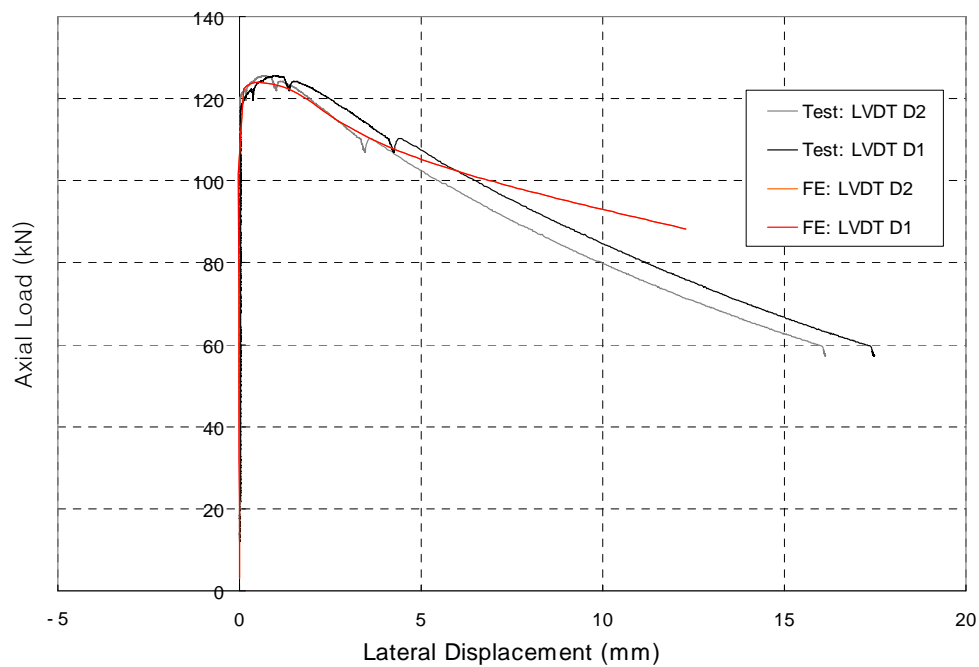


Figure B1.b. C3Cr12_400_1: Axial Load vs. Lateral Displacement

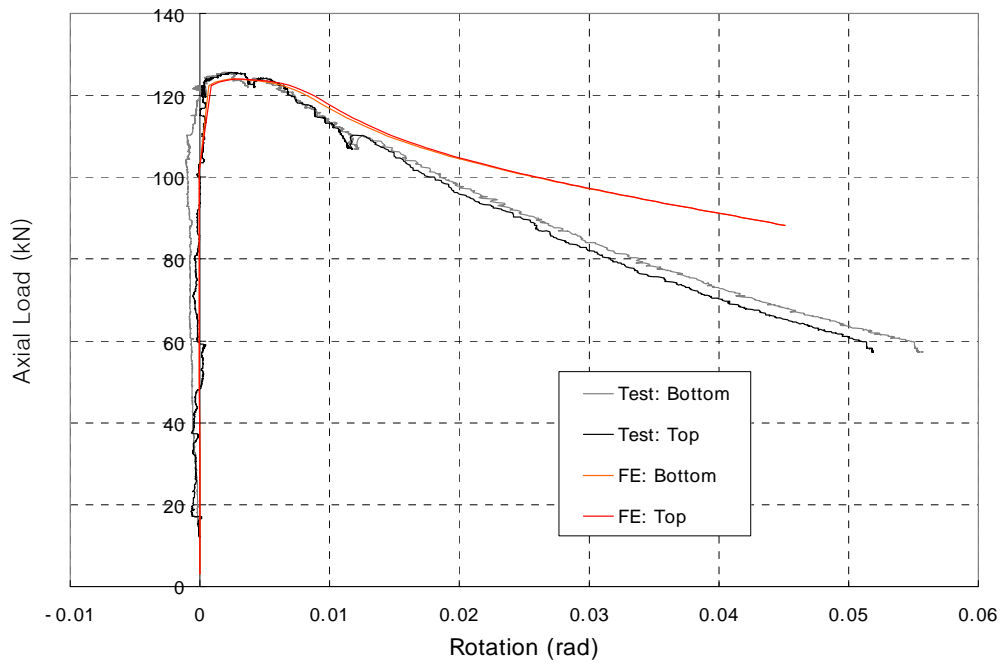


Figure B1.c. C3Cr12_400_1: Axial Load vs. End Rotations

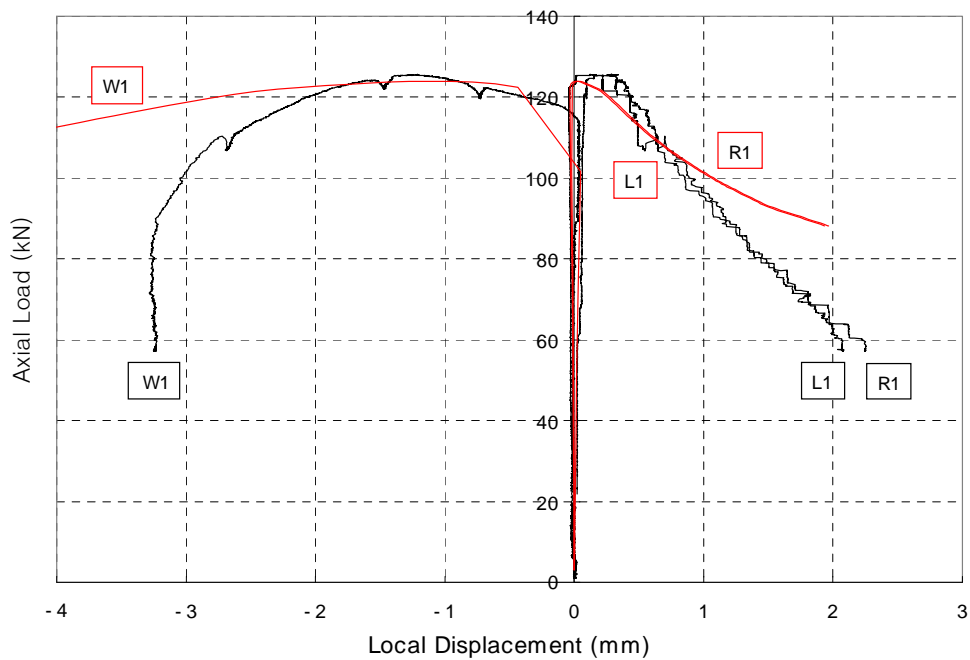


Figure B1.d. C3Cr12_400_1: Axial Load vs. Local Displacements

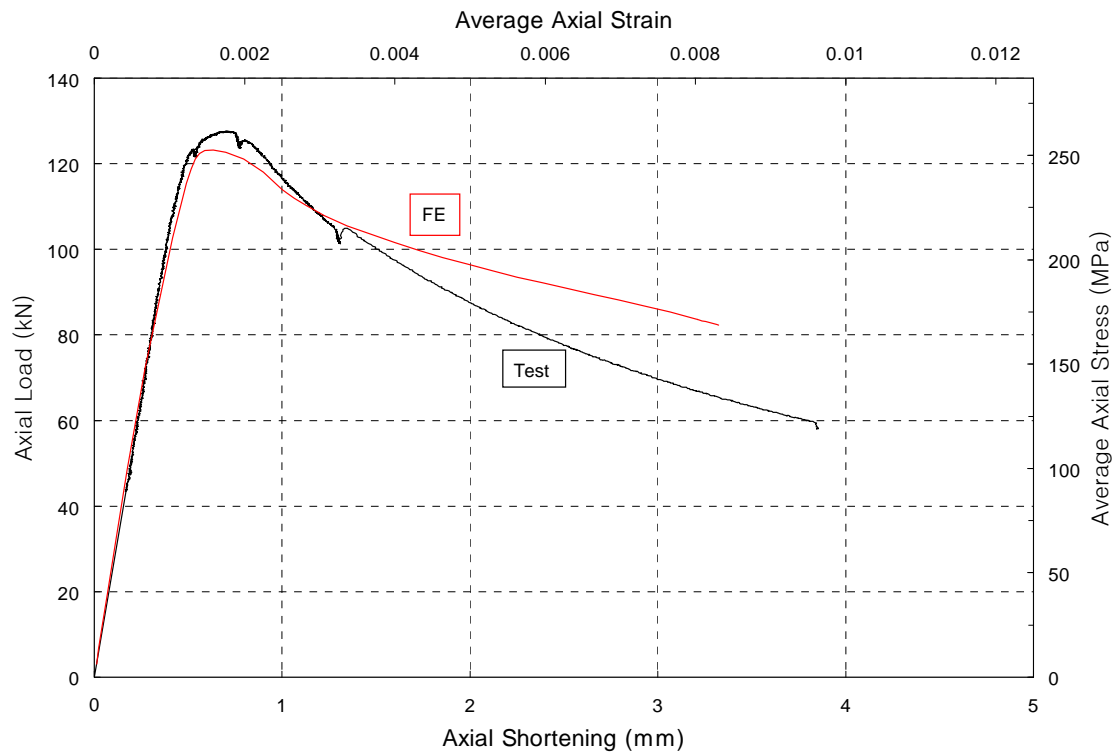


Figure B2.a. C3Cr12_400_2: Axial Load vs. Axial Shortening

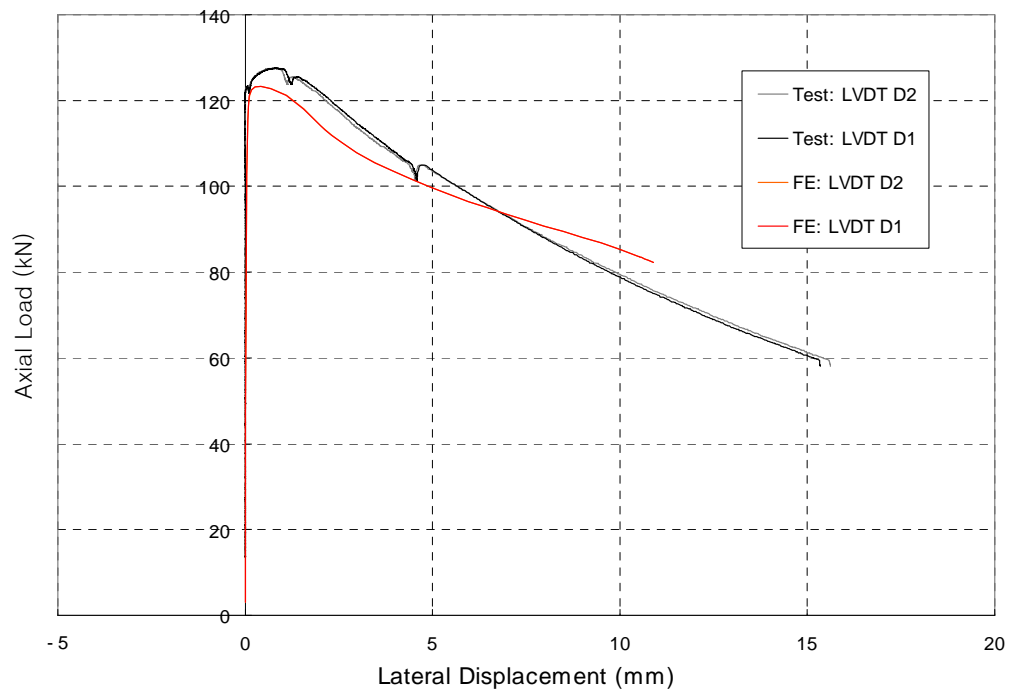


Figure B2.b. C3Cr12_400_2: Axial Load vs. Lateral Displacement

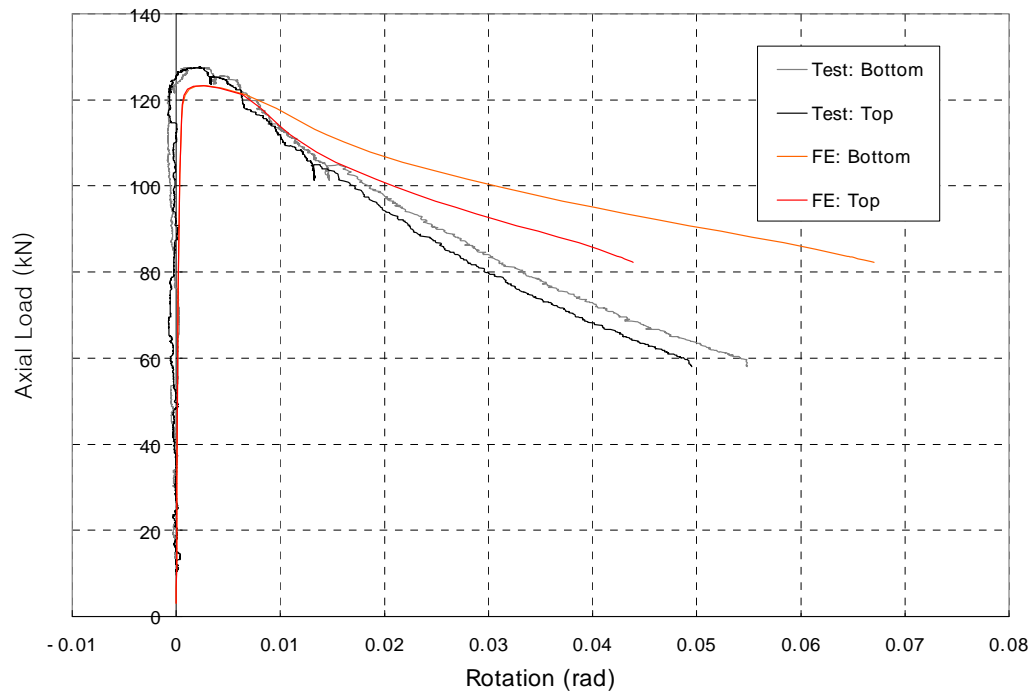


Figure B2.c. C3Cr12_400_2: Axial Load vs. End Rotations

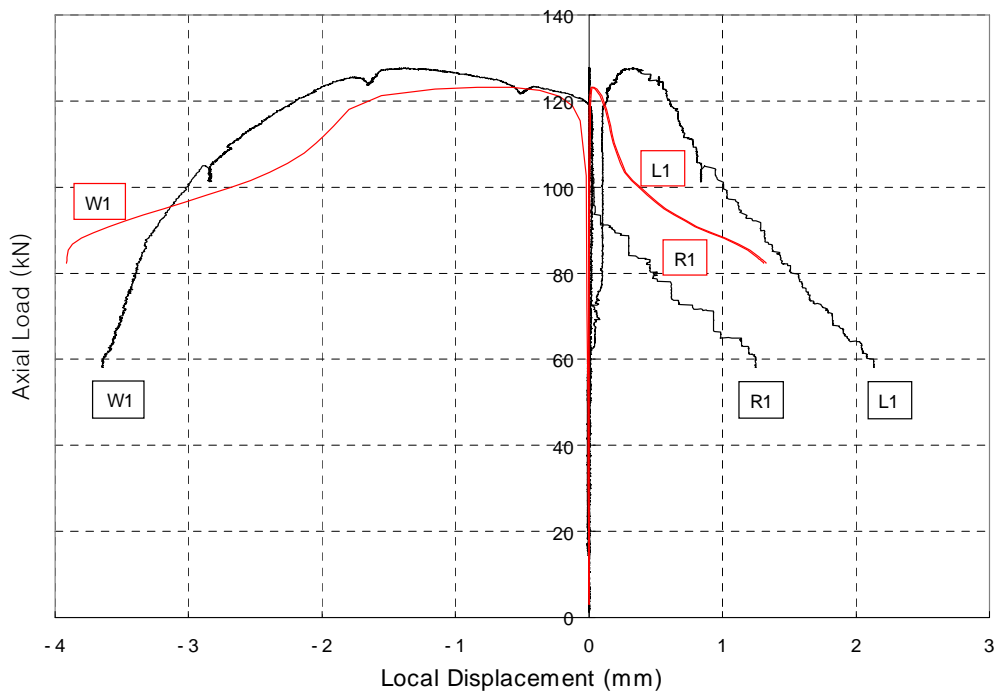


Figure B2.d. C3Cr12_400_2: Axial Load vs. Local Displacements

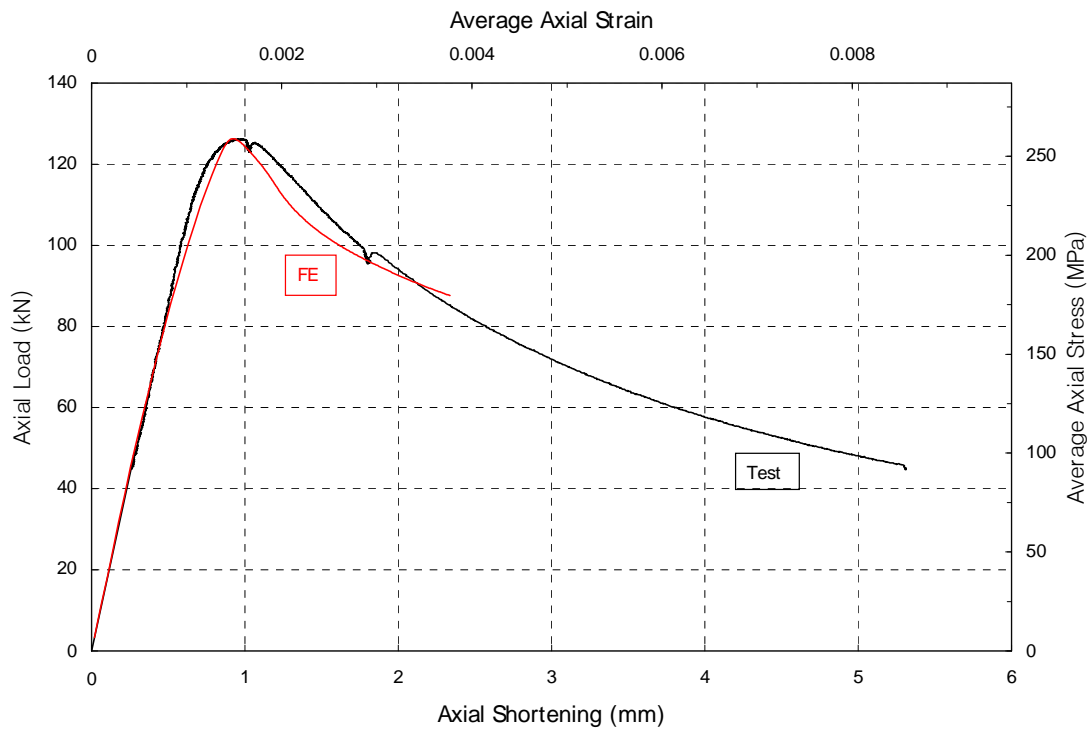


Figure B3.a. C3Cr12_620_1: Axial Load vs. Axial Shortening

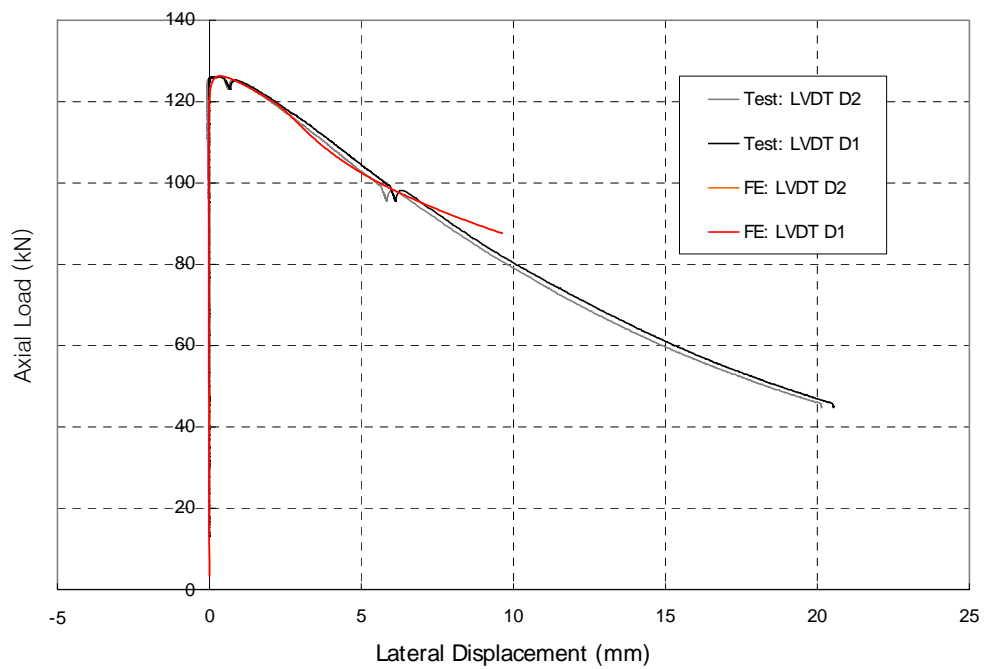


Figure B3.b. C3Cr12_620_1: Axial Load vs. Lateral Displacement

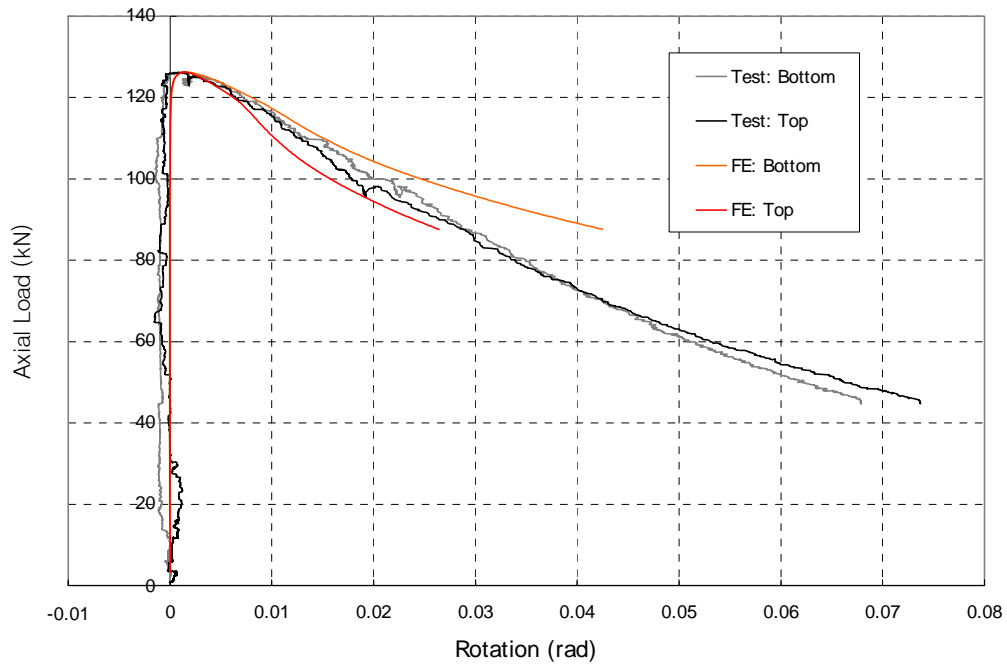


Figure B3.c. C3Cr12_620_1: Axial Load vs. End Rotations

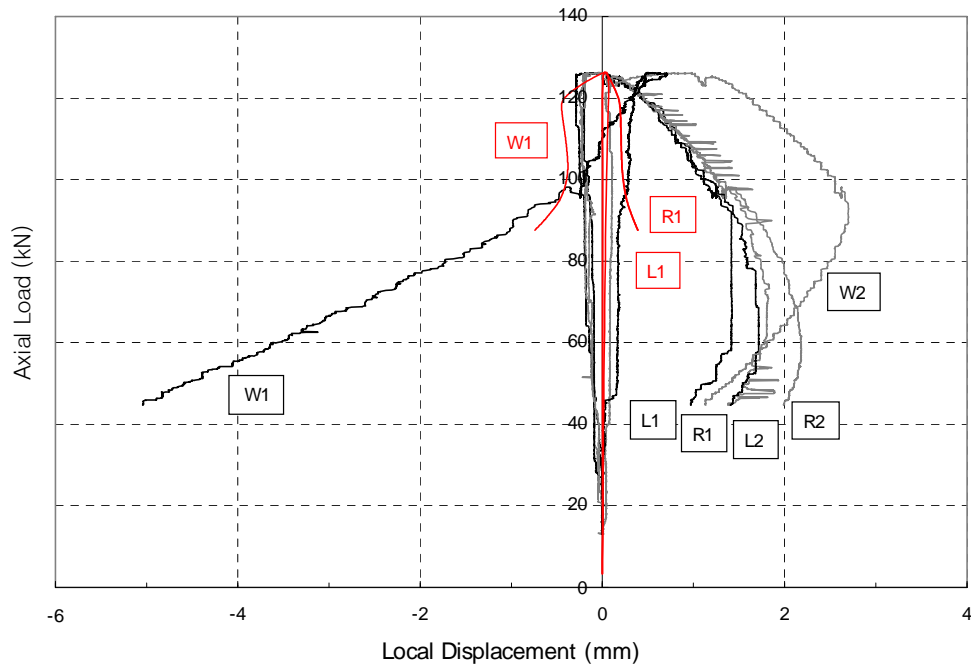


Figure B3.d. C3Cr12_620_1: Axial Load vs. Local Displacements

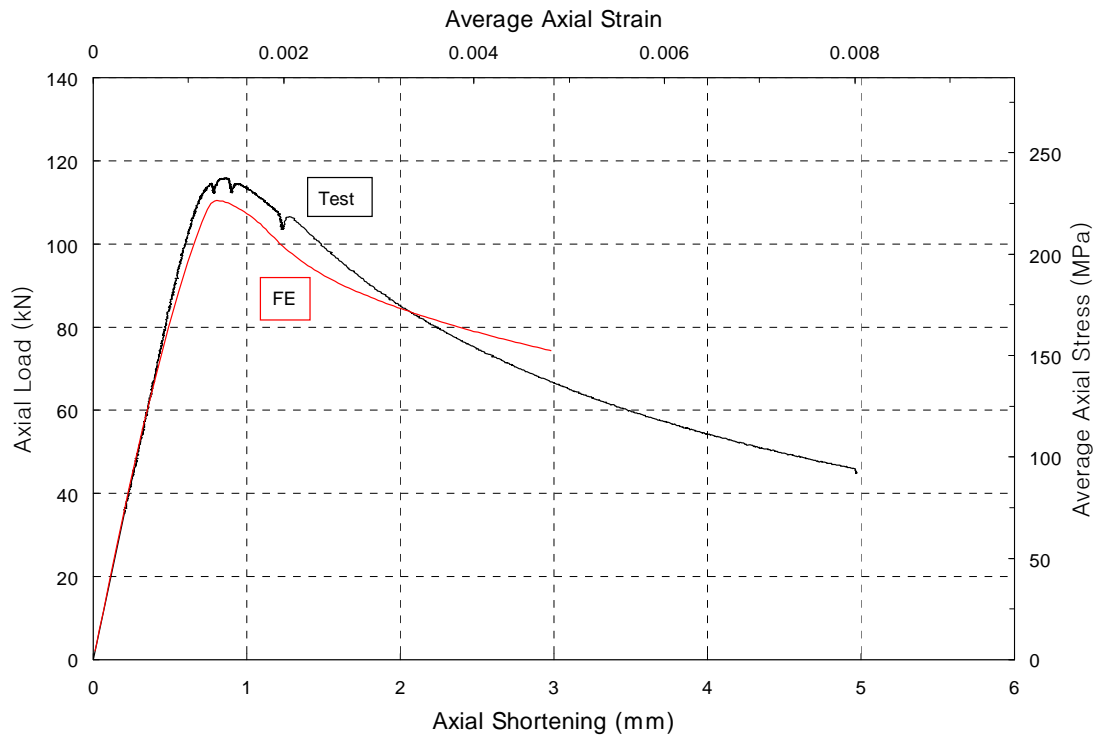


Figure B4.a. C3Cr12_620_2: Axial Load vs. Axial Shortening

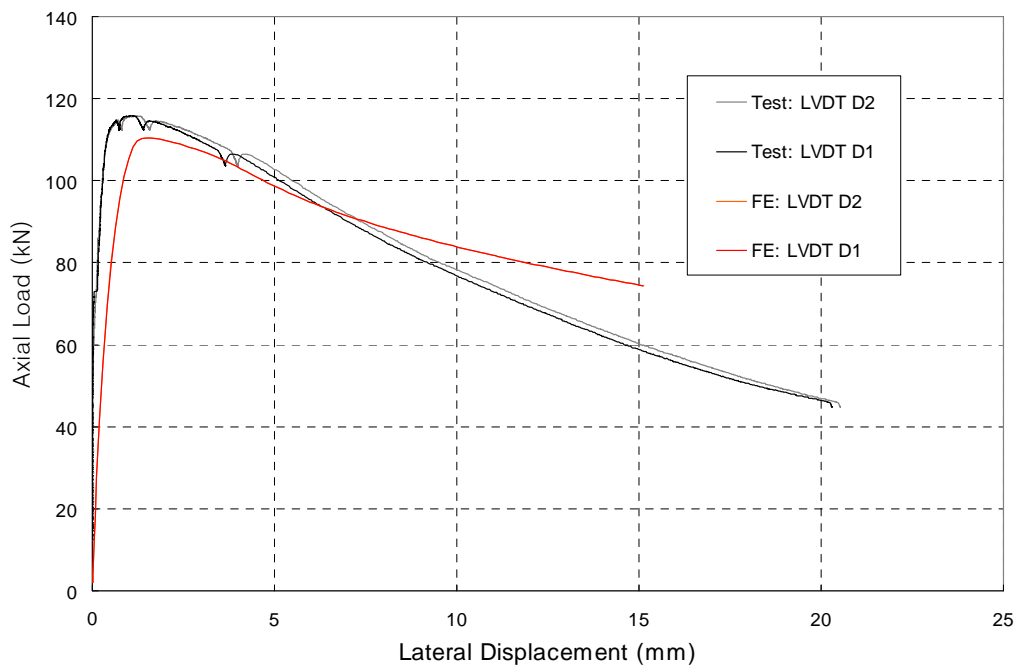


Figure B4.b. C3Cr12_620_2: Axial Load vs. Lateral Displacement

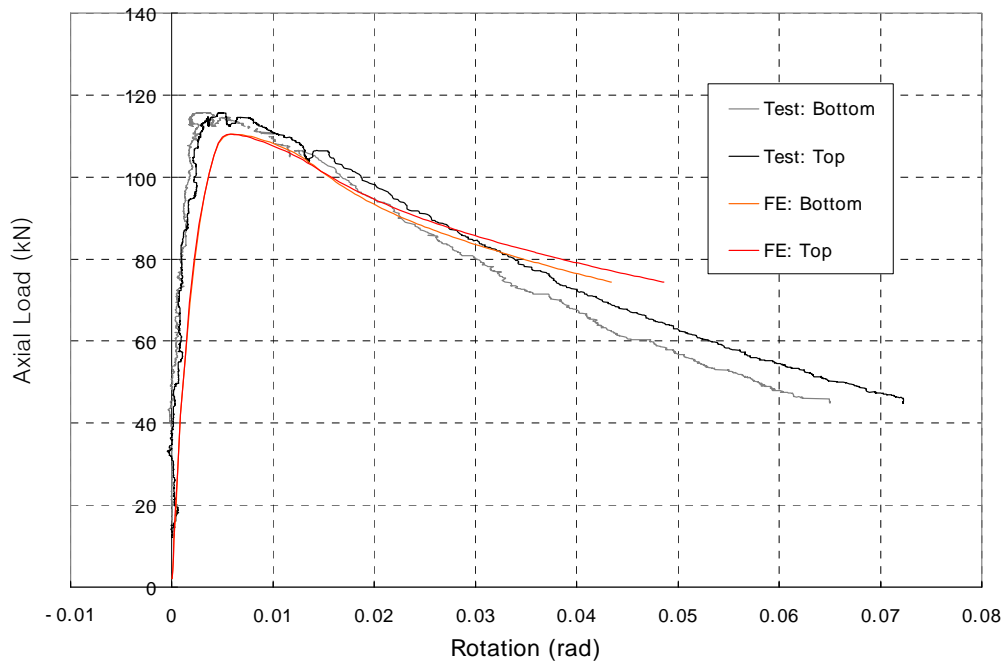


Figure B4.c. C3Cr12_620_2: Axial Load vs. End Rotations

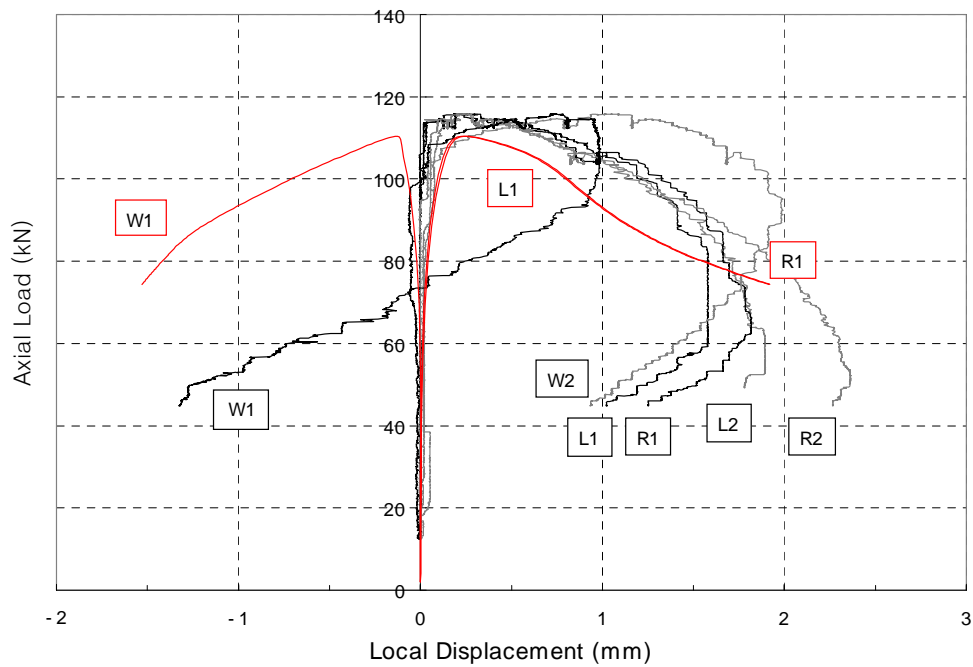


Figure B4.d. C3Cr12_620_2: Axial Load vs. Local Displacements

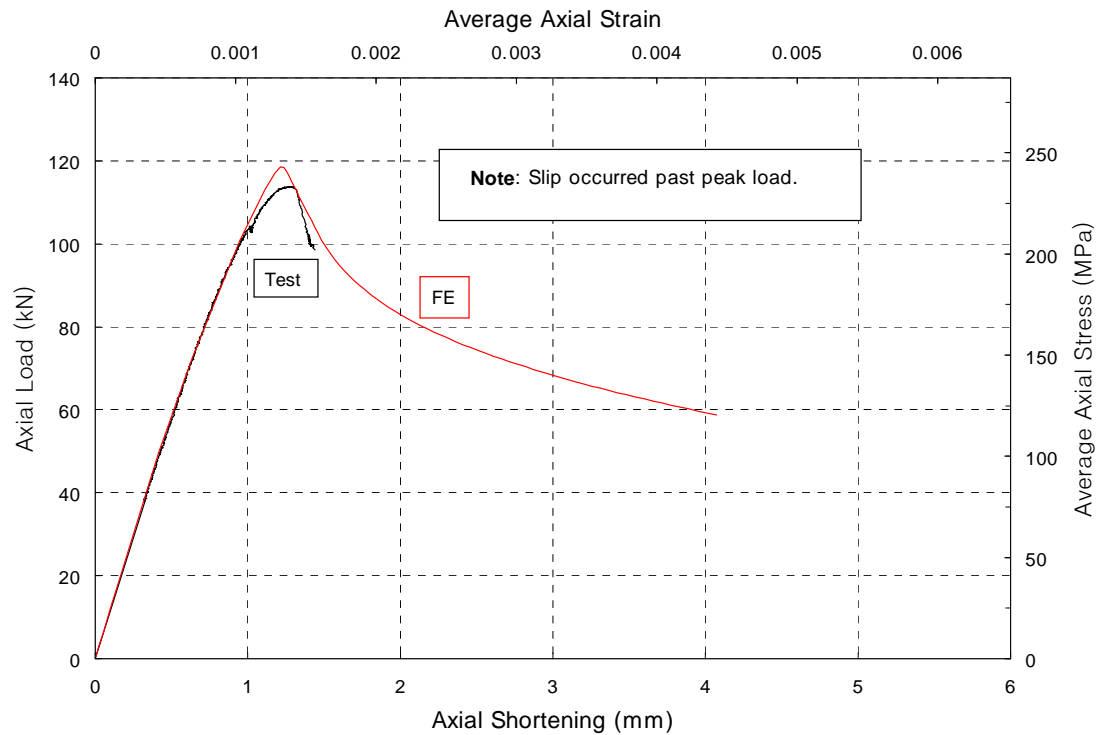


Figure B5.a. C3Cr12_920_1: Axial Load vs. Axial Shortening

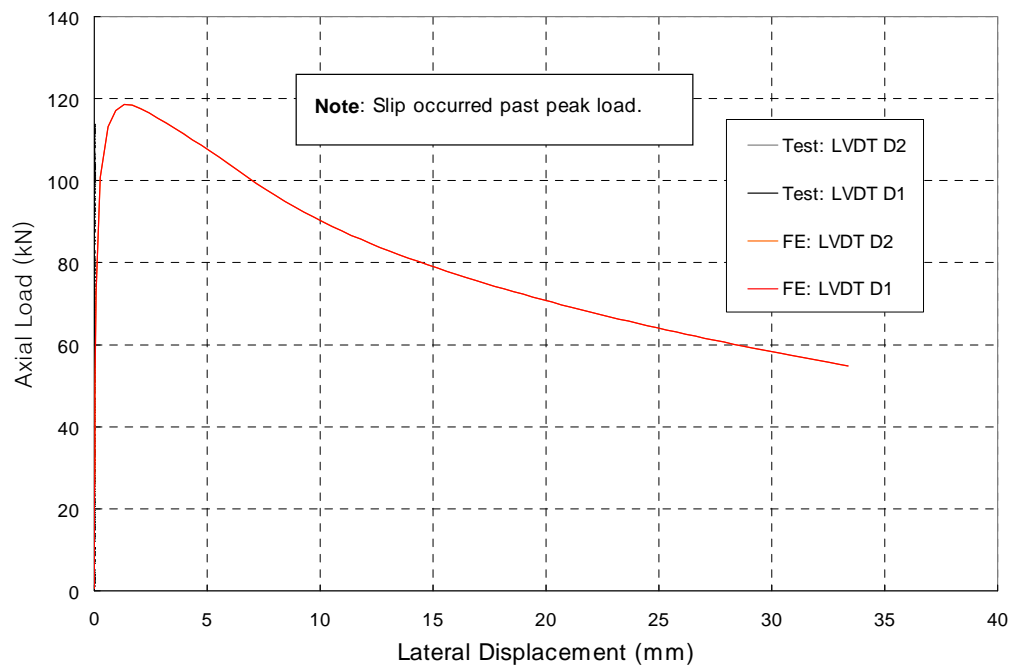


Figure B5.b. C3Cr12_920_1: Axial Load vs. Lateral Displacement

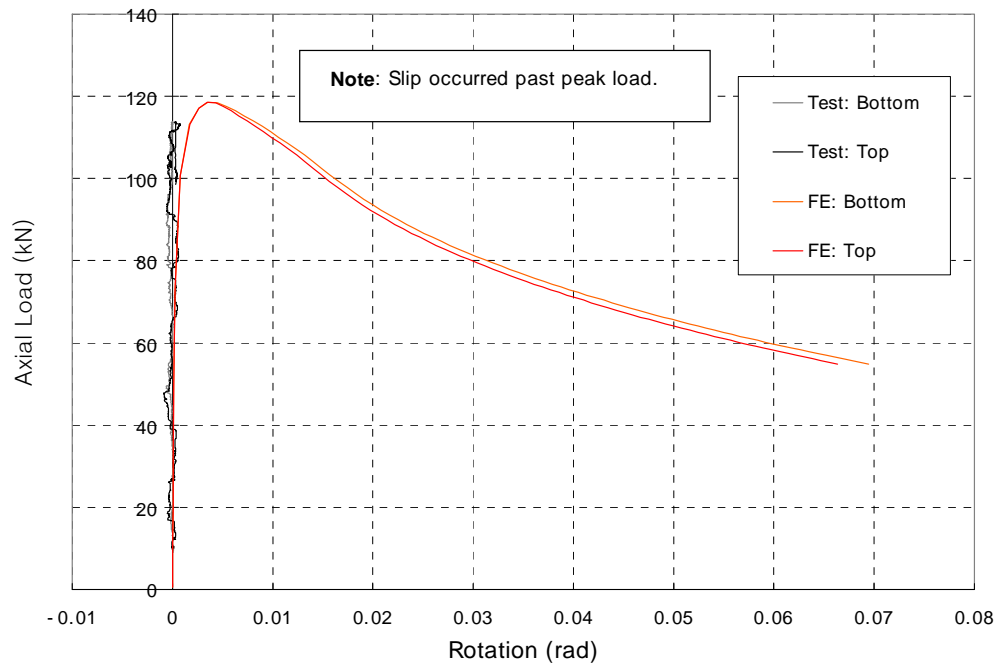


Figure B5.c. C3Cr12_920_1: Axial Load vs. End Rotations

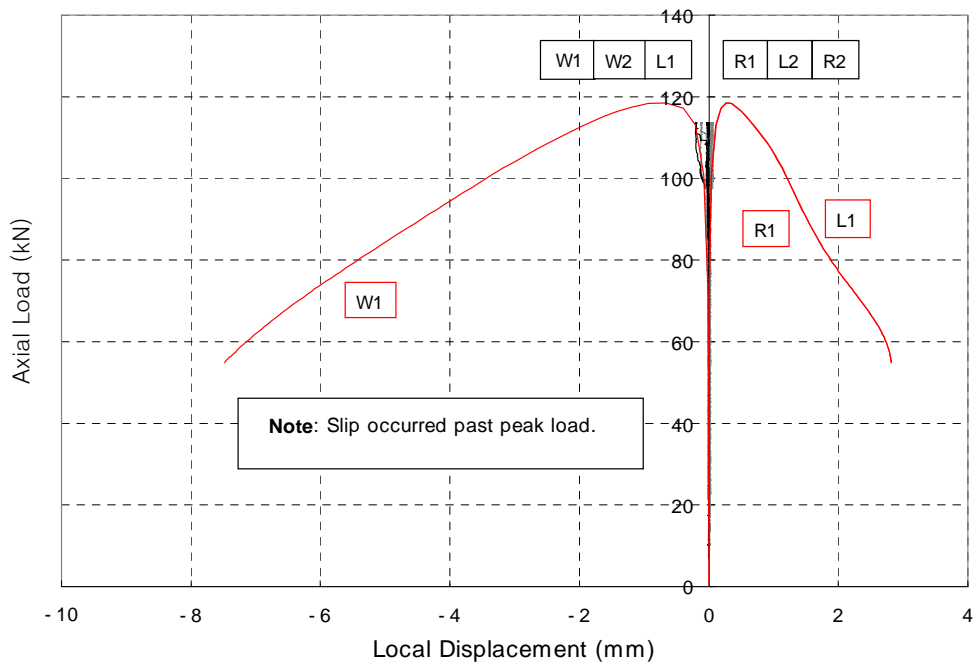


Figure B5.d. C3Cr12_920_1: Axial Load vs. Local Displacements

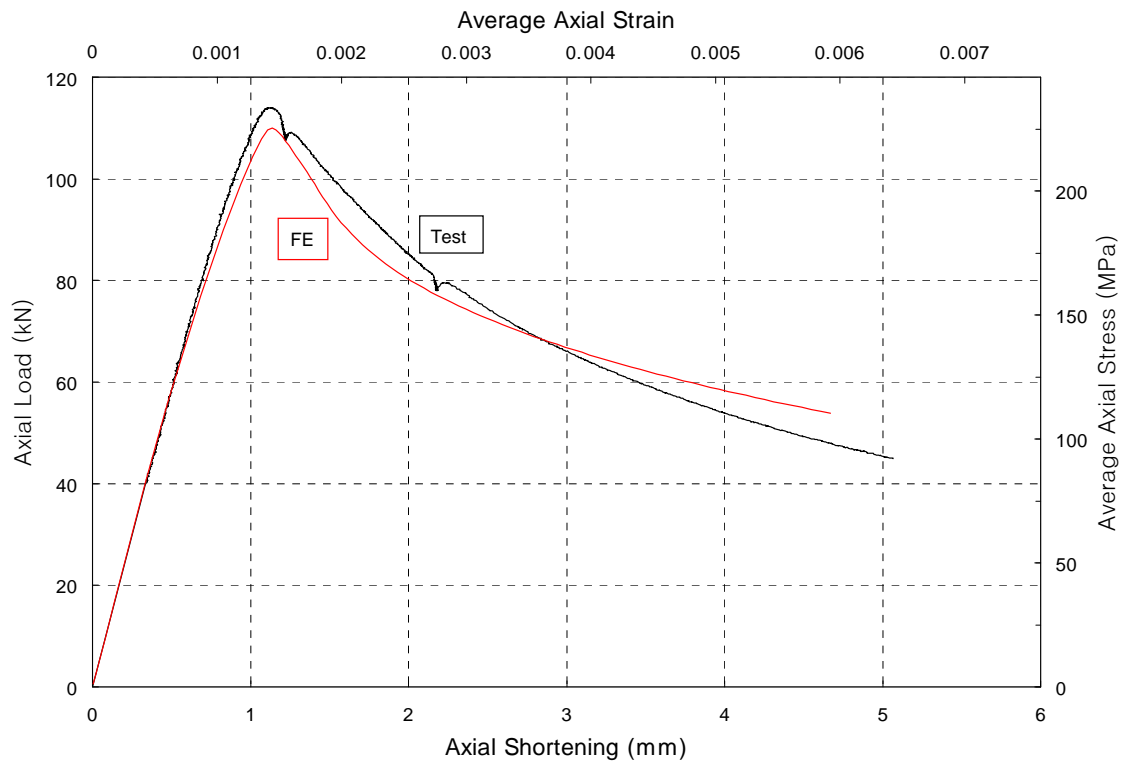


Figure B6.a. C3Cr12_920_2: Axial Load vs. Axial Shortening

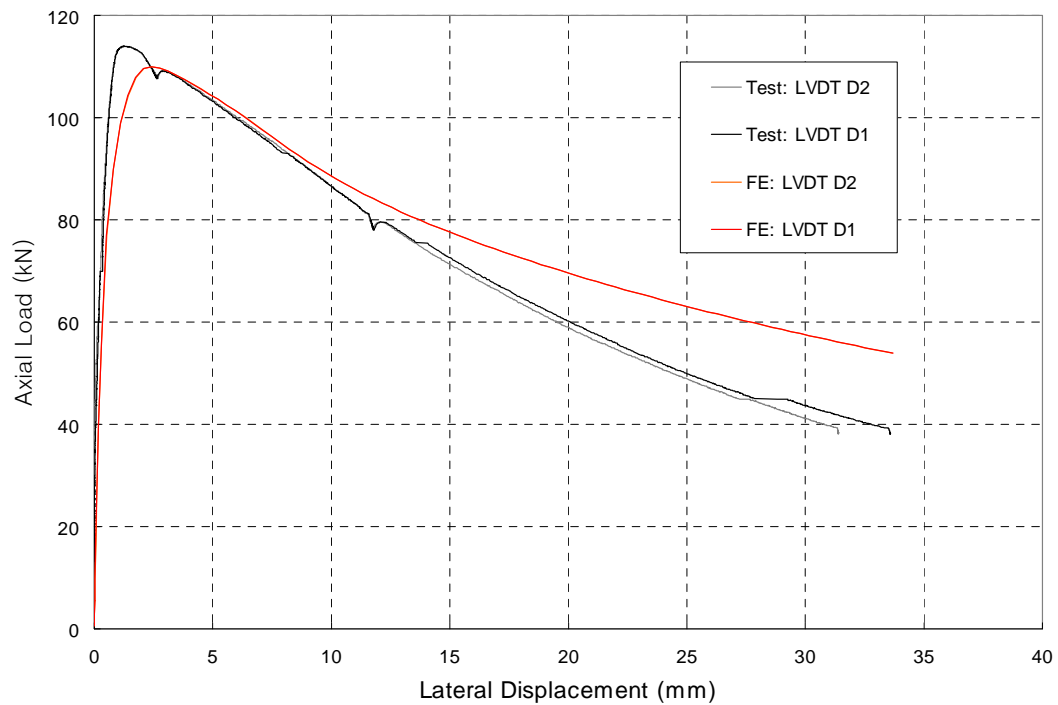


Figure B6.b. C3Cr12_920_2: Axial Load vs. Lateral Displacement

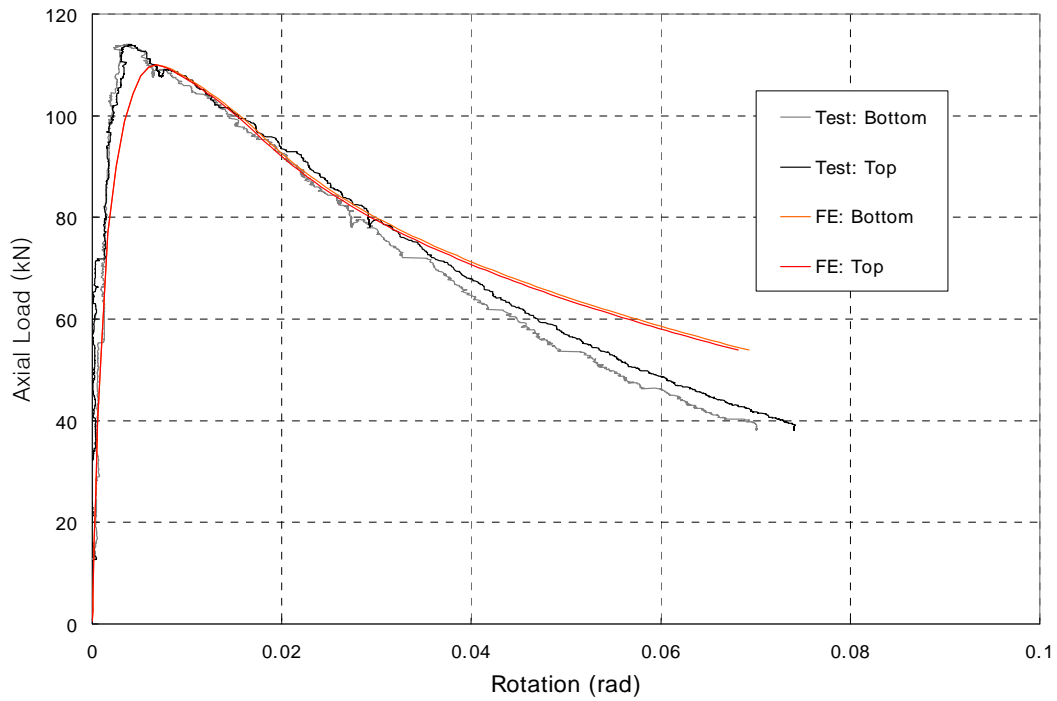


Figure B6.c. C3Cr12_920_2: Axial Load vs. End Rotations

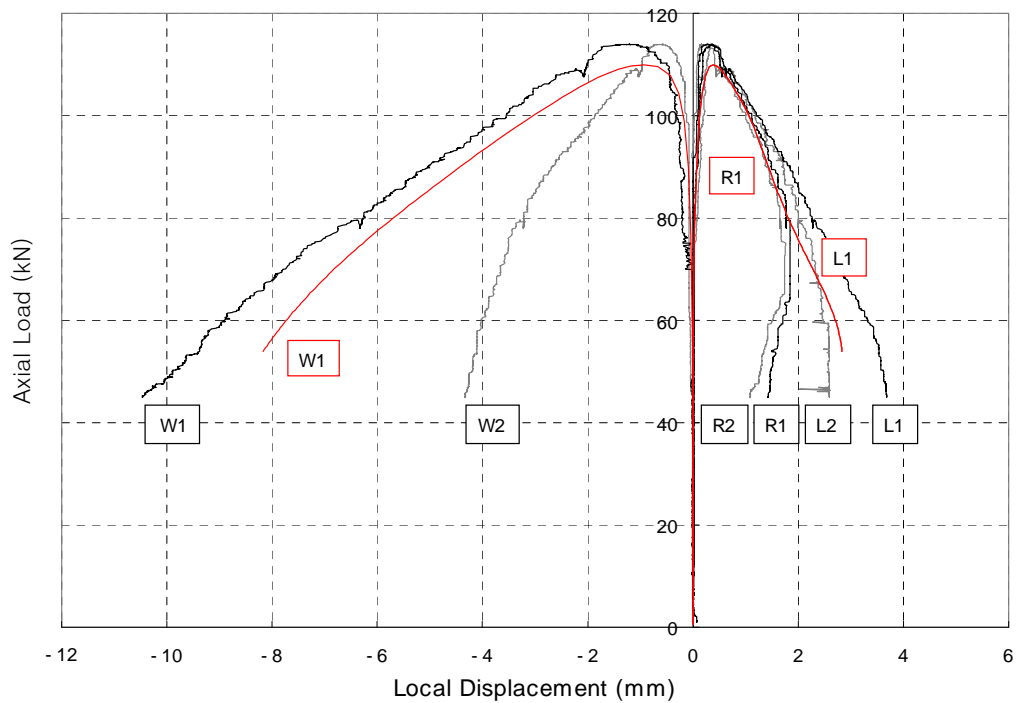


Figure B6.d. C3Cr12_920_2: Axial Load vs. Local Displacements

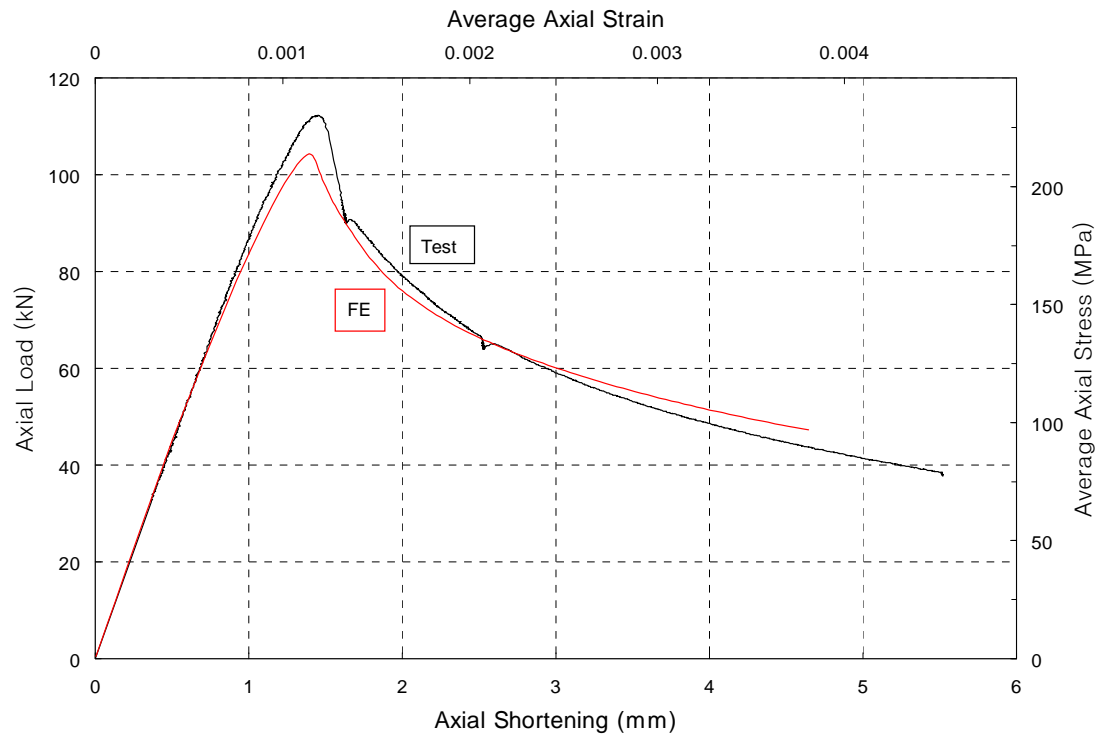


Figure B7.a. C3Cr12_1220_1: Axial Load vs. Axial Shortening

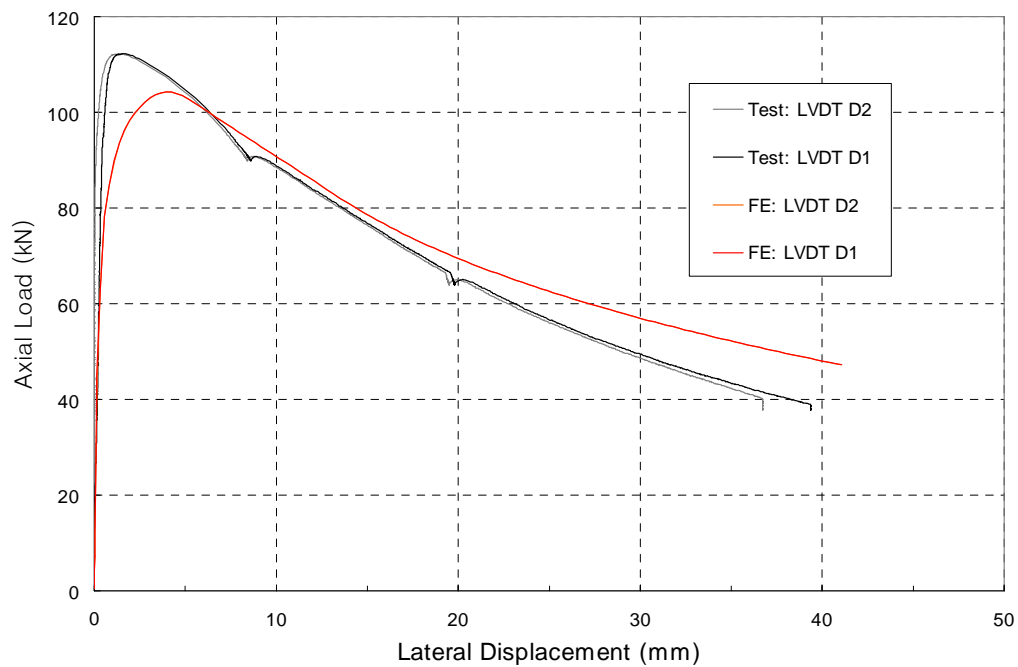


Figure B7.b. C3Cr12_1220_1: Axial Load vs. Lateral Displacement

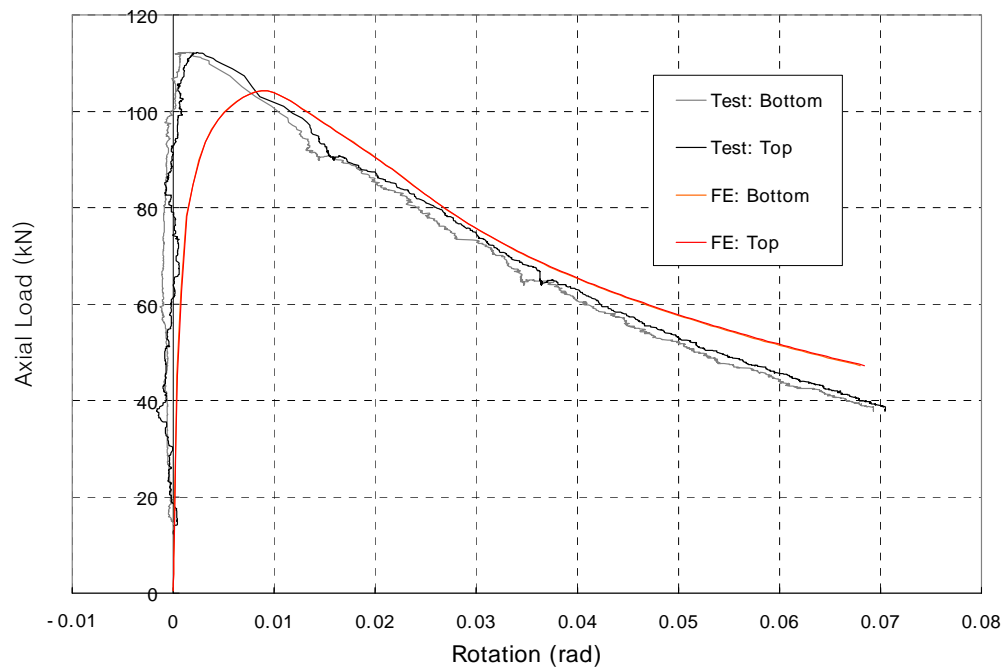


Figure B7.c. C3Cr12_1220_1: Axial Load vs. End Rotations

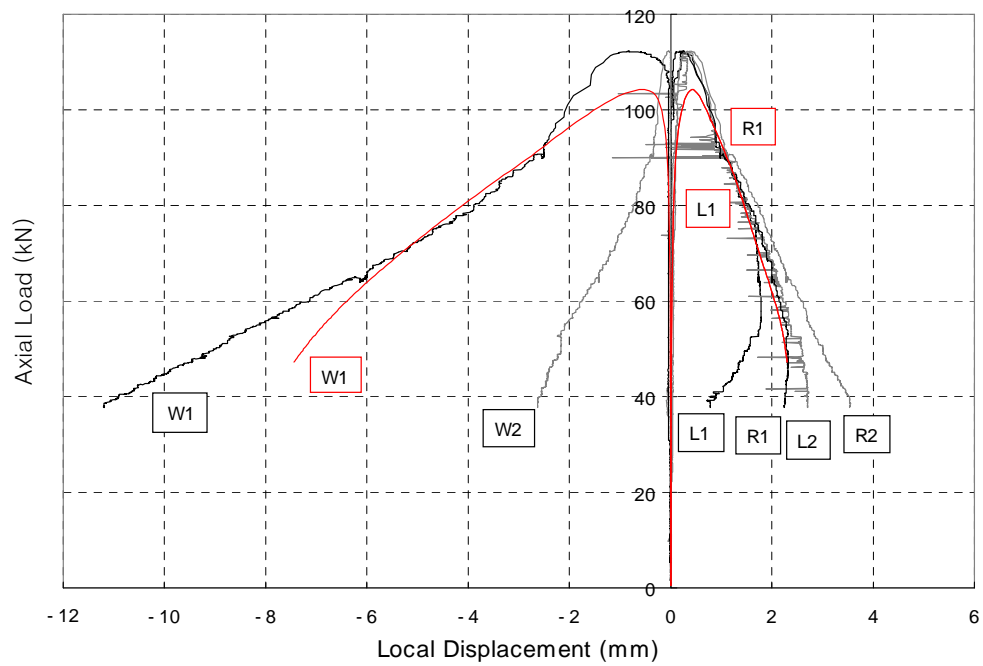


Figure B7.d. C3Cr12_1220_1: Axial Load vs. Local Displacements

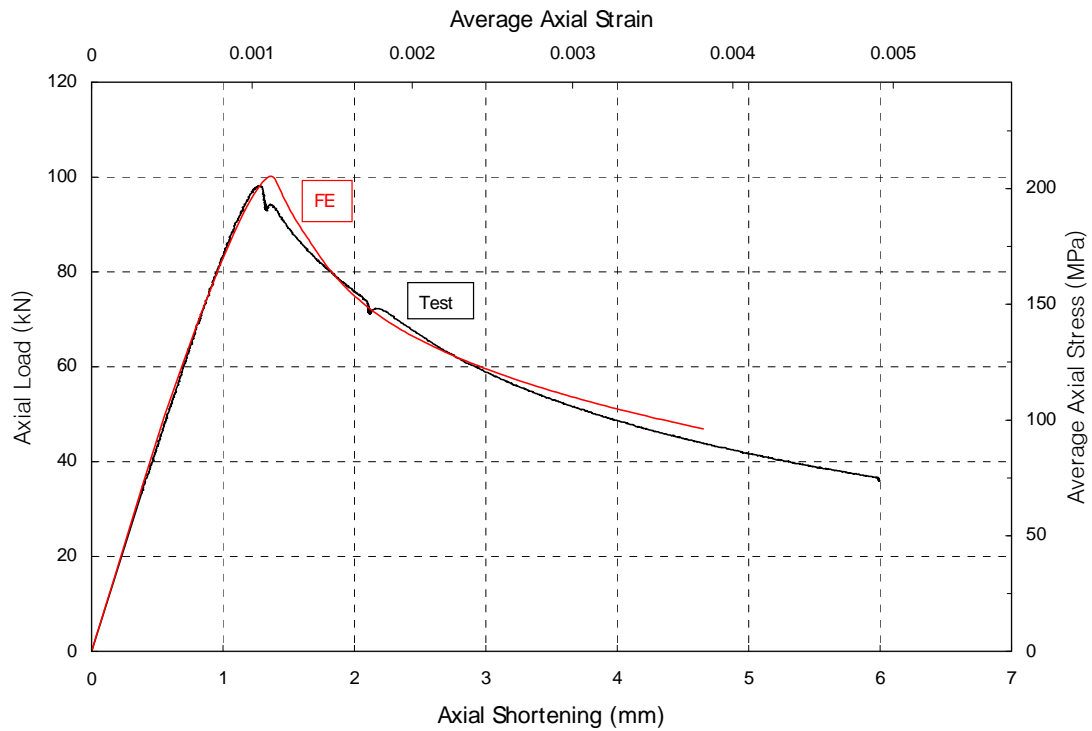


Figure B8.a. C3Cr12_1220_2: Axial Load vs. Axial Shortening

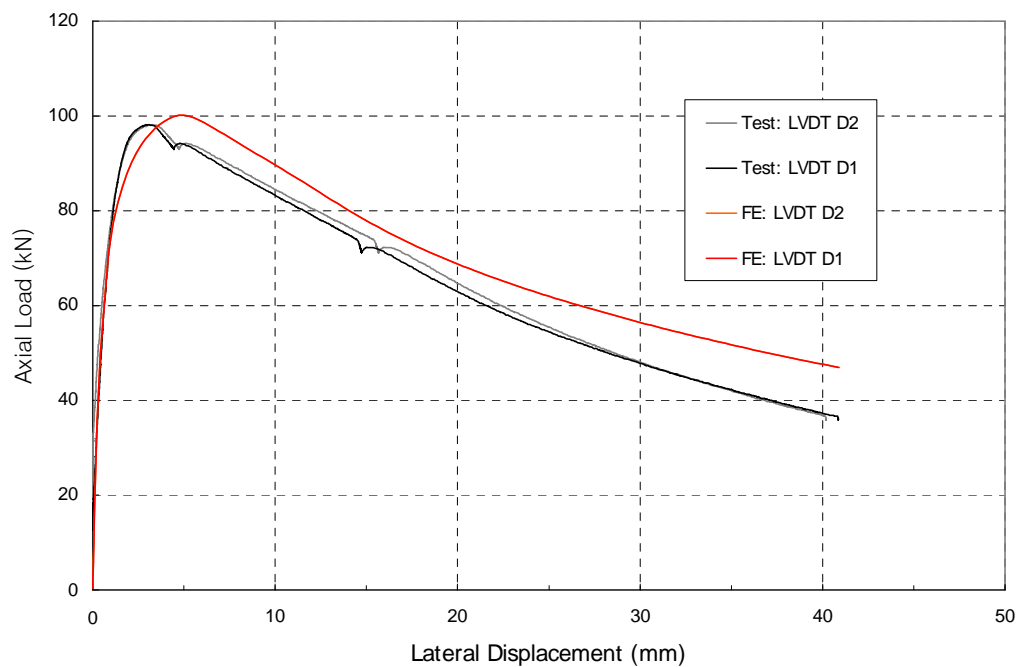


Figure B8.b. C3Cr12_1220_2: Axial Load vs. Lateral Displacement

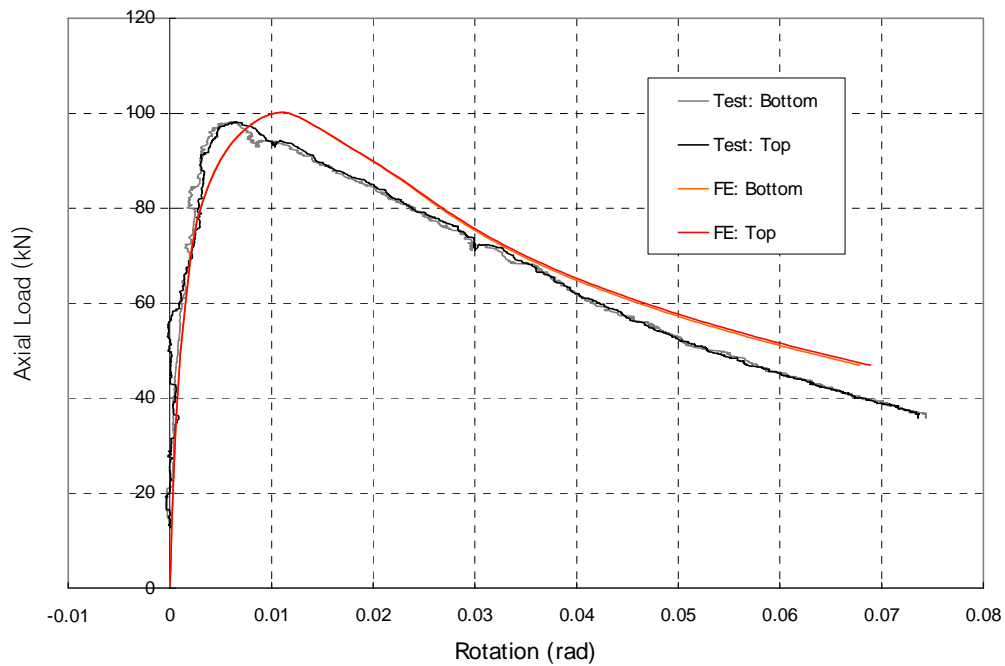


Figure B8.c. C3Cr12_1220_2: Axial Load vs. End Rotations

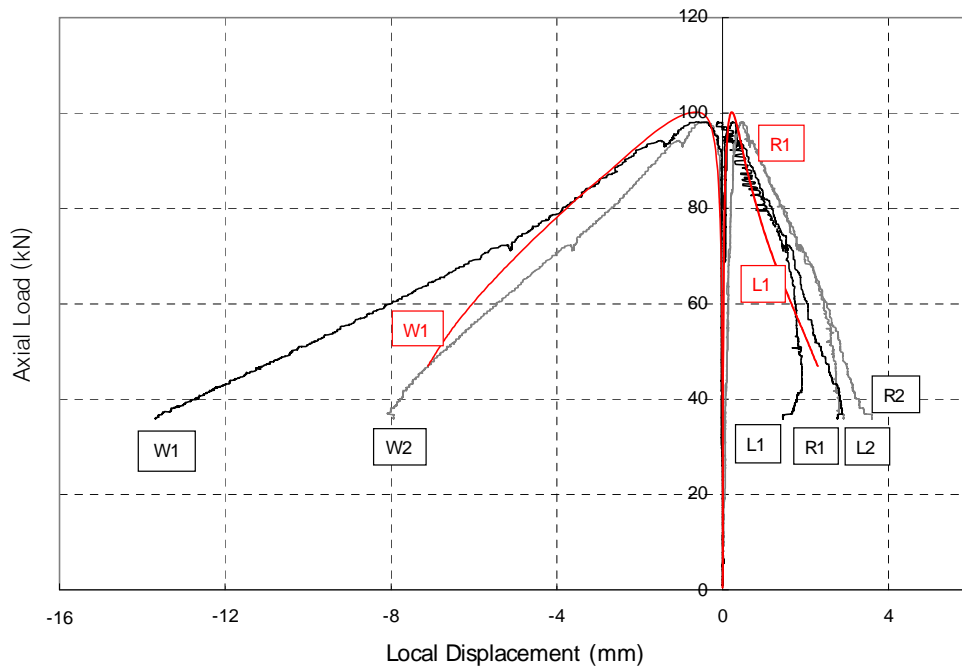


Figure B8.d. C3Cr12_1220_2: Axial Load vs. Local Displacements

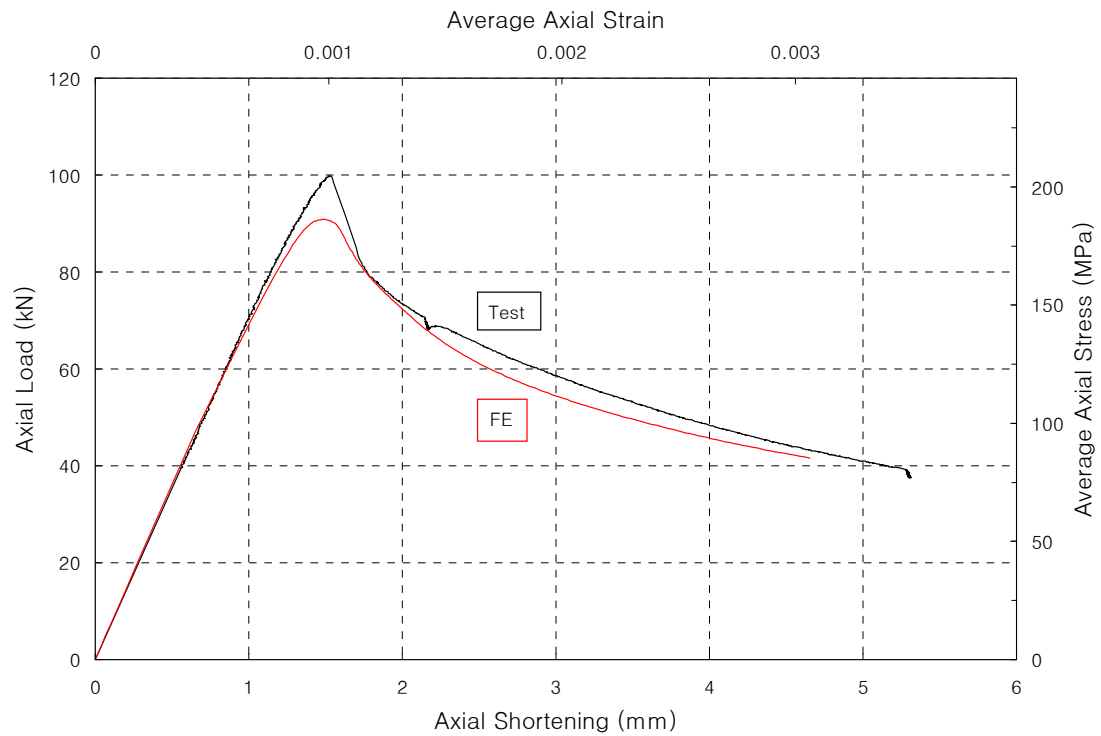


Figure B9.a. C3Cr12_1520_1: Axial Load vs. Axial Shortening

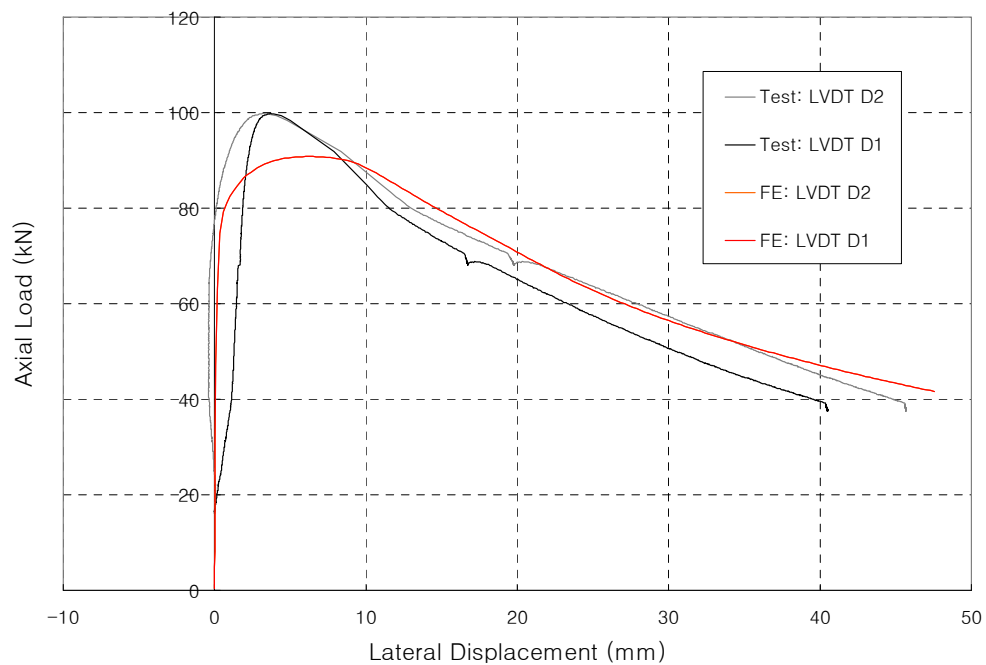


Figure B9.b. C3Cr12_1520_1: Axial Load vs. Lateral Displacement

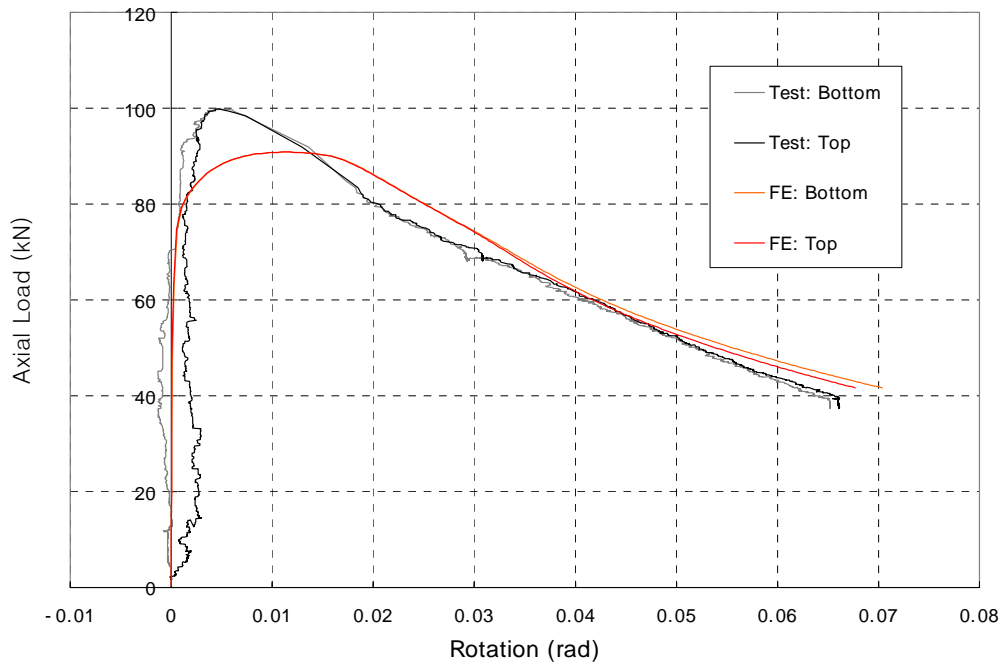


Figure B9.c. C3Cr12_1520_1: Axial Load vs. End Rotations

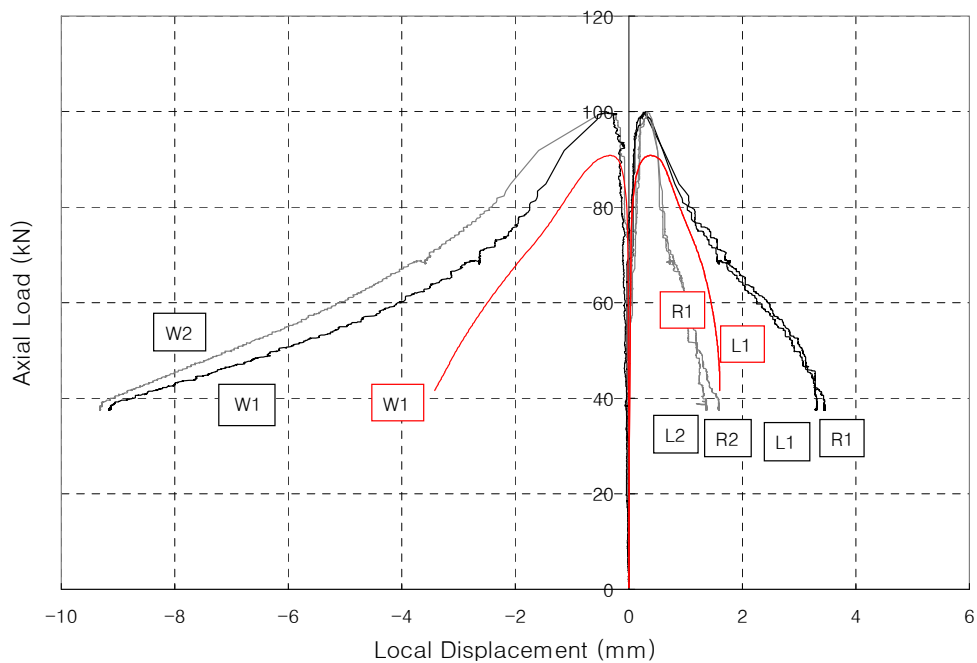


Figure B9.d. C3Cr12_1520_1: Axial Load vs. Local Displacements

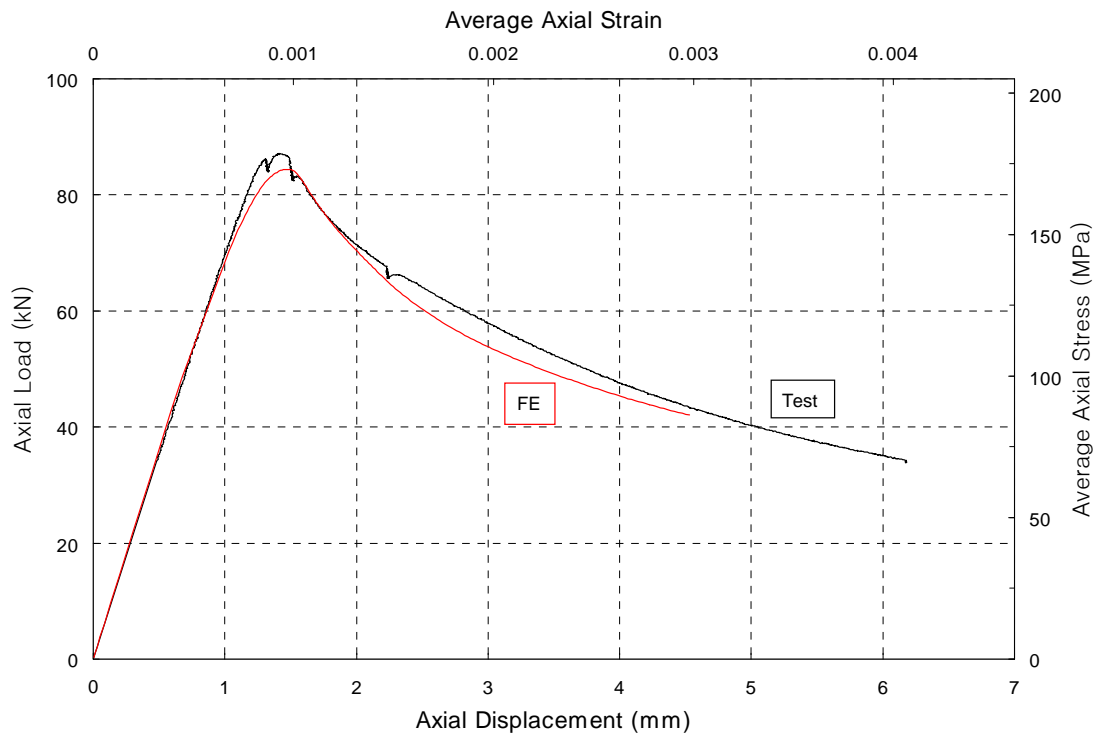


Figure B10.a. C3Cr12_1520_2: Axial Load vs. Axial Shortening

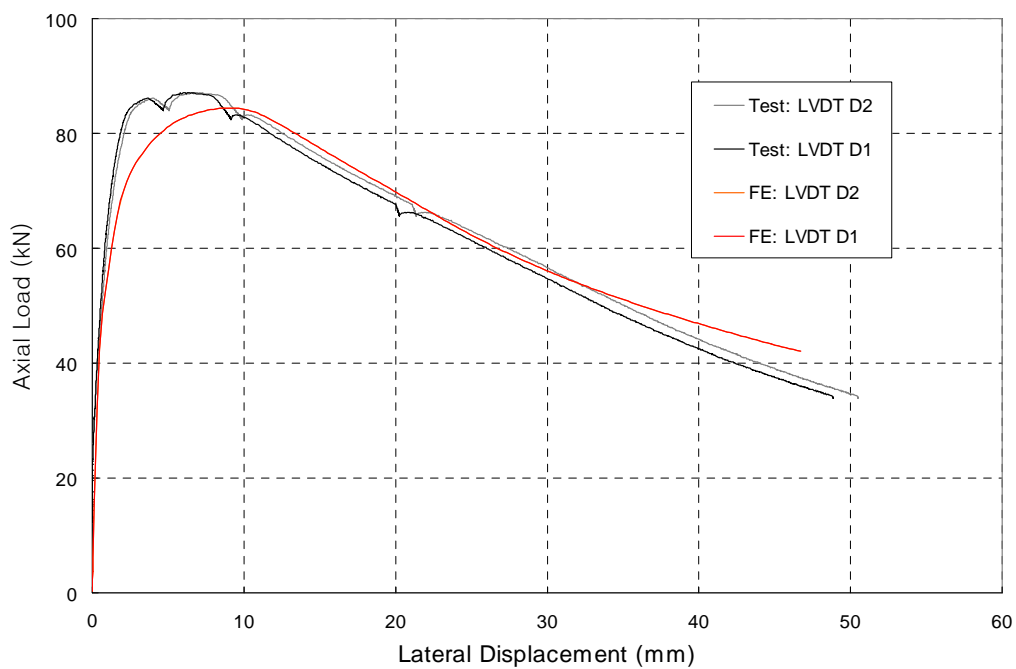


Figure B10.b. C3Cr12_1520_2: Axial Load vs. Lateral Displacement

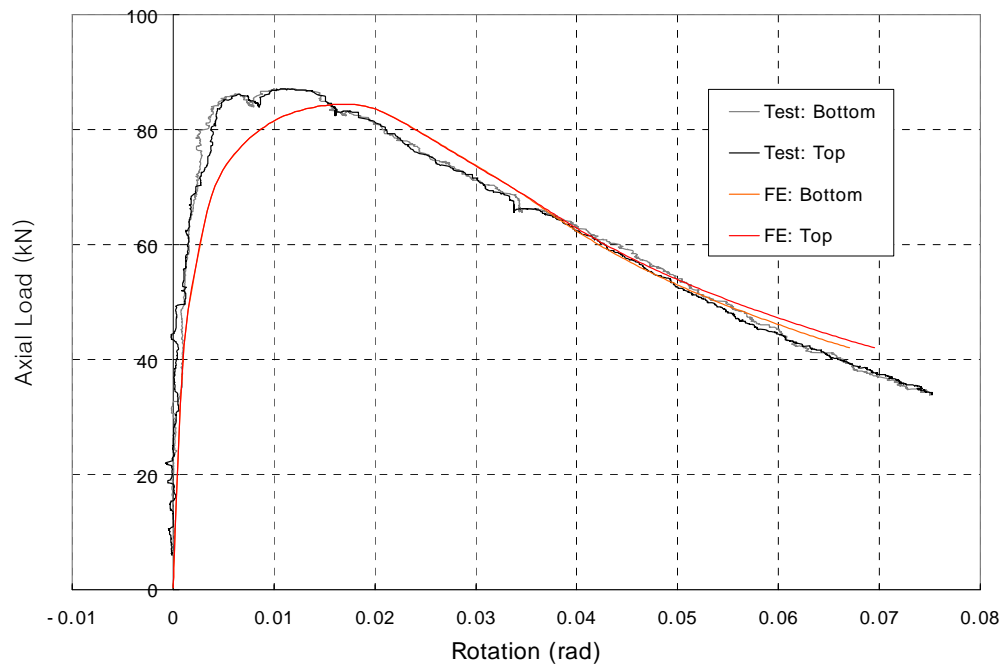


Figure B10.c. C3Cr12_1520_2: Axial Load vs. End Rotations

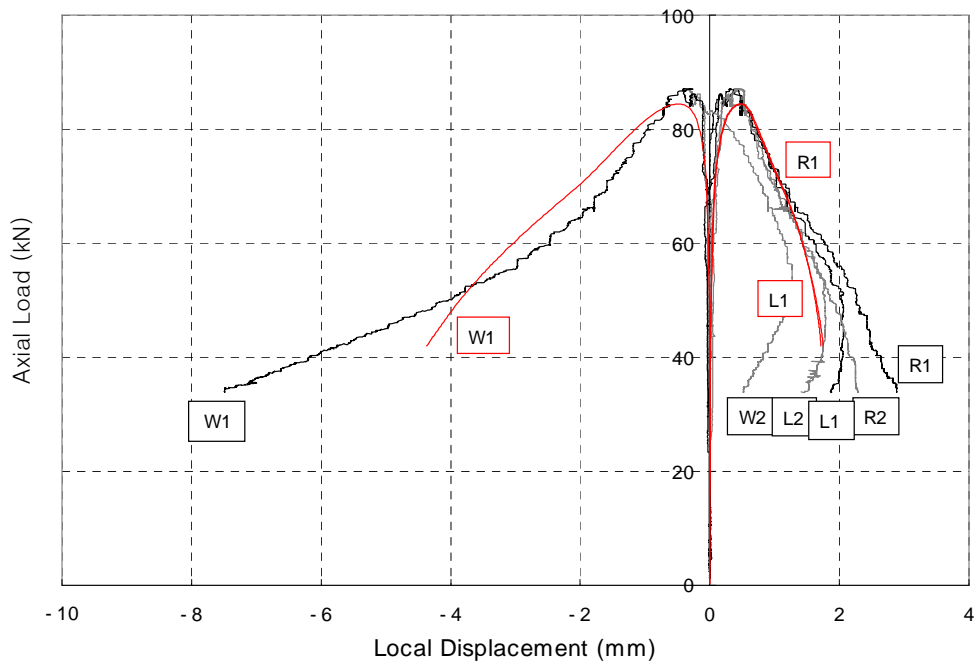


Figure B10.d. C3Cr12_1520_2: Axial Load vs. Local Displacements

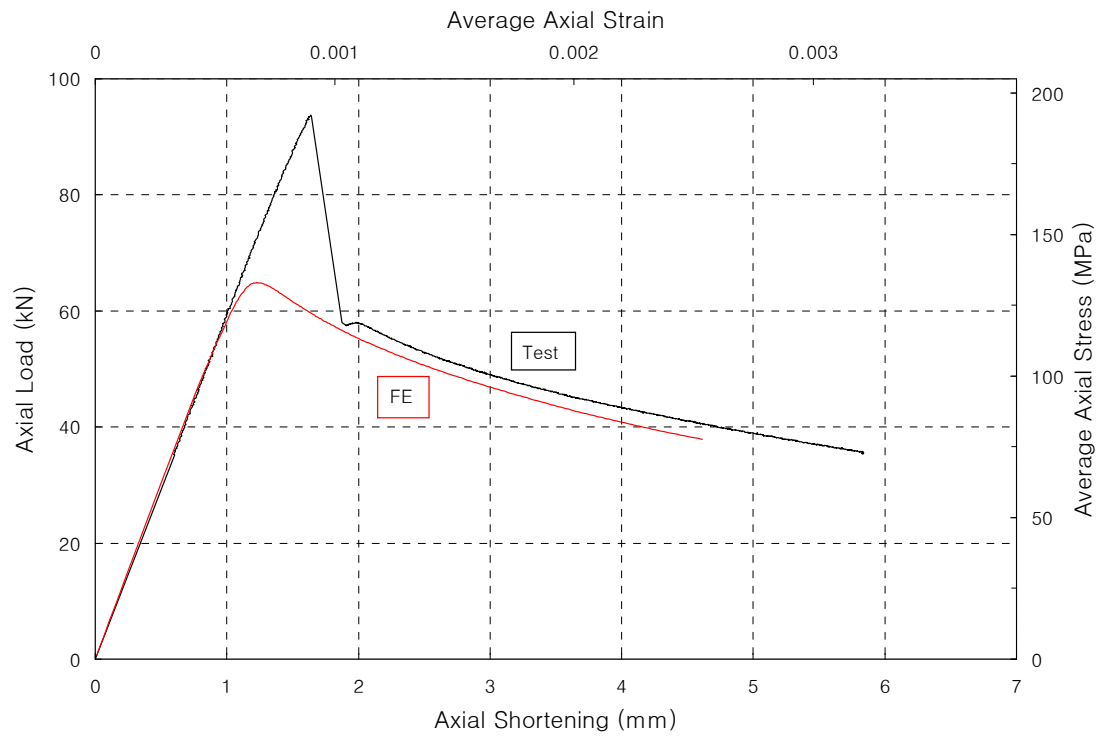


Figure B11.a. C3Cr12_1819_1: Axial Load vs. Axial Shortening

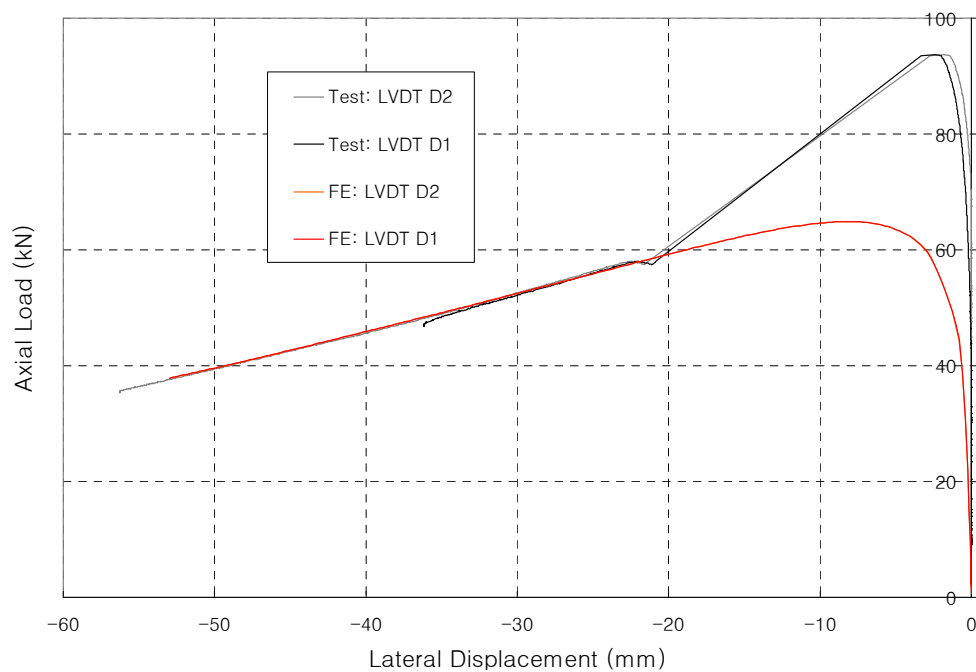


Figure B11.b. C3Cr12_1819_1: Axial Load vs. Lateral Displacement

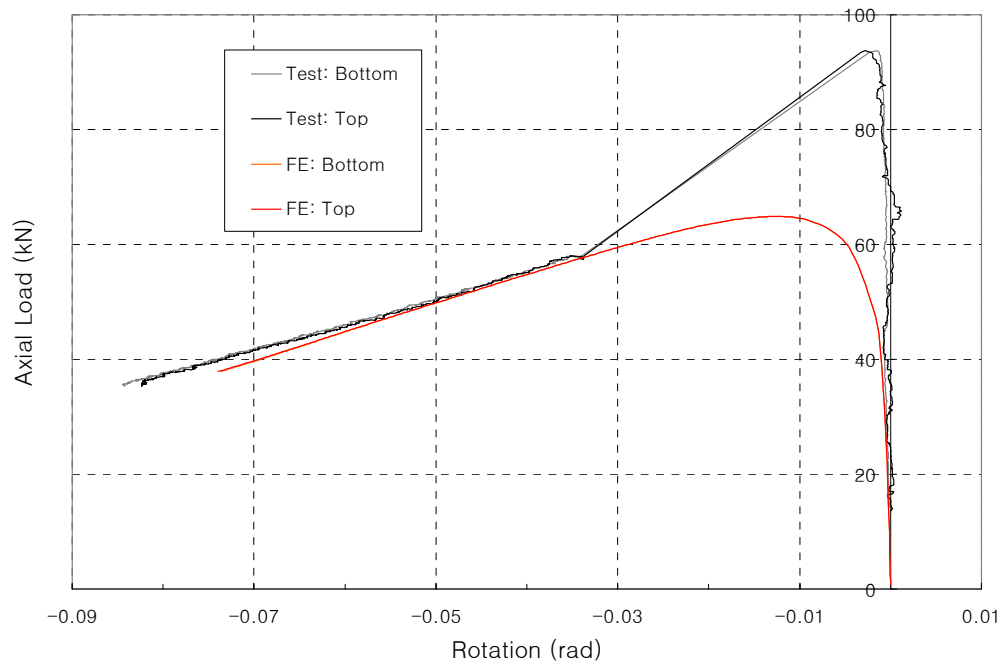


Figure B11.c. C3Cr12_1819_1: Axial Load vs. End Rotations

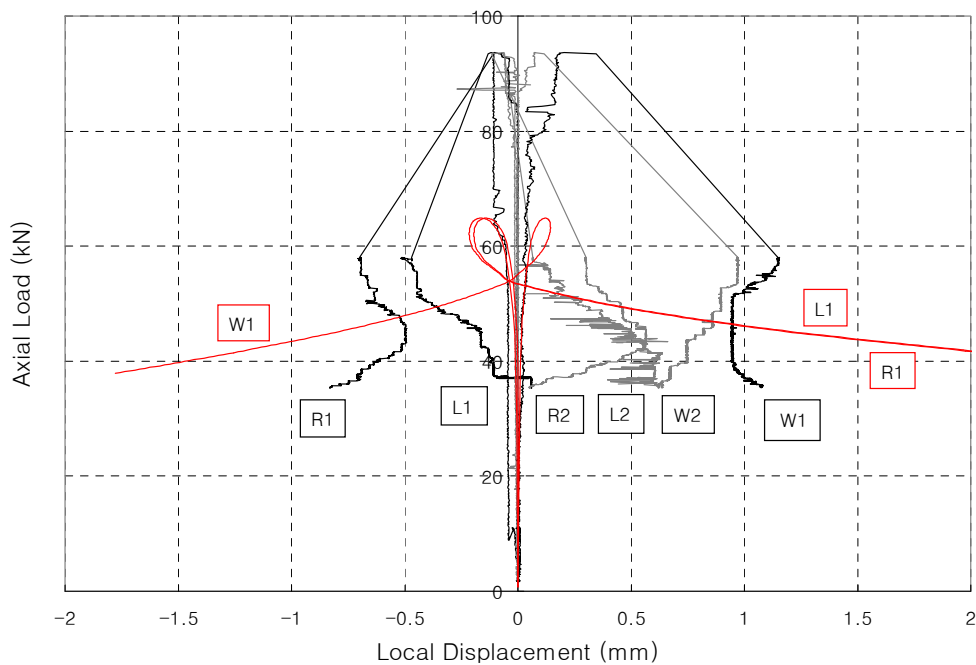


Figure B11.d. C3Cr12_1819_1: Axial Load vs. Local Displacements

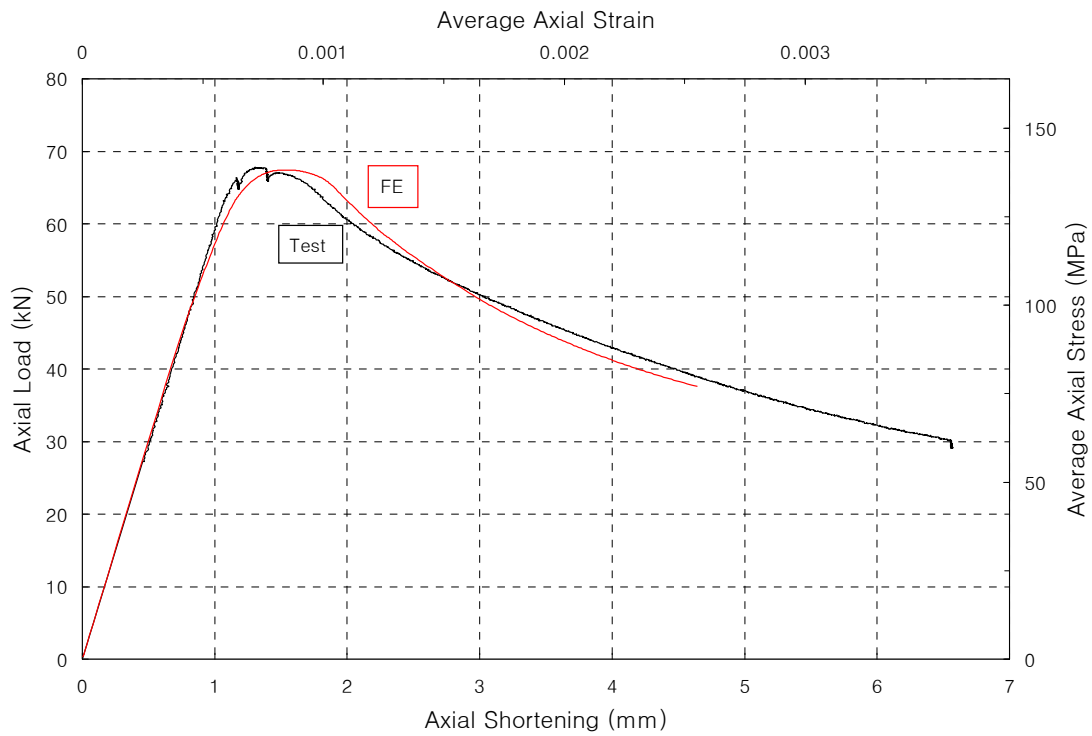


Figure B12.a. C3Cr12_1819_2: Axial Load vs. Axial Shortening

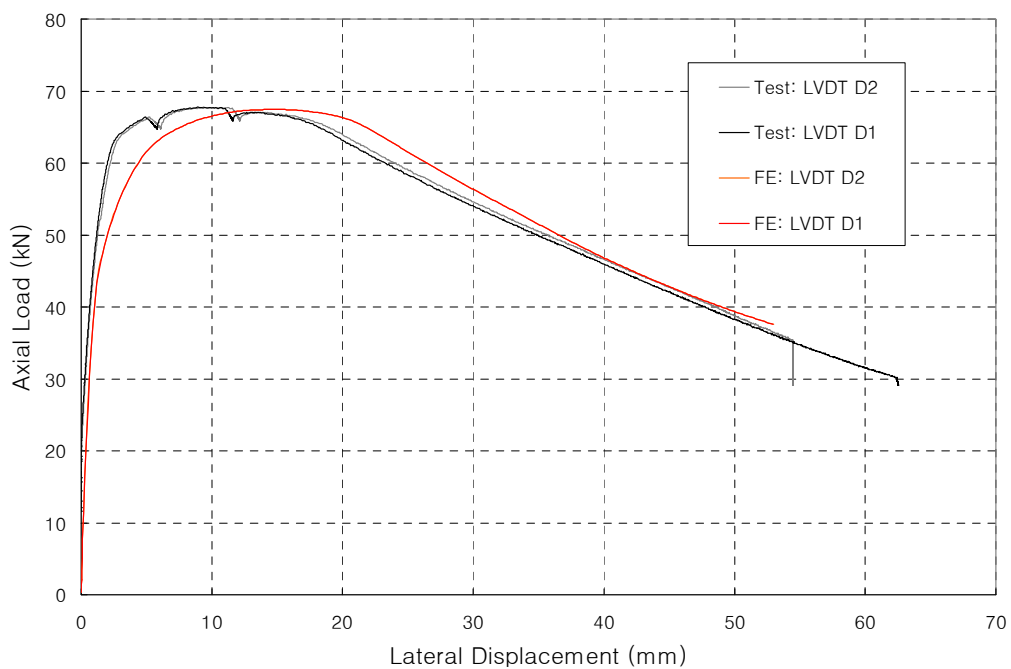


Figure B12.b. C3Cr12_1819_2: Axial Load vs. Local Displacements

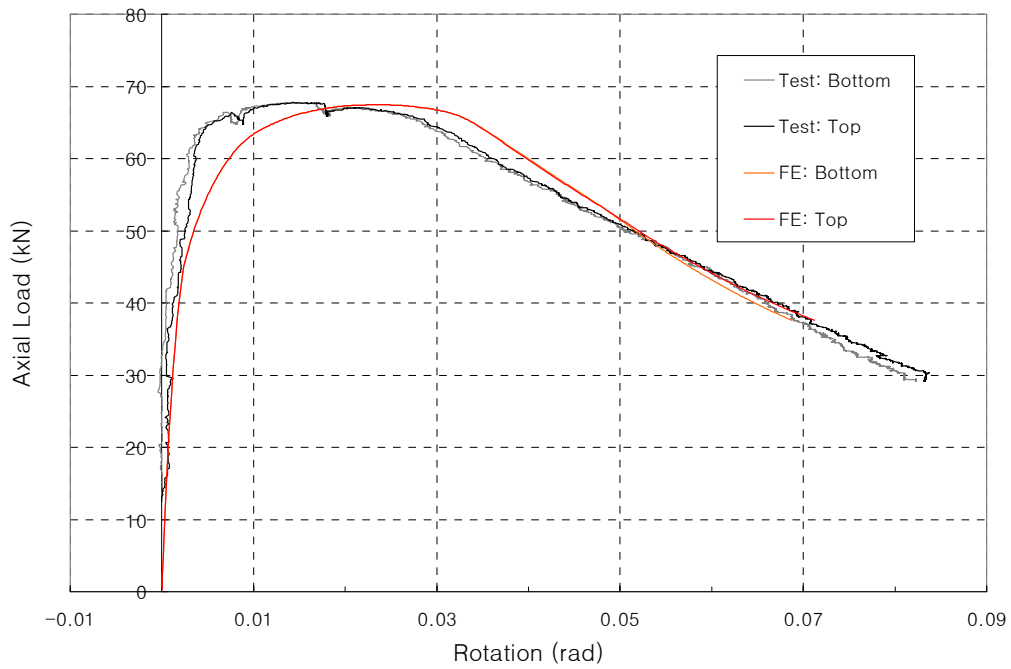


Figure B12.c. C3Cr12_1819_2: Axial Load vs. End Rotations

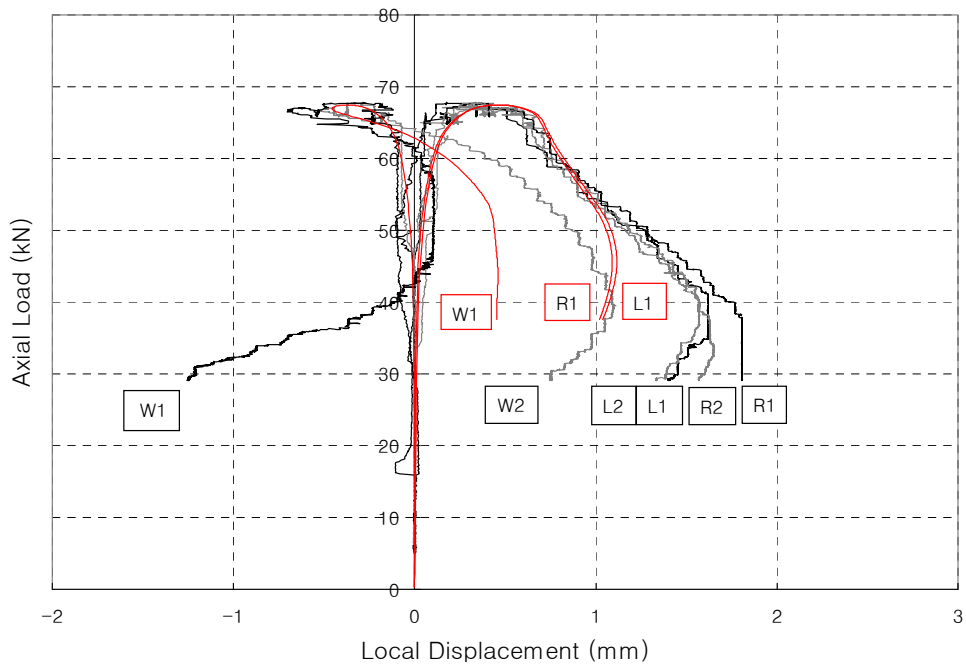


Figure B12.d. C3Cr12_1819_2: Axial Load vs. Local Displacements

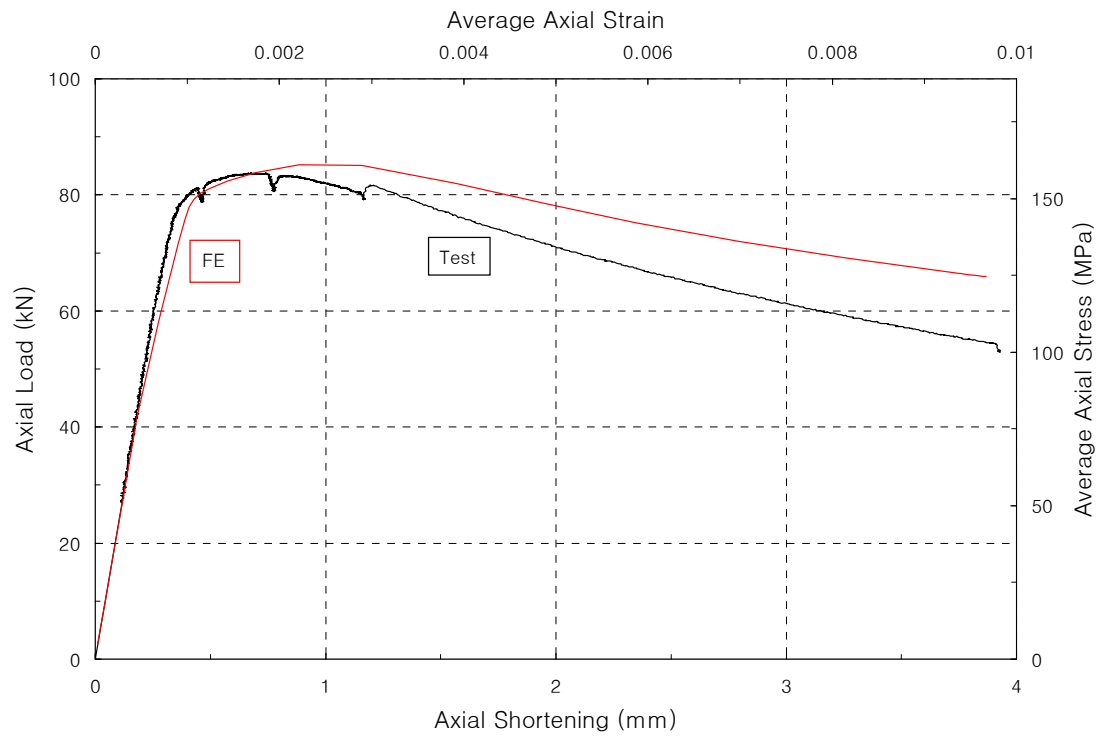


Figure B13.a. C304_400_1 : Axial Load vs. Axial Shortening

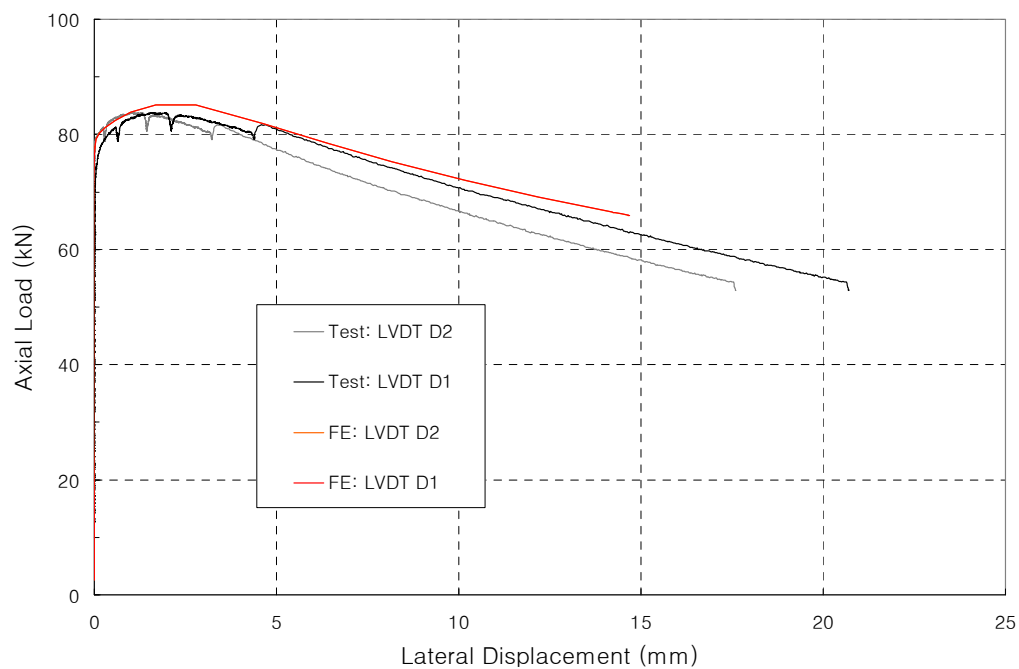


Figure B13.b. C304_400_1 : Axial Load vs. Lateral Displacement

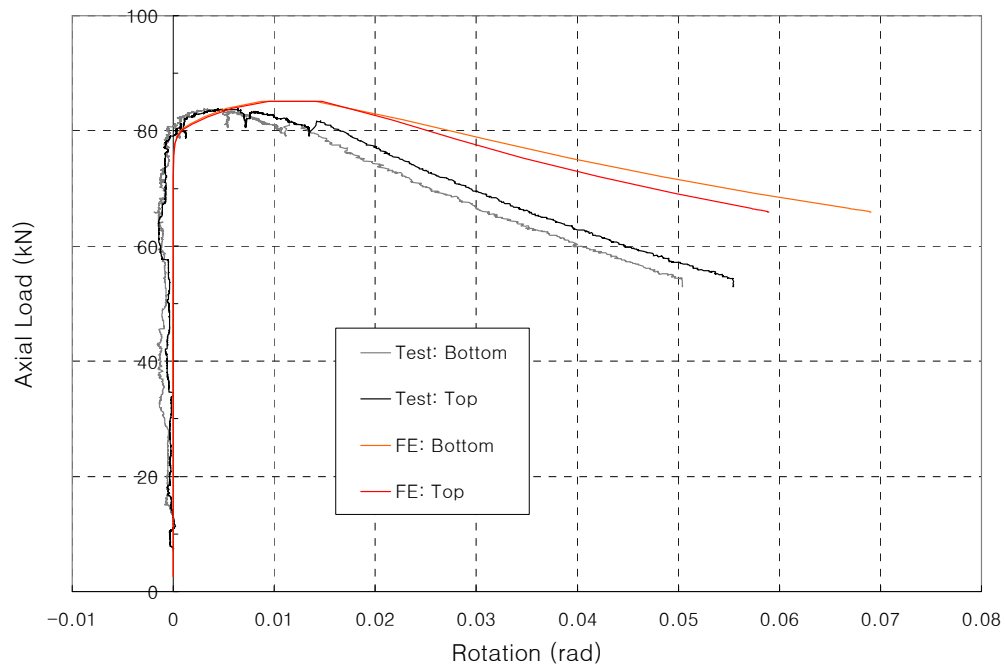


Figure B13.c. C304_400_1 : Axial Load vs. End Rotations

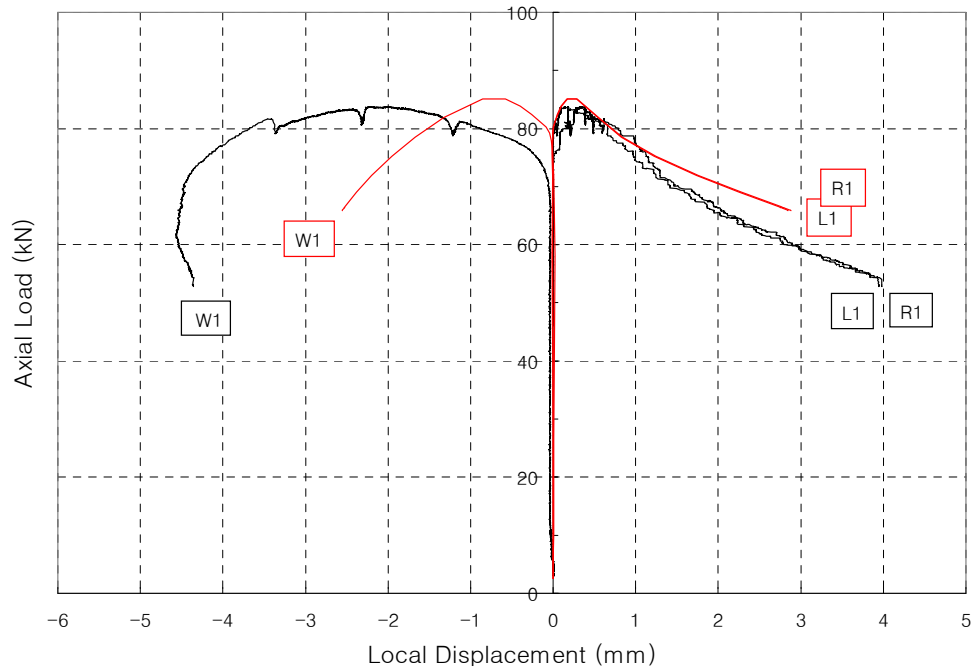


Figure B13.d. C304_400_1 : Axial Load vs. Local Displacements

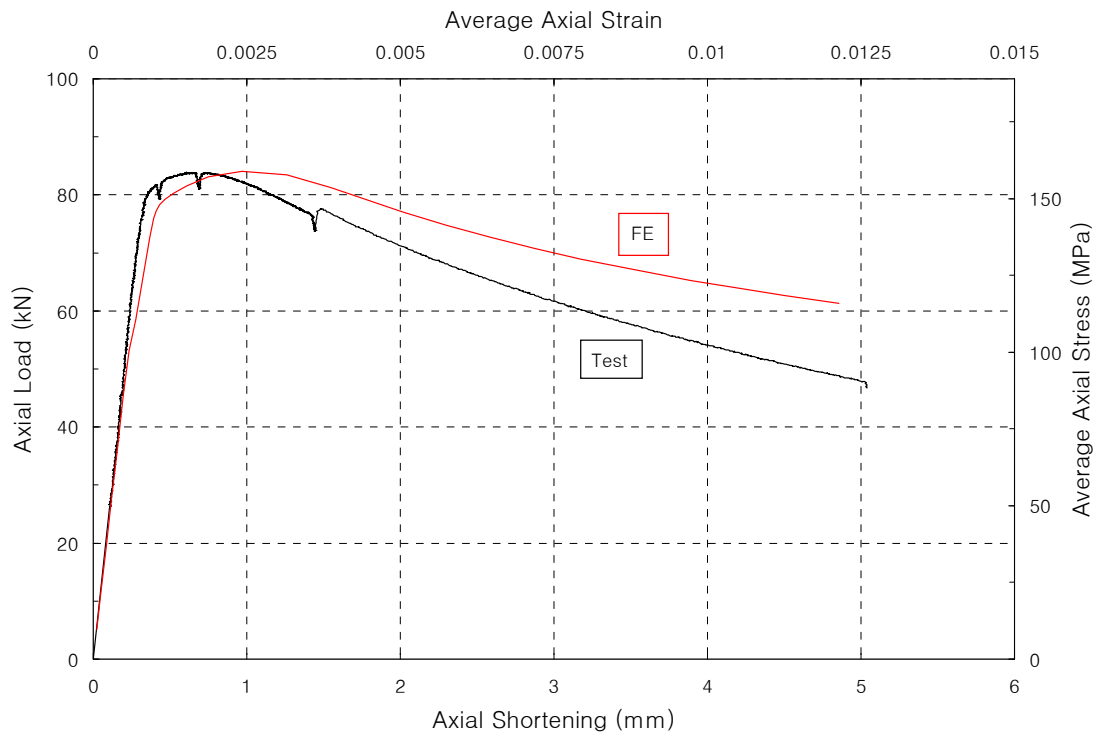


Figure B14.a. C304_400_2 : Axial Load vs. Axial Shortening

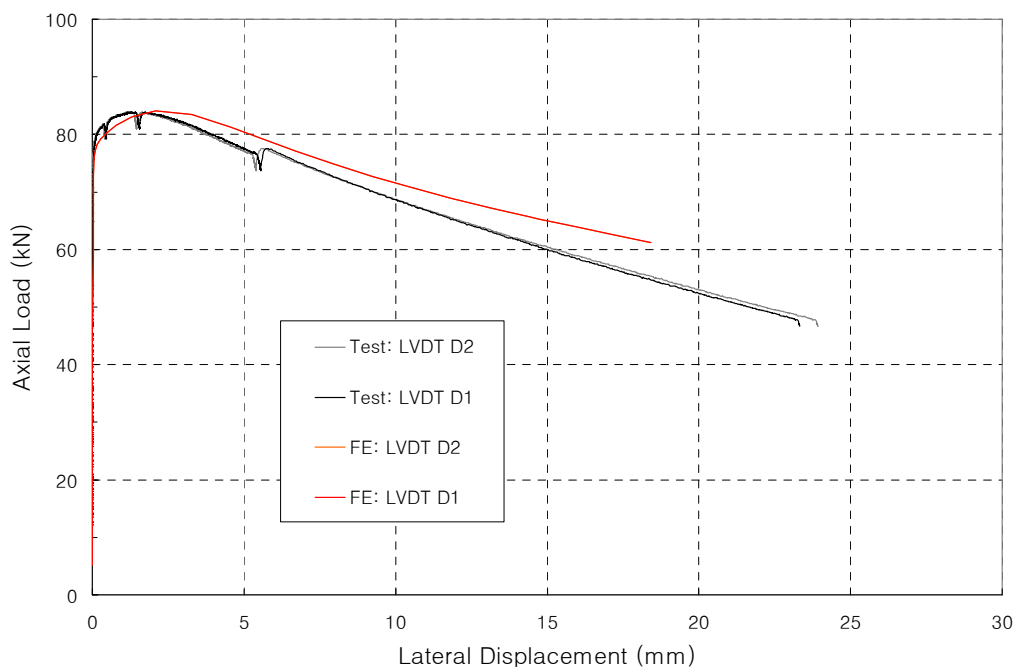


Figure B14.b. C304_400_2 : Axial Load vs. Lateral Displacement

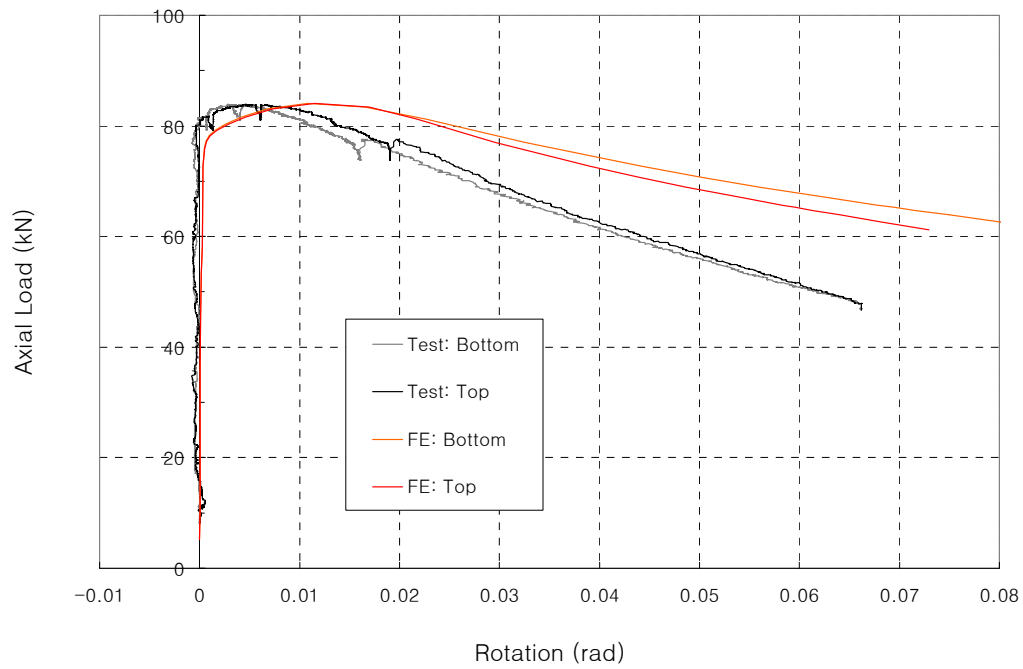


Figure B14.c. C304_400_2 : Axial Load vs. End Rotations

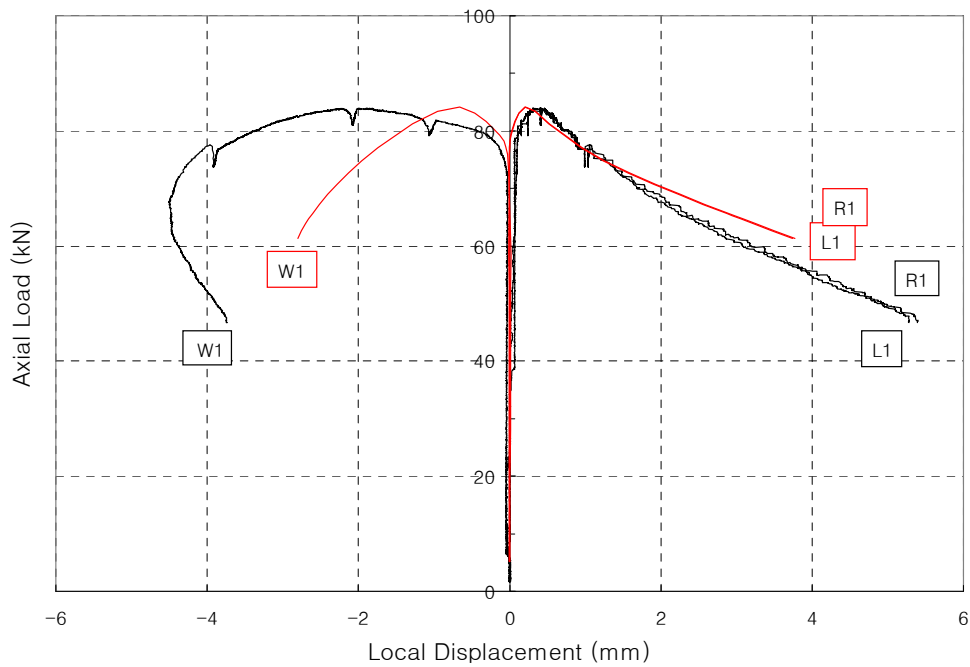


Figure B14.d. C304_400_2 : Axial Load vs. Local Displacements

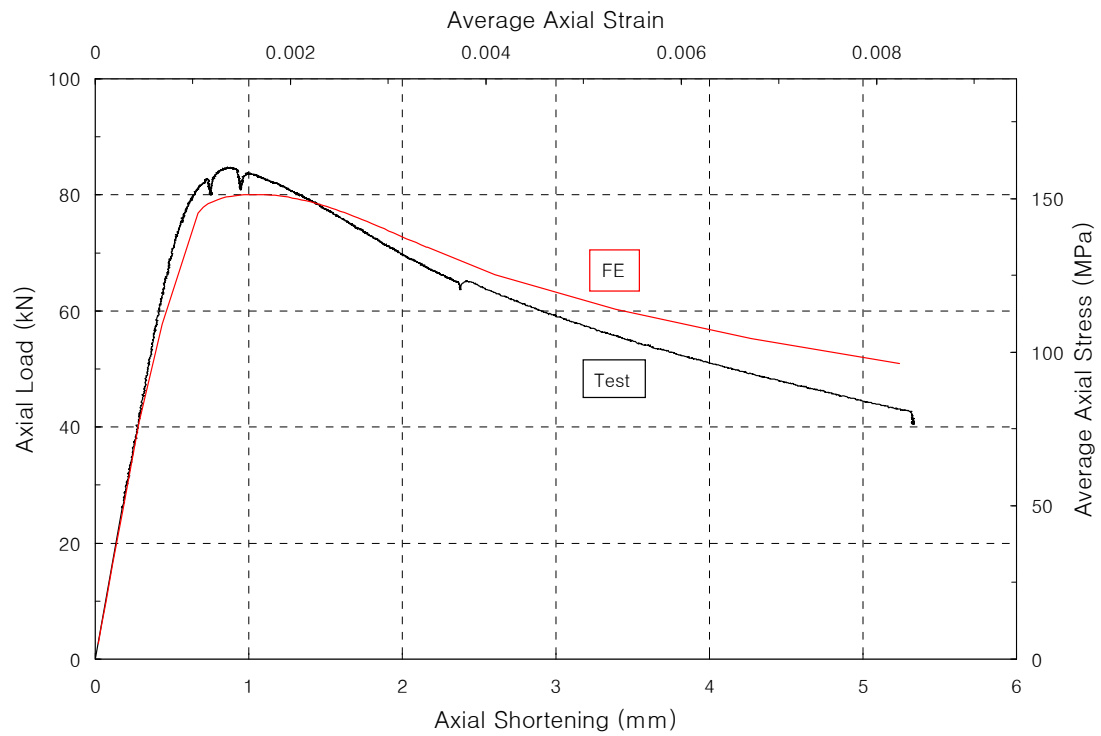


Figure B15.a. C304_636_1 : Axial Load vs. Axial Shortening

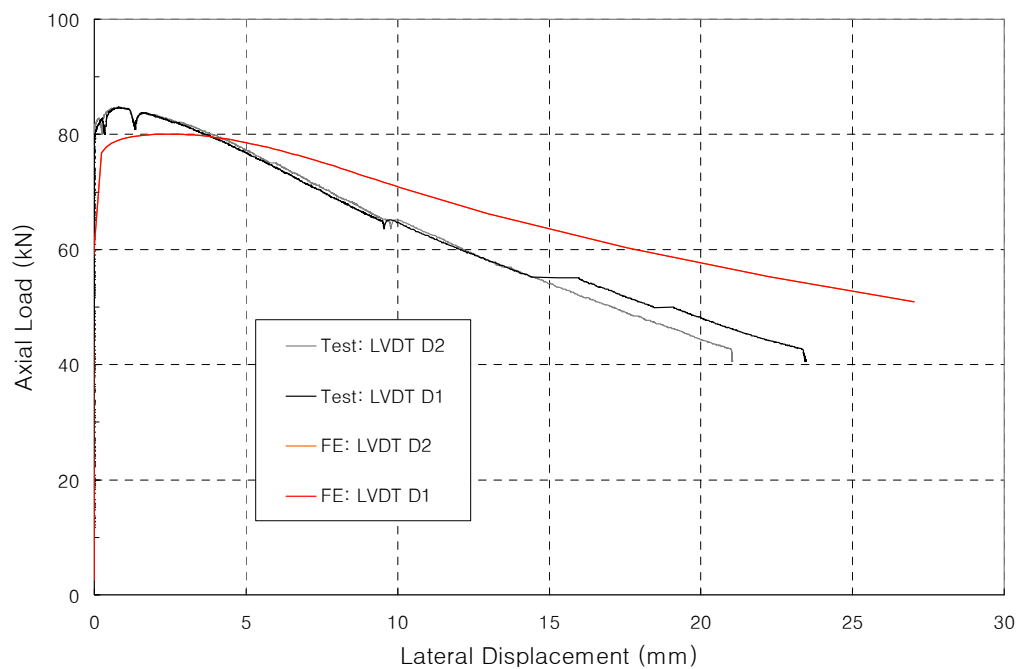


Figure B15.b. C304_636_1 : Axial Load vs. Lateral Displacement

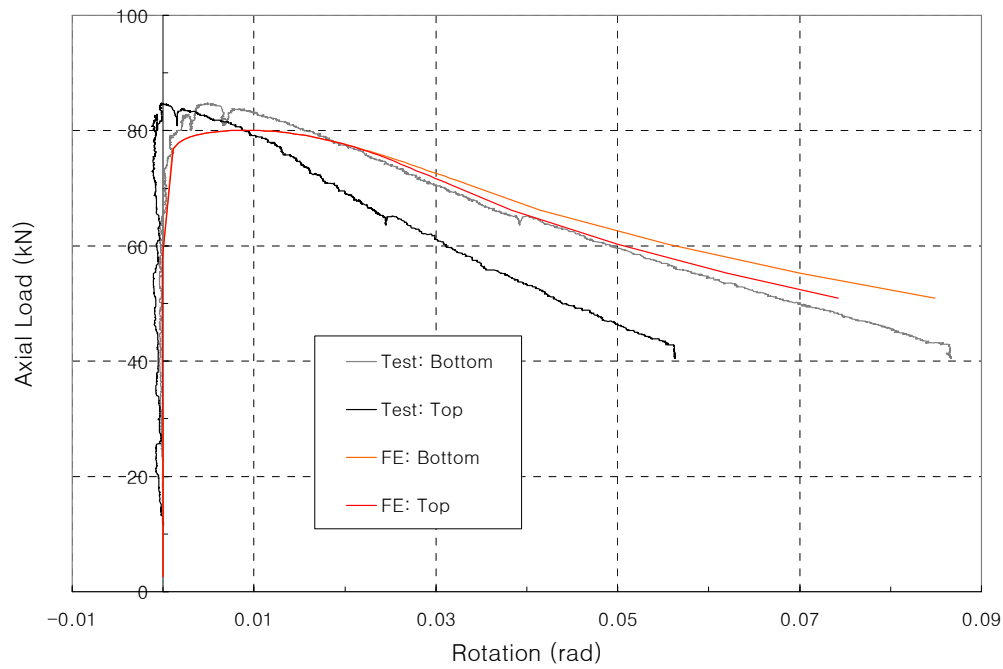


Figure B15.c. C304_636_1 : Axial Load vs. End Rotations

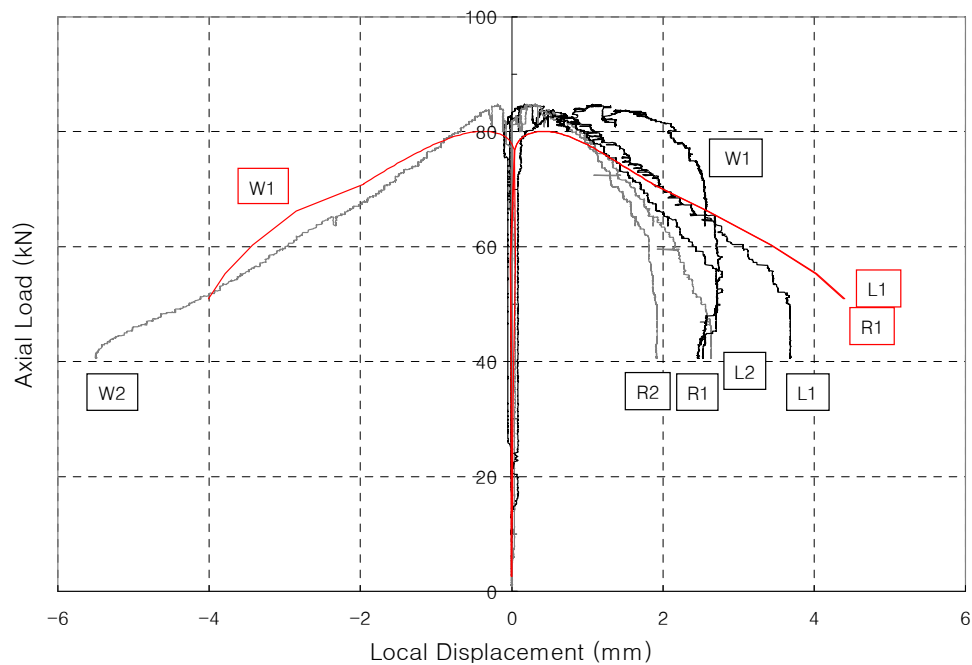


Figure B15.d. C304_636_1 : Axial Load vs. Local Displacements

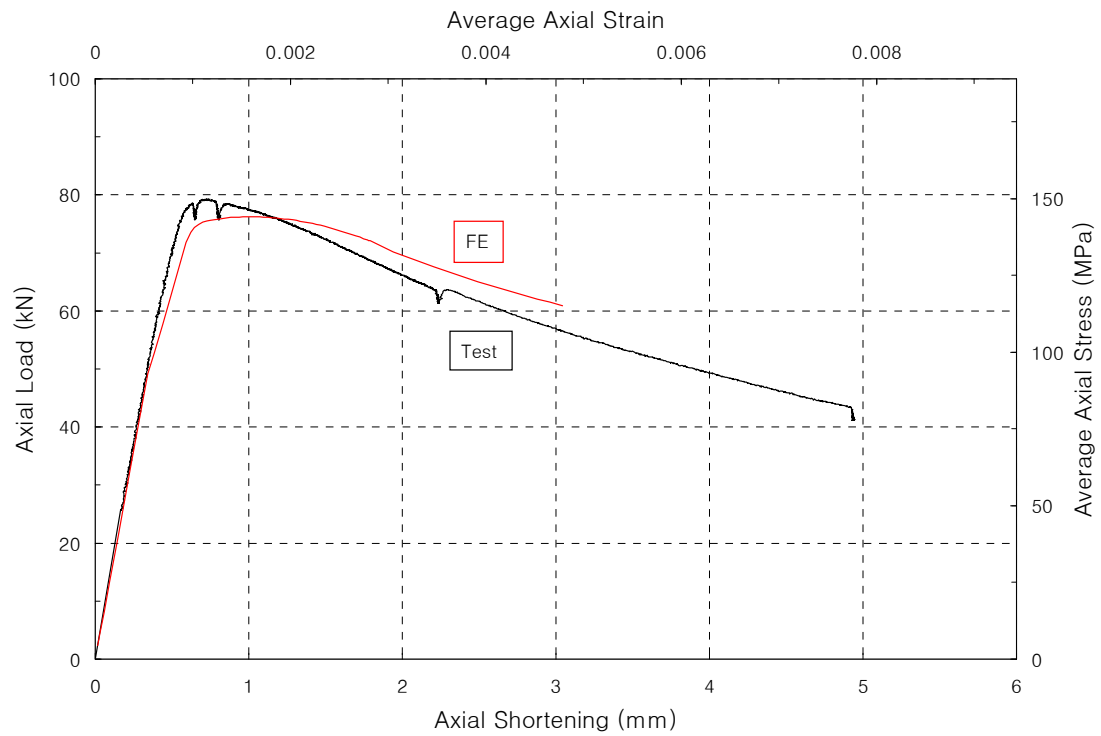


Figure B16.a. C304_636_2 : Axial Load vs. Axial Shortening

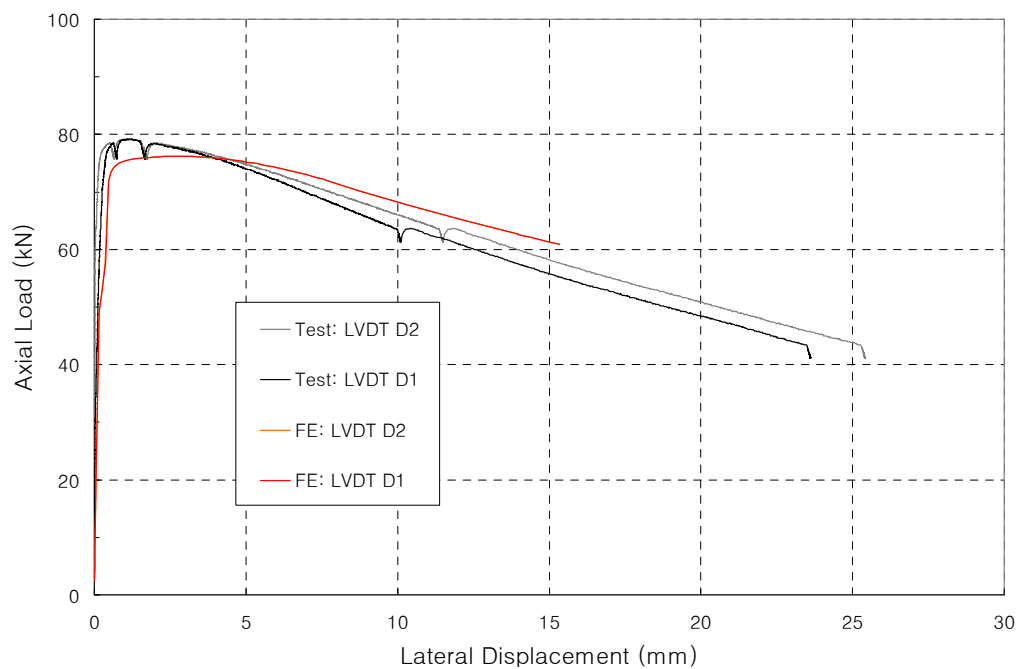


Figure B16.b. C304_636_2 : Axial Load vs. Lateral Displacement

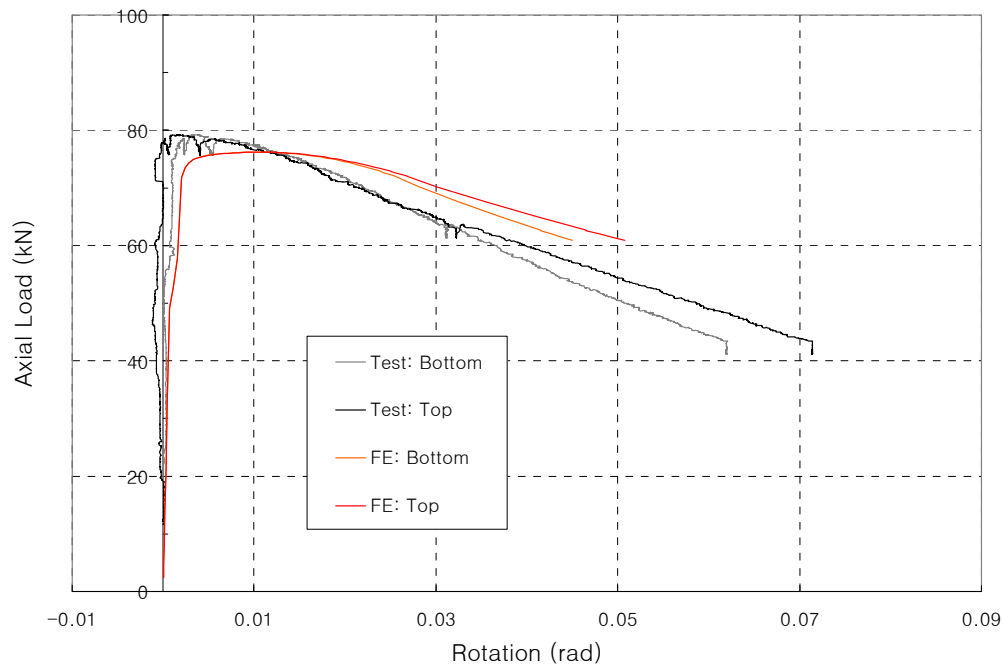


Figure B16.c. C304_636_2 : Axial Load vs. End Rotations

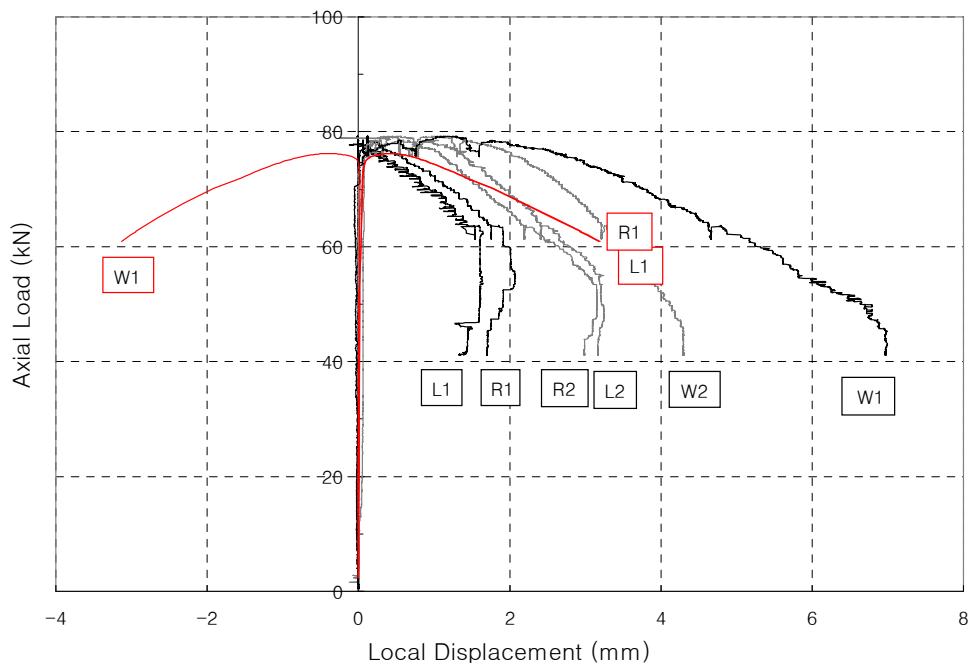


Figure B16.d. C304_636_2 : Axial Load vs. Local Displacements

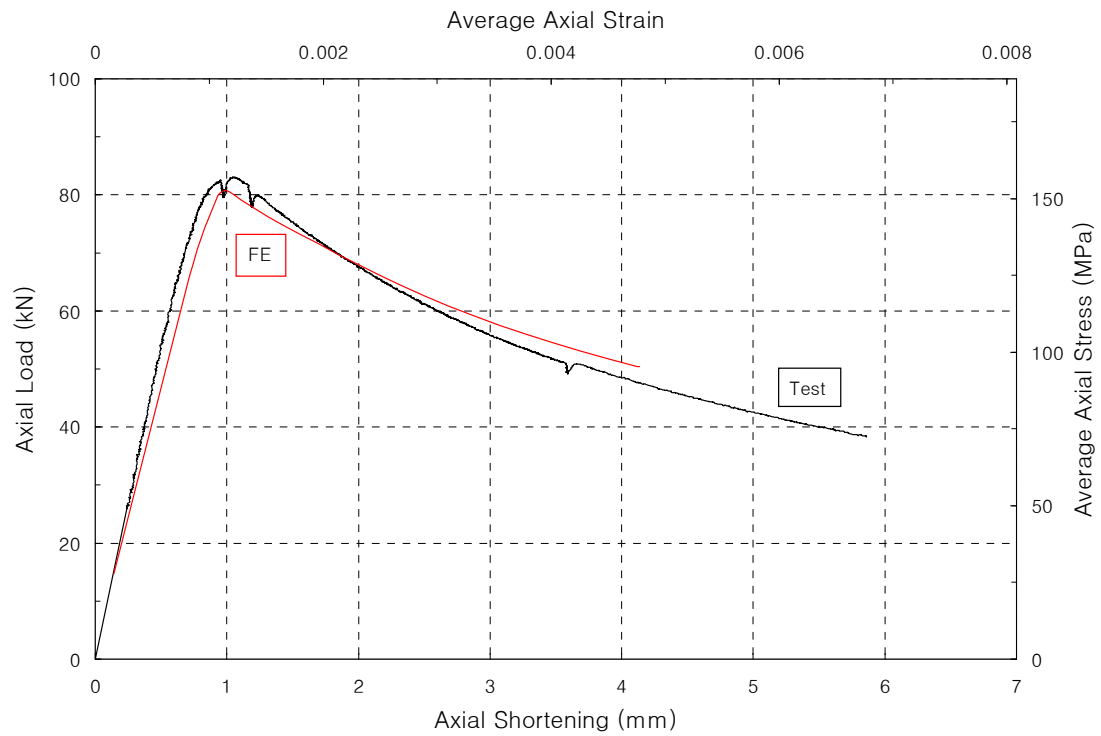


Figure B17.a. C304_866_1 : Axial Load vs. Axial Shortening

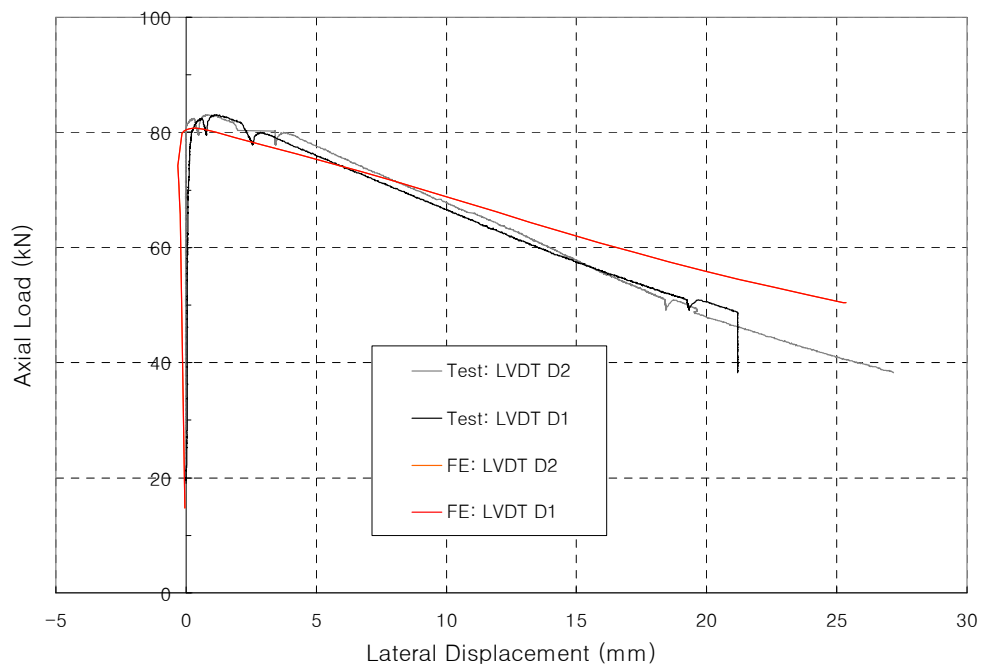


Figure B17.b. C304_866_1 : Axial Load vs. Lateral Displacement

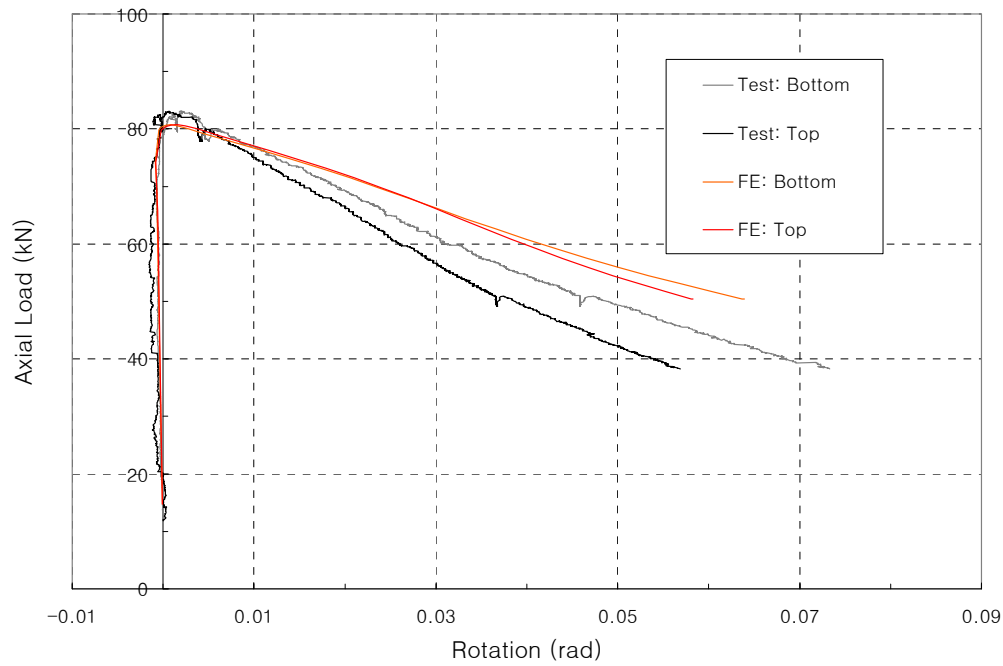


Figure B17.c. C304_866_1 : Axial Load vs. End Rotations

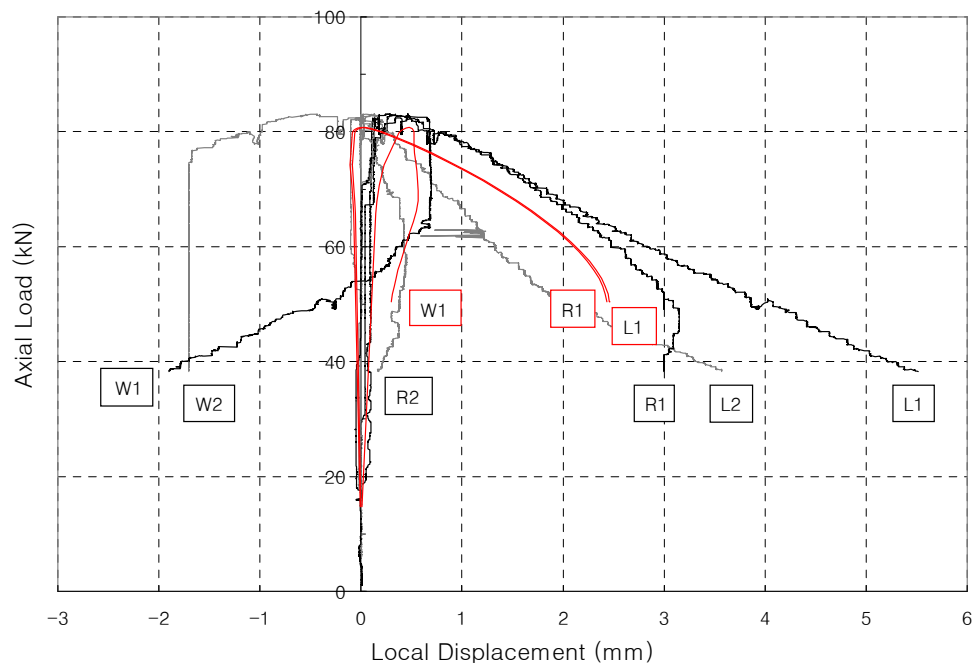


Figure B17.d. C304_866_1 : Axial Load vs. Local Displacements

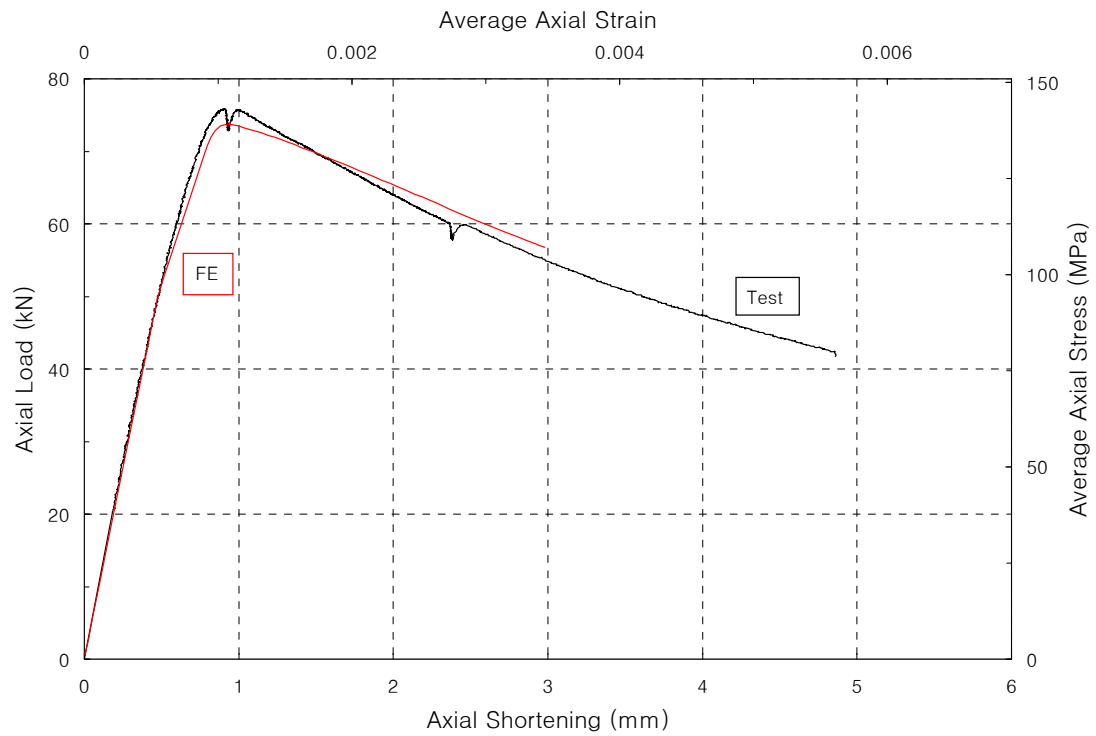


Figure B18.a. C304_866_2 : Axial Load vs. Axial Shortening

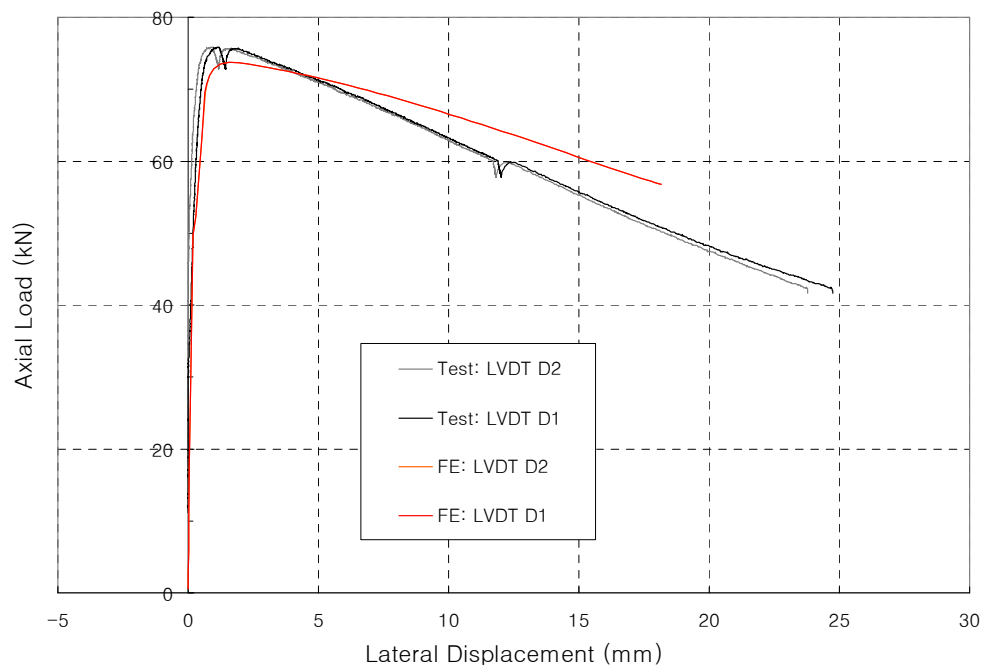


Figure B18.b. C304_866_2 : Axial Load vs. Lateral Displacement

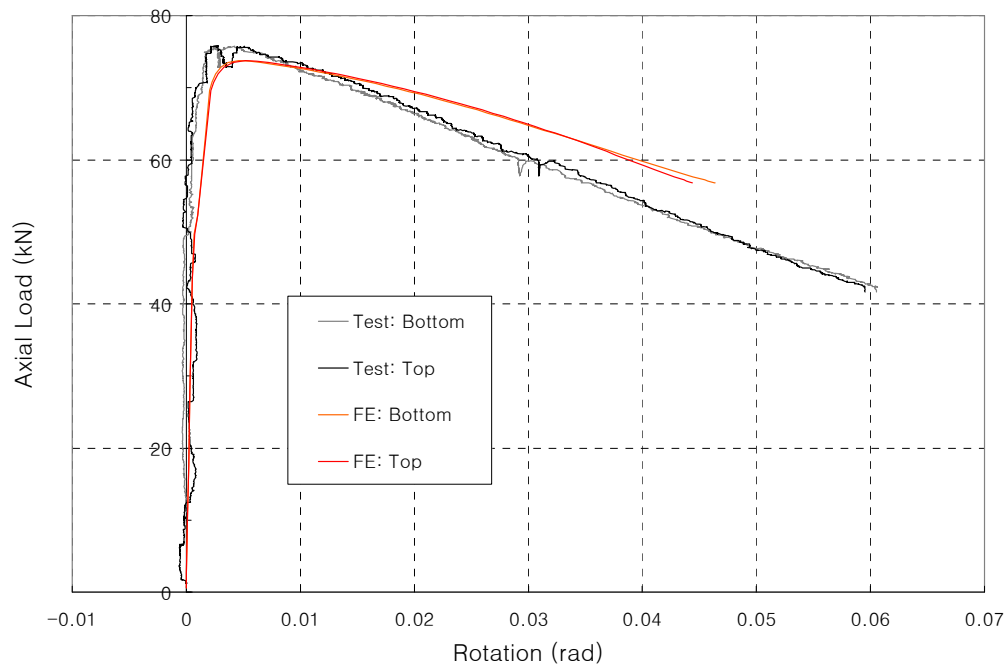


Figure B18.c. C304_866_2 : Axial Load vs. End Rotations

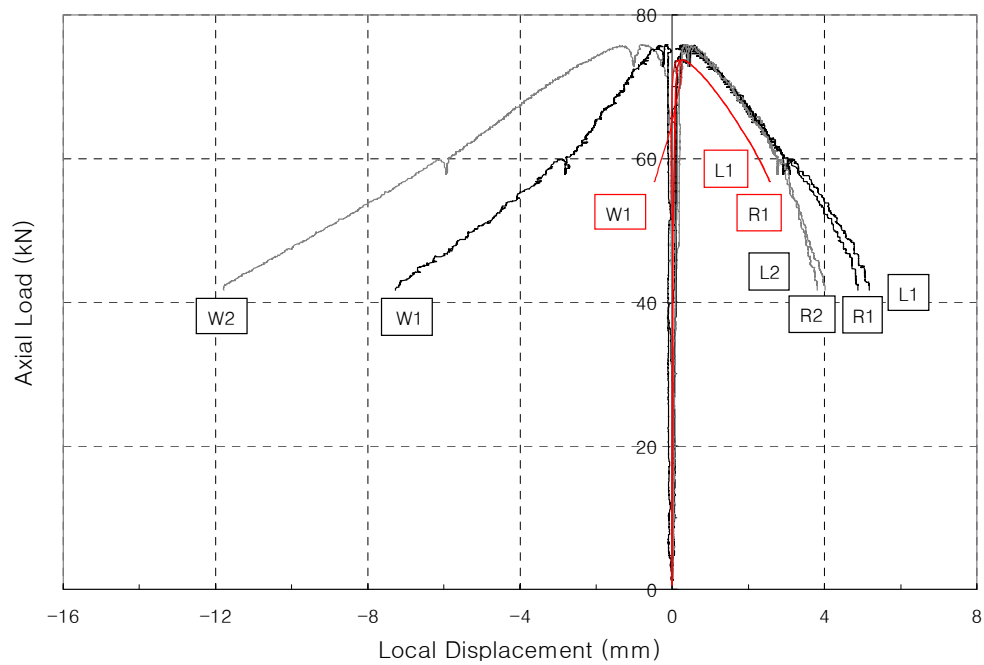


Figure B18.d. C304_866_2 : Axial Load vs. Local Displacements

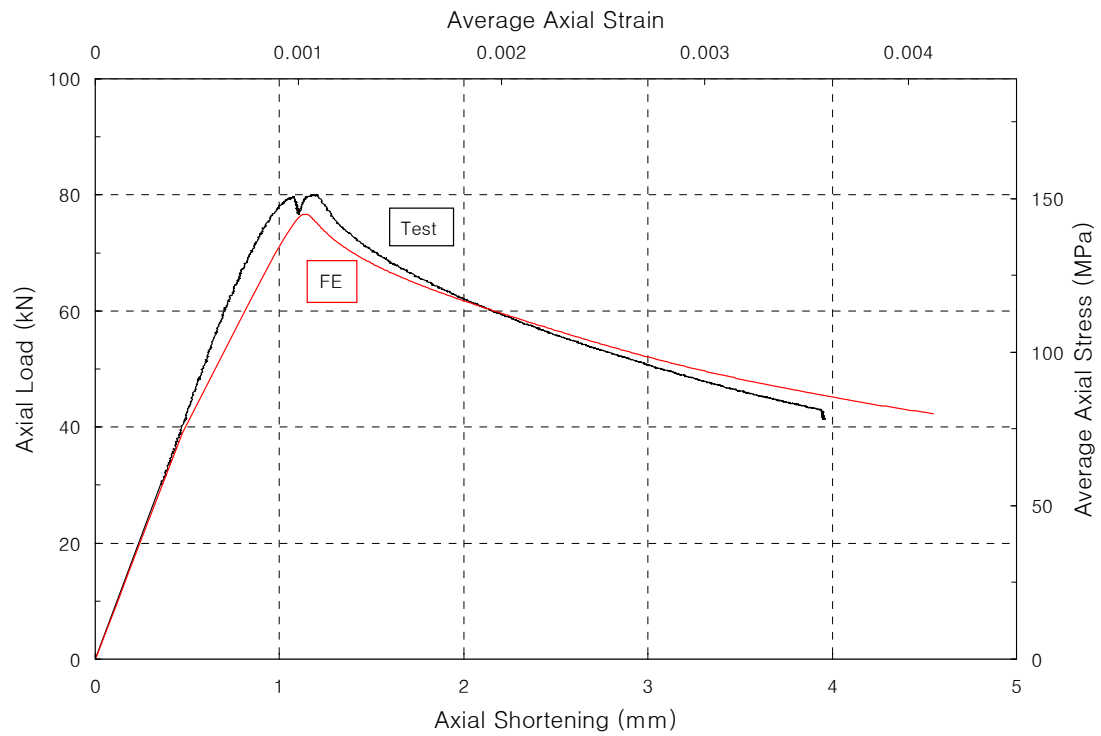


Figure B19.a. C304_1103_1 : Axial Load vs. Axial Shortening

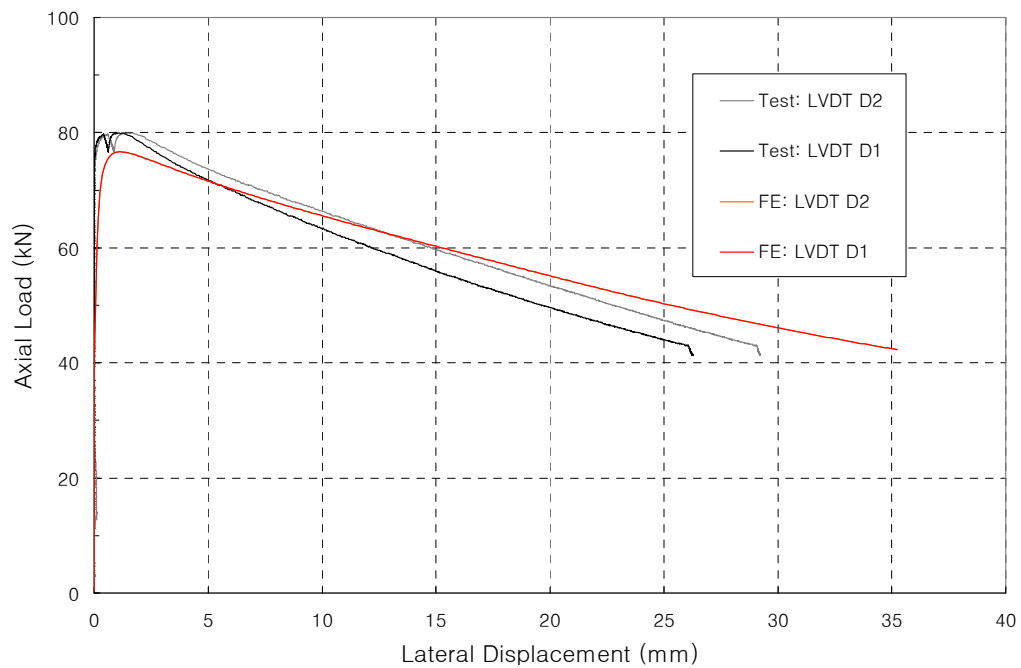


Figure B19.b. C304_1103_1 : Axial Load vs. Lateral Displacement

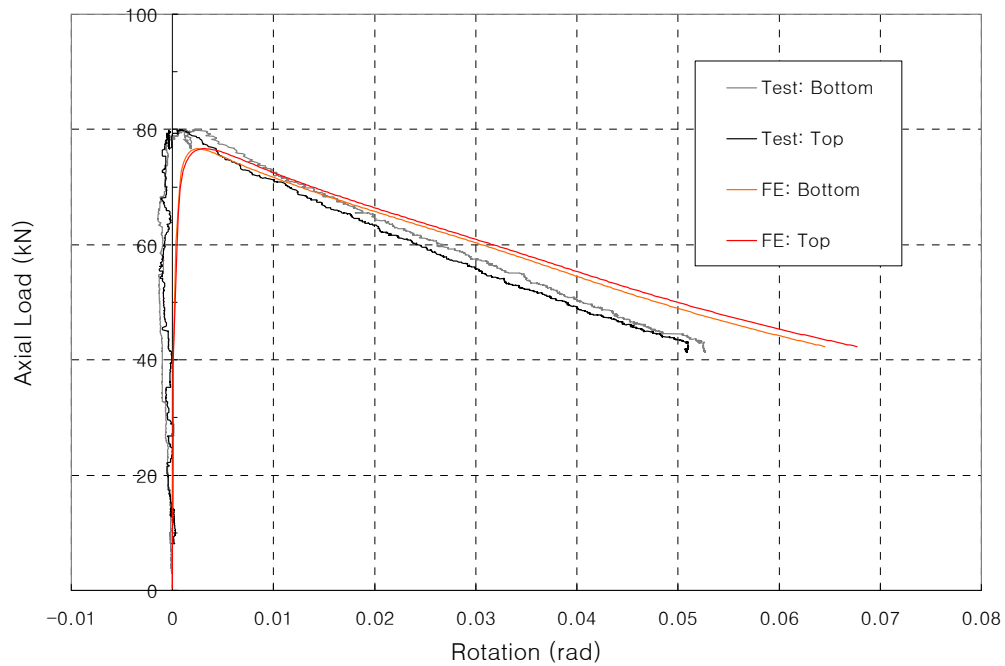


Figure B19.c. C304_1103_1 : Axial Load vs. End Rotations

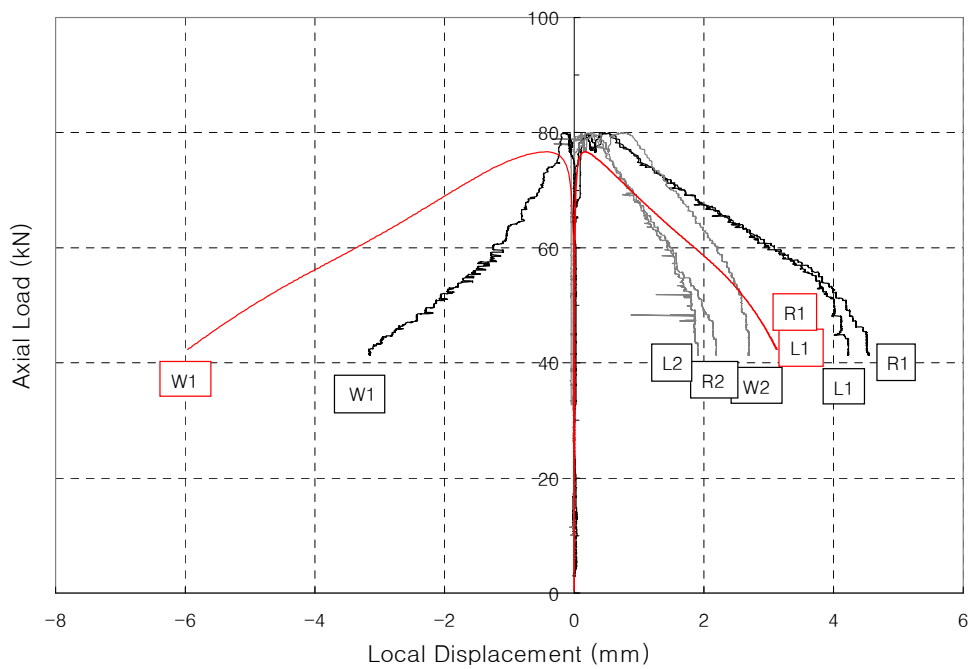


Figure B19.d. C304_1103_1 : Axial Load vs. Local Displacements

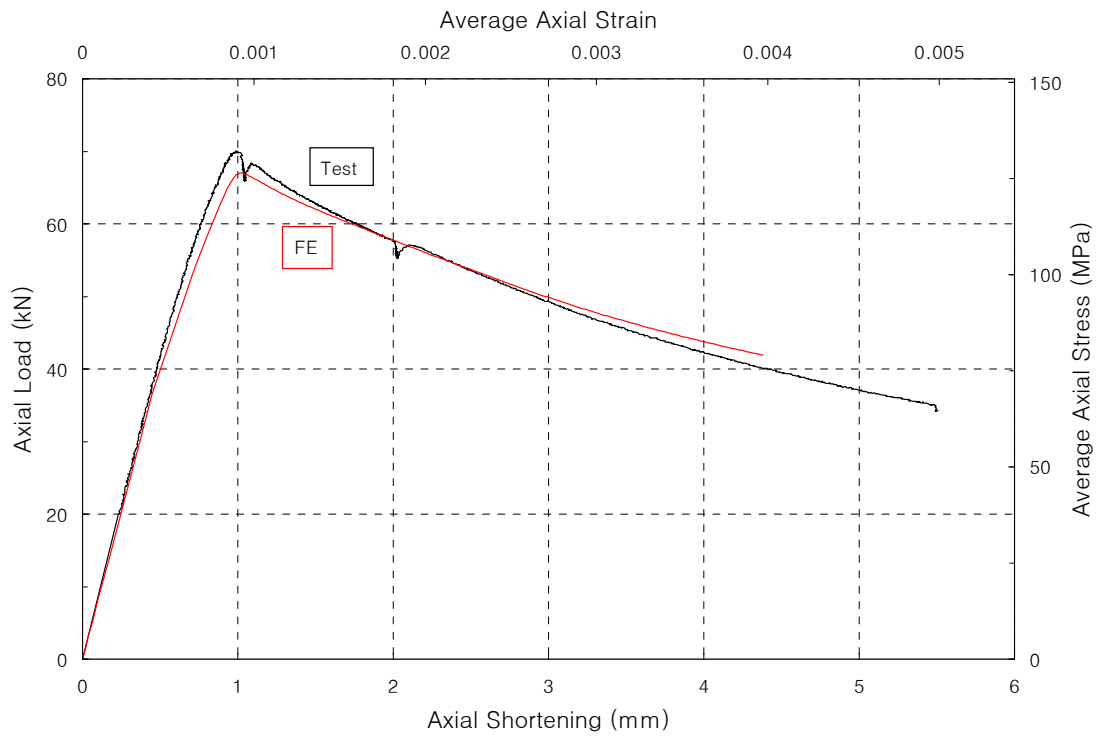


Figure B20.a. C304_1103_2 : Axial Load vs. Axial Shortening

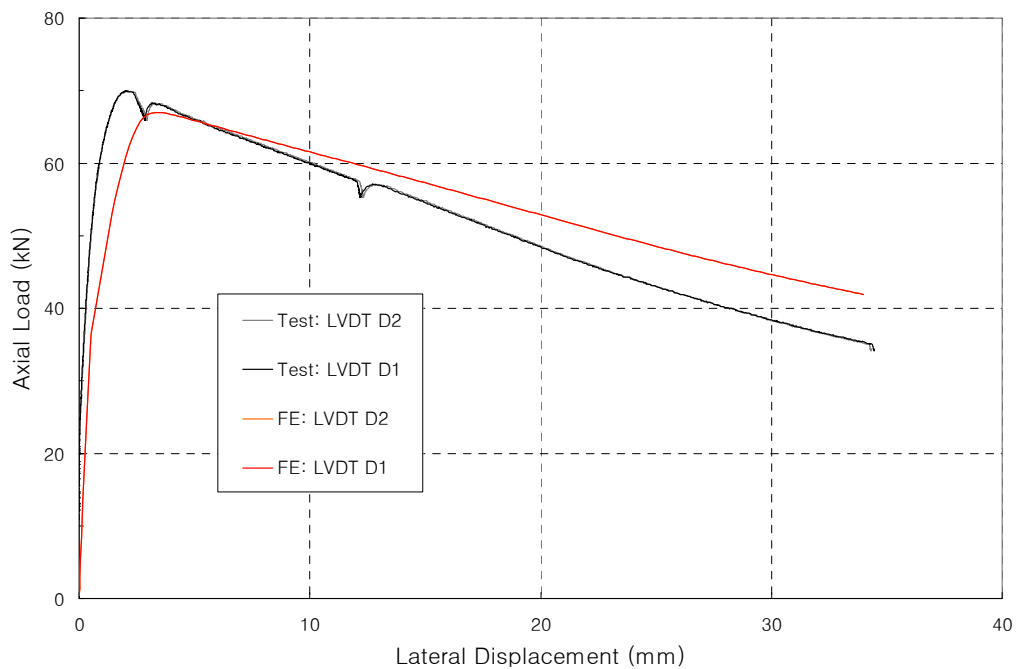


Figure B20.b. C304_1103_2 : Axial Load vs. Lateral Displacement

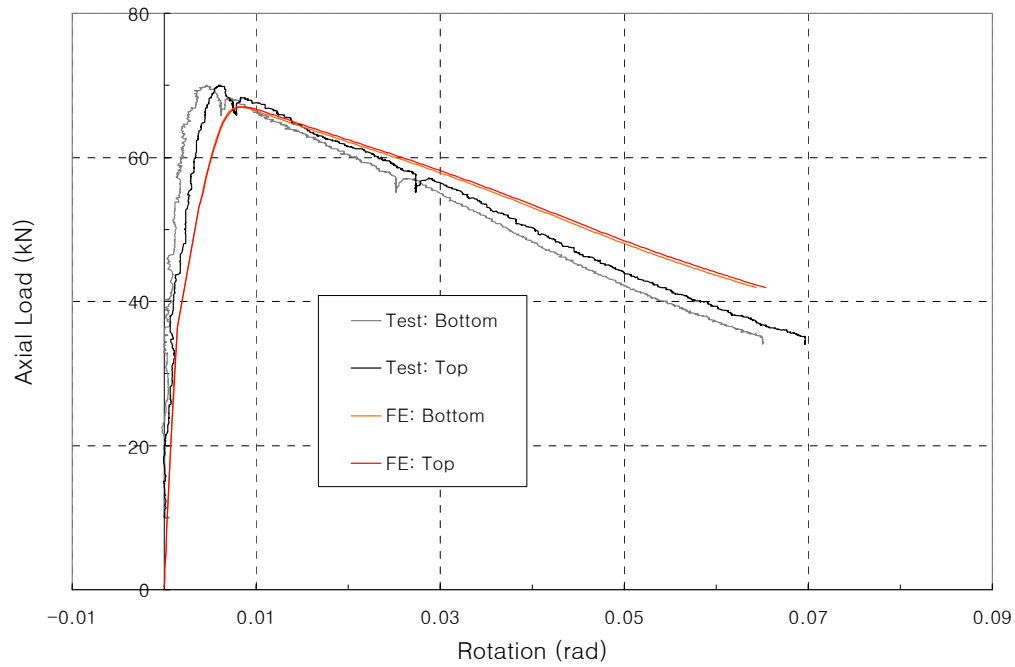


Figure B20.c. C304_1103_2 : Axial Load vs. End Rotations

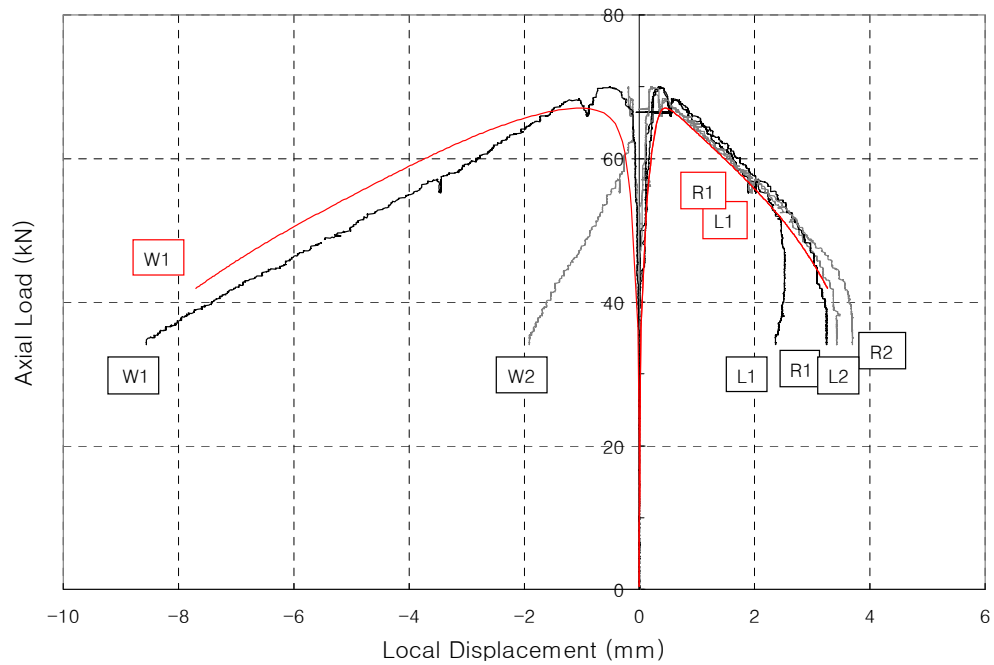


Figure B20.d. C304_1103_2 : Axial Load vs. Local Displacements

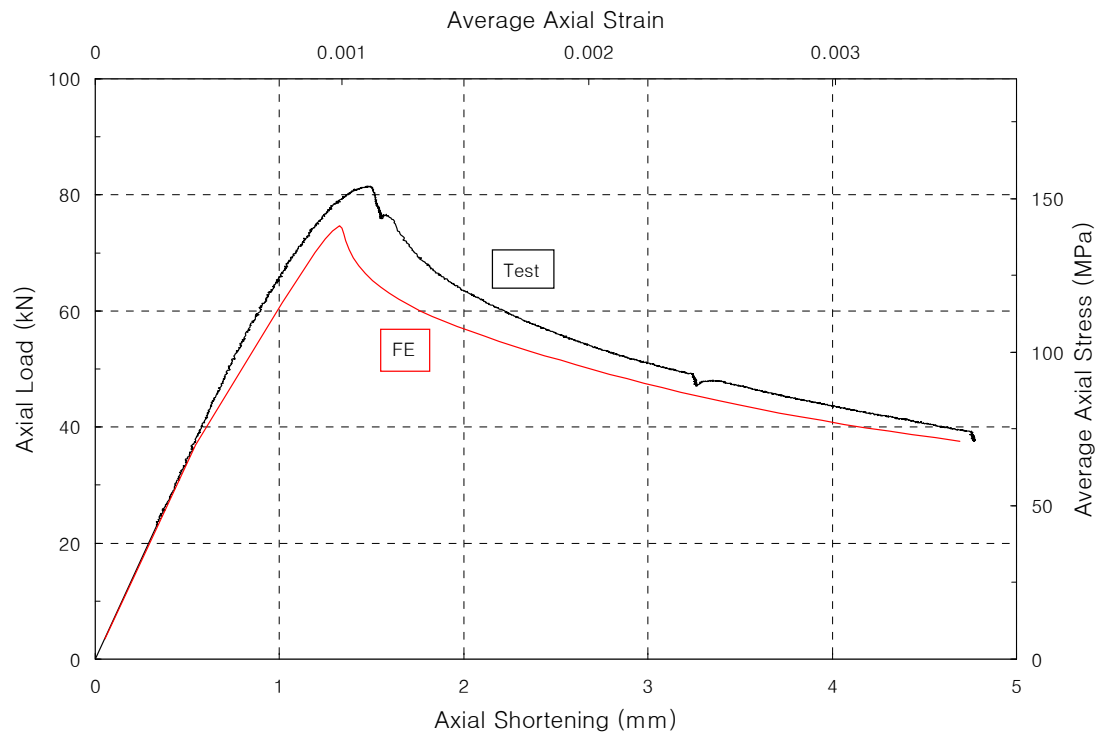


Figure B21.a. C304_1339_1 : Axial Load vs. Axial Shortening

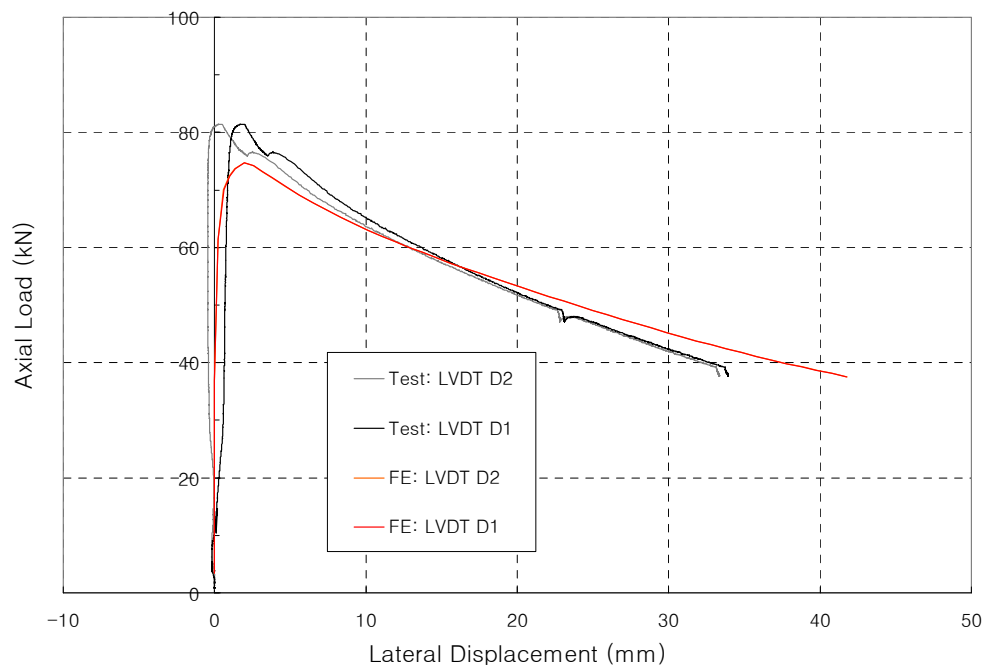


Figure B21.b. C304_1339_1 : Axial Load vs. Lateral Displacement

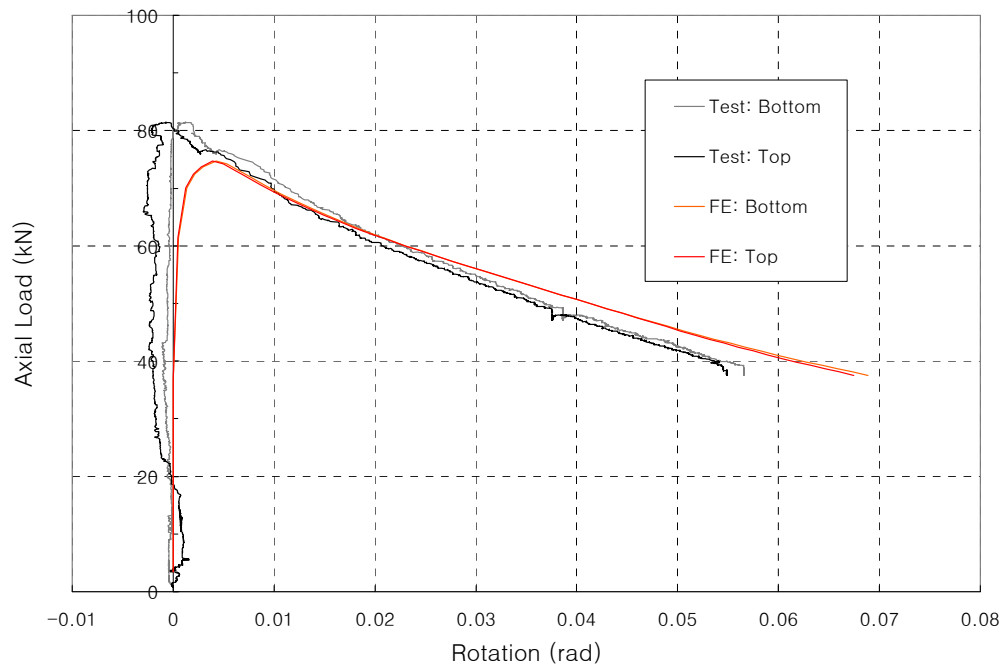


Figure B21.c. C304_1339_1 : Axial Load vs. End Rotations

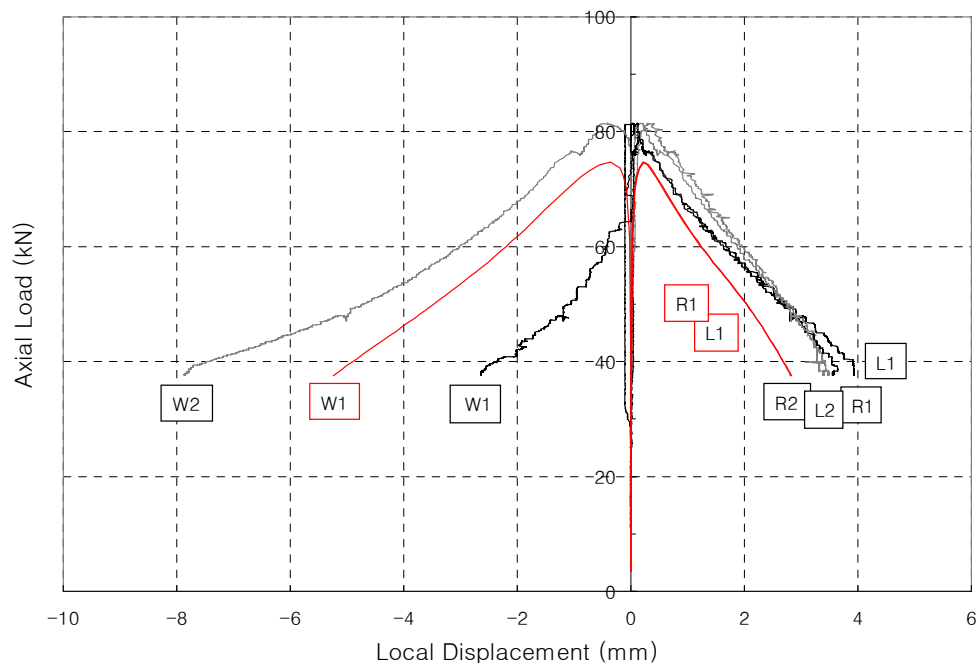


Figure B21.d. C304_1339_1 : Axial Load vs. Local Displacements

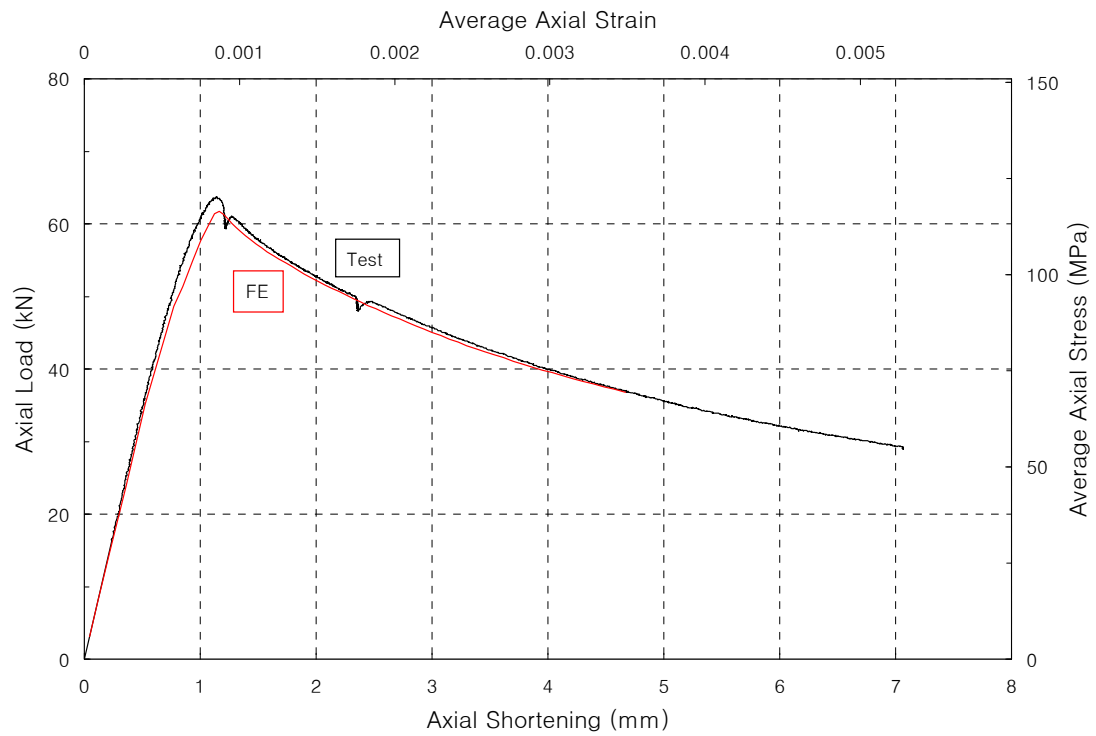


Figure B22.a. C304_1339_2 : Axial Load vs. Axial Shortening

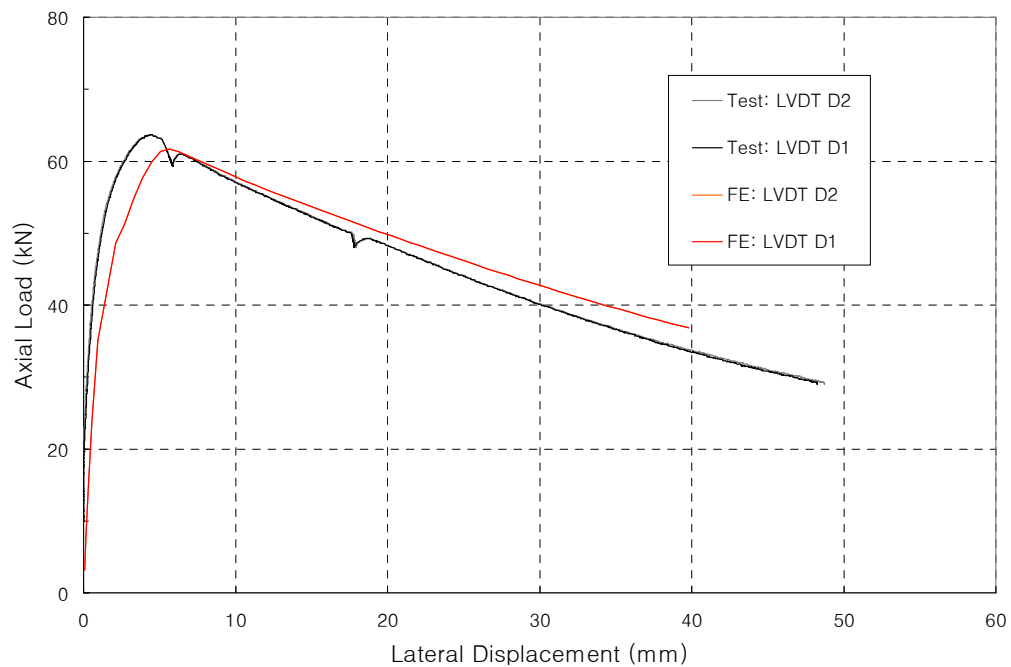


Figure B22.b. C304_1339_2 : Axial Load vs. Lateral Displacement

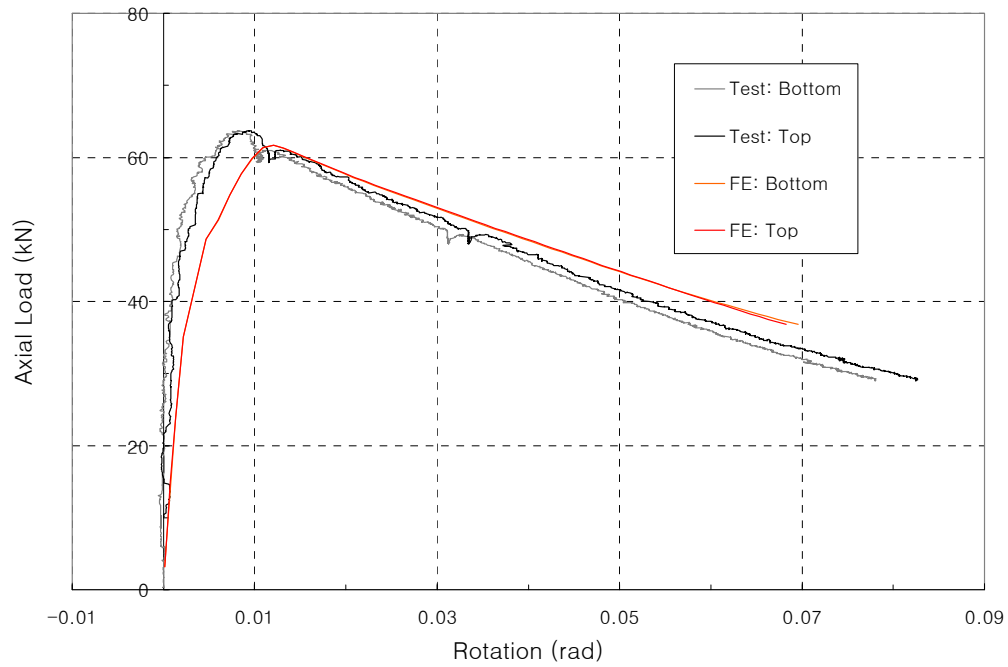


Figure B22.c. C304_1339_2 : Axial Load vs. End Rotations

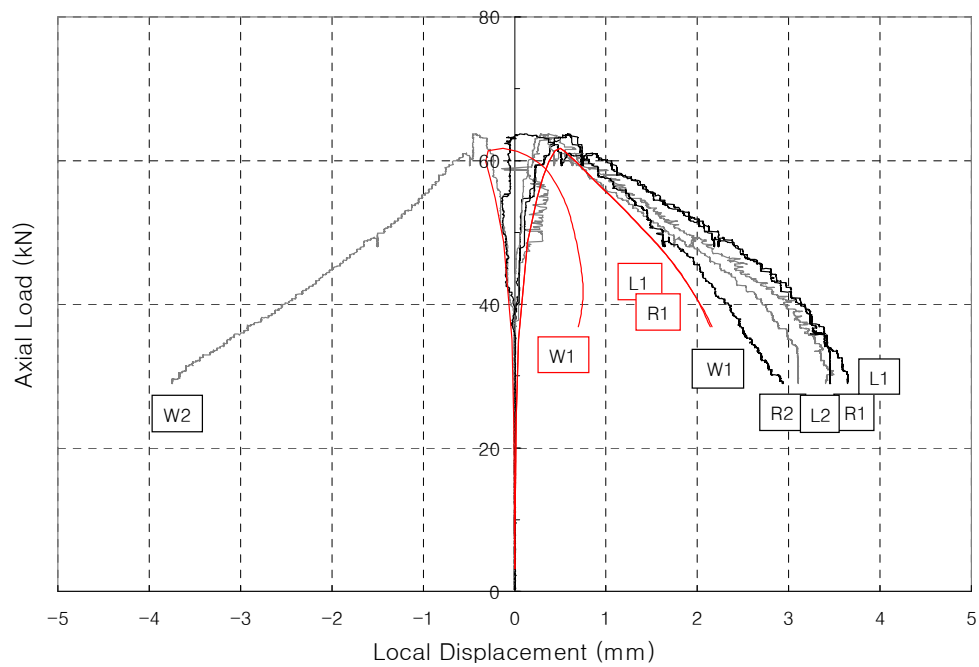


Figure B22.d. C304_1339_2 : Axial Load vs. Local Displacements

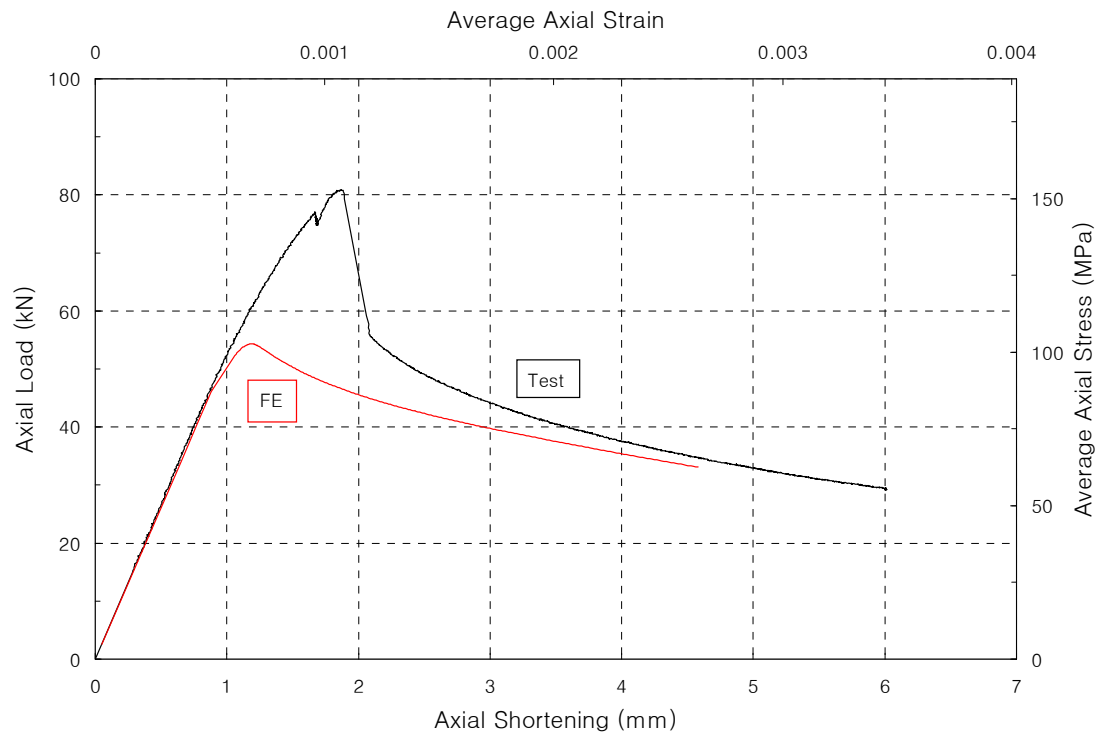


Figure B23.a. C304_1741_1 : Axial Load vs. Axial Shortening

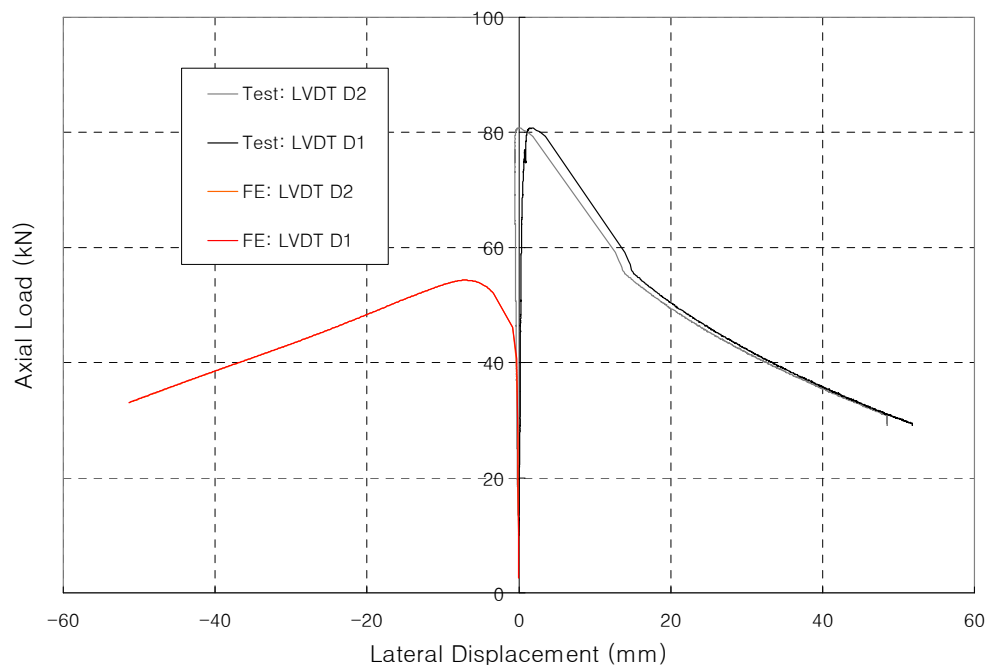


Figure B23.b. C304_1741_1 : Axial Load vs. Lateral Displacement

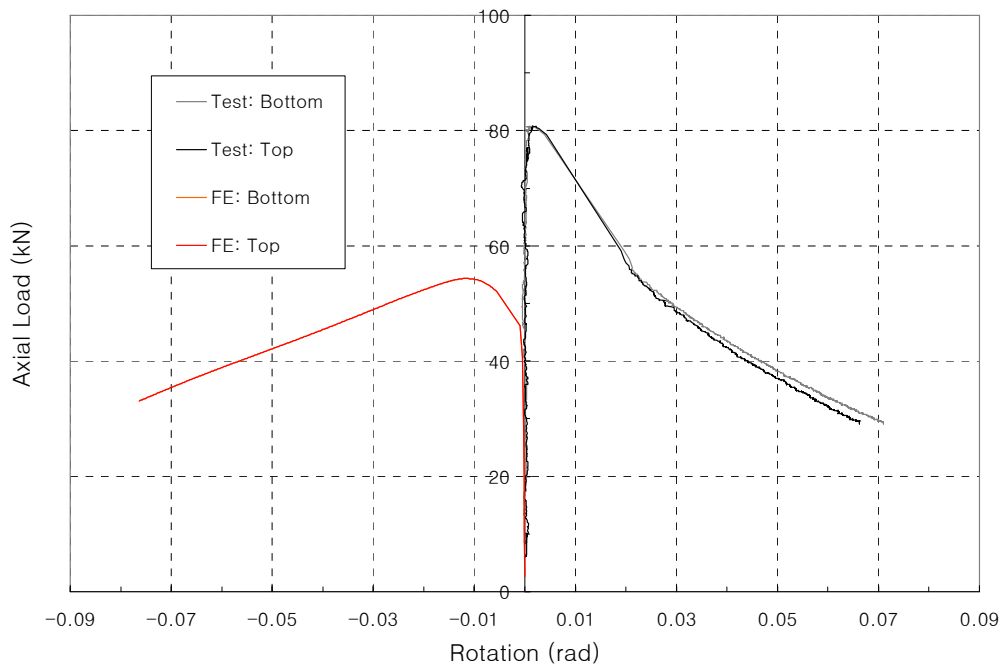


Figure B23.c. C304_1741_1 : Axial Load vs. End Rotations

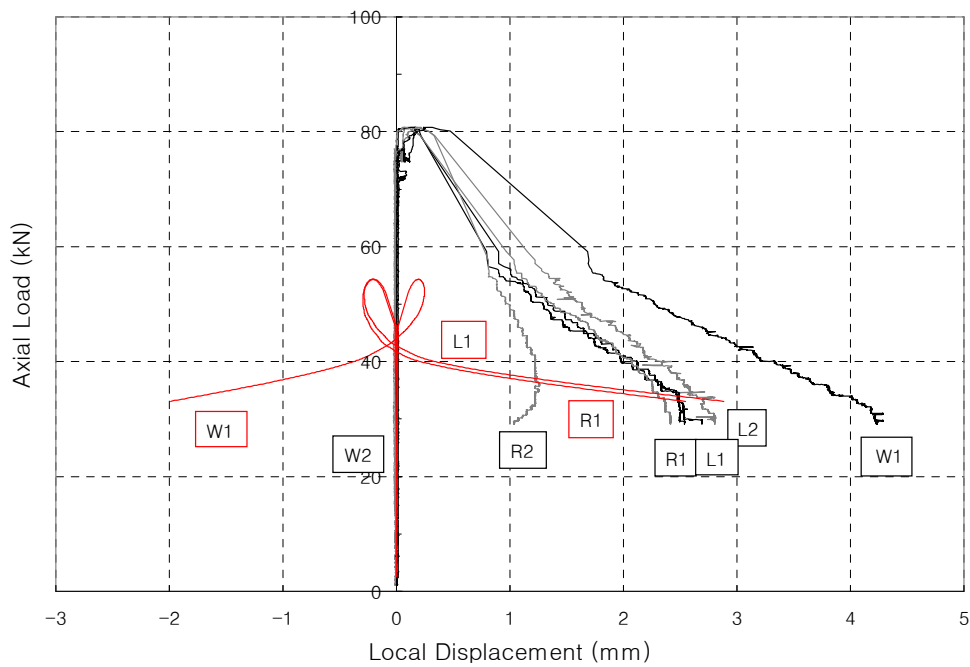


Figure B23.d. C304_1741_1 : Axial Load vs. Local Displacements

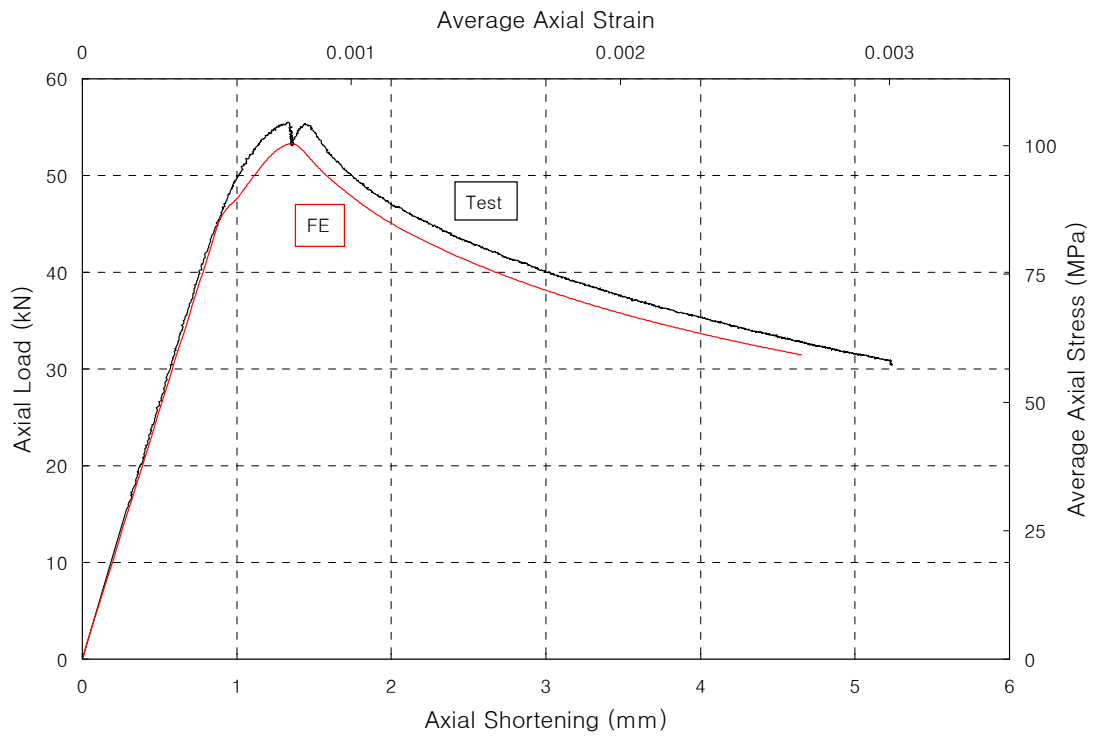


Figure B24.a. C304_1741_2 : Axial Load vs. Axial Shortening

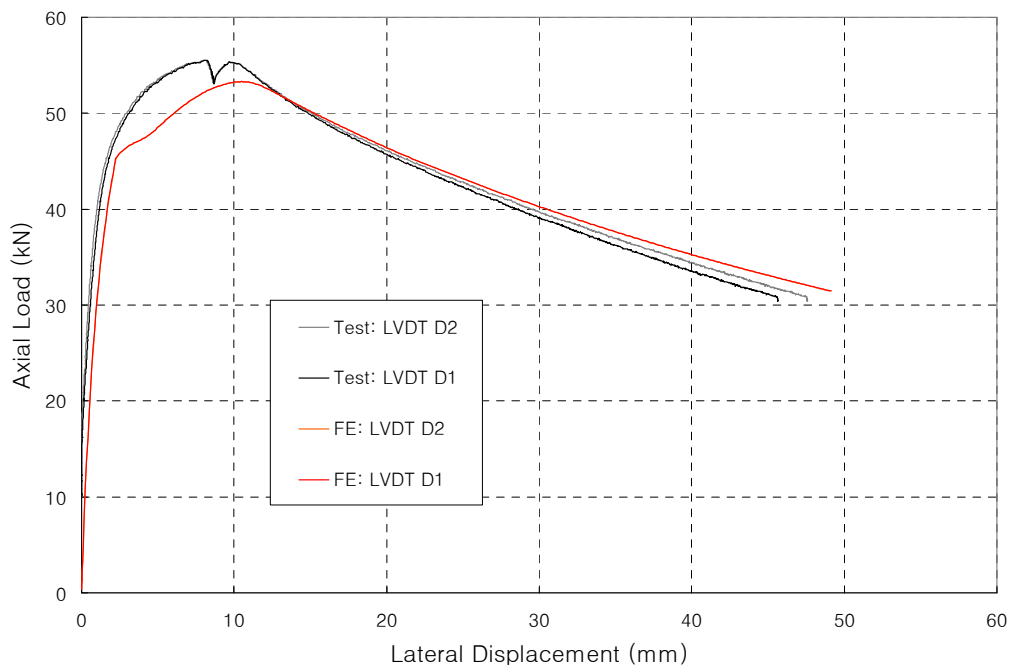


Figure B24.b. C304_1741_2 : Axial Load vs. Lateral Displacement

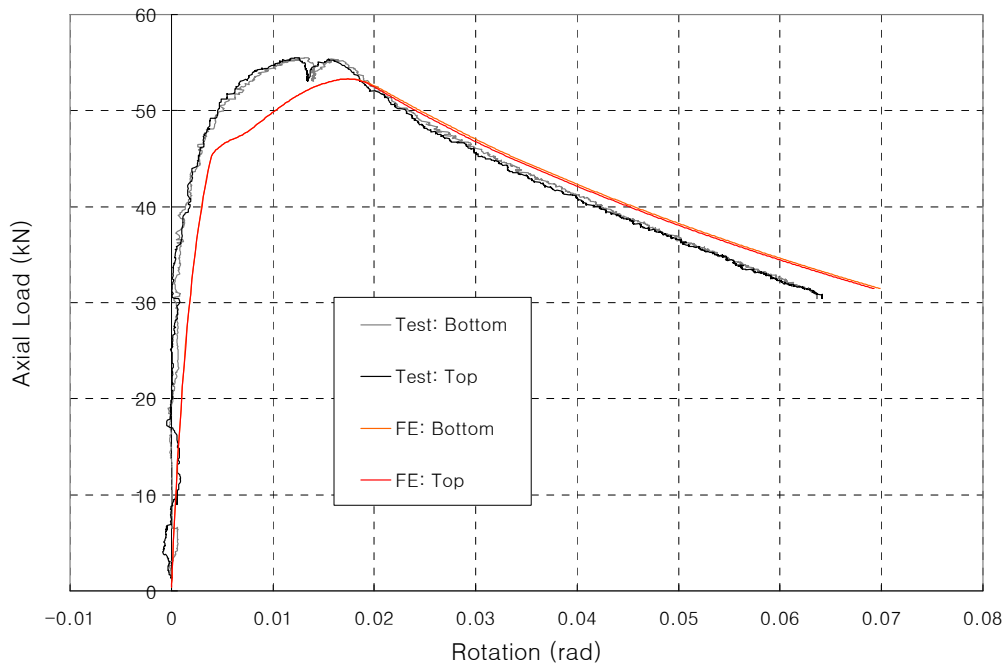


Figure B24.c. C304_1741_2 : Axial Load vs. End Rotations

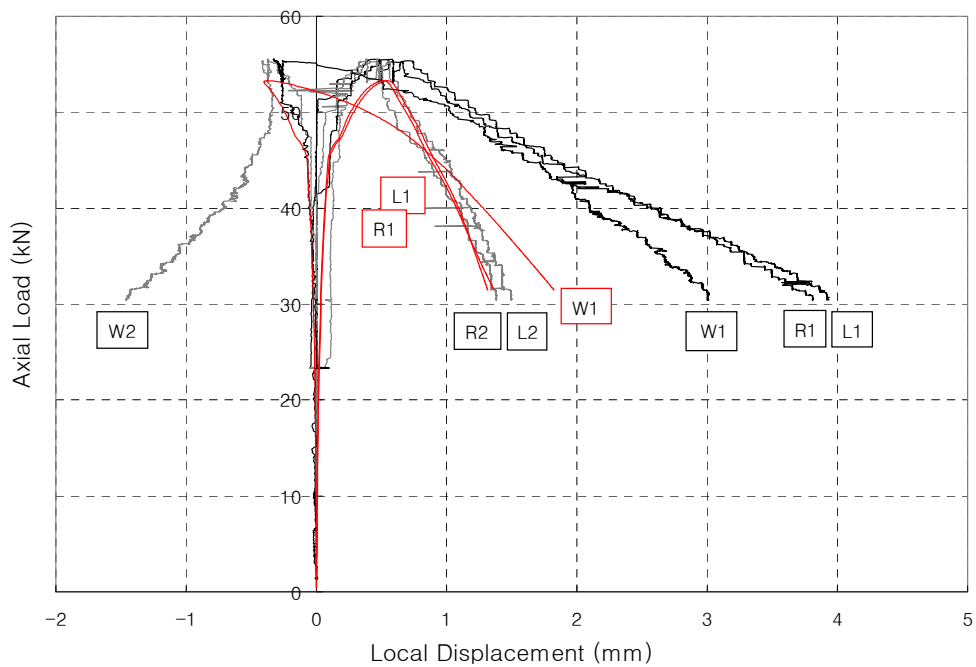


Figure B24.d. C304_1741_2 : Axial Load vs. Local Displacements

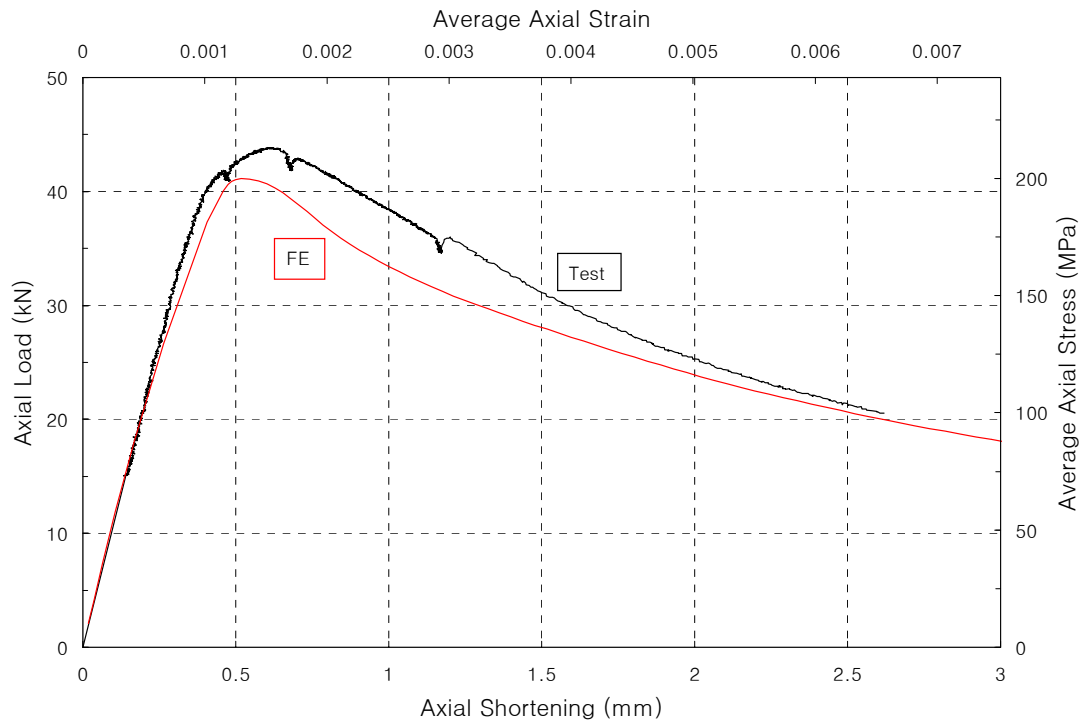


Figure B25.a. C430_399_1 : Axial Load vs. Axial Shortening

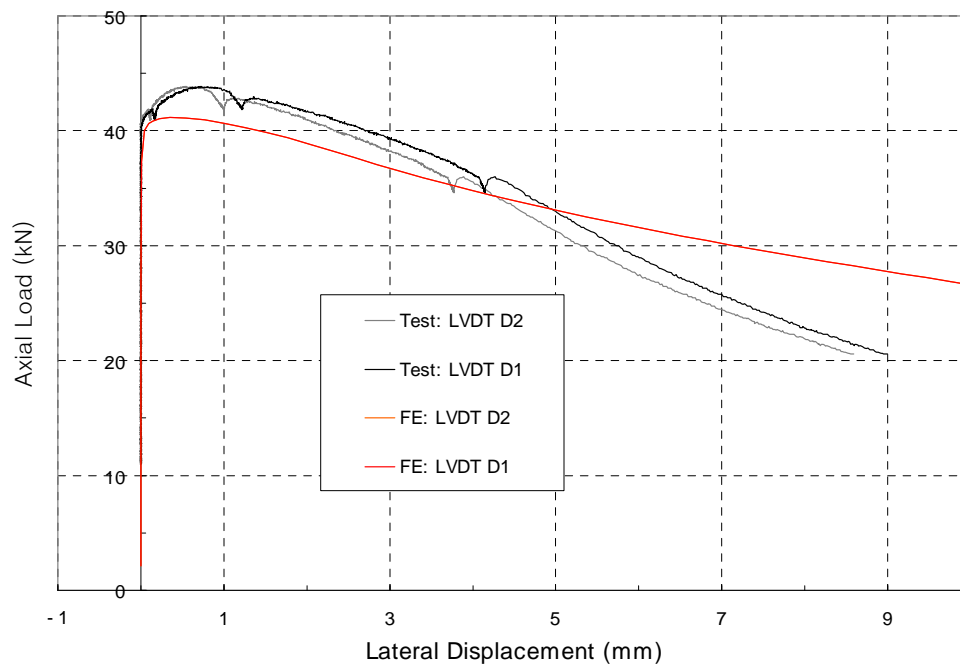


Figure B25.b. C430_399_1 : Axial Load vs. Lateral Displacement

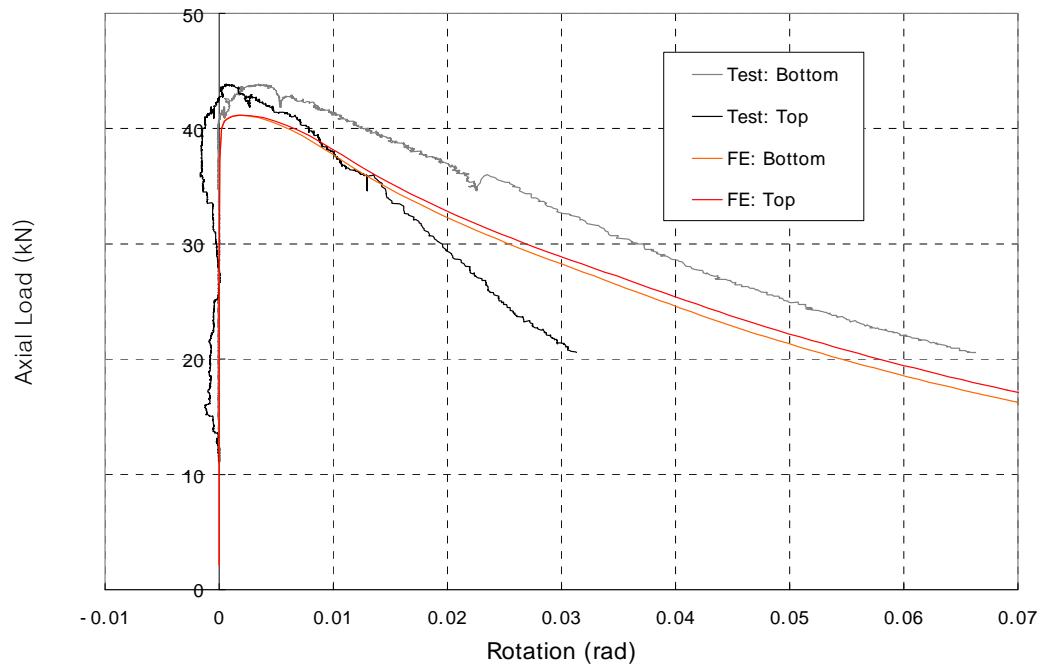


Figure B25.c. C430_399_1 : Axial Load vs. End Rotations

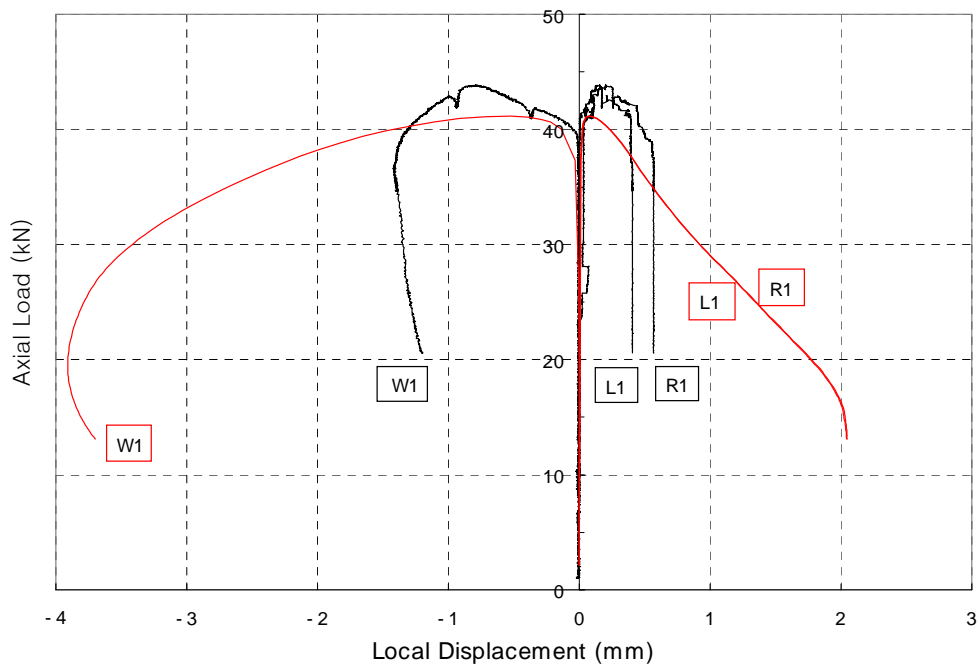


Figure B25.d. C430_399_1 : Axial Load vs. Local Displacements

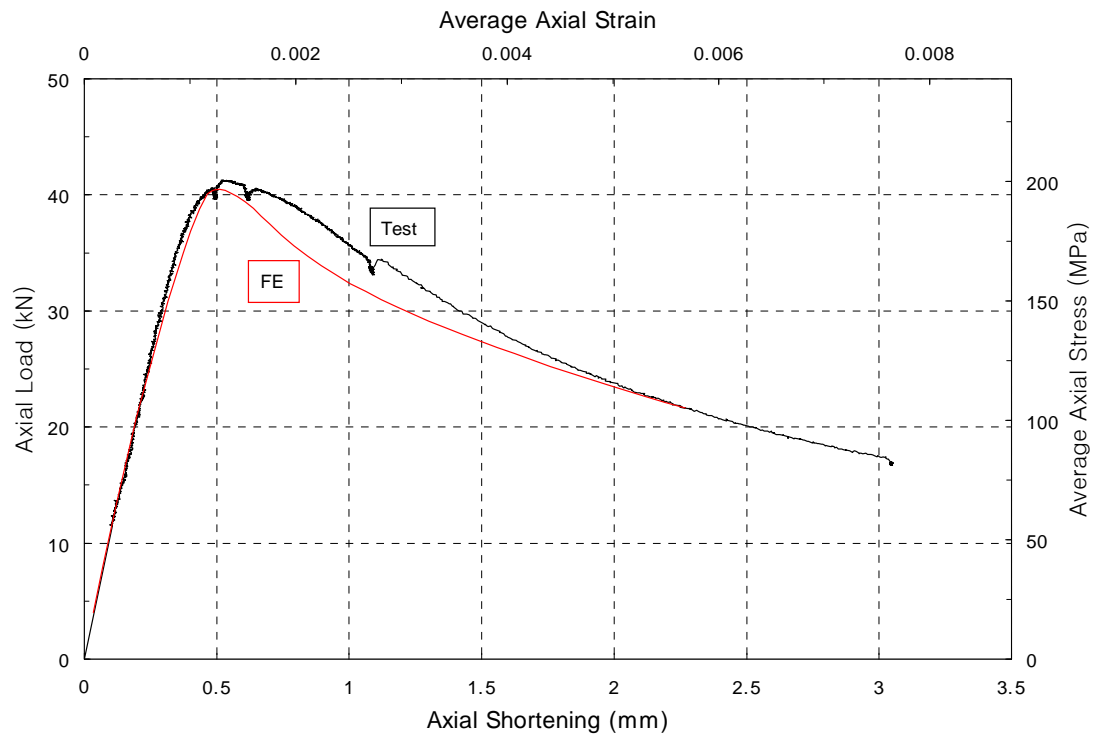


Figure B26.a. C430_399_2 : Axial Load vs. Axial Shortening

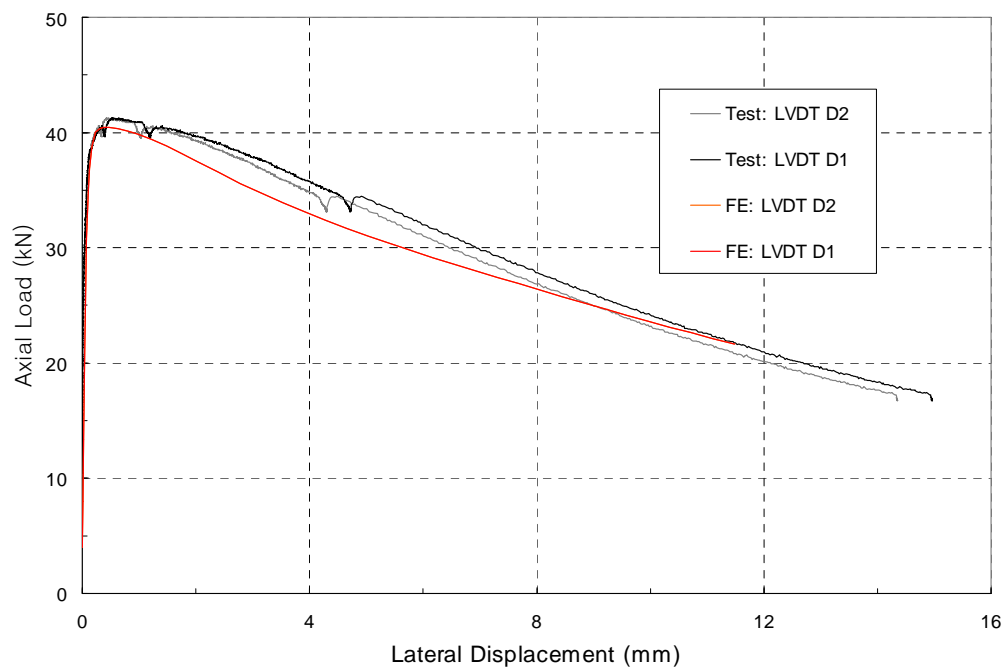


Figure B26.b. C430_399_2 : Axial Load vs. Lateral Displacement

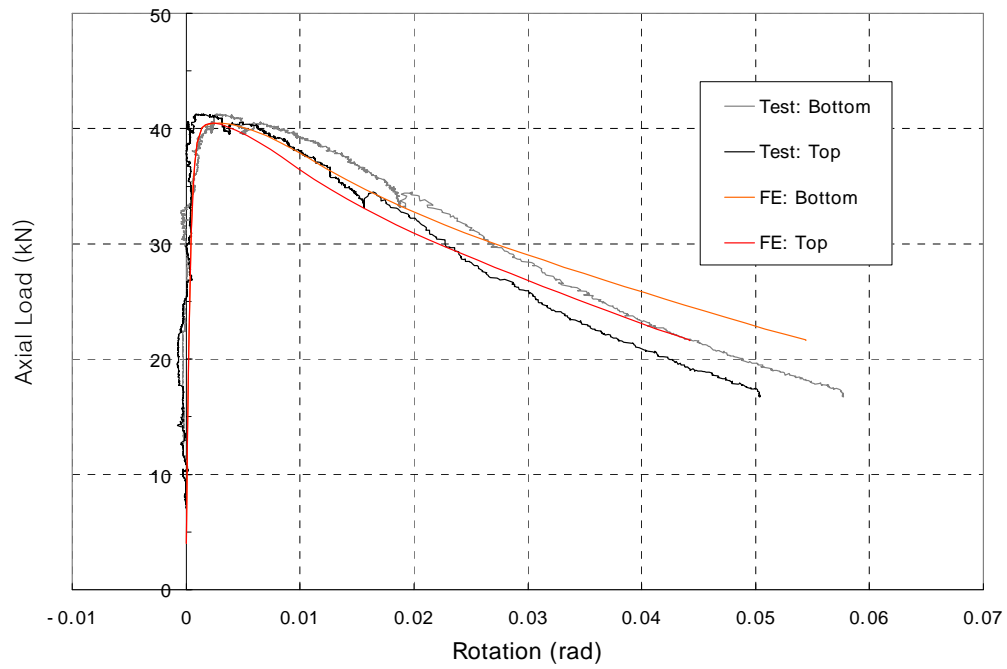


Figure B26.c. C430_399_2 : Axial Load vs. End Rotations

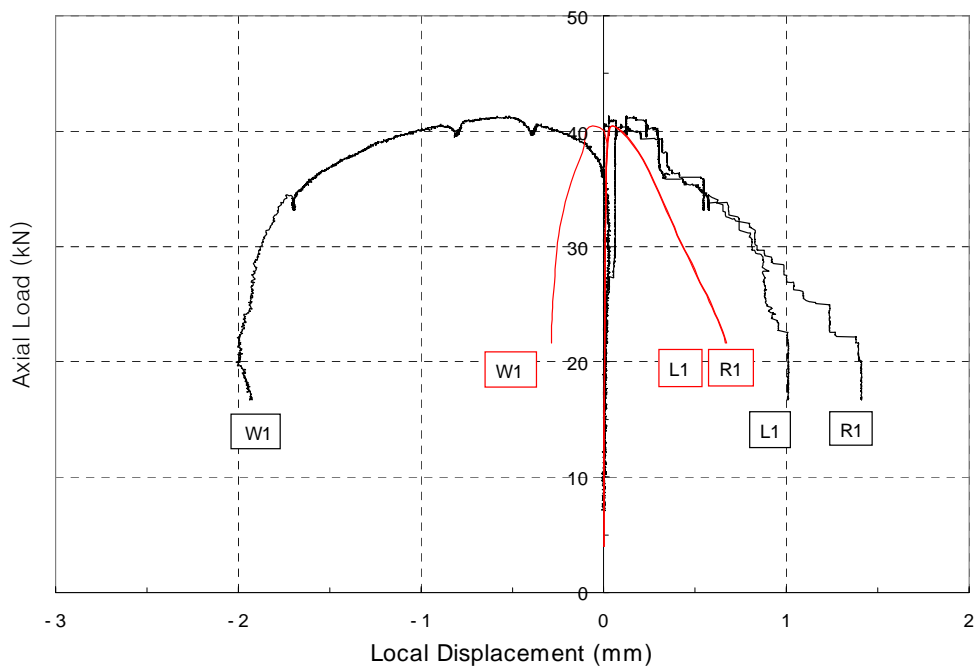


Figure B26.d. C430_399_2 : Axial Load vs. Local Displacements

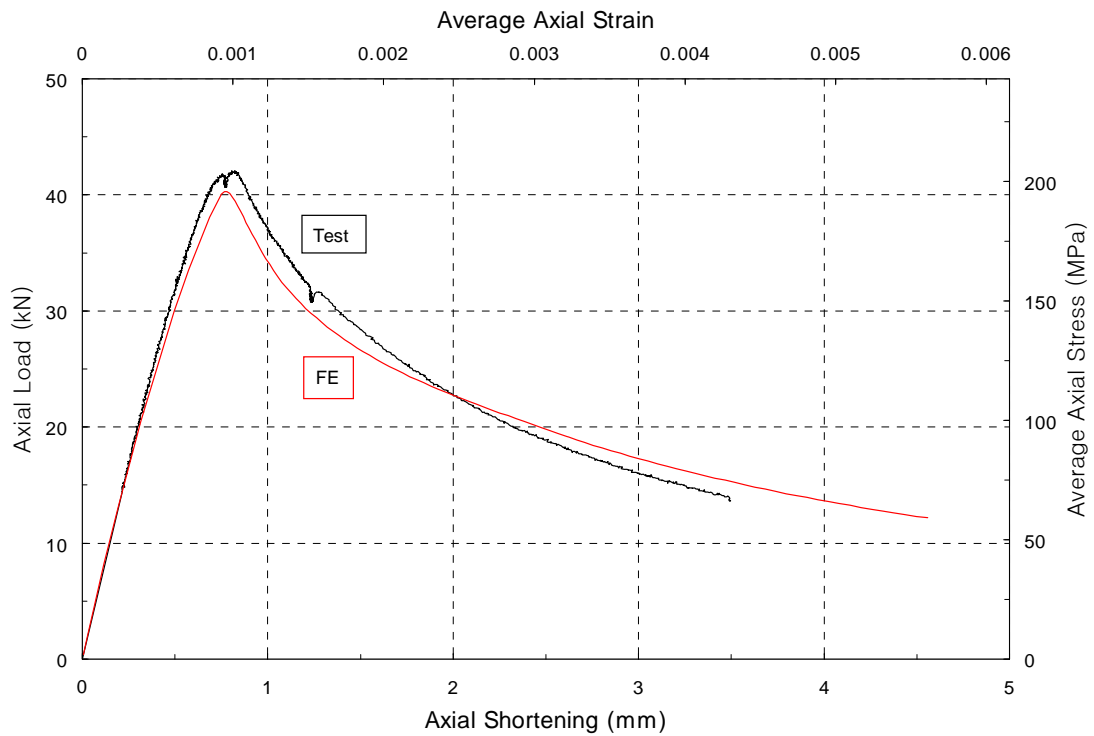


Figure B27.a. C430_650_1 : Axial Load vs. Axial Shortening

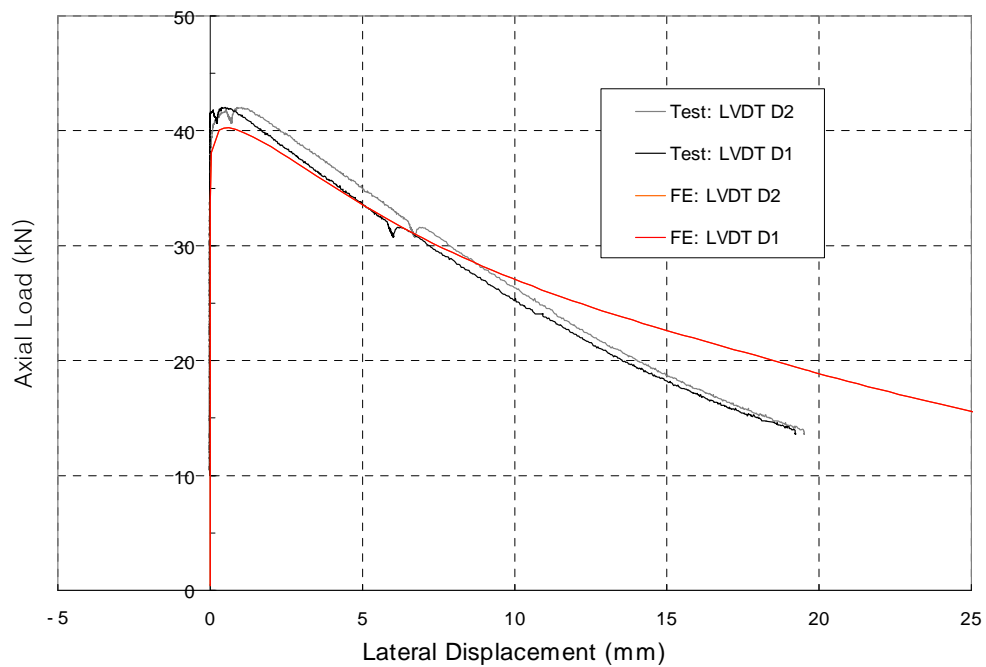


Figure B27.b. C430_650_1 : Axial Load vs. Lateral Displacement

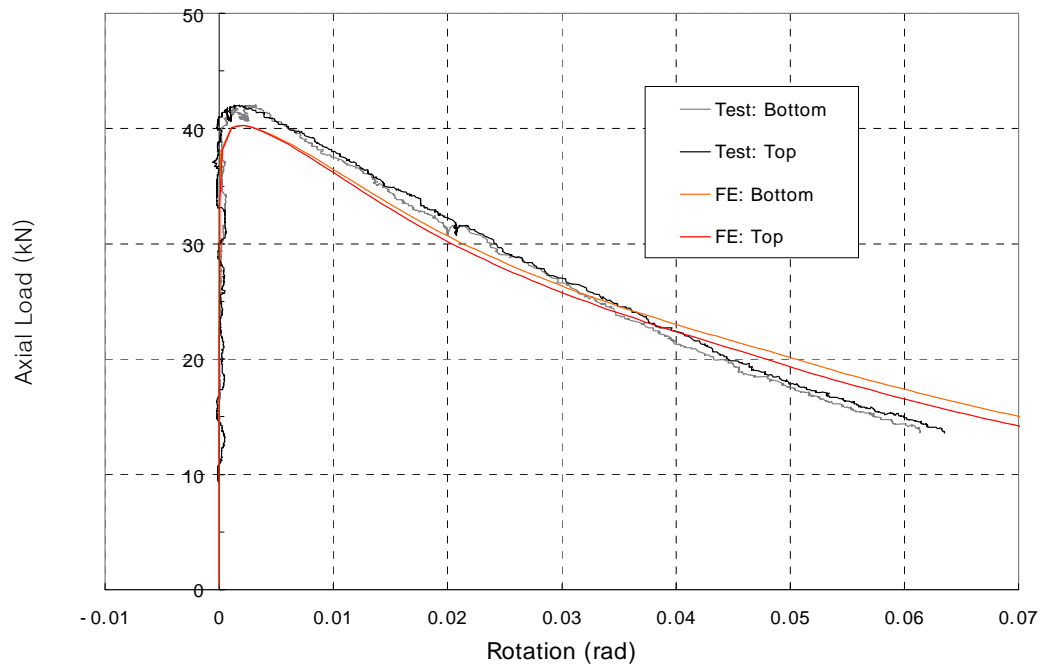


Figure B27.c. C430_650_1 : Axial Load vs. End Rotations

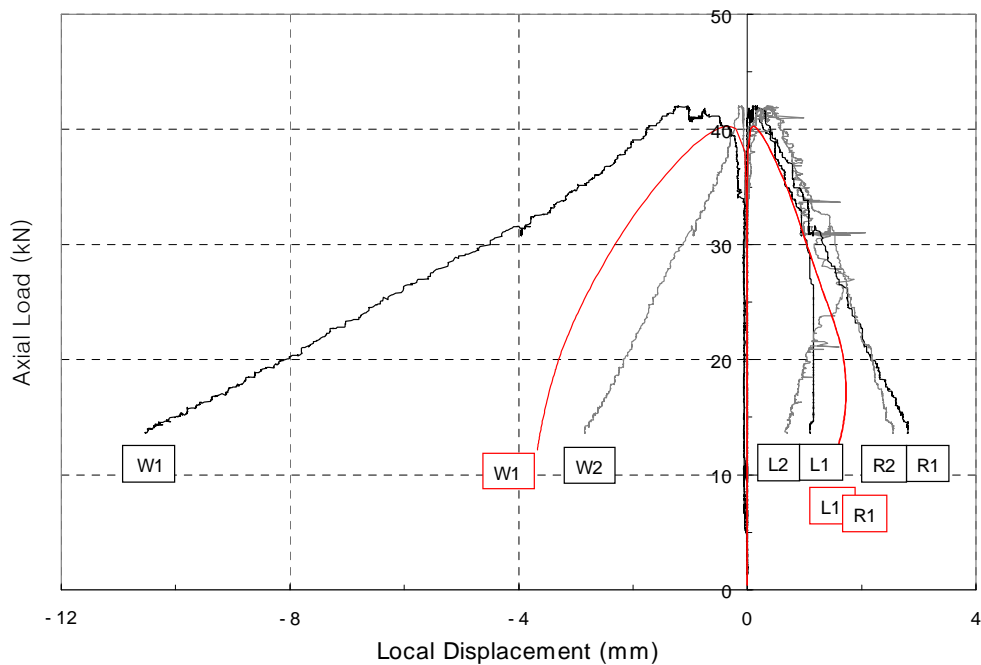


Figure B27.d. C430_650_1 : Axial Load vs. Local Displacements

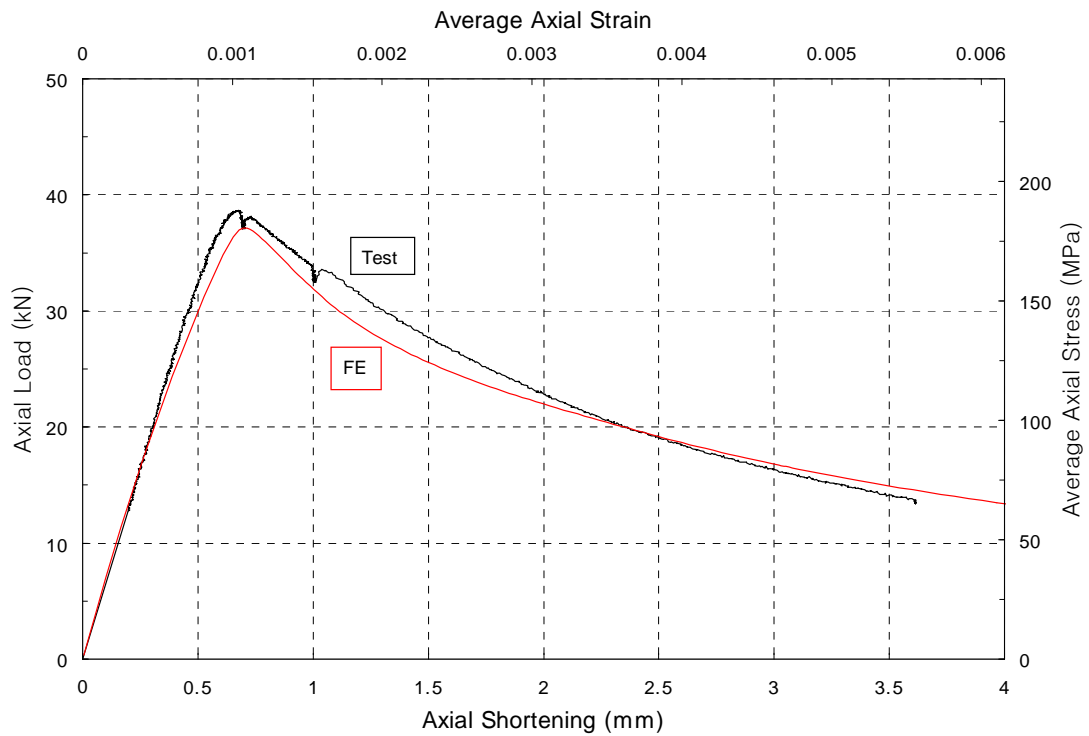


Figure B28.a. C430_650_2 : Axial Load vs. Axial Shortening

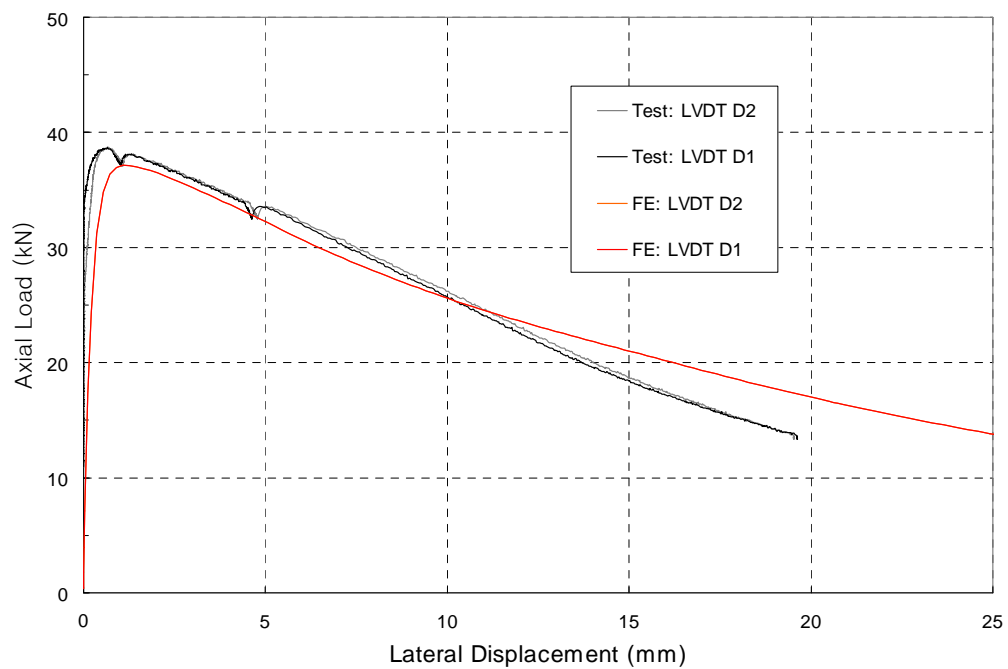


Figure B28.b. C430_650_2 : Axial Load vs. Lateral Displacement

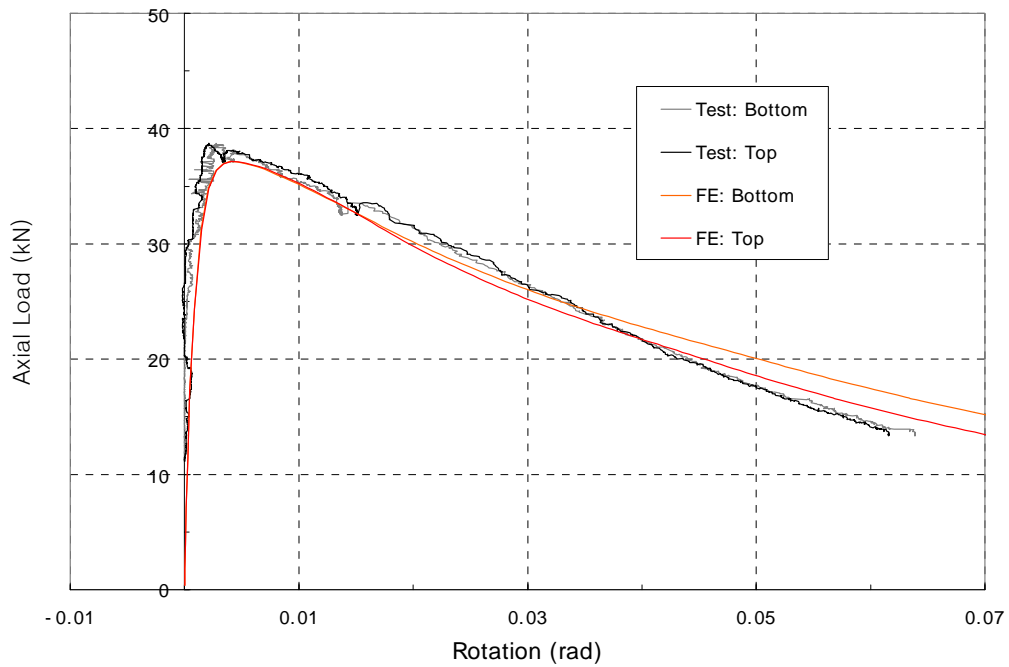


Figure B28.c. C430_650_2 : Axial Load vs. End Rotations

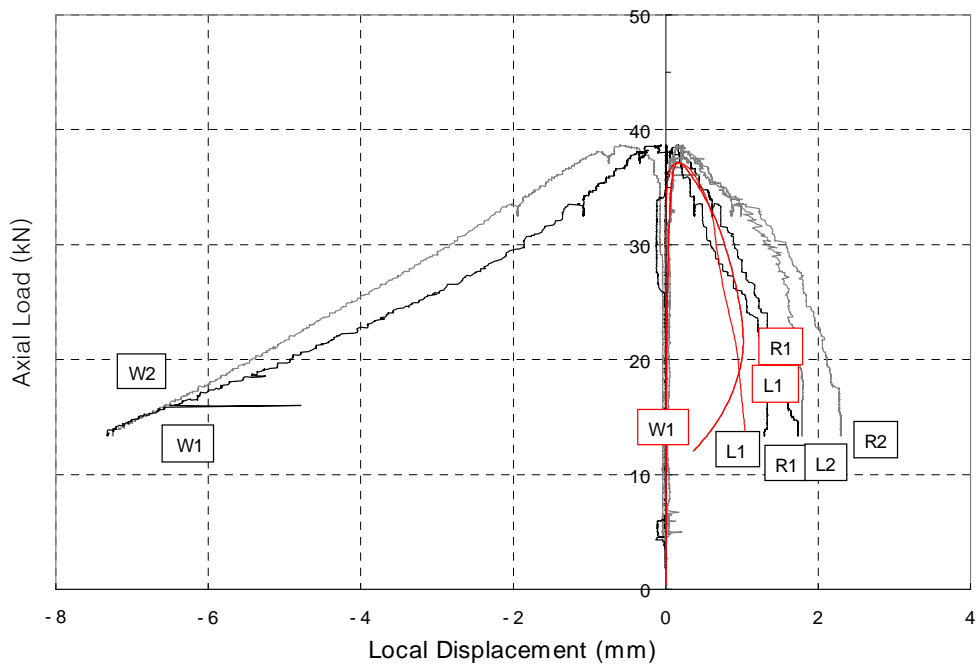


Figure B28.d. C430_650_2 : Axial Load vs. Local Displacements

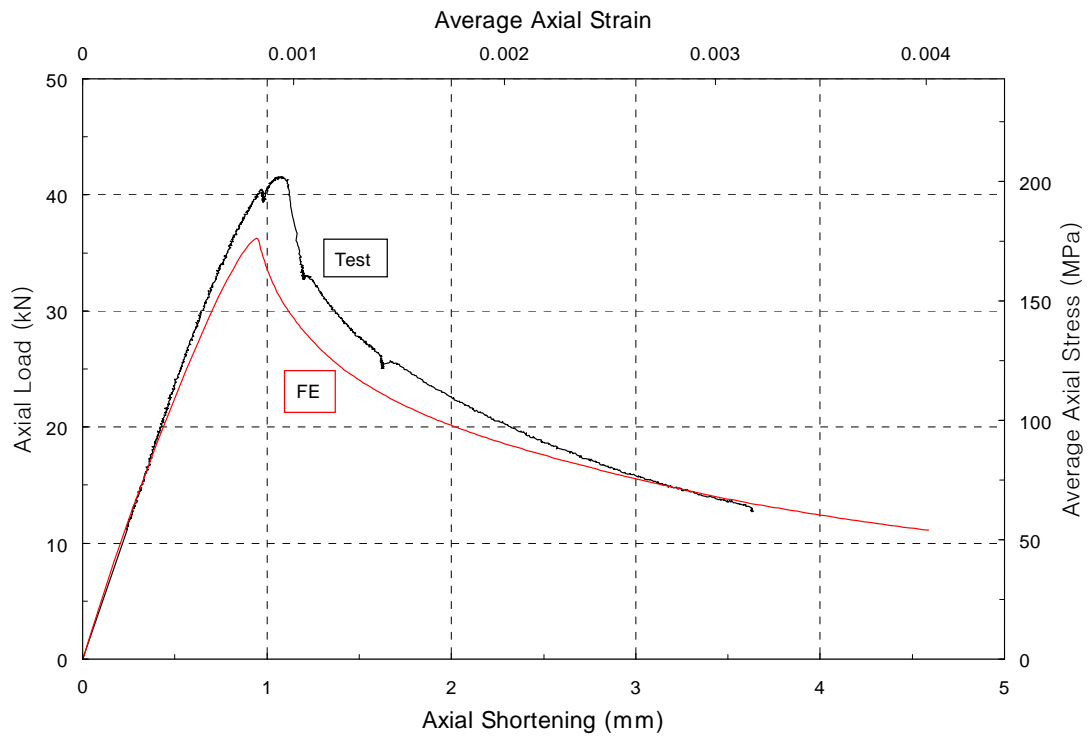


Figure B29.a. C430_915_1 : Axial Load vs. Axial Shortening

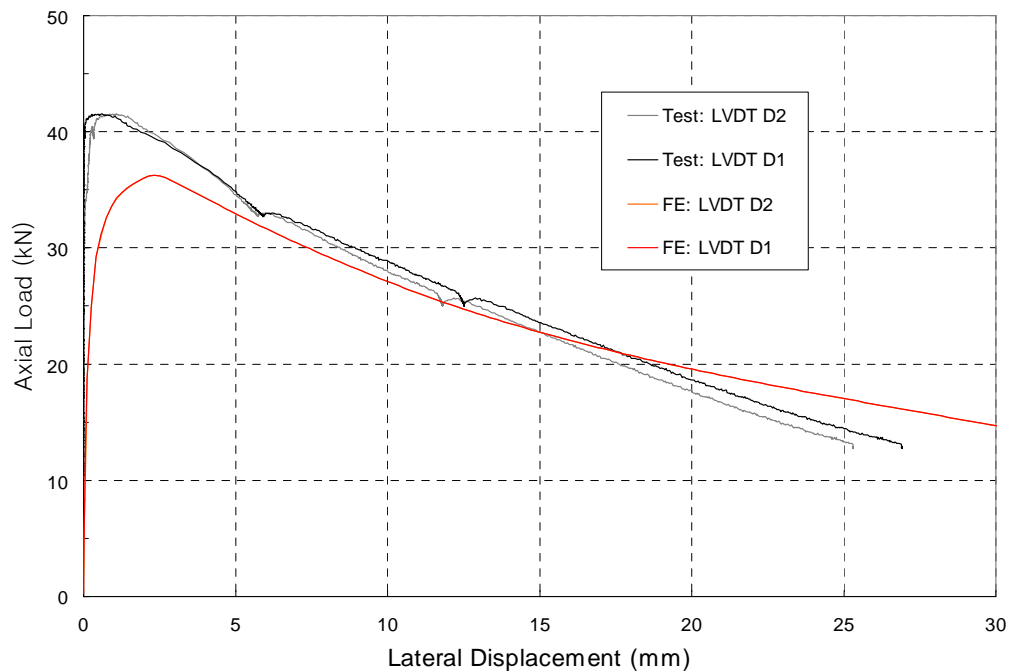


Figure B29.b. C430_915_1 : Axial Load vs. Lateral Displacement

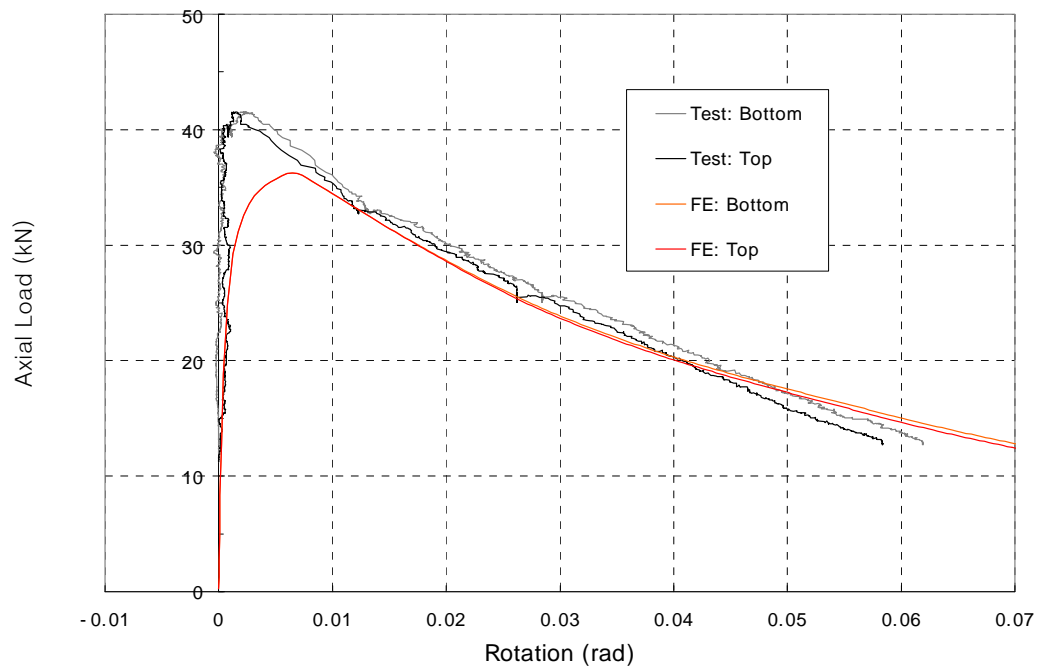


Figure B29.c. C430_915_1 : Axial Load vs. End Rotations

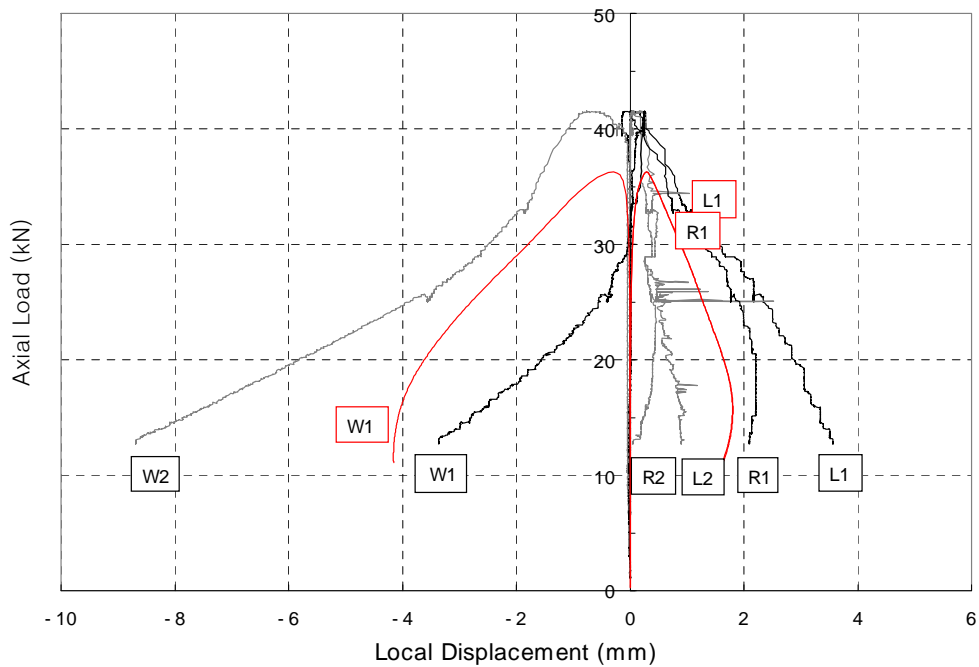


Figure B29.d. C430_915_1 : Axial Load vs. Local Displacements

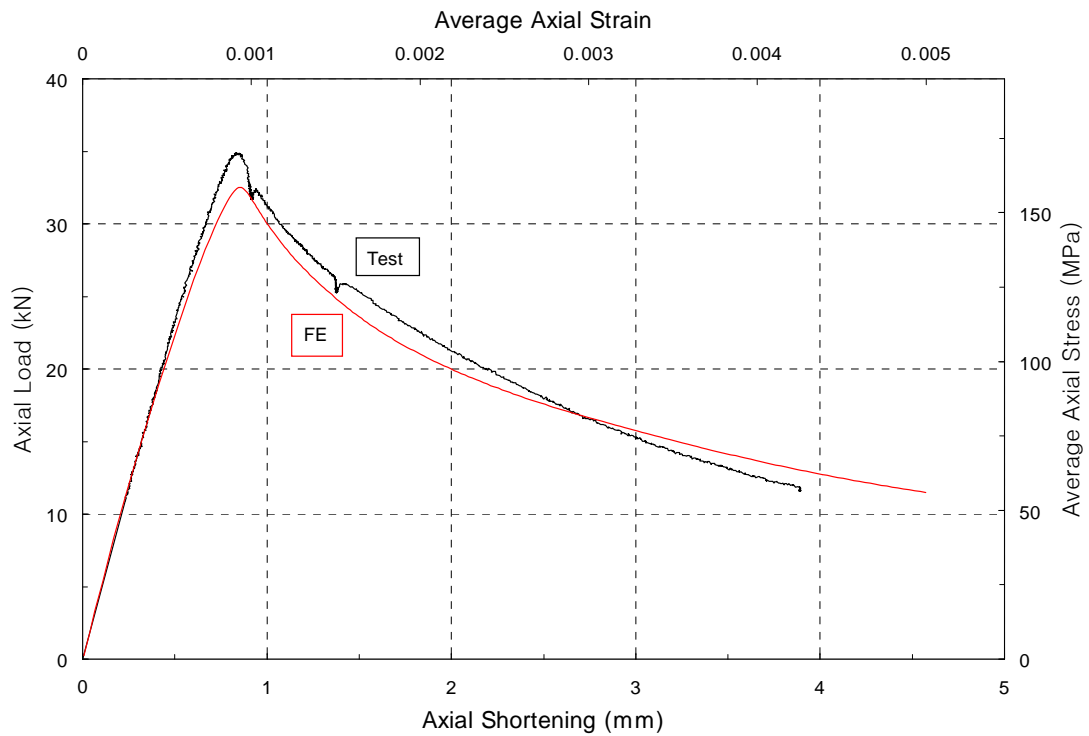


Figure B30.a. C430_915_2 : Axial Load vs. Axial Shortening

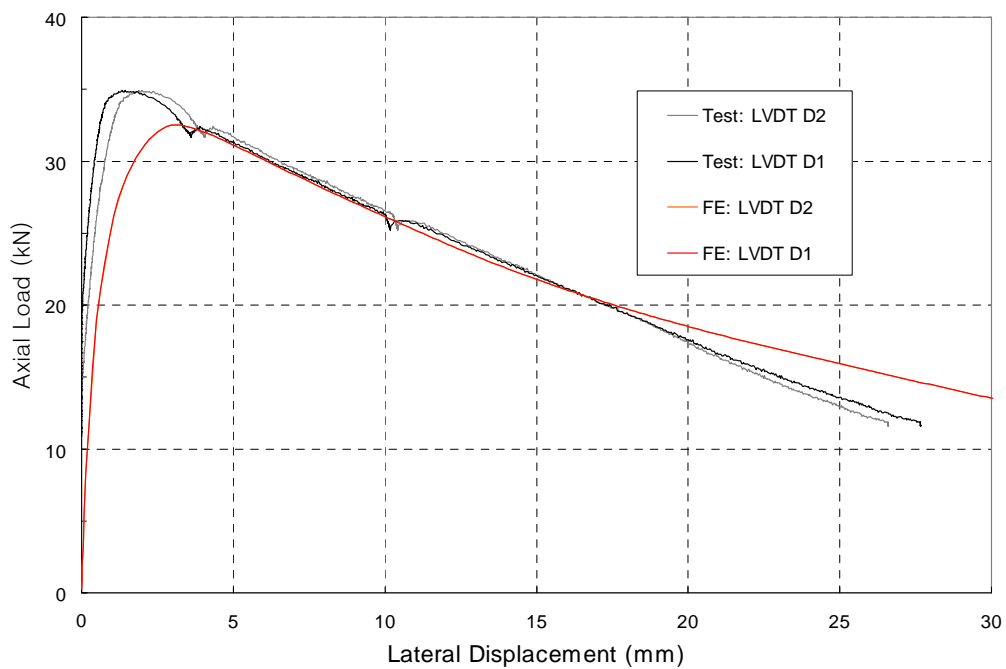


Figure B30.b. C430_915_2 : Axial Load vs. Lateral Displacement

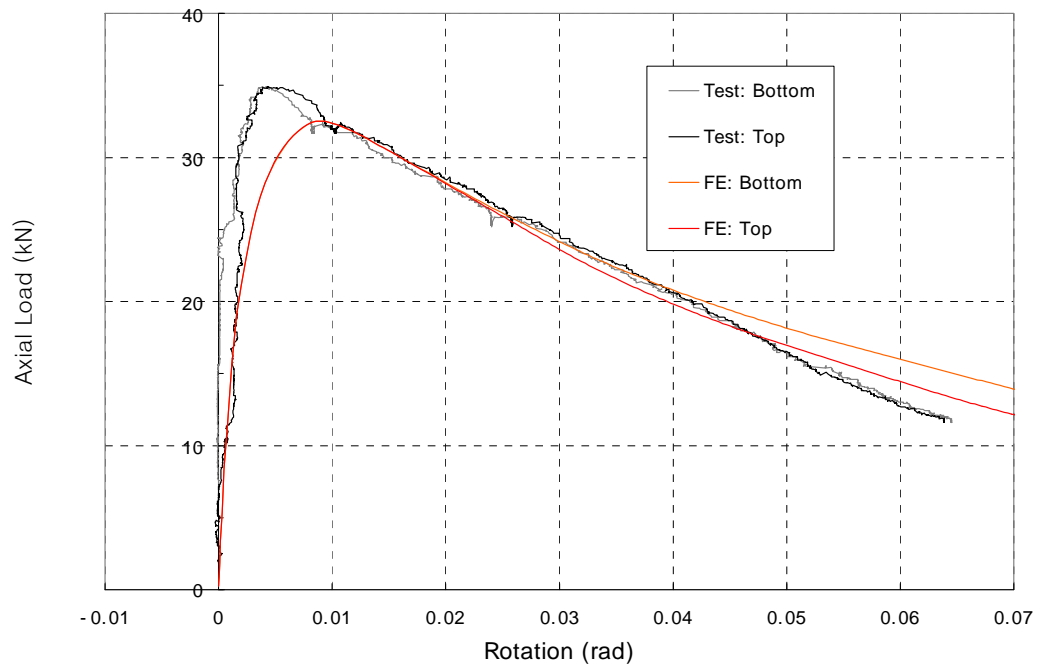


Figure B30.c. C430_915_2 : Axial Load vs. End Rotations

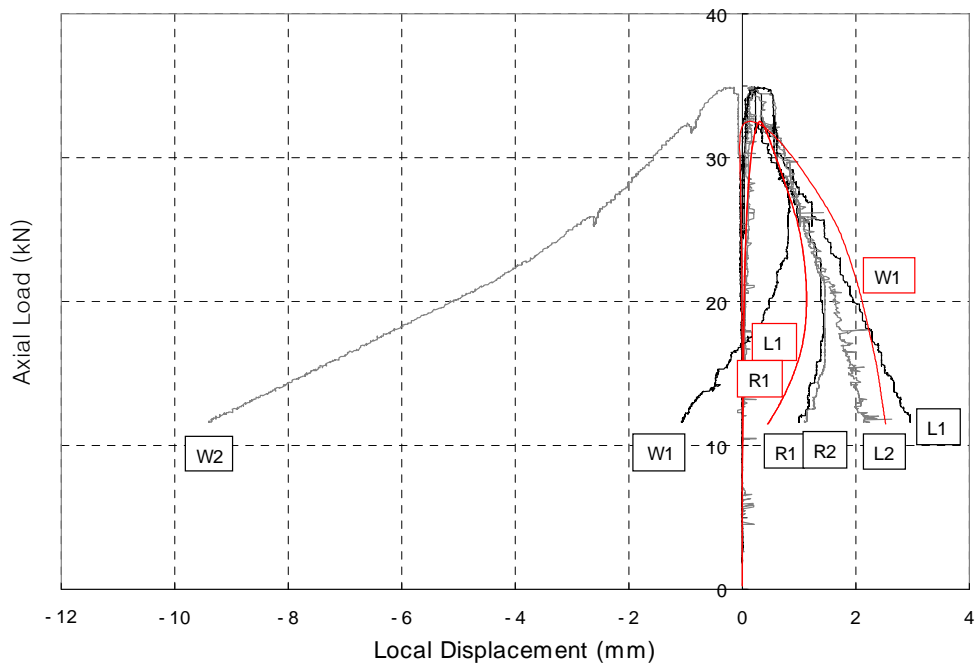


Figure B30.d. C430_915_2 : Axial Load vs. Local Displacements

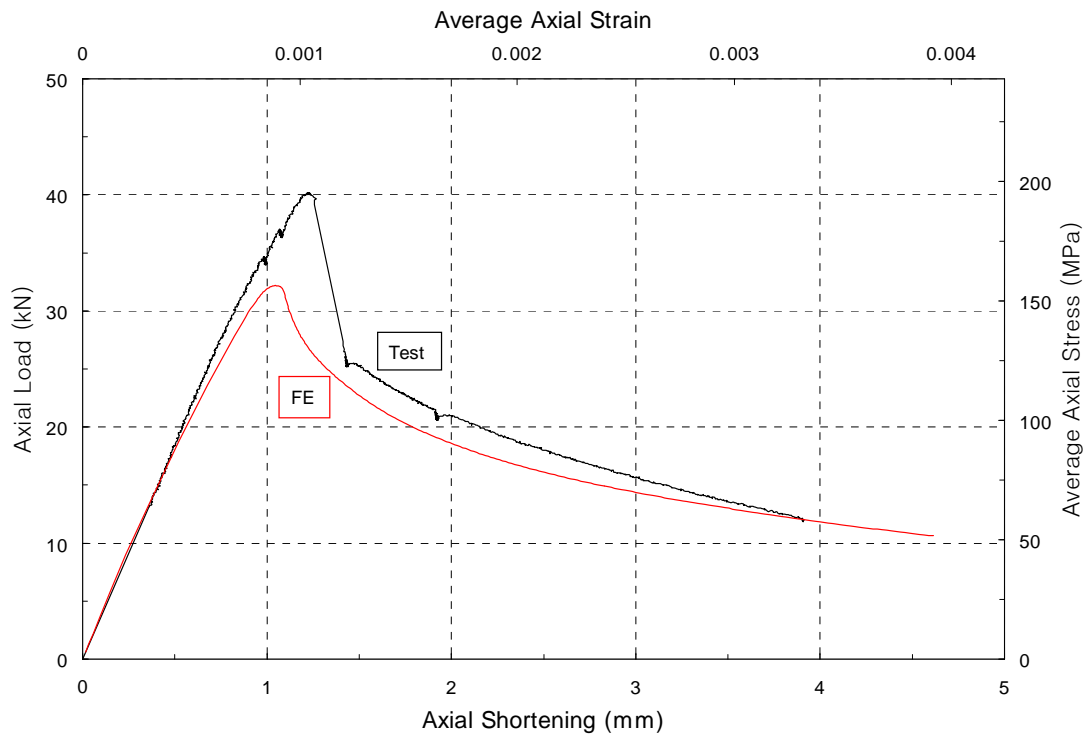


Figure B31.a. C430_1178_1 : Axial Load vs. Axial Shortening

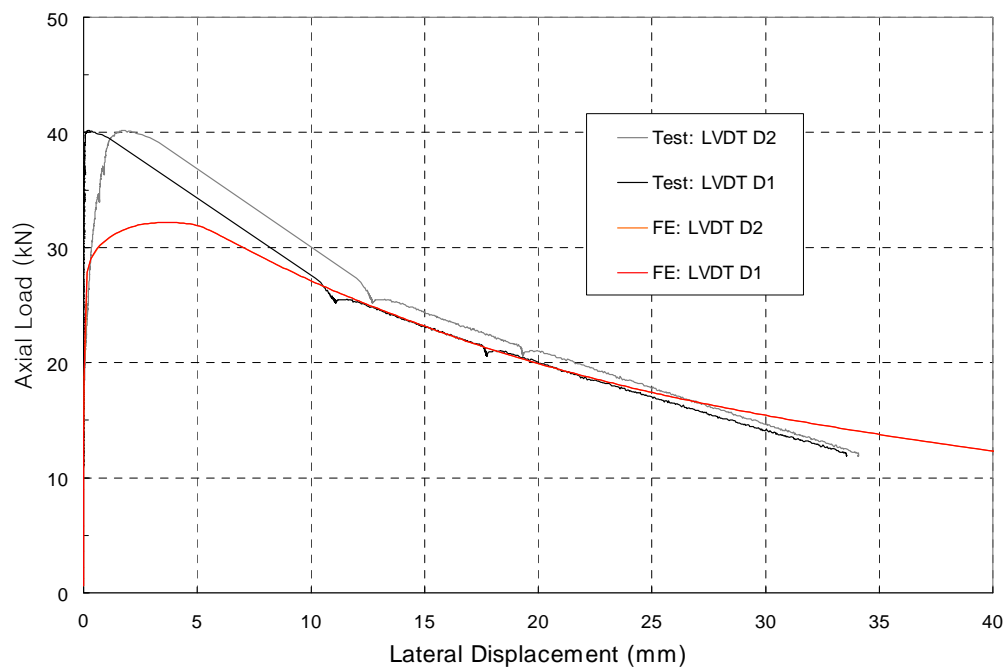


Figure B31.b. C430_1178_1 : Axial Load vs. Lateral Displacement

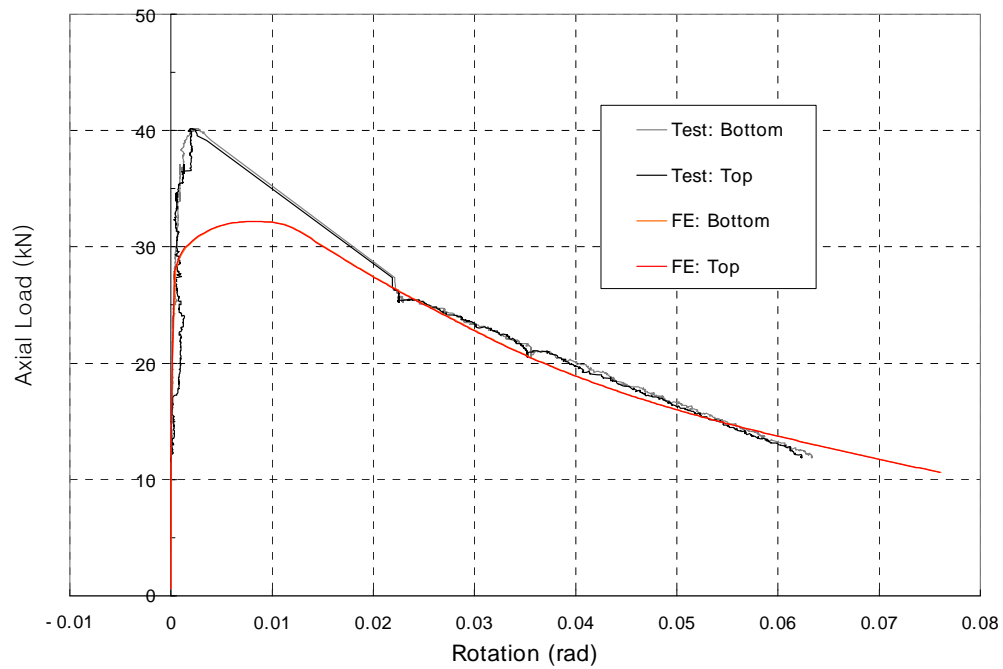


Figure B31.c. C430_1178_1 : Axial Load vs. End Rotations

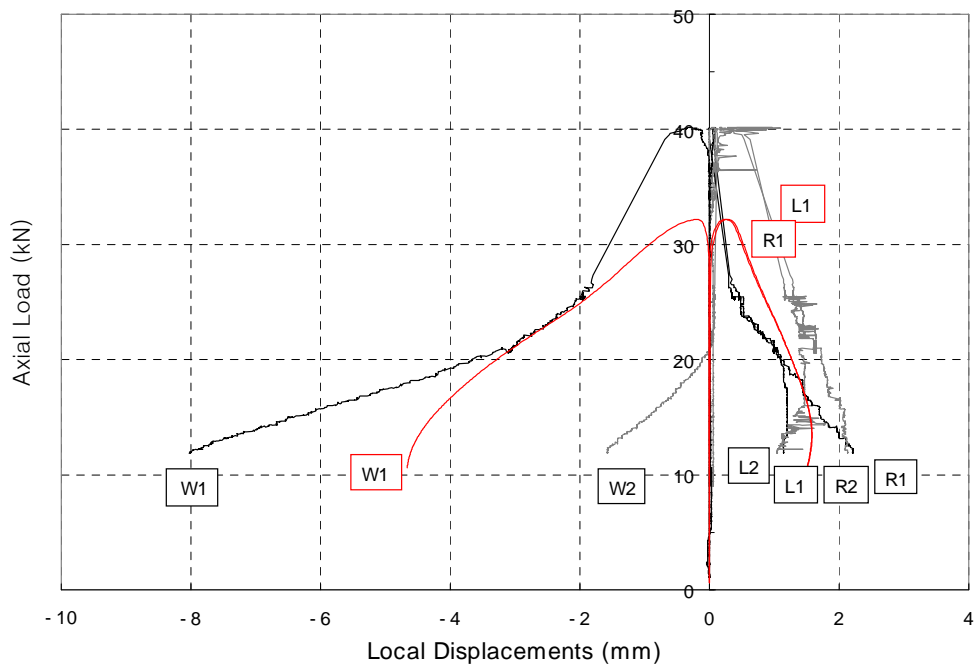


Figure B31.d. C430_1178_1 : Axial Load vs. Local Displacements

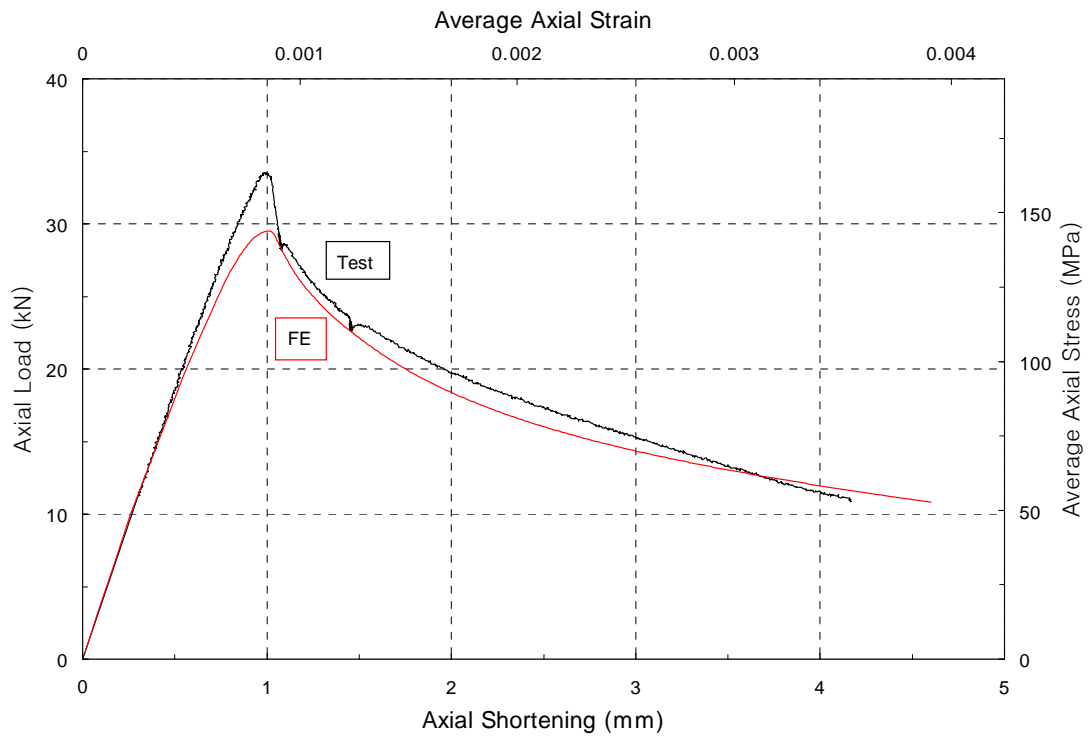


Figure B32.a. C430_1178_2 : Axial Load vs. Axial Shortening

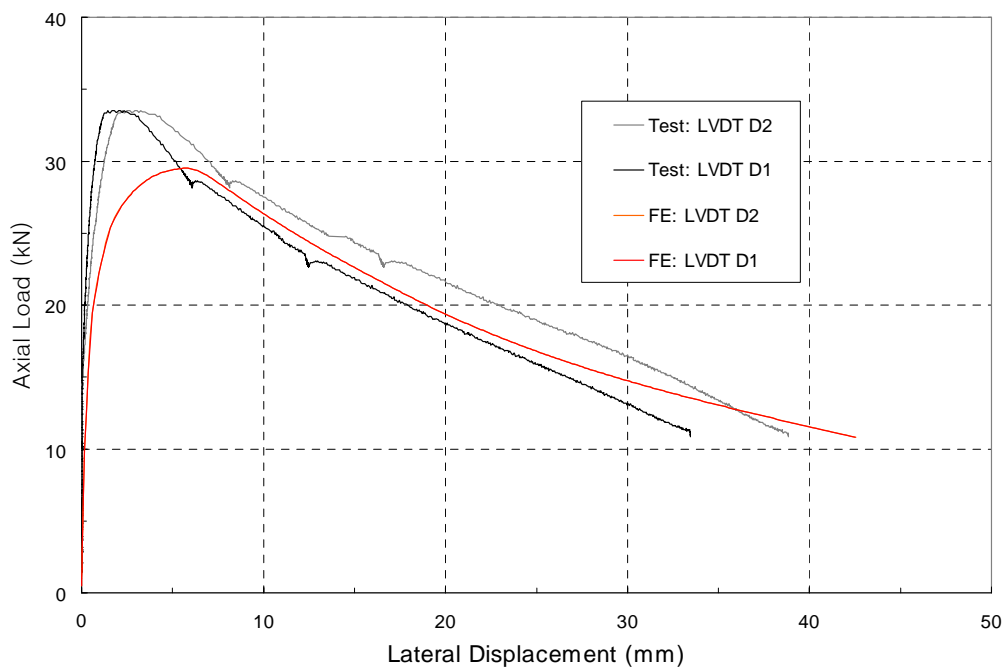


Figure B32.b. C430_1178_2 : Axial Load vs. Lateral Displacement

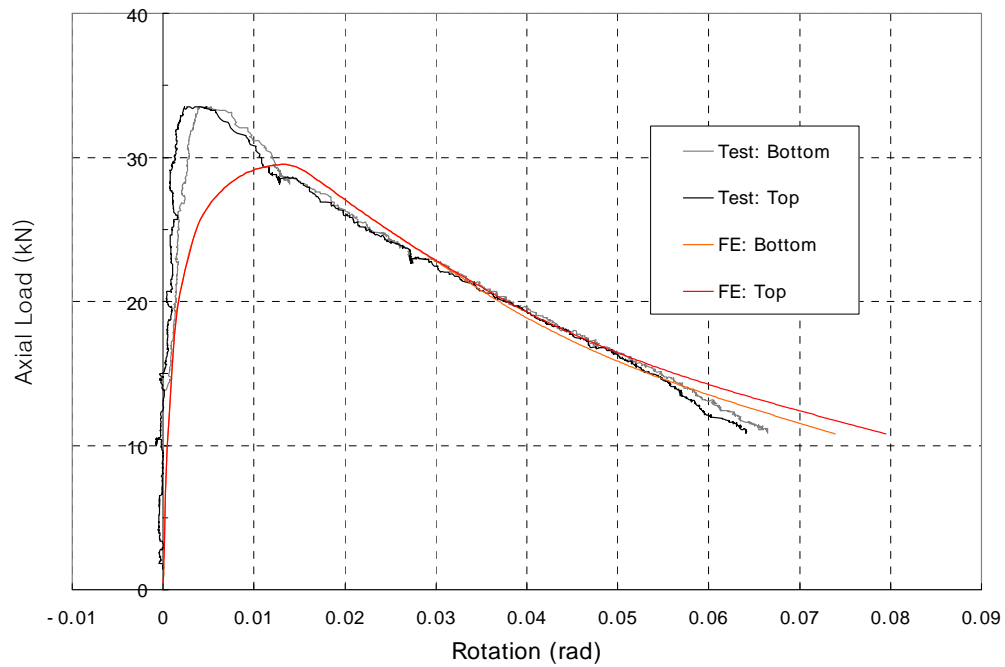


Figure B32.c. C430_1178_2 : Axial Load vs. End Rotations

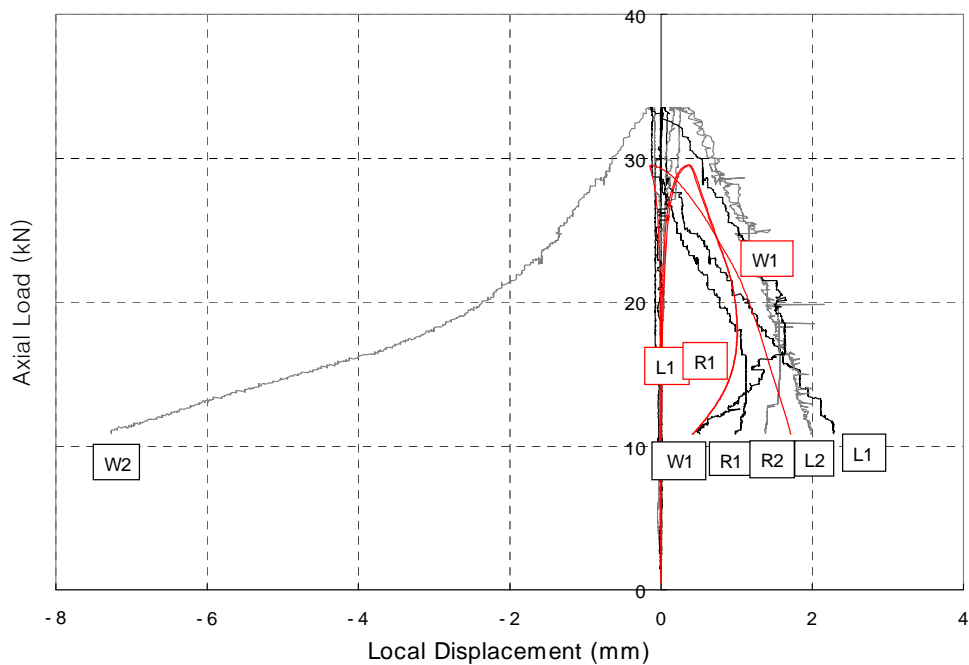


Figure B32.d. C430_1178_2 : Axial Load vs. Local Displacements

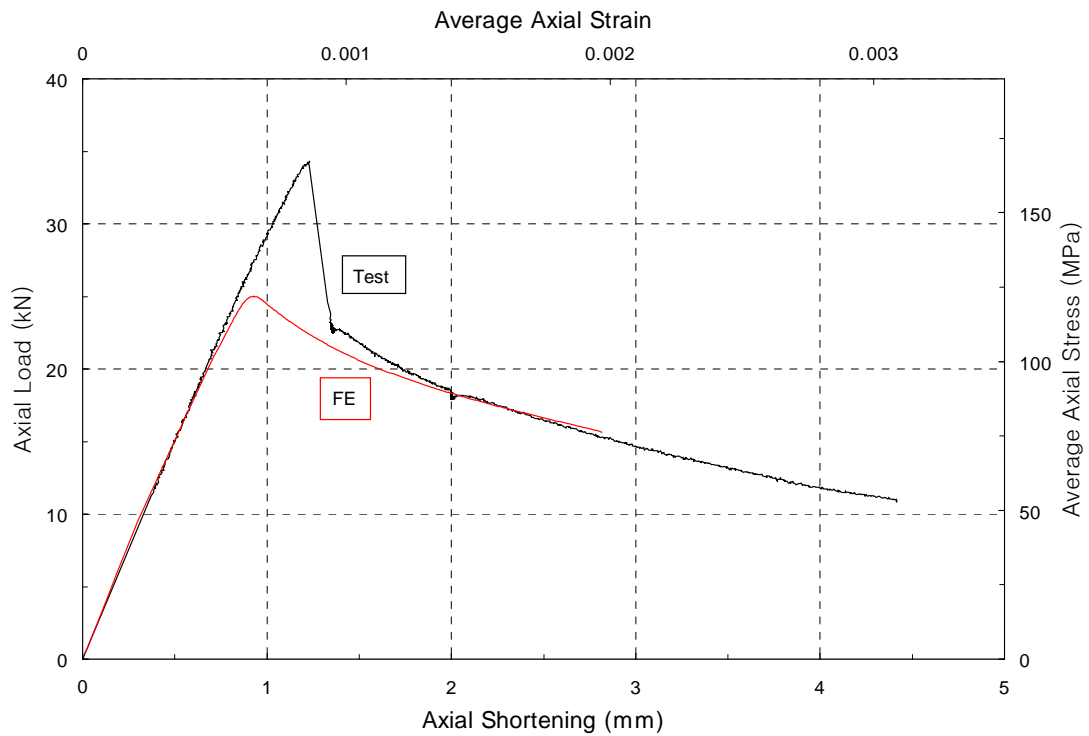


Figure B33.a. C430_1430_1 : Axial Load vs. Axial Shortening

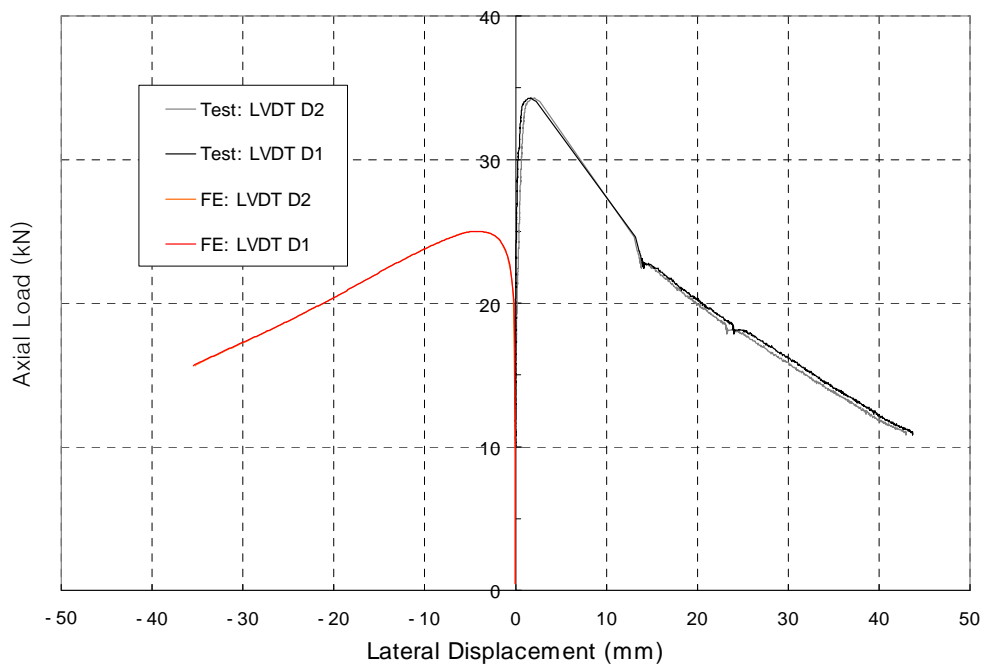


Figure B33.b. C430_1430_1 : Axial Load vs. Lateral Displacement

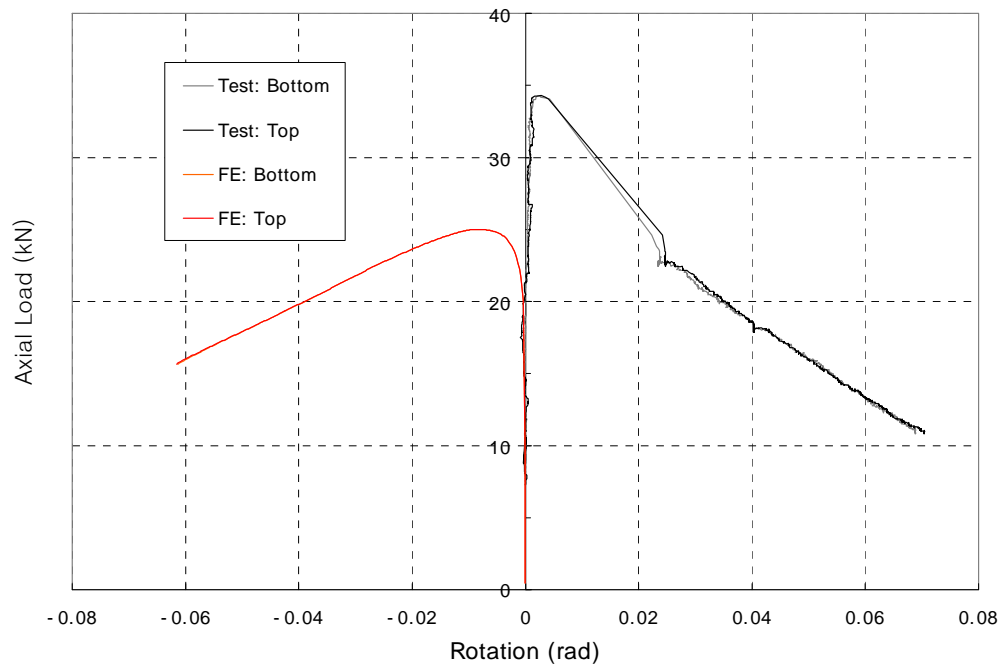


Figure B33.c. C430_1430_1 : Axial Load vs. End Rotations

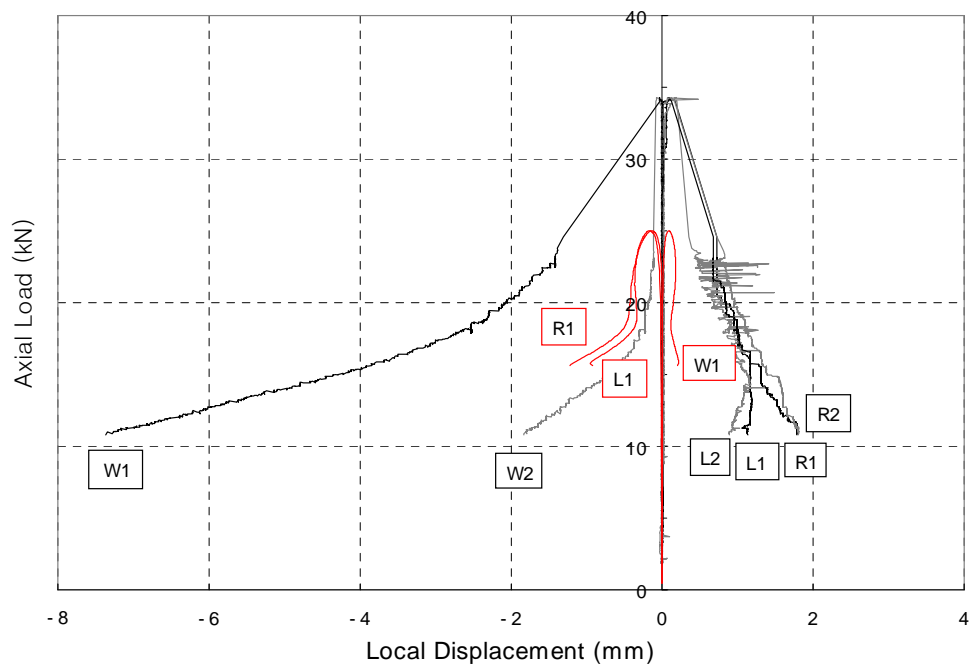


Figure B33.d. C430_1430_1 : Axial Load vs. Local Displacements

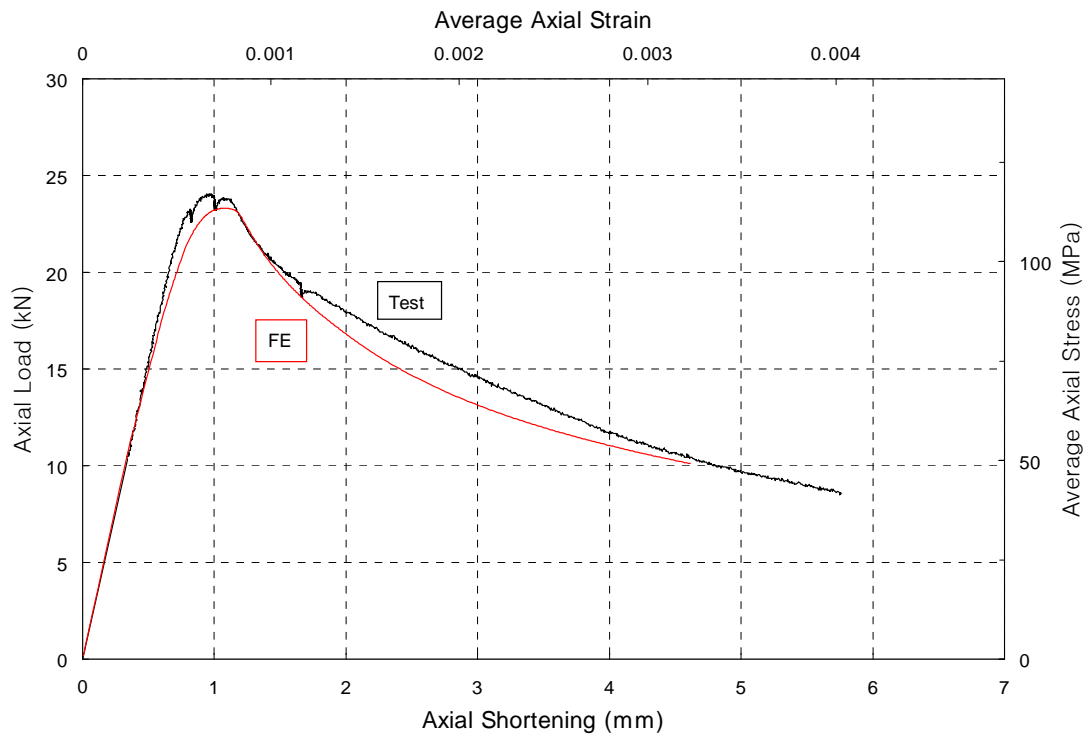


Figure B34.a. C430_1430_2 : Axial Load vs. Axial Shortening

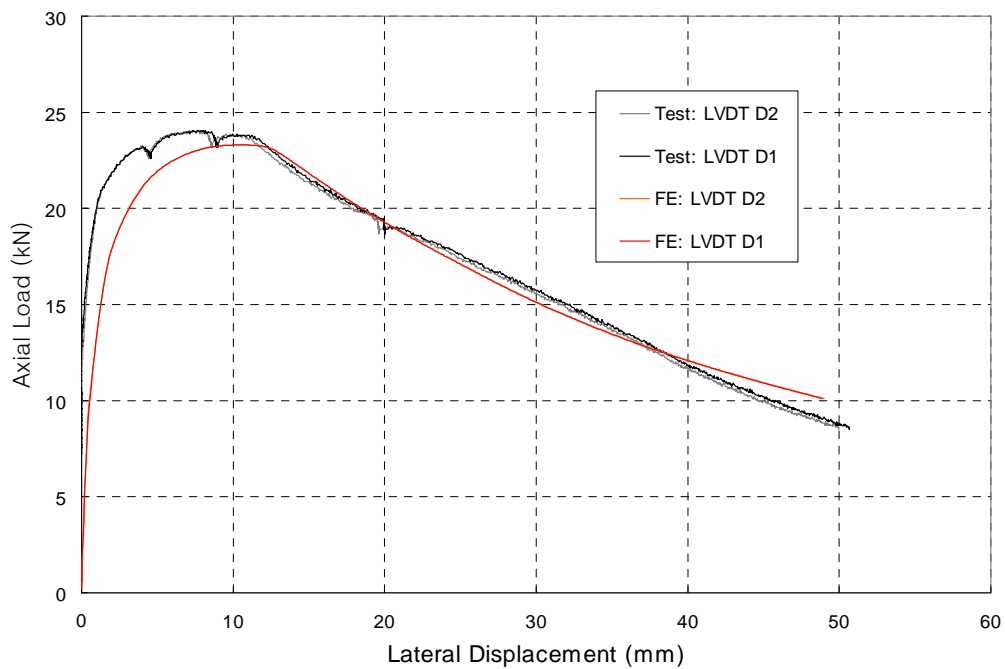


Figure B34.b. C430_1430_2 : Axial Load vs. Lateral Displacement

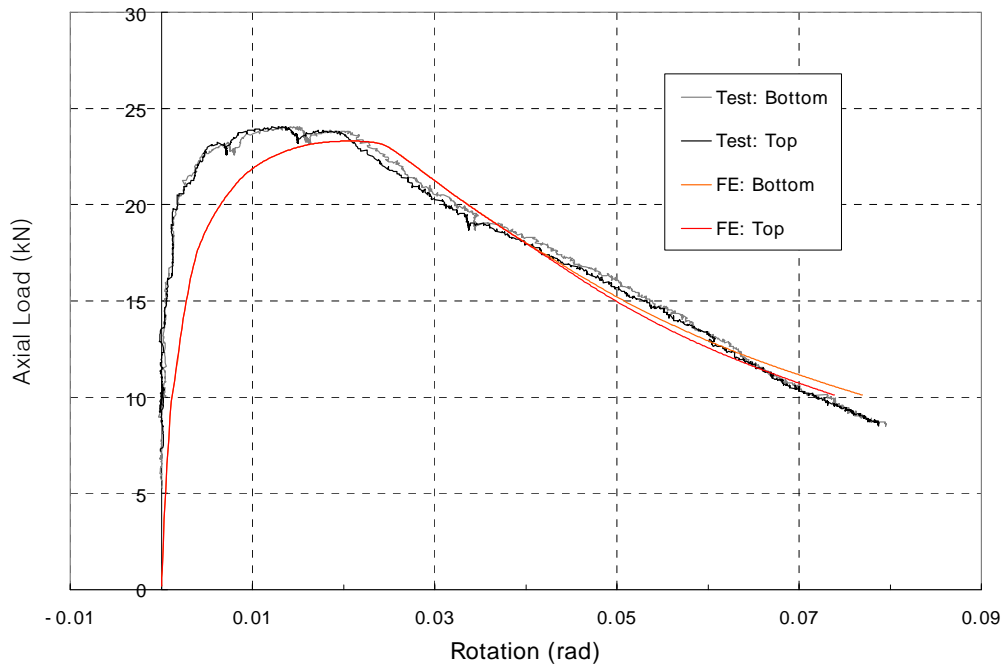


Figure B34.c. C430_1430_2 : Axial Load vs. End Rotations

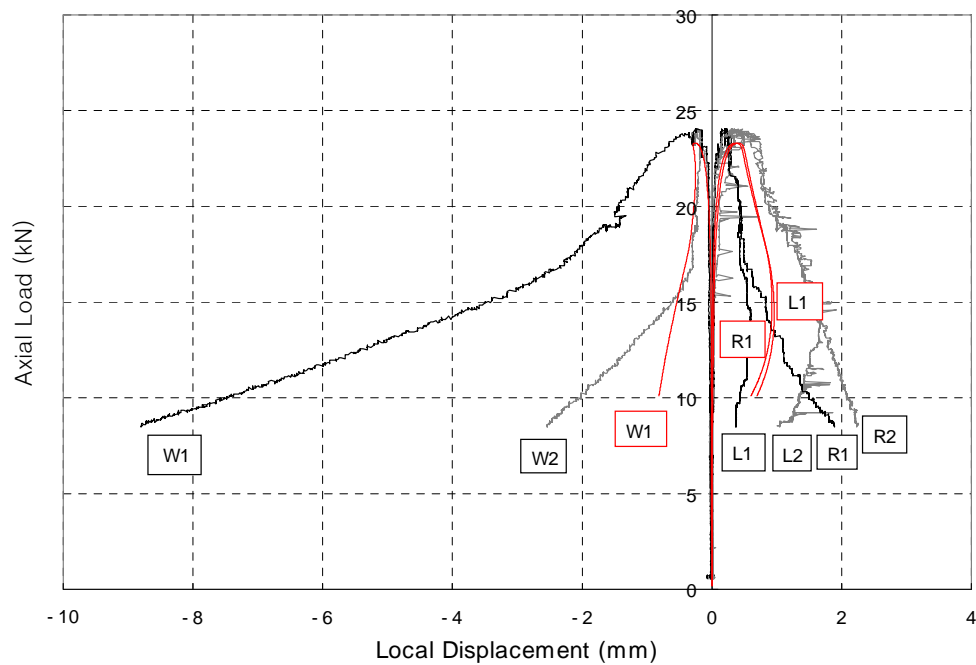


Figure B34.d. C430_1430_2 : Axial Load vs. Local Displacements

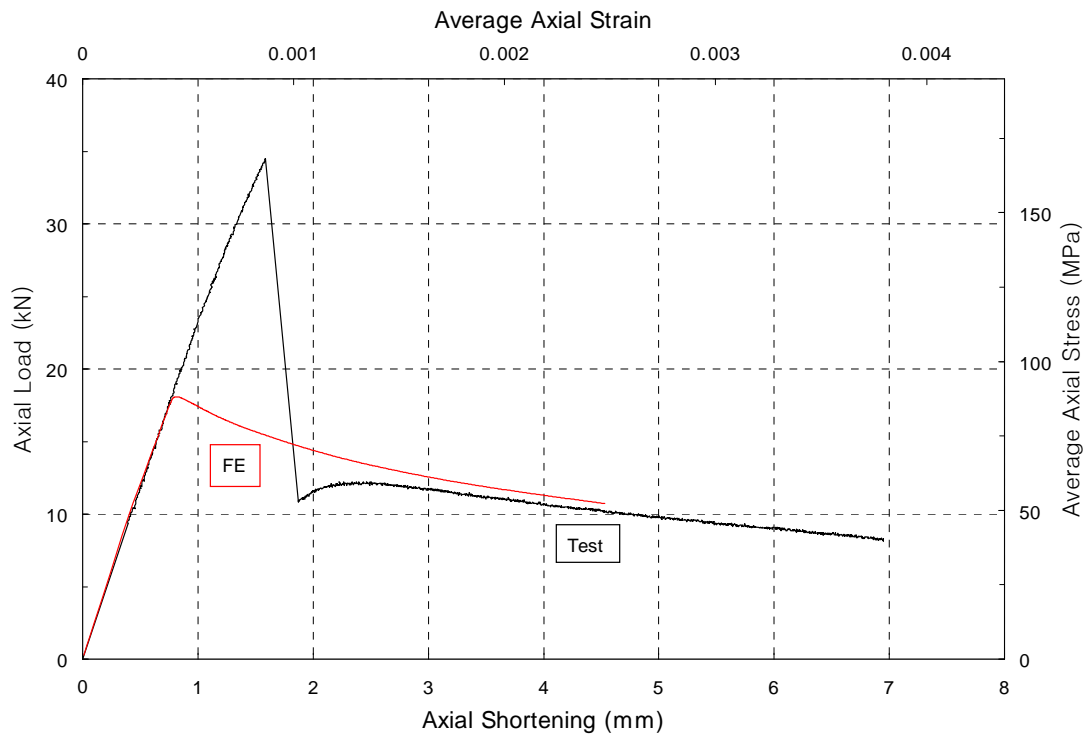


Figure B35.a. C430_1831_1 : Axial Load vs. Axial Shortening

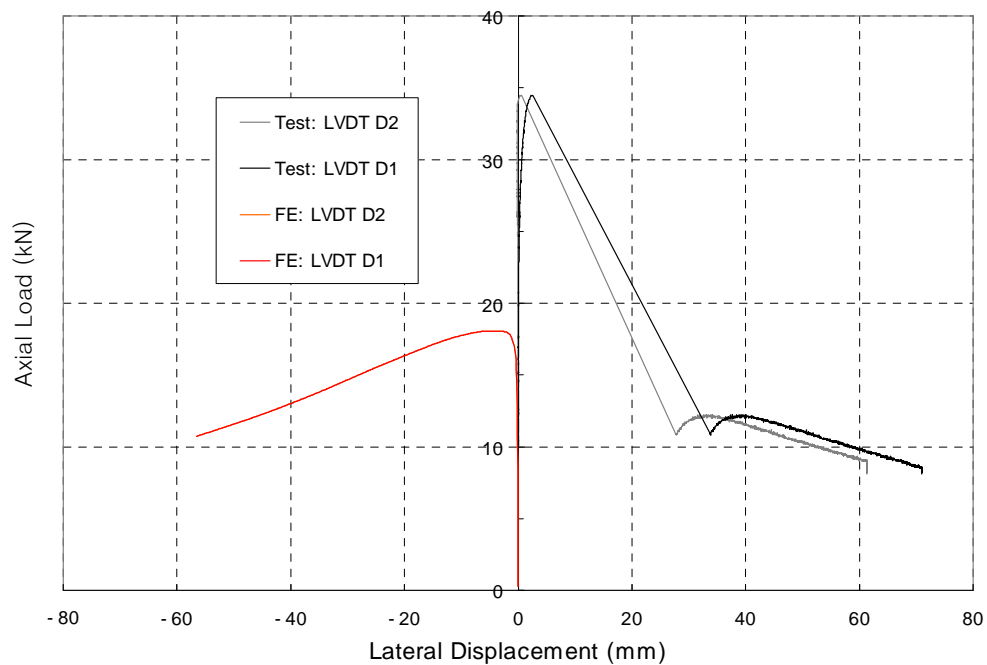


Figure B35.b. C430_1831_1 : Axial Load vs. Lateral Displacement

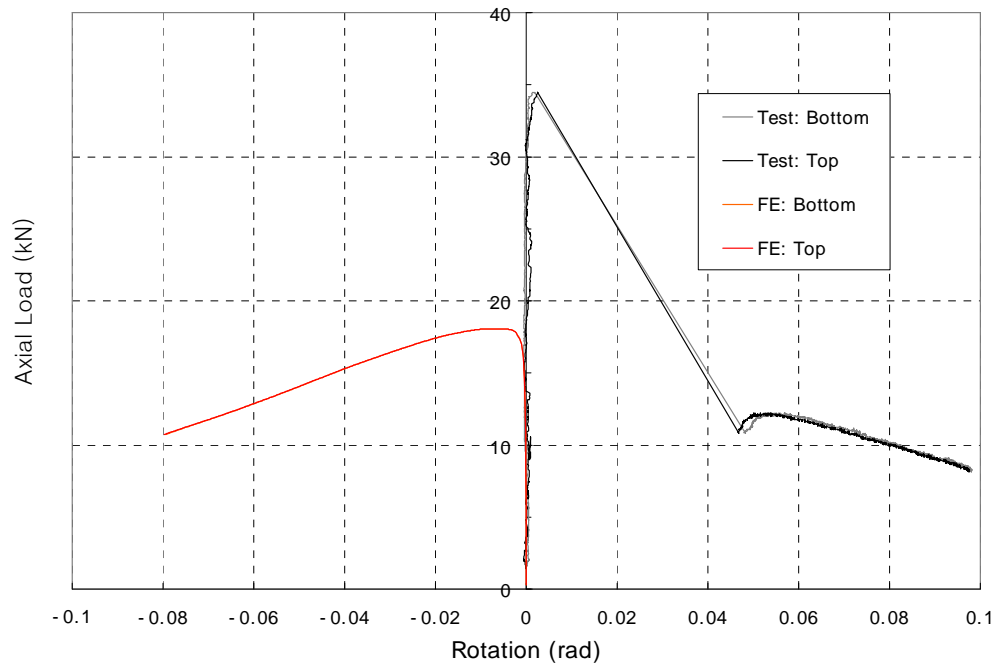


Figure B35.c. C430_1831_1 : Axial Load vs. End Rotations

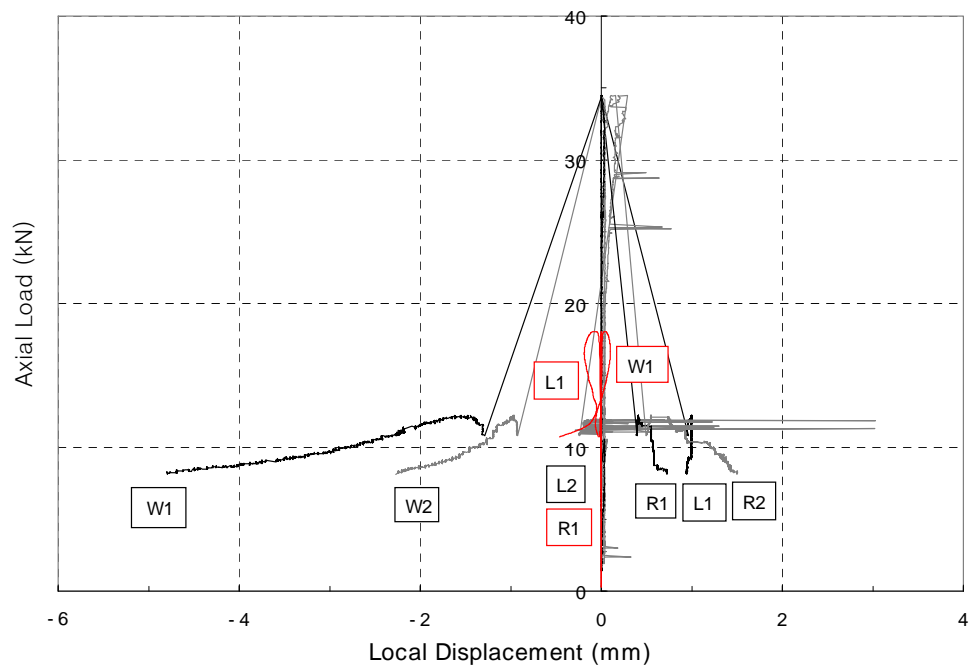


Figure B35.d. C430_1831_1 : Axial Load vs. Local Displacements

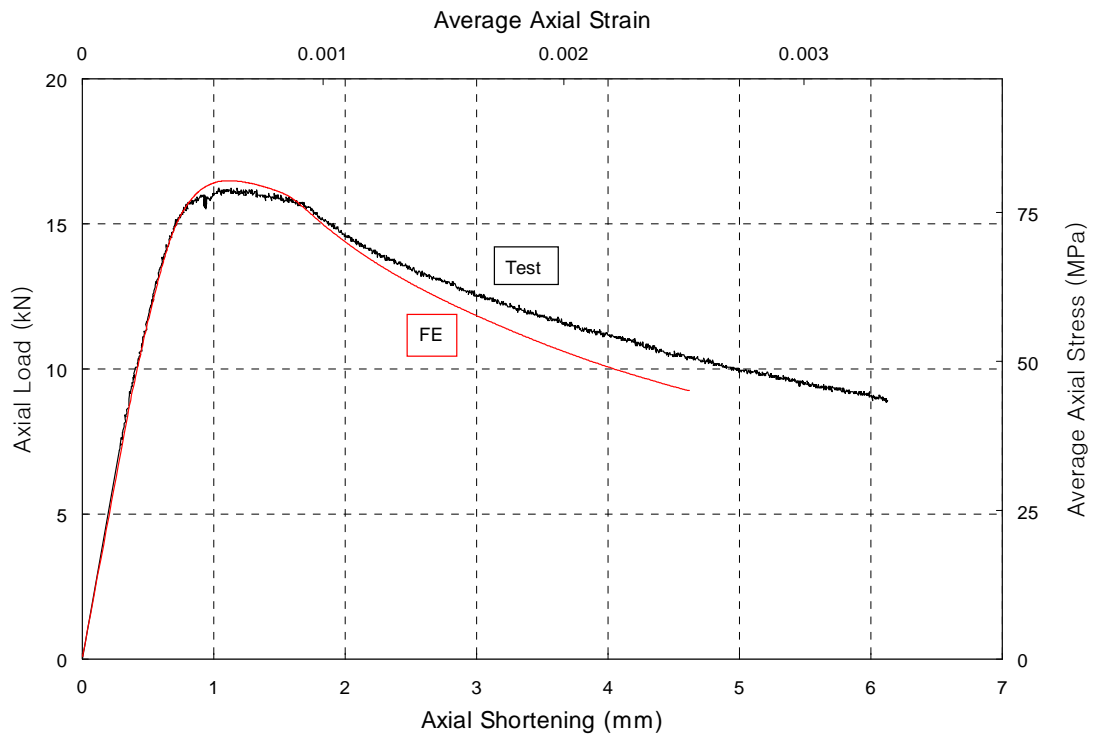


Figure B36.a. C430_1831_2 : Axial Load vs. Axial Shortening

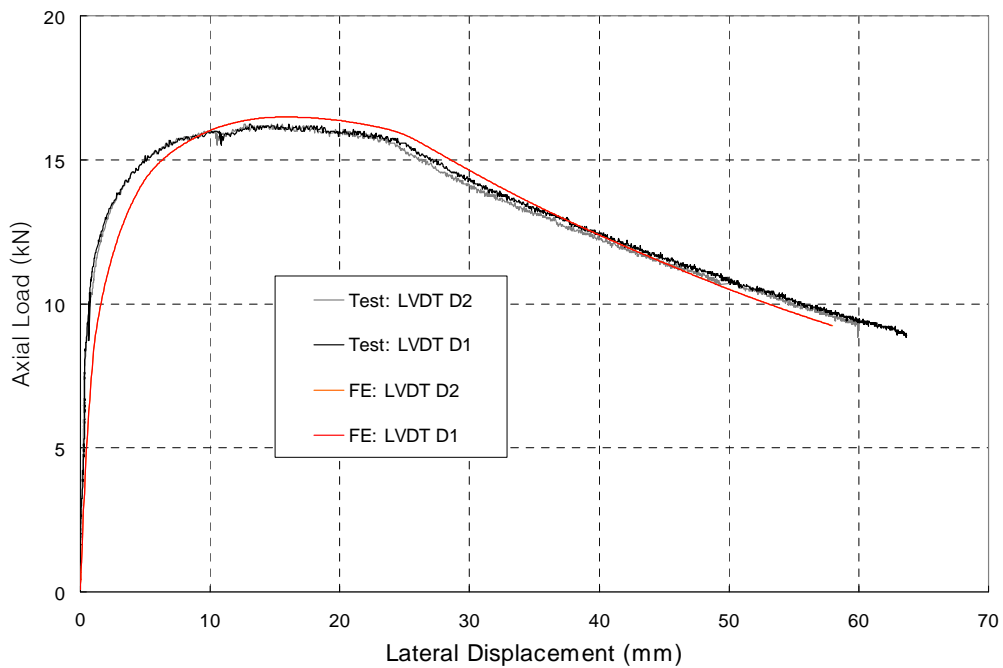


Figure B36.b. C430_1831_2 : Axial Load vs. Lateral Displacement

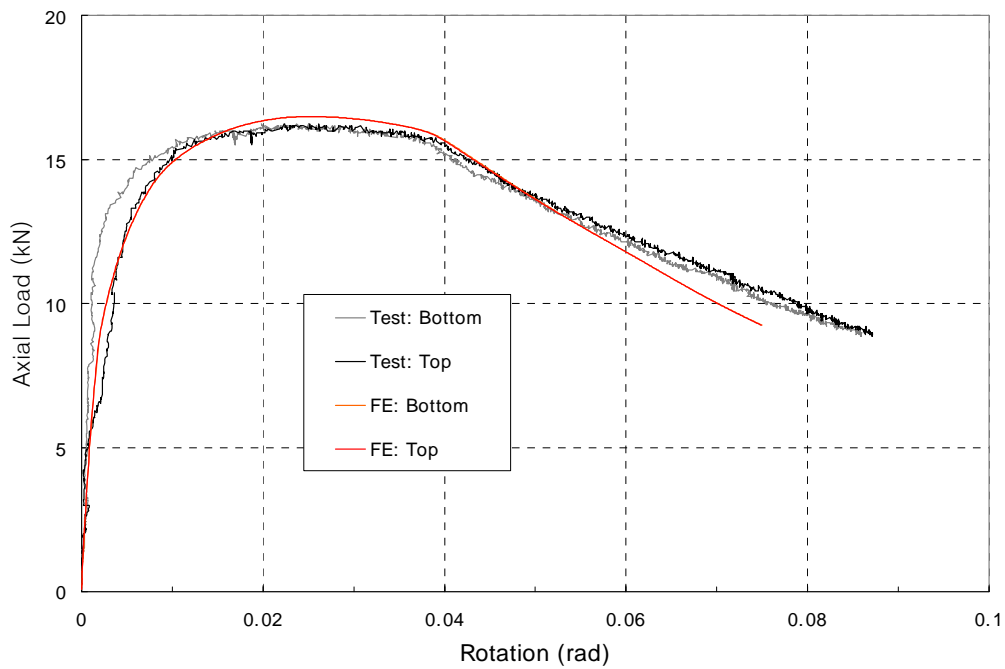


Figure B36.c. C430_1831_2 : Axial Load vs. End Rotations

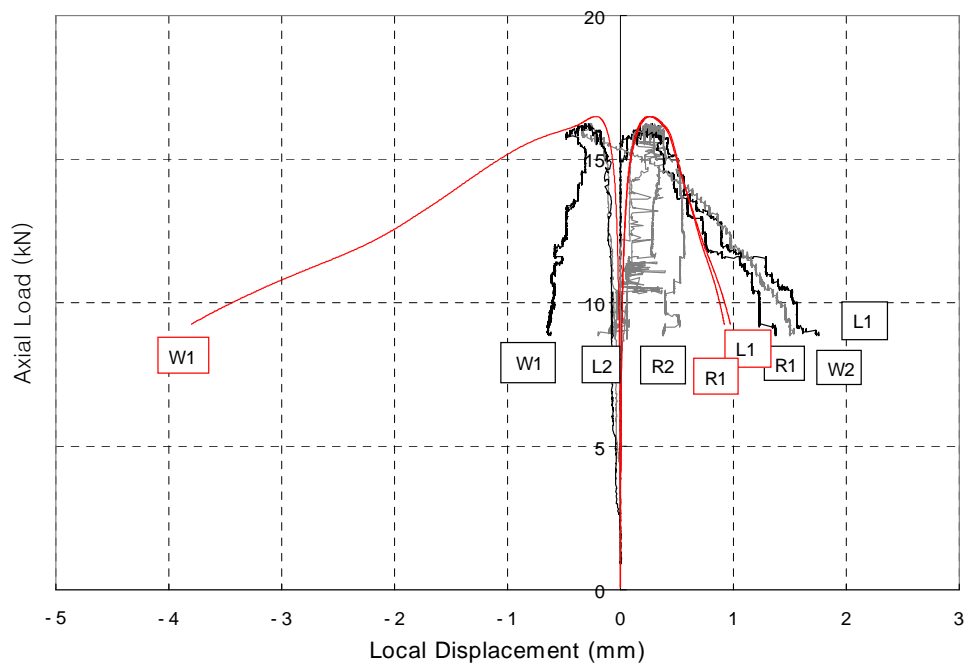


Figure B36.d. C430_1831_2 : Axial Load vs. Local Displacements

Appendix C

Appendix C compares the FE model predictions with the experimental data of 24 I-column tests (Becque and Rasmussen 2007). For each test 4 graphs are presented, showing:

- a. The load vs. axial shortening.
- b. The load vs. lateral displacement.
- c. The load vs. end rotations.
- d. The load vs. local displacements.

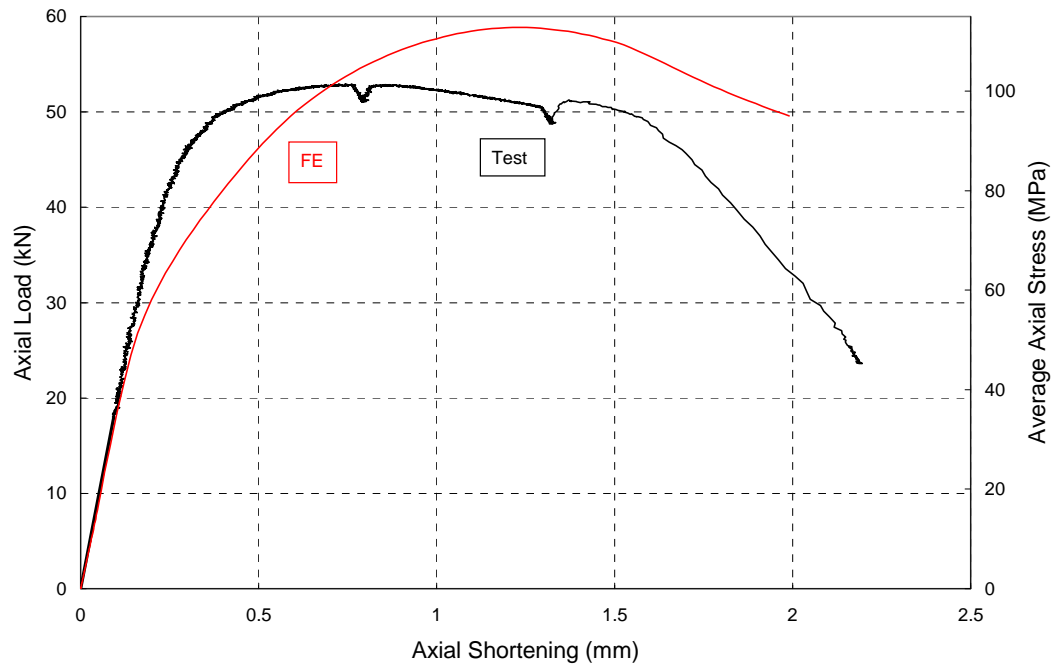


Figure C1.a. I304_500_1 : Axial Load vs. Axial Shortening

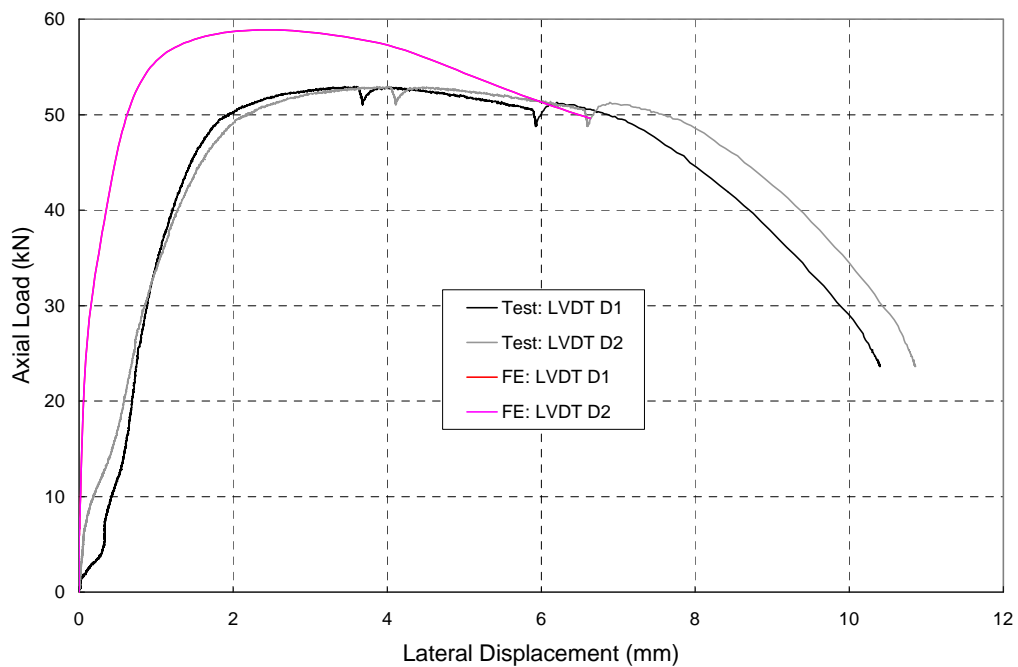


Figure C1.b. I304_500_1 : Axial Load vs. Lateral Displacement

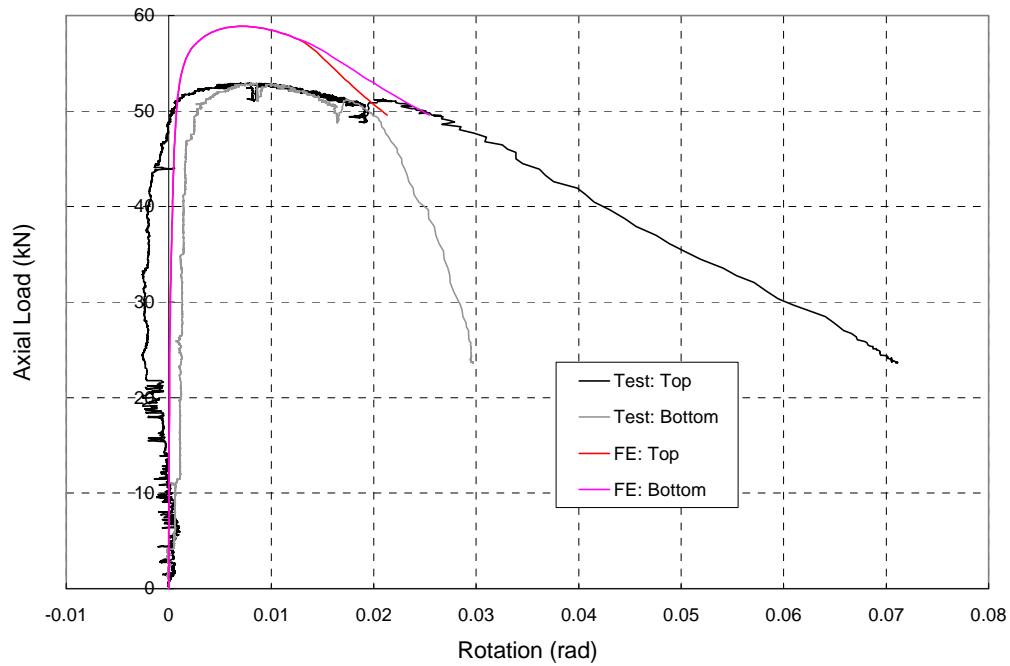


Figure C1.c. I304_500_1 : Axial Load vs. End Rotations

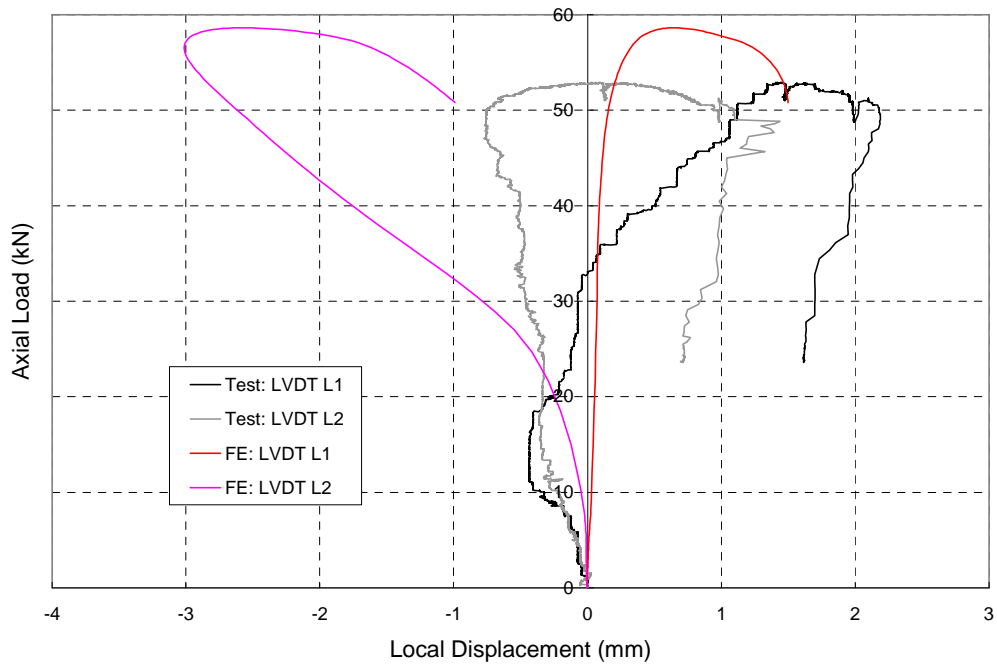


Figure C1.d. I304_500_1 : Axial Load vs. Local Displacements

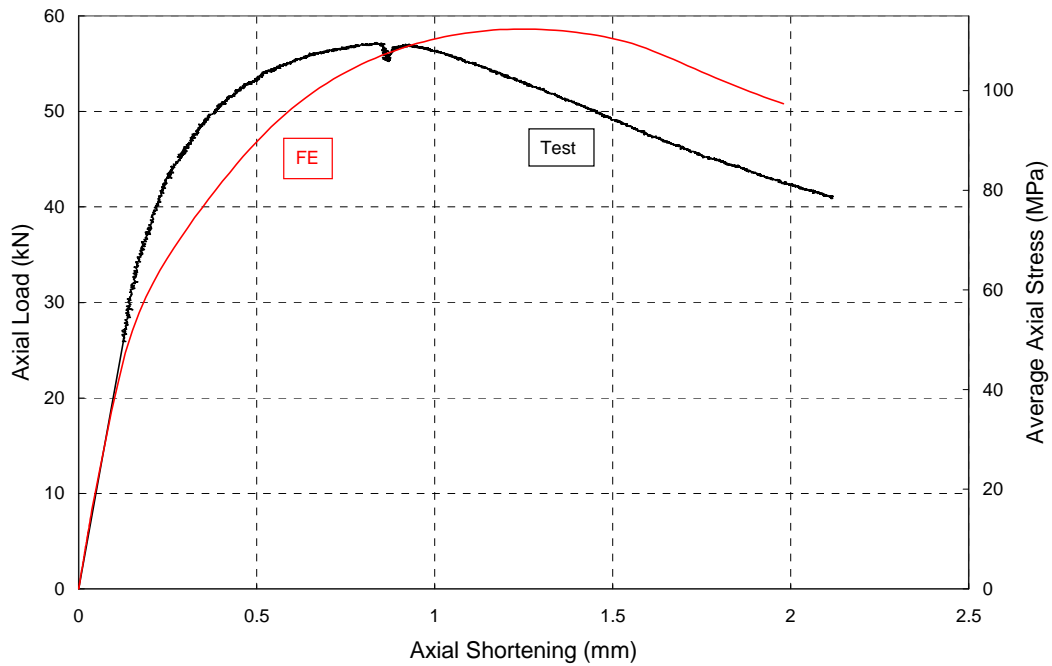


Figure C2.a. I304_500_2 : Axial Load vs. Axial Shortening

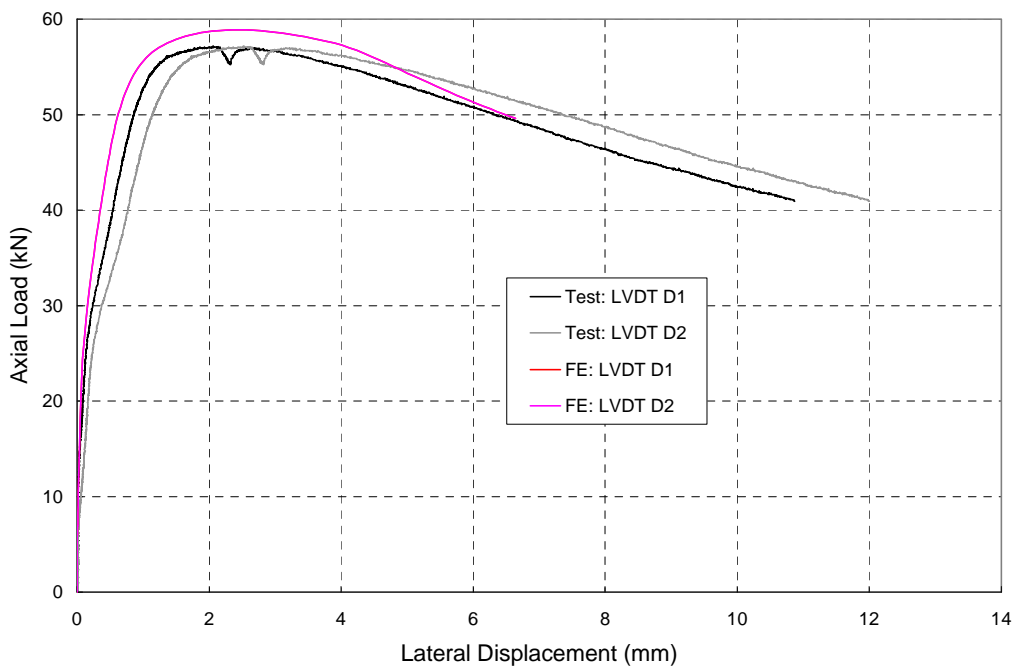


Figure C2.b. I304_500_2 : Axial Load vs. Lateral Displacement

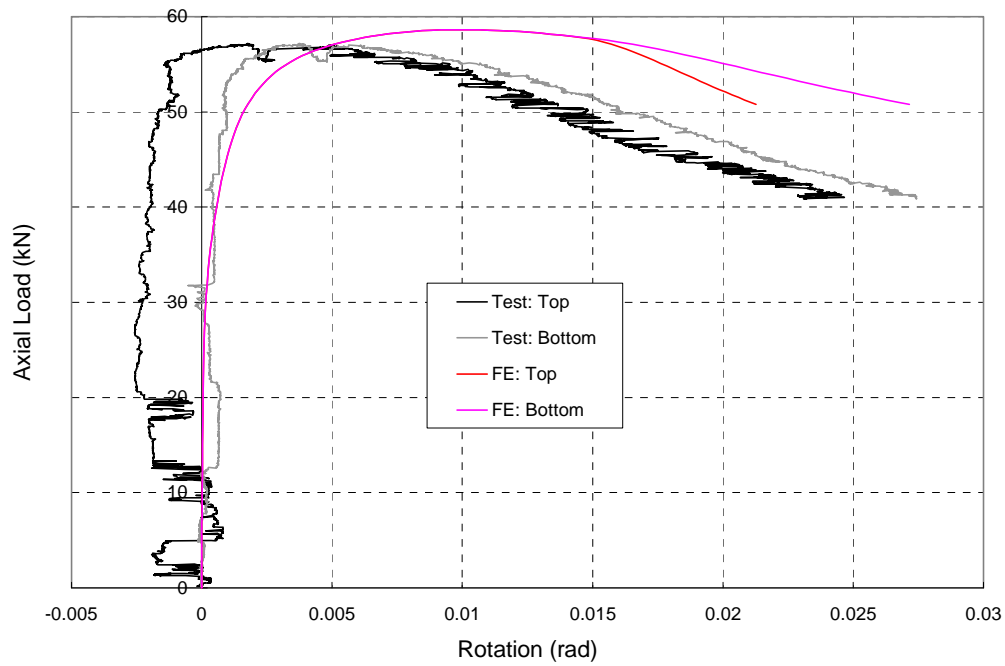


Figure C2.c. I304_500_2 : Axial Load vs. End Rotations

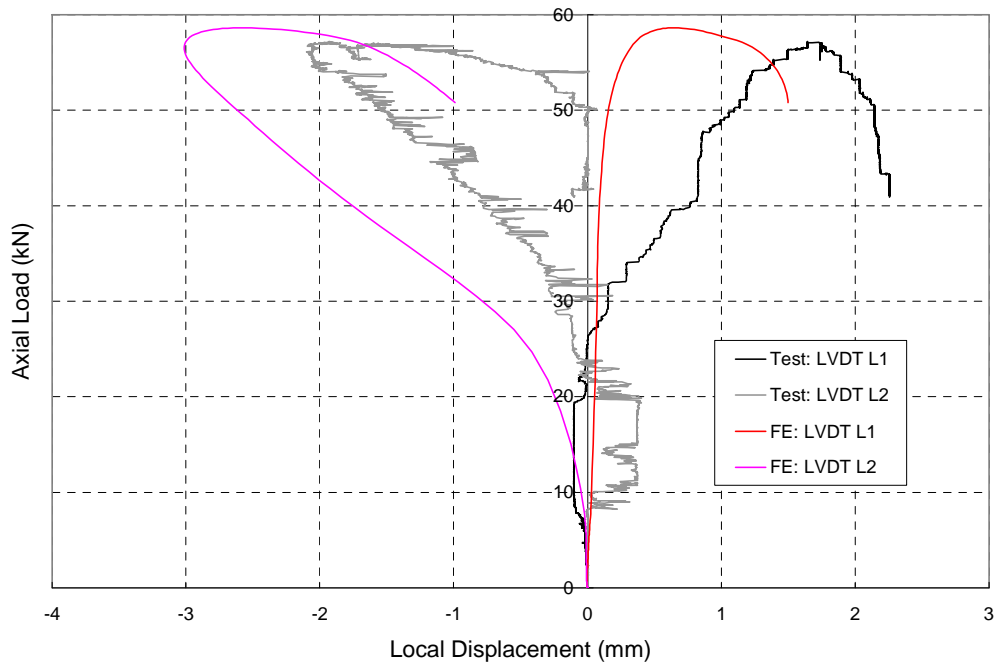


Figure C2.d. I304_500_2 : Axial Load vs. Local Displacements

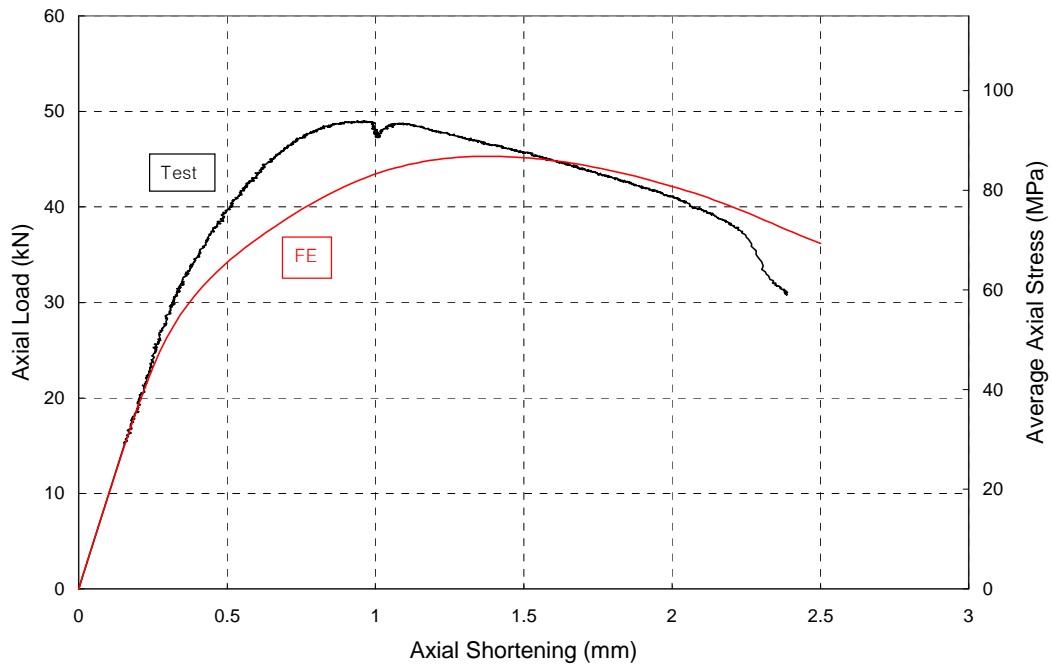


Figure C3.a. I304_1000_1 : Axial Load vs. Axial Shortening

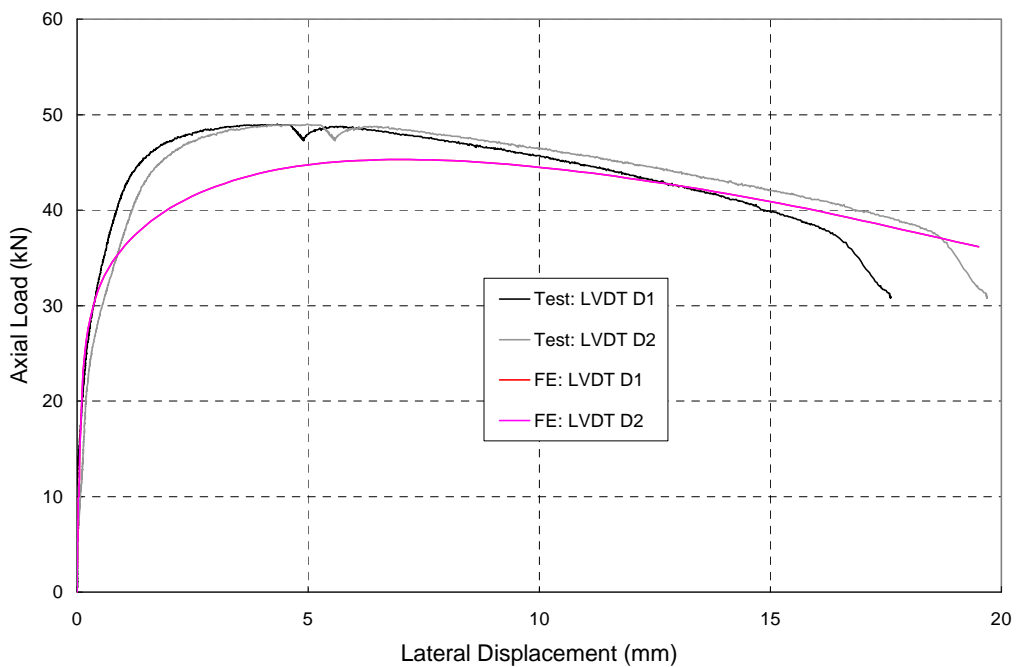


Figure C3.b. I304_1000_1 : Axial Load vs. Lateral Displacement

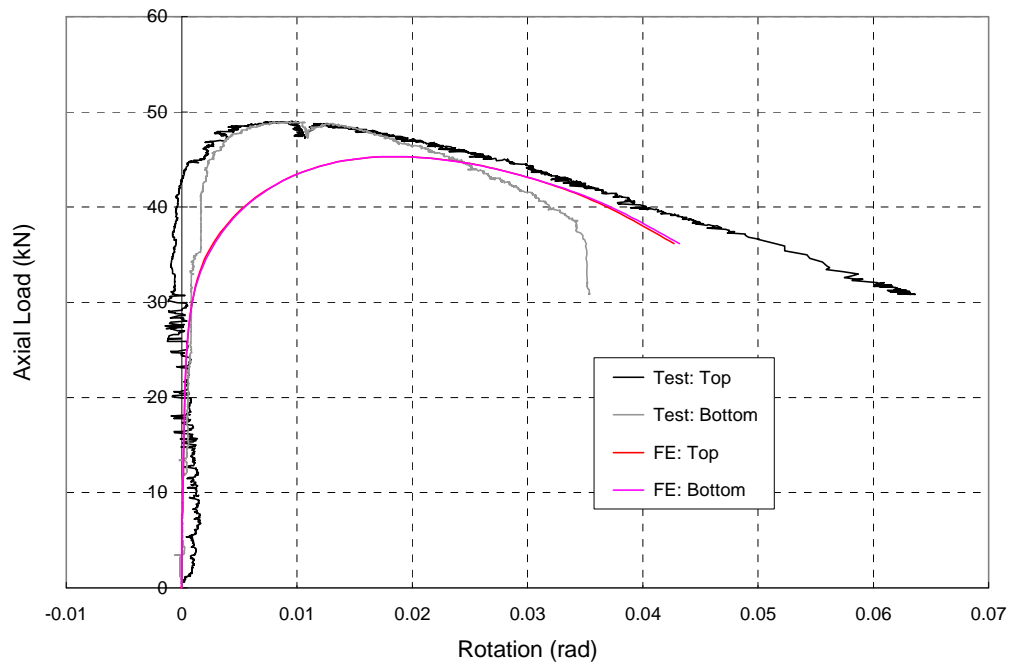


Figure C3.c. I304_1000_1 : Axial Load vs. End Rotations

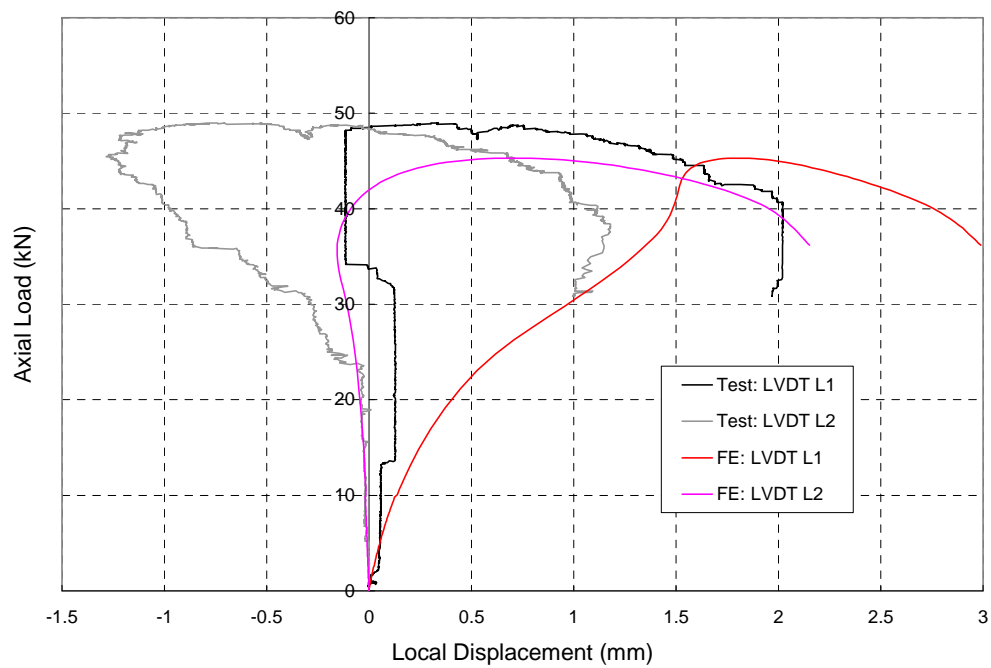


Figure C3.d. I304_1000_1 : Axial Load vs. Local Displacements

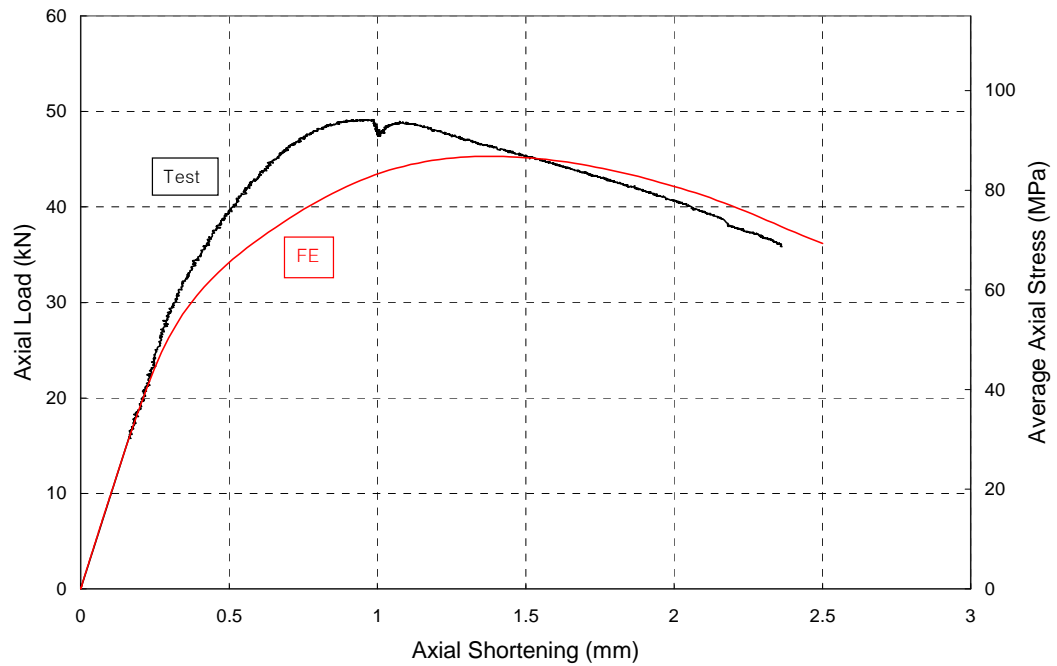


Figure C4.a. I304_1000_2 : Axial Load vs. Axial Shortening

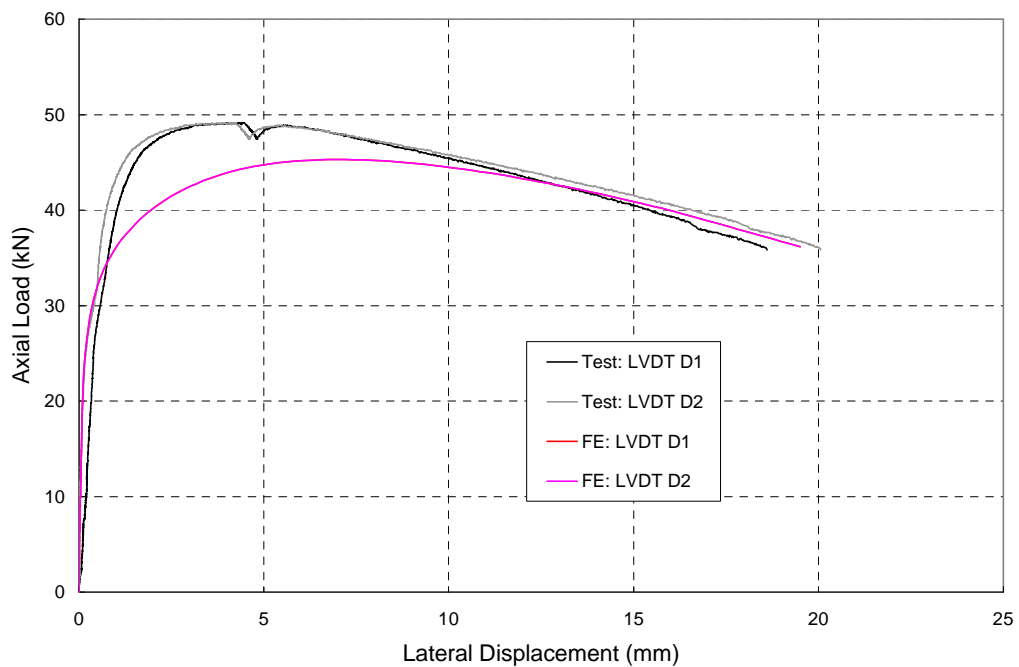


Figure C4.b. I304_1000_2 : Axial Load vs. Lateral Displacement

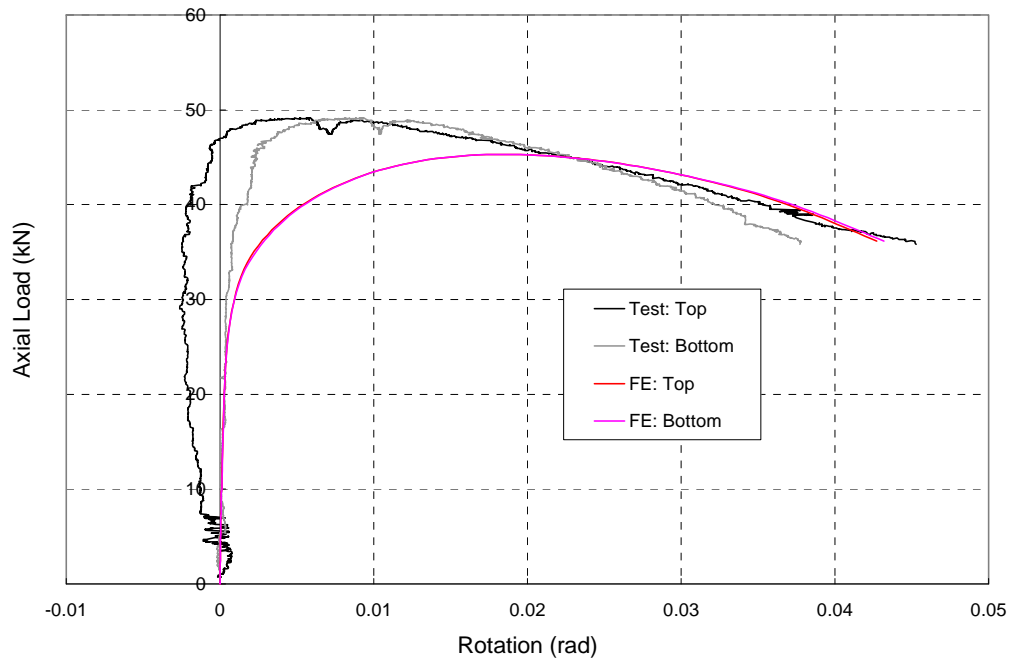


Figure C4.c. I304_1000_2 : Axial Load vs. End Rotations

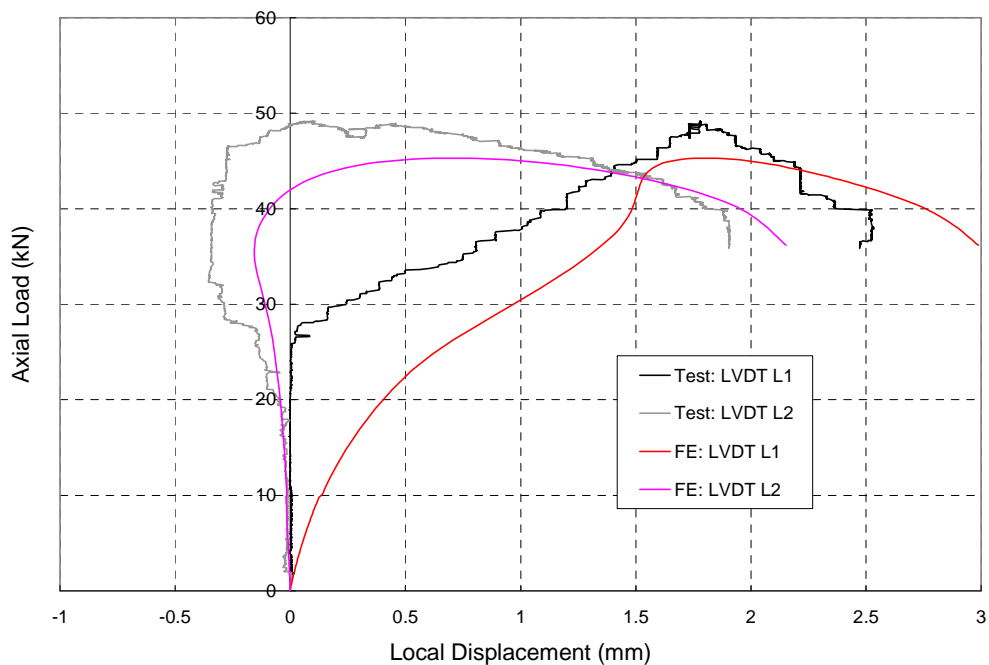


Figure C4.d. I304_1000_2 : Axial Load vs. Local Displacements

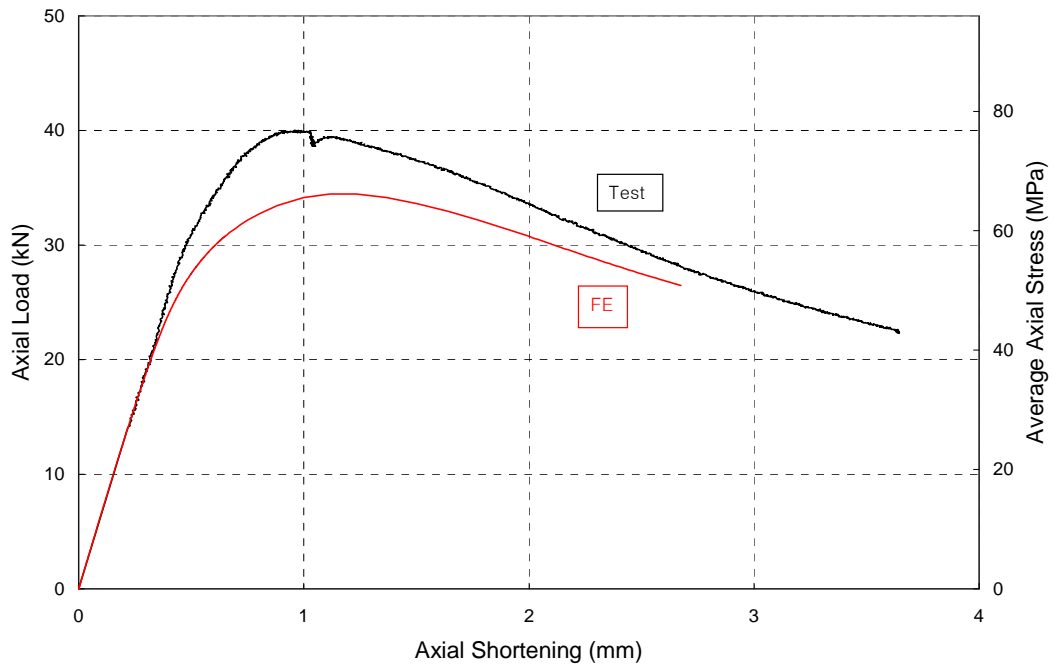


Figure C5.a. I304_1500_1 : Axial Load vs. Axial Shortening

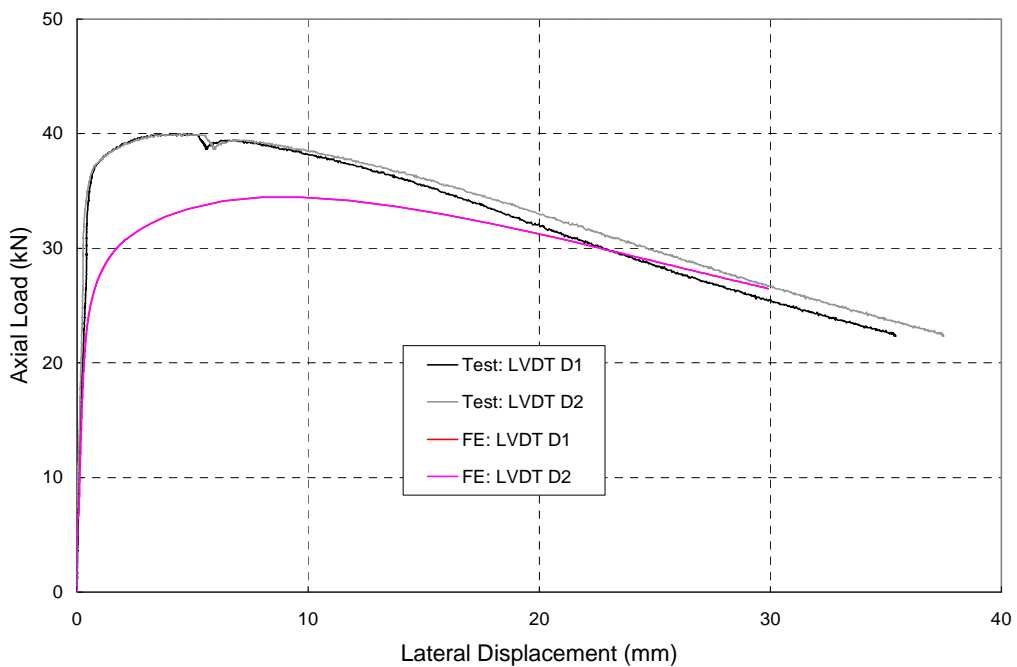


Figure C5.b. I304_1500_1 : Axial Load vs. Lateral Displacement

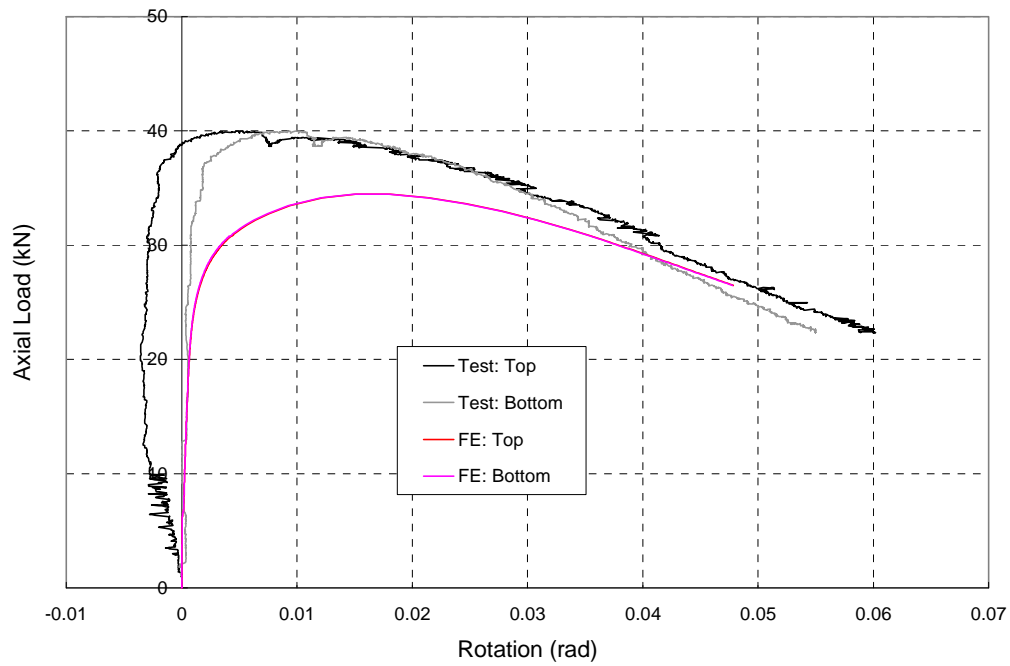


Figure C5.c. I304_1500_1 : Axial Load vs. End Rotations

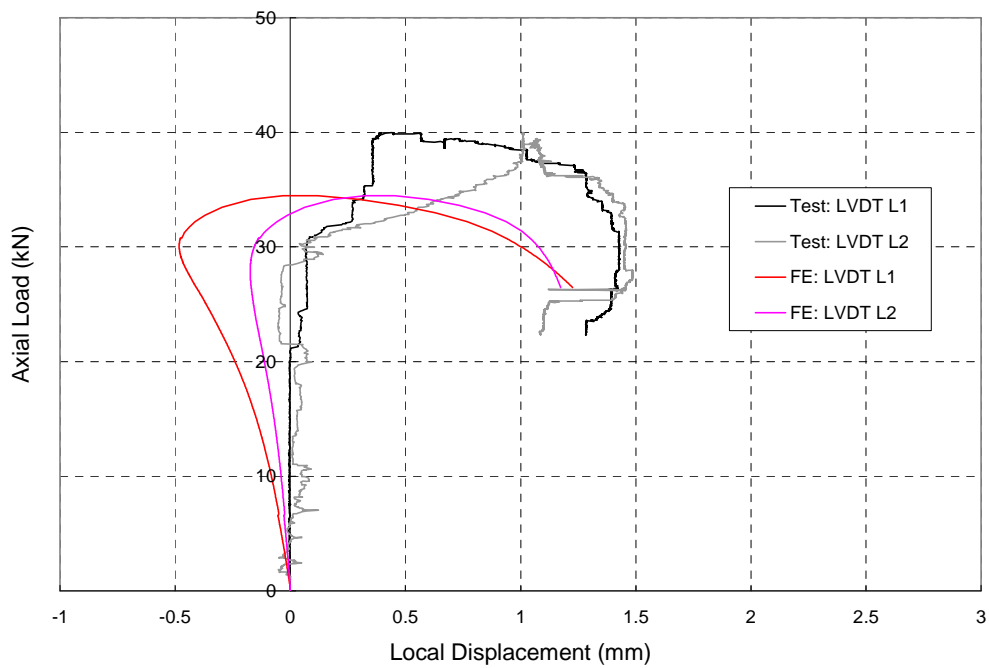


Figure C5.d. I304_1500_1 : Axial Load vs. Local Displacements

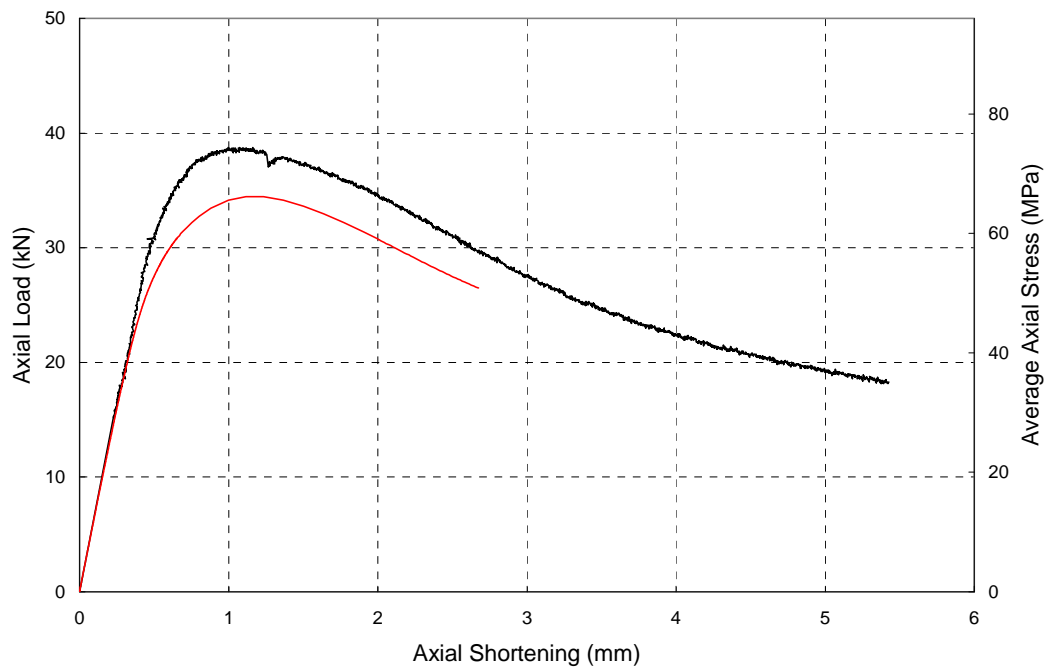


Figure C6.a. I304_1500_2 : Axial Load vs. Axial Shortening

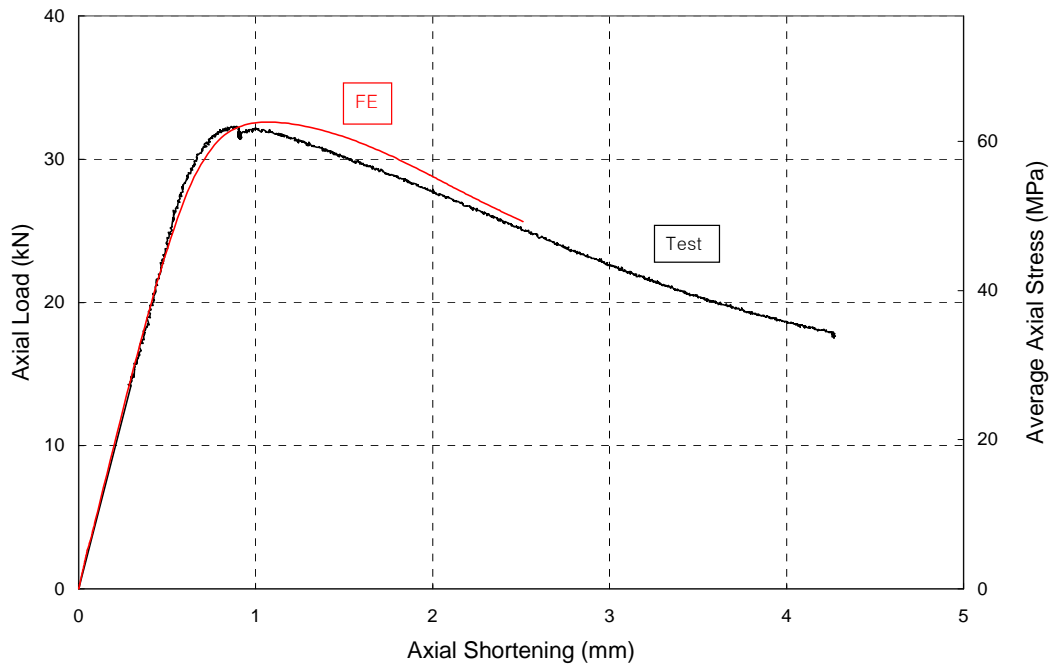


Figure C7.a. I304_2000_1 : Axial Load vs. Axial Shortening

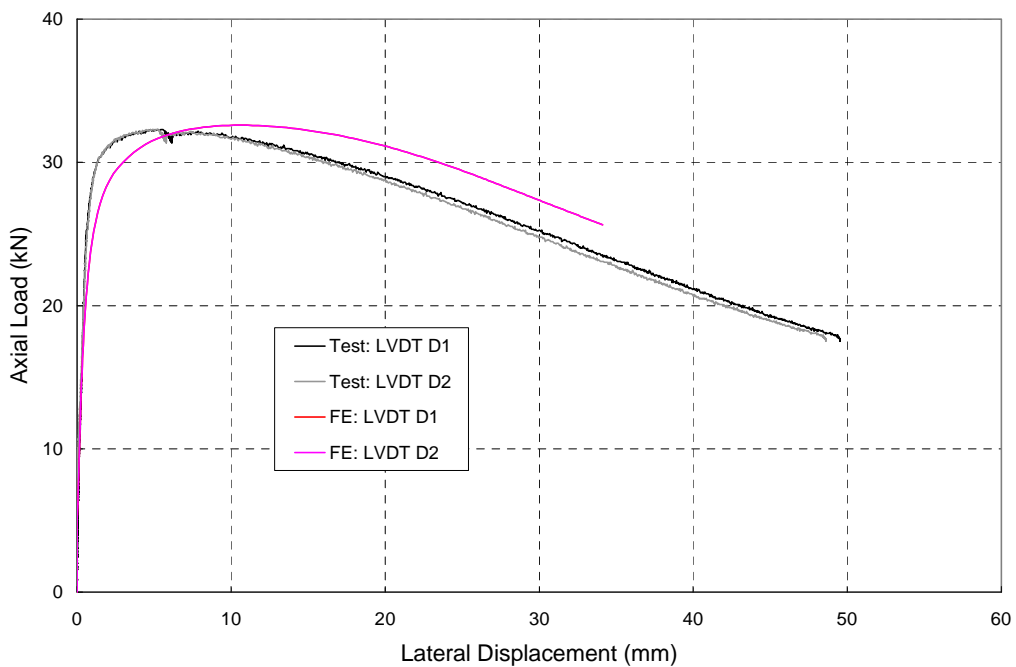


Figure C7.b. I304_2000_1 : Axial Load vs. Lateral Displacement

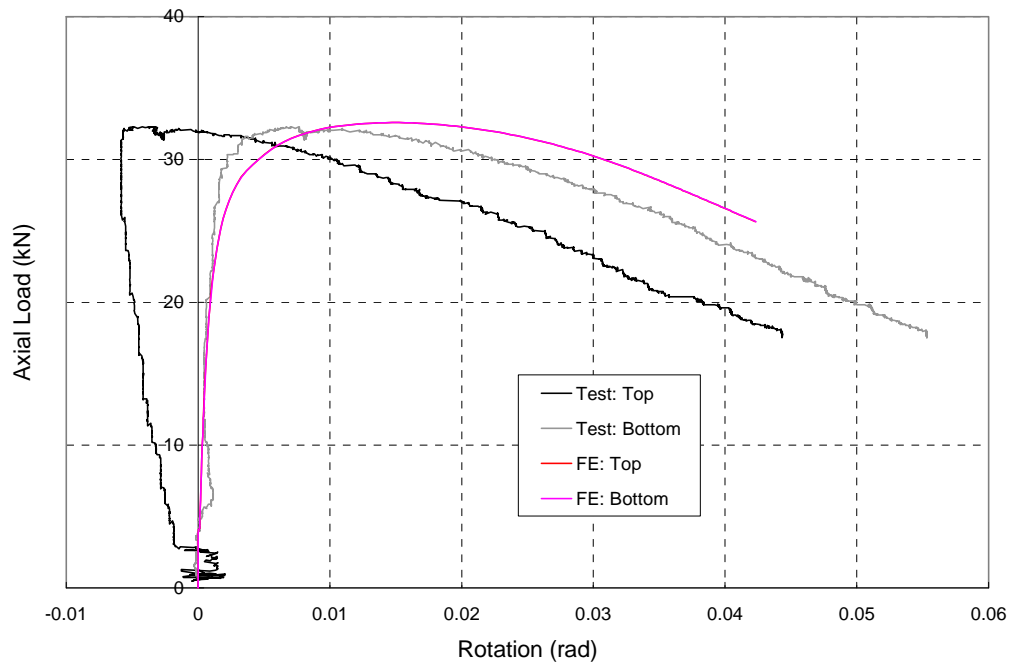


Figure C7.c. I304_2000_1 : Axial Load vs. End Rotations

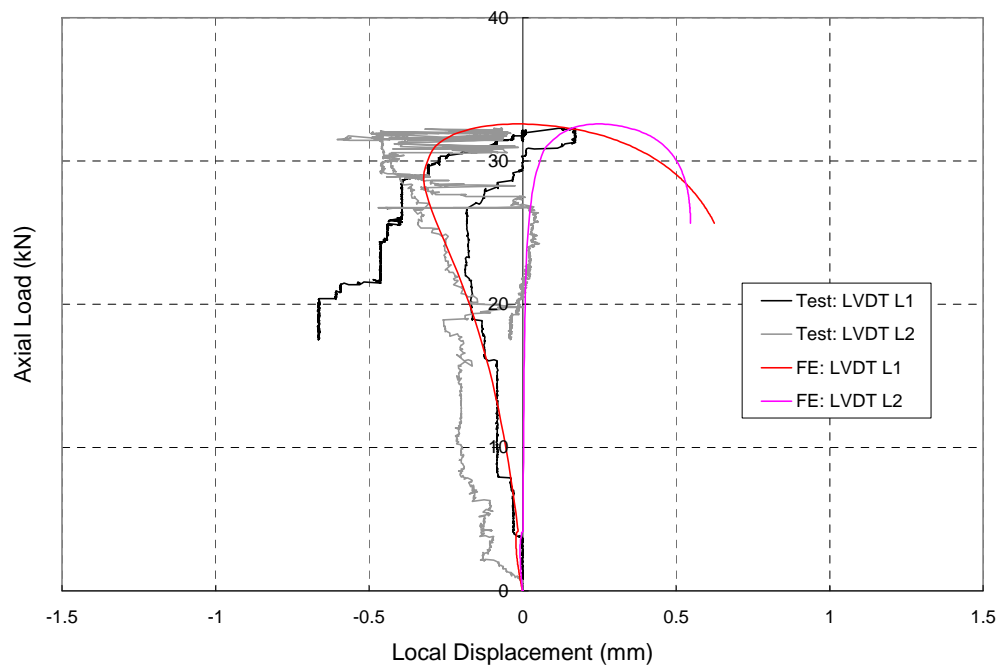


Figure C7.d. I304_2000_1 : Axial Load vs. Local Displacements

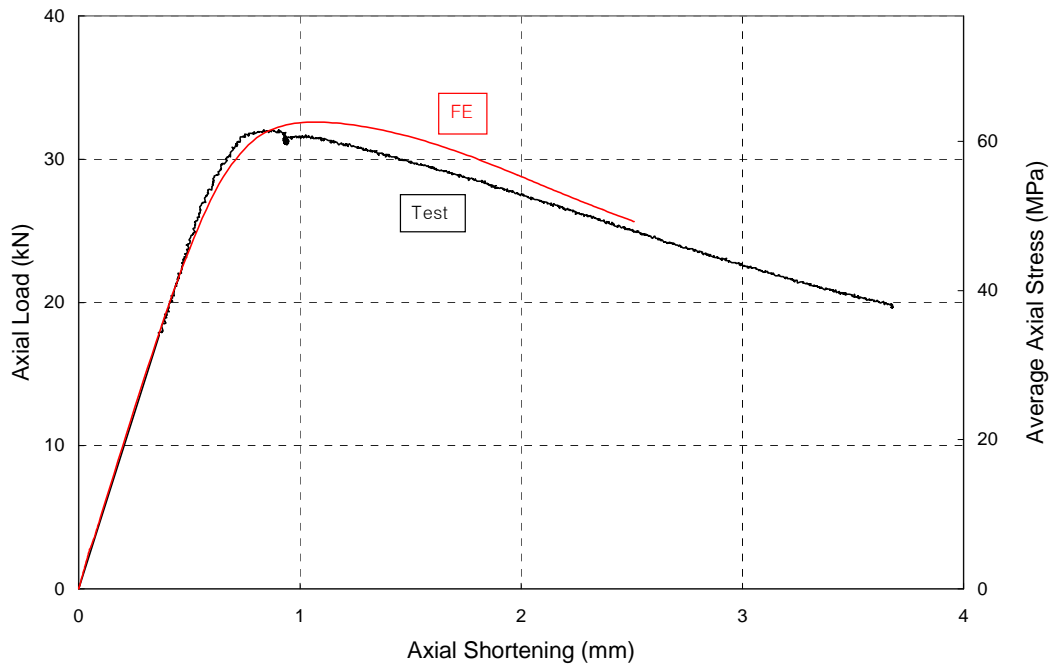


Figure C8.a. I304_2000_2 : Axial Load vs. Axial Shortening

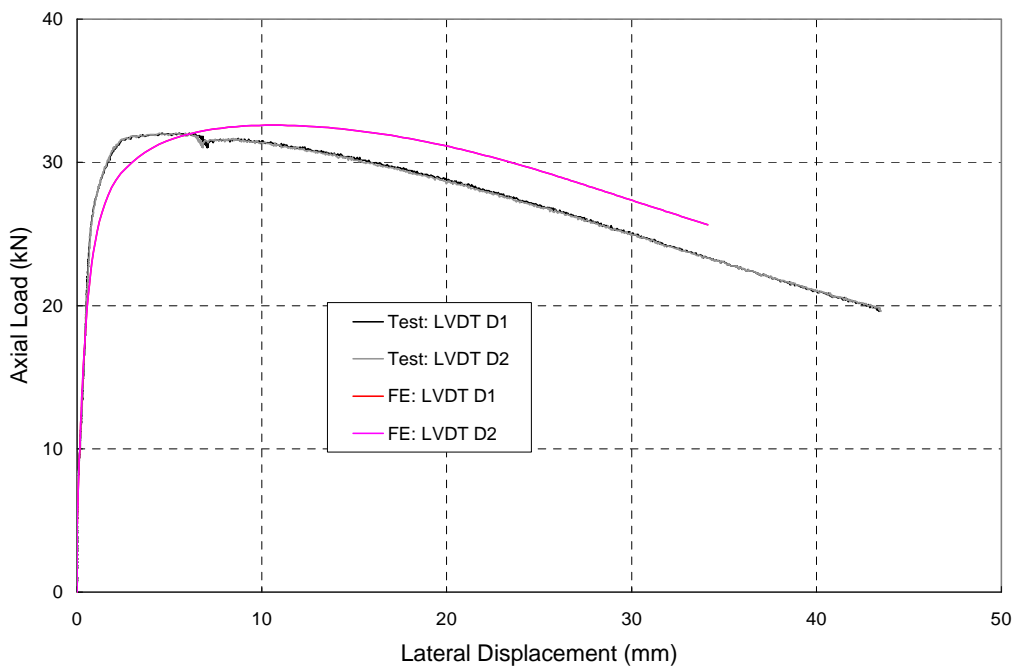


Figure C8.b. I304_2000_2 : Axial Load vs. Lateral Displacement

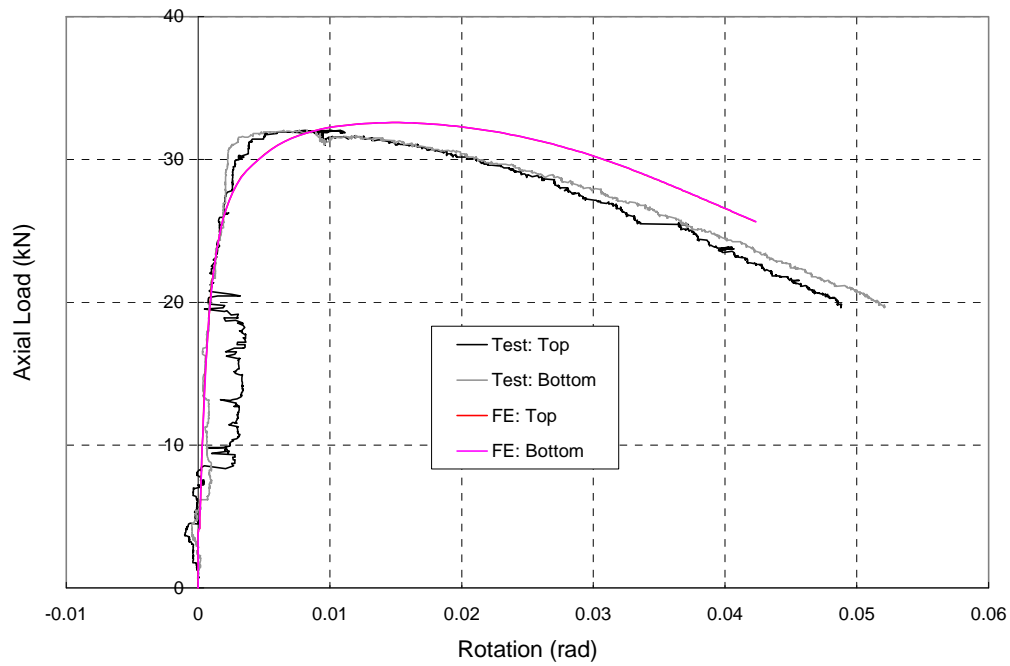


Figure C8.c. I304_2000_2 : Axial Load vs. End Rotations

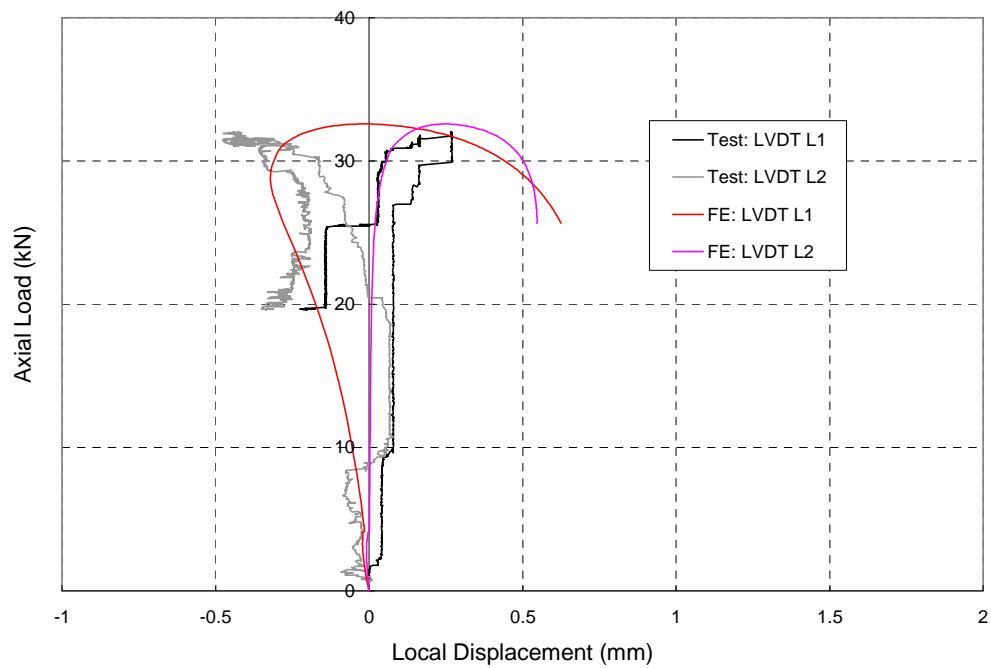


Figure C8.d. I304_2000_2 : Axial Load vs. Local Displacements

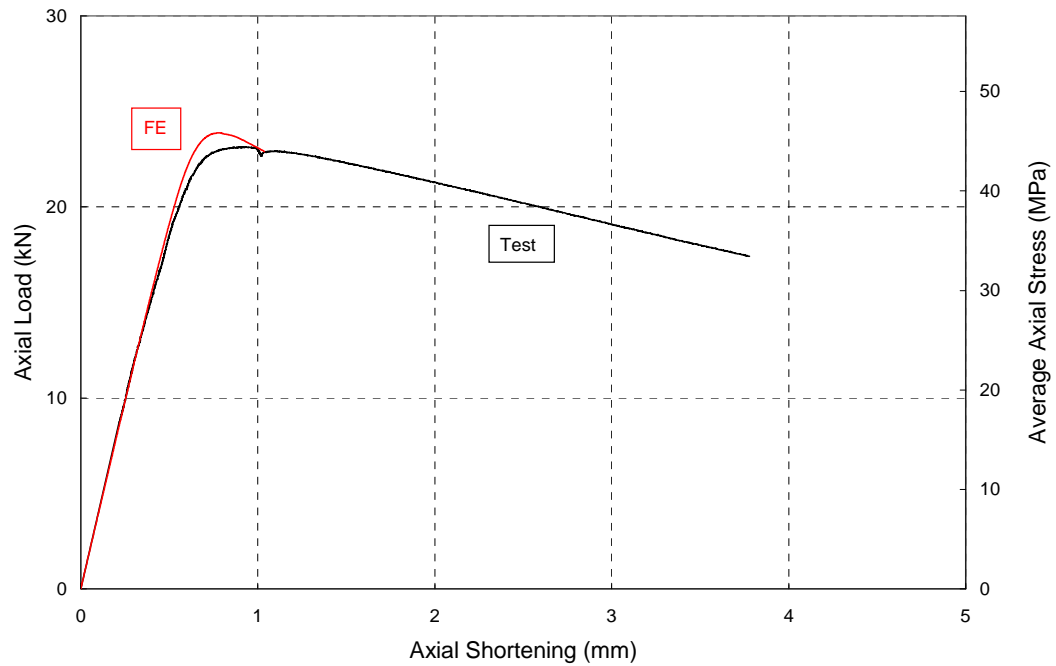


Figure C9.a. I304_2500_1 : Axial Load vs. Axial Shortening

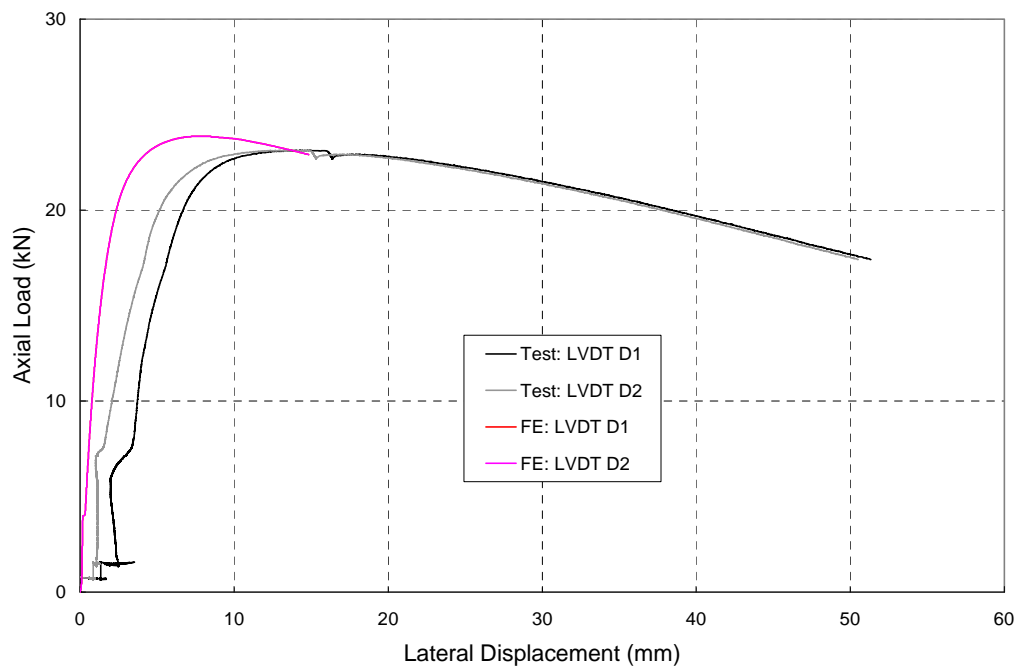


Figure C9.b. I304_2500_1 : Axial Load vs. Lateral Displacement

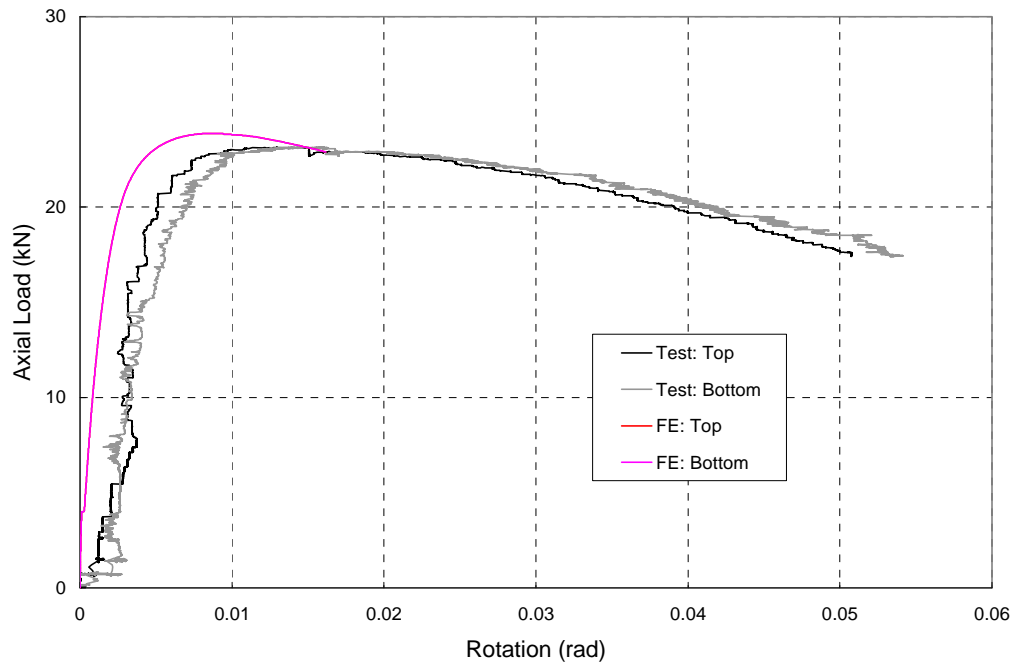


Figure C9.c. I304_2500_1 : Axial Load vs. End Rotations

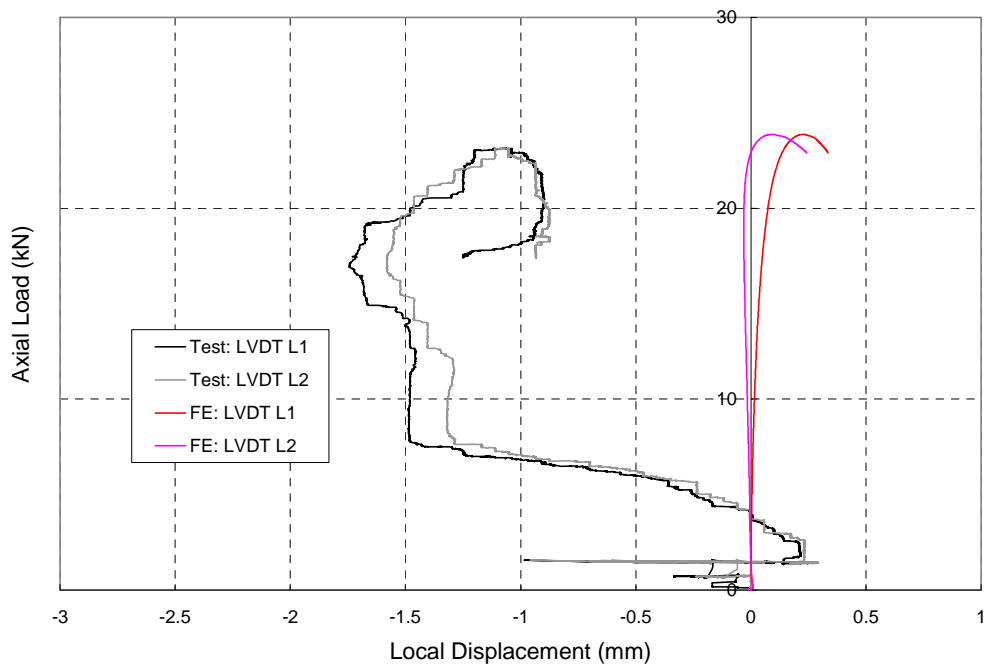


Figure C9.d. I304_2500_1 : Axial Load vs. Local Displacements

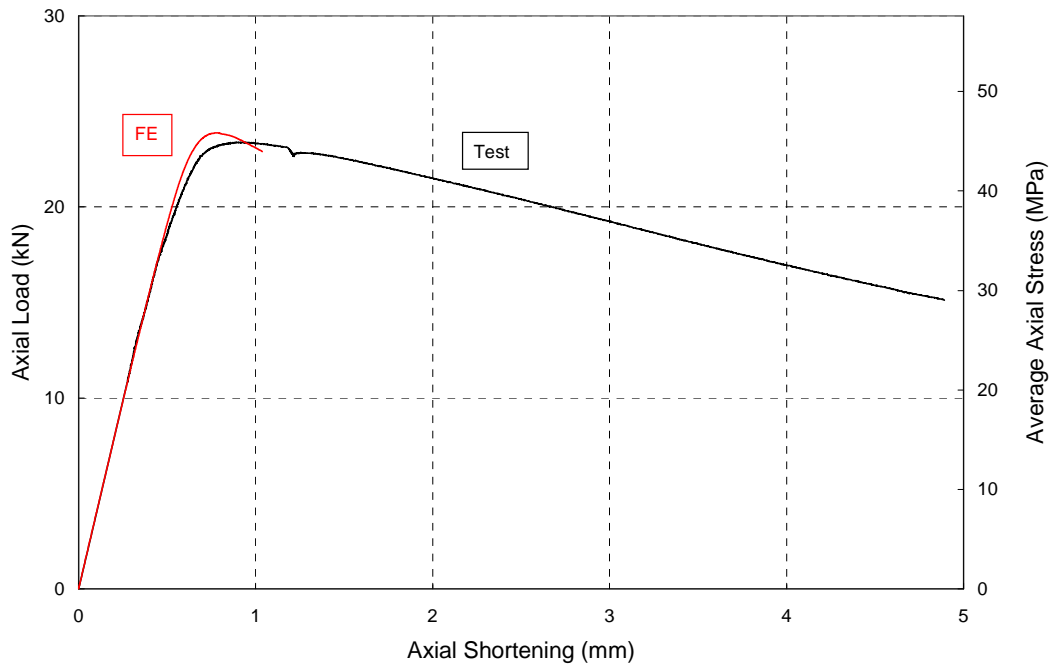


Figure C10.a. I304_2500_2 : Axial Load vs. Axial Shortening

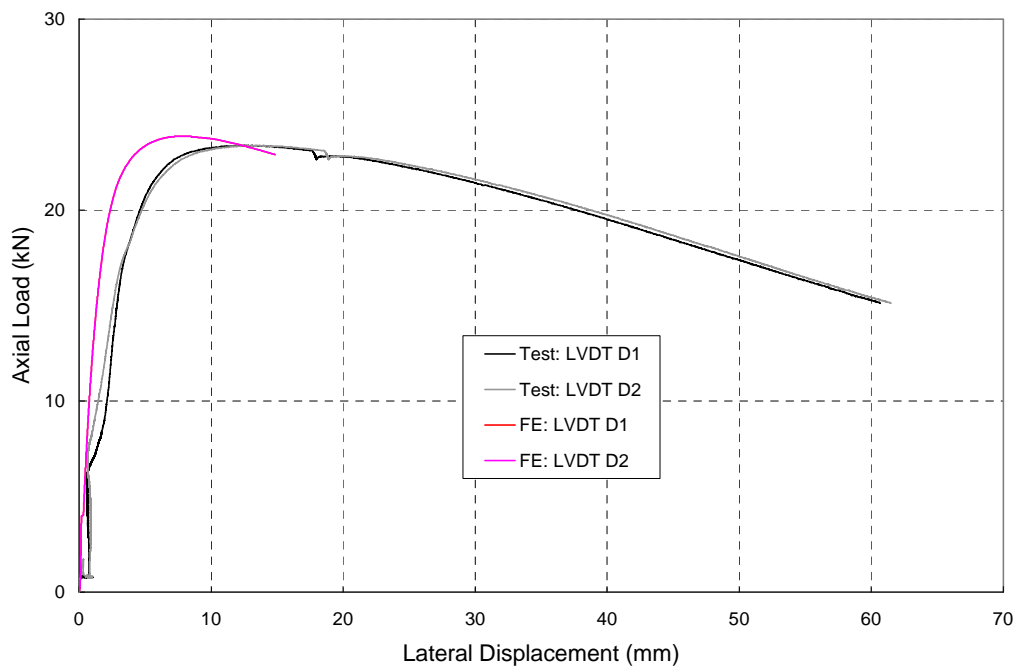


Figure C10.b. I304_2500_2 : Axial Load vs. Lateral Displacement

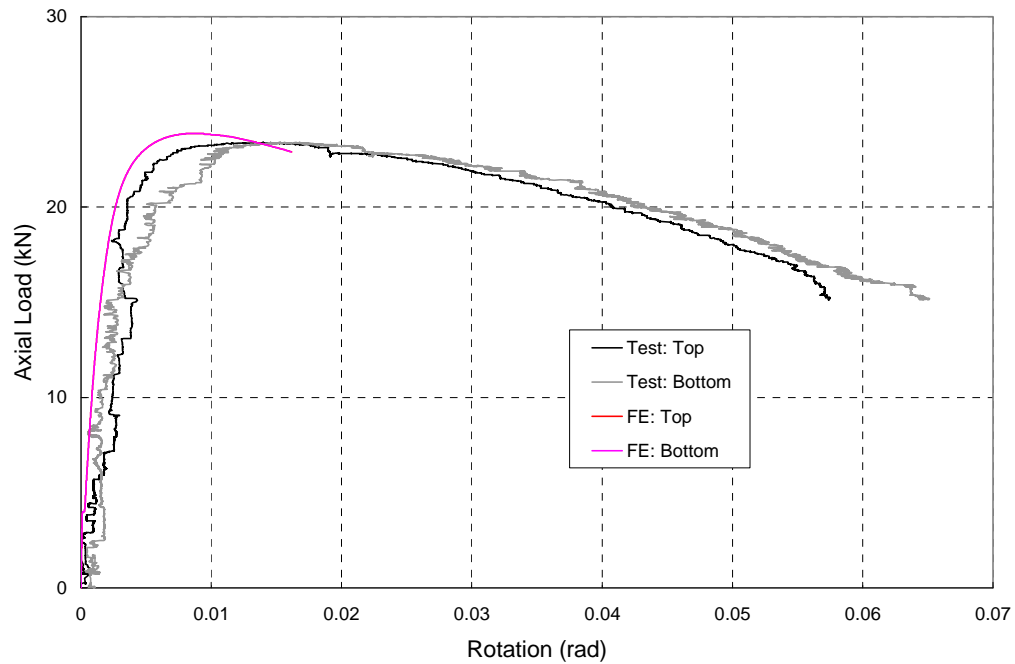


Figure C10.c. I304_2500_2 : Axial Load vs. End Rotations

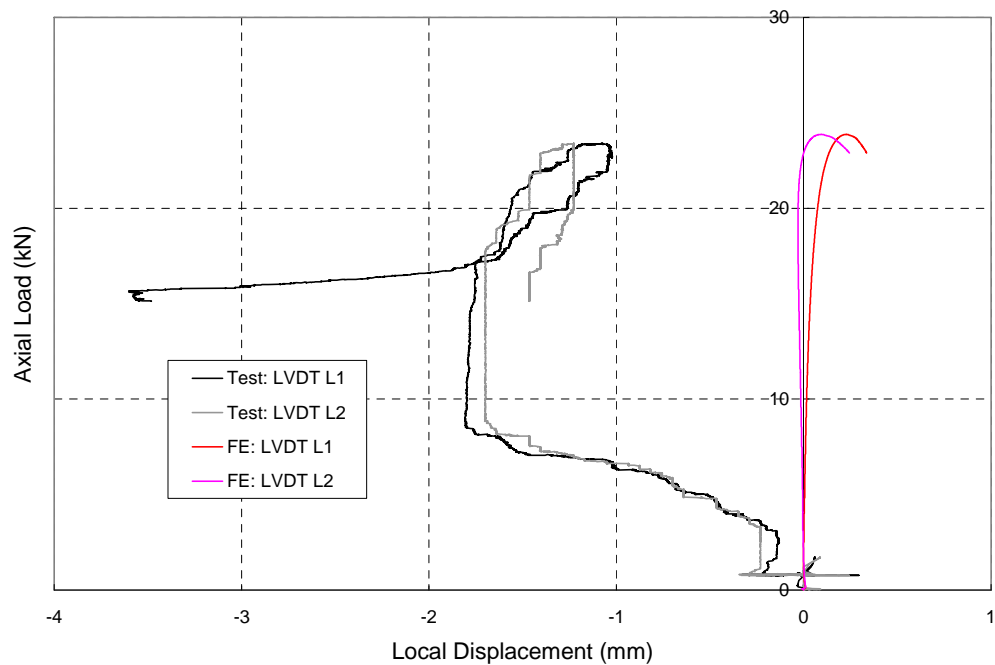


Figure C10.d. I304_2500_2 : Axial Load vs. Local Displacements

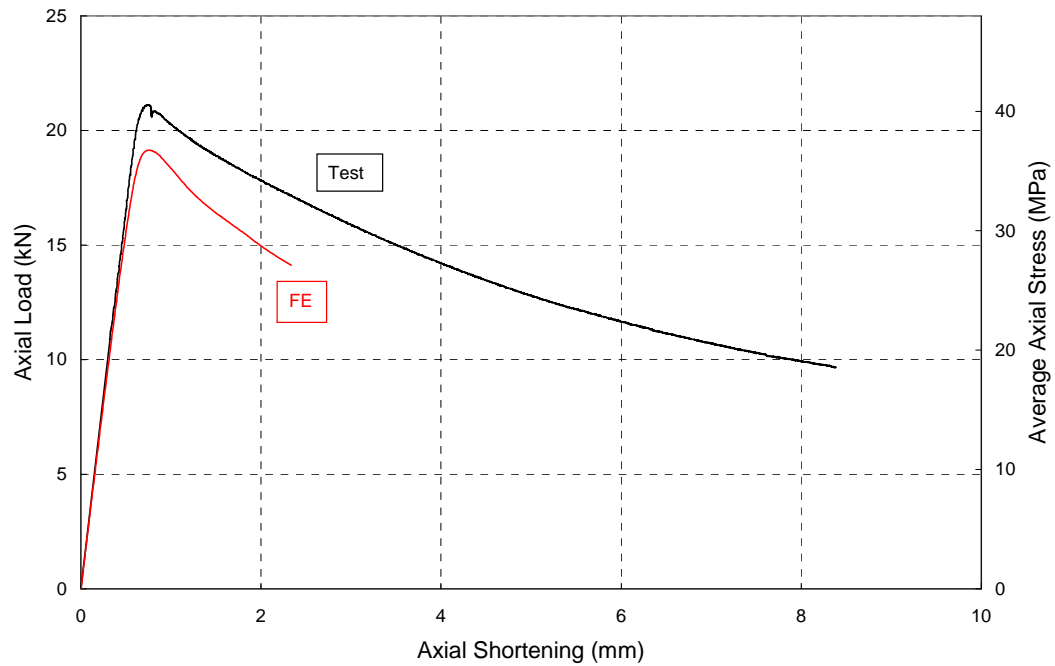


Figure C11.a. I304_3000_1 : Axial Load vs. Axial Shortening

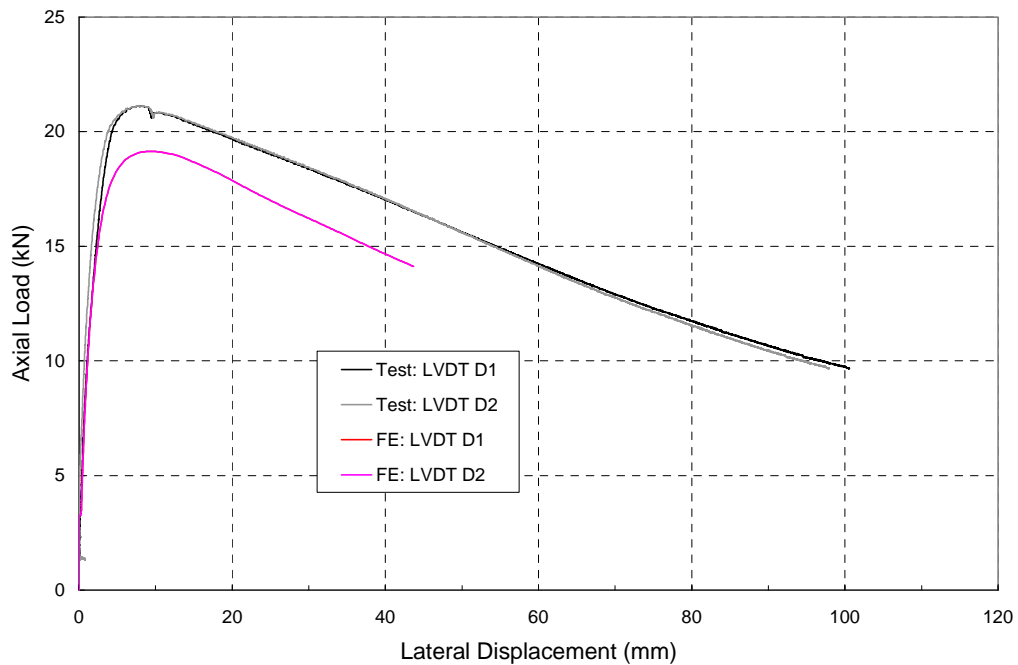


Figure C11.b. I304_3000_1 : Axial Load vs. Lateral Displacement

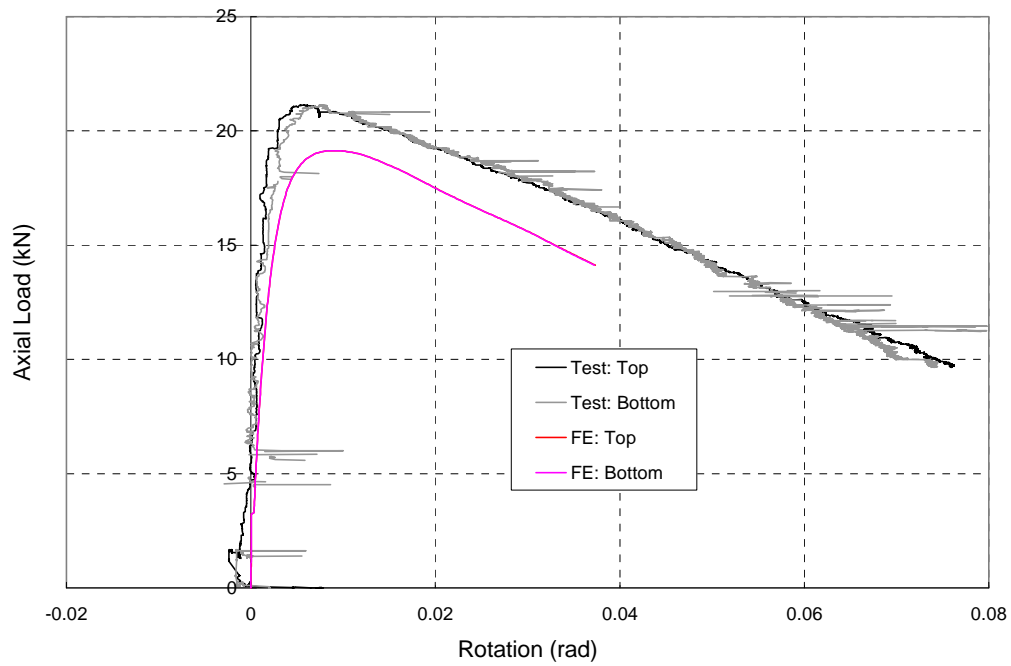


Figure C11.c. I304_3000_1 : Axial Load vs. End Rotations

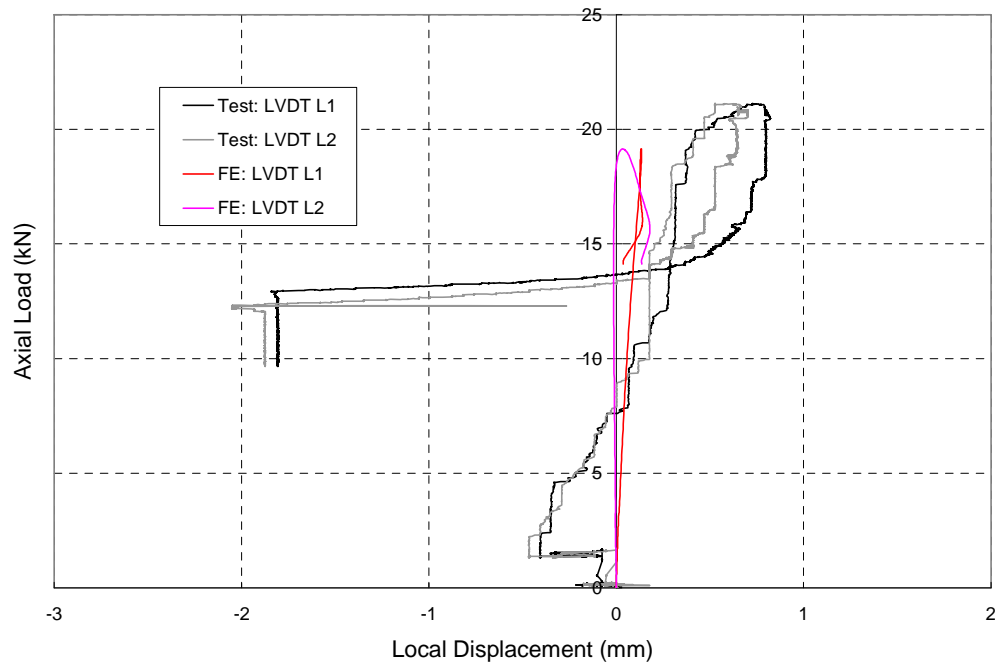


Figure C11.d. I304_3000_1 : Axial Load vs. Local Displacements

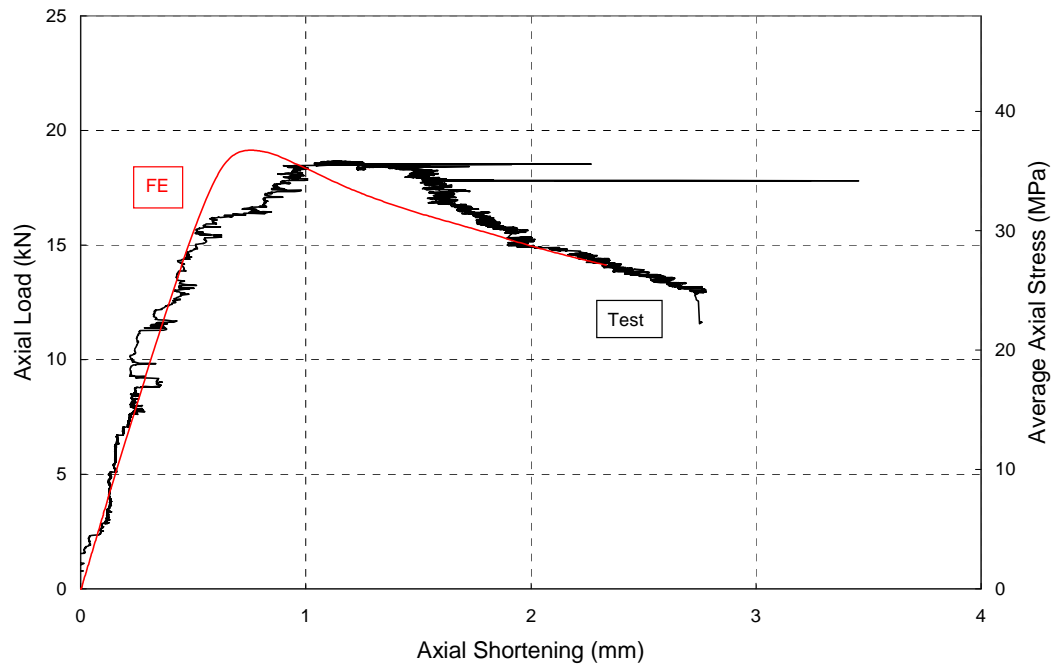


Figure C12.a. I304_3000_2 : Axial Load vs. Axial Shortening

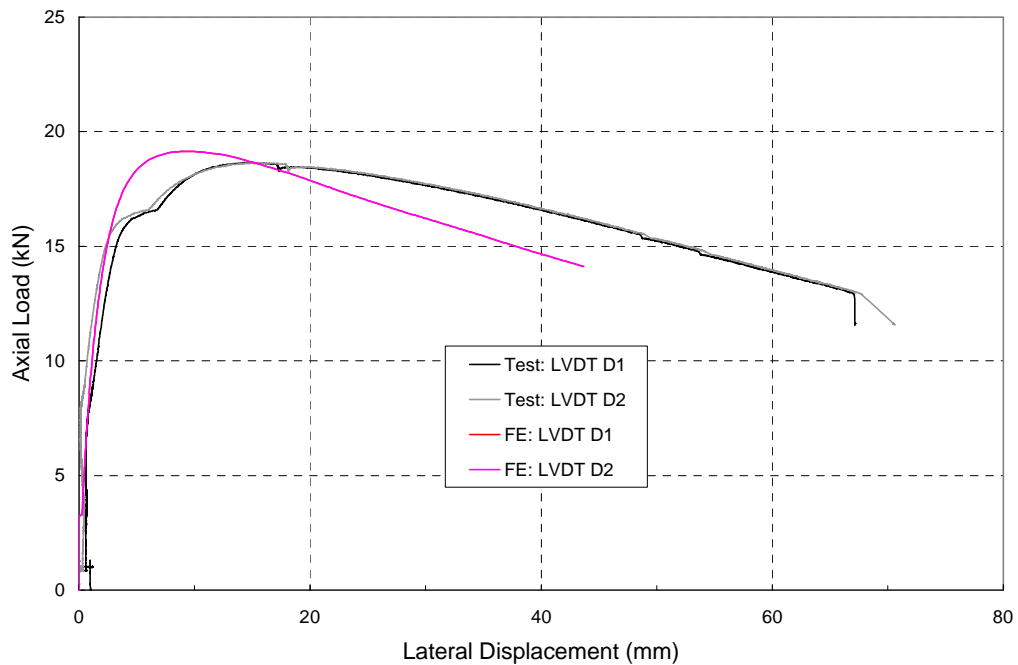


Figure C12.b. I304_3000_2 : Axial Load vs. Lateral Displacement

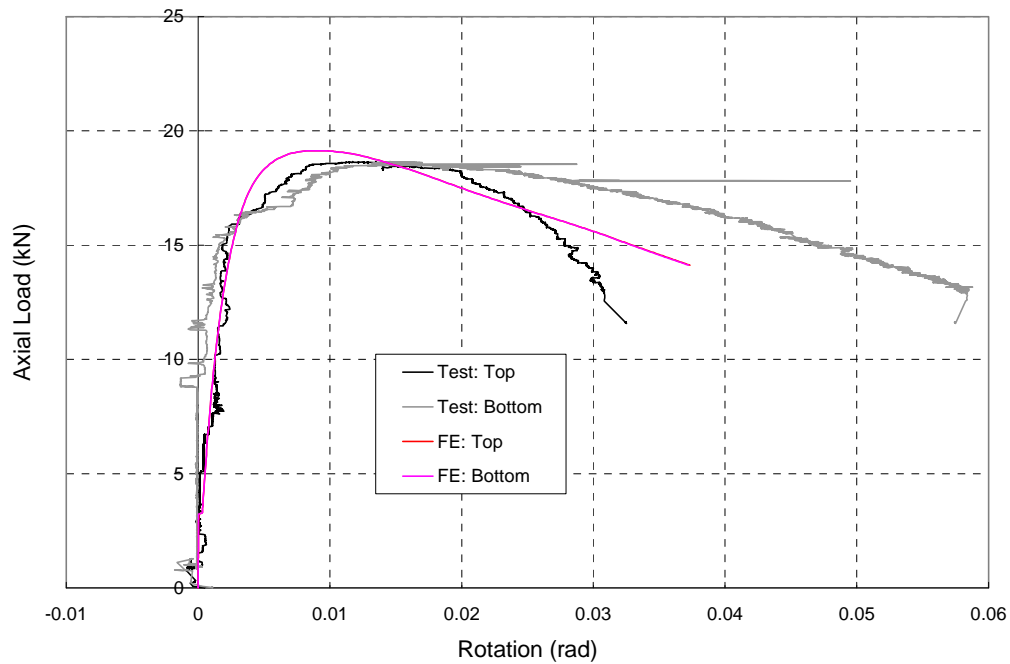


Figure C12.c. I304_3000_2 : Axial Load vs. End Rotations

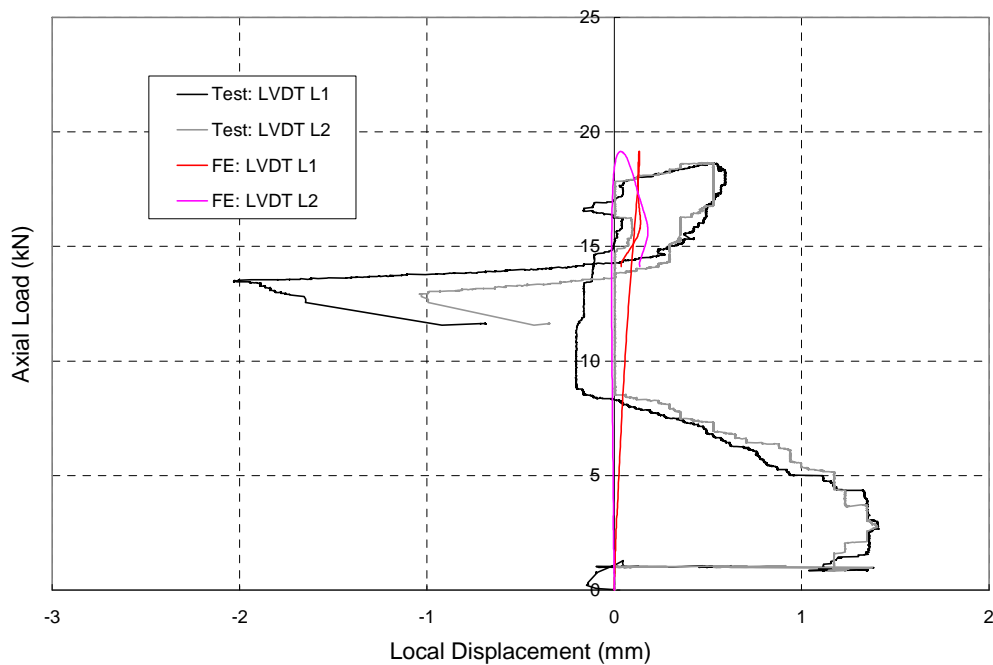


Figure C12.d. I304_3000_2 : Axial Load vs. Local Displacements

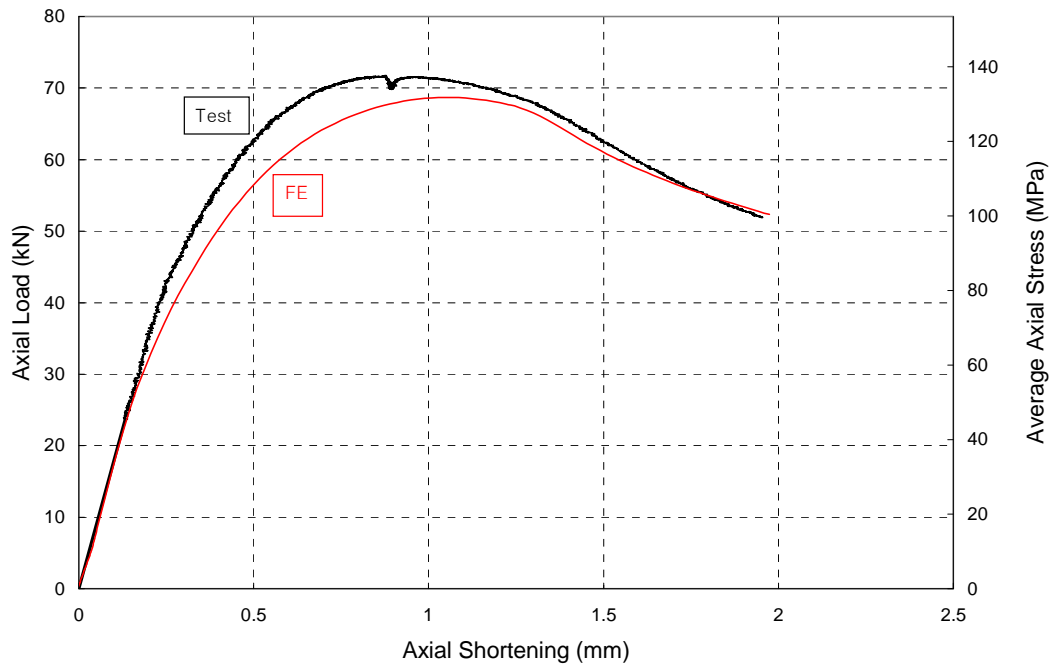


Figure C13.a. I404_500_1 : Axial Load vs. Axial Shortening

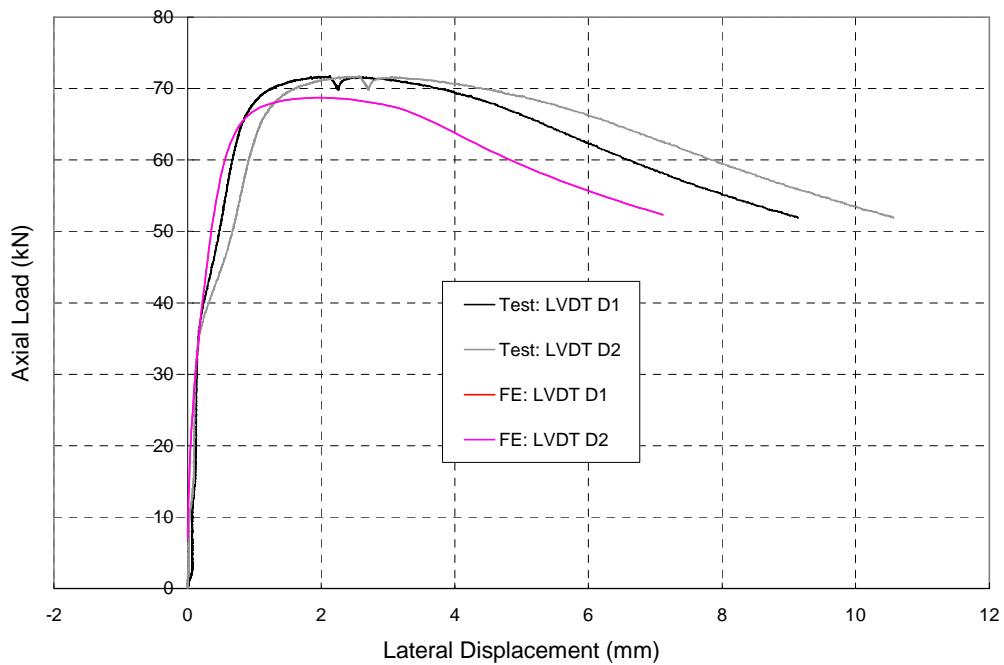


Figure C13.b. I404_500_1 : Axial Load vs. Lateral Displacement

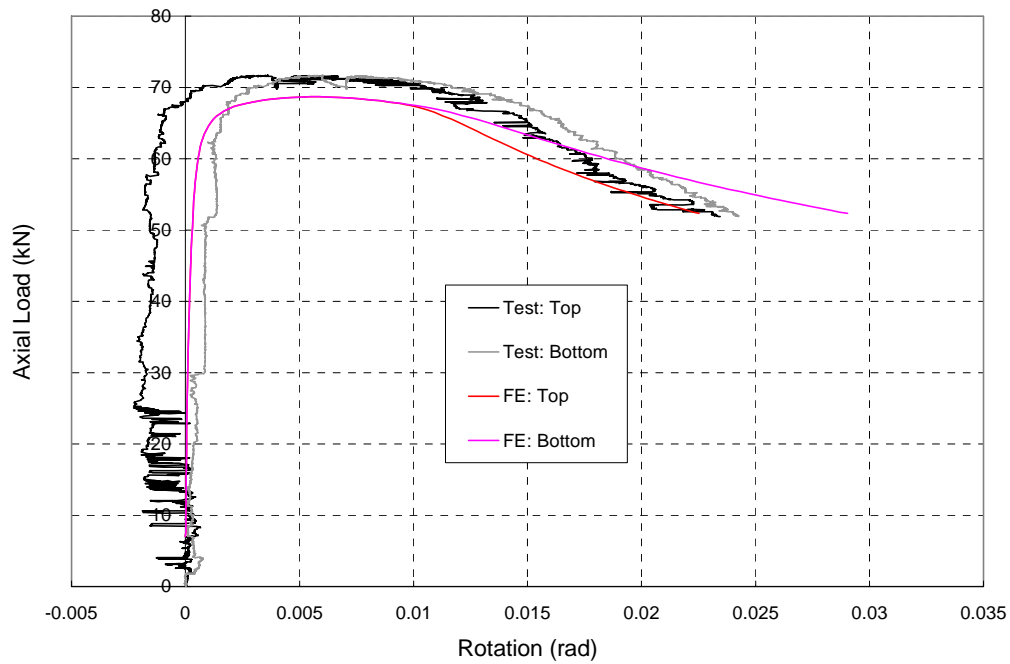


Figure C13.c. I404_500_1 : Axial Load vs. End Rotations

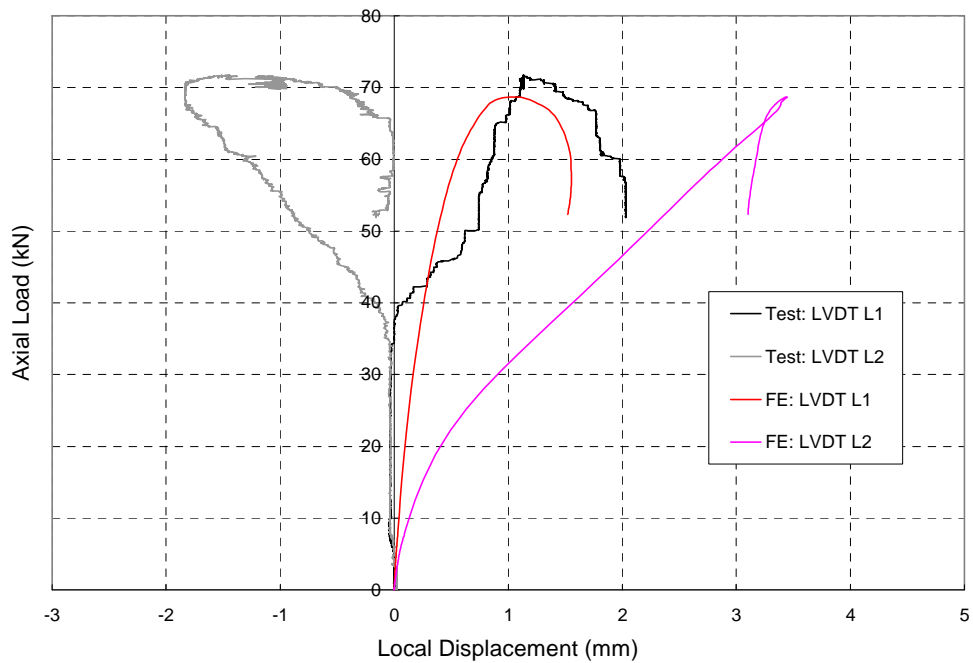


Figure C13.d. I404_500_1 : Axial Load vs. Local Displacements

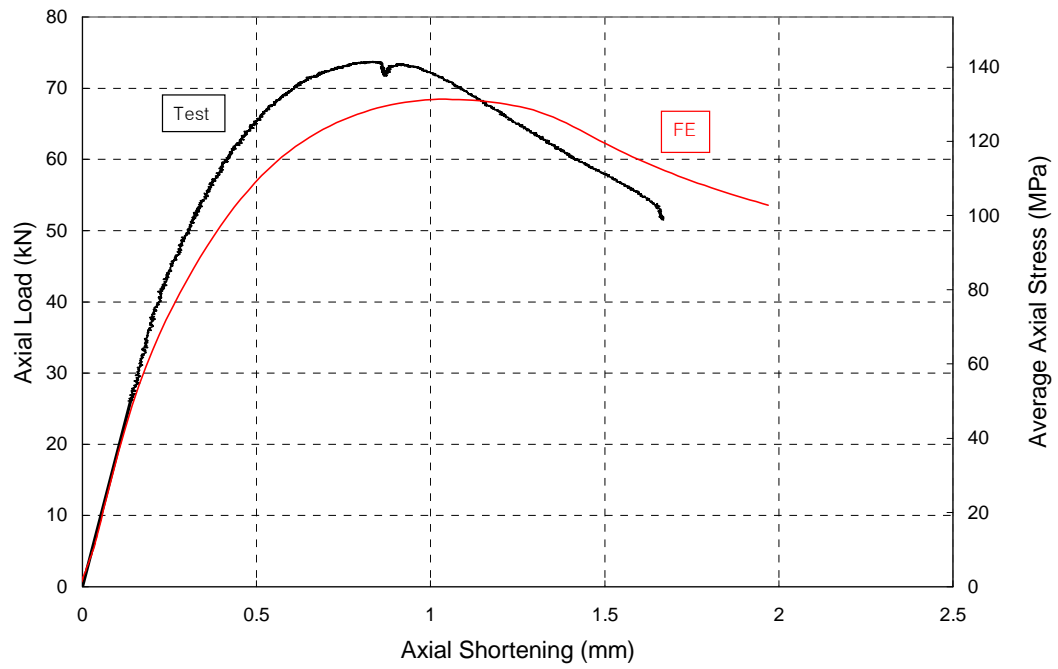


Figure C14.a. I404_500_2 : Axial Load vs. Axial Shortening

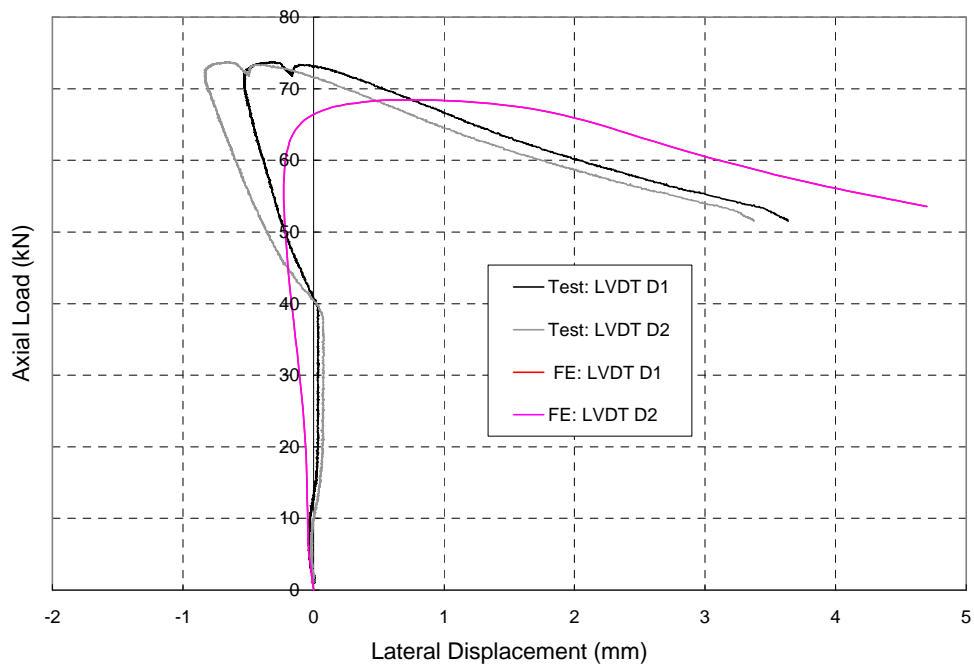


Figure C14.b. I404_500_2 : Axial Load vs. Lateral Displacement

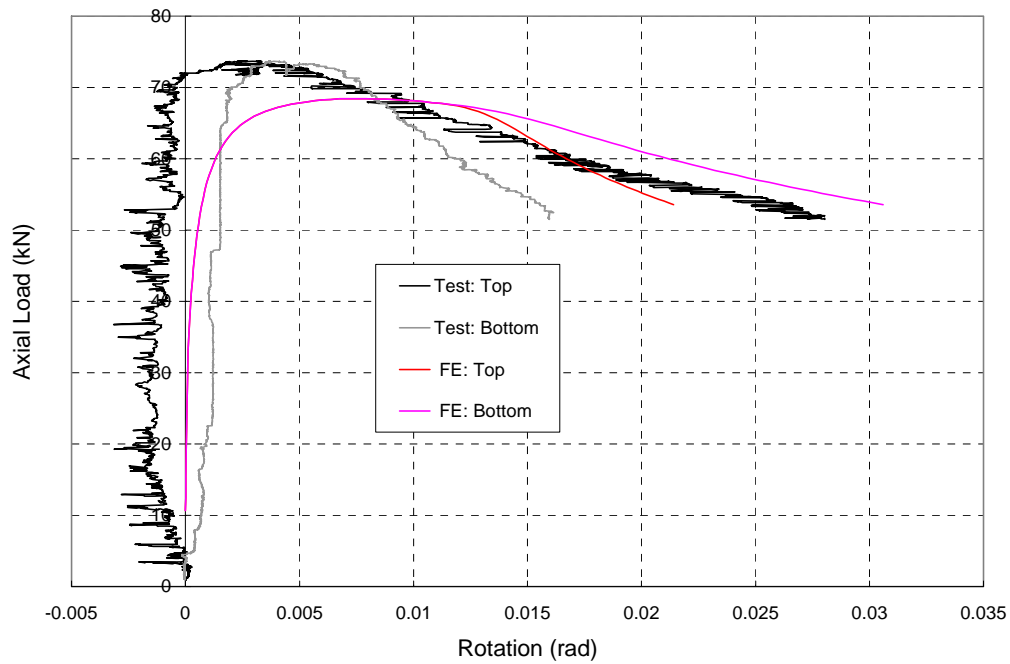


Figure C14.c. I404_500_2 : Axial Load vs. End Rotations

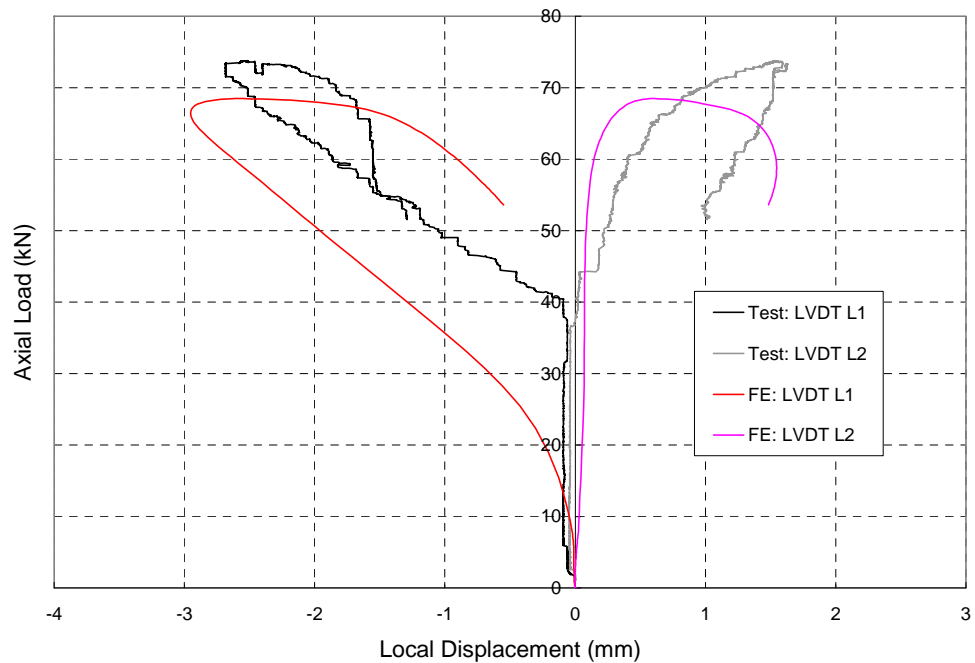


Figure C14.d. I404_500_2 : Axial Load vs. Local Displacements

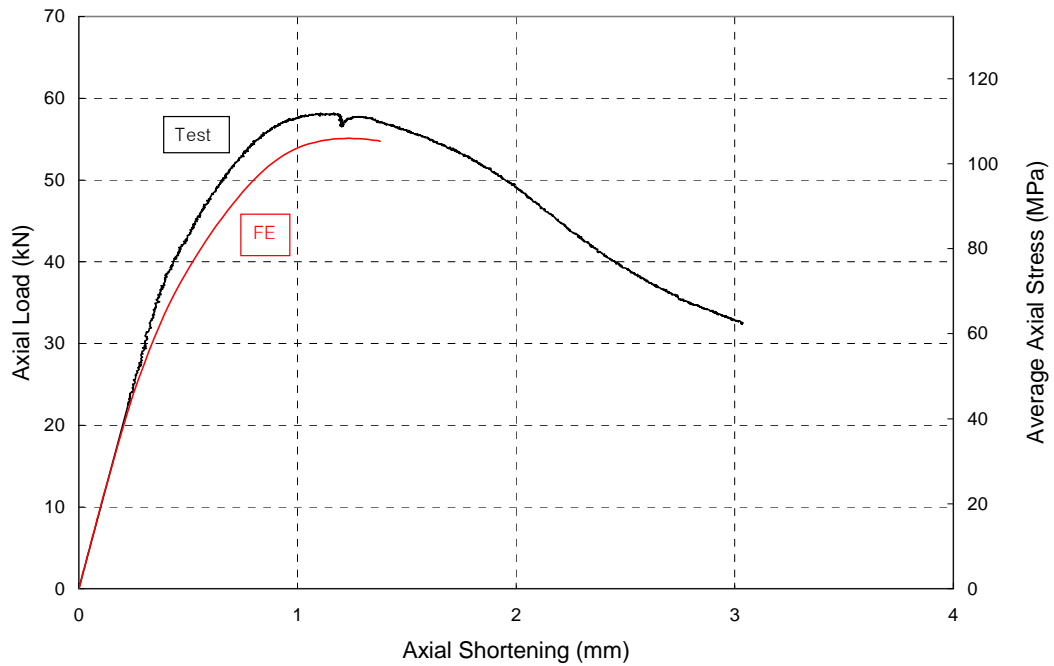


Figure C15.a. I404_1000_1 : Axial Load vs. Axial Shortening

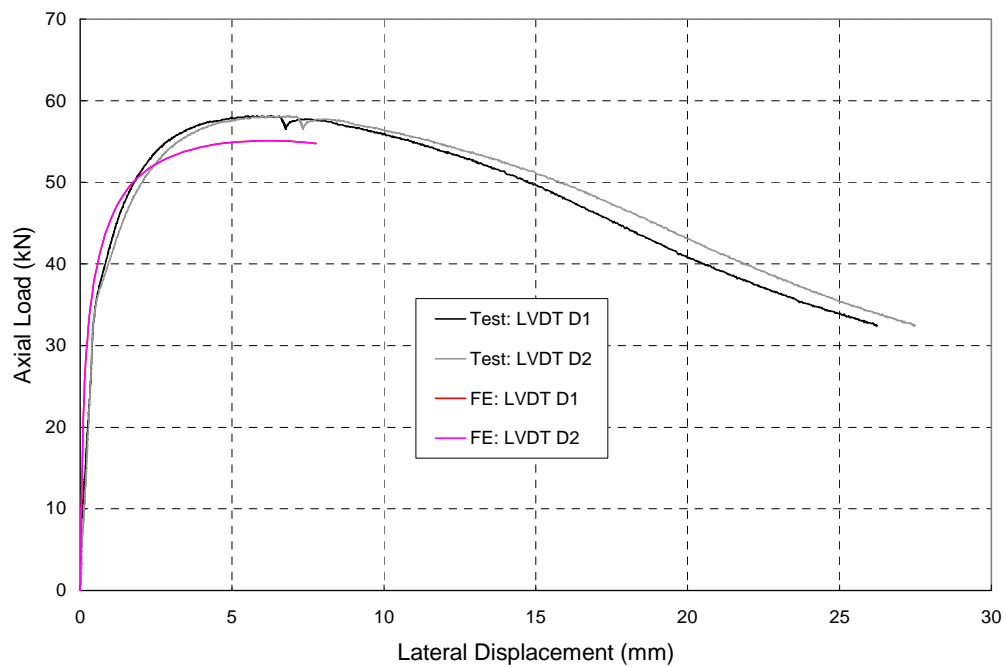


Figure C15.b. I404_1000_1 : Axial Load vs. Lateral Displacement

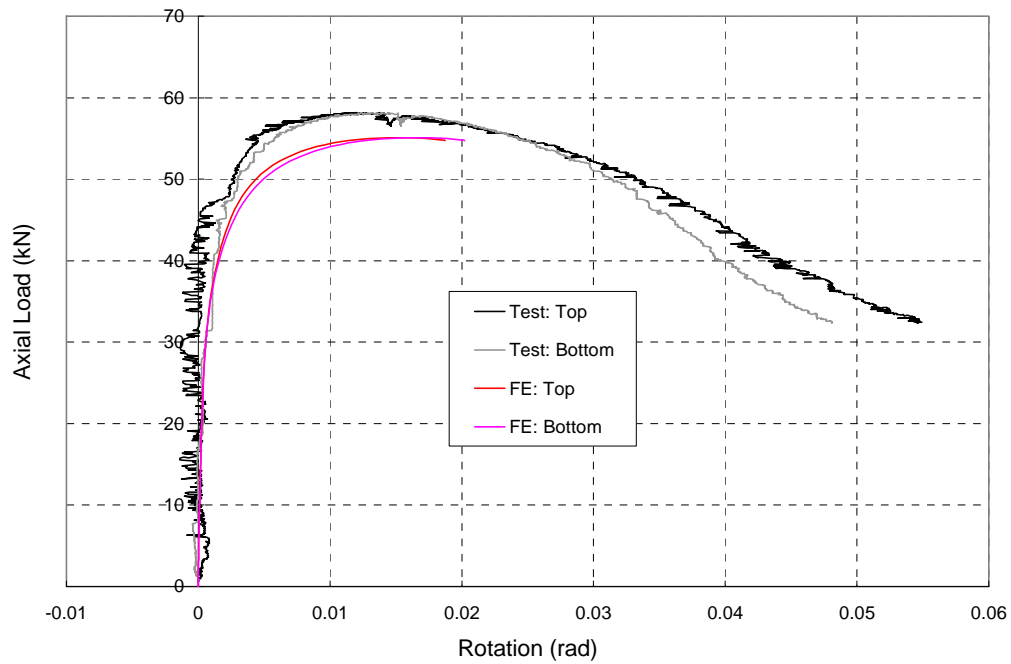


Figure C15.c. I404_1000_1 : Axial Load vs. End Rotations

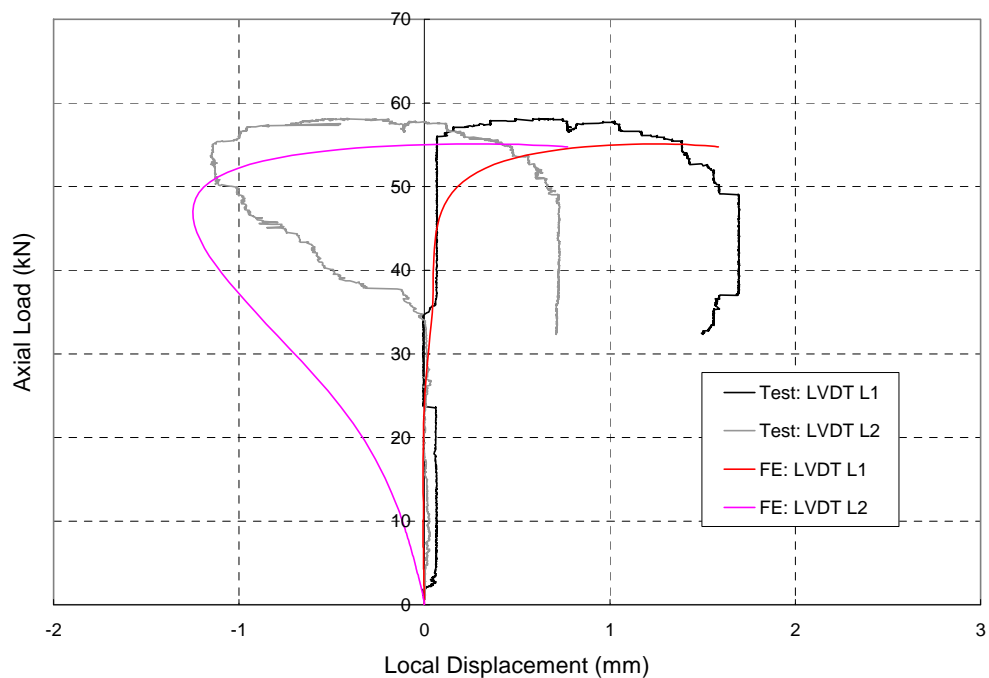


Figure C15.d. I404_1000_1 : Axial Load vs. Local Displacements

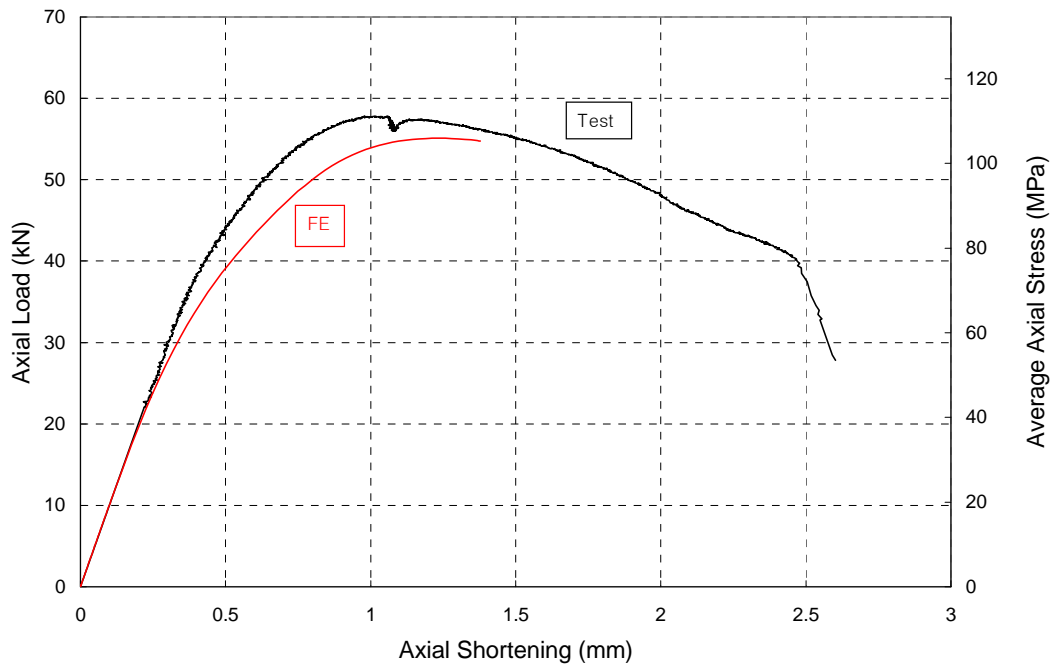


Figure C16.a. I404_1000_2 : Axial Load vs. Axial Shortening

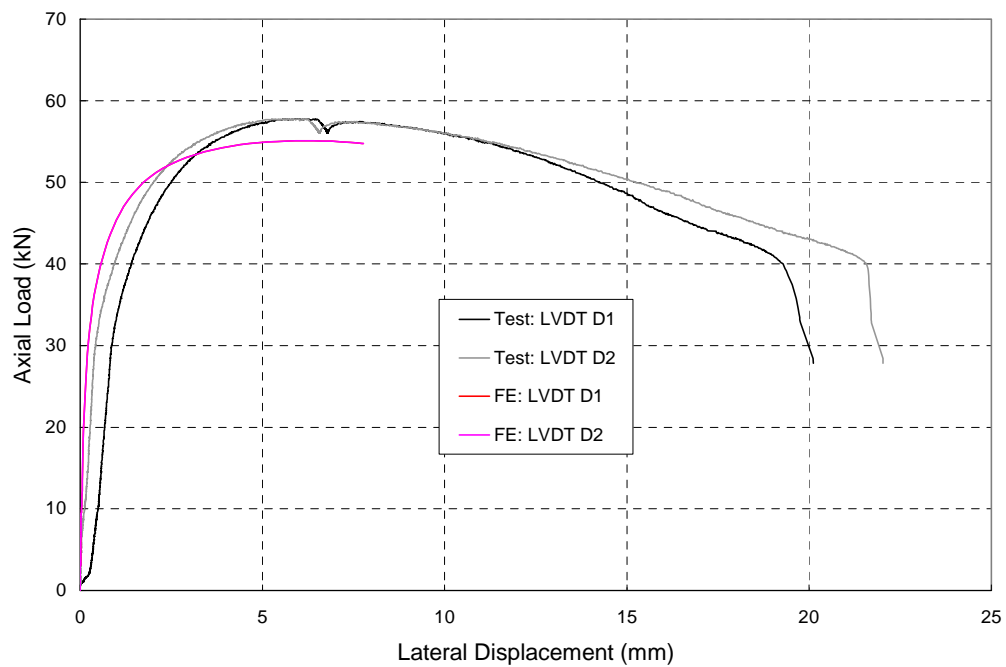


Figure C16.b. I404_1000_2 : Axial Load vs. Lateral Displacement

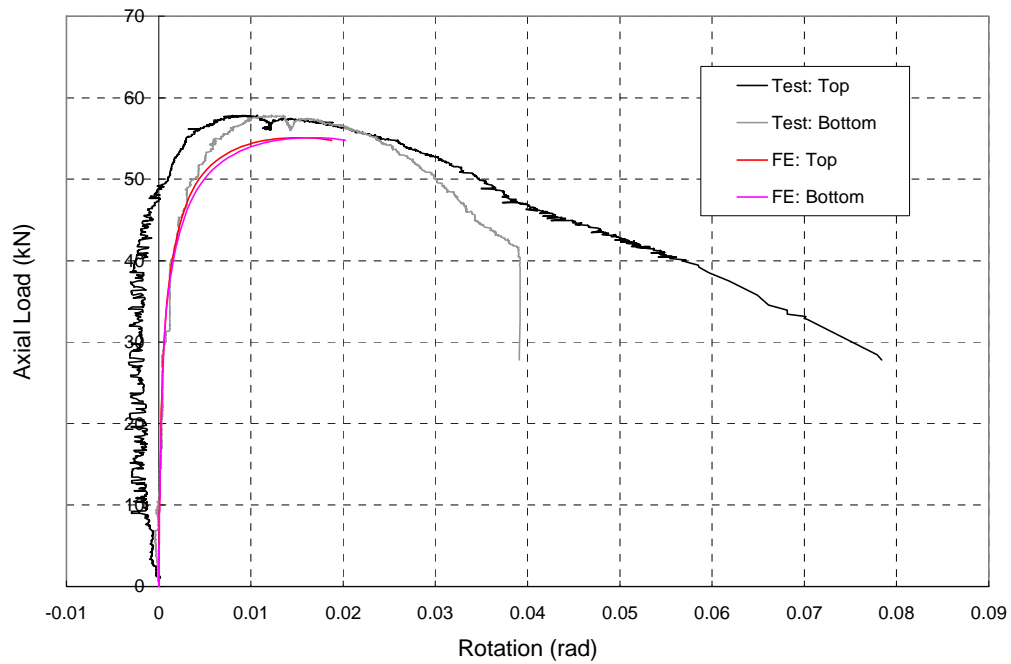


Figure C16.c. I404_1000_2 : Axial Load vs. End Rotations

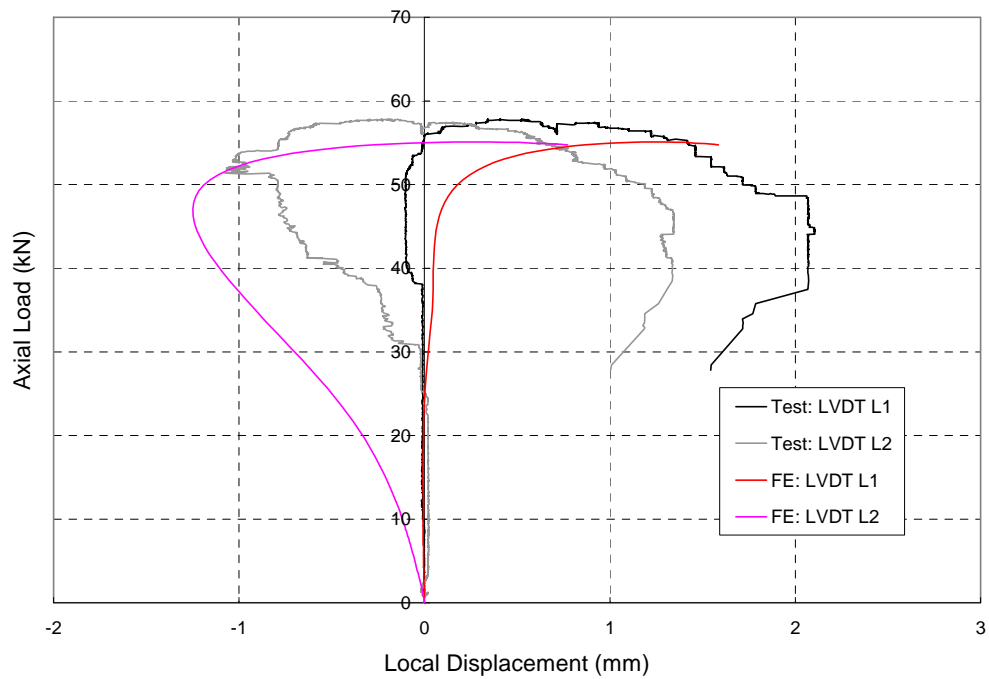


Figure C16.d. I404_1000_2 : Axial Load vs. Local Displacements

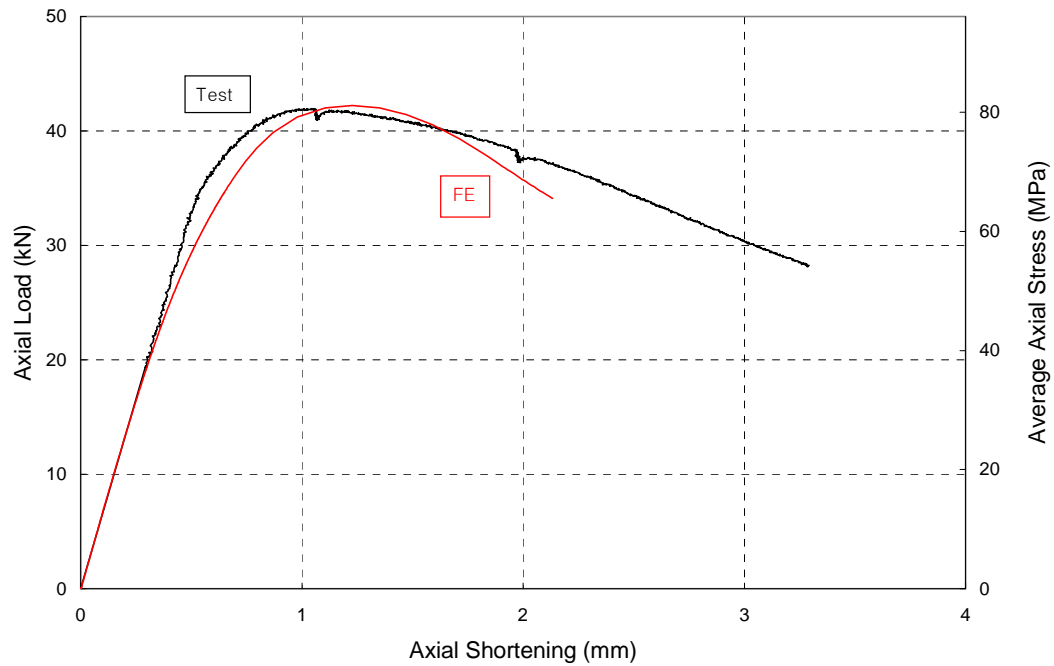


Figure C17.a. I404_1500_1 : Axial Load vs. Axial Shortening

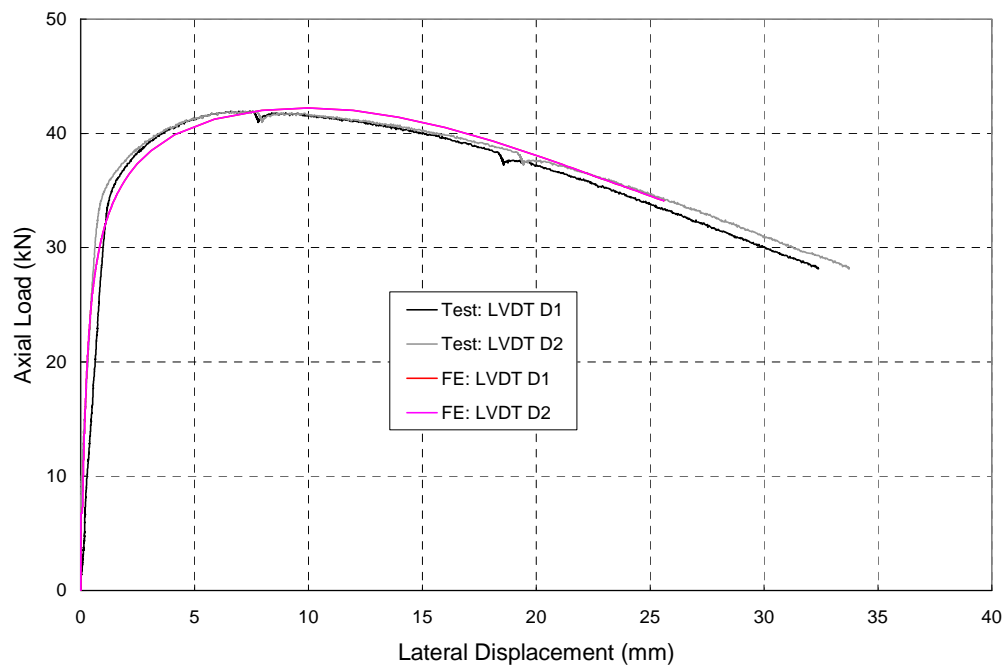


Figure C17.b. I404_1500_1 : Axial Load vs. Lateral Displacement

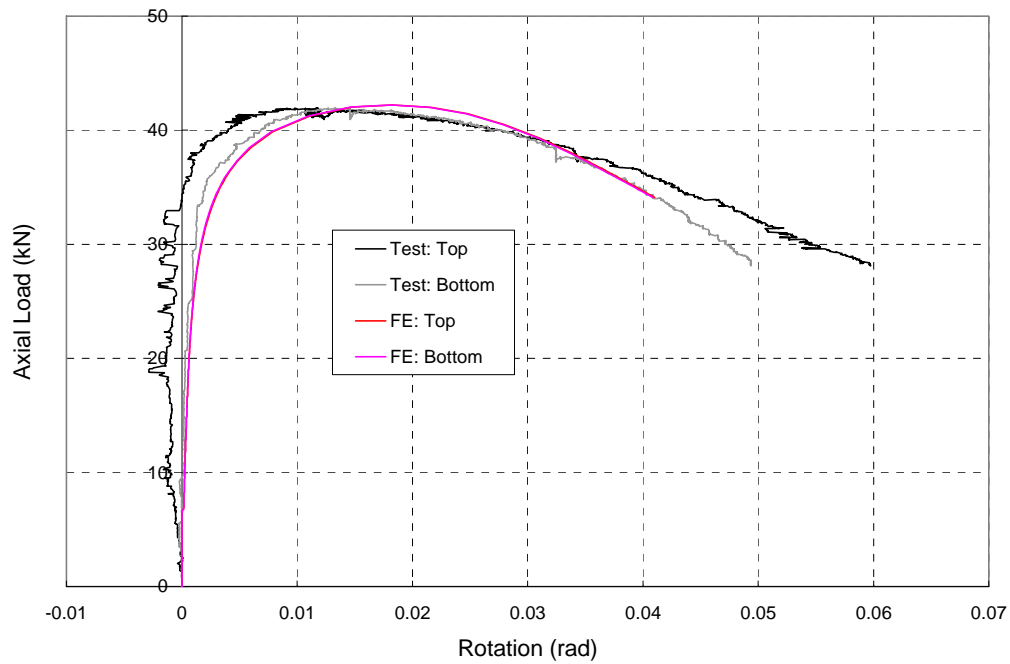


Figure C17.c. I404_1500_1 : Axial Load vs. End Rotations

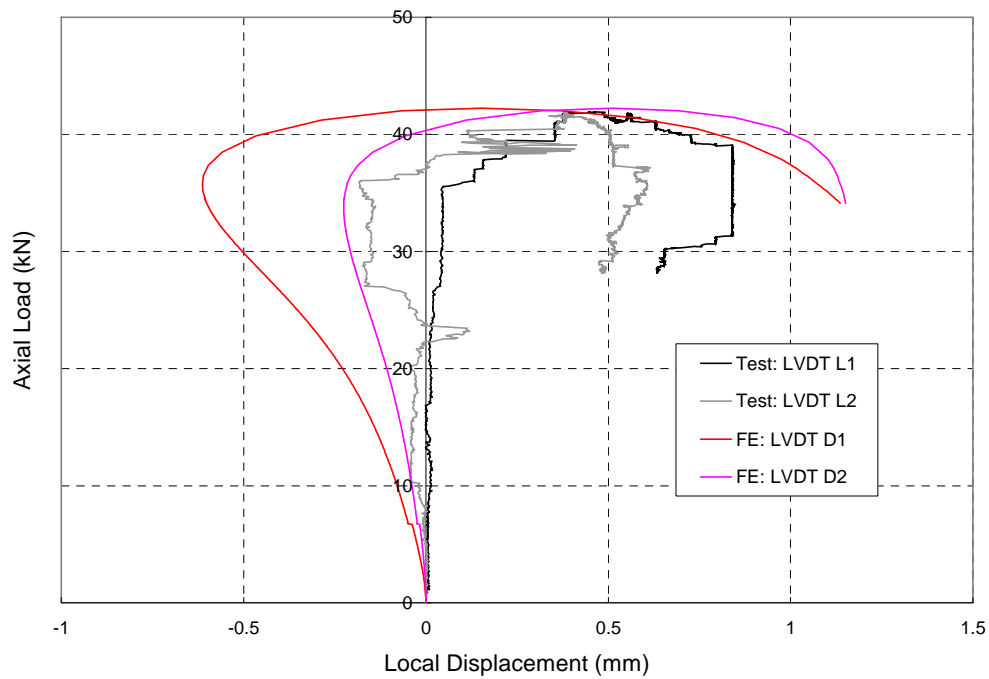


Figure C17.d. I404_1500_1 : Axial Load vs. Local Displacements

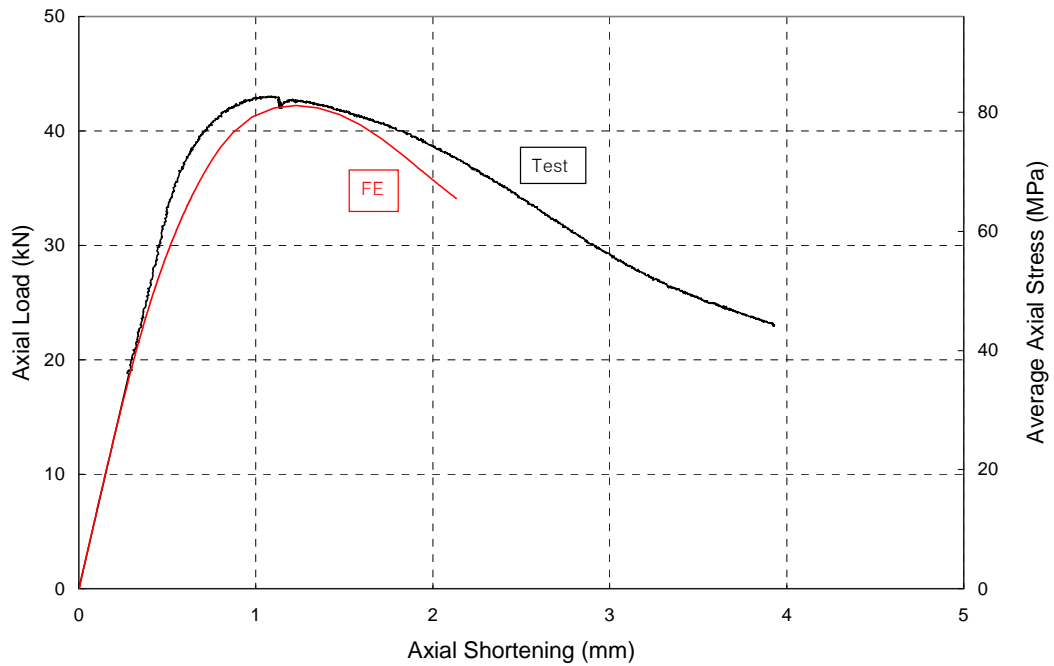


Figure C18.a. I404_1500_2 : Axial Load vs. Axial Shortening

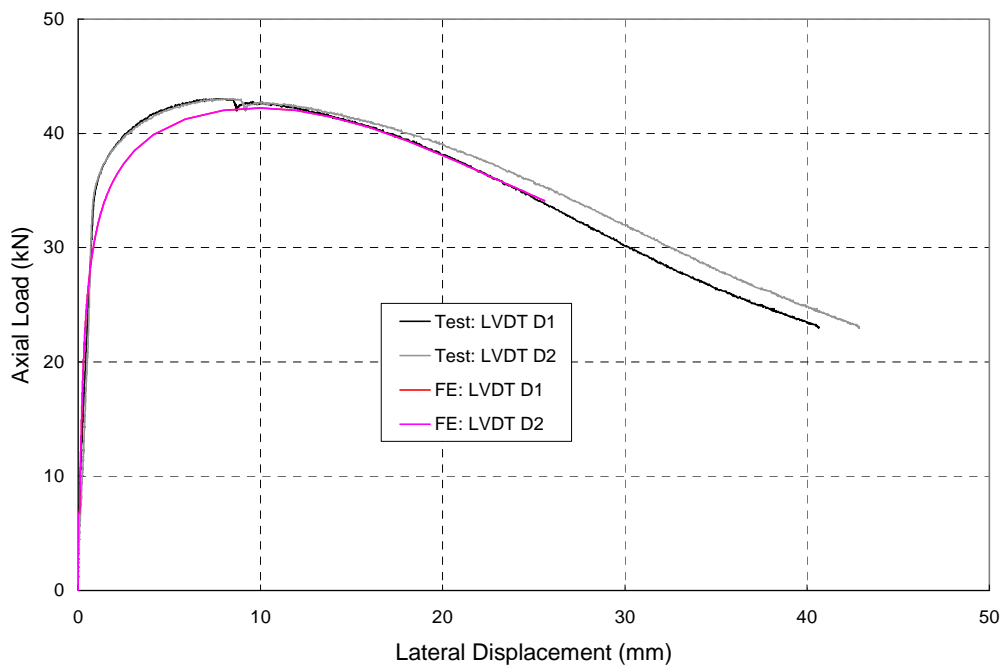


Figure C18.b. I404_1500_2 : Axial Load vs. Lateral Displacement

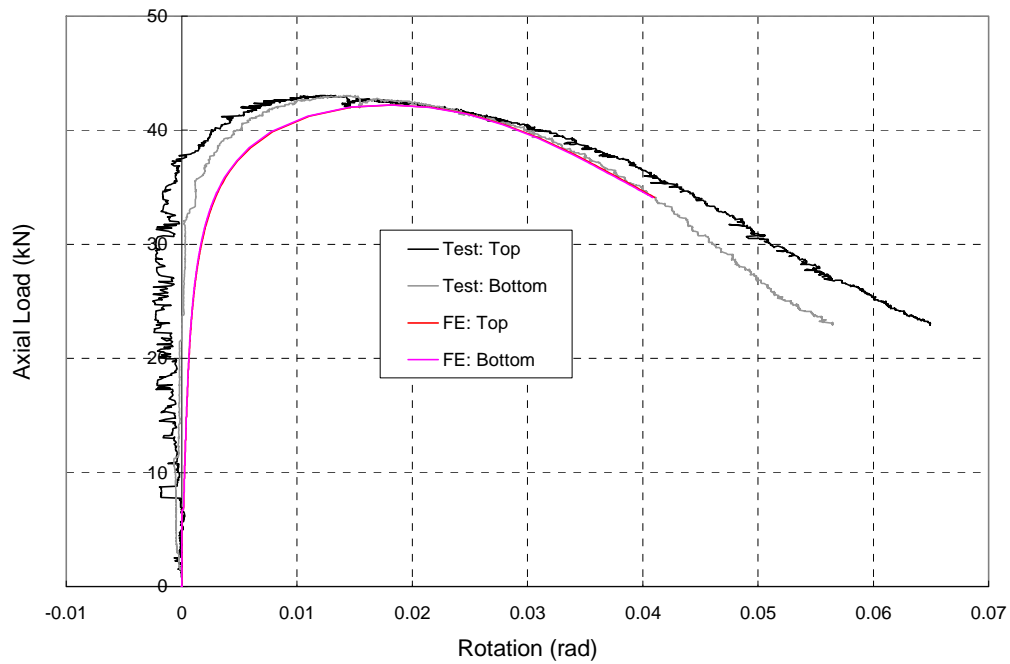


Figure C18.c. I404_1500_2 : Axial Load vs. End Rotations

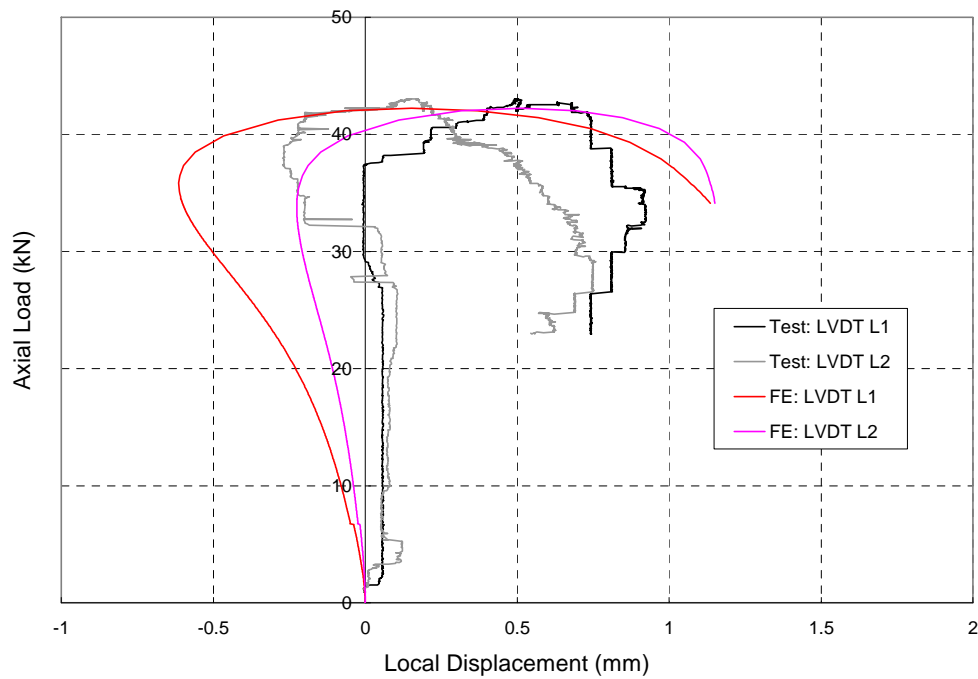


Figure C18.d. I404_1500_2 : Axial Load vs. Local Displacements

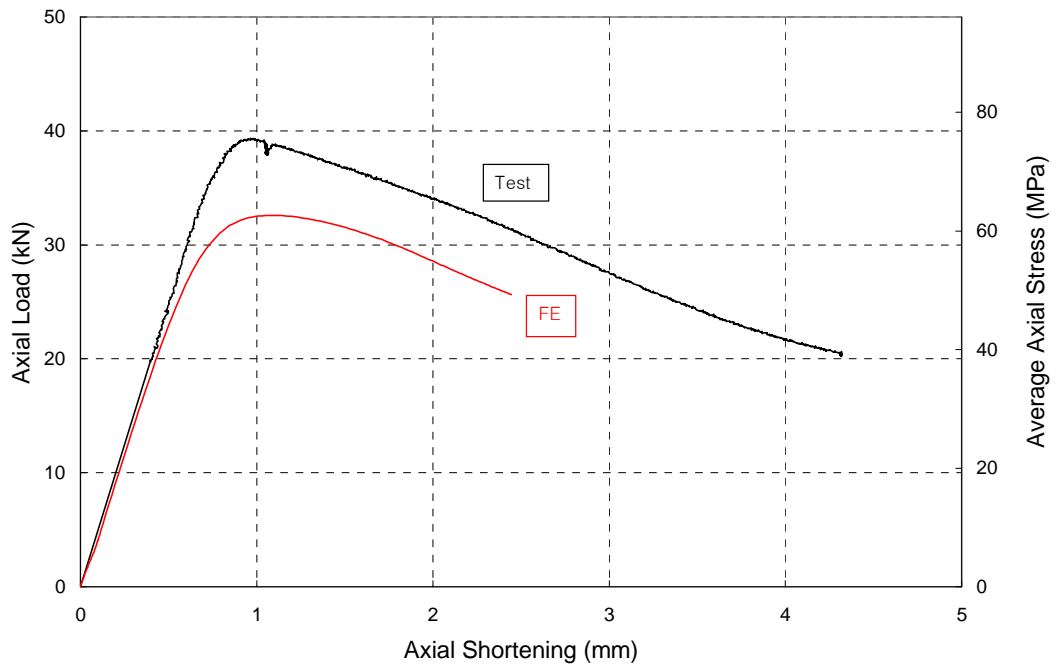


Figure C19.a. I404_2000_1 : Axial Load vs. Axial Shortening

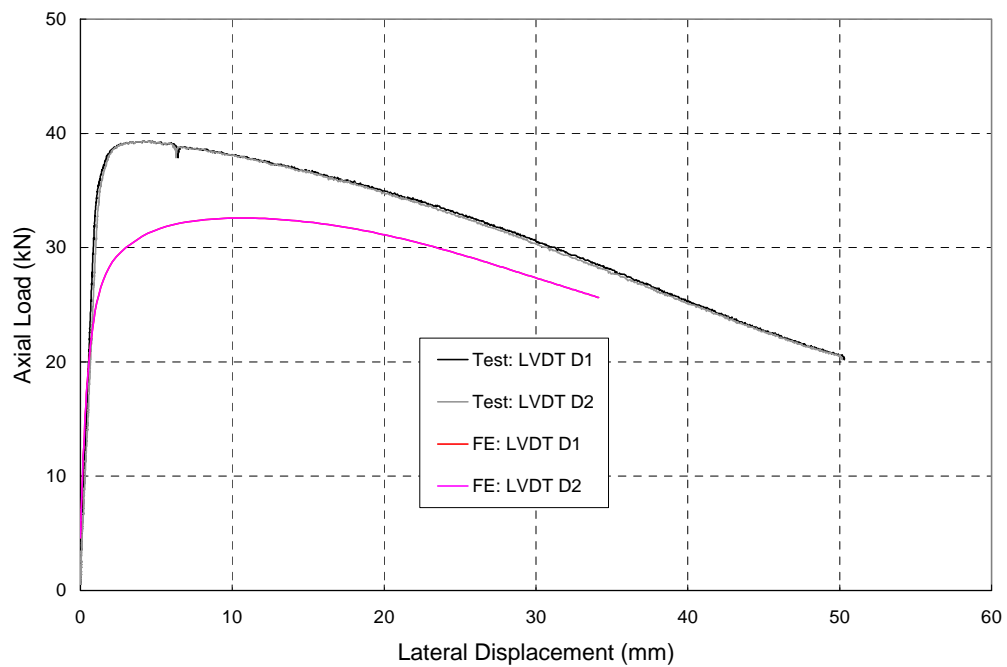


Figure C19.b. I404_2000_1 : Axial Load vs. Lateral Displacement

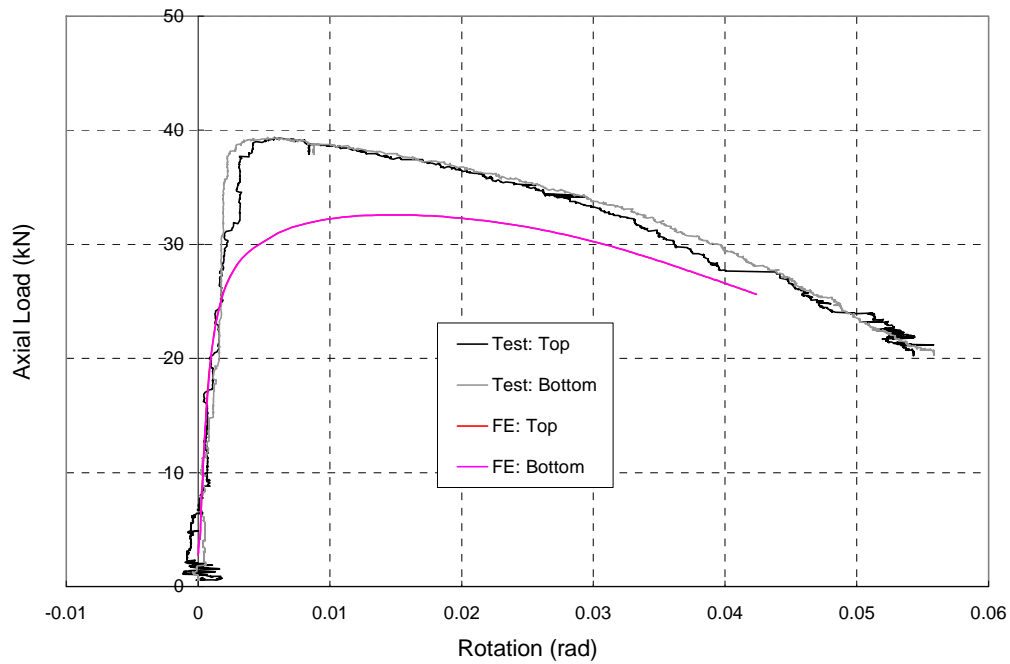


Figure C19.c. I404_2000_1 : Axial Load vs. End Rotations

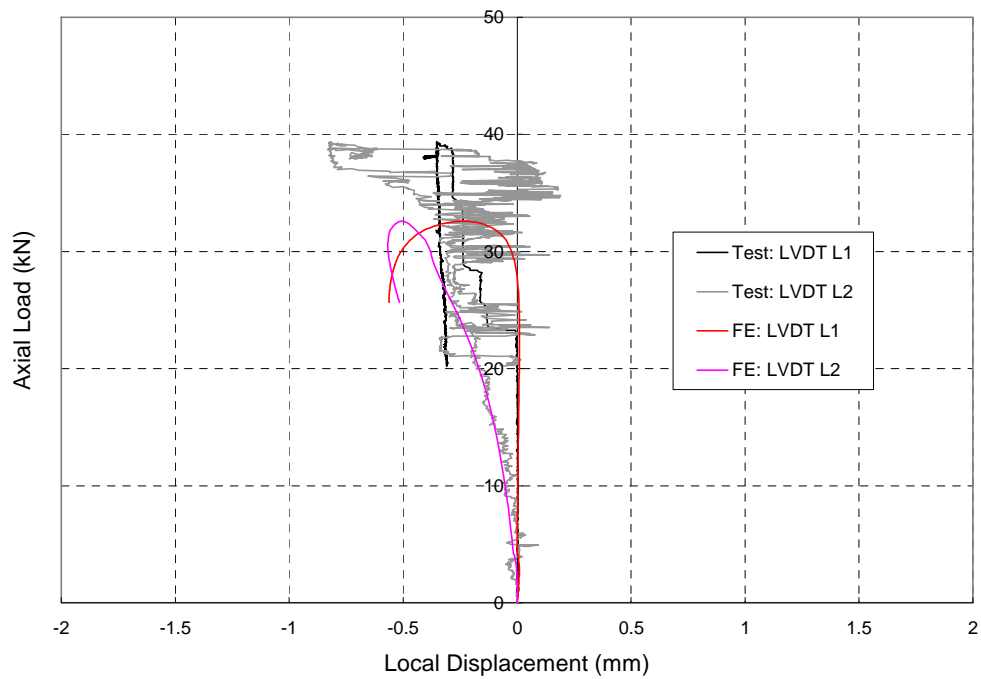


Figure C19.d. I404_2000_1 : Axial Load vs. Local Displacements

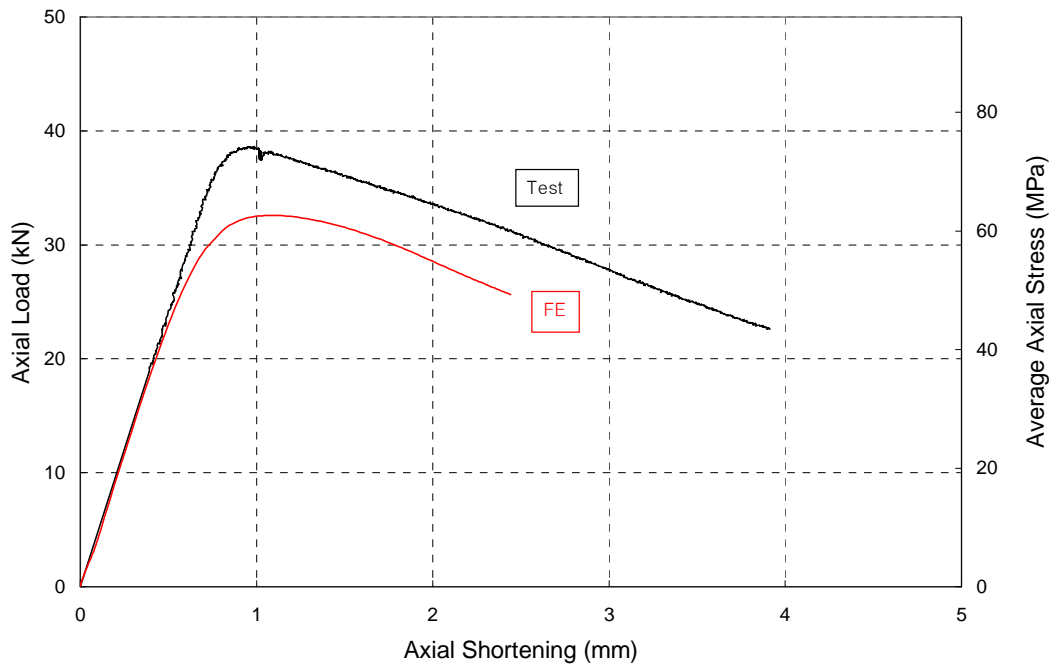


Figure C20.a. I404_2000_2 : Axial Load vs. Axial Shortening

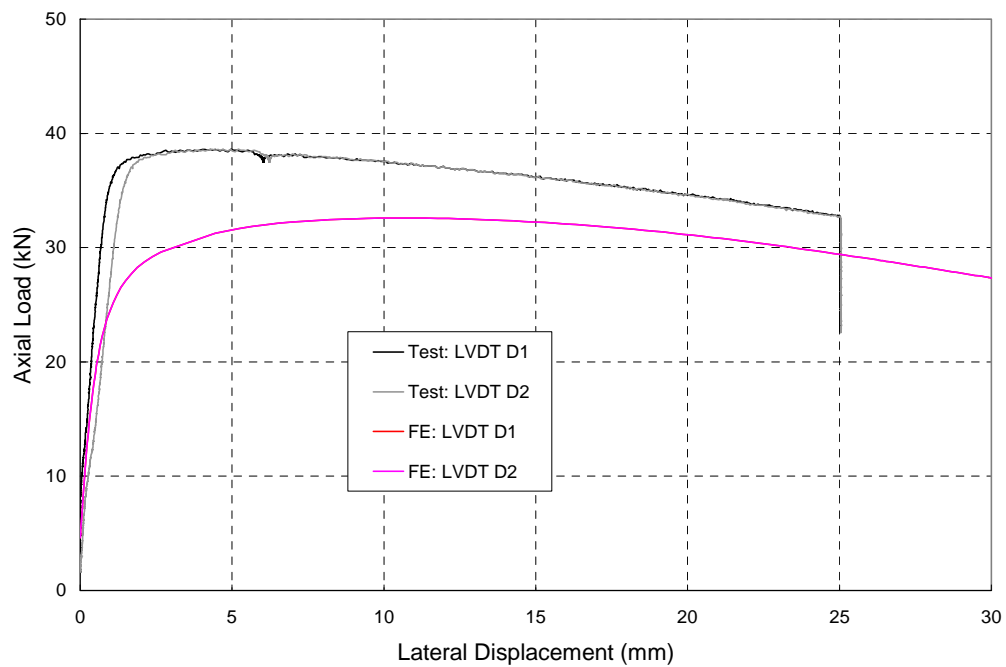


Figure C20.b. I404_2000_2 : Axial Load vs. Lateral Displacement

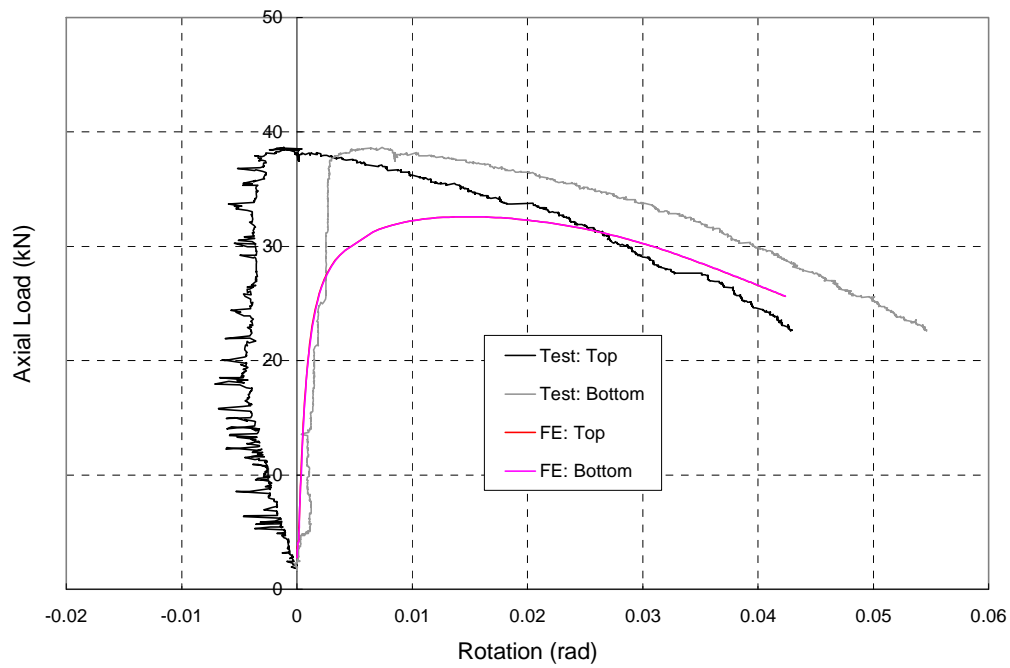


Figure C20.c. I404_2000_2 : Axial Load vs. End Rotations

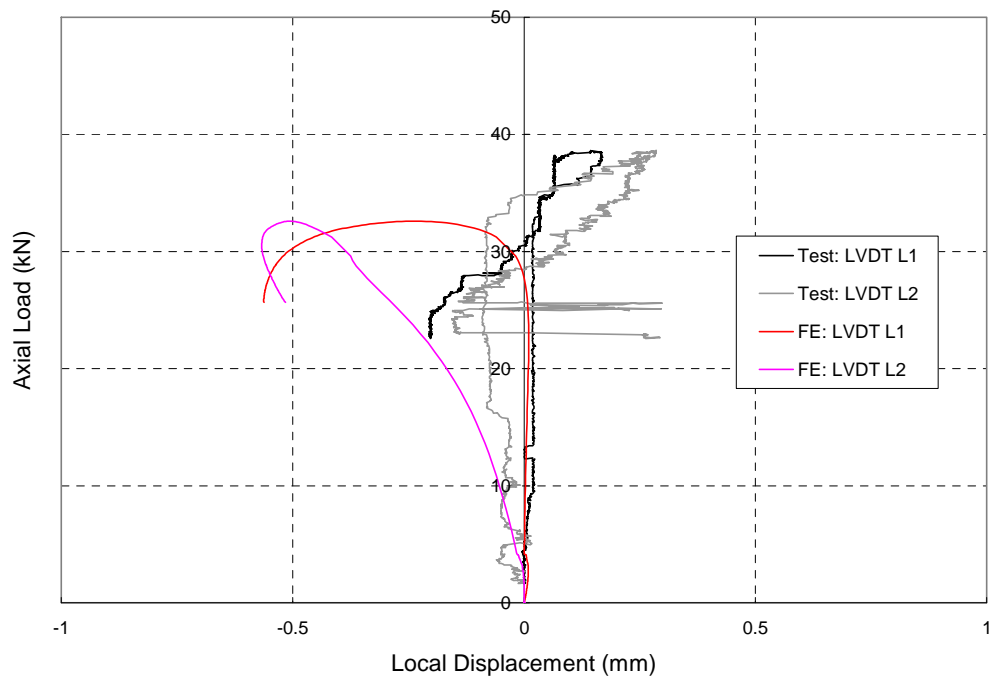


Figure C20.d. I404_2000_2 : Axial Load vs. Local Displacements

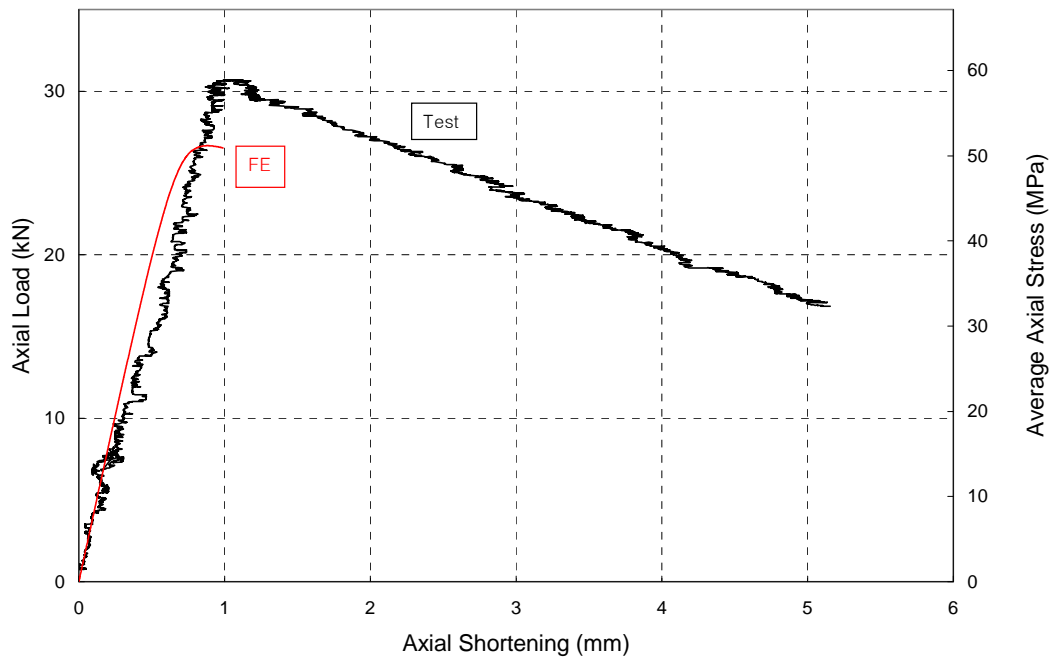


Figure C21.a. I404_2500_1 : Axial Load vs. Axial Shortening

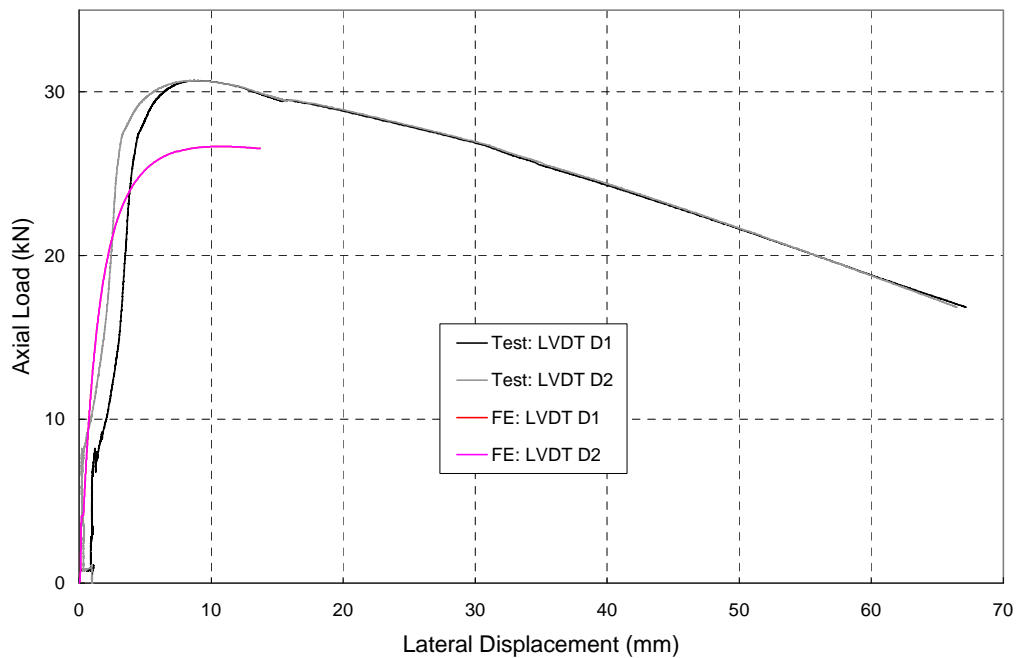


Figure C21.b. I404_2500_1 : Axial Load vs. Lateral Displacement

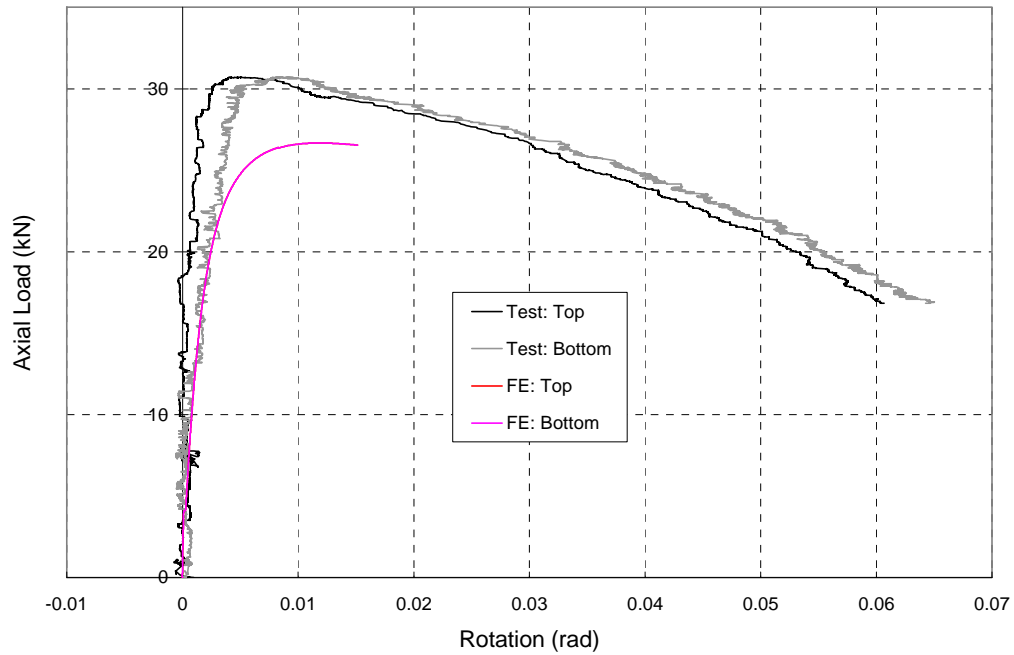


Figure C21.c. I404_2500_1 : Axial Load vs. End Rotations

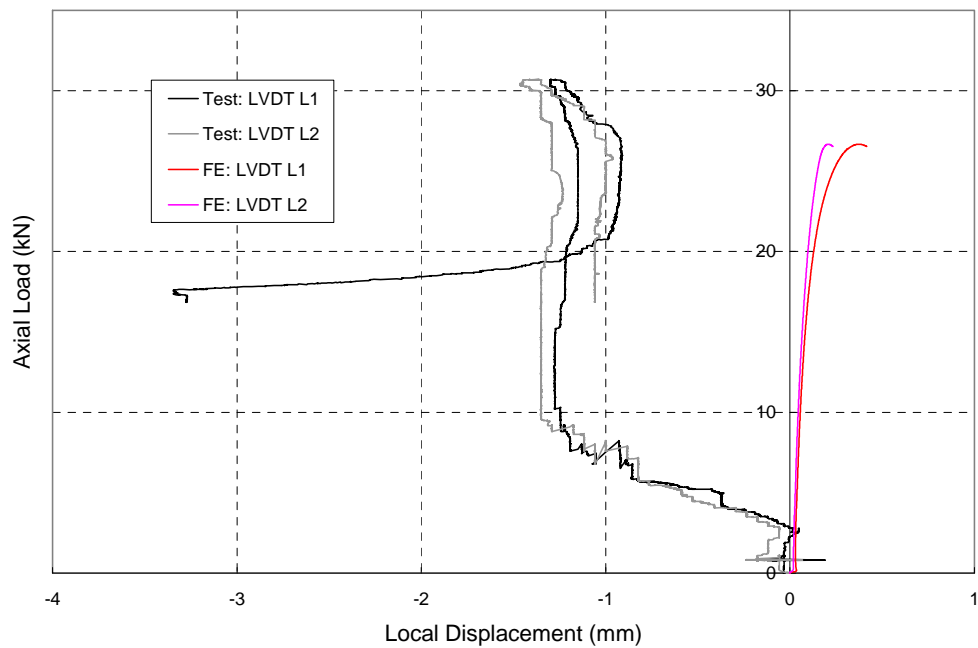


Figure C21.d. I404_2500_1 : Axial Load vs. Local Displacements

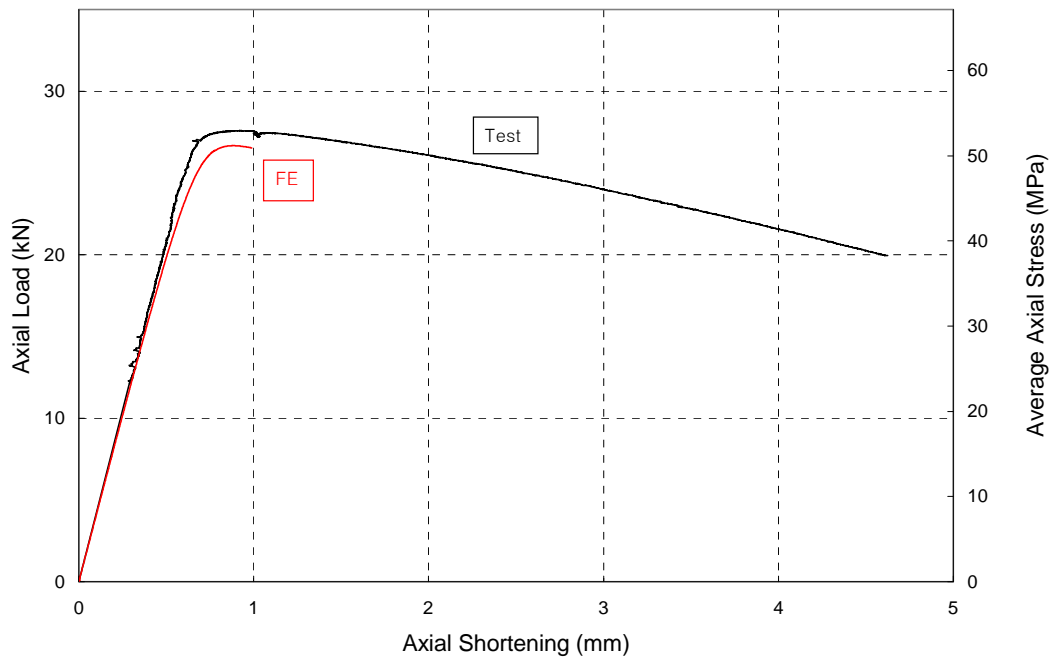


Figure C22.a. I404_2500_2 : Axial Load vs. Axial Shortening

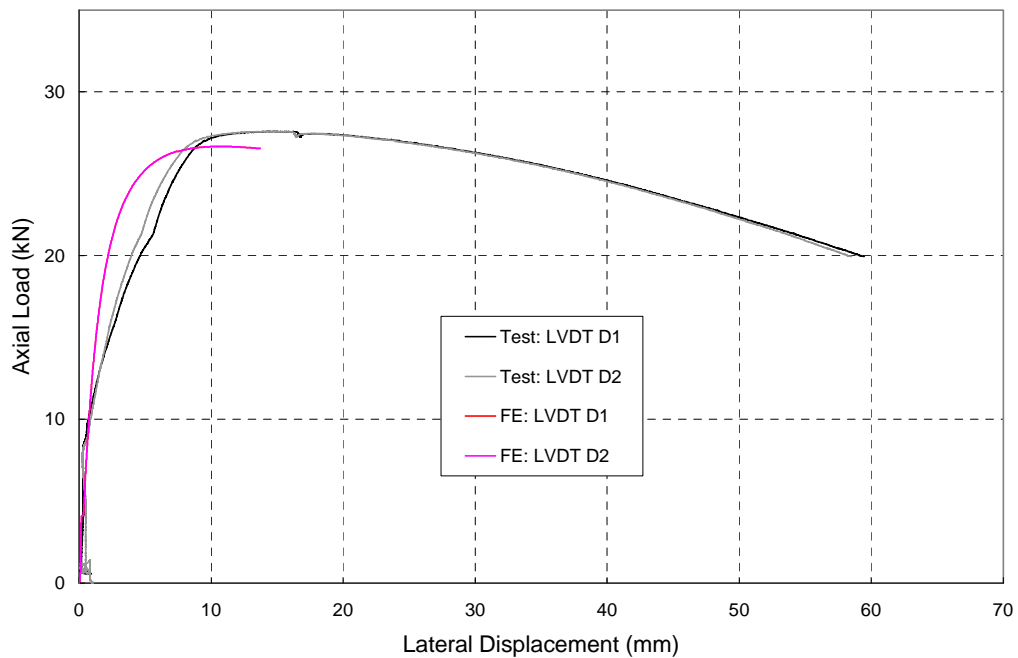


Figure C22.b. I404_2500_2 : Axial Load vs. Lateral Displacement

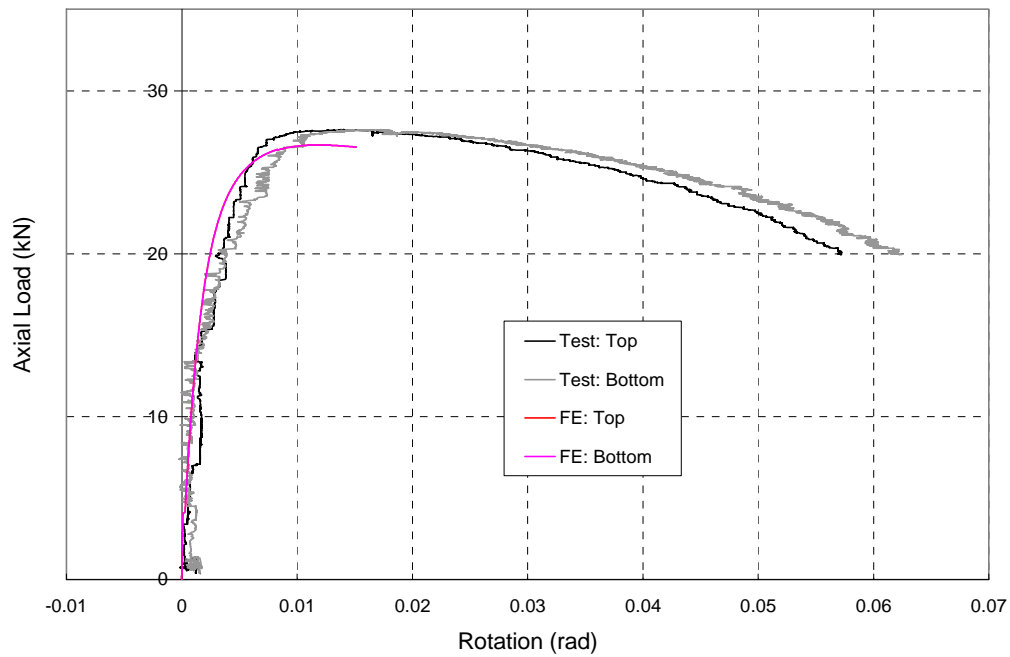


Figure C22.c. I404_2500_2 : Axial Load vs. End Rotations

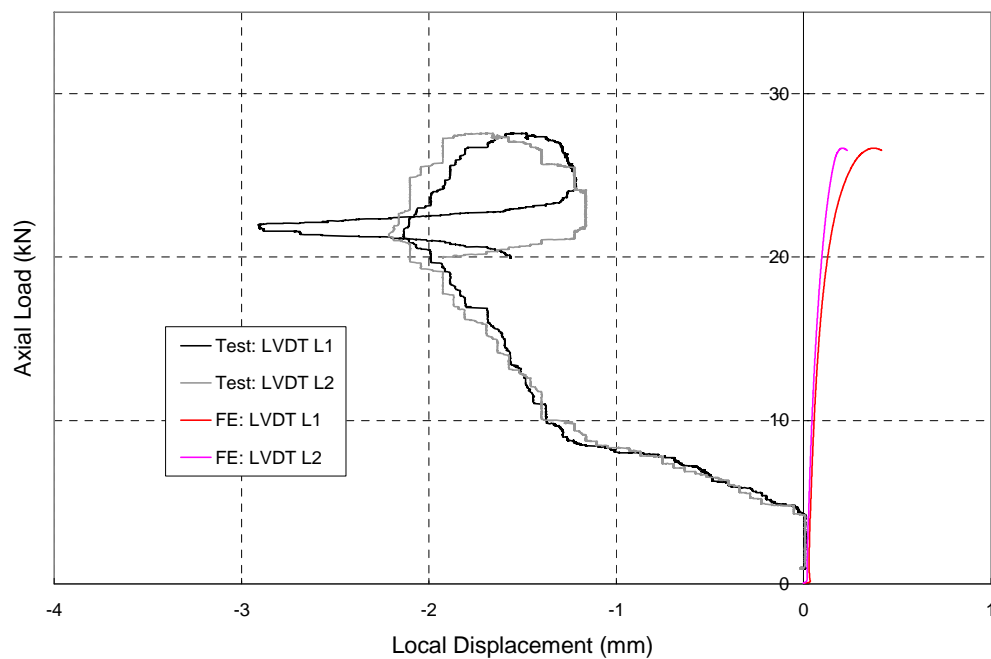


Figure C22.d. I404_2500_2 : Axial Load vs. Local Displacements

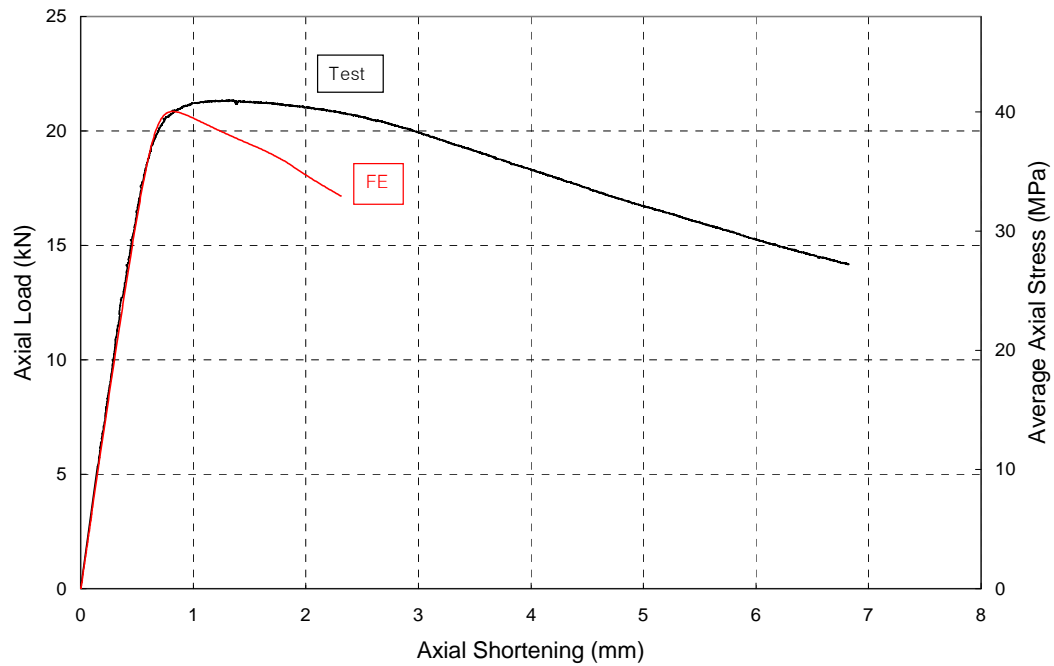


Figure C23.a. I404_3000_1 : Axial Load vs. Axial Shortening

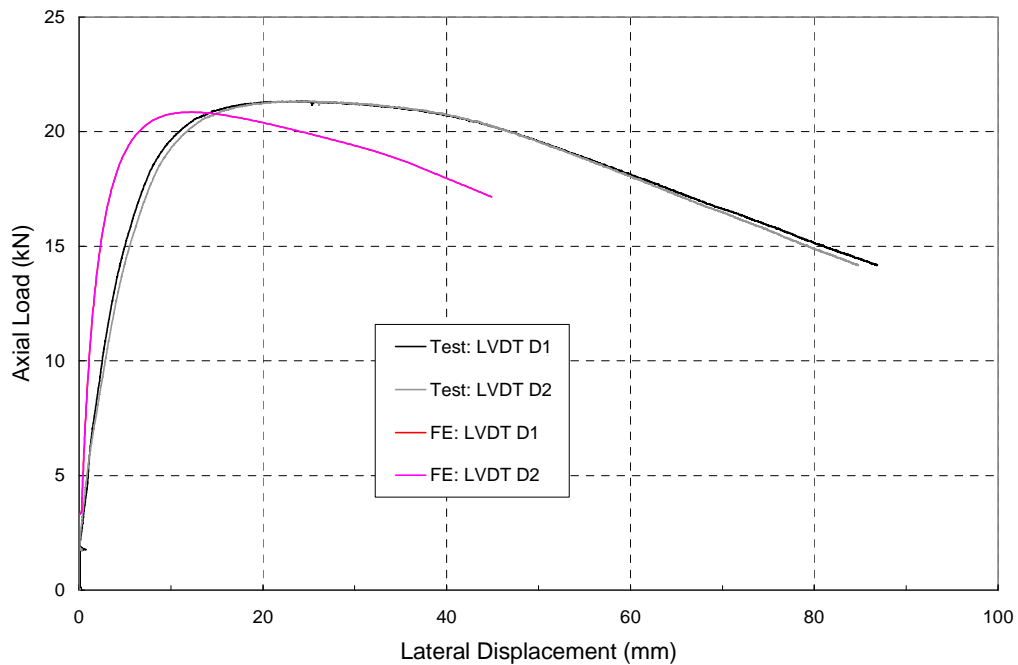


Figure C23.b. I404_3000_1 : Axial Load vs. Lateral Displacement

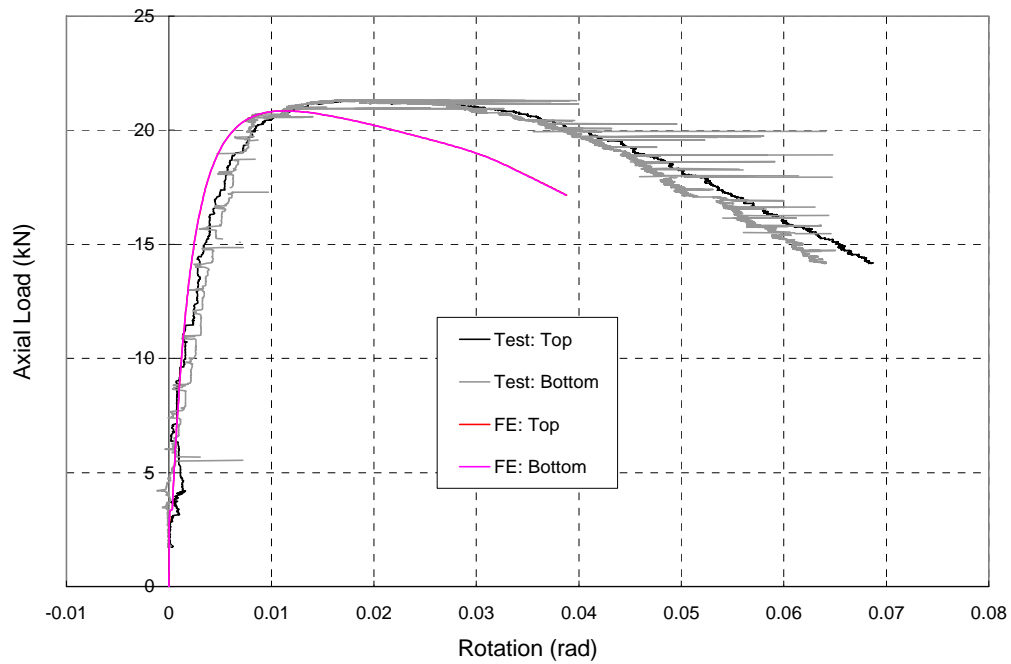


Figure C23.c. I404_3000_1 : Axial Load vs. End Rotations

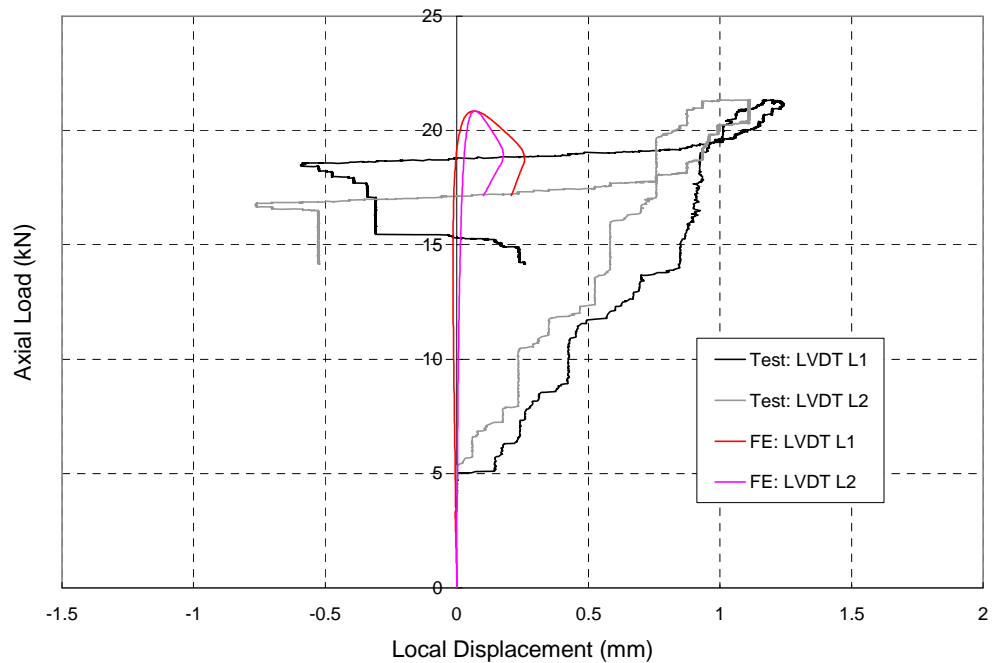


Figure C23.d. I404_3000_1 : Axial Load vs. Local Displacements

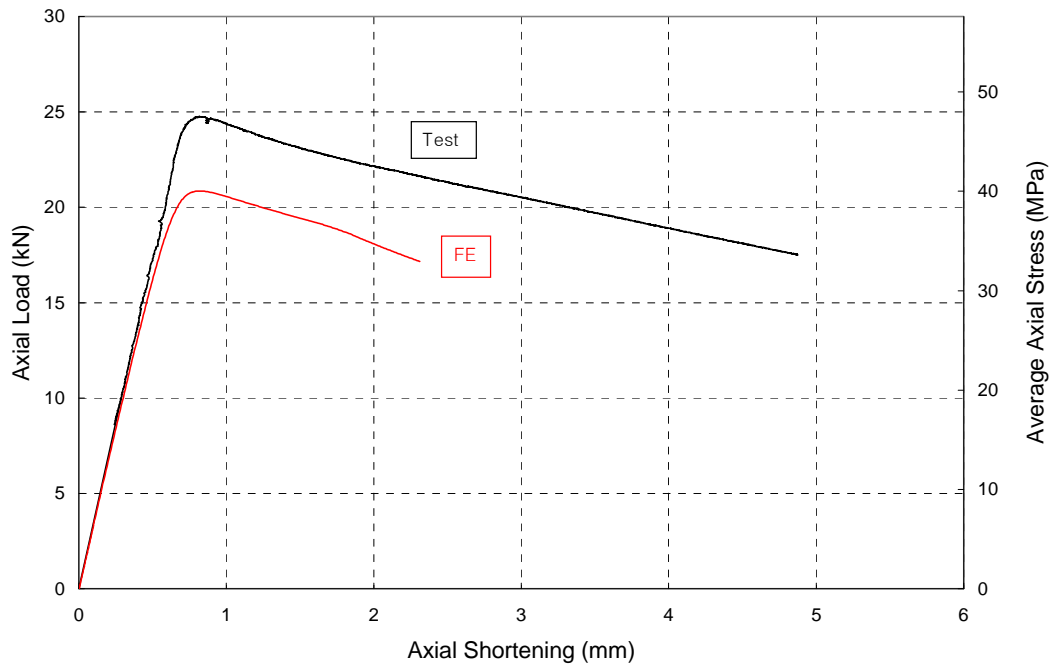


Figure C24.a. I404_3000_2 : Axial Load vs. Axial Shortening

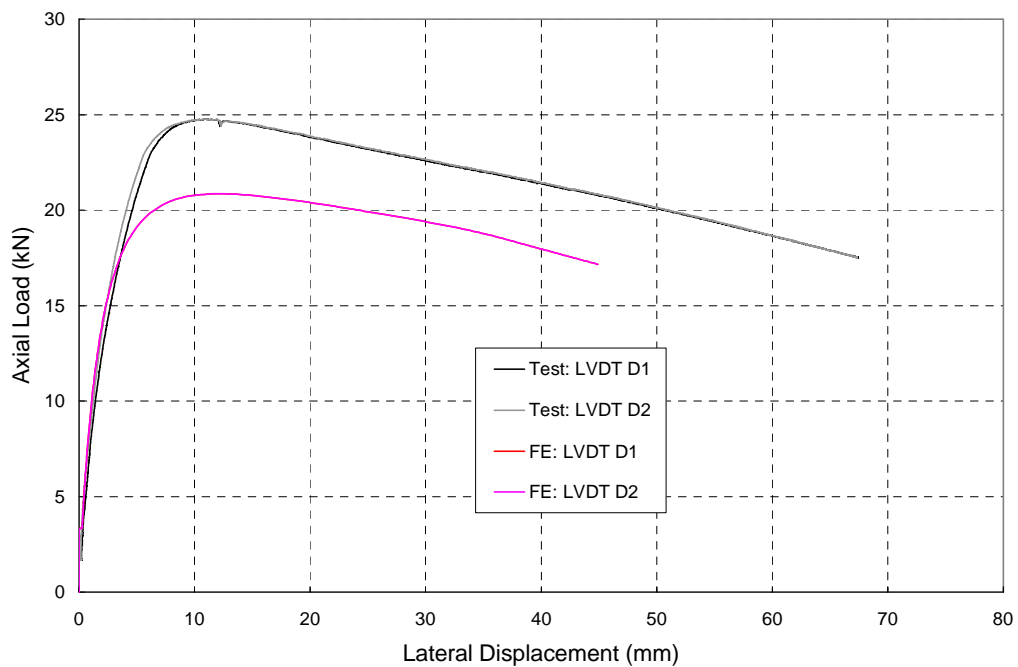


Figure C24.b. I404_3000_2 : Axial Load vs. Lateral Displacement

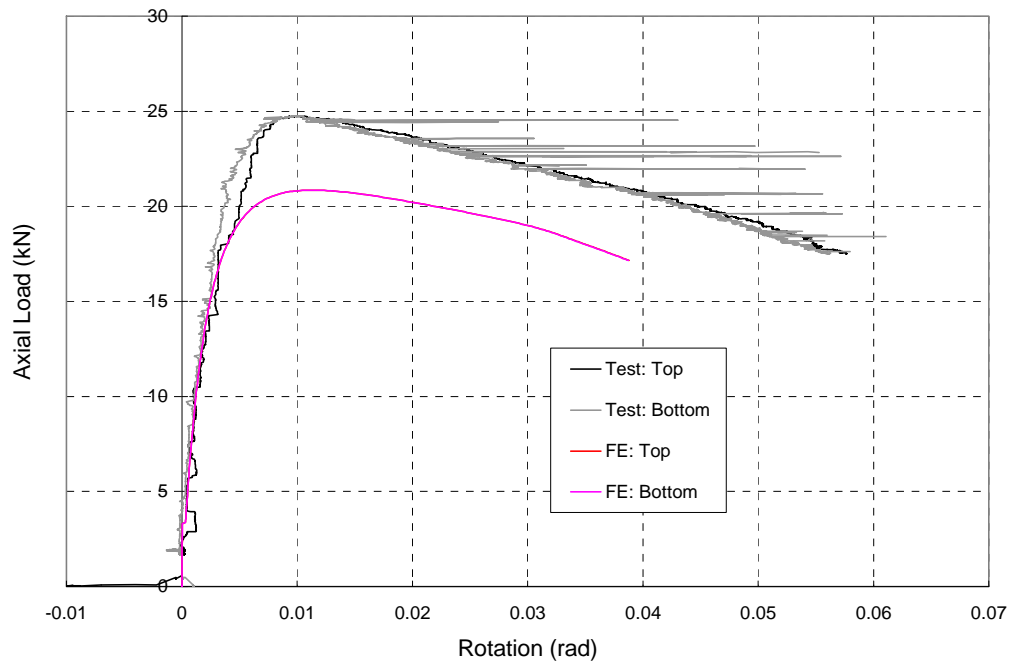


Figure C24.c. I404_3000_2 : Axial Load vs. End Rotations

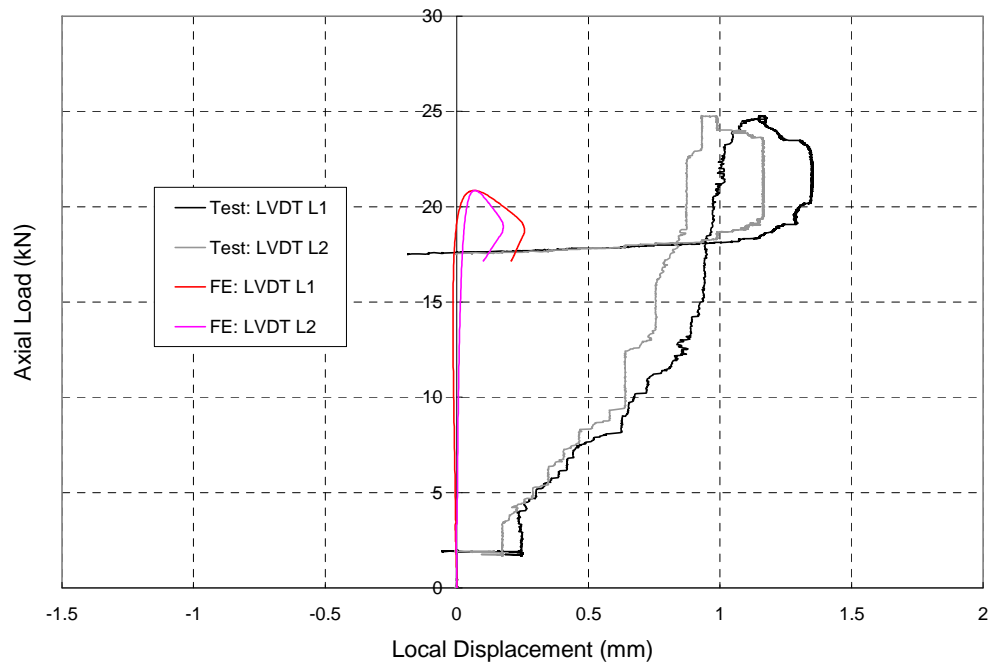


Figure C24.d. I404_3000_2 : Axial Load vs. Local Displacements

Appendix D

Appendix D contains all results of the parametric studies on lipped channels, plain channels, tubular sections and back-to-back channels. The experimental results presented in (Becque and Rasmussen 2006, 2007) are added for completeness. Together, this data forms the basis for the development of a direct strength approach for stainless steel compression members subject to local-overall interaction buckling.

All data are compared to the current Australian, European and North-American design guidelines for stainless steel. The comparison is presented in table format as well as graphically.

Table D1. Lipped Channels: 3Cr12

Specimen	FE/ Exp (1)	Material				Geometry								Slenderness			P _u			
		Alloy	$\sigma_{0.2\%}$	n	E ₀	L _c	d	b	c	r	t	v ₀	ω_d	σ_{cr}	λ_s	λ_o	Test	AS(t)	AS(d)	EC 3
		-	MPa	-	GP	mm	mm	mm	mm	mm	mm	mm	mm	MPa	-	-	kN	kN	kN	kN
C3Cr12_1.98_536	Exp	3Cr12	328	7.5	208	536	125.32	45.20	22.66	4.14	1.98	0.36	(2)	281.0	1.08	0.39	123.20	111.32	105.27	100.55
C3Cr12_1.98_758	Exp	3Cr12	328	7.5	208	758	125.32	45.20	22.66	4.14	1.98	0.51		281.0	1.08	0.55	120.36	103.25	96.77	97.04
C3Cr12_1.98_1056	Exp	3Cr12	328	7.5	208	1056	125.32	45.20	22.66	4.14	1.98	0.70		281.0	1.08	0.76	112.24	93.49	87.03	86.78
C3Cr12_1.98_1356	Exp	3Cr12	328	7.5	208	1356	125.32	45.20	22.66	4.14	1.98	0.90		281.0	1.08	0.98	100.18	84.40	76.80	73.53
C3Cr12_1.98_1656	Exp	3Cr12	328	7.5	208	1656	125.32	45.20	22.66	4.14	1.98	1.10		281.0	1.08	1.19	81.66	74.76	66.27	61.14
C3Cr12_1.98_1955	Exp	3Cr12	328	7.5	208	1955	125.32	45.20	22.66	4.14	1.98	1.30		281.0	1.08	1.41	65.92	64.50	56.74	50.62
C3Cr12_1.32_275	FE	3Cr12	328	7.5	208	275	125.32	35.00	22.66	4.14	1.32	0.18	0.63	127.0	1.61	0.25	60.04	57.03	57.03	47.12
C3Cr12_1.32_550	FE	3Cr12	328	7.5	208	550	125.32	35.00	22.66	4.14	1.32	0.37	0.63	127.0	1.61	0.50	53.85	51.49	48.68	46.96
C3Cr12_1.32_825	FE	3Cr12	328	7.5	208	825	125.32	35.00	22.66	4.14	1.32	0.55	0.63	127.0	1.61	0.75	46.48	46.16	43.31	43.02
C3Cr12_1.32_1100	FE	3Cr12	328	7.5	208	1100	125.32	35.00	22.66	4.14	1.32	0.73	0.63	127.0	1.61	1.00	39.50	40.99	37.47	36.39
C3Cr12_1.32_1370	FE	3Cr12	328	7.5	208	1370	125.32	35.00	22.66	4.14	1.32	0.91	0.63	127.0	1.61	1.25	33.61	35.59	31.72	30.12
C3Cr12_1.32_1645	FE	3Cr12	328	7.5	208	1645	125.32	35.00	22.66	4.14	1.32	1.10	0.63	127.0	1.61	1.50	28.29	29.77	26.53	24.69
C3Cr12_1.32_1920	FE	3Cr12	328	7.5	208	1920	125.32	35.00	22.66	4.14	1.32	1.28	0.63	127.0	1.61	1.75	22.72	24.49	22.27	20.36
C3Cr12_1.32_2195	FE	3Cr12	328	7.5	208	2195	125.32	35.00	22.66	4.14	1.32	1.46	0.63	127.0	1.61	2.00	18.43	20.36	18.87	16.99
C3Cr12_0.87_190	FE	3Cr12	328	7.5	208	190	125.32	24.00	22.66	4.14	0.87	0.13	0.62	57.0	2.40	0.25	28.46			20.89
C3Cr12_0.87_385	FE	3Cr12	328	7.5	208	385	125.32	24.00	22.66	4.14	0.87	0.26	0.62	57.0	2.40	0.50	25.71			20.89
C3Cr12_0.87_575	FE	3Cr12	328	7.5	208	575	125.32	24.00	22.66	4.14	0.87	0.38	0.62	57.0	2.40	0.75	21.73			19.66
C3Cr12_0.87_765	FE	3Cr12	328	7.5	208	765	125.32	24.00	22.66	4.14	0.87	0.51	0.62	57.0	2.40	1.00	18.31			17.36
C3Cr12_0.87_955	FE	3Cr12	328	7.5	208	955	125.32	24.00	22.66	4.14	0.87	0.64	0.62	57.0	2.40	1.25	15.51			14.65
C3Cr12_0.87_1150	FE	3Cr12	328	7.5	208	1150	125.32	24.00	22.66	4.14	0.87	0.77	0.62	57.0	2.40	1.50	13.06		12.61	12.28
C3Cr12_0.87_1340	FE	3Cr12	328	7.5	208	1340	125.32	24.00	22.66	4.14	0.87	0.89	0.62	57.0	2.40	1.75	11.01	11.78	10.73	10.33
C3Cr12_0.87_1530	FE	3Cr12	328	7.5	208	1530	125.32	24.00	22.66	4.14	0.87	1.02	0.62	57.0	2.40	2.00	9.33	9.90	9.17	8.75

(1) Experimental result or FE generated result. (2) Imperfections were modeled as experimentally measured.

Table D1 (Continued). Lipped Channels: 304

Specimen	Exp /FE (1)	Material				Geometry								Slenderness			P _u			
		Alloy	$\sigma_{0.2\%}$	n	E ₀	L _e	d	b	c	r	t	v ₀	ω_d	σ_{cr}	λ_s	λ_o	Test	AS(t)	AS(d)	EC 3
		-	MPa	-	GPa	mm	mm	mm	mm	mm	mm	mm	mm	MPa	-	-	kN	kN	kN	kN
C304_1.96_536	Exp	304	234	6.5	176	536	144.38	46.04	23.85	5.14	1.96	0.36	(2)	185.0	1.12	0.35	84.01	83.03	82.05	73.33
C304_1.96_722	Exp	304	234	6.5	176	772	144.38	46.04	23.85	5.14	1.96	0.51		185.0	1.12	0.51	78.77	75.88	70.97	72.16
C304_1.96_1002	Exp	304	234	6.5	176	1002	144.38	46.04	23.85	5.14	1.96	0.67		185.0	1.12	0.66	74.03	70.25	63.49	67.96
C304_1.96_1239	Exp	304	234	6.5	176	1239	144.38	46.04	23.85	5.14	1.96	0.83		185.0	1.12	0.81	70.67	65.15	57.00	61.80
C304_1.96_1475	Exp	304	234	6.5	176	1475	144.38	46.04	23.85	5.14	1.96	0.98		185.0	1.12	0.97	66.34	60.37	51.21	54.99
C304_1.96_1877	Exp	304	234	6.5	176	1877	144.38	46.04	23.85	5.14	1.96	1.25		185.0	1.12	1.23	53.55	52.21	42.52	44.17
C304_1.35_340	FE	304	234	6.5	176	340	144.38	40.00	24.00	5.14	1.35	0.23	0.65	85.0	1.66	0.25	49.16	46.29	46.29	38.29
C304_1.35_675	FE	304	234	6.5	176	675	144.38	40.00	24.00	5.14	1.35	0.45	0.65	85.0	1.66	0.50	41.62	41.31	38.83	38.20
C304_1.35_1015	FE	304	234	6.5	176	1015	144.38	40.00	24.00	5.14	1.35	0.68	0.65	85.0	1.66	0.75	34.42	36.45	32.52	35.03
C304_1.35_1350	FE	304	234	6.5	176	1350	144.38	40.00	24.00	5.14	1.35	0.90	0.65	85.0	1.66	1.00	29.23	32.22	27.48	29.75
C304_1.35_1690	FE	304	234	6.5	176	1690	144.38	40.00	24.00	5.14	1.35	1.13	0.65	85.0	1.66	1.25	24.27	27.99	23.10	24.55
C304_1.35_2025	FE	304	234	6.5	176	2025	144.38	40.00	24.00	5.14	1.35	1.35	0.65	85.0	1.66	1.50	20.05	23.75	19.52	20.18
C304_1.35_2365	FE	304	234	6.5	176	2365	144.38	40.00	24.00	5.14	1.35	1.58	0.65	85.0	1.66	1.75	16.22	19.76	16.56	16.64
C304_1.35_2705	FE	304	234	6.5	176	2705	144.38	40.00	24.00	5.14	1.35	1.80	0.65	85.0	1.66	2.00	12.12	16.49	14.17	13.88
C304_0.9_235	FE	304	234	6.5	176	235	144.38	27.00	27.00	5.14	0.90	0.16	0.64	39.0	2.45	0.25	24.62			17.77
C304_0.9_475	FE	304	234	6.5	176	475	144.38	27.00	27.00	5.14	0.90	0.32	0.64	39.0	2.45	0.50	20.59			17.77
C304_0.9_710	FE	304	234	6.5	176	710	144.38	27.00	27.00	5.14	0.90	0.47	0.64	39.0	2.45	0.75	16.72			16.73
C304_0.9_945	FE	304	234	6.5	176	945	144.38	27.00	27.00	5.14	0.90	0.63	0.64	39.0	2.45	1.00	13.94			14.77
C304_0.9_1185	FE	304	234	6.5	176	1185	144.38	27.00	27.00	5.14	0.90	0.79	0.64	39.0	2.45	1.25	11.63		11.40	12.36
C304_0.9_1420	FE	304	234	6.5	176	1420	144.38	27.00	27.00	5.14	0.90	0.95	0.64	39.0	2.45	1.50	9.82	11.71	9.76	10.40
C304_0.9_1655	FE	304	234	6.5	176	1655	144.38	27.00	27.00	5.14	0.90	1.10	0.64	39.0	2.45	1.75	8.28	9.88	8.37	8.76
C304_0.9_1895	FE	304	234	6.5	176	1895	144.38	27.00	27.00	5.14	0.90	1.26	0.64	39.0	2.45	2.00	7.32	8.33	7.19	7.39

(1) Experimental result or FE generated result. (2) Imperfections were modeled as experimentally measured.

Table D1 (Continued). Lipped Channels: 430

Specimen	Exp /FE (1)	Material				Geometry								Slenderness			P _u			
		Allo	$\sigma_{0.2\%}$	n	E ₀	L _e	d	b	c	r	t	v ₀	ω_d	σ_{cr}	λ_s	λ_o	Test	AS(t)	AS(d)	EC 3
		-	MPa	-	GPa	mm	mm	mm	mm	mm	mm	mm	mm	MPa	-	-	kN	kN	kN	kN
C430_1.13_535	Exp	430	265	6.5	193	535	79.73	33.29	22.16	3.00	1.13	0.36	(2)	215.0	1.11	0.46	40.45	36.19	35.15	34.41
C430_1.13_785	Exp	430	265	6.5	193	785	79.73	33.29	22.16	3.00	1.13	0.52		215.0	1.11	0.68	37.08	32.56	31.26	31.15
C430_1.13_1049	Exp	430	265	6.5	193	1049	79.73	33.29	22.16	3.00	1.13	0.70		215.0	1.11	0.90	33.29	29.01	27.28	26.33
C430_1.13_1314	Exp	430	265	6.5	193	1314	79.73	33.29	22.16	3.00	1.13	0.88		215.0	1.11	1.13	28.32	25.65	23.38	21.73
C430_1.13_1565	Exp	430	265	6.5	193	1565	79.73	33.29	22.16	3.00	1.13	1.04		215.0	1.11	1.35	23.08	22.32	19.88	17.96
C430_1.13_1967	Exp	430	265	6.5	193	1967	79.73	33.29	22.16	3.00	1.13	1.31		215.0	1.11	1.70	16.50	17.22	15.32	13.35
C430_0.78_210	FE	430	265	6.5	193	210	79.73	24.00	18.00	3.00	0.78	0.14	0.37	101.5	1.62	0.25	19.65	15.15	15.15	15.88
C430_0.78_415	FE	430	265	6.5	193	415	79.73	24.00	18.00	3.00	0.78	0.28	0.37	101.5	1.62	0.50	17.66	13.62	13.20	15.84
C430_0.78_625	FE	430	265	6.5	193	625	79.73	24.00	18.00	3.00	0.78	0.42	0.37	101.5	1.62	0.75	14.98	12.18	11.72	14.34
C430_0.78_835	FE	430	265	6.5	193	835	79.73	24.00	18.00	3.00	0.78	0.56	0.37	101.5	1.62	1.00	12.68	10.93	10.26	11.96
C430_0.78_1045	FE	430	265	6.5	193	1045	79.73	24.00	18.00	3.00	0.78	0.70	0.37	101.5	1.62	1.25	10.69	9.67	8.82	9.84
C430_0.78_1250	FE	430	265	6.5	193	1250	79.73	24.00	18.00	3.00	0.78	0.83	0.37	101.5	1.62	1.50	9.10	8.42	7.48	8.09
C430_0.78_1460	FE	430	265	6.5	193	1460	79.73	24.00	18.00	3.00	0.78	0.97	0.37	101.5	1.62	1.75	7.10	7.08	7.31	6.65
C430_0.78_1670	FE	430	265	6.5	193	1670	79.73	24.00	18.00	3.00	0.78	1.11	0.37	101.5	1.62	2.00	6.04	6.66	6.17	5.54
C430_0.51_140	FE	430	265	6.5	193	140	79.73	16.00	16.00	3.00	0.51	0.09	0.36	45.5	2.41	0.25	9.15			6.67
C430_0.51_280	FE	430	265	6.5	193	280	79.73	16.00	16.00	3.00	0.51	0.19	0.36	45.5	2.41	0.50	8.04			6.67
C430_0.51_420	FE	430	265	6.5	193	420	79.73	16.00	16.00	3.00	0.51	0.28	0.36	45.5	2.41	0.75	6.77			6.26
C430_0.51_560	FE	430	265	6.5	193	560	79.73	16.00	16.00	3.00	0.51	0.37	0.36	45.5	2.41	1.00	5.68			5.48
C430_0.51_700	FE	430	265	6.5	193	700	79.73	16.00	16.00	3.00	0.51	0.47	0.36	45.5	2.41	1.25	4.77			4.58
C430_0.51_835	FE	430	265	6.5	193	835	79.73	16.00	16.00	3.00	0.51	0.56	0.36	45.5	2.41	1.50	4.04		3.95	3.84
C430_0.51_975	FE	430	265	6.5	193	975	79.73	16.00	16.00	3.00	0.51	0.65	0.36	45.5	2.41	1.75	3.43	3.66	3.35	3.23
C430_0.51_1115	FE	430	265	6.5	193	1115	79.73	16.00	16.00	3.00	0.51	0.74	0.36	45.5	2.41	2.00	2.90	3.09	2.87	2.72

(1) Experimental result or FE generated result. (2) Imperfections were modeled as experimentally measured.

Table D2. Plain Channels: 3Cr12

(1) Experimental result or FE generated result.

Specimen	Exp /FE (1)	Material				Geometry							Slenderness			P _u			
		Alloy	$\sigma_{0.2\%}$	n	E ₀	L _e	d	b	r	t	v ₀	ω_d	σ_{cr}	λ_s	λ_0	Test	AS(t)	AS(d)	EC 3
		-	MPa	-	GPa	mm	mm	mm	mm	mm	mm	mm	MPa	-	-	kN	kN	kN	kN
PC3Cr12_1.80_250	FE	3Cr12	328	7.5	208	250	100.00	40.00	4.00	1.80	0.17	0.65	236.6	1.18	0.26	59.85	52.85	52.85	35.61
PC3Cr12_1.80_500	FE	3Cr12	328	7.5	208	500	100.00	40.00	4.00	1.80	0.33	0.65	236.6	1.18	0.51	55.79	49.74	48.33	35.59
PC3Cr12_1.80_750	FE	3Cr12	328	7.5	208	750	100.00	40.00	4.00	1.80	0.50	0.65	236.6	1.18	0.77	50.61	46.41	44.93	34.03
PC3Cr12_1.80_1000	FE	3Cr12	328	7.5	208	1000	100.00	40.00	4.00	1.80	0.67	0.65	236.6	1.18	1.03	44.52	42.96	41.09	30.83
PC3Cr12_1.80_1250	FE	3Cr12	328	7.5	208	1250	100.00	40.00	4.00	1.80	0.83	0.65	236.6	1.18	1.29	37.25	39.43	37.54	27.22
PC3Cr12_1.80_1500	FE	3Cr12	328	7.5	208	1500	100.00	40.00	4.00	1.80	1.00	0.65	236.6	1.18	1.54	30.09	36.11	33.52	24.17
PC3Cr12_1.80_1750	FE	3Cr12	328	7.5	208	1750	100.00	40.00	4.00	1.80	1.17	0.65	236.6	1.18	1.80	24.24	31.39	26.32	21.63
PC3Cr12_1.80_2000	FE	3Cr12	328	7.5	208	2000	100.00	40.00	4.00	1.80	1.33	0.65	236.6	1.18	2.06	19.81	24.12	21.02	18.26
PC3Cr12_1.20_250	FE	3Cr12	328	7.5	208	250	99.40	39.70	4.00	1.20	0.17	0.65	105.9	1.76	0.26	27.57	18.25	18.25	11.63
PC3Cr12_1.20_500	FE	3Cr12	328	7.5	208	500	99.40	39.70	4.00	1.20	0.33	0.65	105.9	1.76	0.51	23.81	17.54	17.24	11.63
PC3Cr12_1.20_750	FE	3Cr12	328	7.5	208	750	99.40	39.70	4.00	1.20	0.50	0.65	105.9	1.76	0.77	20.69	16.72	16.38	11.47
PC3Cr12_1.20_1000	FE	3Cr12	328	7.5	208	1000	99.40	39.70	4.00	1.20	0.67	0.65	105.9	1.76	1.03	18.27	15.82	15.36	11.14
PC3Cr12_1.20_1250	FE	3Cr12	328	7.5	208	1250	99.40	39.70	4.00	1.20	0.83	0.65	105.9	1.76	1.29	16.11	14.78	14.20	10.37
PC3Cr12_1.20_1500	FE	3Cr12	328	7.5	208	1500	99.40	39.70	4.00	1.20	1.00	0.65	105.9	1.76	1.54	13.92	13.59	13.04	9.50
PC3Cr12_1.20_1750	FE	3Cr12	328	7.5	208	1750	99.40	39.70	4.00	1.20	1.17	0.65	105.9	1.76	1.80	11.96	12.38	12.00	8.67
PC3Cr12_1.20_2000	FE	3Cr12	328	7.5	208	2000	99.40	39.70	4.00	1.20	1.33	0.65	105.9	1.76	2.06	10.37	11.44	11.19	7.92
PC3Cr12_0.85_250	FE	3Cr12	328	7.5	208	250	99.05	39.53	4.00	0.85	0.17	0.65	53.7	2.47	0.26	14.69	7.06	7.06	4.16
PC3Cr12_0.85_500	FE	3Cr12	328	7.5	208	500	99.05	39.53	4.00	0.85	0.33	0.65	53.7	2.47	0.51	12.02	6.88	6.80	4.16
PC3Cr12_0.85_750	FE	3Cr12	328	7.5	208	750	99.05	39.53	4.00	0.85	0.50	0.65	53.7	2.47	0.77	9.83	6.66	6.56	4.15
PC3Cr12_0.85_1000	FE	3Cr12	328	7.5	208	1000	99.05	39.53	4.00	0.85	0.67	0.65	53.7	2.47	1.03	8.31	6.41	6.27	4.10
PC3Cr12_0.85_1250	FE	3Cr12	328	7.5	208	1250	99.05	39.53	4.00	0.85	0.83	0.65	53.7	2.47	1.29	7.21	6.11	5.93	4.02
PC3Cr12_0.85_1500	FE	3Cr12	328	7.5	208	1500	99.05	39.53	4.00	0.85	1.00	0.65	53.7	2.47	1.54	6.24	5.75	5.57	3.85
PC3Cr12_0.85_1750	FE	3Cr12	328	7.5	208	1750	99.05	39.53	4.00	0.85	1.17	0.65	53.7	2.47	1.80	5.47	5.36	5.22	3.63
PC3Cr12_0.85_2000	FE	3Cr12	328	7.5	208	2000	99.05	39.53	4.00	0.85	1.33	0.65	53.7	2.47	2.06	4.88	4.99	4.88	3.40

Table D2 (Continued). Plain Channels: 304

(1) Experimental result or FE generated result.

Specimen	Exp /FE	Material				Geometry						Slenderness			P _u				
		Alloy	σ _{0.2%}	n	E ₀	L _e	d	b	r	t	v ₀	ω _d	σ _{cr}	λ _s	λ _o	Test	AS(t)	AS(d)	EC 3
	(1)	-	MPa	-	GPa	mm	mm	mm	mm	mm	mm	mm	MPa	-	-	kN	kN	kN	kN
PC304_1.80_250	FE	304	234	6.5	176	250	100.00	40.00	4.00	1.80	0.17	0.65	200.2	1.08	0.24	40.82	42.62	42.62	29.17
PC304_1.80_500	FE	304	234	6.5	176	500	100.00	40.00	4.00	1.80	0.33	0.65	200.2	1.08	0.47	38.17	40.10	38.94	29.17
PC304_1.80_750	FE	304	234	6.5	176	750	100.00	40.00	4.00	1.80	0.50	0.65	200.2	1.08	0.71	34.96	37.30	35.15	28.00
PC304_1.80_1000	FE	304	234	6.5	176	1000	100.00	40.00	4.00	1.80	0.67	0.65	200.2	1.08	0.94	30.89	34.70	32.12	25.61
PC304_1.80_1250	FE	304	234	6.5	176	1250	100.00	40.00	4.00	1.80	0.83	0.65	200.2	1.08	1.18	26.19	32.36	28.52	22.72
PC304_1.80_1500	FE	304	234	6.5	176	1500	100.00	40.00	4.00	1.80	1.00	0.65	200.2	1.08	1.42	21.53	30.13	22.91	20.25
PC304_1.80_1750	FE	304	234	6.5	176	1750	100.00	40.00	4.00	1.80	1.17	0.65	200.2	1.08	1.65	17.66	25.84	18.56	18.13
PC304_1.80_2000	FE	304	234	6.5	176	2000	100.00	40.00	4.00	1.80	1.33	0.65	200.2	1.08	1.89	14.66	20.25	15.21	15.17
PC304_1.20_250	FE	304	234	6.5	176	250	99.40	39.70	4.00	1.20	0.17	0.65	89.7	1.62	0.24	18.91	15.07	15.07	9.76
PC304_1.20_500	FE	304	234	6.5	176	500	99.40	39.70	4.00	1.20	0.33	0.65	89.7	1.62	0.47	16.49	14.46	14.21	9.76
PC304_1.20_750	FE	304	234	6.5	176	750	99.40	39.70	4.00	1.20	0.50	0.65	89.7	1.62	0.71	14.66	13.75	13.26	9.64
PC304_1.20_1000	FE	304	234	6.5	176	1000	99.40	39.70	4.00	1.20	0.67	0.65	89.7	1.62	0.94	13.20	13.01	12.34	9.37
PC304_1.20_1250	FE	304	234	6.5	176	1250	99.40	39.70	4.00	1.20	0.83	0.65	89.7	1.62	1.18	11.91	12.22	11.42	8.77
PC304_1.20_1500	FE	304	234	6.5	176	1500	99.40	39.70	4.00	1.20	1.00	0.65	89.7	1.62	1.42	10.47	11.36	10.53	8.05
PC304_1.20_1750	FE	304	234	6.5	176	1750	99.40	39.70	4.00	1.20	1.17	0.65	89.7	1.62	1.65	9.07	10.44	9.79	7.35
PC304_1.20_2000	FE	304	234	6.5	176	2000	99.40	39.70	4.00	1.20	1.33	0.65	89.7	1.62	1.89	7.90	9.68	9.16	6.71
PC304_0.85_250	FE	304	234	6.5	176	250	99.05	39.53	4.00	0.85	0.17	0.65	45.5	2.27	0.24	10.14	5.87	5.87	3.54
PC304_0.85_500	FE	304	234	6.5	176	500	99.05	39.53	4.00	0.85	0.33	0.65	45.5	2.27	0.47	8.40	5.71	5.64	3.54
PC304_0.85_750	FE	304	234	6.5	176	750	99.05	39.53	4.00	0.85	0.50	0.65	45.5	2.27	0.71	7.06	5.52	5.38	3.53
PC304_0.85_1000	FE	304	234	6.5	176	1000	99.05	39.53	4.00	0.85	0.67	0.65	45.5	2.27	0.95	6.14	5.31	5.12	3.48
PC304_0.85_1250	FE	304	234	6.5	176	1250	99.05	39.53	4.00	0.85	0.83	0.65	45.5	2.27	1.18	5.45	5.08	4.84	3.42
PC304_0.85_1500	FE	304	234	6.5	176	1500	99.05	39.53	4.00	0.85	1.00	0.65	45.5	2.27	1.42	4.74	4.81	4.55	3.29
PC304_0.85_1750	FE	304	234	6.5	176	1750	99.05	39.53	4.00	0.85	1.17	0.65	45.5	2.27	1.65	4.17	4.52	4.27	3.10
PC304_0.85_2000	FE	304	234	6.5	176	2000	99.05	39.53	4.00	0.85	1.33	0.65	45.5	2.27	1.89	3.73	4.22	4.01	2.91

Table D2 (Continued). Plain Channels: 430

(1) Experimental result or FE generated result.

Specimen	Exp /FE (1)	Material				Geometry							Slenderness			P _u			
		Alloy	$\sigma_{0.2\%}$	n	E ₀	L _e	d	b	r	t	v ₀	ω_d	σ_{cr}	λ_s	λ_o	Test	AS(t)	AS(d)	EC 3
		-	MPa	-	GPa	mm	mm	mm	mm	mm	mm	mm	MPa	-	-	kN	kN	kN	kN
PC430_1.80_250	FE	430	265	6.5	193	250	100.00	40.00	4.00	1.80	0.17	0.65	219.5	1.10	0.24	50.99	47.19	47.19	32.20
PC430_1.80_500	FE	430	265	6.5	193	500	100.00	40.00	4.00	1.80	0.33	0.65	219.5	1.10	0.48	48.13	44.40	43.72	32.20
PC430_1.80_750	FE	430	265	6.5	193	750	100.00	40.00	4.00	1.80	0.50	0.65	219.5	1.10	0.72	44.07	41.28	40.49	30.88
PC430_1.80_1000	FE	430	265	6.5	193	1000	100.00	40.00	4.00	1.80	0.67	0.65	219.5	1.10	0.96	38.91	38.32	37.31	28.19
PC430_1.80_1250	FE	430	265	6.5	193	1250	100.00	40.00	4.00	1.80	0.83	0.65	219.5	1.10	1.20	32.65	35.66	34.24	24.99
PC430_1.80_1500	FE	430	265	6.5	193	1500	100.00	40.00	4.00	1.80	1.00	0.65	219.5	1.10	1.44	26.40	33.12	29.85	22.25
PC430_1.80_1750	FE	430	265	6.5	193	1750	100.00	40.00	4.00	1.80	1.17	0.65	219.5	1.10	1.68	21.33	28.48	23.70	19.92
PC430_1.80_2000	FE	430	265	6.5	193	2000	100.00	40.00	4.00	1.80	1.33	0.65	219.5	1.10	1.92	17.56	22.24	19.06	16.70
PC430_1.20_250	FE	430	265	6.5	193	250	99.40	39.70	4.00	1.20	0.17	0.65	98.3	1.64	0.24	23.48	16.59	16.59	10.72
PC430_1.20_500	FE	430	265	6.5	193	500	99.40	39.70	4.00	1.20	0.33	0.65	98.3	1.64	0.48	20.75	15.93	15.78	10.72
PC430_1.20_750	FE	430	265	6.5	193	750	99.40	39.70	4.00	1.20	0.50	0.65	98.3	1.64	0.72	18.41	15.14	14.96	10.59
PC430_1.20_1000	FE	430	265	6.5	193	1000	99.40	39.70	4.00	1.20	0.67	0.65	98.3	1.64	0.96	16.48	14.32	14.06	10.29
PC430_1.20_1250	FE	430	265	6.5	193	1250	99.40	39.70	4.00	1.20	0.83	0.65	98.3	1.64	1.20	14.63	13.44	13.04	9.62
PC430_1.20_1500	FE	430	265	6.5	193	1500	99.40	39.70	4.00	1.20	1.00	0.65	98.3	1.64	1.44	12.64	12.47	12.01	8.83
PC430_1.20_1750	FE	430	265	6.5	193	1750	99.40	39.70	4.00	1.20	1.17	0.65	98.3	1.64	1.68	10.87	11.45	11.08	8.06
PC430_1.20_2000	FE	430	265	6.5	193	2000	99.40	39.70	4.00	1.20	1.33	0.65	98.3	1.64	1.92	9.44	10.61	10.34	7.36
PC430_0.85_250	FE	430	265	6.5	193	250	99.05	39.53	4.00	0.85	0.17	0.65	49.8	2.31	0.24	12.55	6.46	6.46	3.87
PC430_0.85_500	FE	430	265	6.5	193	500	99.05	39.53	4.00	0.85	0.33	0.65	49.8	2.31	0.48	10.50	6.29	6.25	3.87
PC430_0.85_750	FE	430	265	6.5	193	750	99.05	39.53	4.00	0.85	0.50	0.65	49.8	2.31	0.72	8.80	6.07	6.02	3.87
PC430_0.85_1000	FE	430	265	6.5	193	1000	99.05	39.53	4.00	0.85	0.67	0.65	49.8	2.31	0.96	7.56	5.84	5.76	3.82
PC430_0.85_1250	FE	430	265	6.5	193	1250	99.05	39.53	4.00	0.85	0.83	0.65	49.8	2.31	1.20	6.61	5.58	5.46	3.75
PC430_0.85_1500	FE	430	265	6.5	193	1500	99.05	39.53	4.00	0.85	1.00	0.65	49.8	2.31	1.44	5.75	5.29	5.14	3.60
PC430_0.85_1750	FE	430	265	6.5	193	1750	99.05	39.53	4.00	0.85	1.17	0.65	49.8	2.31	1.68	5.07	4.96	4.82	3.39
PC430_0.85_2000	FE	430	265	6.5	193	2000	99.05	39.53	4.00	0.85	1.33	0.65	49.8	2.31	1.92	4.55	4.63	4.51	3.18

Table D3a. Tubular Sections: Experimental Results

	Specimen	Exp /FE (1)	Material				Geometry						Slenderness			P _u			
			Alloy	$\sigma_{0.2\%}$	n	E ₀	L _e	d	b	r	t	v ₀	σ_{cr}	λ_s	λ_o	Test	AS(t)	AS(d)	EC 3
			-	MPa	-	GPa	mm	mm	mm	mm	mm	mm	MPa	-	-	kN	kN	kN	kN
Young/Liu (2003)	R1L0360	Exp	304	350	5.0	198	179.25	120.0	40.0	4.08	1.96	-	268.1	1.14	0.14	187.8	157.7	157.7	139.4
	R1L0360R	Exp	304	350	5.0	198	179.75	120.0	40.0	4.06	1.93	-	268.1	1.14	0.14	184.7	155.1	155.1	137.1
	R1L1200	Exp	304	350	5.0	198	599.25	120.1	40.1	4.07	1.94	L/4720	268.1	1.14	0.46	167.0	148.3	132.3	139.4
	R1L2000	Exp	304	350	5.0	198	1000.00	120.2	40.0	4.07	1.95	L/4500	268.1	1.14	0.77	141.3	121.0	103.9	119.1
	R1L2800	Exp	304	350	5.0	198	1400.00	120.2	40.0	4.08	1.97	L/1840	268.1	1.14	1.08	96.2	101.2	83.0	93.4
	R1L3600	Exp	304	350	5.0	198	1800.00	120.2	40.0	4.08	1.96	L/4720	268.1	1.14	1.39	83.7	83.4	66.1	69.6
	R3L0360	Exp	304	366	5.0	193	180.00	119.8	79.8	5.29	2.78	-	510.2	0.85	0.08	404.6	364.3	364.3	334.1
	R3L0360R	Exp	304	366	5.0	193	179.75	120.1	79.9	5.30	2.81	-	510.2	0.85	0.08	413.1	364.3	364.3	334.1
	R3L1200	Exp	304	366	5.0	193	599.75	119.9	80.1	5.31	2.82	L/9450	510.2	0.85	0.25	398.3	364.3	364.3	334.1
	R3L2000	Exp	304	366	5.0	193	1000.00	120.0	80.0	5.30	2.80	L/5250	510.2	0.85	0.42	394.0	356.9	313.7	334.1
	R3L2800	Exp	304	366	5.0	193	1399.75	119.4	79.9	5.36	2.92	L/1200	510.2	0.85	0.59	336.8	311.3	266.2	304.8
	R3L3600	Exp	304	366	5.0	193	1799.25	119.7	80.1	5.35	2.9	L/9450	510.2	0.85	0.76	310.6	276.9	229.6	269.3
Liu/Young (2002)	S1L0360	Exp	304	337	4.0	195	180.00	69.9	70.1	2.85	1.91	-	560.0	0.78	0.09	194.0	169.4	169.4	148.0
	S1L0360R	Exp	304	337	4.0	195	180.00	69.9	70.2	2.86	1.93	-	560.0	0.78	0.09	193.1	169.4	169.4	148.0
	S1L1200	Exp	304	337	4.0	195	599.50	69.9	70.0	2.86	1.92	L/4970	560.0	0.78	0.29	189.8	169.4	169.4	148.0
	S1L2000	Exp	304	337	4.0	195	1000.00	69.9	70.1	2.87	1.95	L/2100	560.0	0.78	0.48	188.1	160.4	134.9	144.4
	S1L2800	Exp	304	337	4.0	195	1400.00	69.9	70.2	2.86	1.92	L/4410	560.0	0.78	0.67	159.2	130.7	110.3	127.7
	S1L3600	Exp	304	337	4.0	195	1799.50	70.0	70.1	2.86	1.93	L/950	560.0	0.78	0.86	115.0	109.2	92.0	108.9

(1) Experimental result or FE generated result.

Table D3a (Continued). Tubular Sections: Experimental Results

	Specimen	Exp /FE (1)	Material				Geometry						Slenderness			P_u			
			Alloy	$\sigma_{0.2\%}$	n	E_0	L_e	d	b	r	t	v_0	σ_{cr}	λ_s	λ_o	Test	AS(t)	AS(d)	EC 3
			-	MPa	-	GPa	mm	mm	mm	mm	mm	mm	MPa	-	-	kN	kN	kN	kN
Young/Lui (2006)	SHS2L300	Exp	Duplex	622	5.0	200	150	50.1	50.3	2.29	1.58	-	731.0	0.92	0.13	175.7	164.0	164.0	140.7
	SHS2L300R	Exp	Duplex	622	5.0	200	150	50.0	50.3	2.27	1.55	-	731.0	0.92	0.13	177.6	164.0	164.0	140.7
	SHS2L650	Exp	Duplex	622	5.0	200	325	50.3	50.2	2.30	1.60	L/2326	731.0	0.92	0.29	181.0	164.0	164.0	140.7
	SHS2L1000	Exp	Duplex	622	5.0	200	500	50.2	50.2	2.27	1.54	L/1358	731.0	0.92	0.45	175.1	164.0	164.0	140.7
	SHS2L1500	Exp	Duplex	622	5.0	200	750.5	50.0	50.2	2.27	1.53	L/1790	731.0	0.92	0.67	156.8	145.0	133.5	124.1
	SHS2L2000	Exp	Duplex	622	5.0	200	1000	50.1	50.2	2.27	1.53	L/1500	731.0	0.92	0.90	124.7	126.5	114.7	104.3
	SHS2L2500	Exp	Duplex	622	5.0	200	1250	50.2	50.2	2.27	1.54	L/775	731.0	0.92	1.12	95.1	106.8	93.0	84.1
	SHS2L3000	Exp	Duplex	622	5.0	200	1500	50.1	50.2	2.27	1.54	L/872	731.0	0.92	1.35	72.4	87.1	74.2	66.6
	RHS1L600	Exp	Duplex	486	6.0	212	300	140.0	78.8	8.54	3.08	L/4295	501.0	0.98	0.14	558.2	536.4	536.4	488.9
	RHS1L1400	Exp	Duplex	486	6.0	212	700	139.9	79.9	8.54	3.07	L/7349	501.0	0.98	0.32	553.1	536.4	536.4	488.9
	RHS1L2200	Exp	Duplex	486	6.0	212	1100	139.9	80.0	8.53	3.07	L/5588	501.0	0.98	0.51	525.1	497.4	491.0	474.0
	RHS1L3000	Exp	Duplex	486	6.0	212	1500	140.1	79.9	8.51	3.01	L/3236	501.0	0.98	0.69	513.5	444.4	420.7	422.5
	RHS2L600	Exp	Duplex	536	5.0	208	300	160.1	80.8	7.73	2.87	L/7874	331.0	1.27	0.14	537.3	542.8	542.8	483.2
	RHS2L1400	Exp	Duplex	536	5.0	208	700	160.1	80.8	7.73	2.87	L/5512	331.0	1.27	0.33	537.2	542.8	542.8	483.2
	RHS2L2200	Exp	Duplex	536	5.0	208	1100	160.1	80.8	7.74	2.88	L/6663	331.0	1.27	0.52	515.3	514.4	489.7	474.5
	RHS2L3000	Exp	Duplex	536	5.0	208	1500	160.4	80.8	7.74	2.87	L/3937	331.0	1.27	0.71	439.4	450.4	423.0	427.0
Tajiri-Salmi (1995)	CC-1-RHS-2	Exp	304	305	5.0	205	524	150.7	100.4	4.44	2.89	L/1000	350.0	0.93	0.15	372.0	375.1	375.1	329.6
	CC-2-RHS-2	Exp	304	305	5.0	205	2648	150.2	100.3	4.44	2.89	L/1000	350.0	0.93	0.78	349.0	272.6	236.1	268.3
	CC-3-RHS-2	Exp	304	305	5.0	205	4304	150.1	100.3	4.44	2.89	L/1000	350.0	0.93	1.27	254.0	199.4	153.2	167.9
	CC-4-RHS-2	Exp	304	305	5.0	205	5952	150.4	100.3	4.44	2.89	L/1000	350.0	0.93	1.75	189.0	130.4	99.3	103.0

(1) Experimental result or FE generated result.

Table D3a (Continued). Tubular Sections: Experimental Results

	Specimen	Exp /FE (1)	Material				Geometry						Slenderness			P _u			
			Alloy	$\sigma_{0.2\%}$	n	E ₀	L _e	d	b	r	t	v ₀	σ_{cr}	λ_s	λ_o	Test	AS(t)	AS(d)	EC 3
			-	MPa	-	GPa	mm	mm	mm	mm	mm	mm	MPa	-	-	kN	kN	kN	kN
Gardner/Talja/Baddoo	RHS80x80x3-A	Exp	301LN	520	4.0	187	1148	80.1	80.3	5.54	3.08	1-1.5	1084	0.69	0.62	407.0	422.7	320.1	398.0
	RHS80x80x3-A	Exp	301LN	520	4.0	187	1850	80.1	80.3	5.54	3.08	1-1.5	1084	0.69	0.99	267.0	292.6	223.5	276.3
	RHS80x80x3-A	Exp	301LN	520	4.0	187	2849	80.1	80.3	5.54	3.08	1-1.5	1084	0.69	1.53	150.0	178.1	135.8	150.4
	RHS80x80x3-C850	Exp	301LN	651	4.0	173	1147	80.4	80.0	4.53	3.06	1-1.5	978	0.82	0.72	518.0	507.4	362.9	423.3
	RHS80x80x3-C850	Exp	301LN	651	4.0	173	1847	80.4	80.0	4.53	3.06	1-1.5	978	0.82	1.16	332.0	330.8	240.2	275.8
	RHS80x80x3-C850	Exp	301LN	651	4.0	173	2848	80.4	80.0	4.53	3.06	1-1.5	978	0.82	1.78	162.0	178.8	136.8	143.7
	RHS100x100x3-A	Exp	301LN	481	4.0	195	1447	100.0	100.1	4.04	3.07	1-1.5	700	0.83	0.58	560.0	487.8	389.9	423.9
	RHS100x100x3-A	Exp	301LN	481	4.0	195	2250	100.0	100.1	4.04	3.07	1-1.5	700	0.83	0.90	406.0	365.2	285.9	329.9
	RHS100x100x3-A	Exp	301LN	481	4.0	195	3546	100.0	100.1	4.04	3.07	1-1.5	700	0.83	1.42	220.0	228.2	175.7	191.4
	RHS100x100x3-C850	Exp	301LN	607	4.0	184	1447	100.3	100.0	4.53	3.05	1-1.5	652	0.96	0.67	634.0	551.5	439.3	464.4
	RHS100x100x3-C850	Exp	301LN	607	4.0	184	2250	100.3	100.0	4.53	3.05	1-1.5	652	0.96	1.04	427.0	422.1	313.0	342.9
	RHS100x100x3-C850	Exp	301LN	607	4.0	184	3552	100.3	100.0	4.53	3.05	1-1.5	652	0.96	1.65	222.0	236.8	179.7	186.7
Gardner/Nethercot (2003)	SHS 100x100x2-LC-	Exp	304	370	4.7	207	2000.	99.8	99.9	2.23	1.86	0.1	267	1.18	0.67	176.0	162.6	143.8	149.4
	SHS 100x100x3-LC-	Exp	304	379	3.8	209	2000.	100.1	100.2	2.83	2.92	0.1	635	0.77	0.68	350.0	308.1	257.8	295.4
	SHS 150x150x4-LC-	Exp	304	294	4.5	195	1999.	150.4	150.0	7.69	3.77	0.0	468	0.79	0.42	692.0	596.5	533.8	541.2
	RHS 100x50x2-LCJ-	Exp	304	370	5.2	206	2000.	100.0	50.1	3.22	1.83	0.6	338	1.05	0.75	157.0	123.1	104.6	149.3
	RHS 100x50x3-LC-2m	Exp	304	455	4.1	201	2000.	100.1	50.1	4.54	2.87	1.1	828	0.74	1.46	113.0	144.2	111.3	122.5
	RHS 120x80x3-LC-2m	Exp	304	429	4.2	197	1999.	120.0	80.2	6.06	2.91	1.1	548	0.88	0.90	313.0	297.8	240.5	281.8
	RHS 150x100x4-LC-	Exp	304	319	4.7	200	1999.	149.8	99.9	7.50	3.79	0.1	607	0.72	0.62	515.0	443.9	379.6	454.0
	RHS 100x50x2-LC-1m	Exp	304	370	5.2	206	1000.	99.8	50.0	3.21	1.82	0.1	334	1.05	0.64	163.0	131.1	113.3	129.7
	RHS 100x50x3-LC-1m	Exp	304	455	4.1	201	1000.	100.1	50.0	4.53	2.86	1.0	822	0.74	0.73	304.0	275.1	219.0	260.2
	RHS 120x80x3-LC-1m	Exp	304	429	4.2	197	1000.	120.0	80.2	6.03	2.86	1.0	529	0.90	0.45	448.0	422.8	352.5	382.2

(1) Experimental result or FE generated result.

Table D3b. Tubular Sections: FE Results

(1) Experimental result or FE generated result.

Specimen	Exp /FE (1)	Material				Geometry							Slenderness			P _u			
		Alloy	$\sigma_{0.2\%}$	n	E ₀	L _e	d	b	r	t	v ₀	ω_d	σ_{cr}	λ_s	λ_o	Test	AS(t)	AS(d)	EC 3
		-	MPa	-	GPa	mm	mm	mm	mm	mm	mm	mm	MPa	-	-	kN	kN	kN	kN
SHS304L_1.70_500	FE	304L	415	3.3	195	500	78.7	78.7	4.25	1.70	0.33	0.55	345	1.10	0.24	159.95	172.06	172.06	146.19
SHS304L_1.70_1000	FE	304L	415	3.3	195	1000	78.7	78.7	4.25	1.70	0.67	0.55	345	1.10	0.47	150.56	172.06	145.34	146.19
SHS304L_1.70_1450	FE	304L	415	3.3	195	1450	78.7	78.7	4.25	1.70	0.97	0.55	345	1.10	0.68	137.12	144.92	123.88	131.21
SHS304L_1.70_2000	FE	304L	415	3.3	195	2000	78.7	78.7	4.25	1.70	1.33	0.55	345	1.10	0.94	119.71	118.38	103.27	108.95
SHS304L_1.70_2450	FE	304L	415	3.3	195	2450	78.7	78.7	4.25	1.70	1.63	0.55	345	1.10	1.15	102.50	101.44	85.29	90.02
SHS304L_1.70_3000	FE	304L	415	3.3	195	3000	78.7	78.7	4.25	1.70	2.00	0.55	345	1.10	1.41	79.12	80.13	67.05	69.80
SHS304L_1.70_3450	FE	304L	415	3.3	195	3450	78.7	78.7	4.25	1.70	2.30	0.55	345	1.10	1.62	60.16	66.39	55.48	56.83
SHS304L_1.70_4000	FE	304L	415	3.3	195	4000	78.7	78.7	4.25	1.70	2.67	0.55	345	1.10	1.88	47.76	53.14	44.58	44.86
SHS304L_1.10_500	FE	304L	415	3.3	195	500	78.1	78.1	4.25	1.10	0.33	0.55	148	1.67	0.24	79.26	82.91	82.91	69.25
SHS304L_1.10_1000	FE	304L	415	3.3	195	1000	78.1	78.1	4.25	1.10	0.67	0.55	148	1.67	0.47	72.71	82.91	70.80	69.25
SHS304L_1.10_1450	FE	304L	415	3.3	195	1450	78.1	78.1	4.25	1.10	0.97	0.55	148	1.67	0.68	65.54	70.60	61.13	65.75
SHS304L_1.10_2000	FE	304L	415	3.3	195	2000	78.1	78.1	4.25	1.10	1.33	0.55	148	1.67	0.94	55.31	58.67	51.92	57.31
SHS304L_1.10_2450	FE	304L	415	3.3	195	2450	78.1	78.1	4.25	1.10	1.63	0.55	148	1.67	1.15	48.32	51.10	45.33	49.66
SHS304L_1.10_3000	FE	304L	415	3.3	195	3000	78.1	78.1	4.25	1.10	2.00	0.55	148	1.67	1.41	40.88	43.42	38.33	40.43
SHS304L_1.10_3450	FE	304L	415	3.3	195	3450	78.1	78.1	4.25	1.10	2.30	0.55	148	1.67	1.62	32.52	38.06	33.46	33.81
SHS304L_1.10_4000	FE	304L	415	3.3	195	4000	78.1	78.1	4.25	1.10	2.67	0.55	148	1.67	1.88	26.36	32.43	28.45	27.25
SHS304L_0.80_500	FE	304L	415	3.3	195	500	77.8	77.8	4.25	0.80	0.33	0.55	81	2.26	0.24	47.23	48.01	48.01	40.03
SHS304L_0.80_1000	FE	304L	415	3.3	195	1000	77.8	77.8	4.25	0.80	0.67	0.55	81	2.26	0.47	43.48	48.01	41.08	40.03
SHS304L_0.80_1450	FE	304L	415	3.3	195	1450	77.8	77.8	4.25	0.80	0.97	0.55	81	2.26	0.68	39.10	40.97	35.59	39.28
SHS304L_0.80_2000	FE	304L	415	3.3	195	2000	77.8	77.8	4.25	0.80	1.33	0.55	81	2.26	0.94	32.79	34.19	30.38	35.14
SHS304L_0.80_2450	FE	304L	415	3.3	195	2450	77.8	77.8	4.25	0.80	1.63	0.55	81	2.26	1.15	28.20	29.93	26.69	31.35
SHS304L_0.80_3000	FE	304L	415	3.3	195	3000	77.8	77.8	4.25	0.80	2.00	0.55	81	2.26	1.41	23.25	25.62	22.78	26.47
SHS304L_0.80_3450	FE	304L	415	3.3	195	3450	77.8	77.8	4.25	0.80	2.30	0.55	81	2.26	1.62	19.62	22.63	20.07	22.68
SHS304L_0.80_4000	FE	304L	415	3.3	195	4000	77.8	77.8	4.25	0.80	2.67	0.55	81	2.26	1.88	15.87	17.30	19.49	18.66

Table D4. I-Sections: 3Cr12

(1) Experimental result or FE generated result.

Specimen	Exp /FE (1)	Material				Geometry							Slenderness			P _u			
		Alloy	$\sigma_{0.2\%}$	n	E ₀	L _e	d	2b	r	t	v ₀	ω_d	σ_{cr}	λ_s	λ_o	Test	AS(t)	AS(d)	EC 3
		-	MPa	-	GPa	mm	mm	mm	m	mm	mm	mm	MPa	-	-	kN	kN	kN	kN
I3Cr12_1.80_250	FE	3Cr12	328	7.5	208	250	100.0	70.0	4.0	1.80	0.17	0.60	261	1.12	0.24	134.40	151.14	151.14	123.95
I3Cr12_1.80_500	FE	3Cr12	328	7.5	208	500	100.0	70.0	4.0	1.80	0.33	0.60	261	1.12	0.48	127.35	138.12	128.85	123.95
I3Cr12_1.80_750	FE	3Cr12	328	7.5	208	750	100.0	70.0	4.0	1.80	0.50	0.60	261	1.12	0.72	118.52	124.68	115.91	110.52
I3Cr12_1.80_1000	FE	3Cr12	328	7.5	208	1000	100.0	70.0	4.0	1.80	0.67	0.60	261	1.12	0.96	100.41	113.17	102.21	93.68
I3Cr12_1.80_1250	FE	3Cr12	328	7.5	208	1250	100.0	70.0	4.0	1.80	0.83	0.60	261	1.12	1.19	82.44	101.08	87.23	76.15
I3Cr12_1.80_1500	FE	3Cr12	328	7.5	208	1500	100.0	70.0	4.0	1.80	1.00	0.60	261	1.12	1.43	65.32	86.52	70.27	60.69
I3Cr12_1.80_1750	FE	3Cr12	328	7.5	208	1750	100.0	70.0	4.0	1.80	1.17	0.60	261	1.12	1.67	51.73	67.94	55.85	48.47
I3Cr12_1.80_2000	FE	3Cr12	328	7.5	208	2000	100.0	70.0	4.0	1.80	1.33	0.60	261	1.12	1.91	41.35	52.59	44.92	39.19
I3Cr12_1.10_250	FE	3Cr12	328	7.5	208	250	99.3	69.3	4.0	1.10	0.17	0.60	98	1.83	0.24	63.42	65.40	65.40	51.12
I3Cr12_1.10_500	FE	3Cr12	328	7.5	208	500	99.3	69.3	4.0	1.10	0.33	0.60	98	1.83	0.49	58.15	59.90	56.16	51.12
I3Cr12_1.10_750	FE	3Cr12	328	7.5	208	750	99.3	69.3	4.0	1.10	0.50	0.60	98	1.83	0.73	49.76	54.42	50.87	48.67
I3Cr12_1.10_1000	FE	3Cr12	328	7.5	208	1000	99.3	69.3	4.0	1.10	0.67	0.60	98	1.83	0.97	40.94	49.72	45.23	43.31
I3Cr12_1.10_1250	FE	3Cr12	328	7.5	208	1250	99.3	69.3	4.0	1.10	0.83	0.60	98	1.83	1.21	33.07	44.73	39.18	37.36
I3Cr12_1.10_1500	FE	3Cr12	328	7.5	208	1500	99.3	69.3	4.0	1.10	1.00	0.60	98	1.83	1.46	27.47	38.80	33.46	31.34
I3Cr12_1.10_1750	FE	3Cr12	328	7.5	208	1750	99.3	69.3	4.0	1.10	1.17	0.60	98	1.83	1.70	22.74	32.54	28.53	25.94
I3Cr12_1.10_2000	FE	3Cr12	328	7.5	208	2000	99.3	69.3	4.0	1.10	1.33	0.60	98	1.83	1.94	19.18	27.24	24.44	21.46
I3Cr12_0.80_250	FE	3Cr12	328	7.5	208	250	99.0	69.0	4.0	0.80	0.17	0.60	52	2.52	0.24	40.23	37.62	37.62	28.50
I3Cr12_0.80_500	FE	3Cr12	328	7.5	208	500	99.0	69.0	4.0	0.80	0.33	0.60	52	2.52	0.49	36.50	34.43	32.30	28.50
I3Cr12_0.80_750	FE	3Cr12	328	7.5	208	750	99.0	69.0	4.0	0.80	0.50	0.60	52	2.52	0.73	29.89	31.31	29.29	28.11
I3Cr12_0.80_1000	FE	3Cr12	328	7.5	208	1000	99.0	69.0	4.0	0.80	0.67	0.60	52	2.52	0.98	23.46	28.63	26.08	25.61
I3Cr12_0.80_1250	FE	3Cr12	328	7.5	208	1250	99.0	69.0	4.0	0.80	0.83	0.60	52	2.52	1.22	19.00	25.78	22.65	22.82
I3Cr12_0.80_1500	FE	3Cr12	328	7.5	208	1500	99.0	69.0	4.0	0.80	1.00	0.60	52	2.52	1.47	15.44	22.41	19.45	19.84
I3Cr12_0.80_1750	FE	3Cr12	328	7.5	208	1750	99.0	69.0	4.0	0.80	1.17	0.60	52	2.52	1.71	12.71	18.90	16.71	16.93
I3Cr12_0.80_2000	FE	3Cr12	328	7.5	208	2000	99.0	69.0	4.0	0.80	1.33	0.60	52	2.52	1.96	10.77	15.97	14.46	14.32

Table D4 (Continued). I-Sections: 304

(1) Experimental result or FE generated result.

Specimen	Exp /FE (1)	Material				Geometry							Slenderness			P _u			
		Alloy	$\sigma_{0.2\%}$	n	E ₀	L _e	d	2b	r	t	v ₀	ω_d	σ_{cr}	λ_s	λ_0	Test	AS(t)	AS(d)	EC 3
		-	MPa	-	GPa	mm	mm	mm	m	mm	mm	mm	MPa	-	-	kN	kN	kN	kN
I304_1.80_250	FE	304	234	6.5	176	250	100.0	70.0	4.0	1.80	0.17	0.60	221	1.03	0.22	94.80	113.89	113.89	94.40
I304_1.80_500	FE	304	234	6.5	176	500	100.0	70.0	4.0	1.80	0.33	0.60	221	1.03	0.44	87.74	104.42	98.91	94.40
I304_1.80_750	FE	304	234	6.5	176	750	100.0	70.0	4.0	1.80	0.50	0.60	221	1.03	0.66	79.57	93.50	83.26	85.99
I304_1.80_1000	FE	304	234	6.5	176	1000	100.0	70.0	4.0	1.80	0.67	0.60	221	1.03	0.88	69.55	84.77	70.90	74.08
I304_1.80_1250	FE	304	234	6.5	176	1250	100.0	70.0	4.0	1.80	0.83	0.60	221	1.03	1.10	57.96	76.50	58.17	61.34
I304_1.80_1500	FE	304	234	6.5	176	1500	100.0	70.0	4.0	1.80	1.00	0.60	221	1.03	1.32	47.24	66.84	47.36	49.59
I304_1.80_1750	FE	304	234	6.5	176	1750	100.0	70.0	4.0	1.80	1.17	0.60	221	1.03	1.54	38.00	54.83	38.78	39.97
I304_1.80_2000	FE	304	234	6.5	176	2000	100.0	70.0	4.0	1.80	1.33	0.60	221	1.03	1.75	30.70	43.81	32.05	32.51
I304_1.10_250	FE	304	234	6.5	176	250	99.3	69.3	4.0	1.10	0.17	0.60	83	1.68	0.22	46.93	49.65	49.65	39.17
I304_1.10_500	FE	304	234	6.5	176	500	99.3	69.3	4.0	1.10	0.33	0.60	83	1.68	0.45	41.07	45.64	43.33	39.17
I304_1.10_750	FE	304	234	6.5	176	750	99.3	69.3	4.0	1.10	0.50	0.60	83	1.68	0.67	34.89	41.23	37.05	37.85
I304_1.10_1000	FE	304	234	6.5	176	1000	99.3	69.3	4.0	1.10	0.67	0.60	83	1.68	0.89	29.05	37.69	32.24	34.02
I304_1.10_1250	FE	304	234	6.5	176	1250	99.3	69.3	4.0	1.10	0.83	0.60	83	1.68	1.11	24.02	34.33	28.00	29.75
I304_1.10_1500	FE	304	234	6.5	176	1500	99.3	69.3	4.0	1.10	1.00	0.60	83	1.68	1.34	20.34	30.73	24.28	25.32
I304_1.10_1750	FE	304	234	6.5	176	1750	99.3	69.3	4.0	1.10	1.17	0.60	83	1.68	1.56	17.03	26.76	21.06	21.20
I304_1.10_2000	FE	304	234	6.5	176	2000	99.3	69.3	4.0	1.10	1.33	0.60	83	1.68	1.78	14.49	22.84	18.31	17.69
I304_0.80_250	FE	304	234	6.5	176	250	99.0	69.0	4.0	0.80	0.17	0.60	44	2.31	0.22	29.88	28.59	28.59	21.87
I304_0.80_500	FE	304	234	6.5	176	500	99.0	69.0	4.0	0.80	0.33	0.60	44	2.31	0.45	26.20	26.27	24.94	21.87
I304_0.80_750	FE	304	234	6.5	176	750	99.0	69.0	4.0	0.80	0.50	0.60	44	2.31	0.67	21.16	23.77	21.40	21.83
I304_0.80_1000	FE	304	234	6.5	176	1000	99.0	69.0	4.0	0.80	0.67	0.60	44	2.31	0.90	16.80	21.76	18.68	20.03
I304_0.80_1250	FE	304	234	6.5	176	1250	99.0	69.0	4.0	0.80	0.83	0.60	44	2.31	1.12	13.88	19.86	16.31	18.04
I304_0.80_1500	FE	304	234	6.5	176	1500	99.0	69.0	4.0	0.80	1.00	0.60	44	2.31	1.35	11.52	17.82	14.24	15.89
I304_0.80_1750	FE	304	234	6.5	176	1750	99.0	69.0	4.0	0.80	1.17	0.60	44	2.31	1.57	9.58	15.59	12.46	13.72
I304_0.80_2000	FE	304	234	6.5	176	2000	99.0	69.0	4.0	0.80	1.33	0.60	44	2.31	1.80	8.17	13.41	10.95	11.71

Table D4 (Continued). I-Sections: 430

(1) Experimental result or FE generated result.

Specimen	Exp /FE (1)	Material				Geometry							Slenderness			P _u			
		Alloy	$\sigma_{0.2\%}$	n	E ₀	L _e	d	2b	r	t	v ₀	ω_d	σ_{cr}	λ_s	λ_0	Test	AS(t)	AS(d)	EC 3
		-	MPa	-	GPa	mm	mm	mm	m	mm	mm	mm	MPa	-	-	kN	kN	kN	kN
I430_1.80_250	FE	430	265	6.5	193	250	100.0	70.0	4.0	1.80	0.17	0.60	242	1.05	0.22	111.31	127.68	127.68	105.61
I430_1.80_500	FE	430	265	6.5	193	500	100.0	70.0	4.0	1.80	0.33	0.60	242	1.05	0.45	107.14	117.02	113.47	105.61
I430_1.80_750	FE	430	265	6.5	193	750	100.0	70.0	4.0	1.80	0.50	0.60	242	1.05	0.67	101.72	104.73	100.45	95.82
I430_1.80_1000	FE	430	265	6.5	193	1000	100.0	70.0	4.0	1.80	0.67	0.60	242	1.05	0.89	87.53	94.84	89.16	82.31
I430_1.80_1250	FE	430	265	6.5	193	1250	100.0	70.0	4.0	1.80	0.83	0.60	242	1.05	1.11	72.57	85.39	76.59	67.92
I430_1.80_1500	FE	430	265	6.5	193	1500	100.0	70.0	4.0	1.80	1.00	0.60	242	1.05	1.34	57.79	74.47	62.19	54.76
I430_1.80_1750	FE	430	265	6.5	193	1750	100.0	70.0	4.0	1.80	1.17	0.60	242	1.05	1.56	46.02	60.66	50.04	44.06
I430_1.80_2000	FE	430	265	6.5	193	2000	100.0	70.0	4.0	1.80	1.33	0.60	242	1.05	1.78	36.86	48.20	40.59	35.79
I430_1.10_250	FE	430	265	6.5	193	250	99.3	69.3	4.0	1.10	0.17	0.60	91	1.71	0.23	52.31	55.57	55.57	43.76
I430_1.10_500	FE	430	265	6.5	193	500	99.3	69.3	4.0	1.10	0.33	0.60	91	1.71	0.45	48.81	51.06	49.58	43.76
I430_1.10_750	FE	430	265	6.5	193	750	99.3	69.3	4.0	1.10	0.50	0.60	91	1.71	0.68	43.17	46.09	44.36	42.18
I430_1.10_1000	FE	430	265	6.5	193	1000	99.3	69.3	4.0	1.10	0.67	0.60	91	1.71	0.91	35.48	42.08	39.75	37.85
I430_1.10_1250	FE	430	265	6.5	193	1250	99.3	69.3	4.0	1.10	0.83	0.60	91	1.71	1.13	29.84	38.23	34.86	33.01
I430_1.10_1500	FE	430	265	6.5	193	1500	99.3	69.3	4.0	1.10	1.00	0.60	91	1.71	1.36	25.02	34.07	30.09	28.02
I430_1.10_1750	FE	430	265	6.5	193	1750	99.3	69.3	4.0	1.10	1.17	0.60	91	1.71	1.59	20.84	29.50	25.86	23.41
I430_1.10_2000	FE	430	265	6.5	193	2000	99.3	69.3	4.0	1.10	1.33	0.60	91	1.71	1.81	17.67	25.09	22.26	19.50
I430_0.80_250	FE	430	265	6.5	193	250	99.0	69.0	4.0	0.80	0.17	0.60	48	2.35	0.23	33.12	31.99	31.99	24.43
I430_0.80_500	FE	430	265	6.5	193	500	99.0	69.0	4.0	0.80	0.33	0.60	48	2.35	0.46	30.84	29.38	28.53	24.43
I430_0.80_750	FE	430	265	6.5	193	750	99.0	69.0	4.0	0.80	0.50	0.60	48	2.35	0.68	26.05	26.56	25.58	24.33
I430_0.80_1000	FE	430	265	6.5	193	1000	99.0	69.0	4.0	0.80	0.67	0.60	48	2.35	0.91	20.83	24.28	22.96	22.30
I430_0.80_1250	FE	430	265	6.5	193	1250	99.0	69.0	4.0	0.80	0.83	0.60	48	2.35	1.14	17.11	22.10	20.19	20.05
I430_0.80_1500	FE	430	265	6.5	193	1500	99.0	69.0	4.0	0.80	1.00	0.60	48	2.35	1.37	14.09	19.75	17.53	17.61
I430_0.80_1750	FE	430	265	6.5	193	1750	99.0	69.0	4.0	0.80	1.17	0.60	48	2.35	1.60	11.70	17.18	15.17	15.17
I430_0.80_2000	FE	430	265	6.5	193	2000	99.0	69.0	4.0	0.80	1.33	0.60	48	2.35	1.82	10.00	14.73	13.19	12.93

Table D4 (Continued). I-Sections: Experimental Results

Specimen	Exp /FE (1)	Material				Geometry							Slenderness			P _u			
		Alloy	$\sigma_{0.2\%}$	n	E ₀	L _e	d	2b	r	t	v ₀	ω_d	σ_{cr}	λ_s	λ_o	Test	AS(t)	AS(d)	EC 3
		-	MPa	-	GPa	mm	mm	mm	mm	mm	mm	mm	MPa	-	-	kN	kN	kN	kN
I304_500_2	Exp	304	243	3.0	191	637	126.38	96.86	4.33	1.20	0.33	0.42	62	1.98	0.39	55.24	64.09	59.13	50.43
I304_1000_1	Exp	304	243	3.0	191	1135	126.38	96.86	4.33	1.20	0.75	0.42	62	1.98	0.69	47.25	47.61	49.95	49.36
I304_1000_2	Exp	304	243	3.0	191	1135	126.38	96.86	4.33	1.20	0.76	0.42	62	1.98	0.69	47.43	47.61	49.95	49.36
I304_1500_1	Exp	304	243	3.0	191	1635	126.38	96.86	4.33	1.20	1.15	0.42	62	1.98	1.00	38.67	40.50	39.65	43.15
I304_1500_2	Exp	304	243	3.0	191	1634	126.38	96.86	4.33	1.20	1.09	0.42	62	1.98	1.00	37.63	40.50	39.65	43.15
I304_2000_1	Exp	304	243	3.0	191	2116	126.38	96.86	4.33	1.20	1.38	0.42	62	1.98	1.29	31.37	33.99	33.14	36.34
I304_2000_2	Exp	304	243	3.0	191	2116	126.38	96.86	4.33	1.20	1.12	0.42	62	1.98	1.29	31.07	33.99	33.14	36.34
I304_2500_1	Exp	304	243	3.0	191	2613	126.38	96.86	4.33	1.20	1.14	0.42	62	1.98	1.59	22.71	28.77	27.63	29.38
I304_2500_2	Exp	304	243	3.0	191	2613	126.38	96.86	4.33	1.20	0.69	0.42	62	1.98	1.59	22.94	28.77	27.63	29.38
I304_3000_1	Exp	304	243	3.0	191	3115	126.38	96.86	4.33	1.20	1.91	0.42	62	1.98	1.90	20.62	24.44	23.13	23.35
I304_3000_2	Exp	304	243	3.0	191	3116	126.38	96.86	4.33	1.20	2.05	0.42	62	1.98	1.90	18.30	24.44	23.13	23.35
I404_500_1	Exp	404	290	9.5	195	635	125.24	96.58	3.11	1.20	0.38	0.45	64	2.13	0.42	69.83	65.33	63.13	55.33
I404_500_2	Exp	404	290	9.5	195	635	125.24	96.58	3.11	1.20	0.41	0.45	64	2.13	0.42	71.79	65.33	63.13	55.33
I404_1000_1	Exp	404	290	9.5	195	1135	125.24	96.58	3.11	1.20	0.73	0.45	64	2.13	0.75	56.53	59.18	56.54	53.57
I404_1000_2	Exp	404	290	9.5	195	1135	125.24	96.58	3.11	1.20	0.79	0.45	64	2.13	0.75	56.22	59.18	56.54	53.57
I404_1500_1	Exp	404	290	9.5	195	1636	125.24	96.58	3.11	1.20	1.27	0.45	64	2.13	1.08	40.96	53.48	48.28	46.36
I404_1500_2	Exp	404	290	9.5	195	1635	125.24	96.58	3.11	1.20	1.26	0.45	64	2.13	1.08	42.00	53.48	48.28	46.36
I404_2000_1	Exp	404	290	9.5	195	2115	125.24	96.58	3.11	1.20	1.56	0.45	64	2.13	1.40	37.91	45.32	39.60	38.53
I404_2000_2	Exp	404	290	9.5	195	2115	125.24	96.58	3.11	1.20	1.40	0.45	64	2.13	1.40	37.48	45.32	39.60	38.53
I404_2500_1	Exp	404	290	9.5	195	2613	125.24	96.58	3.11	1.20	1.59	0.45	64	2.13	1.72	29.90	35.46	32.10	30.72
I404_2500_2	Exp	404	290	9.5	195	2615	125.24	96.58	3.11	1.20	1.80	0.45	64	2.13	1.72	27.24	35.46	32.10	30.72
I404_3000_1	Exp	404	290	9.5	195	3117	125.24	96.58	3.11	1.20	1.85	0.45	64	2.13	2.06	21.20	28.24	26.27	24.29
I404_3000_2	Exp	404	290	9.5	195	3115	125.24	96.58	3.11	1.20	1.18	0.45	64	2.13	2.06	24.42	28.24	26.27	24.29

(1) Experimental result or FE generated result.

Table D5. I-Sections: Accuracy of the Solution

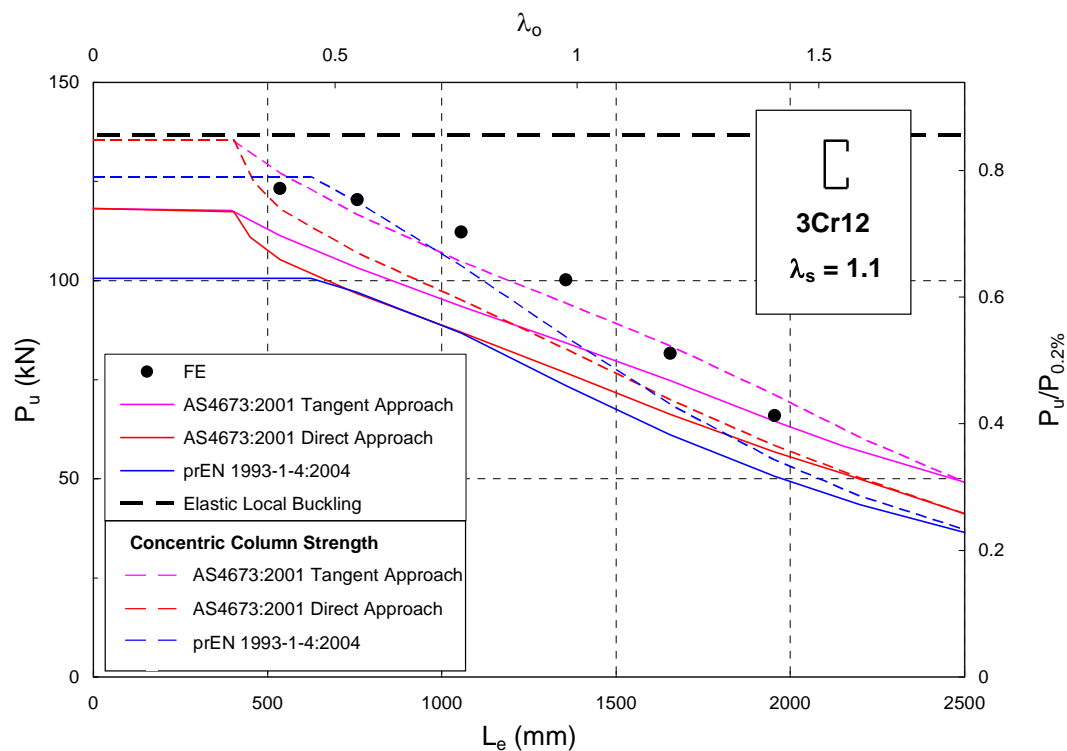
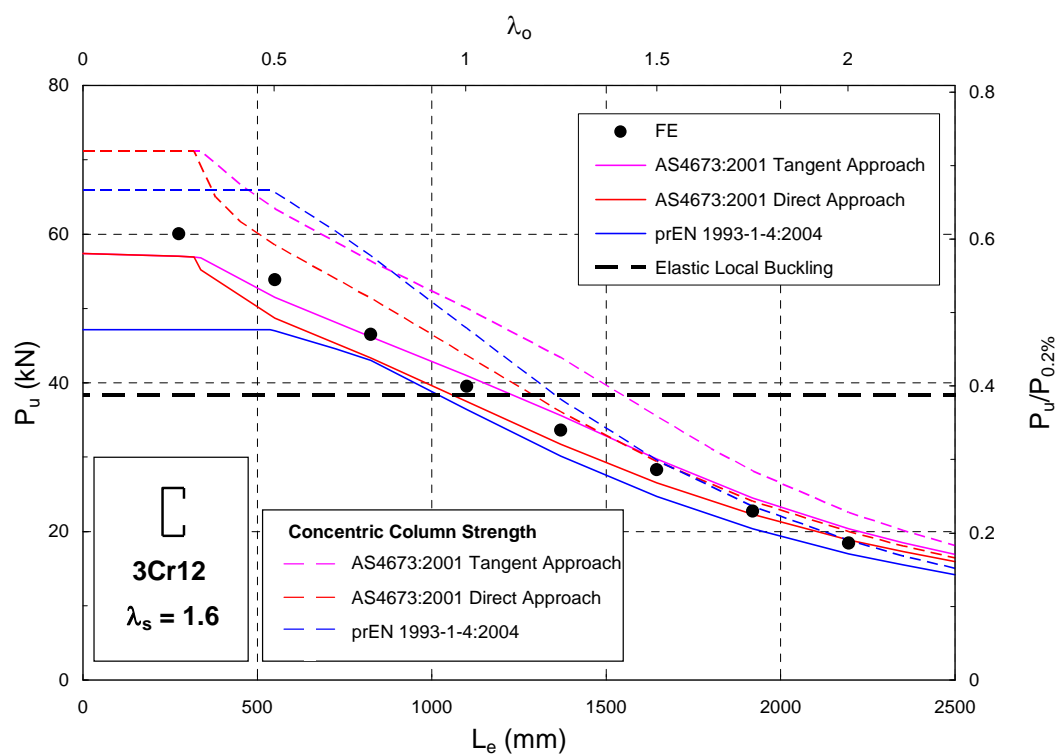
Specimen	ALLSD	ALLSE	ALLPD	ALLIE	μ_1	Step 1	μ_2	Step 2	SD/SE
	J	J	J	J	-	mm	-	mm	%
Verification									
I304_1.20_636	0.0003	27.4	69.6	97.1	0.0002	0.05	-	-	0.001
I304_1.20_1135	0.0025	38.2	55.8	94.1	0.0005	0.1	-	-	0.007
I304_1.20_1635	0.0071	38.9	37.0	76.0	0.001	0.1	0.0001	0.65	0.018
I304_1.20_2118	0.0199	48.1	18.1	66.2	0.0005	0.1	-	-	0.041
I304_1.20_2613	0.2215	14.7	2.5	17.2	0.004	0.1	0.0002	0.8	1.506
I304_1.20_3115	0.0172	24.8	9.7	34.5	0.005	0.1	0.0002	0.8	0.069
I404_1.20_636	0.0003	33.4	76.9	110.3	0.0002	0.05	-	-	0.001
I404_1.20_1135	0.0026	43.5	13.4	56.9	0.0005	0.1	-	-	0.006
I404_1.20_1635	0.0261	51.5	24.0	75.5	0.001	0.1	0.0001	0.65	0.051
I404_1.20_2118	0.0199	48.1	18.1	66.2	0.0005	0.1	-	-	0.041
I404_1.20_2613	0.2260	18.3	0.2	18.4	0.004	0.1	0.0002	0.8	1.235
I404_1.20_3115	0.0174	38.2	4.6	42.8	0.005	0.1	0.0002	0.8	0.045
Parametric Studies									
I3Cr12_1.80_250	0.0163	30.0	32.0	62.0	0.0004	0.15	-	-	0.054
I3Cr12_1.80_500	0.0006	46.0	27.0	73.0	0.0005	0.1	-	-	0.001
I3Cr12_1.80_750	0.0260	54.0	20.0	74.0	0.0002	0.45	-	-	0.048
I3Cr12_1.80_1000	0.0260	50.0	10.0	60.0	0.0002	0.5	-	-	0.052
I3Cr12_1.80_1250	0.0200	40.0	6.5	46.5	0.0002	0.5	-	-	0.050
I3Cr12_1.80_1500	0.0180	32.0	3.9	35.9	0.0002	0.5	-	-	0.056
I3Cr12_1.80_1750	0.0450	24.0	1.8	25.8	0.0002	0.5	-	-	0.188
I3Cr12_1.80_2000	0.0740	19.0	1.0	20.0	0.0002	0.6	-	-	0.389
I3Cr12_1.10_250	0.0077	14.0	17.0	31.0	0.002	0.05	-	-	0.055
I3Cr12_1.10_500	0.0006	25.0	18.0	43.0	0.0005	0.1	-	-	0.002
I3Cr12_1.10_750	0.0180	25.0	9.0	34.0	0.0005	0.1	-	-	0.072
I3Cr12_1.10_1000	0.0013	22.0	4.3	26.3	0.0002	0.2	-	-	0.006
I3Cr12_1.10_1250	0.0224	17.0	2.0	19.0	0.0015	0.1	-	-	0.132
I3Cr12_1.10_1500	0.0162	13.0	0.9	13.9	0.0008	0.1	-	-	0.125
I3Cr12_1.10_1750	0.0426	10.0	0.4	10.4	0.0002	0.1	-	-	0.426
I3Cr12_1.10_2000	0.0121	9.0	0.3	9.3	0.0004	0.1	-	-	0.134
I3Cr12_0.80_250	0.0030	9.1	11.0	20.1	0.002	0.05	-	-	0.033

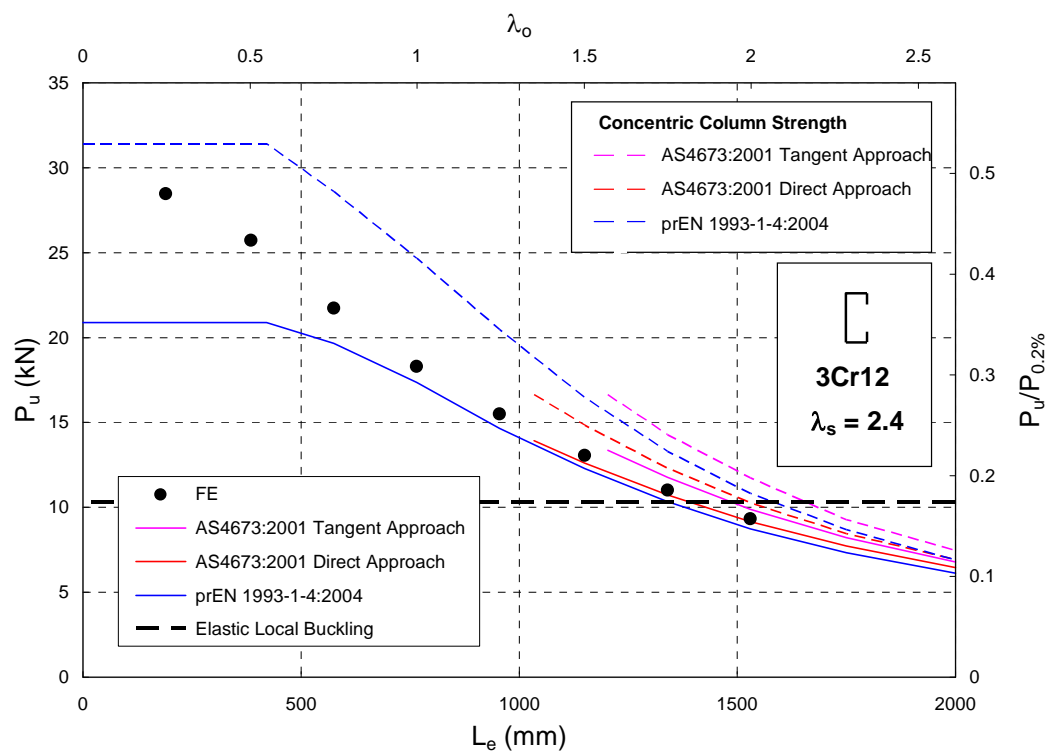
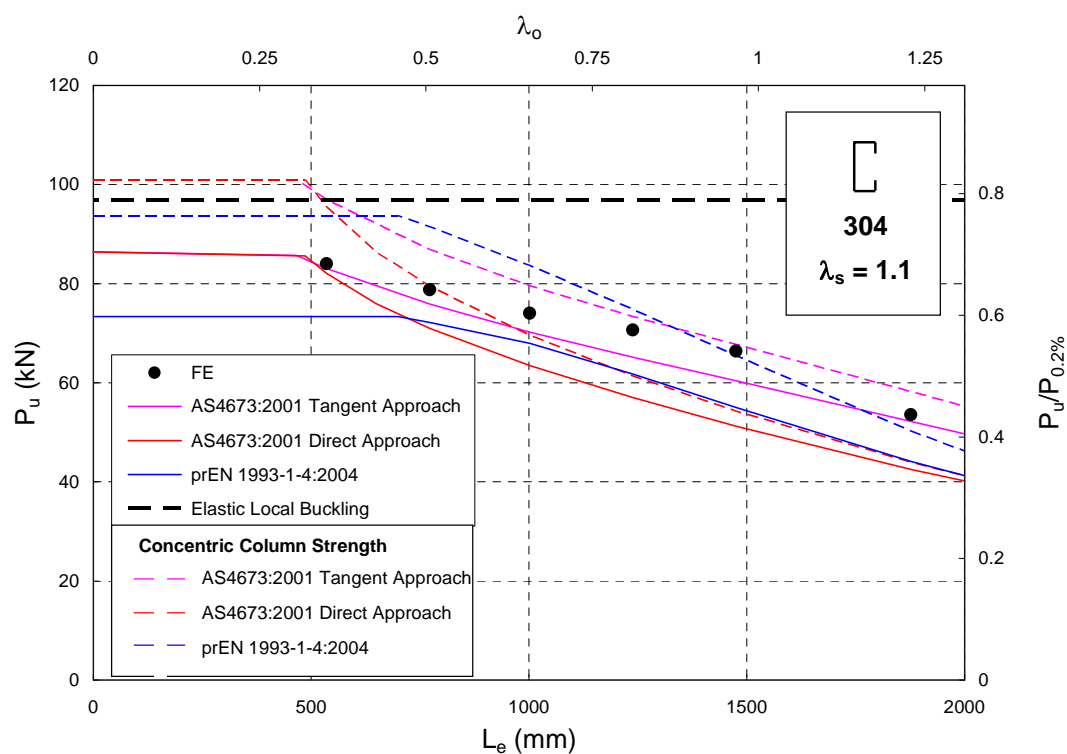
Table D5 (Continued). I-Sections: Accuracy of the Solution

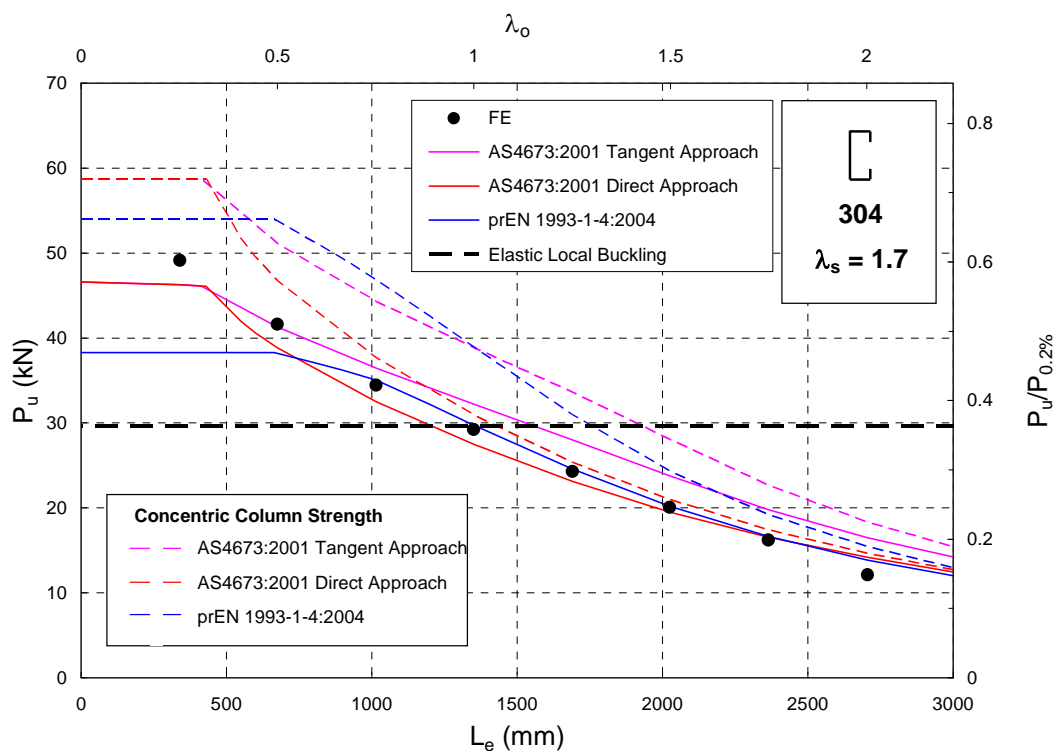
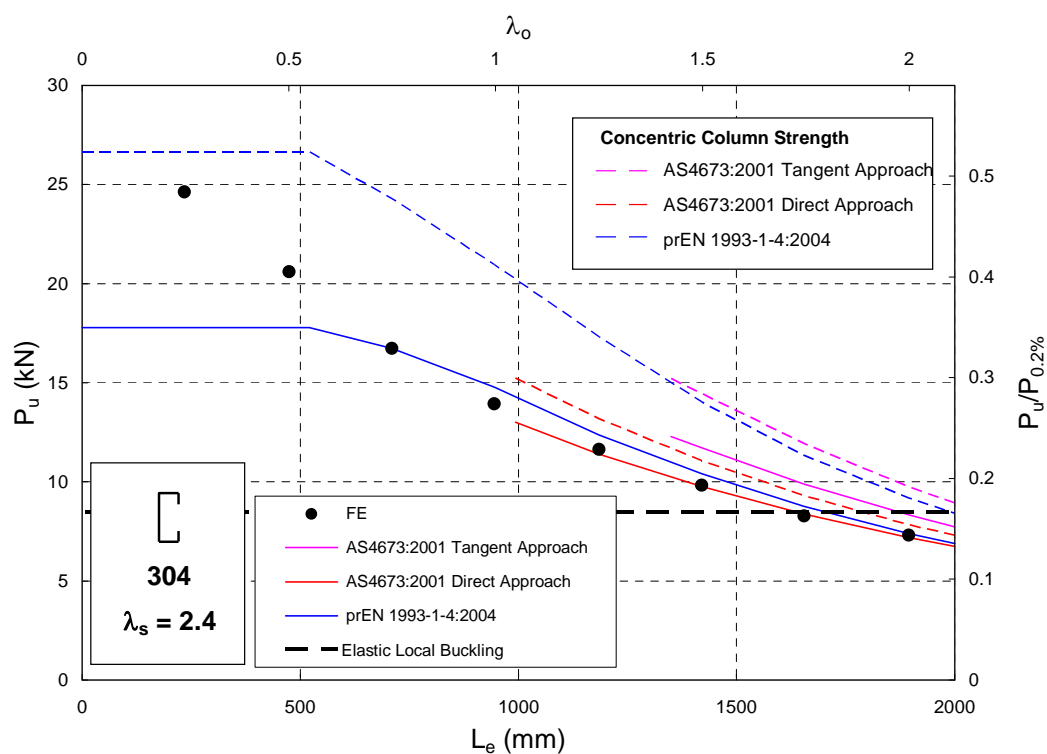
Specimen	ALLSD	ALLSE	ALLPD	ALLIE	μ_1	Step 1	μ_2	Step 2	SD/SE
	J	J	J	J	-	mm	-	mm	%
I3Cr12_0.80_500	0.0090	16.0	12.0	28.0	0.0005	0.1	-	-	0.056
I3Cr12_0.80_750	0.0156	16.0	5.8	21.8	0.0005	0.1	-	-	0.098
I3Cr12_0.80_1000	0.0136	14.0	3.0	17.0	0.0002	0.1	-	-	0.097
I3Cr12_0.80_1250	0.0214	12.0	1.4	13.4	0.0005	0.1	-	-	0.178
I3Cr12_0.80_1500	0.0106	8.7	0.6	9.3	0.0005	0.1	-	-	0.121
I3Cr12_0.80_1750	0.0110	6.7	0.3	7.0	0.0005	0.1	-	-	0.165
I3Cr12_0.80_2000	0.0090	5.5	0.2	5.6	0.0005	0.1	-	-	0.164
I304_1.80_250	0.0013	20.0	40.0	60.0	0.001	0.09	-	-	0.007
I304_1.80_500	0.0004	29.0	27.0	56.0	0.0005	0.1	-	-	0.002
I304_1.80_750	0.0217	34.0	18.0	52.0	0.0002	0.45	-	-	0.064
I304_1.80_1000	0.0150	31.0	11.0	42.0	0.0002	0.5	-	-	0.048
I304_1.80_1250	0.0150	26.0	6.0	32.0	0.0002	0.5	-	-	0.058
I304_1.80_1500	0.0140	21.0	2.8	23.8	0.0002	0.5	-	-	0.067
I304_1.80_1750	0.0188	17.0	1.7	18.7	0.0002	0.5	-	-	0.111
I304_1.80_2000	0.0676	14.0	1.1	15.1	0.0002	0.62	-	-	0.483
I304_1.10_250	0.0240	12.0	24.0	36.0	0.001	0.09	-	-	0.200
I304_1.10_500	0.0002	18.0	18.0	36.0	0.0005	0.05	-	-	0.001
I304_1.10_750	0.0113	16.0	8.2	24.2	0.0005	0.1	-	-	0.071
I304_1.10_1000	0.0092	14.0	4.1	18.1	0.0002	0.2	-	-	0.066
I304_1.10_1250	0.0067	11.0	1.7	12.7	0.0015	0.1	-	-	0.061
I304_1.10_1500	0.0124	9.0	0.6	9.6	0.0008	0.1	-	-	0.137
I304_1.10_1750	0.0324	7.0	0.3	7.3	0.0002	0.1	-	-	0.463
I304_1.10_2000	0.0092	5.8	0.1	5.9	0.0004	0.1	-	-	0.159
I304_0.80_250	0.0037	8.2	16.0	24.2	0.001	0.05	-	-	0.045
I304_0.80_500	0.0006	12.0	11.0	23.0	0.0005	0.05	-	-	0.005
I304_0.80_750	0.0119	11.0	5.1	16.1	0.0005	0.1	-	-	0.108
I304_0.80_1000	0.0104	9.3	2.6	11.9	0.0002	0.1	-	-	0.112
I304_0.80_1250	0.0278	7.1	1.0	8.1	0.0005	0.1	-	-	0.392
I304_0.80_1500	0.0080	6.0	0.5	6.5	0.0005	0.1	-	-	0.134
I304_0.80_1750	0.0060	4.7	0.2	4.9	0.0004	0.1	-	-	0.128
I304_0.80_2000	0.0053	3.6	0.1	3.7	0.0004	0.1	-	-	0.146

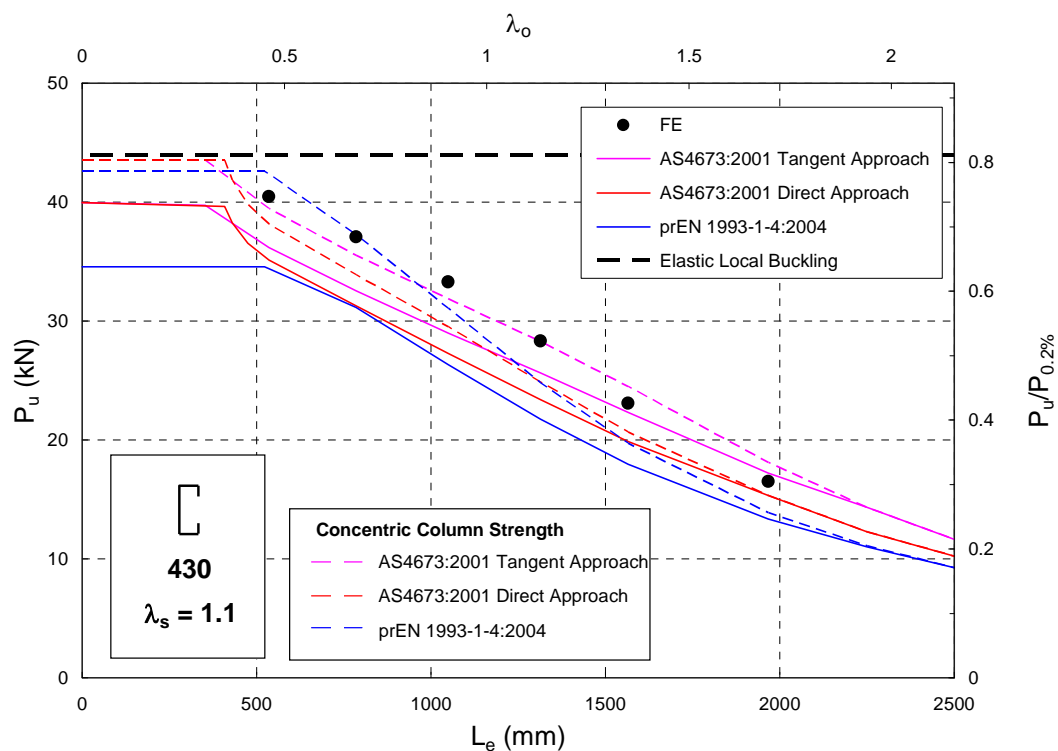
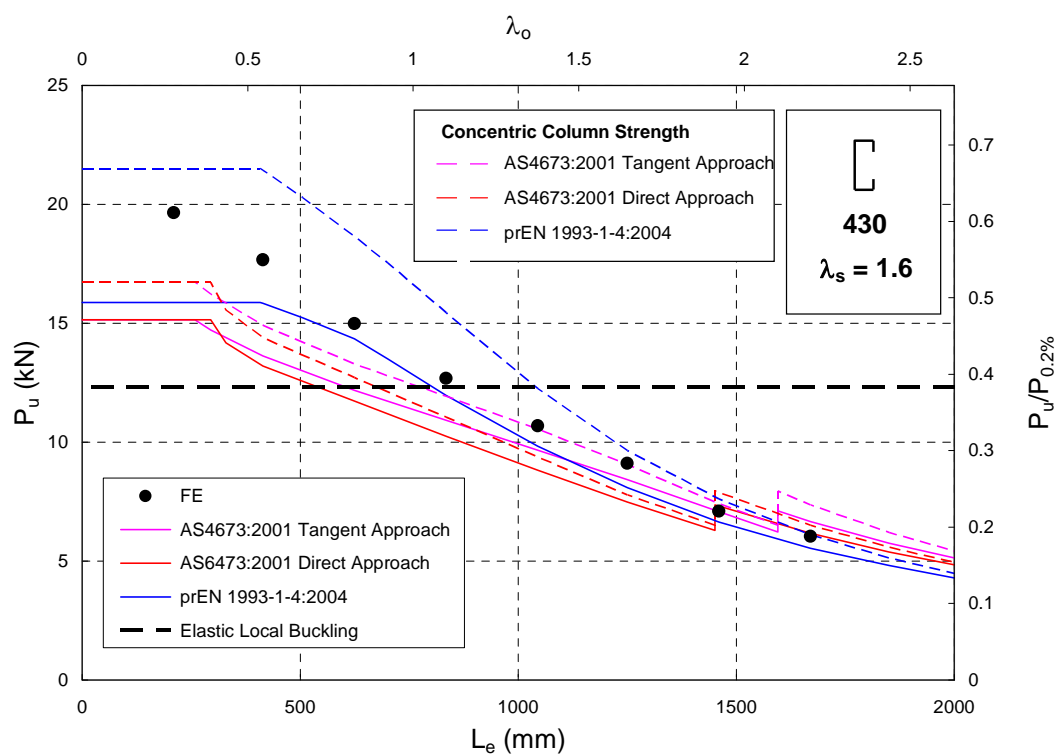
Table D5 (Continued). I-Sections: Accuracy of the Solution

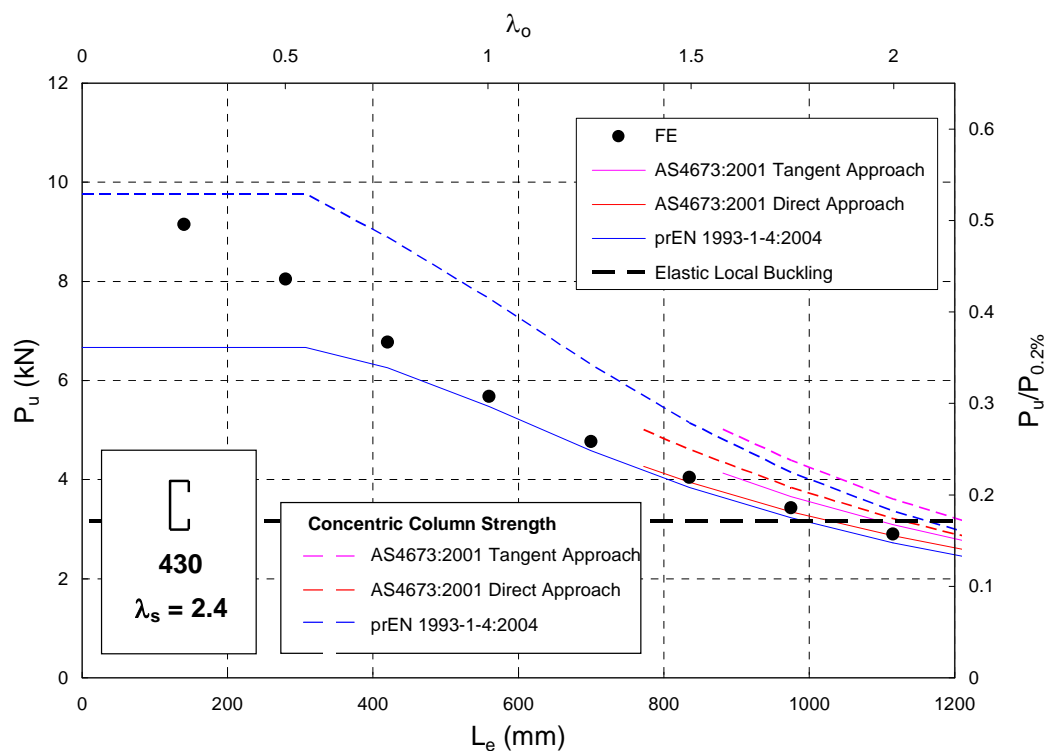
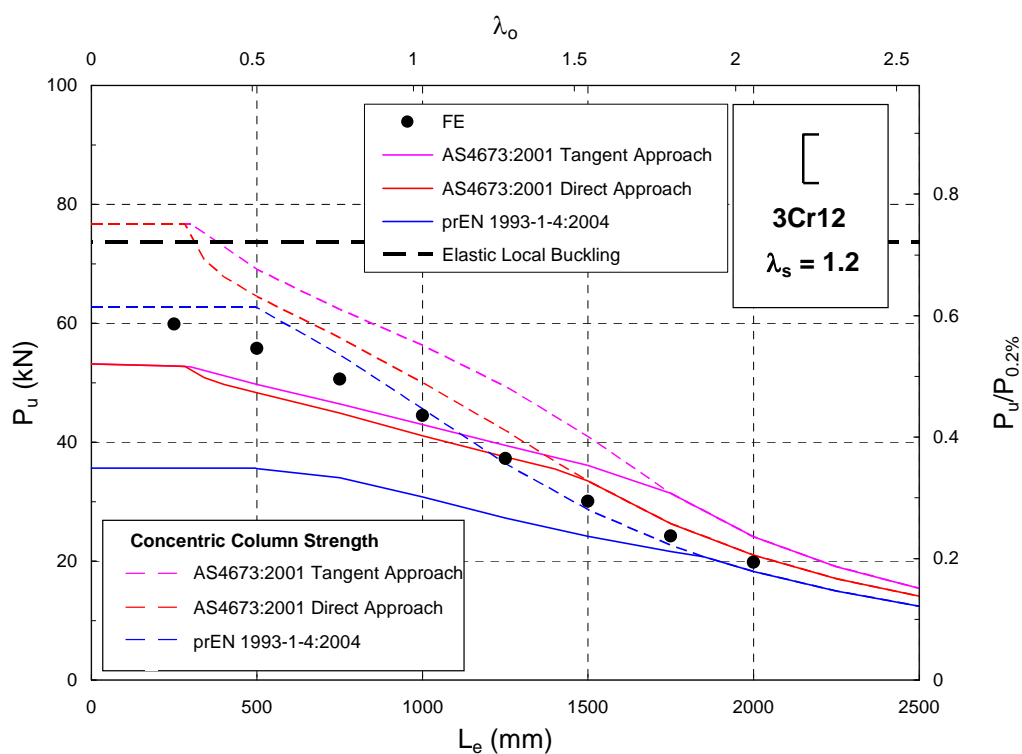
Specimen	ALLSD	ALLSE	ALLPD	ALLIE	μ_1	Step 1	μ_2	Step 2	SD/SE
	J	J	J	J	-	mm	-	mm	%
I430_1.80_250	0.0137	20.0	27.0	47.0	0.0002	0.15	-	-	0.069
I430_1.80_500	0.0003	31.0	24.0	55.0	0.0005	0.05	-	-	0.001
I430_1.80_750	0.0127	40.0	23.0	63.0	0.0002	0.35	-	-	0.032
I430_1.80_1000	0.0108	38.0	15.0	53.0	0.0002	0.4	-	-	0.028
I430_1.80_1250	0.0163	32.0	9.6	41.6	0.0002	0.45	-	-	0.051
I430_1.80_1500	0.0161	25.0	5.7	30.7	0.0002	0.45	-	-	0.064
I430_1.80_1750	0.0202	19.0	3.2	22.2	0.0002	0.45	-	-	0.106
I430_1.80_2000	0.0410	16.0	2.4	18.4	0.0002	0.5	-	-	0.256
I430_1.10_250	0.0012	10.0	15.0	25.0	0.001	0.1	-	-	0.012
I430_1.10_500	0.0002	17.0	16.0	33.0	0.0005	0.05	-	-	0.001
I430_1.10_750	0.0175	19.0	10.0	29.0	0.0005	0.1	-	-	0.092
I430_1.10_1000	0.0131	16.0	5.0	21.0	0.0002	0.1	-	-	0.082
I430_1.10_1250	0.0086	14.0	3.0	17.0	0.0015	0.1	-	-	0.061
I430_1.10_1500	0.0158	11.0	1.6	12.6	0.0008	0.1	-	-	0.144
I430_1.10_1750	0.0138	8.5	1.0	9.5	0.0005	0.1	-	-	0.163
I430_1.10_2000	0.0084	7.0	0.7	7.7	0.0008	0.1	-	-	0.120
I430_0.80_250	0.0002	6.2	9.2	15.4	0.001	0.04	-	-	0.004
I430_0.80_500	0.0008	11.0	10.0	21.0	0.0005	0.05	-	-	0.007
I430_0.80_750	0.0152	12.0	6.3	18.3	0.0005	0.1	-	-	0.127
I430_0.80_1000	0.0133	11.0	3.6	14.6	0.0002	0.1	-	-	0.121
I430_0.80_1250	0.0155	9.0	2.0	11.0	0.0015	0.1	-	-	0.172
I430_0.80_1500	0.0103	7.0	1.0	8.0	0.0005	0.1	-	-	0.147
I430_0.80_1750	0.0108	5.3	0.6	5.9	0.0005	0.1	-	-	0.203
I430_0.80_2000	0.0088	4.1	0.3	4.4	0.0005	0.1	-	-	0.215

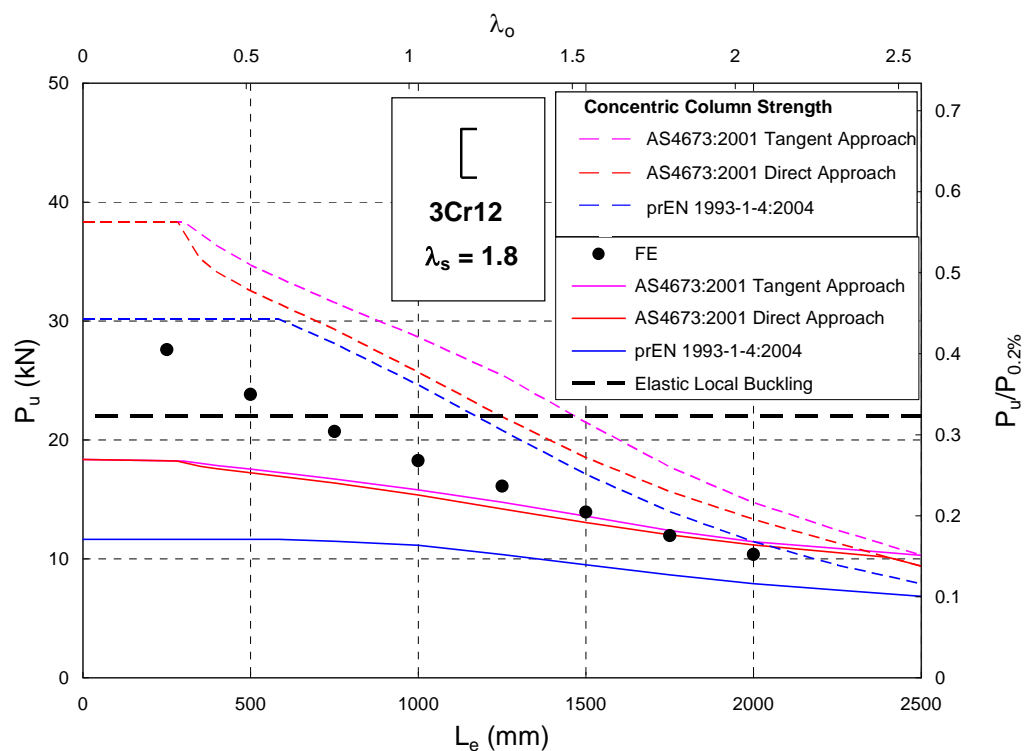
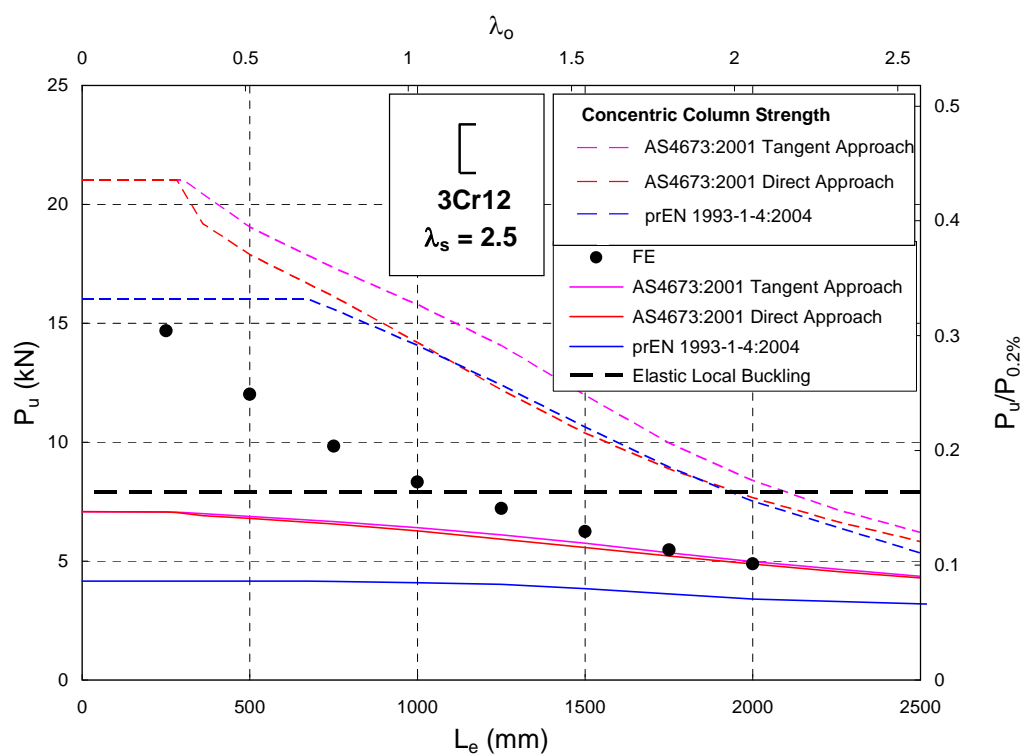

 Figure D.1. Strength Curve of 3Cr12 Lipped Channels with $\lambda_s = 1.1$

 Figure D.2. Strength Curve of 3Cr12 Lipped Channels with $\lambda_s = 1.6$

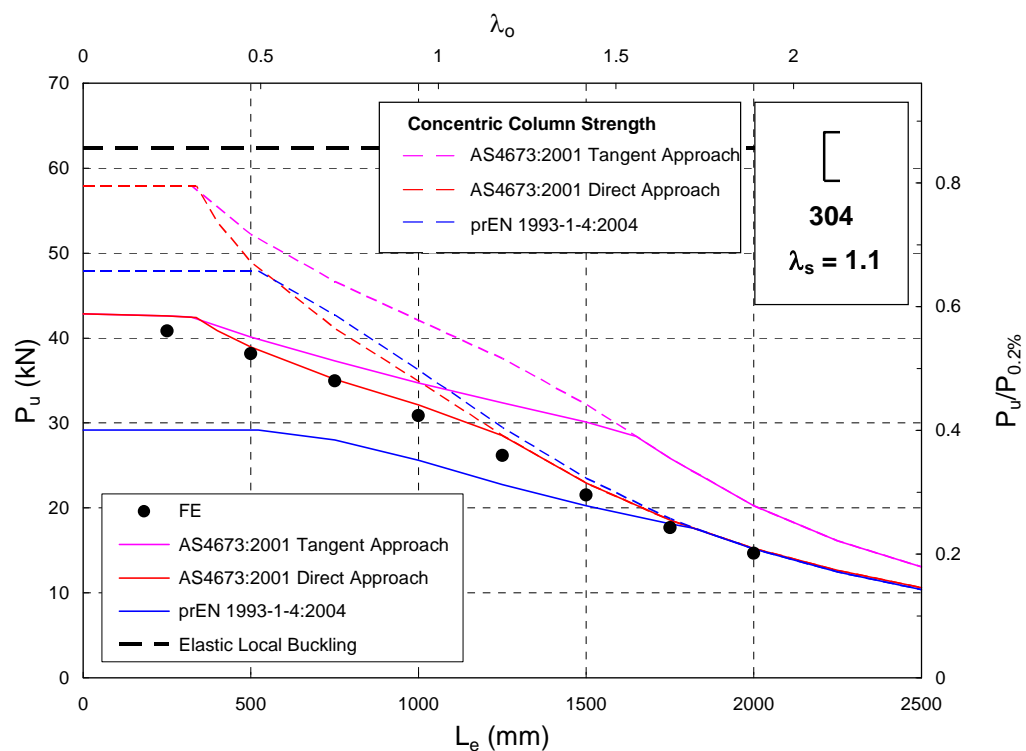
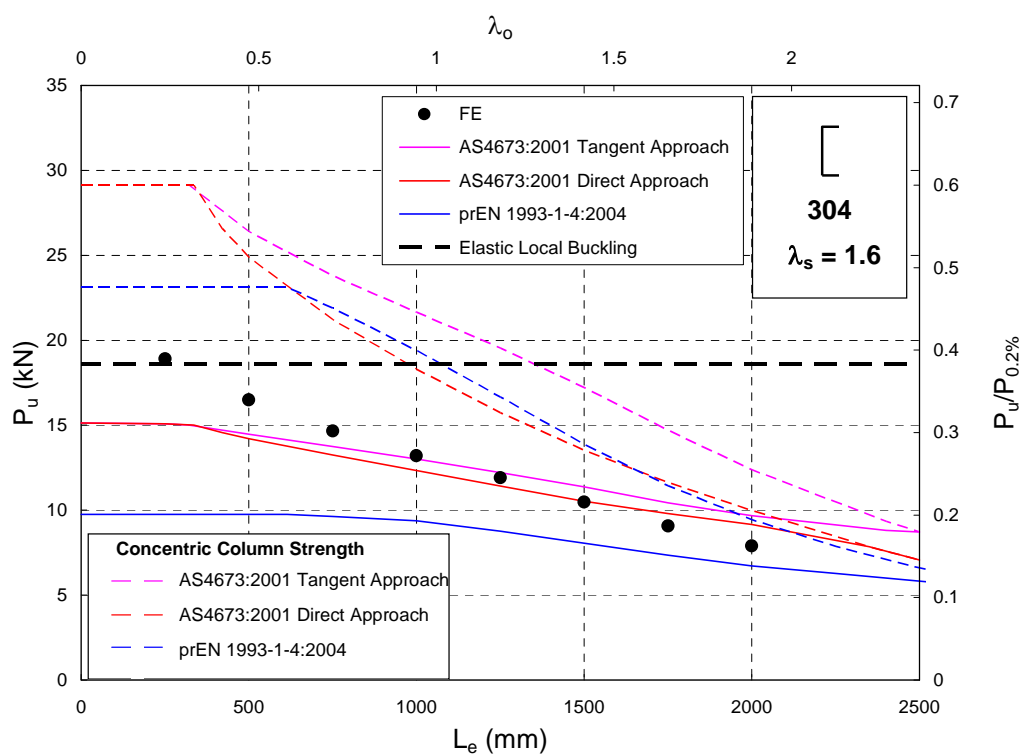

 Figure D.3. Strength Curve of 3Cr12 Lipped Channels with $\lambda_s = 2.4$

 Figure D.4. Strength Curve of 304 Lipped Channels with $\lambda_s = 1.1$

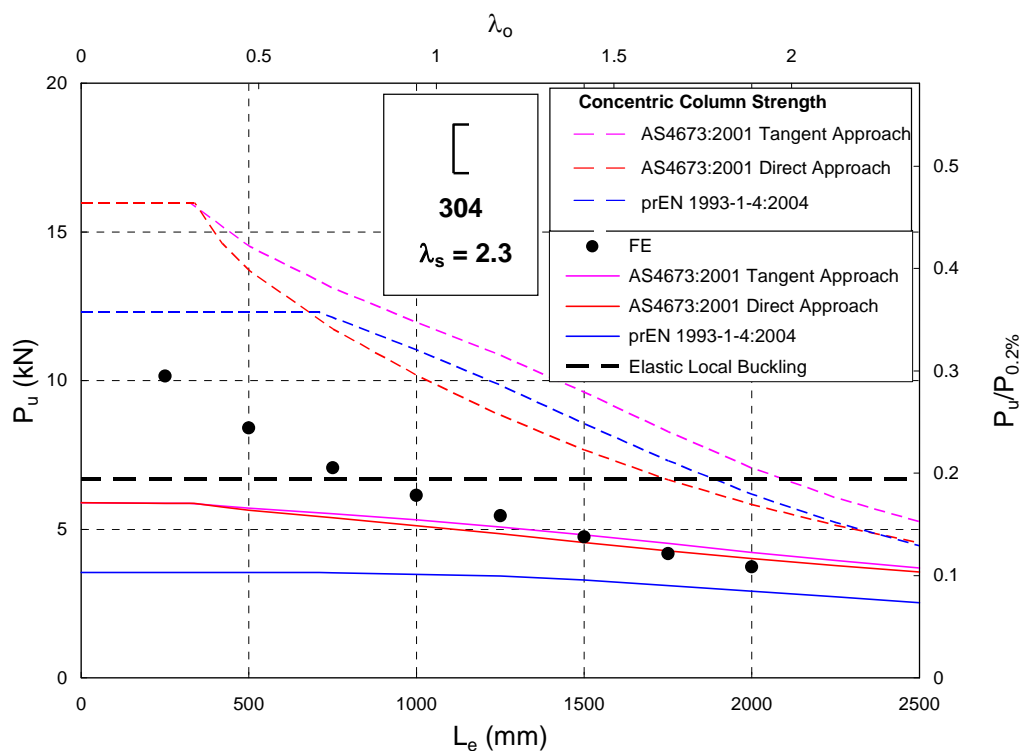
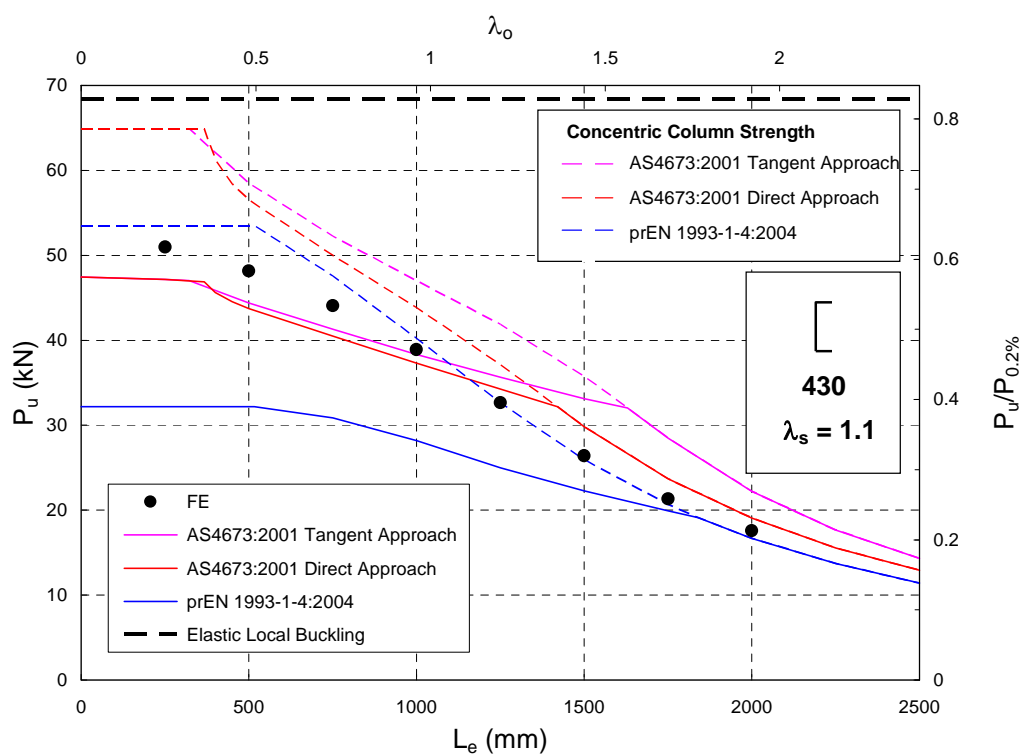

 Figure D.5. Strength Curve of 304 Lipped Channels with $\lambda_s = 1.7$

 Figure D.6. Strength Curve of 304 Lipped Channels with $\lambda_s = 2.4$

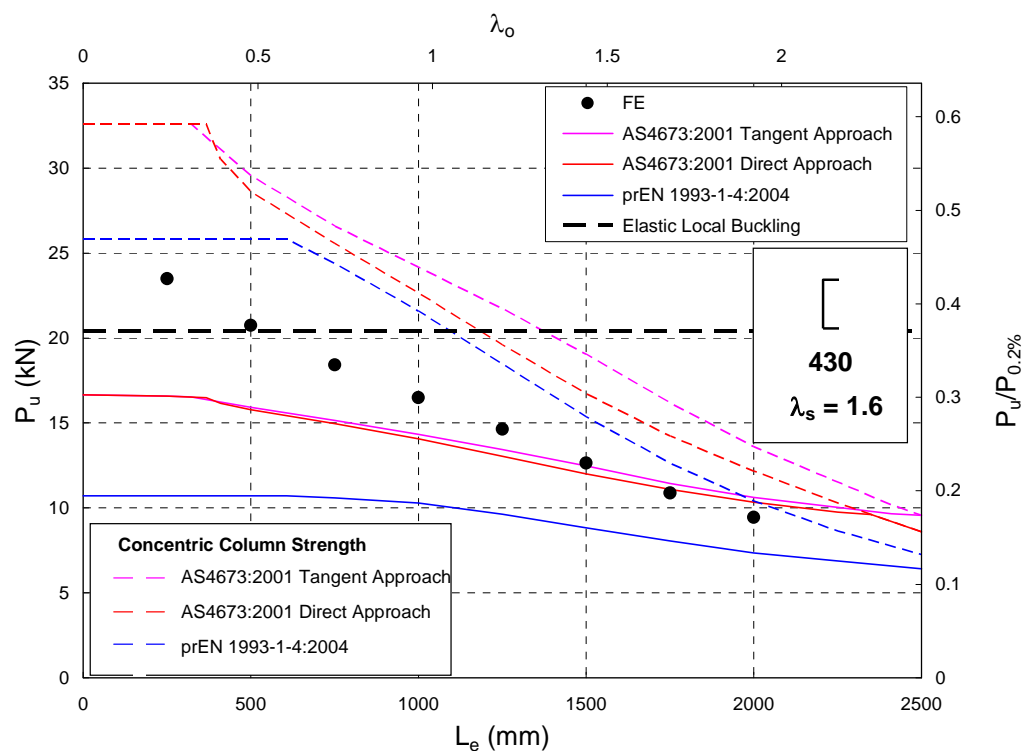
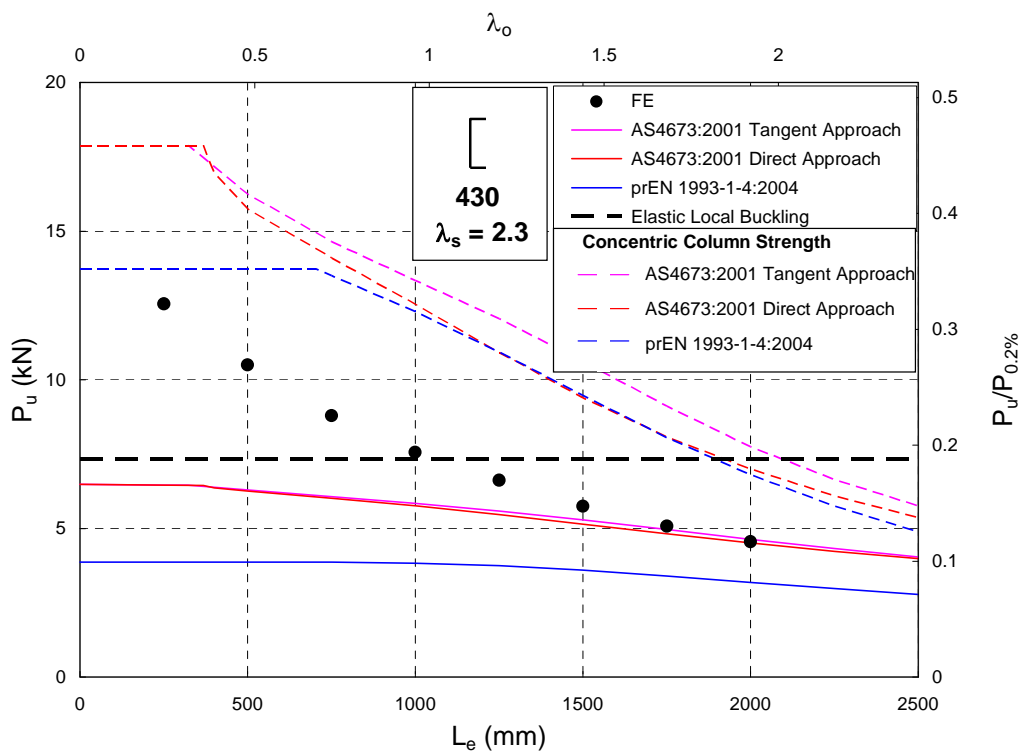

 Figure D.7. Strength Curve of 430 Lipped Channels with $\lambda_s = 1.1$

 Figure D.8. Strength Curve of 430 Lipped Channels with $\lambda_s = 1.6$

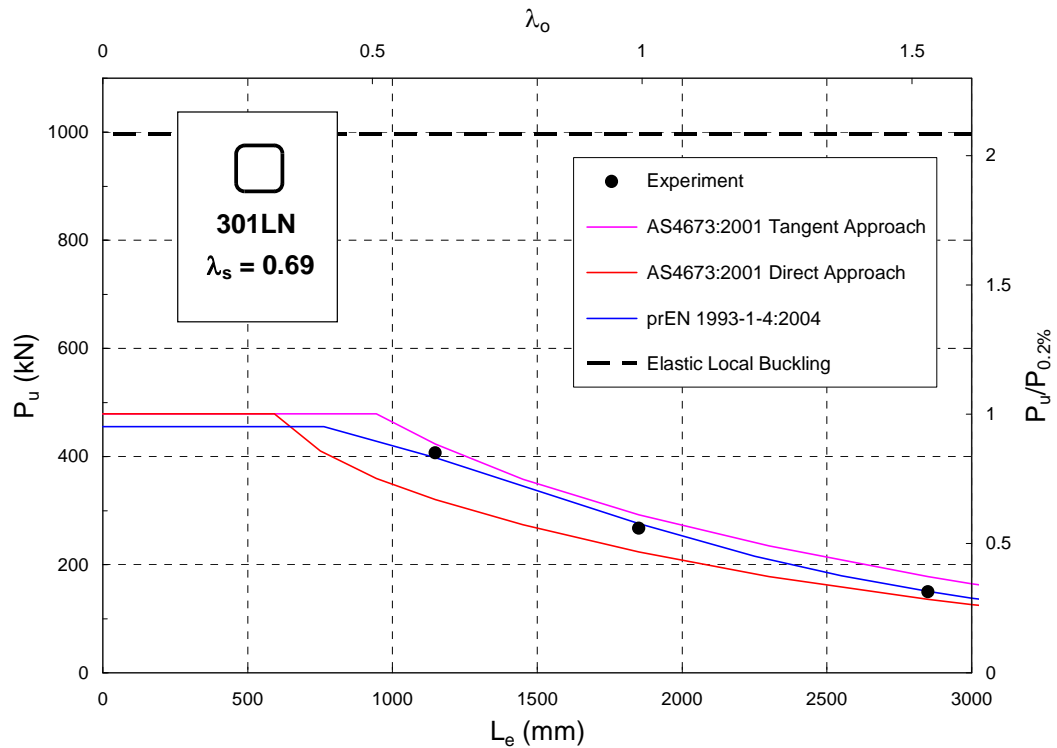
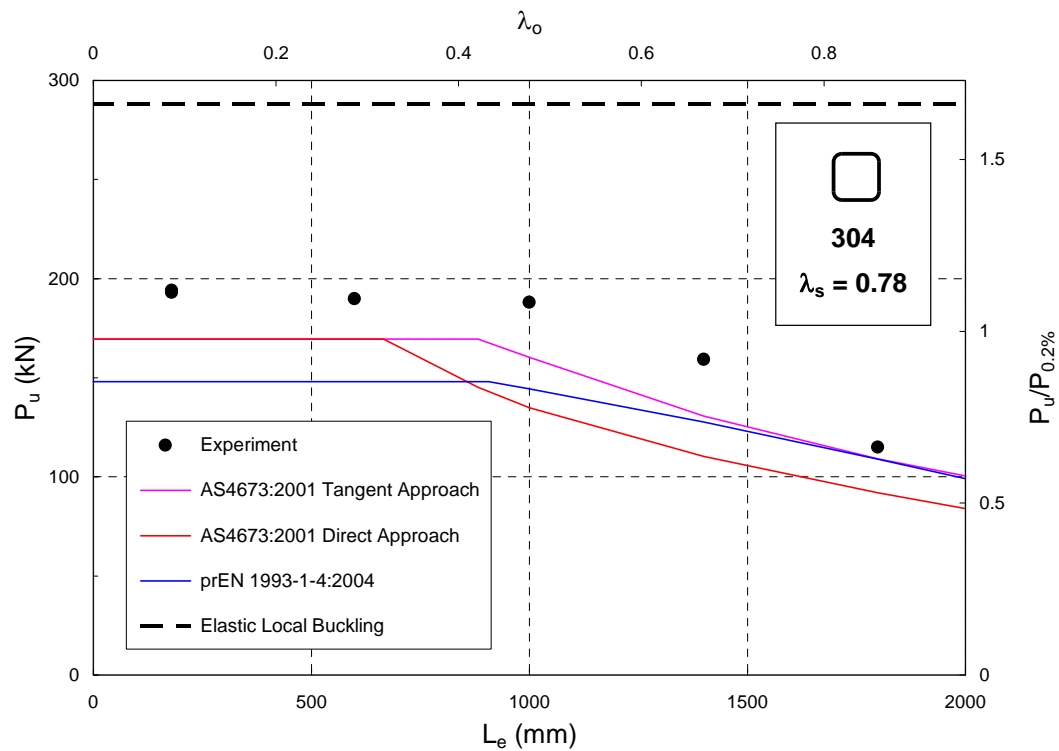

 Figure D.9. Strength Curve of 430 Lipped Channels with $\lambda_s = 2.4$

 Figure D.10. Strength Curve of 3Cr12 Plain Channels with $\lambda_s = 1.2$

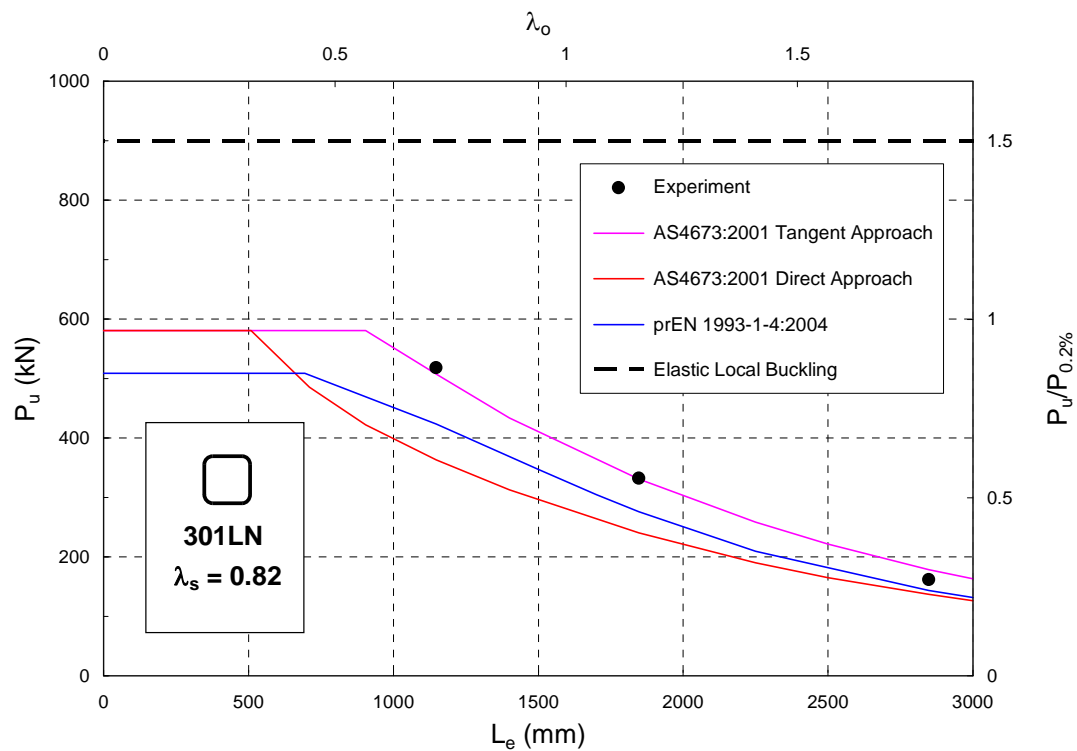
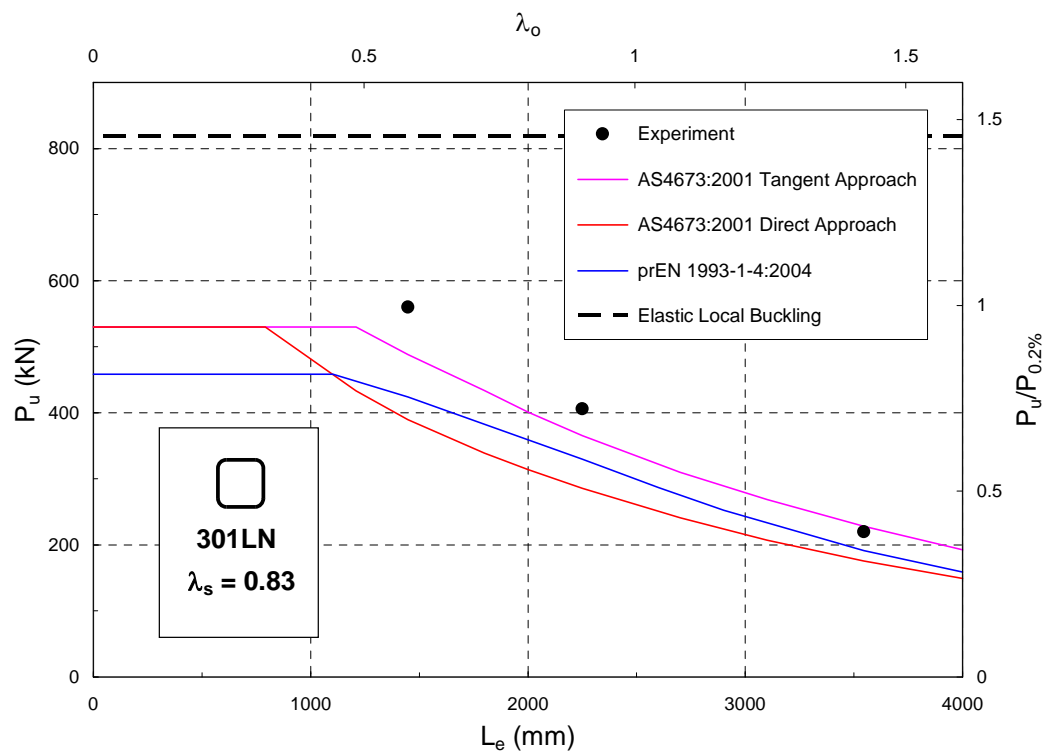

 Figure D.11. Strength Curve of 3Cr12 Plain Channels with $\lambda_s = 1.8$

 Figure D.12. Strength Curve of 3Cr12 Plain Channels with $\lambda_s = 2.5$

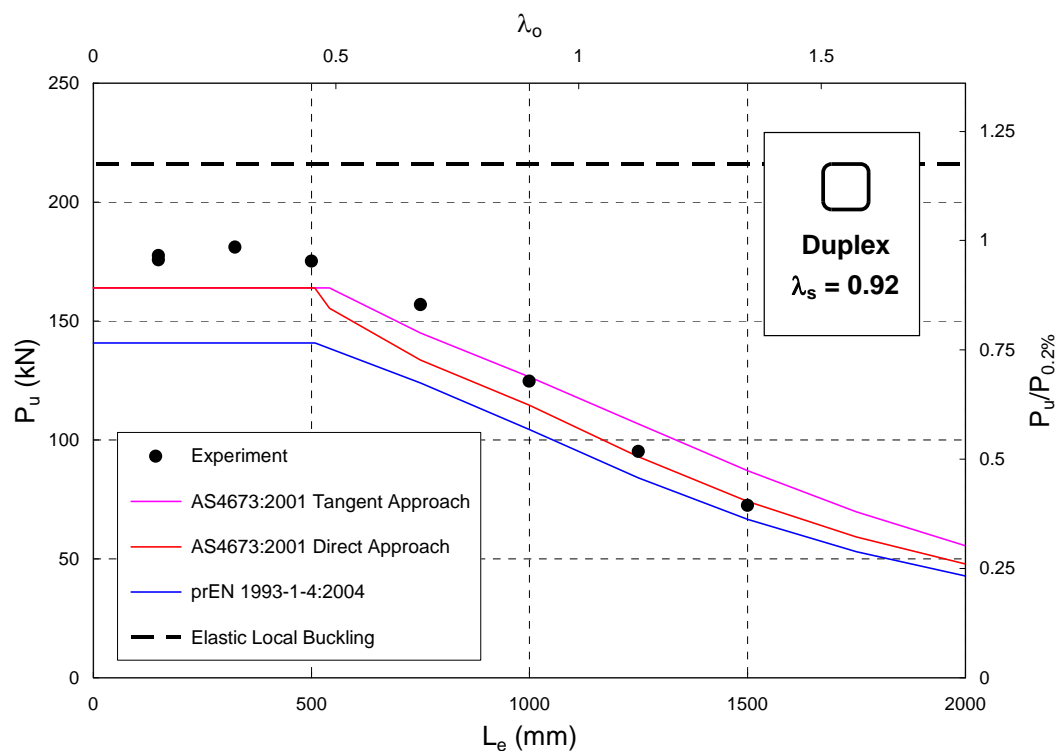
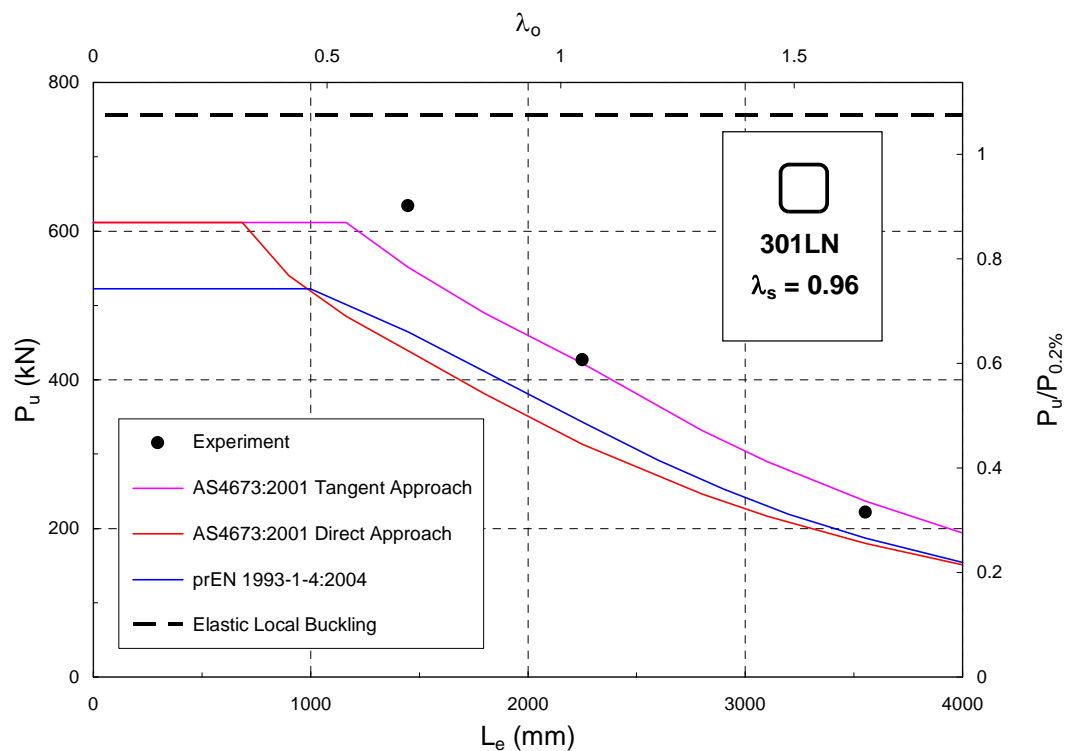

 Figure D.13. Strength Curve of 304 Plain Channels with $\lambda_s = 1.1$

 Figure D.14. Strength Curve of 304 Plain Channels with $\lambda_s = 1.6$

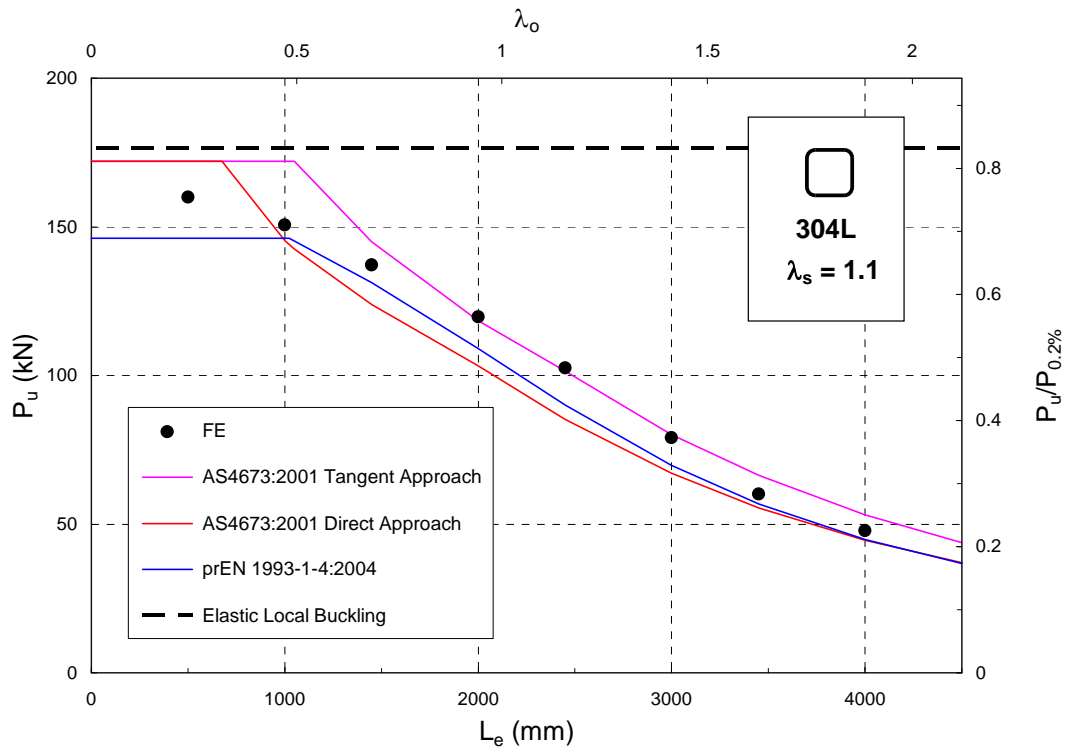
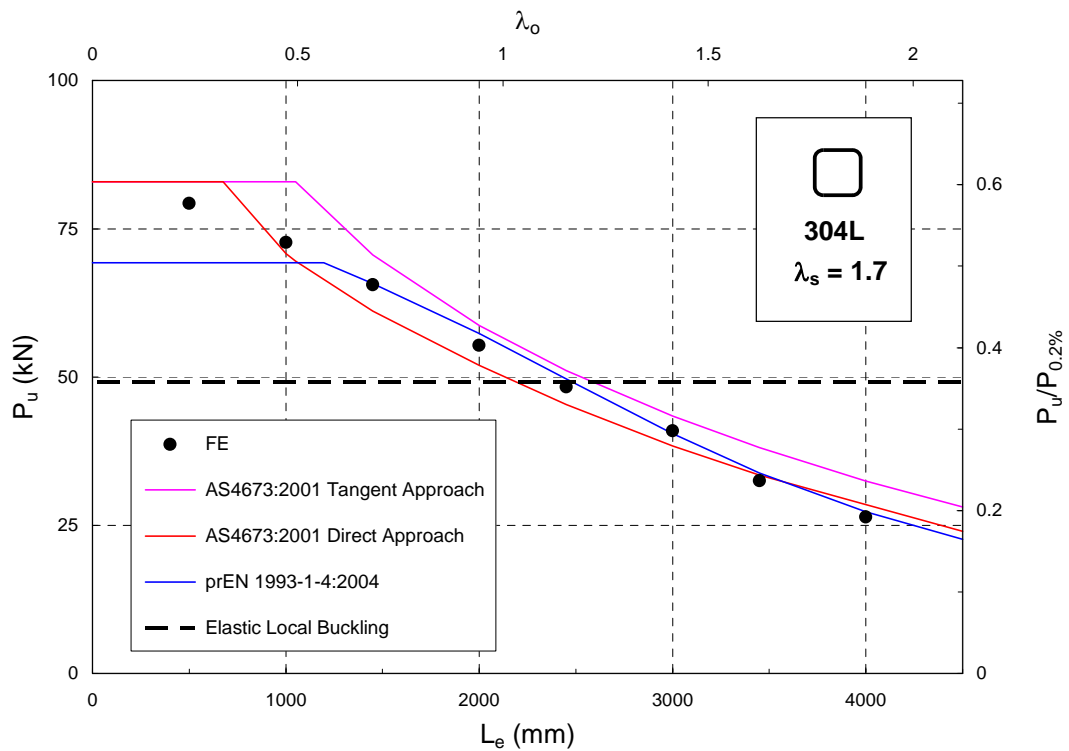

 Figure D.15. Strength Curve of 304 Plain Channels with $\lambda_s = 2.3$

 Figure D.16. Strength Curve of 430 Plain Channels with $\lambda_s = 1.1$

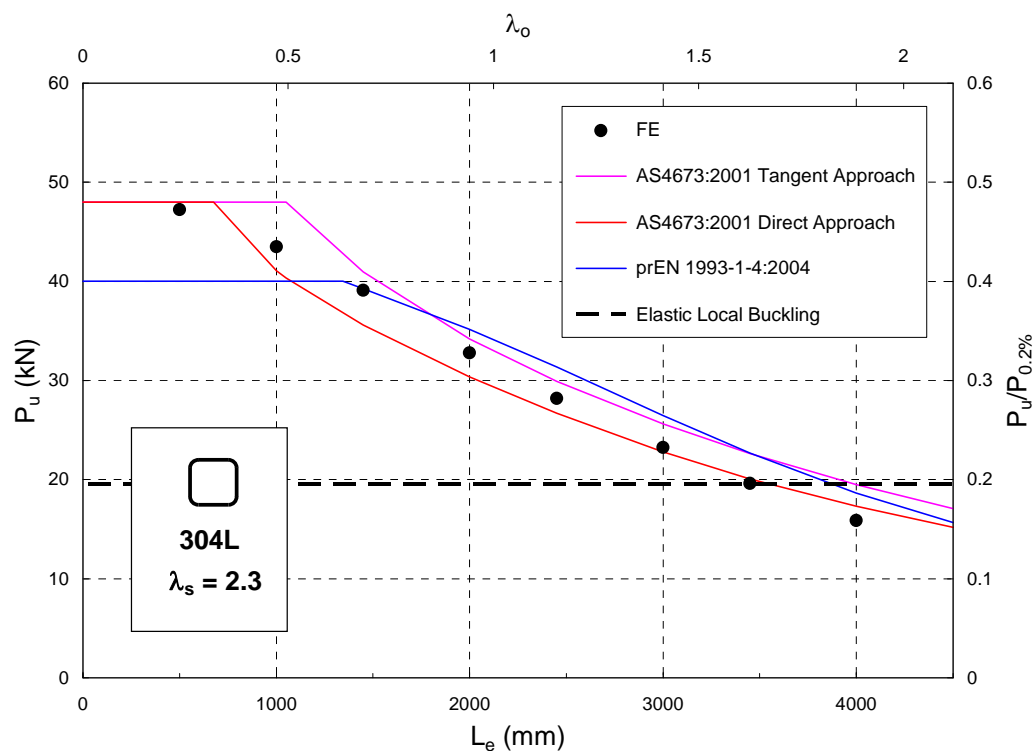
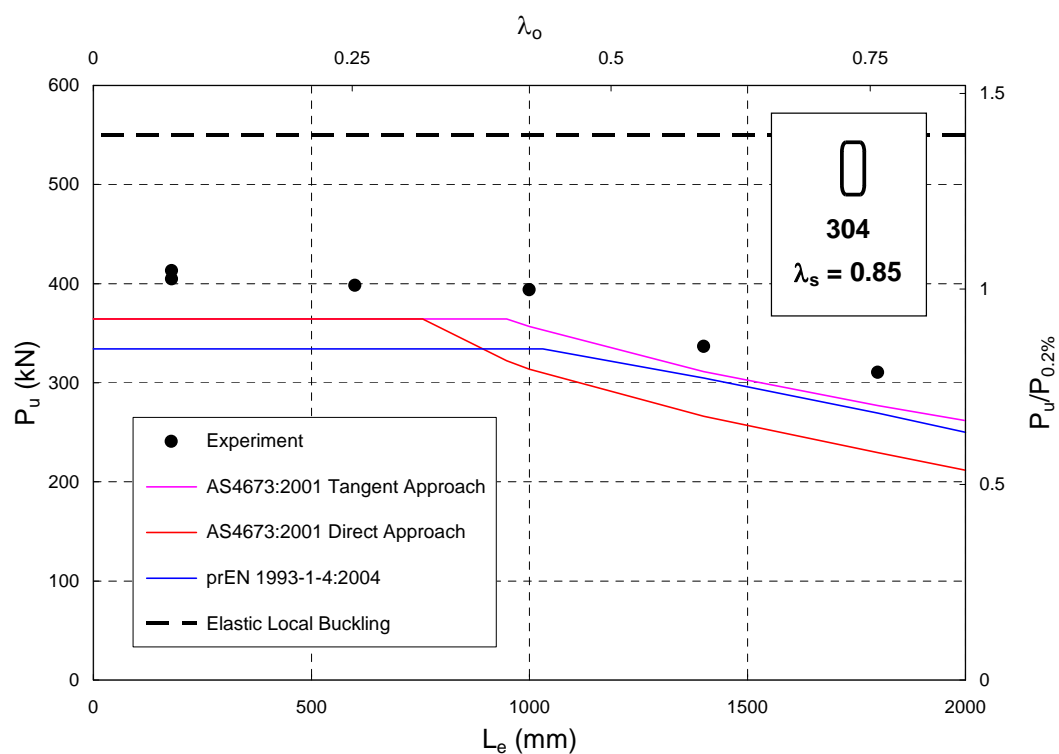

 Figure D.17. Strength Curve of 430 Plain Channels with $\lambda_s = 1.6$

 Figure D.18. Strength Curve of 430 Plain Channels with $\lambda_s = 2.3$

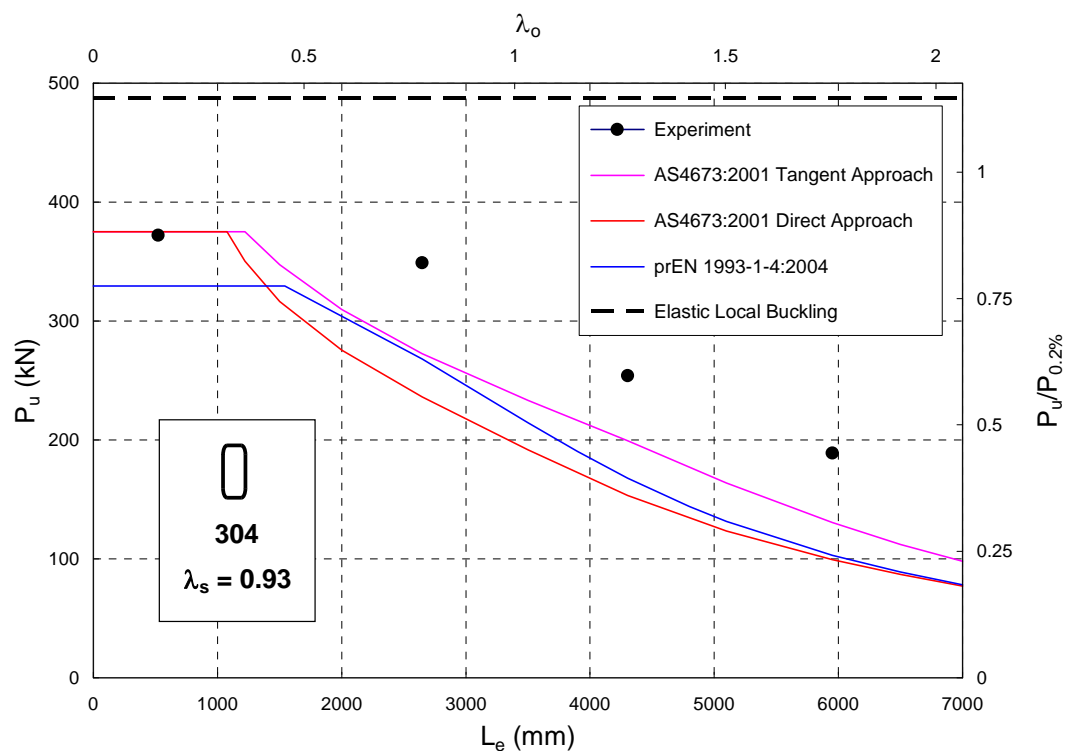
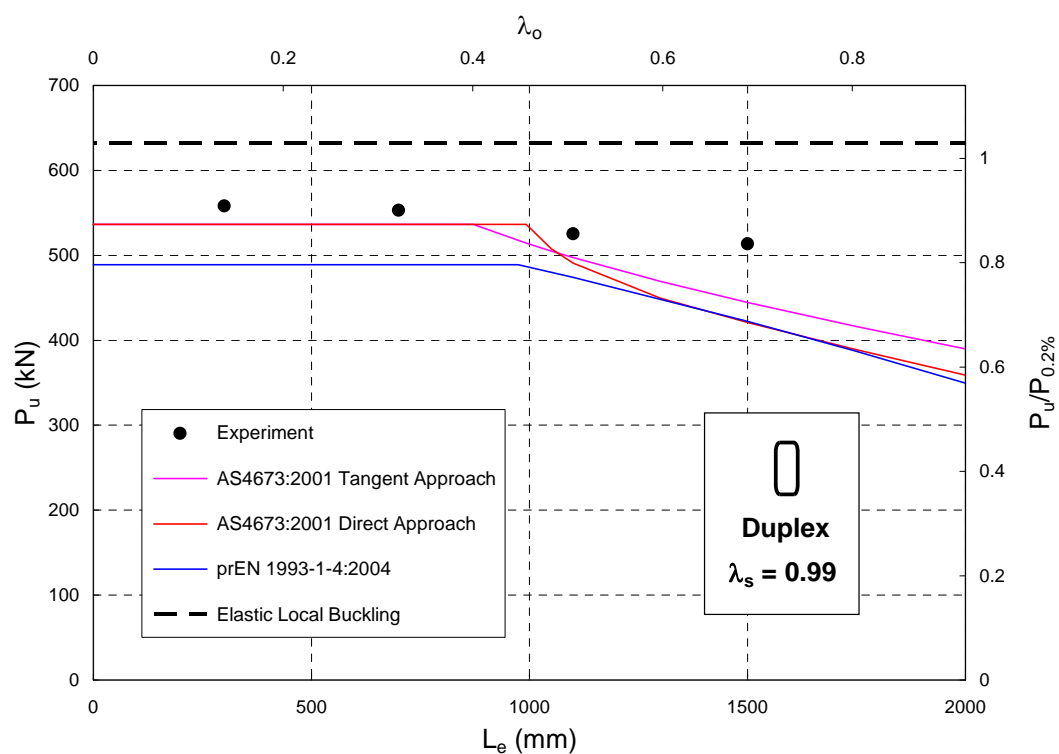

 Figure D.19. Strength Curve of 301LN SHS with $\lambda_s = 0.69$

 Figure D.20. Strength Curve of 304 SHS with $\lambda_s = 0.78$

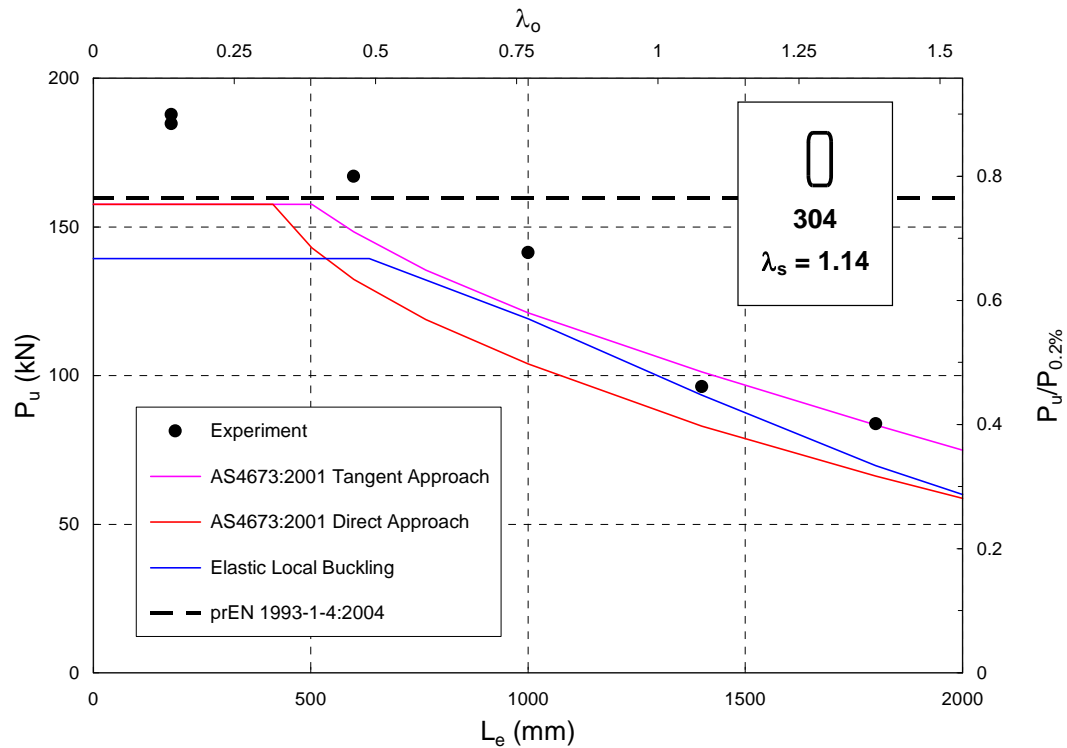
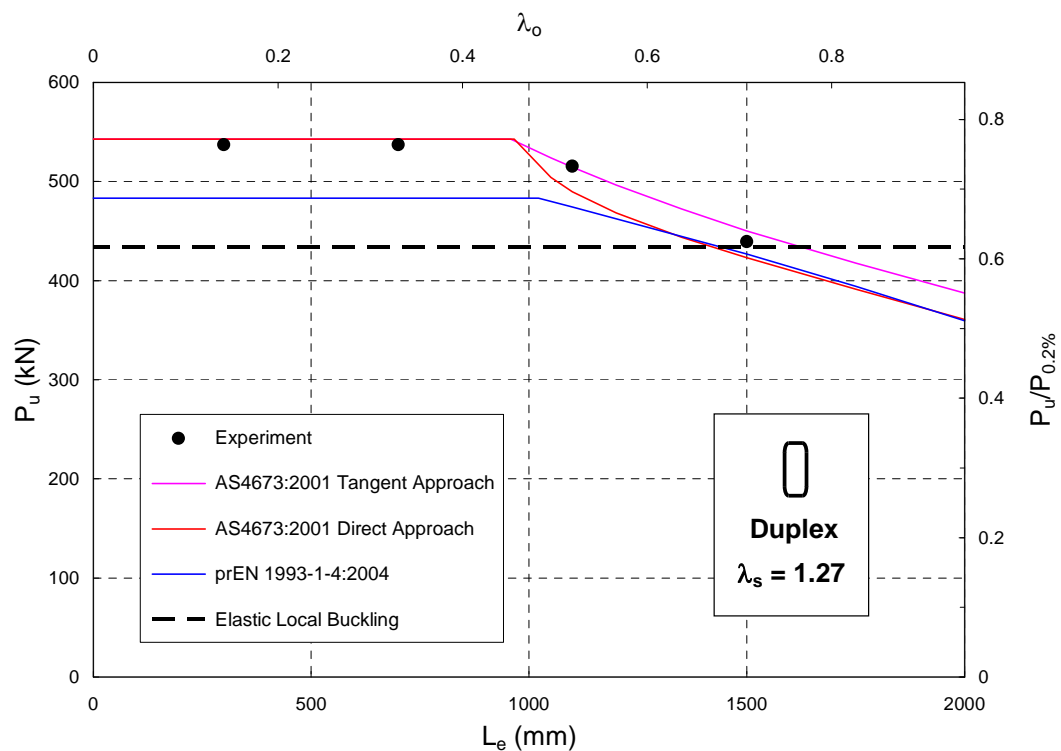

 Figure D.21. Strength Curve of 301LN SHS with $\lambda_s = 0.82$

 Figure D.22. Strength Curve of 301LN SHS with $\lambda_s = 0.83$

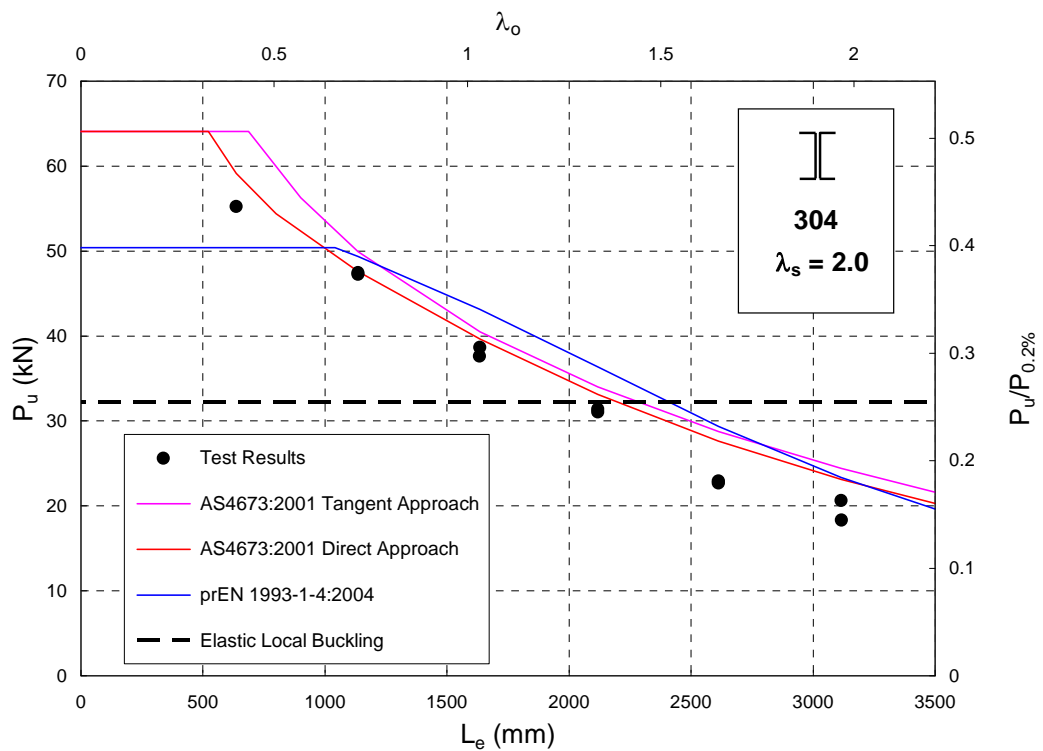
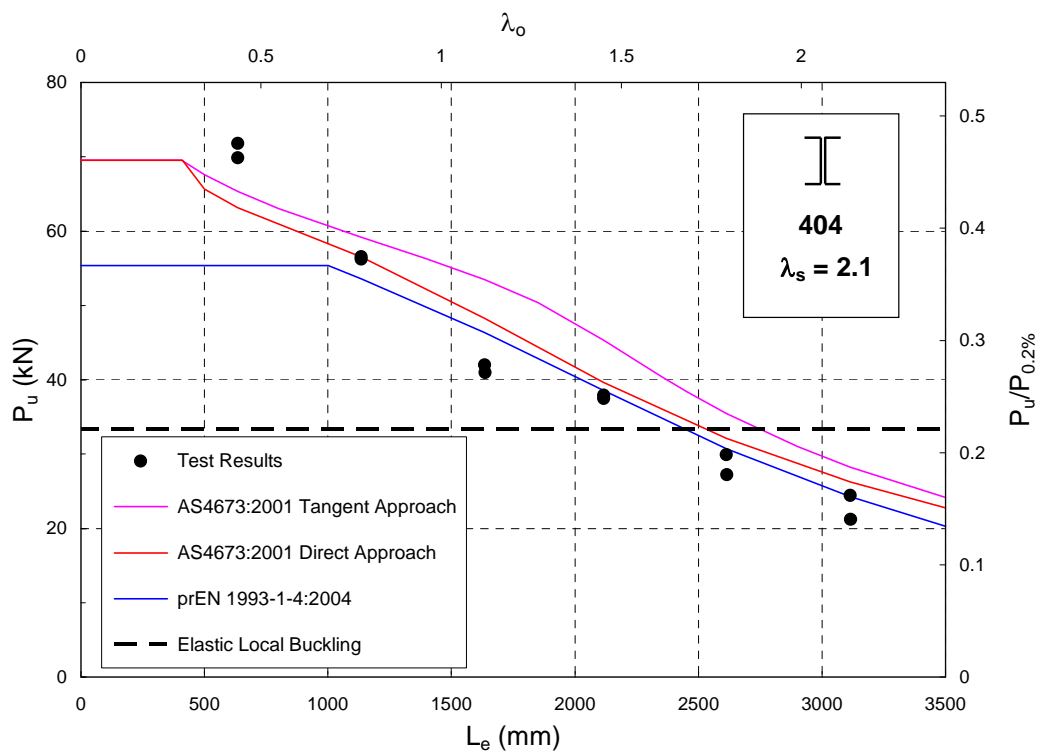

 Figure D.23. Strength Curve of Duplex SHS with $\lambda_s = 0.92$

 Figure D.24. Strength Curve of 301LN SHS with $\lambda_s = 0.96$

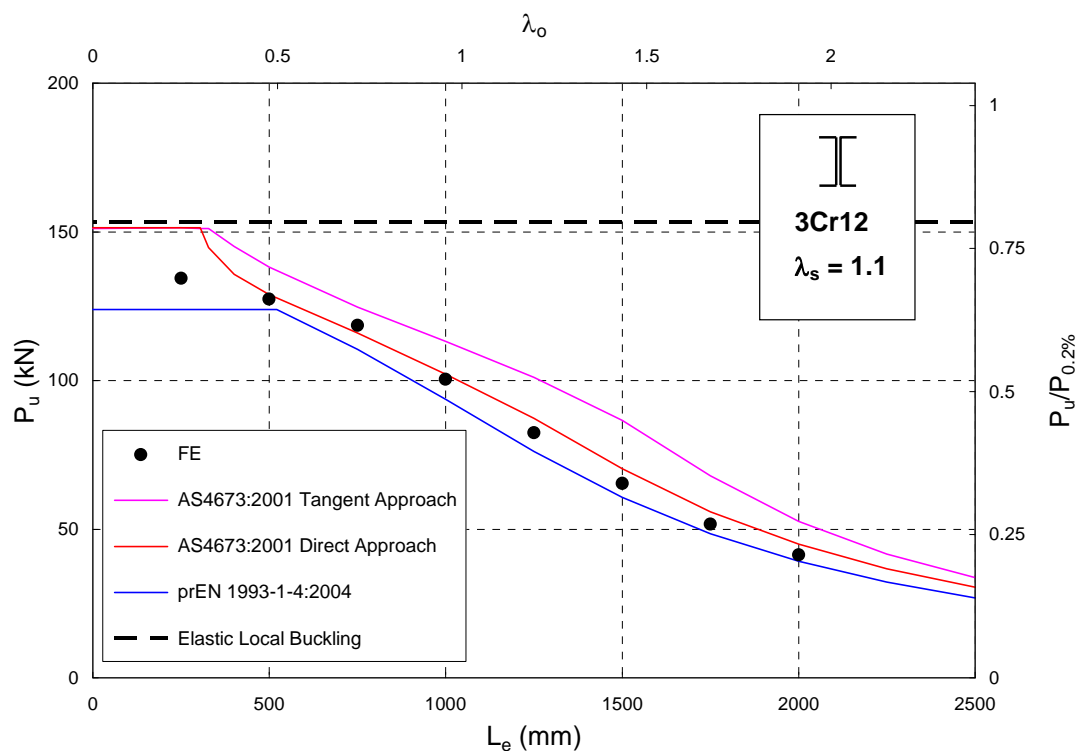
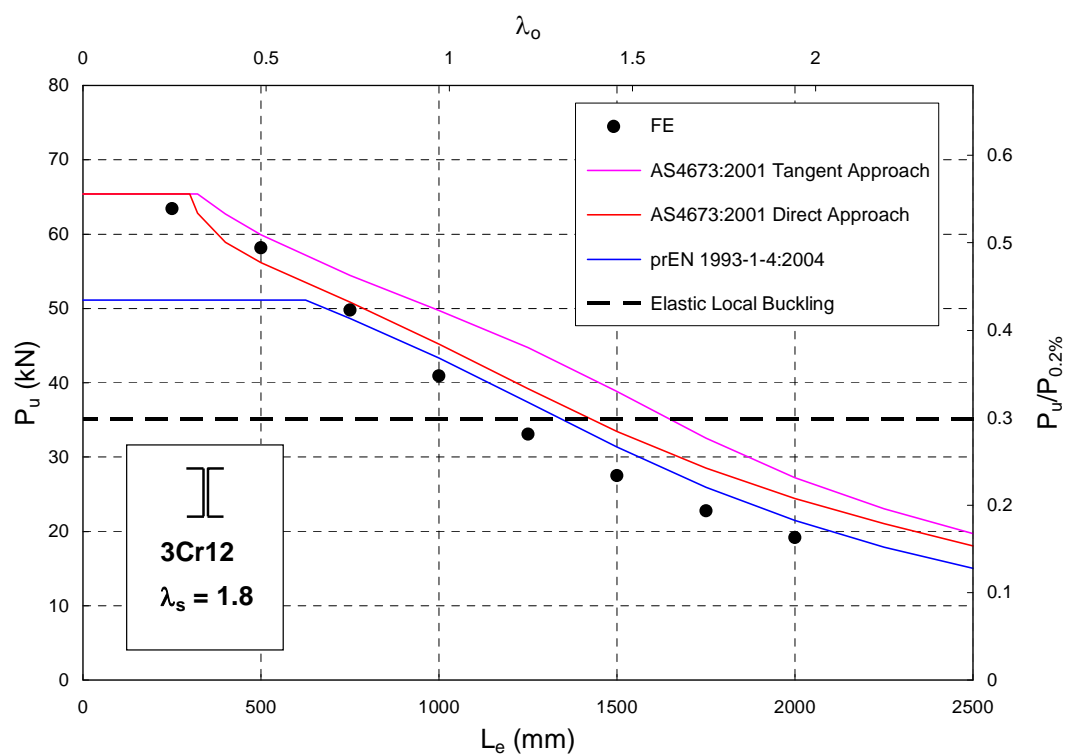

 Figure D.25. Strength Curve of 304L SHS with $\lambda_s = 1.1$

 Figure D.26. Strength Curve of 304L SHS with $\lambda_s = 1.7$

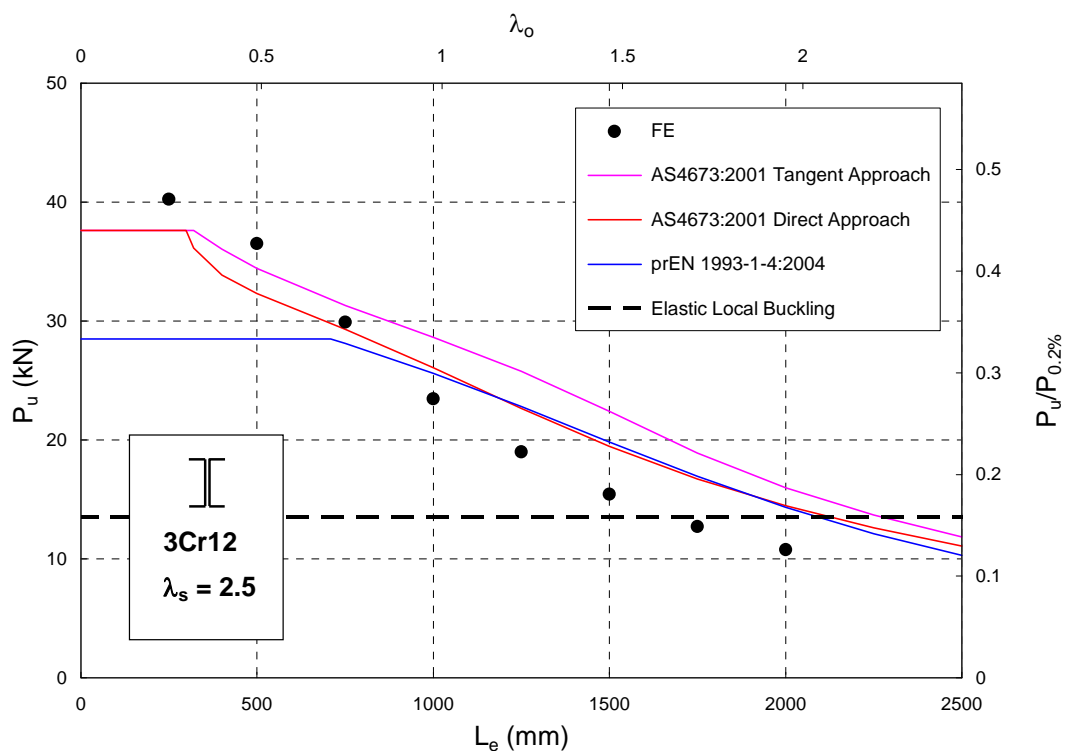
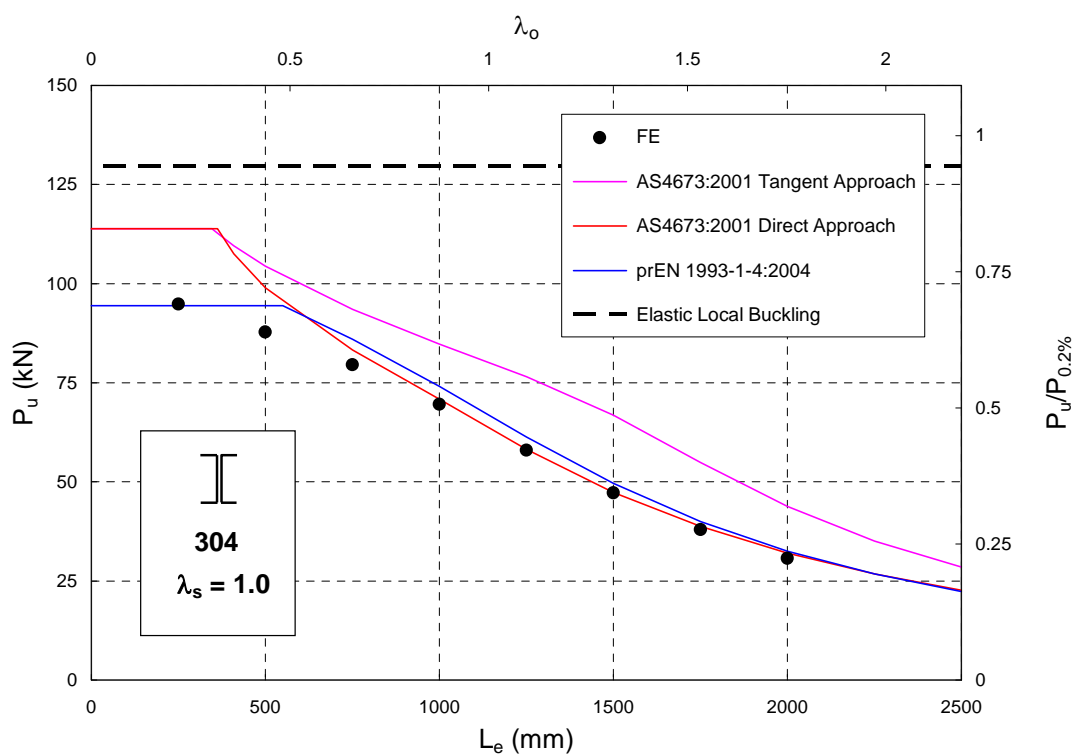

 Figure D.27. Strength Curve of 304L SHS with $\lambda_s = 2.3$

 Figure D.28. Strength Curve of 304 RHS with $\lambda_s = 0.85$

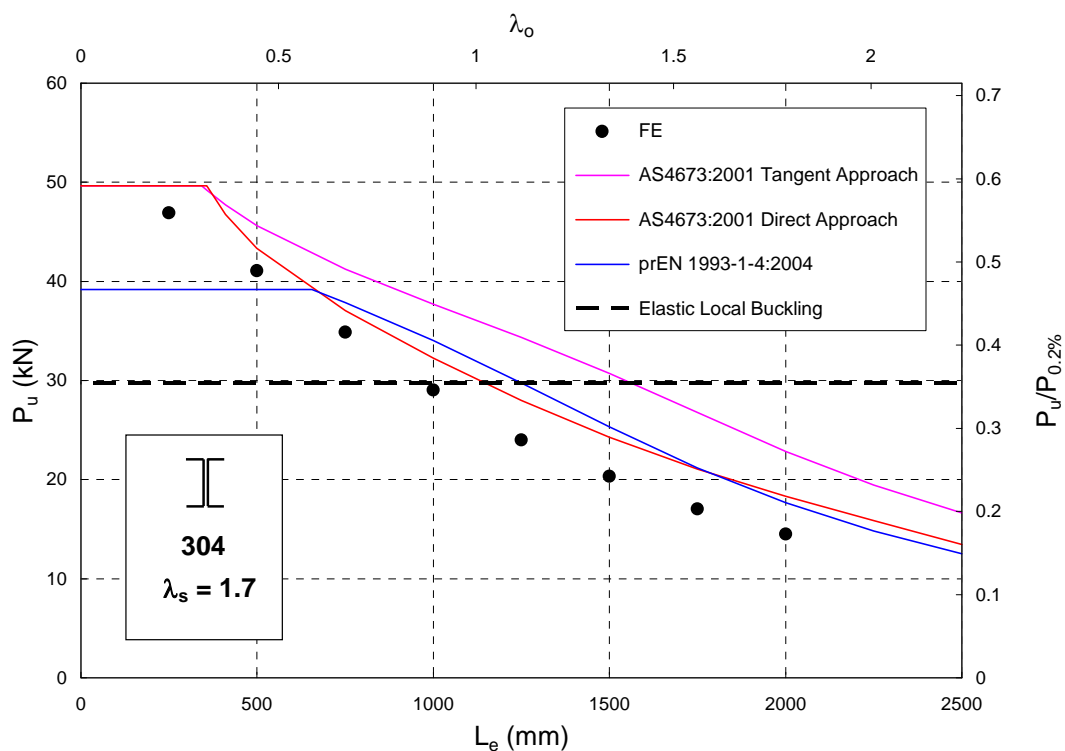
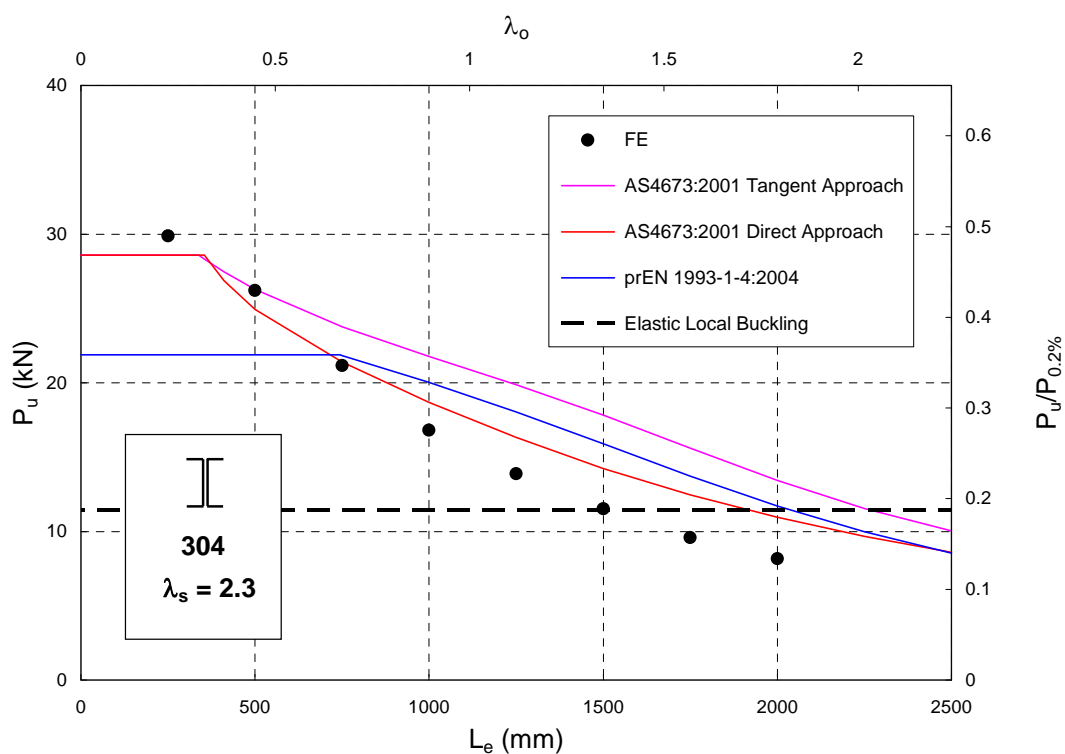

 Figure D.29. Strength Curve of 304 RHS with $\lambda_s = 0.93$

 Figure D.30. Strength Curve of Duplex RHS with $\lambda_s = 0.99$

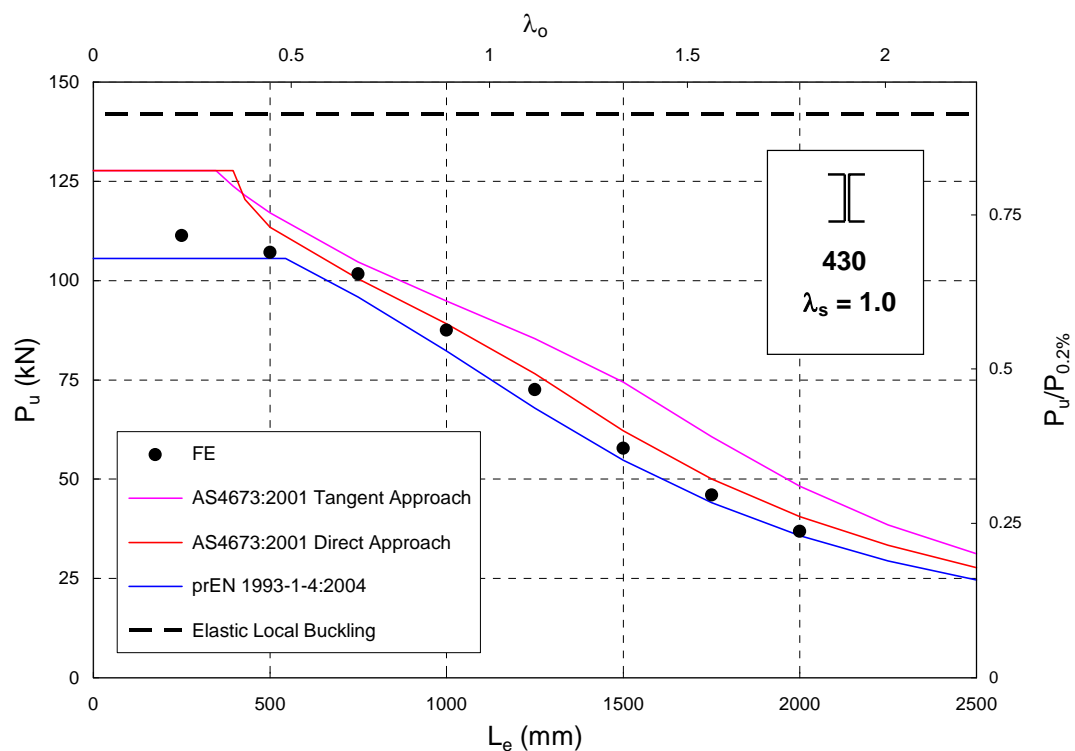
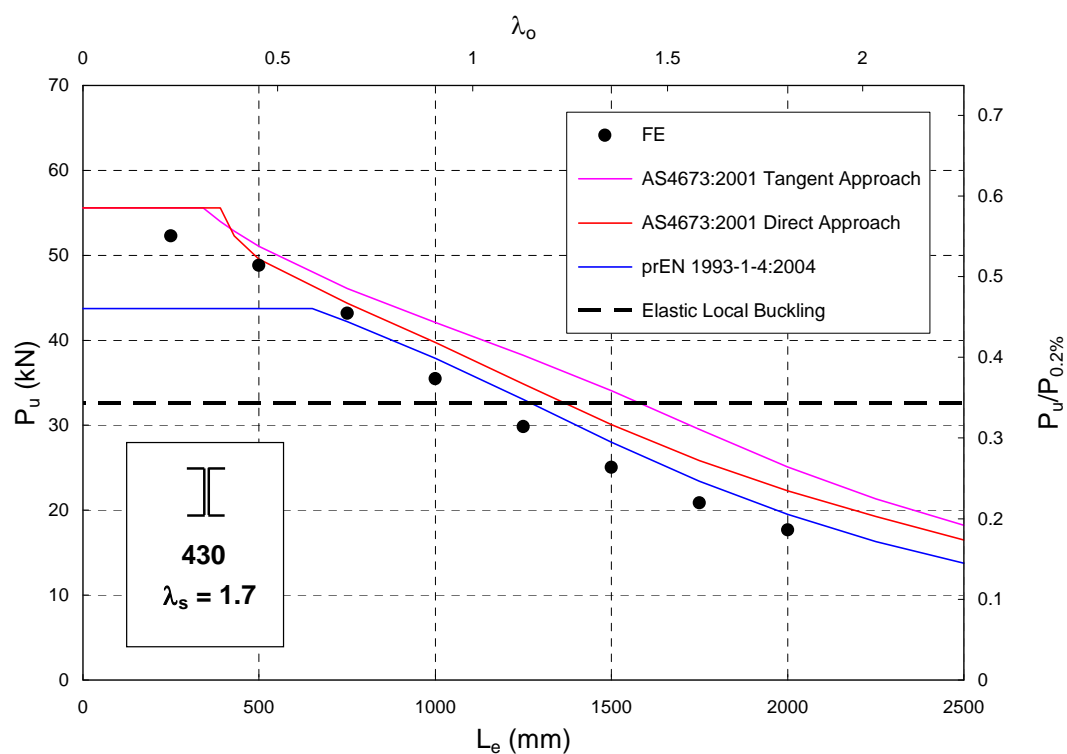

 Figure D.31. Strength Curve of 304 RHS with $\lambda_s = 1.14$

 Figure D.32. Strength Curve of Duplex RHS with $\lambda_s = 1.27$


 Figure D.33. Strength Curve of 304 I-sections with $\lambda_s = 2.0$

 Figure D.34. Strength Curve of 404 I-sections with $\lambda_s = 2.1$


 Figure D.35. Strength Curve of 3Cr12 I-sections with $\lambda_s = 1.1$

 Figure D.36. Strength Curve of 3Cr12 I-sections with $\lambda_s = 1.8$


 Figure D.37. Strength Curve of 3Cr12 I-sections with $\lambda_s = 2.5$

 Figure D.38. Strength Curve of 304 I-sections with $\lambda_s = 1.0$


 Figure D.39. Strength Curve of 304 I-sections with $\lambda_s = 1.7$

 Figure D.40. Strength Curve of 304 I-sections with $\lambda_s = 2.3$


 Figure D.41. Strength Curve of 430 I-sections with $\lambda_s = 1.0$

 Figure D.42. Strength Curve of 430 I-sections with $\lambda_s = 1.7$

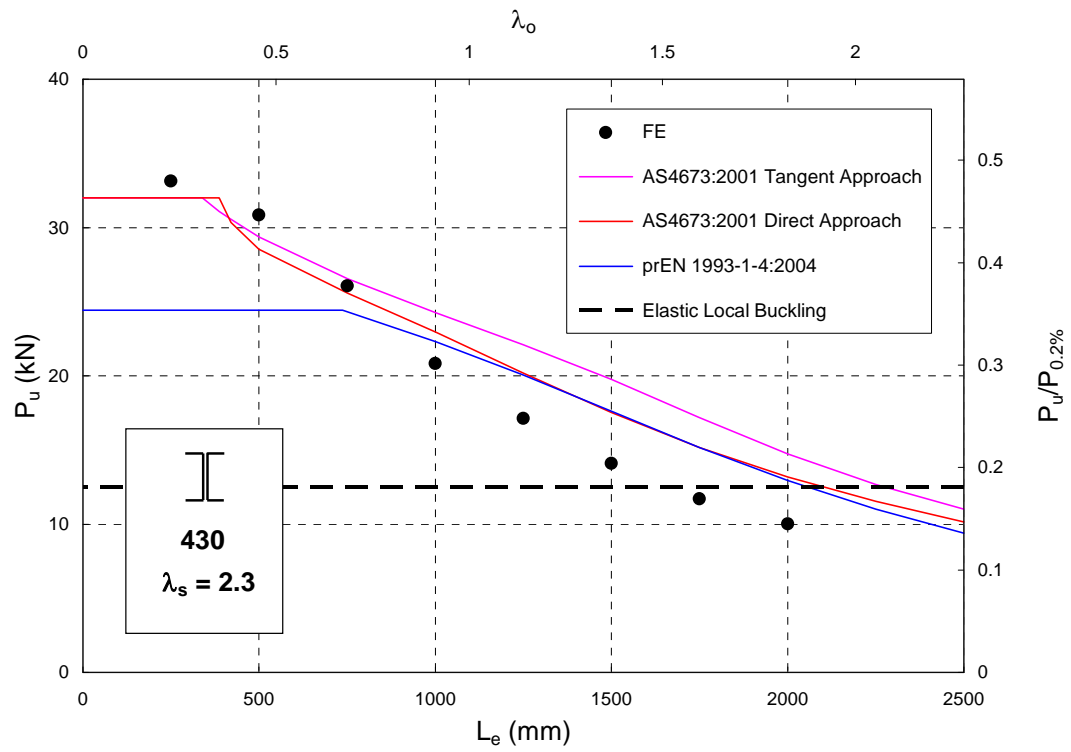


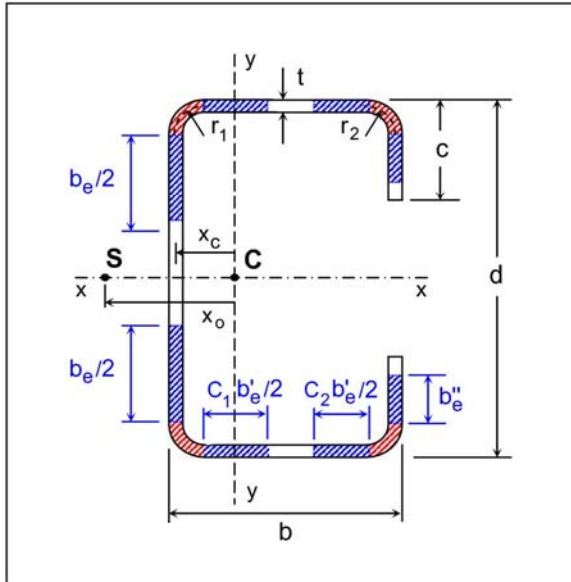
Figure D.43. Strength Curve of 430 I-sections with $\lambda_s = 2.3$

Appendix E

Appendix E contains sample calculations according to AS/NZS 4673 (2004) and prEN 1993-1-4 (2004) of stainless steel lipped channels, plain channels, RHS and back-to-back channels.

E.1. AS/NZS 4673: Lipped Channel Column (Tangent Approach)

Specimen: C3Cr12_1.32_1100



1. Geometry

t	=	1.32	mm
d	=	125.32	mm
b	=	35.00	mm
c	=	22.66	mm
r_1	=	4.14	mm
r_2	=	4.14	mm
L_x	=	1100	mm
k_x	=	0.5	
L_y	=	1100	mm
k_y	=	1.0	
L_t	=	1100	mm
k_t	=	1.0	

2. Material Properties

Stainless Steel :	3Cr12	ϕ_c =	1.00	(Clause 3.4.1)
f_y =	328	MPa		(0.2% proof stress in compression)
n =	7.5			(Ramberg-Osgood parameter)
E_o =	208	GPa	G_o =	75 GPa

3. Maximum b/t Ratios (Clause 2.1.3.1)

Web :	$d(\text{flat})/t$ =	87.7	≤	400	Ok.
Flange :	$b(\text{flat})/t$ =	19.2	≤	50	Ok.
Lip :	$c(\text{flat})/t$ =	13.5	≤	50	Ok.

4. Gross Section Properties

A =	301.29	mm ²	A_c =	34.34	mm ²	(Corner Area)
A_c/A =	11.40	%	x_c =	-10.94	mm	
I_x =	668182.8	mm ⁴	r_x =	47.09	mm	
I_y =	57985	mm ⁴	r_y =	13.87	mm	
S_x =	10664	mm ³	S_y =	2478	mm ³	
x_o =	-30.33	mm	r_o =	57.71	mm	
J =	175.0	mm ⁴	C_w =	2.32E+08	mm ⁶	

5. Buckling Stresses

5.1 Flexural buckling about y-y axis (Clause 3.4.2 - Tangent Approach)

$$f_{oc} = \frac{\pi^2 E_t}{(k_y L_y / r_y)^2} \quad \text{with} \quad E_t = \frac{f_y E_o}{f_y + 0.002 n E_o \left[\frac{f}{f_y} \right]^{n-1}}$$

$$f_{oc} = 211.28 \text{ MPa}$$

5.2 Flexural-torsional buckling (Clause 3.4.4)

$$f_n = \frac{1}{2\beta} \left[\sigma_{ex} + \sigma_t - \sqrt{(\sigma_{ex} + \sigma_t)^2 - 4\beta\sigma_{ex}\sigma_t} \right] \quad \text{with} \quad \beta = 1 - \left(\frac{x_o}{r_o} \right)^2$$

$$f_n = 223.86 \text{ MPa}$$

$$\beta = 0.724$$

6. Effective width calculations (Clause 2.2.1.2)

$$f^* = \min(f_{oc}, f_n, f_y) = 211.28 \text{ MPa} \quad S = 40.16$$

6.1 Web $k = 4.0$

$$d(\text{flat}) = 115.7 \text{ mm}$$

$$\lambda = 1.470$$

$$\rho = 0.579$$

$$b_e = 66.95 \text{ mm}$$

6.2 Flange

$$b(\text{flat}) = 25.4 \text{ mm}$$

$$b(\text{flat})/t = 19.2$$

$$I_a = 4 \text{ mm}^4$$

$$I_s = 627 \text{ mm}^4$$

$$C_1 = 1.00$$

$$C_2 = 1.00$$

$$n = 0.50$$

$$k_a = 0.79$$

$$k = 0.8$$

$$\lambda' = 0.550$$

$$\rho' = 1.000$$

$$b_e' = 25.40 \text{ mm}$$

$$C_1 b_e' / 2 = 12.70 \text{ mm}$$

$$C_2 b_e' / 2 = 12.70 \text{ mm}$$

6.3 Lip $k = 0.5$

$$c(\text{flat}) = 17.9 \text{ mm}$$

$$\lambda'' = 0.642$$

$$\rho'' = 1.000$$

$$C_2 b_e'' = 17.86 \text{ mm}$$

6.4 A_e

$$A_e = 236.92 \text{ mm}^2$$

7. Shift in Effective Centroid

$$e_N = 2.97 \text{ mm} \quad (\text{Positive away from the Web})$$

8. Member Capacity under Concentric Axial Load

$$\phi_c N_c = 50.06 \text{ kN} \quad (\text{Tangent Modulus Approach})$$

9. Weak Axis Section Bending Capacity under a Moment which puts the Web into COMPRESSION

9.1 Yield Moment (Clause 3.3.2.2)

$$f_1^* = 242.02 \text{ MPa} \quad (\text{Compression})$$

$$f_2^* = 328.00 \text{ MPa} \quad (\text{Tension})$$

9.1.1 Web k = 4.0

$$d(\text{flat}) = 115.7 \text{ mm} \quad \lambda = 1.573$$

$$\rho = 0.547 \quad b_e = 63.28 \text{ mm}$$

9.1.2 Flanges

Assume that the flanges are fully effective. (1)

9.1.3 Z_e

$$x_{ce} = -14.20 \text{ mm} \quad (\text{Centroid of the Effective Section})$$

$$A_e = 232.07 \text{ mm}^2$$

$$I_e = 47224 \text{ mm}^4$$

$$Z_e = 2345 \text{ mm}^3$$

9.1.4 Check Assumption (1)

$$\psi = -1.355 \quad \lambda = 0.117$$

$$k = 34.84 \quad \rho = 1.00$$

Assumption (1) is valid.

9.1.5 M_{sy}

$$M_{sy} = 0.769 \text{ kNm} \quad 1.25 M_{sy} = 0.961 \text{ kNm}$$

9.2 Plastic Reserve Capacity (Clause 3.3.2.3)

$$f_1^* = 328.00 \text{ MPa} \quad (\text{Compression})$$

$$\lambda_1 = 27.95 \quad \lambda_2 = 32.23 \quad C_y = 1.0$$

9.2.1 Web $k = 4.0$

$$\begin{aligned} d(\text{flat}) &= 115.7 \text{ mm} & \lambda &= 1.831 \\ \rho &= 0.480 & b_e &= 55.60 \text{ mm} \end{aligned}$$

9.2.2 S_e

$$\begin{aligned} x_N &= -11.87 \text{ mm} & (\text{Neutral Axis}) \\ S_e &= 2918 \text{ mm}^3 \\ 1.25 Z_e &= 2931 \text{ mm}^3 \end{aligned}$$

9.2.3 Flanges

$$d_w/t = 5.86 \leq \lambda_1 = 27.95 \quad \text{Ok.}$$

9.2.4 M_{sp}

$$M_{sp} = 0.957 \text{ kNm}$$

10. Interaction Equation (Clause 3.5)

$$\phi_b = 1.0$$

$$N_e = 98 \text{ kN}$$

$$N^* = 40.99 \text{ kN}$$

$$f^* = 166.73 \text{ MPa}$$

10.1 Effective Section under a Stress f^*
10.1.1 Web $k = 4.0$

$$\begin{aligned} d(\text{flat}) &= 115.7 \text{ mm} & \lambda &= 1.306 \\ \rho &= 0.637 & b_e &= 73.70 \text{ mm} \end{aligned}$$

10.1.2 Flange

$$\begin{aligned} S &= 45.21 \\ b(\text{flat}) &= 25.4 \text{ mm} & b(\text{flat})/t &= 19.2 \\ I_a &= 1 \text{ mm}^4 & I_s &= 627 \text{ mm}^4 \\ C_1 &= 1.00 & C_2 &= 1.00 \\ n &= 0.50 & k_a &= 0.79 \\ k &= 0.8 & \lambda' &= 0.489 \\ \rho' &= 1.000 & b_e' &= 25.40 \text{ mm} \\ C_1 \cdot b_e'/2 &= 12.70 \text{ mm} & C_2 \cdot b_e'/2 &= 12.70 \text{ mm} \end{aligned}$$

10.1.3 Lip

$$k = 0.5$$

$$c(\text{flat}) = 17.9 \text{ mm}$$

$$\lambda'' = 0.570$$

$$\rho'' = 1.000$$

$$C_2 \cdot b_e'' = 17.86 \text{ mm}$$

10.1.4 A_e

$$A_e = 245.83 \text{ mm}^2$$

10.2 Shift in Effective Centroid

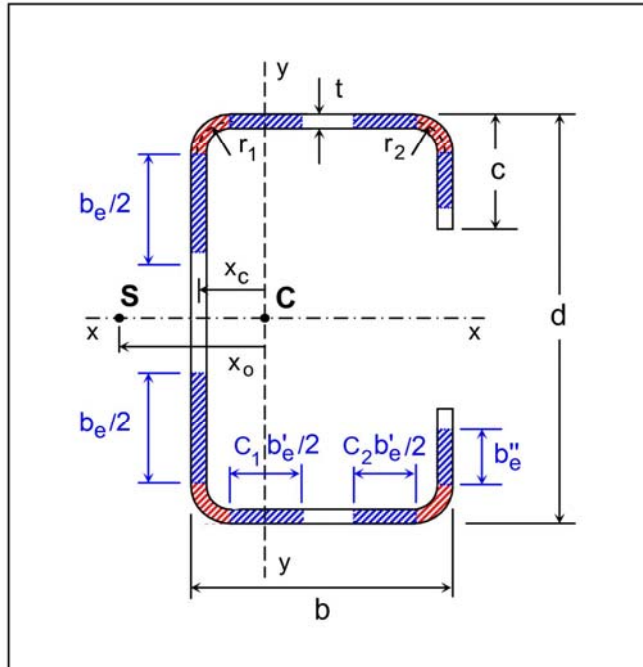
$$e_N = 2.47 \text{ mm}$$

(Positive away from the Web)

E.2. AS/NZS 4673: Lipped Channel Column (Direct Approach)

Specimen: C3Cr12_1.32_1100

1. Geometry



t	=	1.32	mm
d	=	125.32	mm
b	=	35.00	mm
c	=	22.66	mm
r_1	=	4.14	mm
r_2	=	4.14	mm
L_x	=	1100	mm
k_x	=	0.5	
L_y	=	1100	mm
k_y	=	1.0	
L_t	=	1100	mm
k_t	=	1.0	

2. Material Properties

Stainless Steel :	3Cr12	ϕ_c =	1.00	(Clause 3.4.1)
f_y =	328	MPa	(0.2% proof stress in compression)	
n =	7.5	(Ramberg-Osgood parameter)		
E_o =	208	GPa	G_o =	75 GPa

3. Maximum b/t Ratios (Clause 2.1.3.1)

Web :	$d(\text{flat})/t$ =	87.7	≤	400	Ok.
Flange :	$b(\text{flat})/t$ =	19.2	≤	50	Ok.
Lip :	$c(\text{flat})/t$ =	13.5	≤	50	Ok.

4. Gross Section Properties

A =	301.29	mm ²	A_c =	34.34	mm ²	(Corner Area)
A_c/A =	11.40	%	x_c =	-10.94	mm	
I_x =	668182.8	mm ⁴	r_x =	47.09	mm	
I_y =	57985	mm ⁴	r_y =	13.87	mm	

Gross Section Properties (Continued)

$S_x =$	10664 mm ³	$S_y =$	2478 mm ³
$x_o =$	-30.33 mm	$r_o =$	57.71 mm
$J =$	175.0 mm ⁴	$C_w =$	2.32E+08 mm ⁶

5. Buckling Stresses
5.1 Flexural buckling about y-y axis (Clause 3.4.2)

Direct Approach:

$\phi_c =$	1.00	$\lambda_o =$	0.56
$\alpha =$	0.94	$\lambda_1 =$	0.27
$\beta =$	0.15	$\eta =$	0.371
$\lambda =$	1.00	$f_{oc} =$	179.76 MPa
$\phi =$	1.19		

5.2 Flexural-torsional buckling (Clause 3.4.4)

$$f_n = \frac{1}{2\beta} \left[\sigma_{ex} + \sigma_t - \sqrt{(\sigma_{ex} + \sigma_t)^2 - 4\beta\sigma_{ex}\sigma_t} \right] \quad \text{with} \quad \beta = 1 - \left(\frac{x_o}{r_o} \right)^2$$

$$f_n = 223.86 \text{ MPa} \quad \beta = 0.724$$

6. Effective width calculations (Clause 2.2.1.2)

$$f^* = \min(f_{oc}, f_n, f_y) = 179.76 \text{ MPa} \quad S = 43.54$$

6.1 Web $k = 4.0$

$d(\text{flat}) =$	115.7 mm	$\lambda =$	1.356
$\rho =$	0.618	$b_e =$	71.51 mm

6.2 Flange

$b(\text{flat}) =$	25.4 mm	$b(\text{flat})/t =$	19.2
$I_a =$	2 mm ⁴	$I_s =$	627 mm ⁴
$C_1 =$	1.00	$C_2 =$	1.00
$n =$	0.50	$k_a =$	0.79
$k =$	0.8	$\lambda' =$	0.507

$$\begin{aligned} \rho' &= 1.000 & b_e' &= 25.40 \text{ mm} \\ C_1 \cdot b_e' / 2 &= 12.70 \text{ mm} & C_2 \cdot b_e' / 2 &= 12.70 \text{ mm} \end{aligned}$$

6.3 Lip $k = 0.5$

$$\begin{aligned} c(\text{flat}) &= 17.9 \text{ mm} & \lambda'' &= 0.592 \\ \rho'' &= 1.000 & C_2 \cdot b_e'' &= 17.86 \text{ mm} \end{aligned}$$

6.4 A_e

$$A_e = 242.94 \text{ mm}^2$$

7. Shift in Effective Centroid

$$e_N = 2.63 \text{ mm} \quad (\text{Positive away from the Web})$$

8. Member Capacity under Concentric Axial Load

$$\phi_c \cdot N_c = 43.67 \text{ kN} \quad (\text{Direct Approach})$$

9. Weak Axis Section Bending Capacity

under a Moment which puts the Web into COMPRESSION

9.1 Yield Moment (Clause 3.3.2.2)

$$f_1^* = 242.02 \text{ MPa} \quad (\text{Compression})$$

$$f_2^* = 328.00 \text{ MPa} \quad (\text{Tension})$$

9.1.1 Web $k = 4.0$

$$\begin{aligned} d(\text{flat}) &= 115.7 \text{ mm} & \lambda &= 1.573 \\ \rho &= 0.547 & b_e &= 63.28 \text{ mm} \end{aligned}$$

9.1.2 Flanges

Assume that the flanges are fully effective. (1)

9.1.3 Z_e

$$x_{ce} = -14.20 \text{ mm} \quad (\text{Centroid of the Effective Section})$$

$$A_e = 232.07 \text{ mm}^2$$

$$I_e = 47224 \text{ mm}^4$$

$$Z_e = 2345 \text{ mm}^3$$

9.1.4 Check Assumption (1)

$$\begin{aligned}\psi &= -1.355 & \lambda &= 0.117 \\ k &= 34.84 & \rho &= 1.00\end{aligned}$$

Assumption (1) is valid.

9.1.5 M_{sy}

$$M_{sy} = 0.769 \text{ kNm}$$

9.2 Plastic Reserve Capacity (Clause 3.3.2.3)

$$f_1^* = 328.00 \text{ MPa (Compression)}$$

$$\lambda_1 = 27.95 \quad \lambda_2 = 32.23 \quad C_y = 1.0$$

9.2.1 Web $k = 4.0$

$$\begin{aligned}d(\text{flat}) &= 115.7 \text{ mm} & \lambda &= 1.831 \\ \rho &= 0.480 & b_e &= 55.60 \text{ mm}\end{aligned}$$

9.2.2 S_e

$$\begin{aligned}x_N &= -11.87 \text{ mm (Plastic Neutral Axis)} \\ S_e &= 2918 \text{ mm}^3 \\ 1.25 Z_e &= 2931 \text{ mm}^3\end{aligned}$$

9.2.3 Flanges

$$d_w/t = 5.86 \leq \lambda_1 = 27.95 \quad \text{Ok.}$$

9.2.4 M_{sp}

$$M_{sp} = 0.957 \text{ kNm}$$

10. Interaction Equation (Clause 3.5)

$$\phi_b = 1.0$$

$$N_e = 98 \text{ kN}$$

$$N^* = 37.47 \text{ kN}$$

$$f^* = 149.89 \text{ MPa}$$

10.1 Effective Section under a Stress f^*

10.1.1 Web

$$k = 4.0$$

$$d(\text{flat}) = 115.7 \text{ mm} \quad \lambda = 1.238$$

$$\rho = 0.664 \quad b_e = 76.87 \text{ mm}$$

10.1.2 Flange

$$S = 47.68$$

$$b(\text{flat}) = 25.4 \text{ mm} \quad b(\text{flat})/t = 19.2$$

$$I_a = 1 \text{ mm}^4 \quad I_s = 627 \text{ mm}^4$$

$$C_1 = 1.00 \quad C_2 = 1.00$$

$$n = 0.50 \quad k_a = 0.79$$

$$k = 0.8 \quad \lambda' = 0.463$$

$$\rho' = 1.000 \quad b_e' = 25.40 \text{ mm}$$

$$C_1 \cdot b_e'/2 = 12.70 \text{ mm} \quad C_2 \cdot b_e'/2 = 12.70 \text{ mm}$$

10.1.3 Lip

$$k = 0.5$$

$$c(\text{flat}) = 17.9 \text{ mm} \quad \lambda'' = 0.540$$

$$\rho'' = 1.000 \quad C_2 \cdot b_e'' = 17.86 \text{ mm}$$

10.1.4 A_e

$$A_e = 250.01 \text{ mm}^2$$

10.2 Shift in Effective Centroid

$$e_N = 2.24 \text{ mm} \quad (\text{Positive away from the Web})$$

Specimen
<div style="border: 1px solid black; height: 100px; width: 100%;"></div>



1. Geometry

2. Material Properties

$$f_{yb} = 328 \text{ MPa} \quad (0.2\% \text{ proof stress})$$
$$E_o = 208 \text{ GPa} \qquad G_o = 80 \text{ GPa}$$
$$\gamma_{M0} = 1.00 \qquad \gamma_{M1} = 1.00$$

prEN 1993-1-4 (2004) 5.2.1

4. Other Limitations

prEN 1993-1-3 (2002)

5. Classification

prEN 1993-1-4 (2004) 5.2.2



Web :	$d(\text{flat})/t =$	87.7	Class	4
Flange :	$b(\text{flat})/t =$	19.2	Class	1
Lip :	$c/t =$	17.2	Class	4
Overall Class :			Class	4

6. Gross Section Properties

$A =$	301.29 mm ²	$A_c =$	34.34 mm ²	(Corner Area)
$A_c/A =$	11.40 %	$x_c =$	-10.94 mm	
$I_x =$	668182.8 mm ⁴	$r_x =$	47.09 mm	
$I_y =$	57985 mm ⁴	$r_y =$	13.87 mm	
$S_x =$	10664 mm ³	$S_y =$	2478 mm ³	
$x_o =$	-30.33 mm	$r_o =$	57.71 mm	
$J =$	175.0 mm ⁴	$C_w =$	2.19E+08 mm ⁶	
$\beta =$	0.724	$\delta =$	0.0254	

7. Effective width calculations

7.1 Web $k = 4.00$

$\bar{b} =$	115.72 mm	$\bar{\lambda}_p =$	1.831
$\rho =$	0.384	$b_e =$	44.47 mm

7.2 Flange $k = 4.00$

$\bar{b}' =$	25.40 mm	$\bar{\lambda}_{p'} =$	0.402
$\rho' =$	1.000	$b_{e1}' =$	12.70 mm

$\chi_d =$	0.99
------------	------

$\rho'_{red} =$	1.000	$\bar{\lambda}'_{p,red} =$	0.400
		$b_{e2}' =$	12.70 mm

7.3 Lip $k = 0.88$

$b_p'' =$	22.66 mm	$\bar{\lambda}_p'' =$	0.758
$\rho' =$	0.917	$b_e'' =$	20.78 mm

7.4 Stiffener Properties (EN 1993-1-3: 5.5.3.2)

$A_s =$	46.45 mm ²	$I_s =$	2036 mm ⁴
---------	-----------------------	---------	----------------------

$$\begin{aligned}
 K &= 0.695 \text{ N/mm}^2 & \sigma_{cr} &= 738.6 \text{ MPa} \\
 \bar{\lambda}_d &= 0.666 & \chi_d &= 0.988 \\
 A_{s,red} &= 45.90 \text{ mm}^2 & t_{red} &= 1.30 \text{ mm}
 \end{aligned}$$

7.5 A_e

$$A_e = 201.19 \text{ mm}^2$$

8. Shift in Effective Centroid

$$e_N = 4.45 \text{ mm} \quad (\text{Positive Shift away from the Web})$$

9. Flexural Buckling *prEN 1993-1-4 (2004) 5.4.2*

$$\begin{aligned}
 \alpha &= 0.49 & \bar{\lambda}_o &= 0.40 \\
 \beta_A &= 0.668 & \bar{\lambda} &= 0.819 \\
 \phi &= 0.938 & \chi &= 0.717
 \end{aligned}$$

$$N_{b,y,Rd} = 47.29 \text{ kN}$$

10. Weak Axis Section Bending Capacity

under a Moment which puts the Web into Compression *EN1993-1-3 : 6.1.4.2*

10.1 Web

$$b_e = 44.47 \text{ mm}$$

10.2 Flange $k = 23.9$

Check if flange is fully effective : **Ok.**

$$\bar{\lambda}_p' = 0.164 \quad \rho' = 1.000$$

10.3 Effective Properties

$$\begin{aligned}
 A_e &= 207.25 \text{ mm}^2 \\
 d_c' &= 15.85 \text{ mm} \quad (\text{Depth of the Compressive Portion of the Flange.}) \\
 W_{pp,eff} &= 2460 \text{ mm}^3 \quad (\text{Partially Plastic Section Modulus})
 \end{aligned}$$

10.4 Section Bending Capacity

$$M_{cy,Rd} = 0.807 \text{ kNm}$$

11. Interaction

$$\begin{aligned}
 N_{Ed} &= 36.39 \text{ kN} & N_{Ed}/N_{b,Rd} &= 0.769 \\
 e_N &= 3.43 \text{ mm} & & (\text{Shift in Effective Centroid under } N_{Ed}) \\
 N_{Ed} \cdot e_N &= 0.12 \text{ kNm} & M_{Ed}/M_{b,Rd} &= 0.155 \\
 \lambda_y &= 0.819 & k'_y &= 1.491
 \end{aligned}$$

$$N_{Ed} = 36.39 \text{ kN}$$

12. Effective Section under a Load N_{Ed}

$$f_{Ed} = 158.6 \text{ MPa}$$

12.1 Web

$$k = 4.00$$

$$\bar{b} = 115.72 \text{ mm} \quad \bar{\lambda}_p = 1.274$$

$$\rho = 0.529 \quad b_e = 61.23 \text{ mm}$$

12.2 Flange

$$k = 4.00 \quad b_{p'} = 31.25$$

$$b_{p'} = 25.4 \text{ mm} \quad \bar{\lambda}_{p'} = 0.280$$

$$\rho' = 1.000 \quad b_{e1'} = 12.70 \text{ mm}$$

$$\chi_d = 1.000 \quad \bar{\lambda}_{p,red}' = 0.280$$

$$\rho'_{red} = 1.000 \quad b_{e2'} = 12.70 \text{ mm}$$

12.3 Lip

$$k = 0.88 \quad b_p'' = 20.79$$

$$b_p'' = 22.7 \text{ mm} \quad \bar{\lambda}_p'' = 0.530$$

$$\rho' = 1.000 \quad b_e'' = 22.66 \text{ mm}$$

12.4 Stiffener Properties (EN 1993-1-3: 5.5.3.2)

$$A_s = 48.92 \text{ mm}^2 \quad I_s = 2586 \text{ mm}^4$$

$$K = 0.685 \text{ N/mm}^2 \quad \sigma_{cr} = 784.4 \text{ MPa}$$

$$\bar{\lambda}_d = 0.450 \quad \chi_d = 1.000$$

$$A_{s,red} = 48.92 \text{ mm}^2 \quad t_{red} = 1.32 \text{ mm}$$

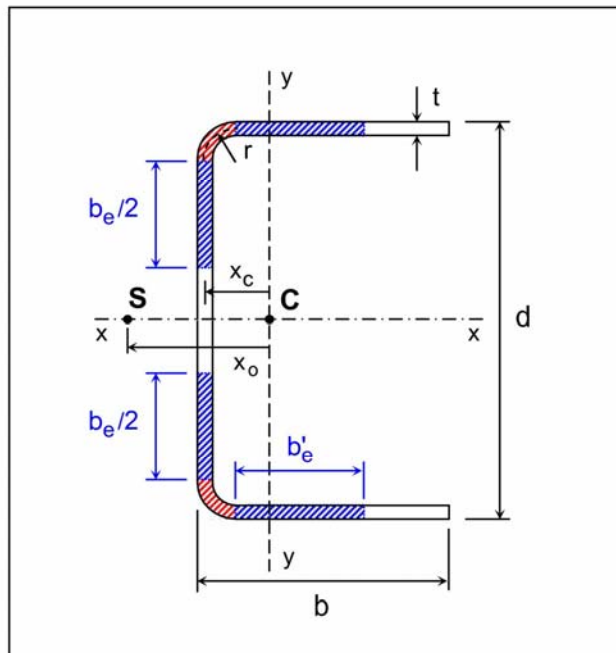
12.5 A_e

$A_e = 229.37 \text{ mm}^2$

12.6 Shift in Effective Centroid

$$e_N = 3.43 \text{ mm} \quad (\text{Positive Shift away from the Web})$$

E.4. AS/NZS 4673: Plain Channel Column (Tangent Approach)



Specimen

PC304_1.80_750

1. Geometry

t	=	1.80	mm
d	=	100.0	mm
b	=	40.0	mm
r	=	4.0	mm
L_x	=	750	mm
k_x	=	0.5	
L_y	=	750	mm
k_y	=	1.0	
L_t	=	750	mm
k_t	=	1.0	

2. Material Properties

Stainless Steel :	304	ϕ_c =	1.00	(Clause 3.4.1)
f_y =	234 MPa	(0.2% proof stress in compression)		
n =	6.5	(Ramberg-Osgood parameter)		
E_o =	176 GPa	G_o =	75 GPa	

3. Maximum b/t Ratios (Clause 2.1.3.1)

Web :	$d(\text{flat})/t$	=	50.1	\leq	400	Ok.
Flange :	$b(\text{flat})/t$	=	19.5	\leq	50	Ok.

4. Gross Section Properties

A	=	311.34	mm ²	A_c	=	22.62	mm ²	(Corner Area)
A_c/A	=	7.27	%	x_c	=	-8.85	mm	
I_x	=	463714.3	mm ⁴	r_x	=	38.59	mm	
I_y	=	47039	mm ⁴	r_y	=	12.29	mm	
S_x	=	9274	mm ³	S_y	=	1555	mm ³	

Gross Section Properties (Continued)

$$x_o = -22.45 \text{ mm}$$

$$r_o = 46.31 \text{ mm}$$

$$J = 336.2 \text{ mm}^4$$

$$C_w = 8.15\text{E}+07 \text{ mm}^6$$

5. Flexural buckling about y-y axis

(Clause 3.4.2)

$$f_{oc} = \frac{\pi^2 E_t}{(k_y L_y / r_y)^2} \quad \text{with}$$

$$E_t = \frac{f_y E_o}{f_y + 0.002 n E_o \left[\frac{f}{f_y} \right]^{n-1}}$$

$$f_{oc} = 170.81 \text{ MPa}$$

6. Effective width calculations

(Clause 2.2.1.2)

$$f^* = \min(f_{oc}, f_y) = 170.81 \text{ MPa}$$

6.1. Web $k = 4.0$

$$d(\text{flat}) = 90.2 \text{ mm}$$

$$\lambda = 0.821$$

$$\rho = 0.892$$

$$b_e = 80.42 \text{ mm}$$

6.2. Flange $k = 0.5$

$$b(\text{flat}) = 35.1 \text{ mm}$$

$$\lambda' = 0.904$$

$$\rho' = 0.837$$

$$b_e' = 29.38 \text{ mm}$$

6.3. Ae

$$A_e = 273.15 \text{ mm}^2$$

7. Shift in Effective Centroid

$$e_N = -1.49 \text{ mm}$$

(Positive away from the Web)

8. Member Capacity under Concentric Axial Load

$$\phi_c N_c = 46.66 \text{ kN}$$

(Tangent Approach)

9. Weak Axis Section Bending Capacity

under a Moment which puts the Web into TENSION

(Clause 3.3.2.2)

$$f_1^* = 234.00 \text{ MPa} \quad (\text{Compression})$$

$$f_2^* = -18.63 \text{ MPa} \quad (\text{Tension})$$

9.1.1 Web

The web is in tension and is thus fully effective.

9.1.2 Flanges $k = 0.59$ (Appendix I) $\psi = -0.080$

$b(\text{flat}) = 35.1 \text{ mm}$ $\lambda = 0.976$

$\rho = 0.794$ $b_e = 25.80 \text{ mm}$

9.1.3 Z_e

$x_{ce} = -6.59 \text{ mm}$ (Centroid of the Effective Section)

$A_e = 287.17 \text{ mm}^2$

$I_e = 28119 \text{ mm}^4$

$Z_e = 865 \text{ mm}^3$

9.1.5 M_{sy}

$M_{sy} = 0.202 \text{ kNm}$

10. Interaction Equation (Clause 3.5)

$\phi_b = 1.00$

$N_e = 145 \text{ kN}$

$N^* = 37.30 \text{ kN}$

$f^* = 125.06 \text{ MPa}$

10.1 Effective Section under a Stress f^*

10.1.1 Web $k = 4.0$

$d(\text{flat}) = 90.2 \text{ mm}$ $\lambda = 0.703$

$\rho = 0.978$ $b_e = 88.18 \text{ mm}$

10.1.2 Flange $k = 0.5$

$b(\text{flat}) = 35.1 \text{ mm}$ $\lambda' = 0.773$

$\rho' = 0.925$ $b_e' = 32.48 \text{ mm}$

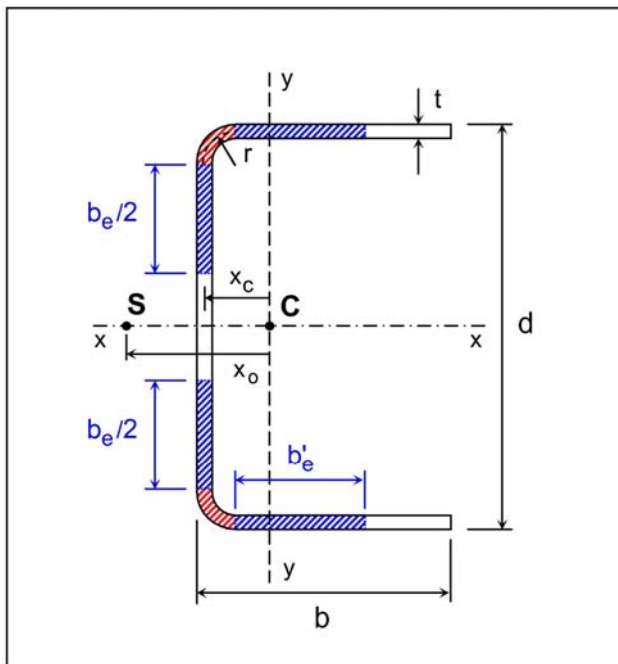
10.1.4 A_e

$A_e = 298.26 \text{ mm}^2$

10.2 Shift in Effective Centroid

$$e_N = -0.81 \text{ mm} \quad (\text{Positive away from the Web})$$

E.5. AS/NZS 4673: Plain Channel Column (Direct Approach)



Specimen

PC304_1.80_750

1. Geometry

t	=	1.80	mm
d	=	100.0	mm
b	=	40.0	mm
r	=	4.0	mm
L_x	=	750	mm
k_x	=	0.5	
L_y	=	750	mm
k_y	=	1.0	
L_t	=	750	mm
k_t	=	1.0	

2. Material Properties

Stainless Steel :	304	ϕ_c	=	1.00	(Clause 3.4.1)
f_y	=	234	MPa		(0.2% proof stress in compression)
n	=	6.5			(Ramberg-Osgood parameter)
E_o	=	176	GPa	G_o	= 75 GPa

3. Maximum b/t Ratios (Clause 2.1.3.1)

Web :	$d(\text{flat})/t$	=	50.1	\leq	400	Ok.
Flange :	$b(\text{flat})/t$	=	19.5	\leq	50	Ok.

4. Gross Section Properties

A	=	311.34	mm ²	A_c	=	22.62	mm ²	(Corner Area)
A_c/A	=	7.27	%	x_c	=	-8.85	mm	
I_x	=	463714.3	mm ⁴	r_x	=	38.59	mm	
I_y	=	47039	mm ⁴	r_y	=	12.29	mm	
S_x	=	9274	mm ³	S_y	=	1555	mm ³	

Gross Section Properties (Continued)

$$x_o = -22.45 \text{ mm}$$

$$r_o = 46.31 \text{ mm}$$

$$J = 336.2 \text{ mm}^4$$

$$C_w = 8.15\text{E}+07 \text{ mm}^6$$

5. Flexural buckling about y-y axis

(Clause 3.4.2)

Direct Approach:

$$\phi_c = 1.00$$

$$\alpha = 1.59$$

$$\lambda_o = 0.55$$

$$\beta = 0.28$$

$$\lambda_1 = 0.2$$

$$\lambda = 0.71$$

$$\eta = 0.441$$

$$\phi = 0.97$$

$$f_{oc} = 143.04 \text{ MPa}$$

6. Effective width calculations

(Clause 2.2.1.2)

$$f^* = \min(f_{oc}, f_y) = 143.04 \text{ MPa}$$

6.1. Web $k = 4.0$

$$d(\text{flat}) = 90.2 \text{ mm}$$

$$\lambda = 0.751$$

$$\rho = 0.941$$

$$b_e = 84.89 \text{ mm}$$

6.2. Flange $k = 0.5$

$$b(\text{flat}) = 35.1 \text{ mm}$$

$$\lambda' = 0.827$$

$$\rho' = 0.887$$

$$b_e' = 31.15 \text{ mm}$$

6.3. Ae

$$A_e = 287.57 \text{ mm}^2$$

7. Shift in Effective Centroid

$$e_N = -1.10 \text{ mm}$$

(Positive away from the Web)

8. Member Capacity under Concentric Axial Load

$$\phi_c N_c = 41.13 \text{ kN}$$

(Direct Approach)

9. Weak Axis Section Bending Capacity

under a Moment which puts the Web into TENSION

(Clause 3.3.2.2)

$$f_1^* = 234.00 \text{ MPa} \quad (\text{Compression})$$

$$f_2^* = -18.63 \text{ MPa} \quad (\text{Tension})$$

9.1.1 Web

The web is in tension and is thus fully effective.

9.1.2 Flanges

$$k = 0.59 \quad (\text{Appendix I})$$

$$\psi = -0.080$$

$$b(\text{flat}) = 35.1 \text{ mm}$$

$$\lambda = 0.976$$

$$\rho = 0.794$$

$$b_e = 25.80 \text{ mm}$$

9.1.3 Z_e

$$x_{ce} = -6.59 \text{ mm} \quad (\text{Centroid of the Effective Section})$$

$$A_e = 287.17 \text{ mm}^2$$

$$I_e = 28119 \text{ mm}^4$$

$$Z_e = 865 \text{ mm}^3$$

9.1.5 M_{sy}

$$M_{sy} = 0.202 \text{ kNm}$$

10. Interaction Equation

(Clause 3.5)

$$\phi_b = 1.00$$

$$N_e = 145 \text{ kN}$$

$$N^* = 35.15 \text{ kN}$$

$$f^* = 115.47 \text{ MPa}$$

10.1 Effective Section under a Stress f^*

10.1.1 Web

$$k = 4.0$$

$$d(\text{flat}) = 90.2 \text{ mm}$$

$$\lambda = 0.675$$

$$\rho = 0.999$$

$$b_e = 90.07 \text{ mm}$$

10.1.2 Flange

$$k = 0.5$$

$$b(\text{flat}) = 35.1 \text{ mm}$$

$$\lambda' = 0.743$$

$$\rho' = 0.947$$

$$b_e' = 33.25 \text{ mm}$$

10.1.4 A_e

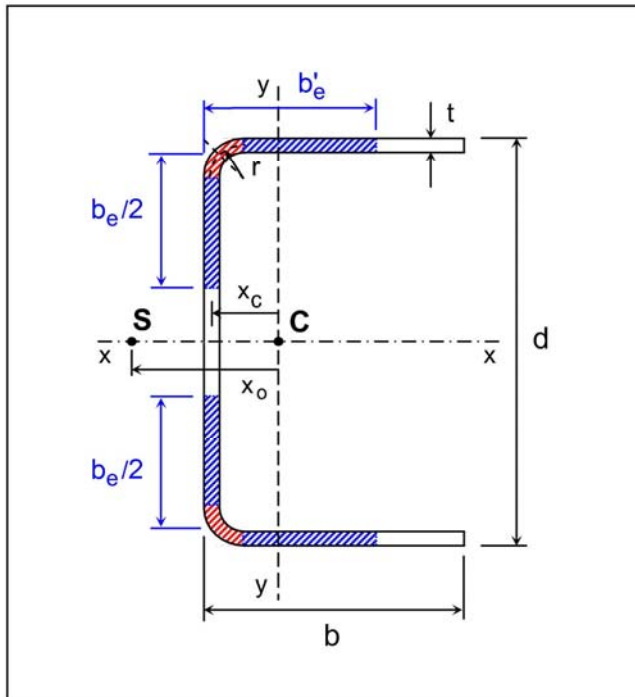
$A_e = 304.44 \text{ mm}^2$

10.2 Shift in Effective Centroid

$$e_N = -0.63 \text{ mm}$$

(Positive away from the Web)

E.6. EC3 (prEN 1993-1-4): Plain Channel Column



Specimen

PC304_1.80_750

1. Geometry

t	=	1.80	mm
d	=	100.0	mm
b	=	40.0	mm
r	=	4.0	mm
L_x	=	750	mm
k_x	=	1.0	
L_y	=	750	mm
k_y	=	1.0	
L_t	=	750	mm
k_t	=	1.0	

2. Material Properties

Stainless Steel : 304

 $f_{yb} = 234$ MPa (0.2% proof stress)

 $E_o = 176$ GPa $G_o = 67.69$ GPa

 $\gamma_{Mo} = 1.00$ $\gamma_{M1} = 1.00$

3. Maximum Width-to-Thickness Ratios prEN 1993-1-4 (2004) 5.2.1

 Web : $d/t = 55.6 \leq 400$ Ok.

 Flange : $b/t = 22.2 \leq 50$ Ok.

4. Other Limitations prEN 1993-1-3 (2002)

 $0.45 \text{ mm} \leq t \leq 15 \text{ mm}$ Ok.
 $r_i \leq 0.04 t E / f_y = 54.15$ Ok.

5. Classification prEN 1993-1-4 (2004) 5.2.2

 $\varepsilon = 0.917$

Web :	$d(\text{flat})/t =$	50.1	Class	4
Flange :	$b/t =$	22.2	Class	4
Overall Class :			Class	4

6. Gross Section Properties

$A =$	311.34 mm ²	$A_c =$	22.62 mm ²	(Corner Area)
$A_c/A =$	7.27 %	$x_c =$	-8.85 mm	
$I_x =$	463714.3 mm ⁴	$r_x =$	38.59 mm	
$I_y =$	47039 mm ⁴	$r_y =$	12.29 mm	
$S_x =$	9274 mm ³	$S_y =$	1555 mm ³	
$x_o =$	-22.45 mm	$r_o =$	46.31 mm	
$J =$	336.2 mm ⁴	$C_w =$	7.66E+07 mm ⁶	
$\beta =$	0.765	$\delta =$	0.0151	

7. Effective width calculations

7.1. Web $k = 4.00$

$\bar{b} =$	90.20 mm	$\bar{\lambda}_p =$	0.961
$\rho =$	0.668	$b_e =$	60.25 mm

7.2. Flange $k = 0.43$

$\bar{b} =$	40.00 mm	$\bar{\lambda}'_p =$	1.300
$\rho' =$	0.633	$b_e' =$	25.30 mm

7.3. A_e

$A_e = 204.51 \text{ mm}^2$

8. Shift in Effective Centroid

$$e_N = -3.59 \text{ mm} \quad (\text{Positive away from the Web})$$

9. Flexural Buckling prEN 1993-1-4:2004 5.4.2

$\alpha =$	0.49	$\bar{\lambda}_o =$	0.40
$\beta_A =$	0.657	$\bar{\lambda} =$	0.574
$\phi =$	0.707	$\chi =$	0.892

$$N_{b,y,Rd} = 42.70 \text{ kN}$$

10. Member Capacity under Concentric Axial Load

$$N_{b,Rd} = 42.70 \text{ kN}$$

11. Weak Axis Section Bending Capacity

under a Moment which puts the Web into TENSION

$$f_1^* = 234.00 \text{ MPa} \quad (\text{Compression})$$

$$f_2^* = -47.12 \text{ MPa} \quad (\text{Tension})$$

11.1.1 Web

The web is in tension and is thus fully effective.

$$11.1.2 \text{ Flanges} \quad k = 0.62 \quad \psi = -0.201$$

$$b = 40.0 \text{ mm} \quad \bar{\lambda}_p = 1.087$$

$$\rho = 0.725 \quad b_e = 24.12 \text{ mm}$$

11.1.3 Z_e

$$x_{ce} = -5.80 \text{ mm} \quad (\text{Centroid of the Effective Section})$$

$$A_e = 278.32 \text{ mm}^2$$

$$I_e = 22640 \text{ mm}^4$$

$$Z_e = 680 \text{ mm}^3$$

11.1.5 M_{sy}

$$M_{sy} = 0.159 \text{ kNm}$$

12. Interaction Equation

$$N_{Ed} = 28.00 \text{ kN} \quad N_{Ed}/N_{b,Rd} = 0.656$$

$$e_N = -1.63 \text{ mm} \quad (\text{Shift in Effective Centroid under } N_{Ed})$$

$$N_{Ed} \cdot e_N = 0.05 \text{ kNm} \quad M_{Ed}/M_{b,Rd} = 0.287$$

$$\lambda_y = 0.574 \quad k'_y = 1.200$$

$$N_{Ed} = 28.00 \text{ kN}$$

13. Effective Section under a Load N_{Ed}

$$f_{Ed} = 101.90 \text{ MPa}$$

13.1.1 Web

$$k = 4.0$$

$$\bar{b} = 90.20 \text{ mm} \quad \bar{\lambda}_p = 0.634$$

$$\rho = 0.906 \quad b_e = 81.76 \text{ mm}$$

13.1.2 Flange

$$k = 0.43$$

$$\bar{b} = 40.00 \text{ mm} \quad \bar{\lambda}'_p = 0.858$$

$$\rho' = 0.852 \quad b_{e'} = 34.07 \text{ mm}$$

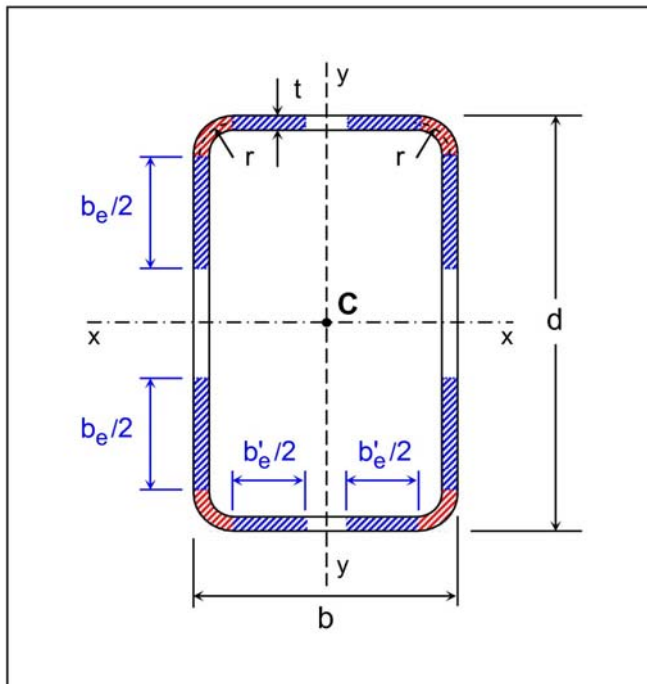
13.1.3 A_e

$$A_e = 274.82 \text{ mm}^2$$

13.2 Shift in Effective Centroid

$$e_N = -1.63 \text{ mm} \quad (\text{Positive away from the Web})$$

E.7. AS/NZS 4673: SHS/RHS Column



Specimen

Young/Liu R1L1200

1. Geometry

$$t = 1.95 \text{ mm}$$

$$d = 120.1 \text{ mm}$$

$$b = 40.0 \text{ mm}$$

$$r = 4.08 \text{ mm}$$

$$L_y = 599.25 \text{ mm}$$

$$k_y = 1.0$$

Note: d is the long dimension.

b is the short dimension.

2. Material Properties

Stainless Steel : 304

$$\phi = 1.00 \text{ (Clause 3.4.1)}$$

$$f_y = 350 \text{ MPa} \text{ (0.2\% proof stress in compression)}$$

$$n = 5 \text{ (Ramberg-Osgood parameter)}$$

$$E_o = 198 \text{ GPa}$$

$$G_o = 75 \text{ GPa}$$

3. Maximum b/t Ratios (Clause 2.1.3.1)

$$d_{\text{flat}}/t = 56.4 \leq 400 \text{ Ok.}$$

$$b_{\text{flat}}/t = 15.3 \leq 400 \text{ Ok.}$$

4. Gross Section Properties

$$A = 596.17 \text{ mm}^2$$

$$A_c = 49.98 \text{ mm}^2 \text{ (Corner Area)}$$

$$A_c/A = 8.38 \%$$

$$I_x = 1006959 \text{ mm}^4$$

$$r_x = 41.10 \text{ mm}$$

$$I_y = 179974 \text{ mm}^4$$

$$r_y = 17.37 \text{ mm}$$

$$S_x = 16766 \text{ mm}^3$$

$$S_y = 8995 \text{ mm}^3$$

5. Buckling Stresses

5.1. Tangent Approach

(Clause 3.4.2)

$$f_{oc} = \frac{\pi^2 E_t}{(k_y L_y / r_y)^2} \quad \text{with}$$

$$E_t = \frac{f_y E_o}{f_y + 0.002 n E_o \left[\frac{f}{f_y} \right]^{n-1}}$$

$$f_{oc} = 322.74 \text{ MPa}$$

5.2. Direct Approach

$$\phi_c = 1.00$$

$$\alpha = 1.59$$

$$\lambda_o = 0.55$$

$$\beta = 0.28$$

$$\lambda_1 = 0.2$$

$$\lambda = 0.46$$

$$\eta = 0.218$$

$$\phi = 0.72$$

$$f_{oc} = 277.34 \text{ MPa}$$

6. Tangent Approach: Effective width calculations

(Clause 2.2.1.2)

$$f^* = \min(f_{oc}, f_y) = 322.74 \text{ MPa}$$

6.1. Face 1 $k = 4.0$

$$d_{flat} = 110.0 \text{ mm}$$

$$\lambda = 1.197$$

$$\rho = 0.682$$

$$b_e = 75.01 \text{ mm}$$

6.2. Face 2 $k = 4.0$

$$b_{flat} = 29.9 \text{ mm}$$

$$\lambda' = 0.325$$

$$\rho' = 1.000$$

$$b_e' = 29.91 \text{ mm}$$

6.3. A_e

$$A_e = 459.55 \text{ mm}^2$$

6.4. Member Capacity

$$\phi N_c = 148.32 \text{ kN}$$

(Tangent Approach)

7. Direct Approach: Effective width calculations (Clause 2.2.1.2)

$$f^* = \min (f_{oc}, f_y) = 277.34 \text{ MPa}$$

7.1. Face 1 $k = 4.0$

$$d_{flat} = 110.0 \text{ mm} \quad \lambda = 1.110$$

$$\rho = 0.723 \quad b_e = 79.49 \text{ mm}$$

7.2. Face 2 $k = 4.0$

$$b_{flat} = 29.9 \text{ mm} \quad \lambda' = 0.302$$

$$\rho' = 1.000 \quad b_e' = 29.91 \text{ mm}$$

7.3. Ae

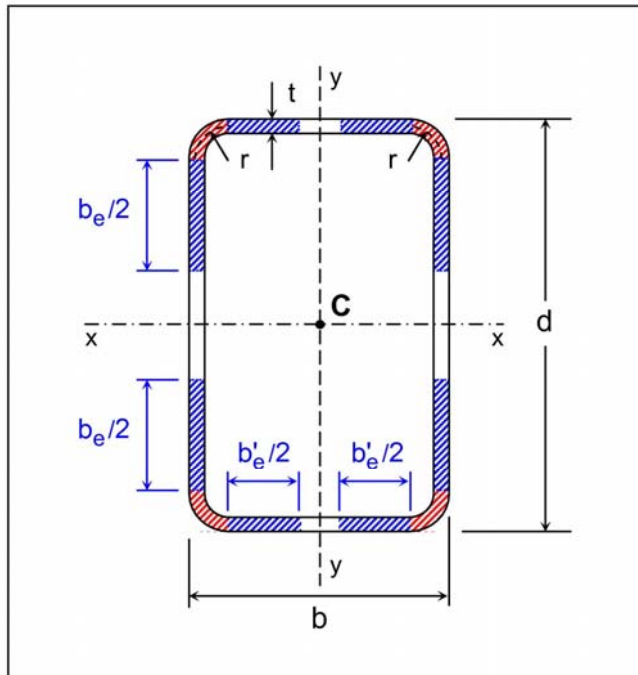
$$A_e = 477.01 \text{ mm}^2$$

7.4. Member Capacity

$$\phi.N_c = 132.29 \text{ kN}$$

(Direct Approach)

E.8. EC3 (prEN 1993-1-4): SHS/RHS Column



Specimen

Young/Liu R1L1200

1. Geometry

$$t = 1.95 \text{ mm}$$

$$d = 120.1 \text{ mm}$$

$$b = 40.0 \text{ mm}$$

$$r = 4.08 \text{ mm}$$

$$L_y = 599.25 \text{ mm}$$

$$k_y = 1.0$$

Note: d is the long dimension.

b is the short dimension.

2. Material Properties

Stainless Steel : 304

$$f_y = 350 \text{ MPa} \quad (0.2\% \text{ proof stress in compression})$$

$$E_o = 198 \text{ GPa} \quad G_o = 76.2 \text{ GPa}$$

$$\gamma_{Mo} = 1.00 \quad \gamma_{M1} = 1.00$$

3. Maximum b/t Ratios prEN 1993-1-4 (2004) 5.2.1

$$d_{flat}/t = 56.4 \leq 400 \quad \text{Ok.}$$

$$b_{flat}/t = 15.3 \leq 400 \quad \text{Ok.}$$

Other Limitations prEN 1993-1-3 (2002)

$$0.45 \text{ mm} \leq t \leq 15 \text{ mm} \quad \text{Ok.}$$

$$r_i \leq 0.04 t E / f_y = 44.16 \quad \text{Ok.}$$

4. Classification prEN 1993-1-4 (2004) 5.2.2

$$\varepsilon = 0.796$$

$$d_{flat}/t = 56.4 \quad \text{Class } 4$$

5. Gross Section Properties

$A =$	596.17 mm ²	$A_c =$	49.98 mm ²	(Corner Area)
$A_c/A =$	8.38 %			
$I_x =$	1006959 mm ⁴	$r_x =$	41.10 mm	
$I_y =$	179974 mm ⁴	$r_y =$	17.37 mm	
$S_x =$	16766 mm ³	$S_y =$	8995 mm ³	

6. Effective width calculations

6.1. Face 1 $k = 4.0$

$d_{\text{flat}} =$	110.0 mm	$\lambda =$	1.247
$\rho =$	0.539	$b_e =$	59.28 mm

6.2. Face 2 $k = 4.0$

$b_{\text{flat}} =$	29.9 mm	$\lambda' =$	0.339
$\rho' =$	1.000	$b_e' =$	29.91 mm

6.3. A_e

$A_e =$	398.15 mm ²
---------	------------------------

7. Flexural Buckling prEN 1993-1-4 (2004) 5.4.2

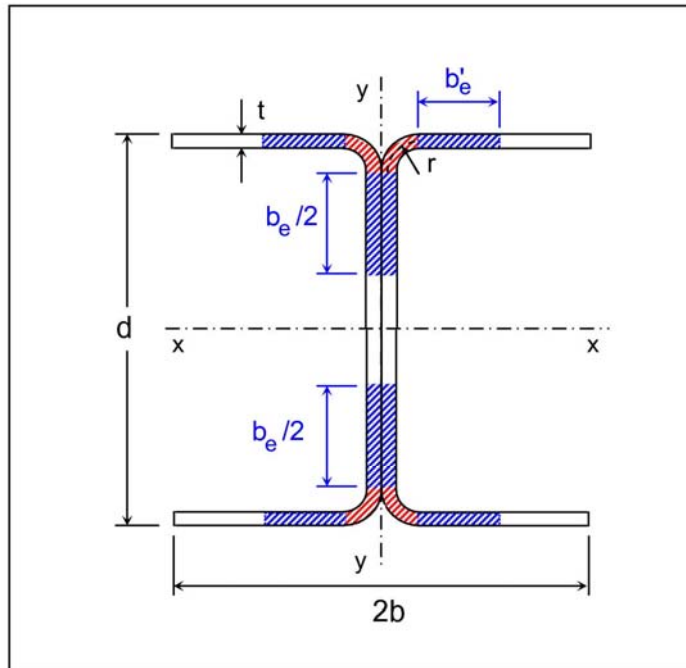
$\alpha =$	0.49	$\bar{\lambda}_o =$	0.40
$\beta_A =$	0.668	$\bar{\lambda} =$	0.377
$\phi =$	0.566	$\chi =$	1.000

$$N_{b,y,Rd} = 139.35 \text{ kN}$$

8. Member Capacity

$N_{b,Rd} =$	139.35 kN
--------------	-----------

E.9. AS/NZS 4673: Back-to-back Channels



Specimen

I404_1.20_1000

1. Geometry

t	=	1.20	mm
d	=	125.24	mm
b	=	48.29	mm
r	=	3.11	mm
L_x	=	1135	mm
k_x	=	1.0	
L_y	=	1135	mm
k_y	=	1.0	

2. Material Properties

Stainless Steel :	404	ϕ =	1.00	(Clause 3.4.1)
f_y =	290 MPa	(0.2% proof stress in compression)		
n =	9.5	(Ramberg-Osgood parameter)		
E_o =	195 GPa	G_o =	75 GPa	

3. Maximum b/t Ratios (Clause 2.1.3.1)

Web :	d_{flat}/t	=	98.2	\leq	400	Ok.
Flange :	b_{flat}/t	=	37.2	\leq	50	Ok.
	b/d_{flat}	=	0.41	\leq	0.8	Ok.

4. Gross Section Properties

A	=	520.20	mm ²	A_c	=	23.45	mm ²	(Corner Area)
A_c/A	=	4.51	%					
I_x	=	1234699	mm ⁴	r_x	=	48.72	mm	
I_y	=	179942	mm ⁴	r_y	=	18.60	mm	

Gross Section Properties (Continued)

$$S_x = 19717 \text{ mm}^3$$

$$S_y = 3726 \text{ mm}^3$$

$$J = 249.7 \text{ mm}^4$$

$$C_w = 6.92\text{E}+08 \text{ mm}^6$$

5. Overall Buckling Stress
Flexural buckling about y-y axis

(Clause 3.4.2)

$$f_{oc} = \frac{\pi^2 E_t}{(k_y L_y / r_y)^2} \quad \text{with}$$

$$E_t = \frac{f_y E_o}{f_y + 0.002 n E_o \left[\frac{f}{f_y} \right]^{n-1}}$$

$$f_{oc} = 222.16 \text{ MPa}$$

Alternatively (Direct Approach):

$$\alpha = 0.73$$

$$\phi_c = 1.00$$

$$\lambda_o = 0.568$$

$$\beta = 0.147$$

$$\lambda_1 = 0.25$$

$$\lambda = 0.75$$

$$\eta = 0.244$$

$$\phi = 0.90$$

$$f_{oc} = 206.15 \text{ MPa}$$

6. Tangent Approach: Effective width calculations

(Clause 2.2.1.2)

$$f^* = \min(f_{oc}, f_y) = 222.16 \text{ MPa}$$

6.1. Web $k = 4.0$

$$d_{flat} = 117.8 \text{ mm}$$

$$\lambda = 1.743$$

$$\rho = 0.501$$

$$b_e = 59.06 \text{ mm}$$

6.2. Flange $k = 0.5$

$$b_{flat} = 44.6 \text{ mm}$$

$$\lambda' = 1.866$$

$$\rho' = 0.473$$

$$b_e' = 21.08 \text{ mm}$$

6.3. A_e

$$A_e = 266.37 \text{ mm}^2$$

6.4. Member Capacity

$$\phi.N_c = 59.18 \text{ kN}$$

(Tangent Approach)

7. Direct Approach: Effective width calculations

$$f^* = \min(f_{oc}, f_y) = 206.15 \text{ MPa}$$

7.1. Web

$$k = 4.0$$

$$d_{flat} = 117.8 \text{ mm}$$

$$\lambda = 1.679$$

$$\rho = 0.518$$

$$b_e = 60.97 \text{ mm}$$

7.2. Flange

$$k = 0.5$$

$$b_{flat} = 44.6 \text{ mm}$$

$$\lambda' = 1.797$$

$$\rho' = 0.488$$

$$b_{e'} = 21.77 \text{ mm}$$

7.3. A_e

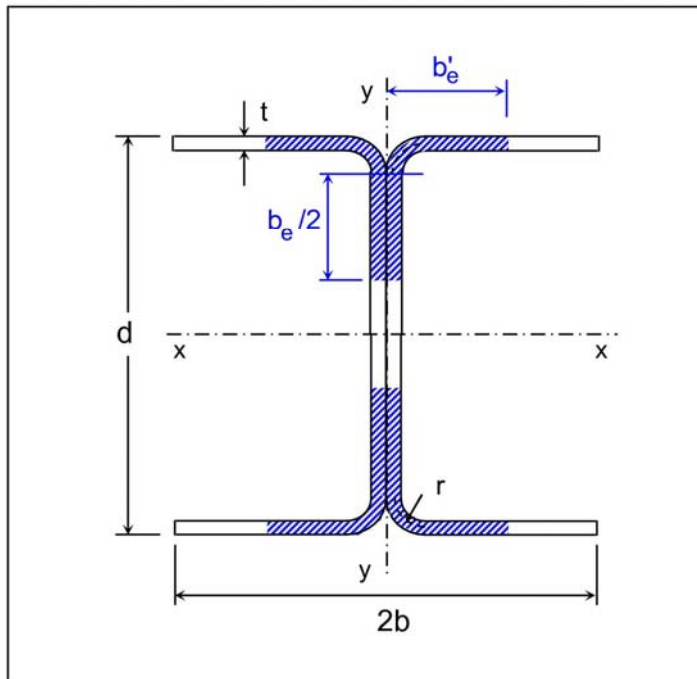
$$A_e = 274.28 \text{ mm}^2$$

7.4. Member Capacity

$$\phi.N_c = 56.54 \text{ kN}$$

(Direct Approach)

E.10. EC3 (prEN 1993-1-4): Back-to-back Channels



Specimen

I404_1000_1

1. Geometry

t	=	1.2	mm
d	=	125.24	mm
b	=	48.29	mm
r	=	3.11	mm
L_x	=	1135	mm
k_x	=	1.0	
L_y	=	1135	mm
k_y	=	1.0	

2. Material Properties

Stainless Steel : 404

 $f_{yb} = 290$ MPa (0.2% proof stress)

 $E_o = 195$ GPa

 $G_o = 75$ GPa

 $\gamma_{Mo} = 1.00$
 $\gamma_{M1} = 1.00$

3. Maximum Width-to-Thickness Ratios *prEN 1993-1-4 (2004) 5.2.1*

 Web : $d/t = 104.4 \leq 400$ Ok.

 Flange : $b/t = 40.2 \leq 50$ Ok.

Other Limitations *prEN 1993-1-3 (2002)*

 $0.45 \text{ mm} \leq t \leq 15 \text{ mm}$ Ok.
 $r_i \leq 0.04 t E / f_y = 32.28$ Ok.

4. Classification *prEN 1993-1-4 : 2004 5.2.2*

 $\varepsilon = 0.867$

Web :	$d_{\text{flat}}/t =$	98.2	Class	4
Flange :	$b/t =$	40.2	Class	4
Overall Class :			Class	4

5. Gross Section Properties

$A =$	520.20 mm ²	$A_c =$	23.45 mm ²	(Corner Area)
$A_c/A =$	4.51 %			
$I_x =$	1234699 mm ⁴	$r_x =$	48.72 mm	
$I_y =$	179942 mm ⁴	$r_y =$	18.60 mm	
$S_x =$	19717 mm ³	$S_y =$	3726 mm ³	

6. Effective width calculations

6.1. Web $k = 4.00$

$\bar{b} =$	117.82 mm	$\bar{\lambda}_p =$	1.992
$\rho =$	0.356	$b_e =$	41.96 mm

6.2. Flange $k = 0.43$

$\bar{b}' =$	48.29 mm	$\bar{\lambda}'_p =$	2.490
$\rho' =$	0.364	$b_{e'} =$	17.60 mm

6.3. A_e

$$A_e = 190.80 \text{ mm}^2$$

7. Flexural Buckling *prEN 1993-1-4 (2004) 5.4.2*

$\alpha =$	0.49	$\bar{\lambda}_o =$	0.40
$\beta_A =$	0.367	$\bar{\lambda} =$	0.454
$\phi =$	0.616	$\chi =$	0.968
$N_{b,y,Rd} =$	53.57 kN		

8. Member Capacity

$$N_{b,Rd} = 53.57 \text{ kN}$$